DEVELOPMENT OF NANO-FERRITE COMPOSITES FOR TUNABLE MICROWAVE ABSORBER APPLICATION

Thesis Submitted for the Award of the Degree of

DOCTOR OF PHILOSOPHY

in

Electronics and Communication Engineering

By

Ankit Jain

Registration Number: 42000313

Supervised by

Dr. Charanjit Singh (21882)

Electronics and Communication (Professor)

School of Electronics and Electrical Engineering

Lovely Professional University, Punjab

Co-Supervised by

Dr. Sachin Kumar Godara

Apparel and Textile Technology

(Assistant Professor)

Guru Nanak Dev University, Punjab

LOVELY PROFESSIONAL UNIVERSITY, PUNJAB

2024

DECLARATION

I, hereby declared that the presented work in the thesis entitled "**Development of Nano-Ferrite Composites for Tunable Microwave Absorber Application**" in fulfilment of degree of **Doctor of Philosophy (Ph. D.)** is outcome of research work carried out by me under the supervision of **Dr. Charanjit Singh** working as **Professor**, in the **Electronics and Communication Engineering, School of Electronics and Electrical Engineering** of **Lovely Professional University, Punjab**, **India**. In keeping with general practice of reporting scientific observations, due acknowledgements have been made whenever work described here has been based on findings of other investigator. This work has not been submitted in part or full to any other University or Institute for the award of any degree.

(Signature of Scholar)

Name of the scholar: Ankit Jain
Registration No.: 42000313
Department/school: Electronics and Communication Engineering, School of Electronics and Electrical Engineering
Lovely Professional University,
Punjab, India

CERTIFICATE

This is to certify that the work reported in the Ph. D. thesis entitled "**Development of Nano-Ferrite Composites for Tunable Microwave Absorber Application**" submitted in fulfillment of the requirement for the award of degree of **Doctor of Philosophy (Ph.D.)** in the **Electronics and Communication Engineering, School of Electronics and Electrical Engineering,** is a research work carried out by **Ankit Jain, 42000313**, is bonafide record of his/her original work carried out under my supervision and that no part of thesis has been submitted for any other degree, diploma or equivalent course.

(Signature of Supervisor)

Name of supervisor: Dr. Charanjit Singh

Designation: Professor

Department/school: Electronics and Communication Engineering

School of Electronics and Electrical Engineering

University: Lovely Professional University, Punjab

(Signature of Co-Supervisor)

Name of Co-Supervisor: Dr. Sachin Kumar Godara

Designation: Assistant Professor

Department/school: Apparel and Textile Technology

University: Guru Nanak Dev University, Punjab

ABSTRACT

The rapid development of wireless communication technology and nano-electronic devices has contributed to electromagnetic (EM) pollution, affecting human health, national security, and electronic systems via the generation of undesirable high-frequency electromagnetic waves. The increasing problem necessitates the need for efficient electromagnetic suppressors, particularly microwave absorbers, intended to absorb or reduce harmful emissions. Effective microwave absorbers need attributes like impedance matching, extensive absorption bandwidth, affordability, lightweight design, and resilient dielectric/magnetic loss mechanisms. This work utilizes M-type hexaferrite, recognized for its advantageous magnetic characteristics, as the foundational material. To overcome the limits of pure M-type hexaferrite, doped and mixed substances were developed to improve these qualities. This research examines divalent and trivalent substitutions in M-type hexaferrite $BaCo_xAl_xFe_{12-2x}O_{19}$ ($0.0 \leq x \leq 1.0$), $BaCo_xCe_xFe_{12-2x}O_{19}$ ($0.0 \leq x \leq 1.0$), $BaCo_xCd_xFe_{12-2x}O_{19}$ ($0.0 \leq x \leq 1.0$) and $BaCo_xCr_xFe_{12-2x}O_{19}$ ($0.0 \leq x \leq 1.0$), utilizing a sol-gel auto-combustion method. Composite materials were synthesized by amalgamating these substituted hexaferrites with polyaniline (PANI) in an 80:20 ratio, yielding hybrid structures intended to improve microwave absorption [$BaCo_xAl_xFe_{12-2x}O_{19}$ (80%) + PANI(20%)], [$BaCo_xCe_xFe_{12-2x}O_{19}$ (80%) + PANI(20%)], [$BaCo_xCd_xFe_{12-2x}O_{19}$ (80%) + PANI(20%)], [$BaCo_xCe_xFe_{12-2x}O_{19}$ (80%) + PANI(20%)] and [$BaCo_xCr_xFe_{12-2x}O_{19}$ (80%) + PANI(20%)].

A careful characterization was conducted utilizing X-ray Diffraction (XRD) for phase identification, Field Emission Scanning Electron Microscopy (FESEM) for morphological assessment, Energy Dispersive X-ray Analysis (EDX) for compositional evaluation, and Vector Network Analyzer (VNA) for electromagnetic property analysis. Furthermore, impedance, dielectric, and magnetic characteristics were examined using impedance analyzers and LCR meters.

In this study synthesized Co-Al substituted $BaCo_xAl_xFe_{12-2x}O_{19}$ hexaferrites via sol-gel combustion to investigate their structural, dielectric, magnetic, and electromagnetic properties. X-ray diffraction confirmed the formation of a hexagonal M-type phase with systematic reductions in lattice parameters and crystallite sizes

across doping levels. FESEM analysis revealed a transition from large fused grains in undoped samples to smaller, needle-like grains in doped samples, enhancing interfacial resistance crucial for microwave absorption. Dielectric measurements showed lower permittivity and enhanced polarization in Co-Al doped samples, supporting improved high-frequency performance. Magnetic properties showed decreased saturation magnetization and coercivity with doping, aligning with reduced magnetic hardness favourable for flexible magnetic applications. The W5 sample exhibited a high reflection loss of -46.55 dB at 10.05 GHz due to optimal impedance matching, positioning Co-Al substituted $BaCo_xAl_xFe_{12-2x}O_{19}$ as a promising material for electromagnetic interference (EMI) shielding and microwave absorption.

The Co-Ce substituted $BaCo_xCe_xFe_{12-2x}O_{19}$ hexaferrites were developed to explore modifications in their structural, dielectric, magnetic, and microwave absorption properties. XRD confirmed the hexagonal M-type phase, with lattice parameters decreasing slightly with Ce substitution. FESEM analysis displayed significant grain agglomeration and voids, contributing to enhanced grain boundary effects, critical for dielectric and impedance matching. Dielectric constants and losses decreased with frequency, while impedance spectroscopy and electric modulus analysis indicated substantial grain boundary polarization, beneficial for EMI shielding. A peak reflection loss of -49.46 dB was achieved by X3 at 12.15 GHz, highlighting its excellent impedance matching properties. These findings support the suitability of Co-Ce substituted hexaferrites in high-frequency applications for EMI shielding and microwave absorption.

In this study synthesized Co-Cd substituted $BaCo_xCd_xFe_{12-2x}O_{19}$ hexaferrites, examining their structural, dielectric, magnetic, and electromagnetic absorption properties. XRD confirmed structural integrity with minor lattice contraction due to Cd doping. FESEM images displayed varied grain sizes, with optimal morphology in Y4 enhancing electromagnetic absorption. Dielectric properties exhibited frequency-dependent relaxation, with low dielectric loss values in high-frequency regions, ideal for EMI applications. The Y4 sample showed an optimal reflection loss of -40.49 dB at 10.39 GHz due to effective impedance matching, marking it as a strong candidate for EMI shielding. This study demonstrates the potential of Co-Cd substituted

hexaferrites in applications requiring tuned magnetic and dielectric properties with efficient microwave absorption.

The Co-Cr substituted $BaCo_xCr_xFe_{12-2x}O_{19}$ series was synthesized to analyze the impact of Cr doping on structural, dielectric, magnetic, and microwave absorption properties. XRD results confirmed the hexagonal M-type structure, with slight lattice contraction observed across samples. FESEM revealed increased grain boundary density with Cr substitution, which improved dielectric relaxation and enhanced magnetic properties. AC conductivity and electric modulus measurements indicated high grain boundary polarization, conducive to EMI shielding. Samples Z2 and Z4 exhibited maximum reflection loss values of -40.8 dB and -43.4 dB, respectively, with optimal impedance matching, making them effective for microwave absorption. The Co-Cr substituted $BaCo_xCr_xFe_{12-2x}O_{19}$ materials demonstrate versatile dielectric and magnetic properties, positioning them as potential materials for high-frequency EMI shielding applications.

This study explored the structural, dielectric, magnetic, and microwave absorption properties of polyaniline (PANI) composites with Co-Al substituted $BaCo_xAl_xFe_{12-2x}O_{19}$ hexaferrites. Structural analysis via XRD confirmed a stable hexagonal M-type phase across all composites. FESEM imaging revealed morphology changes, with smaller, densely packed grains enhancing charge mobility and dielectric relaxation. Dielectric studies showed a reduction in permittivity and dielectric loss with increasing frequency, while impedance measurements indicated efficient impedance matching for microwave absorption. Magnetic properties displayed a controlled reduction in magnetization and coercivity due to Co-Al substitution, ideal for flexible magnetic applications. The WP2 composite achieved a reflection loss of -41.38 dB at 9.71 GHz, demonstrating strong EMI shielding with effective impedance matching. The study concludes that Co-Al/PANI composites offer promising applications in microwave absorption and EMI shielding.

The Co-Ce substituted $BaCo_xCe_xFe_{12-2x}O_{19}$/PANI composites were synthesized to investigate the impact of PANI on the structural, dielectric, magnetic, and microwave absorption properties. XRD confirmed a hexagonal M-type structure across doping levels, while FESEM revealed that grain coalescence and boundary density increased with Co-Ce and PANI inclusion. Dielectric analysis indicated stable responses at

higher frequencies with reduced dielectric loss, while impedance spectroscopy suggested strong charge mobility due to PANI's conductive nature. Magnetic characterizations showed a decline in saturation magnetization and coercivity, supporting applications in tunable magnetic devices. The XP1 composite achieved a high reflection loss of -36.34 dB at 10.05 GHz with near-ideal impedance matching, highlighting its suitability for microwave absorption and EMI shielding applications.

The Co-Cd substituted $BaCo_xCd_xFe_{12-2x}O_{19}$/PANI composites were analyzed for their structural, dielectric, magnetic, and electromagnetic absorption properties. XRD results showed a stable M-type hexagonal structure with Co-Cd doping, while FESEM imaging revealed increased porosity and varied grain structures that improved dielectric performance and microwave absorption. Dielectric studies showed high permittivity at lower frequencies, with a rapid decrease indicating effective dielectric relaxation. Magnetic measurements revealed optimal coercivity and anisotropy for EMI applications, with PANI enhancing conductivity and impedance matching. The YP2 composite achieved a peak reflection loss of -55.54 dB at 10.56 GHz, marking it as a superior candidate for EMI shielding and high-frequency absorption.

The Co-Cr substituted $BaCo_xCr_xFe_{12-2x}O_{19}$/PANI composites were synthesized to assess the effect of PANI on structural, dielectric, magnetic, and microwave absorption properties. XRD confirmed the hexagonal M-type structure with minimal structural variation, while FESEM images displayed significant grain boundary formation with increased porosity due to PANI integration. Dielectric properties exhibited frequency-dependent behaviour with improved impedance matching at high frequencies. Magnetic characterization showed reduced saturation magnetization and coercivity with Co-Cr doping, favouring applications in flexible magnetic devices. The ZP2 composite achieved a high reflection loss of -41.09 dB at 8.37 GHz, with impedance values near free-space impedance, supporting its effectiveness in EMI shielding. These results highlight Co-Cr/PANI composites as strong candidates for microwave absorption and EMI shielding applications requiring tunable dielectric and magnetic properties across a wide frequency range.

ACKNOWLEDGMENT

First of all, I show my gratitude and thanks to GOD for giving me the strength, zeal, and courage to complete my research work. It is he who always takes me out of difficult situations and shows me the correct path to face and overcome the challenges during this research journey.

I would like to present my gratitude to my supervisor **Dr. Charanjit Singh** (Professor), and Co-Supervisor **Dr. Sachin Kumar Godara** (Assistant Professor) for their guidance, support, and motivation throughout the research work. They always stood as a guiding torch whenever I was in need during my research.

I am thankful to all the faculty members of the Electronics and Communication Engineering Department for their help and support. I sincerely thank Dr. R.B Jotania (Department of Physics, Gujarat University, Ahmedabad, India) and Dr. Suwarna Datar (Department of Applied Physics, Defence Institute of Advanced Technology, Pune, India) for providing various supports in characterization.

Last but not least, a special thanks to my lovely parents (Mr. Vijay K Jain and Mrs. Sarita Jain), my wife (Mrs. Ankita Jain), my daughters (Ashvi and Anvi), my brothers (Ashish Jain and Anshul Jain) and all my family members for their consistent support, motivation, and prayers throughout my research.

Ankit Jain
Registration No: 42000313
Date: 31-10-2024

Table of Contents

DECLARATION ii

CERTIFICATE iii

ABSTRACT iv

ACKNOWLEDGMENT viii

CHAPTER–1 22

INTRODUCTION 22

1.1 Ferrites 23

1.1.1. Historical Development of Ferrites 23

1.2 Classification of Ferrites 24

1.2.1 Based on Magnetic Behaviour 24

1.2.2 Based on crystal structure 25

1.3 Hexagonal ferrites 26

1.3.1 M-type hexagonal ferrites 27

1.3.2 Crystal structure of M-type hexagonal ferrites 28

1.4 Microwave absorbers 29

1.4.1 Types of Microwave Absorbers 29

1.5 Application of ferrites 30

1.6 Synthesis of M-type Hexaferrite 32

1.7 Polyaniline 34

1.7.1 The Role of Polyaniline (PANI) in Microwave Absorption 34

1.8 Chapter Outline 34

CHAPTER-2 37

REVIEW OF LITERATURE, RESEARCH GAP, AND OBJECTIVES 37

2.1. Review of literature 37

2.2. Research Gaps 75

2.3. Objective of this study 76

CHAPTER-3 78

RESEARCH METHODOLOGY AND CHARACTERIZATION 78

3.1. Method of Synthesis 78

3.1.1. Sol-gel Auto Combustion Methodology 78

3.1.2. Polyaniline (PANI) synthesis method 81

3.1.3. Pellet formation and sintering 81

3.2. Synthesis of Co^{2+} and Al^{3+} substituted BaM hexaferrite with composition $BaCo_xAl_xFe_{12-2x}O_{19}$ 82

3.3. Synthesis of Co^{2+} and Ce^{3+} substituted BaM hexaferrite with composition $BaCo_xCe_xFe_{12-2x}O_{19}$ 83

3.4. Synthesis of Co^{2+} and Cd^{2+} substituted BaM hexaferrite with composition $BaCo_xCd_xFe_{12-2x}O_{19}$ 84

3.5. Synthesis of Co^{2+} and Cr^{3+} substituted BaM hexaferrite with composition $BaCo_xCr_xFe_{12-2x}O_{19}$ 86

3.6. Structural Characterization 87

3.6.1. X-ray diffraction analysis 87

3.7. Field Emission Scanning Electron Microscopy 89

3.8. Vibrating Sample Magnetometer (VSM) 90

3.9. Impedance Analyzer 91

3.10. Vector Network Analyzer 92

3.11. Application / Design-specific parameters 92

3.11.2. Complex permeability 93

3.11.3. Loss tangent 93

CHAPTER-4 102

RESULTS AND DISCUSSION 102

4.1. Co^{2+}- Al^{3+} substituted $BaCo_xAl_xFe_{12-2x}O_{19}$ hexaferrite. 102

4.1.1 Structural Analysis 102

4.1.1.1 X-ray Analysis 102

4.1.2 Field Emission Scanning Electron Microscopy 105

4.1.3 Electrical Characterization 106

4.1.3.1 Dielectric constant 106

4.1.3.2 Analysis of Dielectric Loss and Loss Tangent in $BaCo_xAl_xFe_{12-2x}O_{19}$ Ferrites 107

4.1.3.3 AC Conductivity 111

4.1.3.4 Electric modulus analysis 113

4.1.3.5 Impedance spectroscopy 116

4.1.3.6 Computational Impedance Simulation and Validation 119

4.1.3.7 Investigating the Relationship between EIS Data and Microstructure 120

4.1.3.8 Impact of Microstructure on Dielectric Loss 125

4.1.3.9 Impact of Microstructure on AC Conductivity 126

4.1.3.10 Investigating the Influence of Simulated Grain Boundaries on Electric Modulus Responses 126

4.1.3.11 Incorporating Simulated Grain Boundaries into Impedance Spectroscopy Analysis 127

4.1.4 Magnetic Analysis 127

4.1.5 Electromagnetic Characteristics 132

4.1.5.1 Complex permeability and complex permittivity 132

4.1.5.2 Microwave absorption in $BaCo_xAl_xFe_{12-2x}O_{19}$ 134

4.1.5.3 Quarter Wavelength Mechanism 134

4.1.5.4 Impedance matching mechanism 153

4.1.5.5 Eddy Current Loss 158

4.1.5.6 Bandwidth to Thickness Ratio 159

4.1.5.7 S – Parameter 160

4.2 Co^{2+}- Ce^{3+} substituted $BaCo_xCe_xFe_{12-2x}O_{19}$ hexaferrite. 162

4.2.1. X-ray diffraction analysis 162

4.2.2 Field Formulation and Morphological Analysis of Nanoferrite Composites via FESEM Characterization 165

4.2.3 Electrical Characterization 166

4.2.3.1 Dielectric constant 166

4.2.3.2 Dielectric Loss and Tangent Loss factor 166

4.2.3.3 AC Conductivity 169

4.2.3.4 Electric modulus analysis 171

4.2.3.5 Impedance spectroscopy 174

4.2.3.6 Software-based Impedance Simulation and Validation 177

4.2.4 Magnetic Analysis 179

4.2.5 Electromagnetic Characteristics 183

4.2.5.1 Complex permeability and complex permittivity 183

4.2.5.2 Microwave absorption in $BaCo_xCe_xFe_{12-2x}O_{19}$ 185

4.2.5.3 Quarter Wavelength Mechanism 185

4.2.5.4 Impedance matching mechanism 200

4.2.5.5 Eddy Current Loss 204

4.2.5.6 Bandwidth to Thickness Ratio 204

4.2.5.7 S – Parameter 205

4.3 Co^{2+}- Cd^{2+} substituted $BaCo_xCd_xFe_{12-2x}O_{19}$ hexaferrite 207

4.3.1 X-ray diffraction analysis 207

4.3.2 Formulation and Morphological Analysis of Nanoferrite Composites via FESEM Characterization 210

4.3.3 Electrical Characterization 211

4.3.3.1 Dielectric constant 211

4.3.3.2 Dielectric Loss and Tangent Loss factor 212

4.3.3.3 AC Conductivity 214

4.3.3.4 Electric modulus analysis 217

4.3.3.5 Impedance spectroscopy 221

4.3.3.6 Software-based Impedance Simulation and Validation 223

4.3.3.7 Correlation between EIS parameters and Morphology 224
4.3.3.8 Simulated Grain/Grain boundary parameters and AC Conductivity 229
4.3.3.9 Simulated Grain/Grain boundary parameters and Electric Modulus 230
4.3.3.10 Simulated Grain/Grain boundary parameters and Impedance spectroscopy 231
4.3.4 Magnetic Analysis 232
4.3.5 Electromagnetic Characteristics 237
4.3.5.1 Complex permeability and complex permittivity 237
4.3.5.2 Microwave absorption and Quarter Wavelength Mechanism in $BaCo_xCd_xFe_{12-2x}O_{19}$ 238
4.3.5.3 Impedance matching mechanism 245
4.3.5.4 Eddy Current Loss 249
4.3.5.5 Bandwidth to Thickness Ratio 250
4.3.5.6 S – Parameter 251
4.4 Co^{2+}- Cr^{3+} substituted $BaCo_xCr_xFe_{12-2x}O_{19}$ hexaferrite. 254
4.4.1 X-ray diffraction analysis 254
4.4.2 Formulation and Morphological Analysis of Nanoferrite Composites via FESEM Characterization 256
4.4.3 Electrical Characterization 258
4.4.3.1 Dielectric constant 258
4.4.3.2 Dielectric Loss and Tangent Loss factor 259
4.4.3.3 AC Conductivity 264
4.4.3.4 Electric modulus analysis 265
4.4.3.5 Impedance spectroscopy 269
5.3.1.1 Software-based Impedance Simulation and Validation 272
5.3.1.2 Correlation between EIS parameters and Morphology 275
5.3.2 Magnetic Analysis 280
5.3.3 Electromagnetic Characteristics 285
5.3.3.1 Complex permeability and complex permittivity 285
5.3.3.2 Microwave absorption in $BaCo_xCr_xFe_{12-2x}O_{19}$ 287
5.3.3.3 Quarter Wavelength Mechanism 287
5.3.3.4 Impedance matching mechanism 300

5.3.3.5 Eddy Current Loss.....305
4.4.5.6 Bandwidth to Thickness Ratio.....305
4.4.5.7 S – Parameter.....306
4.5 Co^{2+}- Al^{3+} substituted $BaCo_xAl_xFe_{12-2x}O_{19}$ / PANI Composite.....307
4.5.1 Field Emission Scanning Electron Microscopy.....308
4.5.2 Electrical Characterization.....308
4.5.2.1 Dielectric constant.....308
4.5.2.2 Electric modulus analysis.....312
4.5.2.3 Impedance spectroscopy.....315
4.5.2.4 Computational Impedance Simulation and Validation.....317
4.5.2.5 Investigating the Relationship between EIS Data and Microstructure 318
4.5.2.6 Investigating the Relationship between EIS Data and Electric Parameters.....319
4.5.3 Magnetic Analysis.....320
4.5.4 Electromagnetic Characteristics.....322
4.5.4.1 Complex permeability and complex permittivity.....322
4.5.4.2 Microwave absorption in $BaCo_xAl_xFe_{12-2x}O_{19}$ / PANI.....323
4.5.4.3 Quarter Wavelength Mechanism.....323
4.5.4.4 Impedance matching mechanism.....333
4.5.4.5 Eddy Current Loss.....336
4.5.4.6 S – Parameter.....338
4.6 Co^{2+}- Ce^{3+} substituted $BaCo_xCe_xFe_{12-2x}O_{19}$ / PANI Composite.....339
4.6.1 Field Emission Scanning Electron Microscopy.....339
4.6.2 Electrical Characterization.....339
4.6.2.1 Dielectric constant.....339
4.6.2.2 Electric modulus analysis.....343
4.6.2.3 Impedance spectroscopy.....346
4.6.2.4 Computational Impedance Simulation and Validation.....348
4.6.2.5 Investigating the Relationship between EIS Data and Microstructure 349

4.6.2.6 Investigating the Relationship between EIS Data and Electric Parameters....350
4.6.3 Magnetic Analysis....351
4.6.4 Electromagnetic Characteristics....354
4.6.4.1 Complex permeability and complex permittivity....354
4.6.4.2 Microwave absorption in $BaCo_xCe_xFe_{12-2x}O_{19}$ / PANI....356
4.6.4.3 Quarter Wavelength Mechanism....358
4.6.4.4 Impedance matching mechanism....363
4.6.4.5 Eddy Current Loss....366
4.6.4.6 Bandwidth to Thickness Ratio....366
4.6.4.6 S – Parameter....367
4.7 Co^{2+}- Cd^{2+} substituted $BaCo_xCd_xFe_{12-2x}O_{19}$ hexaferrite / PANI....368
4.7.1 Field Emission Scanning Electron Microscopy....368
4.7.2 Electrical Characterization....369
4.7.2.1 Dielectric constant....369
4.7.2.2 Electric modulus analysis....372
4.7.2.3 Impedance spectroscopy....375
4.7.2.4 Computational Impedance Simulation and Validation....377
4.7.2.5 Investigating the Relationship between EIS Data and Microstructure 378
4.7.2.6 Investigating the Relationship between EIS Data and Electric Parameters....380
4.7.3 Magnetic Analysis....382
4.7.4 Electromagnetic Characteristics....384
4.7.4.1 Complex permeability and complex permittivity....384
4.7.4.2 Microwave absorption and Quarter Wavelength Mechanism in $BaCo_xCd_xFe_{12-2x}O_{19}$ / PANI....386
4.7.4.3 Impedance matching mechanism....394
4.7.4.4 Eddy Current Loss....397
4.7.4.5 Bandwidth to Thickness Ratio....398
4.7.4.6 S – Parameter....398

4.8 Co^{2+}- Cr^{3+} substituted $BaCo_xCr_xFe_{12-2x}O_{19}$ hexaferrite / PANI.....399
4.8.1 Field Emission Scanning Electron Microscopy.....400
4.8.2 Electrical Characterization.....400
4.8.2.1 Dielectric constant.....400
4.8.2.2 Electric modulus analysis.....404
4.8.2.3 Impedance spectroscopy.....407
4.8.2.4 Investigating the Relationship between EIS Data and Microstructure 411
4.8.3 Magnetic Analysis.....412
4.8.4 Electromagnetic Characteristics.....416
4.8.4.1 Complex permeability and complex permittivity.....416
4.8.4.2 Microwave absorption in $BaCo_xCr_xFe_{12-2x}O_{19}$ / PANI.....418
4.8.4.3 Quarter Wavelength Mechanism.....418
4.8.4.4 Impedance matching mechanism.....427
4.8.4.5 Eddy Current Loss.....430
4.8.4.6 Bandwidth to Thickness Ratio.....431
CHAPTER 5 434
SUMMARY AND CONCLUSION 434
5.1 Future Scope.....446
REFERENCES 447

List of Tables

Table 1.1. Characteristics of Soft and Hard Ferrites.....24

Table 1.2. Comparative Properties of Different Types of Ferrites 25

Table 1.3. Comparison of Different Types of Hexaferrite.....26

Table 1.4. Overview of Hexaferrite Types and Structures 27

Table 1.5. Site occupancy of Fe^{3+} ion at different crystallographic sites. 29

Table 1.6. Comparison of Microwave Absorbers.....30

Table 1.7. Comparison of Various Synthesis Methods of M-type hexaferrite. 33

Table 3.1. Detailed description of chemicals used in quantity (g) and performed characterization of $BaCo_xAl_xFe_{12-2x}O_{19}$ 83

Table 3.2. Detailed description of chemicals used in quantity (g) and performed characterization of $BaCo_xCe_xFe_{12-2x}O_{19}$.....83

Table 3.3. Detailed description of chemicals used in quantity (g) and performed characterization of $BaCo_xCd_xFe_{12-2x}O_{19}$ 85

Table 3.4 Detailed description of chemicals used in quantity (g) and performed characterization of $BaCo_xCr_xFe_{12-2x}O_{19}$ 86

Table 3.5 Application-Specific Parameters for Electromagnetic Ferrite Materials.....98

Table 4.1. Presents the assignment of sample names corresponding to various substitution levels in $BaCo_xAl_xFe_{12-2x}O_{19}$ hexaferrite.....102

Table 4.2. Effect of Co-Al Doping on Structural Parameters of $BaCo_xAl_xFe_{12-2x}O_{19}$ Ferrites (W0 (x = 0.0), W1 (x = 0.2), W2 (x = 0.4), W3 (x = 0.6), W4 (x = 0.8), W5 (x = 1.0)).....103

Table 4.3. Elemental Composition of $BaCo_xAl_xFe_{12-2x}O_{19}$ Determined by EDX Analysis (W0 (x = 0.0), W1 (x = 0.2), W2 (x = 0.4), W3 (x = 0.6), W4 (x = 0.8), W5 (x = 1.0)). 104

Table 4.4. Extracted Grain and Grain Boundary Parameters from EIS Modelling...120

Table 4.5. Magnetic parameters determined from M-H curves.....132

Table 4.6. REL with matching thickness/frequency, BW, and PBW for $BaCo_xAl_xFe_{12-2x}O_{19}$ (W1 to W5).....147

Table 4.7. Z_{in}, Z_{real}, and Z_{imag} values corresponding to REL for $BaCo_xAl_xFe_{12-2x}O_{19}$. 158

Table 4.8. Presents the assignment of sample names corresponding to various substitution levels in $BaCo_xCe_xFe_{12-2x}O_{19}$ hexaferrite. 162

Table 4.9. Effect of Co-Ce Doping on Lattice Parameters and Unit Cell Volume of $BaCo_xCe_xFe_{12-2x}O_{19}$ (X0 to X5) 163

Table 4.10. Elemental Composition (Weight % and Atomic %) of $BaCo_xCe_xFe_{12-2x}O_{19}$ (x = X0 to X5, 0.0-1.0) determined by EDX Analysis 165

Table 4.11 Extracted Grain and Grain Boundary Parameters (EIS) 177

Table 4.12. Magnetic parameters determined from M-H curves 181

Table 4.13 REL with matching thickness/frequency, BW, and PBW for $BaCo_xCe_xFe_{12-2x}O_{19}$ (X1 to X5). 195

Table 4.14 Z_{in}, Z_{real}, and Z_{imag} values corresponding to REL_{max} for $BaCo_xCe_xFe_{12-2x}O_{19}$. 202

Table 4.15. Presents the assignment of sample names corresponding to various substitution levels in $BaCo_xCd_xFe_{12-2x}O_{19}$ hexaferrite. 207

Table 4.16 Co-Cd content, Lattice constants, ratio c/a and unit cell volume of ferrite sample $BaCo_xCd_xFe_{12-2x}O_{19}$ (Y0 to Y5, x =0.0, 0.2, 0.4, 0.6, 0.8, and 1.0) 208

Table 4.17 Weight % and Atomic % of all the elements in the final compositions $BaCo_xCd_xFe_{12-2x}O_{19}$ (Y0 to Y5, x =0.0, 0.2, 0.4, 0.6, 0.8, and 1.0) as evaluated from EDX analysis. 209

Table 4.18 Grain and Grain boundary parameters derived from EIS software 223

Table 4.19. Magnetic parameters determined from M-H curves 235

Table 4.20 REL with matching thickness/frequency, BW, and PBW for $BaCo_xCd_xFe_{12-2x}O_{19}$ (Y1 to Y5). 243

Table 4.21 Z_{in}, Z_{real}, and Z_{imag} values corresponding to REL_{max} for $BaCo_xCd_xFe_{12-2x}O_{19}$. 249

Table 4.22. Presents the assignment of sample names corresponding to various substitution levels in $BaCo_xCr_xFe_{12-2x}O_{19}$ hexaferrite 254

Table 4.23. Influence of Co-Cr Doping on the Lattice Parameters (a, c), c/a Ratio, and Unit Cell Volume of $BaCo_xCr_xFe_{12-2x}O_{19}$ Hexaferrites 255

Table 4.24 Qualitative Assessment of Elemental Presence in $BaCo_xCr_xFe_{12-2x}O_{19}$ using EDX Analysis 256

Table 4.25 Extracted Grain and Grain Boundary Parameters from Electrical Impedance Spectroscopy 275

Table 4.26. Magnetic parameters determined from M-H curves 281

Table 4.27 REL with matching thickness/frequency, BW, and PBW for $BaCo_xCr_xFe_{12-2x}O_{19}$ (Z1 to Z4). 297

Table 4.28 Z_{in}, Z_{real}, and Z_{imag} values corresponding to REL_{max} for $BaCo_xCr_xFe_{12-2x}O_{19}$. 305

Table 4.29. Presents the assignment of sample names corresponding to various substitution levels in $BaCo_xAl_xFe_{12-2x}O_{19}$ hexaferrite.....307

Table 4.30 Extracted Grain and Grain Boundary Parameters from EIS Modelling ..318

Table 4. 31 Magnetic parameters M_s, H_c, H_a, M_r and M_r/M_s value of all hexaferrite samples.....322

Table 4.32 REL with matching thickness/frequency, BW, and PBW for $BaCo_xAl_xFe_{12-2x}O_{19}$ (WP1 to WP3).....329

Table 4.33 Z_{in}, Z_{real}, and Z_{imag} values corresponding to REL_{max} for $BaCo_xAl_xFe_{12-2x}O_{19}$/PANI. 336

Table 4.34. Presents the assignment of sample names corresponding to various substitution levels in $BaCo_xCe_xFe_{12-2x}O_{19}$ hexaferrite. 339

Table 4.35 Extracted Grain and Grain Boundary Parameters from EIS Modelling ..348

Table 4.36 Magnetic parameters M_s , H_c , H_a, M_r, and M_r / M_s value of all hexaferrite samples.....354

Table 4.37 REL with matching thickness/frequency, BW, and PBW for $BaCo_xCe_xFe_{12-2x}O_{19}$ (XP1 to XP3). 361

Table 4.38 Z_{in}, Z_{real}, and Z_{imag} values corresponding to REL_{max} for $BaCo_xCe_xFe_{12-2x}O_{19}$ / PANI.....366

Table 4.39. Presents the assignment of sample names corresponding to various substitution levels in $BaCo_xCd_xFe_{12-2x}O_{19}$ hexaferrite. 368

Table 4.40 Extracted Grain and Grain Boundary Parameters from EIS Modelling ..378

Table 4.41 Magnetic parameters M_s, H_c, H_a, M_r and M_r/M_s value of all hexaferrite samples.....384

Table 4.42 REL with matching thickness/frequency, BW, and PBW for $BaCo_xCd_xFe_{12-2x}O_{19}$ (YP1 to YP3). 392

Table 4.43 Z_{in}, Z_{real}, and Z_{imag} values corresponding to REL_{max} for $BaCo_xCd_xFe_{12-2x}O_{19}$. 397

Table 4.44. Presents the assignment of sample names corresponding to various substitution levels in $BaCo_xCr_xFe_{12-2x}O_{19}$ hexaferrite.....400

Table 4.45 Extracted Grain and Grain Boundary Parameters from EIS Modelling ..410

Table 4.46 Magnetic parameters M_s, H_c, H_a, M_r and M_r/M_s value of all hexaferrite samples.....416

Table 4.47 REL with matching thickness/frequency, BW, and PBW for $BaCo_xCr_xFe_{12-2x}O_{19}$ (Z1 to Z5).....424

Table 4.48 Z_{in}, Z_{real}, and Z_{imag} values corresponding to REL_{max} for $BaCo_xCr_xFe_{12-2x}O_{19}$ / PANI. 430

List of Figures

Figure 1.1. Classification of Ferrites.....24

Figure 1.2. Advantages of M-type Hexaferrite.....27

Figure 1.3. Magnetoplumbite crystal structure of M-type hexaferrite.....28

Figure 1.4. Types of Microwave Absorbers 29

Figure 1.5. Application of Ferrites.....32

Figure 1.6. Various synthesis methods of M-type hexaferrite.....33

Figure 3.1. Synthesis Flowchart for Sol-Gel Auto-Combustion.....80

Figure 3.2. Rectangular pellets prepared for VNA measurement.....81

Figure 3.3. Chemicals along with their company for the preparation of $BaCo_xAl_xFe_{12-2x}O_{19}$. 82

Figure 3.4. Chemicals along with their company for the preparation of $BaCo_xCe_xFe_{12-2x}O_{19}$ 84

Figure 3.5. Chemicals along with their company for the preparation of $BaCo_xCd_xFe_{12-2x}O_{19}$ 85

Figure 3.6. Chemicals along with their company for the preparation of $BaCo_xCr_xFe_{12-2x}O_{19}$ 86

Figure 3.7. X-ray Diffraction Setup: Rigaku Miniflex-II System. 87

Figure 3.8. X-ray Diffractometer: Schematic Overview. 88

Figure 3.9. Morphological Analysis via FESEM and HR-TEM (JEOL Instruments).89

Figure 3.10. Magnetic Characterization using Microsense EV-90 Vibrating Sample Magnetometer 91

Figure 3.11. LCR meter used for electrical characterization.....92

Figure 3.12. Vector network analyzer (VNA). 98

Figure 4.1. X-ray Diffraction Analysis of M-type $BaCo_xAl_xFe_{12-2x}O_{19}$ Hexaferrites103

Figure 4.2. Energy-Dispersive X-ray Spectroscopy (EDX) Analysis of $BaCo_xAl_xFe_{12-2x}O_{19}$ Hexaferrites (W0 and W2).....104

Figure 4.3. SEM Micrographs of $BaCo_xAl_xFe_{12-2x}O_{19}$ Ferrites (W0 (x = 0.0), W1 (x = 0.2), W2 (x = 0.4), W3 (x = 0.6), W4 (x = 0.8), W5 (x = 1.0)). 105

Figure 4.4(a). Dielectric Constant Dependence on Frequency in $BaCo_xAl_xFe_{12-2x}O_{19}$ (W0 (x = 0.0), W1 (x = 0.2), W2 (x = 0.4), W3 (x = 0.6), W4 (x = 0.8) and W5 (x = 1.0)) Hexaferrites 108

Figure 4.5. n-Value Analysis of AC Conductivity in $BaCo_xAl_xFe_{12-2x}O_{19}$ Ferrites (W0 (x = 0.0), W1 (x = 0.2), W2 (x = 0.4), W3 (x = 0.6), W4 (x = 0.8) and W5 (x = 1.0)). 113

Figure 4.6(a). Real Modulus (M′) Dependence on Frequency in $BaCo_xAl_xFe_{12-2x}O_{19}$ (W0 (x = 0.0), W1 (x = 0.2), W2 (x = 0.4), W3 (x = 0.6), W4 (x = 0.8) and W5 (x = 1.0)) Hexaferrites 114

Figure 4.7(a) Real Impedance (Z′) Dependence on Frequency in BaCoxAlxFe12-2xO19 (W0 (x = 0.0), W1 (x = 0.2), W2 (x = 0.4), W3 (x = 0.6), W4 (x = 0.8) and W5 (x = 1.0)) Hexaferrites 117

Figure 4.8. Measured and Fitted Impedance Data with Equivalent Circuit (W0 to W5) 120

Figure 4.9. SEM Characterization of $BaCo_xAl_xFe_{12-2x}O_{19}$ Ferrites (x = 0.0-1.0 (W0 to W5)) 123

Figure 4.10. Hysteresis loops of W0, W1, W2, W3, W4 and W5 hexaferrite.....130

Figure 4.11. M_s versus 1/ H^2 plots for all hexaferrite samples. 131

Figure 4.12. Complex permittivity and permeability versus frequency plots for $BaCo_xAl_xFe_{12-2x}O_{19}$. 133

Figure 4.13. REL versus frequency for different thickness (W1) and calculate thickness versus frequency for $BaCo_xAl_xFe_{12-2x}O_{19}$ 136

Figure 4.14. REL versus frequency for different thickness (W2) and calculate thickness versus frequency for $BaCo_xAl_xFe_{12-2x}O_{19}$ 138

Figure 4.15. REL versus frequency for different thickness (W3) and calculate thickness versus frequency for $BaCo_xAl_xFe_{12-2x}O_{19v}$.....141

Figure 4.16. REL versus frequency for different thickness (W4) and calculate thickness versus frequency for $BaCo_xAl_xFe_{12-2x}O_{19}$ 143

Figure 4.17. REL versus frequency for different thickness (W5) and calculate thickness versus frequency for $BaCo_xAl_xFe_{12-2x}O_{19}$ 146

Figure 4.18. Three-dimensional (3D) plots of reflection loss at various frequencies and thicknesses for all samples of BaCoAl-series. 151

Figure 4.19. Zin and REL curve against frequency for $BaCo_xAl_xFe_{12-2x}O_{19}$.....156

Figure 4.20. Z_{real}, $Z_{imag,}$ and REL v/s frequency for $BaCo_xAl_xFe_{12-2x}O_{19}$.....158

Figure 4.21. C_0 versus frequency curve for $BaCo_xAl_xFe_{12-2x}O_{19}$. 159

Figure 4.22. S_{11} versus frequency curve for $BaCo_xAl_xFe_{12-2x}O_{19}$. 161

Figure 4.23. S_{21} versus frequency curve for $BaCo_xAl_xFe_{12-2x}O_{19}$.....161

Figure 4.24. XRD Patterns of Co^{2+} and Ce^{3+} Doped M-type Ba Hexaferrites.....163

Figure 4.25. EDX Spectra of Barium Hexaferrite ($BaCo_xCe_xFe_{12-2x}O_{19}$) with Varying Doping Levels (X0 and X2).....164

Figure 4.26. Microstructure Analysis: SEM Images of Co-Doped $BaFe_{12}O_{19}$ (x = 0.0-1.0 (X0 to X5)).....165

Figure 4.27(a). Frequency Dependence of Dielectric Constant for Co-Ce Doped $BaFe_{12}O_{19}$ (X0 to X5 (x = 0.0-1.0)).....167

Figure 4.28. Frequency Dependence of AC Exponent (n) for $BaCo_xCe_xFe_{12-2x}O_{19}$ (X0 to X5 (x = 0.0-1.0)).....171

Figure 4. 29(a) M' vs. Frequency of Co- Ce Doped $BaFe_{12}O_{19}$ (X0 to X5, x = 0.0-1.0) Hexaferrites (900°C, 5h).....172

Figure 4.30(a) Frequency Dependence of Real Impedance (Z') in $BaCo_xCe_xFe_{12-2x}O_{19}$ (x = 0.0-1.0) Hexaferrites (900°C, 5h).....175

Figure 4.31 Complex Impedance Plots: Measured vs. Fitted Data (Equivalent Circuit Included), Where X0 = 0.0, X1 = 0.2, X2 = 0.4, X3 = 0.6, X4 = 0.8 and X5 = 1.0..178

Figure 4.32. Hysteresis loops of X0, X1, X2, X3, X4 and X5 hexaferrite. 182

Figure 4.33 M_s versus 1/ H^2 plots for all hexaferrite samples. 183

Figure 4.34 Complex permittivity and permeability versus frequency plots for $BaCo_xCe_xFe_{12-2x}O_{19}$.....184

Figure 4.35 REL versus frequency for different thickness (X2) and calculate thickness versus frequency for $BaCo_xCe_xFe_{12-2x}O_{19}$.....187

Figure 4.36 REL versus frequency for different thickness (X3) and calculate thickness versus frequency for $BaCo_xCe_xFe_{12-2x}O_{19}$.....189

Figure 4.37 REL versus frequency for different thickness (X4) and calculate thickness versus frequency for $BaCo_xCe_xFe_{12-2x}O_{19}$.....192

Figure 4.38 REL versus frequency for different thickness (X5) and calculate thickness versus frequency for $BaCo_xCe_xFe_{12-2x}O_{19}$.....194

Figure 4.39 Three-dimensional (3D) plots of reflection loss at various frequencies and thicknesses for all samples of BaCoCe-series. 198

Figure 4.40 Zin and REL curve against frequency for $BaCo_xCe_xFe_{12-2x}O_{19}$. 202

Figure 4.41 Z_{real}, $Z_{imag,}$ and REL v/s frequency for $BaCo_xCe_xFe_{12-2x}O_{19}$.....204

Figure 4.42 C_0 versus frequency curve for $BaCo_xAl_xFe_{12-2x}O_{19}$. 205

Figure 4.43 S_{11} and S_{21} versus frequency curve for $BaCo_xCe_xFe_{12-2x}O_{19}$. 206

Figure 4.44 X-ray diffractions of M -type $BaCo_xCd_xFe_{12-2x}O_{19}$ (Y0 to Y5, x = 0.0, 0.2, 0.4, 0.6, 0.8, and 1.0) hexaferrites.....208

Figure 4.45 EDX spectra of $BaCo_xCd_xFe_{12-2x}O_{19}$ (Y0 to Y5, x =0.0, 0.2, 0.4, 0.6, 0.8, and 1.0) hexaferrite for samples Y0 and Y2. 209

Figure 4.46 SEM micrographs of ferrite samples of $BaCo_xCd_xFe_{12-2x}O_{19}$ (Y0 to Y5, x =0.0, 0.2, 0.4, 0.6, 0.8, and 1.0) 210

Figure 4.47(a) Variation of dielectric constant with frequency for $BaCo_xCd_xFe_{12-2x}O_{19}$ (Y0 to Y5, x = 0.0, 0.2, 0.4, 0.6, 0.8, and 1.0) hexaferrites samples heated at 900° C for 5 hours. 214

Figure 4.48 Calculation of n for AC conductivity with respect to frequency for ferrite sample $BaCo_xCd_xFe_{12-2x}O_{19}$ (Y0 to Y5, x =0.0, 0.2, 0.4, 0.6, 0.8, and 1.0) which is less than 1.....217

Figure 4.49(a) Variation of the real part of the electric modulus (M′) with frequency of $BaCo_xCd_xFe_{12-2x}O_{19}$ (Y0 to Y5, x =0.0, 0.2, 0.4, 0.6, 0.8, and 1.0) hexaferrite samples heated at 900° C for 5 hours. 218

Figure 4.50(a) Variation of the real part of the Impedance (Z') with frequency of $BaCo_xCd_xFe_{12-2x}O_{19}$ (Y0 to Y5, x = 0.0, 0.2, 0.4, 0.6, 0.8, and 1.0) hexaferrite samples heated at 900° C for 5 hours. 222

Figure 4.50(c) 51Variation of the Cole-Cole type plot of $BaCo_xCd_xFe_{12-2x}O_{19}$ (Y0 to Y5, x =0.0, 0.2, 0.4, 0.6, 0.8, and 1.0) hexaferrite samples heated at 900° C for 5 hours.....223

Figure 4.52 Complex impedance plots for ferrite samples (red points-measured values, green lines-fitted values) and an applied equivalent circuit. 224

Figure 4. 53 (a) Migration of grain process; (b) Represent Grain and Grain Boundaries; (c) Separation of grain and identification of grain boundaries; (d) Diffusion across boundary for $BaCo_xCd_xFe_{12-2x}O_{19}$ (Y0 to Y5, x =0.0, 0.2, 0.4, 0.6, 0.8, and 1.0). 226

Figure 4.54 SEM micrographs of ferrite samples of $BaCo_xCd_xFe_{12-2x}O_{19}$ (Y1 and Y3) 227

Figure 4.55. Hysteresis loops of Y0, Y1, Y2, Y3, Y4 and Y5 hexaferrite. 235

Figure 4.56 M_s versus 1/ H^2 plot for all hexaferrite samples. 236

Figure 4.57 Complex permittivity and permeability versus frequency plots for $BaCo_xCd_xFe_{12-2x}O_{19}$. 238

Figure 4.58 REL versus frequency for different thickness (Y1) and calculate thickness versus frequency for $BaCo_xCd_xFe_{12-2x}O_{19}$ 240

Figure 4.59 REL versus frequency for different thickness (Y2) and calculate thickness versus frequency for $BaCo_xCd_xFe_{12-2x}O_{19}$ 242

Figure 4.60 REL versus frequency for different thickness (Y3) and calculate thickness versus frequency for $BaCo_xCd_xFe_{12-2x}O_{19}$ 242

Figure 4.61 REL versus frequency for different thickness (Y4) and calculate thickness versus frequency for $BaCo_xCd_xFe_{12-2x}O_{19}$ 242

Figure 4.62 REL versus frequency for different thickness (Y5) and calculate thickness versus frequency for $BaCo_xCd_xFe_{12-2x}O_{19}$ 243

Figure 4.63 Three-dimensional (3D) plots of reflection loss at various frequencies and thicknesses for all samples of BaCoCd-series. 244

Figure 4.64 Z_{in} and REL curve against frequency for $BaCo_xCd_xFe_{12-2x}O_{19}$. 247

Figure 4.65 Z_{real}, $Z_{imag,}$ and REL v/s frequency for $BaCo_xCd_xFe_{12-2x}O_{19}$. 249

Figure 4.66 C_0 versus frequency curve for $BaCo_xCd_xFe_{12-2x}O_{19}$. 250

Figure 4.67 S_{11} versus frequency curve for $BaCo_xCd_xFe_{12-2x}O_{19}$.....252

Figure 4.68 S_{21} versus frequency curve for $BaCo_xCd_xFe_{12-2x}O_{19}$. 253

Figure 4.69 X-Ray Diffraction Analysis of M-Type $BaCo_xCr_xFe_{12-2x}O_{19}$ (Z0 (x = 0.0), Z1 (x = 0.2), Z2 (x = 0.4), Z3 (x = 0.6), Z4 (x = 0.8), Z5 (x = 1.0)) 255

Figure 4.70 Focused EDX Analysis of $BaCo_xCr_xFe_{12-2x}O_{19}$ Hexaferrites for Z0 and Z2 256

Figure 4.71 SEM micrographs of ferrite samples of $BaCo_xCr_xFe_{12-2x}O_{19}$ (Z0 (x = 0.0), Z1 (x = 0.2), Z2 (x = 0.4), Z3 (x = 0.6), Z4 (x = 0.8), Z5 (x = 1.0)). 257

Figure 4.72(a) Frequency Dependence of Dielectric Constant in $BaCo_xCr_xFe_{12-2x}O_{19}$ (Z0 (x = 0.0), Z1 (x = 0.2), Z2 (x = 0.4), Z3 (x = 0.6), Z4 (x = 0.8), Z5 (x = 1.0)) Hexaferrites.....261

Figure 4.73 Frequency Exponent (n) of AC Conductivity in $BaCo_xCr_xFe_{12-2x}O_{19}$ (Z0 (x = 0.0), Z1 (x = 0.2), Z2 (x = 0.4), Z3 (x = 0.6), Z4 (x = 0.8), Z5 (x = 1.0)). 263

Figure 4.74(a) Frequency Dependence of Real Electric Modulus (M′) in Co-Cr Doped of $BaCo_xCr_xFe_{12-2x}O_{19}$ hexaferrite. 266

Figure 4.75(a) Frequency Dependence of Real Impedance (Z') in Co-Cr Doped $BaCo_xCd_xFe_{12-2x}O_{19}$ (Z0 (x = 0.0), Z1 (x = 0.2), Z2 (x = 0.4), Z3 (x = 0.6), Z4 (x = 0.8), Z5 (x = 1.0)) hexaferrite. 270

Figure 4.76(b) Frequency Dependence of Imaginary Impedance (Z″) in Co-Cr Doped $BaCo_xCd_xFe_{12-2x}O_{19}$ (Z0 (x = 0.0), Z1 (x = 0.2), Z2 (x = 0.4), Z3 (x = 0.6), Z4 (x = 0.8), Z5 (x = 1.0)) hexaferrite. 270

Figure 4.77 Complex Impedance Spectroscopy of Ferrite Samples: Measured Data (Red Points) and Equivalent Circuit Fitting (Green Lines) where Z0 = 0.0, Z1 = 0.2, Z2 = 0.4, Z3 = 0.6, Z4 = 0.8 and Z5 = 1.0 274

Figure 4.78 (a) Migration of grain process; (b) Represent Grain and Grain Boundaries; (c) Separation of grain and identification of grain boundaries; (d) Diffusion across boundary for $BaCo_xCr_xFe_{12-2x}O_{19}$ (Z0 (x = 0.0), Z1 (x = 0.2), Z2 (x = 0.4), Z3 (x = 0.6), Z4 (x = 0.8), Z5 (x = 1.0)). 279

Figure 4.79. Hysteresis loops of Z0, Z1, Z2, Z3, Z4 and Z5 hexaferrite. 283

Figure 4.80 M_s versus 1/ H^2 plot for all hexaferrite samples. 284

Figure 4.81 Complex permittivity and permeability versus frequency plots for $BaCo_xCr_xFe_{12-2x}O_{19}$ (Z0 to Z4). 286

Figure 4.82 REL versus frequency for different thickness (Z1) and calculate thickness versus frequency for $BaCo_xCr_xFe_{12-2x}O_{19}$ 287

Figure 4.83 REL versus frequency for different thickness (Z2) and calculate thickness versus frequency for $BaCo_xCr_xFe_{12-2x}O_{19}$ 290

Figure 4.84 REL versus frequency for different thickness (Z3) and calculate thickness versus frequency for $BaCo_xCr_xFe_{12-2x}O_{19}$ 292

Figure 4.85 REL versus frequency for different thickness (Z4) and calculate thickness versus frequency for $BaCo_xCr_xFe_{12-2x}O_{19}$ 295

Figure 4.86 Three-dimensional (3D) plots of reflection loss at various frequencies and thicknesses for all samples of BaCoCr-series. 298

Figure 4.87 Z_{in} and REL curve against frequency for $BaCo_xCr_xFe_{12-2x}O_{19}$. 302

Figure 4.88 Z_{real}, $Z_{imag,}$ and REL v/s frequency for $BaCo_xCr_xFe_{12-2x}O_{19}$. 304

Figure 4.89 C_0 versus frequency curve for $BaCo_xCr_xFe_{12-2x}O_{19}$. 305

Figure 4.90 S_{11} versus frequency curve for $BaCo_xCr_xFe_{12-2x}O_{19}$. 306

Figure 4.91 S_{21} versus frequency curve for $BaCo_xCr_xFe_{12-2x}O_{19}$. 307

Figure 4.92 SEM Micrographs of $BaCo_xAl_xFe_{12-2x}O_{19}$ Ferrites (WP1 (x = 0.0), WP2 (x = 0.8), WP3 (x = 1.0)). 308

Figure 4.93(a) Dielectric Constant Dependence on Frequency in $BaCo_xAl_xFe_{12-2x}O_{19}$ (WP1 (x = 0.0), WP2 (x = 0.8), WP3 (x = 1.0)) Hexaferrites 309

Figure 4.94(b) Imaginary Modulus (M'') Dependence on Frequency in $BaCo_xAl_xFe_{12-2x}O_{19}$ (WP1 (x = 0.0), WP2 (x = 0.8), WP3 (x = 1.0)) Hexaferrites 314

Figure 4.95(a) Real Impedance (Z′) Dependence on Frequency in $BaCo_xAl_xFe_{12-2x}O_{19}$ (WP1 (x = 0.0), WP2 (x = 0.8), WP3 (x = 1.0)) Hexaferrites 316

Figure 4.96 Measured and Fitted Impedance Data with Equivalent Circuit (WP1 to WP3) 318

Figure 4.97 M_s versus 1/ H^2 plots for all hexaferrite samples. 321

Figure 4.98 Hysteresis loops of WP1, WP2 and WP3 hexaferrite. 322

Figure 4.99 Complex permittivity and permeability versus frequency plots for $BaCo_xAl_xFe_{12-2x}O_{19}$ / PANI. 323

Figure 4.100 REL versus frequency for different thickness (WP1) and calculate thickness versus frequency for $BaCo_xAl_xFe_{12-2x}O_{19}$/PANI 325

Figure 4.101 REL versus frequency for different thickness (WP2) and calculate thickness versus frequency for $BaCo_xAl_xFe_{12-2x}O_{19}$/PANI 327

Figure 4.102 REL versus frequency for different thickness (WP3) and calculate thickness versus frequency for $BaCo_xAl_xFe_{12-2x}O_{19}$/PANI 328

Figure 4.103 Three-dimensional (3D) plots of reflection loss at various frequencies and thicknesses for all samples of BaCoAl / PANI-series. 331

Figure 4.104 Zin and REL curve against frequency for $BaCo_xAl_xFe_{12-2x}O_{19}$ /PANI. 335

Figure 4.105 Z_{real}, $Z_{imag,}$ and REL v/s frequency for $BaCo_xAl_xFe_{12-2x}O_{19}$ /PANI. 336

Figure 4.106 C_0 versus frequency curve for $BaCo_xAl_xFe_{12-2x}O_{19}$ / PANI. 337

Figure 4.107 S_{11} and S_{21} versus frequency curve for $BaCo_xAl_xFe_{12-2x}O_{19}$ / PANI. ... 338

Figure 4.108 SEM Micrographs of $BaCo_xCe_xFe_{12-2x}O_{19}$ Ferrites. 339

Figure 4.109(a) Dielectric Constant Dependence on Frequency in $BaCo_xCe_xFe_{12-2x}O_{19}$ (XP1 (x = 0.0), XP2 (x = 0.6), XP3 (x = 1.0)) Hexaferrites 341

Figure 4.110(a) Real Modulus (M′) Dependence on Frequency in $BaCo_xCe_xFe_{12-2x}O_{19}$ (XP1 (x = 0.0), XP2 (x = 0.6), XP3 (x = 1.0)) Hexaferrites. 344

Figure 4.111(a) Real Impedance (Z′) Dependence on Frequency in $BaCo_xCe_xFe_{12-2x}O_{19}$ (XP1 (x = 0.0), XP2 (x = 0.6), XP3 (x = 1.0)) Hexaferrites 347

Figure 4.112 Measured and Fitted Impedance Data with Equivalent Circuit (XP1 to XP3) 349

Figure 4.113 M_s versus 1/ H^2 plots for all hexaferrite samples. 353

Figure 4.114 Hysteresis loops of XP1, XP2 and XP3 hexaferrite. 353

Figure 4.115 Complex permittivity and permeability versus frequency plots for $BaCo_xCe_xFe_{12-2x}O_{19}$ / PANI 355

Figure 4.116 REL versus frequency for different thickness (XP1) and calculate thickness versus frequency for $BaCo_xCe_xFe_{12-2x}O_{19}$ 357

Figure 4.117 REL versus frequency for different thickness (XP2) and calculate thickness versus frequency for $BaCo_xCe_xFe_{12-2x}O_{19}$ 358

Figure 4.118 REL versus frequency for different thickness (XP3) and calculate thickness versus frequency for $BaCo_xCe_xFe_{12-2x}O_{19}$ 359

Figure 4.119 Three-dimensional (3D) plots of reflection loss at various frequencies and thicknesses for all samples of BaCoCe-series. 362

Figure 4.120 Z_{in} and REL curve against frequency for $BaCo_xCe_xFe_{12-2x}O_{19}$ / PANI 364

Figure 4.121 Z_{real}, $Z_{imag,}$ and REL v/s frequency for $BaCo_xCe_xFe_{12-2x}O_{19}$ / PANI 365

Figure 4.122 C_0 versus frequency curve for $BaCo_xAl_xFe_{12-2x}O_{19}$ / PANI..... 366

Figure 4.123 S_{11} and S_{21} versus frequency curve for $BaCo_xCe_xFe_{12-2x}O_{19}$ / PANI.... 368

Figure 4.124 SEM Micrographs of $BaCo_xCd_xFe_{12-2x}O_{19}$ Ferrites (YP1 (x = 0.0), YP2 (x = 0.6), YP3 (x = 1.0)). 368

Figure 4.125(a) Dielectric Constant Dependence on Frequency in $BaCo_xCd_xFe_{12-2x}O_{19}$ (YP1 (x = 0.0), YP2 (x = 0.6), YP3 (x = 1.0)) Hexaferrites. 370

Figure 4.126 (a) Real Modulus (M′) Dependence on Frequency in $BaCo_xCd_xFe_{12-2x}O_{19}$ (YP1 (x = 0.0), YP2 (x = 0.6), YP3 (x = 1.0)) Hexaferrites 373

Figure 4.127(a) Real Impedance (Z′) Dependence on Frequency in $BaCo_xCd_xFe_{12-2x}O_{19}$ (YP1 (x = 0.0), YP2 (x = 0.6), YP3 (x = 1.0)) Hexaferrites. 376

Figure 4.128 Measured and Fitted Impedance Data with Equivalent Circuit (YP1 to YP3) 378

Figure 4.129 M_s versus 1/ H^2 plots for all hexaferrite samples. 383

Figure 4.130 Hysteresis loops of Y1, Y2 and Y3 hexaferrite. 383

Figure 4.131 Complex permittivity and permeability versus frequency plots for $BaCo_xCd_xFe_{12-2x}O_{19}$ / PANI. 385

Figure 4.132 REL versus frequency for different thickness (YP1) and calculate thickness versus frequency for $BaCo_xCd_xFe_{12-2x}O_{19}$ / PANI 390

Figure 4.133 REL versus frequency for different thickness (YP2) and calculate thickness versus frequency for $BaCo_xCd_xFe_{12-2x}O_{19}$ / PANI 390

Figure 4.134 REL versus frequency for different thickness (YP3) and calculate thickness versus frequency for $BaCo_xCd_xFe_{12-2x}O_{19}$ / PANI 391

Figure 4.135 Three-dimensional (3D) plots of reflection loss at various frequencies and thicknesses for all samples of BaCoCd-series. 394

Figure 4.136 Z_{in} and REL curve against frequency for $BaCo_xCd_xFe_{12-2x}O_{19}$ / PANI 395

Figure 4.137 Z_{real}, $Z_{imag,}$ and REL v/s frequency for $BaCo_xCd_xFe_{12-2x}O_{19}$ / PANI 396

Figure 4.138 C_0 versus frequency curve for $BaCo_xCd_xFe_{12-2x}O_{19}$ / PANI.....397

Figure 4.139 S_{11} and S_{21} versus frequency curve for $BaCo_xCd_xFe_{12-2x}O_{19}$ / PANI....399

Figure 4.140 SEM Micrographs of $BaCo_xCr_xFe_{12-2x}O_{19}$ Ferrites (ZP1 (x = 0.0), ZP2 (x = 0.6), ZP3 (x = 0.8)).....400

Figure 4.141(a) Dielectric Constant Dependence on Frequency in $BaCo_xCr_xFe_{12-2x}O_{19}$ (ZP1 (x = 0.0), ZP2 (x = 0.6), ZP3 (x = 0.8)) Hexaferrites. 402

Figure 4.142(a) Real Modulus (M′) Dependence on Frequency in $BaCo_xCr_xFe_{12-2x}O_{19}$ (ZP1 (x = 0.0), ZP2 (x = 0.6), ZP3 (x = 0.8)) Hexaferrites 405

Figure 4.143(a) Real Impedance (Z′) Dependence on Frequency in $BaCo_xCr_xFe_{12-2x}O_{19}$ (ZP1 (x = 0.0), ZP2 (x = 0.6), ZP3 (x = 0.8)) Hexaferrites. 408

Figure 4.144 Measured and Fitted Impedance Data with Equivalent Circuit (ZP1 to ZP3).....410

Figure 4.145 M_s versus 1/ H^2 plots for all hexaferrite samples. 415

Figure 4.146 Hysteresis loops of ZP1, ZP2 and ZP3 hexaferrite. 415

Figure 4.147 Complex permittivity and permeability versus frequency plots for $BaCo_xCr_xFe_{12-2x}O_{19}$ (ZP1 to ZP3).....417

Figure 4.148 REL versus frequency for different thickness (ZP1) and calculate thickness versus frequency for $BaCo_xCr_xFe_{12-2x}O_{19}$ / PANI.....420

Figure 4.149. REL versus frequency for different thickness (ZP2) and calculate thickness versus frequency for $BaCo_xCr_xFe_{12-2x}O_{19}$ / PANI.....421

Figure 4.150 REL versus frequency for different thickness (ZP3) and calculate thickness versus frequency for $BaCo_xCr_xFe_{12-2x}O_{19}$ / PANI.....422

Figure 4.151 Three-dimensional (3D) plots of reflection loss at various frequencies and thicknesses for all samples of BaCoCr-series. 426

Figure 4.152 Z_{in} and REL curve against frequency for $BaCo_xCr_xFe_{12-2x}O_{19}$ / PANI.429

Figure 4.153 Z_{real}, $Z_{imag,}$ and REL v/s frequency for $BaCo_xCr_xFe_{12-2x}O_{19}$ / PANI.....430

Figure 4.154 C_0 versus frequency curve for $BaCo_xCr_xFe_{12-2x}O_{19}$ / PANI.....431

Figure 4.155 S_{11} and S_{21} versus frequency curve for $BaCo_xCr_xFe_{12-2x}O_{19}$ / PANI. ...432

CHAPTER–1

INTRODUCTION

Our modern world is filled with advanced technology, from super-fast electronics to wireless communication, sensors, automated systems, advanced antennas, and even military platforms equipped with stealth technology [1-2]. This widespread use of wireless technology has filled our environment with electromagnetic (EM) waves. Everyday items like laptops, cell phones, Wi-Fi routers, and microwave ovens all give off this EM energy. Outside, sources such as cell towers, satellites, and medical equipment like CT scanners also add to this exposure, which can be harmful to our health [1].

Beyond health concerns, EM waves can interfere with how electronic devices work, a problem known as electromagnetic interference (EMI). This happens when electronic parts near each other mess with each other's performance. Small circuit boards, often used in electronics, can actually act like antennas if their wiring is a certain length, sending out EM energy and causing interference [2]. This EMI can affect nearby electronics, the environment, and even human safety [4-5].

To fight against this interference, special materials are used that can absorb or weaken EM waves through their electrical or magnetic properties [6]. That's why it's so important to develop inexpensive and effective materials that can absorb these waves [7-8]. Communication systems, which rely on EM waves, operate across various microwave frequencies [9]. Good absorbing materials need to be lightweight, low density, broad bandwidth, antioxidant capability, excellent thermal stability, and the ability to absorb EM radiation at multiple frequencies [10-11].

Composites, which are materials made by combining different substances, are excellent at absorbing EM waves. They do this by improving properties like magnetism, electrical flow, and how they handle electrical and magnetic energy [12-13]. Their varied characteristics make them useful for many different applications [14-15]. Among various materials, ferrites show great promise for absorbing microwaves [5].

In today's digital age, hackers can use EM waves to get into or disrupt sensitive information. Microwave absorbers help protect against these threats by reducing EM

radiation, shielding electronic circuits, and keeping data safe. They also offer protection for human health and come in different forms such as fabrics, foams, paints, and sheets, designed for specific uses [3-4].

1.1Ferrites

Ferrites are extensively used in technology because of their distinctive amalgamation of magnetic and insulating characteristics. The composition of these ceramic materials consists mostly of iron oxides along with metal oxides including barium, strontium, manganese, nickel, and zinc. Ferrites are categorized according to several characteristics such as permittivity, permeability, dielectric loss, magnetic loss, saturation magnetization, and coercivity. Ferrimagnetism is a fascinating form of magnetism observed in ferrites, where certain magnetic moments line up with one another while others line up with the opposite. The resulting net magnetic field is stronger than in antiferromagnetic materials, yet not as strong as in purely ferromagnetic materials. This unique magnetic behaviour was first described by Louis Neel. The structural and electrical characteristics of ferrites are significantly affected by the synthesis technique, chemical composition, porosity and grain size.

1.1.1. Historical Development of Ferrites

The journey of understanding magnetism and its applications began around 800 BC with the discovery of magnetite in Magnesia, Asia Minor. This naturally magnetic ferrite played a crucial role in early navigation. Centuries later, in 1600 AD, William Gilbert's seminal work, De Magnete, provided a clear distinction between electricity and magnetism and accurately described Earth's magnetic field.

The early 20th century marked a new era for ferrites. In 1930, Dr. Takeshi Takie recognized ferrite's high permeability, making it suitable for high-frequency technologies. This understanding quickly led to practical applications; by 1936, the first quarter-wavelength resonant absorber was developed in the Netherlands, driven by advancements in radar technology.

World War II spurred significant innovations in radar-absorbing materials, with the U.S. developing solutions like HARP and the Salisbury Screen. The post-war period (1945–1950) saw a shift towards creating broadband absorbers. Further theoretical groundwork was laid by J.L. Snoek in 1947, who highlighted the benefits of soft ferrites in New Development in Ferromagnetic Materials. In 1948, Louis Néel's

research provided deeper insights into ferrimagnetic spin interactions. A major breakthrough occurred in 1956 with the creation of garnet and hexagonal ferrites, including barium and strontium ferrites, which were particularly valuable due to their ease of production and cost-effectiveness [57].

1.2 Classification of Ferrites

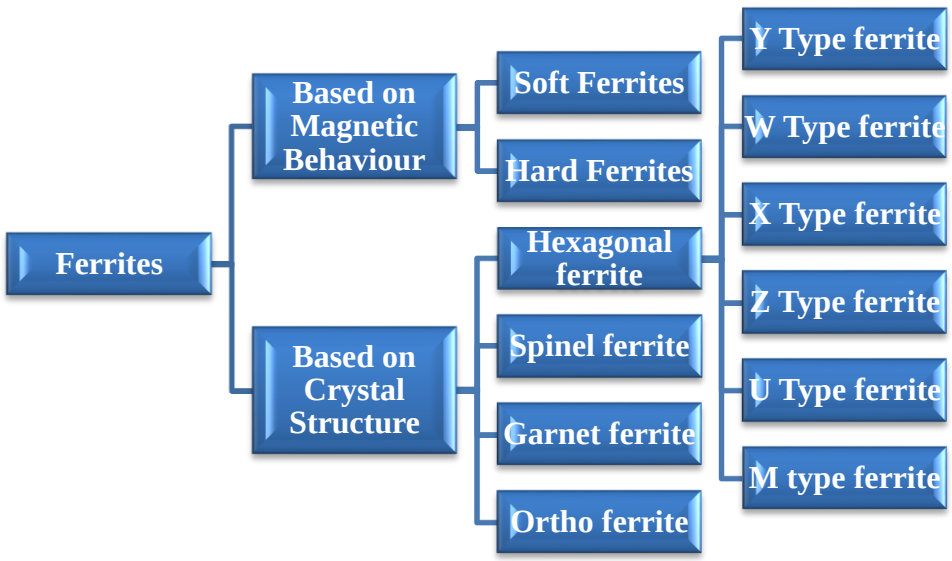

Figure 1.1. Classification of Ferrites

1.2.1 Based on Magnetic Behaviour

Ferrites may be categorized into two main groups according to their magnetic properties: soft ferrites and hard ferrites [16]. Table 1.1 presents the key distinctions between soft ferrites and hard ferrites, aiding in the selection of the appropriate ferrite type for different applications based on their distinct magnetic characteristics.

Table 1.1. Characteristics of Soft and Hard Ferrites

Feature	**Soft Ferrites**	**Hard Ferrites**
Magnetization and Demagnetization	Easily magnetized and demagnetized	Retain significant magnetization
Coercivity (H_c)	Low	High
Hysteresis Loop Area	Small (indicates less energy loss)	Large (indicates more energy dissipation)
Saturation Magnetization (M_s)	Relatively large	Generally lower compared to soft ferrites
Examples	Manganese-zinc ferrite (Mn-Zn), Nickel-zinc ferrite (Ni-Zn)	Barium ferrite (BaFe12O19), Strontium ferrite ($SrFe_{12}O_{19}$)

Common Applications	Transformer cores, Inductor cores, LC filters	Magnetic recording devices such disks and cassettes, as well as permanent magnets

1.2.2 Based on crystal structure

The atomic arrangement of a ferrite material's crystal structure is essential for influencing its magnetic interactions and, therefore, its magnetic characteristics. Ferrites may be categorized into four principal types based on their crystal structure: ortho ferrites, garnet ferrites, spinel ferrites, and hexagonal ferrites. Each kind demonstrates distinct characteristics and uses that arise from its particular crystalline structure [58-60].

Table 1.2. Comparative Properties of Different Types of Ferrites

Feature	**Spinel Ferrites**	**Garnet Ferrites**	**Ortho Ferrites**	**Hexagonal Ferrites**
General Formula	XY_2O_4	$X_3Y_5O_{12}$	XYO_3	$XY_{12}O_{19}$
Elements Represented by X	Mg, Fe, Zn, Mn, Ni, etc.	Trivalent ions such as Gd, Dy, Nd	Large trivalent metals or rare earth ions such as Bi	Sr, Ba, Pb
Elements Represented by Y	Al, Cr, Fe	Fe	Fe	Fe
Primary Use Case	Microwave-absorbing materials	Soft ferromagnetic applications	Exhibits mild ferromagnetic properties	Suitable for absorbing high-frequency waves due to GHz range resonance
Magnetic Resonance Frequency	Low natural magnetic resonance frequency	Comparable to spinel ferrite but with additional sites	Antiferromagnetic behaviour due to antisymmetric exchange interaction	High, naturally resonates in the gigahertz (GHz) range
Saturation Magnetization (M_s)	20-80 emu/g (depending on composition)	100-140 emu/g depending on specific garnet composition	1-10 emu/g (varies significantly with composition)	72-110 emu/g
Coercivity (H_c)	10-100 Oe (varies depending on composition)	Generally low, under 10 Oe	100-500 Oe (varies by composition)	High, around 3000- 7000 Oe
Crystal Structure	Cubic (similar to spinel structure)	Comparable to spinel with additional dodecahedral	Orthorhombic	Hexagonal (hexaferrite)

1.3 Hexagonal ferrites

Hexaferrites are a class of intricate oxides that have extensive applications in diverse technological fields including sensors, magnetic recording, biomedicine, microwave absorbers, magnetoelectric devices, radar absorbing materials, low-power spintronics devices, memory storage devices, radiation shielding for electronic devices, circulators, phase shifters, and stealth technology. The materials can be categorized into six distinct groups: M, W, X, Y, Z, and U, based on their composition and crystalline structure. Each variety exhibits distinct magnetic and structural characteristics that make them appropriate for certain purposes [61-65].

Table 1.3. Comparison of Different Types of Hexaferrite

Feature	M-Type	W-Type	X-Type	Y-Type	Z-Type	U-Type
General Formula	$MY_{12}O_{19}$	$XY_2Fe_{16}O_{27}$	$X_2Y_2Fe_{28}O_{46}$	$X_2Y_2Fe_{12}O_{22}$	$X_3Y_2Fe_{24}O_{41}$	$X_4Y_2Fe_{32}O_{60}$
Elements Represented by M/X	Ba, Sr	Ba, Sr, Mg, Pb	Ba, Sr, Mg, Pb	Ba, Sr, Mg, Pb	Ba, Sr, Mg, Pb	Ba, Sr, Mg, Pb
Elements Represented by Y	Fe	Divalent metal cation (e.g., Co, Ni)	Divalent metal cation (e.g., Co, Ni)	Cu, Zn, Co, etc.	Divalent metal cation (e.g., Co, Ni)	Divalent metal cation (e.g., Co, Ni)
Primary Use Case	High-density magnetic recording, permanent magnets, telecommunications, magneto-optical recording, microwave devices	Household appliances, permanent magnets, recording heads, microwave equipment	Applications requiring alternating M-type and W-type structures	Soft magnets, microwave devices	Microwave devices like antennas, inductors, and absorbers	Applications requiring large unit cells and complex structures
Magnetic Properties	Strong coercivity, large saturation magnetization, high uniaxial anisotropy, excellent corrosion resistance	Relatively high saturation magnetization, good electrical conductivity due to Fe^{2+} ions	Combination of magnetism from M and W structures, moderate properties	Soft magnetic properties, low coercivity, moderate magnetization	High permeability, high resonance frequency	Complex magnetic properties due to intricate and large crystal structure

Coercivity (H_c)	3000-6000 Oe	2000-3000 Oe	500-2000 Oe	~100-300 Oe	1000-3000 Oe	1000–3000 Oe
Saturation Magnetization (M_s)	72-80 emu/g	70-90 emu/g	60-80 emu/g	40-60 emu/g	50-70 emu/g	60-80 emu/g

1.3.1 M-type hexagonal ferrites

M-type ferrites, with the formula $MFe_{12}O_{19}$ (where M = barium, lead, or strontium), were first studied by Phillips in the early 1950s. They exhibit high coercivity, strong saturation magnetization, uniaxial anisotropy, and excellent corrosion resistance, making them ideal for microwave devices, high-density magnetic storage, magneto-optical recording, telecommunications, and permanent magnets.

Table 1.4. Overview of Hexaferrite Types and Structures

Hexaferrite Type	Combination	Stacking Sequence	Molecular Formula
M	M	RSR* S*	$MFe_{12}O_{19}$
Y	Y	TSTSTS	$X_2Y_2Fe_{12}O_{22}$
W	M + S	RSSR* S* S*	$XY_2Fe_{16}O_{27}$
Z	M + Y	RSTSR* S* T* S*	$X_3Y_2Fe_{24}O_{41}$
X	2M + S	RSR* S* S*	$X_2Y_2Fe_{28}O_{46}$
U	2M + Y	RSR* S* T* S*	$X_4Y_2Fe_{32}O_{60}$

The M-type hexaferrite distinguishes itself from other varieties due to its many significant benefits and distinctive characteristics as follows:

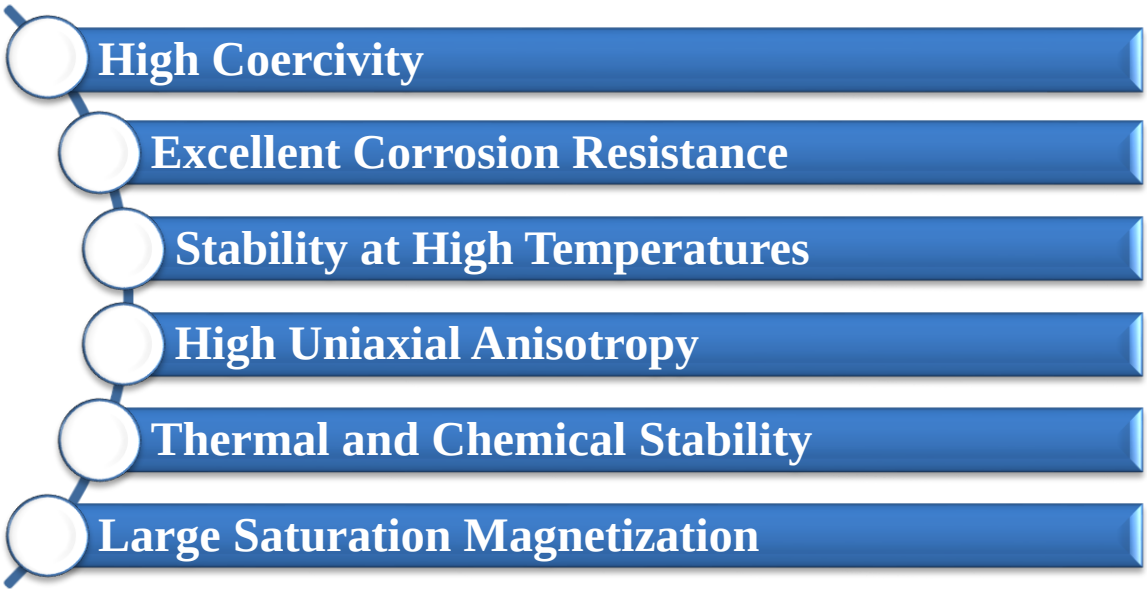

Figure 1.2. Advantages of M-type Hexaferrite

1.3.2 Crystal structure of M-type hexagonal ferrites

M-type hexagonal ferrites are highly valued for their robust properties, including high resistance to demagnetization (coercivity), cost-effectiveness, and excellent chemical and thermal stability, along with a high Curie temperature. These characteristics make them ideal for a wide range of applications, such as permanent magnets, supercapacitors, data storage, microwave devices, and materials for absorbing electromagnetic (EM) radiation.

Their structure is based on a magnetoplumbite configuration within the $P6_3/mmc$ space group. This arrangement features two spinel blocks (S and S*) separated by an R block, which typically contains barium or strontium. The characteristic stacking sequence is RSR*S*. The R Block consists of three layers of oxygen ions and is represented as $[Me^{2+}Fe_6^{3+}O_{11}]^{2-}$ with the chemical composition $(O_4\text{-}MeO_3)\text{-}O_4$. The S Block is composed of a spinel structure featuring two layers of oxygen ions, represented as $[Me_2^{2+}Fe_4^{3+}O_{11}]^0$ or $[Fe_6^{3+}O_8]^{2+}$ [66-67].The asterisk (*) denotes a 180° rotation around the hexagonal c-axis. Each unit cell of these ferrites contains 38 O^{2-} ions, 24 Fe^{3+} ions, and 2 Me ions (which can be Ba^{2+}, Sr^{2+}, Pb^{2+}, or La^{2+}). The Fe^{3+} ions occupy five distinct crystallographic sites: three octahedral sites (2a, 12k, $4f_1$), one trigonal bipyramidal site (2b), and one tetrahedral site ($4f_2$).

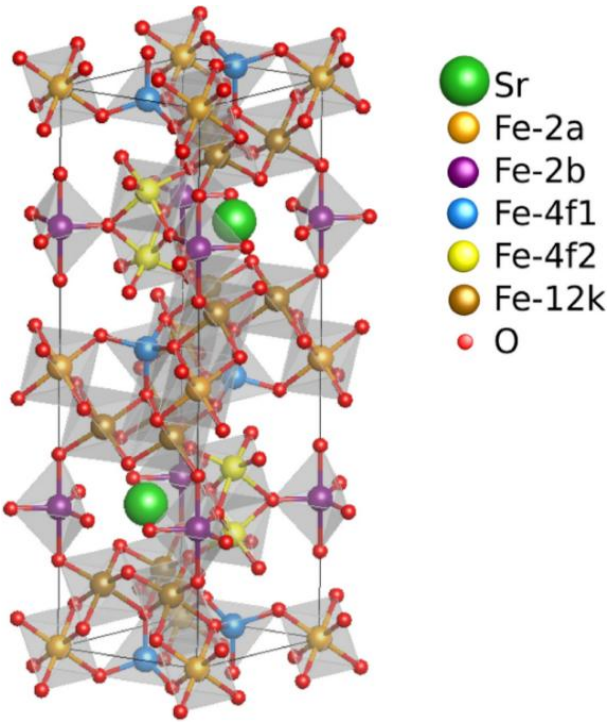

Figure 1.3. Magnetoplumbite crystal structure of M-type hexaferrite.

Table 1.5. Site occupancy of Fe^{3+} ion at different crystallographic sites.

Site	Geometry	Spin	No. of Fe^{3+} ions	No. of ions
2a	Octahedral	Up (↑)	1	2
12k	Octahedral	Up (↑)	6	12
$4f_2$	Octahedral	Down (↓)	2	4
$4f_1$	Tetrahedral	Down (↓)	2	4
2b	Trigonal bi-pyramidal	Up (↑)	1	2

1.4Microwave absorbers

Microwave-absorbing materials are predominantly designed to prevent the transmission or reflection of EM waves, which can be achieved by combining metal plates with dielectrics at specific intervals or wavelengths. The effectiveness of microwave absorbers relies on their material preparation, component arrangement, thickness, and absorption frequencies. All the advantages of an EM absorber are not fulfilled by a single material. So, we need to consider a composite of EM absorbers in which the matrix is embedded by some filler. Generally, filler involves one or more material that is responsible for absorption, and it controls how and at what frequency the material will absorb the electromagnetic wave [26-27]. For example, polyaniline, polypyrrole, wax, rubber, etc. On the other hand, matrix material will hold the filler and protect it from mechanical and environmental damage. The matrix material is commonly selected for its physical properties such as weather resistance, flexibility, and temperature resistance.

1.4.1 Types of Microwave Absorbers

The microwave absorbers that are utilized to attenuate or absorb microwave radiation are categorized into two categories, as seen in Figure 1.4.

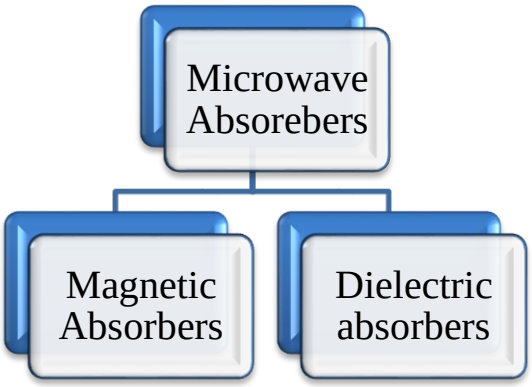

Figure 1.4. Types of Microwave Absorbers

Table 1.6. Comparison of Microwave Absorbers

Feature	Magnetic Absorbers	Dielectric Absorbers
Absorption Mechanism	Magnetic hysteresis and eddy current losses	Dielectric loss via internal polarization processes
Key Properties	High magnetic permeability, high magnetic loss	High electrical conductivity, high dielectric loss
Form Factors	Elastomers (silicone, nitrile, neoprene, urethane), hard epoxy	Low-cost foam, elastomers, composite materials
Weight	Heavier due to dense ferromagnetic materials	Generally lightweight
Cost	Expensive due to costly ferromagnetic fillers	Low cost, depending on filler materials
Applications	Environments with magnetic fields, EMI suppression	General EMI suppression, stealth technology
Examples	Ferrites, iron particles	Ceramic composites, carbon nanotubes (CNT), silicon rubber, $BaTiO_3$, conductive polymers
Advantages	Efficient microwave absorption in specific frequencies, high magnetic loss	Ease of fabrication, cost-effective, tunable absorption properties
Disadvantages	Heavy and expensive	Less effective at low frequencies, temperature limitations

1.5 Application of ferrites

Ferrites possess a diverse range of magnetic, electrical, and thermal properties, making them incredibly versatile across numerous applications (as illustrated in Figure 1.5). Some of their primary uses include:

1. Magnetic Recording
    - Data Storage: They are integral to tapes and hard drives for efficient storage of magnetic charges.
    - Tape Recorder Heads: Their strong magnetic characteristics make them ideal for this purpose [25–28].
2. Permanent Magnets
    - Motors & Generators: Ferrites provide durable magnetic components for electric motors and generators [29].
    - Speakers & Headphones: They play a key role in converting electrical signals into sound.
3. Transformers and Inductors

- Power Supplies: Ferrites serve as core materials in high-frequency inductors and transformers.
- RF/Microwave Inductors: They are used in filters and chokes to maintain signal integrity [30–31].

4. EMI Shielding
    - Suppressors: Ferrites help minimize electromagnetic interference in electronic devices.
    - Cable Shielding: Ferrite beads are employed to eliminate noise in cables [32].
5. Microwave Absorbers
    - Stealth Applications: They are used in defense technologies to reduce radar signatures.
    - EM Wave Blocking: Ferrites find use in both radar and various civilian applications for blocking electromagnetic waves [33–35].
6. Biomedicine
    - MRI: They function as contrast agents in magnetic resonance imaging.
    - Drug Delivery: Superparamagnetic iron oxide nanoparticles (SPIONs) enable targeted drug delivery and imaging [36–37].
7. Communication Systems
    - Antennas: Ferrites enhance signal reception in antennas.
    - Phase Shifters & Circulators: They are essential components in telecommunication systems [38].
8. Magneto-Optical Devices
    - Sensors/Actuators: These devices are sensitive to magnetic fields.
    - Data Storage: Ferrites are utilized in magneto-optical memory solutions [39].
9. Energy Applications
    - Supercapacitors: They improve the performance of energy storage in supercapacitors [40].
10. Radar Absorbent Materials (RAM)
    - Military Use: Ferrites are crucial in defense technology to decrease radar visibility [41].
11. Ferrite Cores in Electronics

- SMPS (Switched-Mode Power Supplies): They enable efficient power conversion in electronic devices [42].

12. Microwave Devices
    - Isolators & Circulators: Ferrites are core components in radar and communication systems [43].
13. Household Appliances
    - Washing Machines & Microwaves: They are used for magnetic coupling in various household appliances [44].

Ferrite materials are highly valued for their magnetic and electrical properties, which play a crucial role in a wide range of applications. Their versatility and significance in modern technology cannot be overstated.

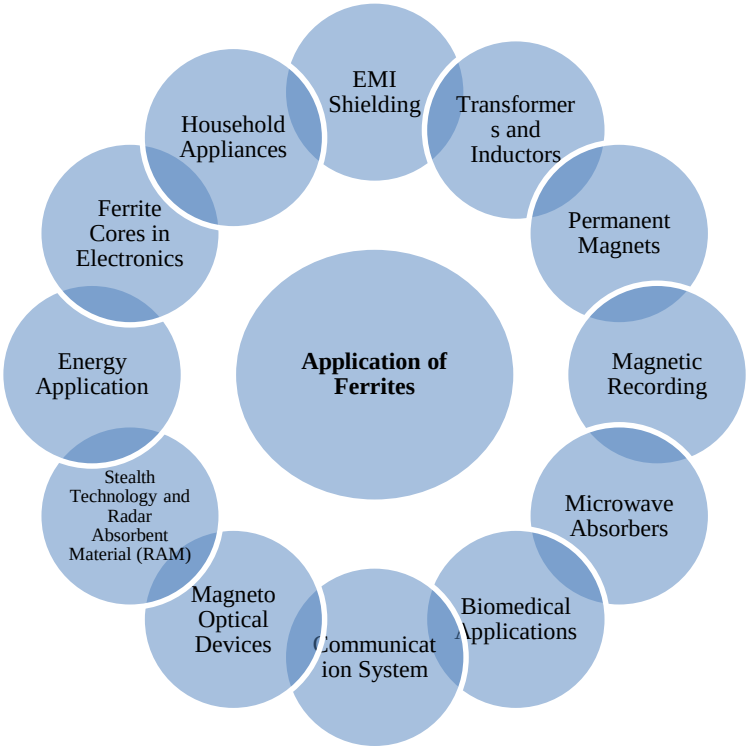

Figure 1.5. Application of Ferrites.

1.6 Synthesis of M-type Hexaferrite

M-type hexaferrites have garnered significant attention due to their exceptional structural, morphological, electrical, and magnetic characteristics. The method used to produce these materials greatly influences their final characteristics. The crystal structures, compositions, homogeneity, morphology, and scalability of the resulting hexaferrites can be influenced by various synthesis techniques. In addition, different

methods may differ in terms of how quickly they can be completed and how cost-effective they are. Scientists have utilized different synthesis methods to produce M-type hexaferrites, each with its own benefits and unique difficulties. Here is a brief summary of the main synthesis methods, including their characteristics, advantages, and difficulties [45-53].

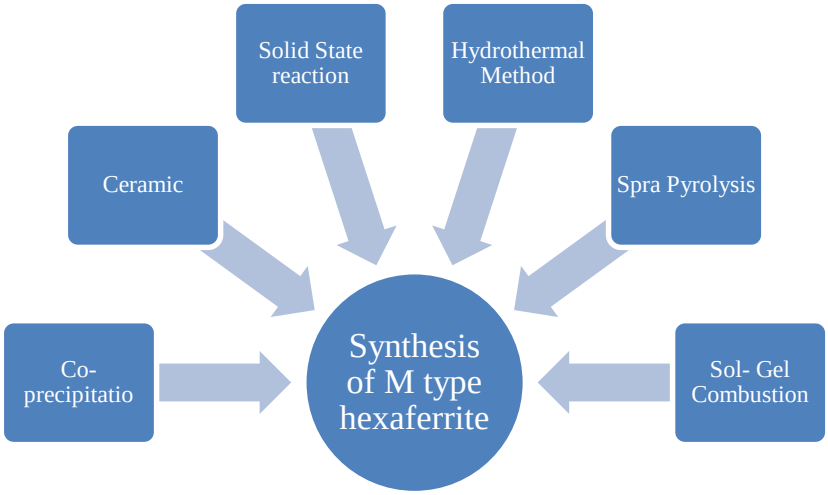

Figure 1.6. Various synthesis methods of M-type hexaferrite.

Table 1.7. Comparison of Various Synthesis Methods of M-type hexaferrite.

Synthesis Method	**Key Features**	**Benefits**	**Challenges**
Solid-State Reaction	Mixing solid reactants, followed by high-temperature calcination.	Simplicity, ability to produce phase-pure materials.	Requires high temperatures and long reaction times.
Hydrothermal Method	Reacting precursors in an aqueous solution at elevated temperatures and pressures.	Controlled particle size and shape, high purity.	Requires precise control of synthesis conditions, time-consuming.
Sol-Gel Combustion	Preparation of a sol from metal salts and organic fuel, followed by gel combustion.	Homogeneous particle distribution, cost-effective, environmentally friendly.	Handling of combustible materials, precise control needed.
Co-Precipitation	Co-precipitating metal ions from solution, followed by heat treatment.	Homogeneous materials, controlled particle size, good reproducibility.	Requires careful control of pH and temperature during precipitation.

Microemulsion	Using water-in-oil microemulsions as nanoreactors.	Produces uniform nanoparticles with controlled size and shape.	Requires surfactants and organic solvents, thorough washing is needed.
Combustion Synthesis	Rapid heating of a precursor mixture to ignite a self-sustaining combustion reaction.	Simple and fast synthesis, suitable for nanosized powders.	High temperatures can lead to non-uniform particle sizes and agglomeration.

1.7 Polyaniline

Polymers are composed of macromolecules, which are substantial molecules formed from repeating units. Conductivity can vary depending on the composition and structure of these materials. Polyaniline (PANI) is a conductive polymer that finds extensive use in a wide range of applications owing to its exceptional physiochemical properties. It is worth mentioning that PANI exhibits excellent thermal stability, is cost-effective to synthesize, possesses impressive corrosion resistance, and demonstrates enhanced conductivity. It has proven to be highly valuable in the realm of microwave absorption [54-56].

1.7.1 The Role of Polyaniline (PANI) in Microwave Absorption

PANI possesses various advantageous properties that make it suitable for microwave absorption. These encompass eddy current loss and a significant dielectric constant, which contribute to its conduction loss and facilitate polarization. In recent times, there has been a growing trend in utilizing PANI alongside various metallic and ferromagnetic materials. This is done to take advantage of PANI's mechanical strength, corrosion resistance, and EMI shielding capabilities, all while reducing the weight and corrosive nature of these materials. Out of the three forms of PANI (leucoemeraldine, pernigraniline, and emeraldine), the emeraldine form stands out as the most conductive, making it highly suitable for microwave absorption applications.

1.8 Chapter Outline

Chapter 1: This Chapter highlights the increasing significance of addressing electromagnetic (EM) interference in the context of rapid technological advancement. The proliferation of wireless devices, electronic systems, and military platforms has led to an environment saturated with EM radiation, posing health risks, operational challenges, and security vulnerabilities.

The chapter emphasizes the critical role of materials that can absorb or mitigate EM waves, such as ferrites and composites, which are essential for various applications, including stealth technology, EMI shielding, and microwave absorption. These materials work through mechanisms like dielectric and magnetic losses, with a focus on optimizing their performance through tuning of properties such as permittivity, permeability, and magnetic loss.

Chapter 2: This Chapter presents a comprehensive review of existing literature, identifies key research gaps, and outlines the objectives of the study. It synthesizes findings from prior studies on M-type hexaferrites and their composites, emphasizing their potential for electromagnetic interference (EMI) suppression and microwave absorption applications.

Chapter 3: This Chapter outlines the methodologies and techniques employed to synthesize and characterize the pure and doped barium hexaferrite materials and their composites, focusing on their structural, magnetic, electrical, and electromagnetic properties. The primary synthesis method utilized is the sol-gel auto-combustion technique, renowned for its precision in producing nanoscale materials with uniform properties. The study further explores the incorporation of polyaniline (PANI) to enhance the flexibility and electromagnetic performance of hexaferrite composites.

Chapter 4: This chapter presents the results and discussions regarding the investigated research work. The obtained results of ferrites and composites doped with Al, Ce, Cd and Cr are discussed and analyzed in detail. The structural analysis using XRD and morphological investigation using SEM has been explained. The electric/dielectric characteristics like dielectric constant, loss, electric modulus, ac conductivity, and impedance of the developed compositions have been explained in detail. This chapter also discusses the microwave absorption analysis of the prepared compositions based on Quarter wavelength and impedance matching mechanisms.

Chapter 5: This chapter presents the summary and conclusion of the investigated research work. The outcomes of the research performed are discussed in this chapter. This chapter also discussed the future aspects of the investigation performed.

Conclusion:

The introduction establishes the foundation for the research by:

- Identifying the critical need to address EMI challenges in modern technology.

- Showcasing the potential of ferrites, particularly M-type hexaferrites, in mitigating EMI through efficient microwave absorption.
- Highlighting the complementary role of materials like PANI in enhancing the performance of ferrite-based absorbers.

This chapter provides a roadmap for the subsequent exploration of novel ferrite composites tailored for high-performance EM absorption across multiple applications. The synthesis and characterization of these materials aim to bridge the gaps in existing technologies, ultimately contributing to advancements in stealth, communication, and EMI management.

CHAPTER-2
REVIEW OF LITERATURE, RESEARCH GAP, AND OBJECTIVES

2.1. Review of literature

The literature review is a crucial component of any research, providing a comprehensive foundation for achieving the research objectives. In this section, an extensive survey of existing literature is conducted to support and guide the research work.

Jing et al. (2024) synthesized praseodymium (Pr) and dysprosium (Dy) doped strontium ferrites using the sol-gel method. They studied the structural, magnetic, and absorption characteristics under varying calcination temperatures and doping levels. XRD analysis revealed the presence of both M-type phase and heterophase, induced by Pr and Dy doping. Micrograph images confirmed that grain size decreased with higher doping levels. The study found that saturation magnetization decreased while coercivity increased with increased Pr-Dy doping. The maximum reflection loss (RL) reported was -52.51 dB, with an absorption bandwidth of 4.81 GHz [66].

Wang et al. (2024) $Lu_xLa_ySr_{1-x}Fe_{12-x}O_{19}$, an M-type strontium ferrite, was synthesized via the co-precipitation method with rare-earth element doping aimed at enhancing its dielectric properties. X-ray diffraction (XRD) confirmed the formation of a hexagonal single-phase magnetoplumbite structure, while scanning electron microscopy (SEM) revealed a regular hexagonal grain morphology. Vibrating sample magnetometer (VSM) analysis indicated that the material is hard magnetic with high coercivity, which significantly decreased from 2065.3 to 910.3 Oe with increased doping of rare-earth elements (Lu–La). Dielectric measurements showed a substantial increase in the relative dielectric constant, ranging from 6.71×10^3 to 1.28×10^5 at low frequencies and from 3.09×10^3 to 2.03×10^4 at high frequencies. The high dielectric constant and low coercivity achieved through rare-earth doping make these ferrites suitable for use in electromagnetic shielding applications, where they can

effectively reduce interference from magnetic fields and block electromagnetic waves [67].

Jin et al. (2024) Ce^{3+}- doped M-type barium ferrite $BaCe_xFe_{12-x}O_{19}$ (x = 0–1.2) was synthesized using the sol-gel method to investigate the impact of Ce^{3+} doping on the crystal structure, microstructure, and electromagnetic properties. X-ray diffraction (XRD) analysis showed that the crystal structure of the M-type ferrite remained stable despite increasing Ce^{3+} content, with the grain size remaining constant in the micrometer range. Ce^{3+} doping significantly improved the electromagnetic and microwave absorption properties of $BaFe_{12}O_{19}$, primarily due to enhanced magnetic and dielectric losses. Among the various doping concentrations, $BaCe_{0.2}Fe_{11.8}O_{19}$ exhibited the best performance, achieving a minimum reflection loss of -58 dB and an effective absorption bandwidth of 9.44 GHz at a thickness of 2.3 mm. This research highlights the potential of Ce^{3+} - doped M-type barium ferrites as efficient electromagnetic wave absorbers with broad absorption bandwidths for applications in electromagnetic interference (EMI) shielding [68].

Wei et al. (2024) M-type barium ferrites ($Ba_{1-x}Nd_xFe_{12-x}M_xO_{19}$, x = 0–0.3) were synthesized with Nd^{3+} - M^{5+} (M = Nb^{5+}, Ta^{5+}) ion substitutions via a solid-state reaction to enhance their electromagnetic wave absorption properties. The substitution reduced the anisotropic field, lowering the natural resonance frequency and increasing the complex permittivity through interfacial and dipole polarization. This led to multiple natural resonances and improved impedance matching. The substituted ferrites achieved reflection losses of -35 to -50 dB, an ultrabroad bandwidth (~13.5 GHz), and low matching thickness (<0.75 mm) in the 26.5–40 GHz range. In the 2–18 GHz range, the x = 0.1 sample performed well with a matching thickness below 1.5 mm, making these materials excellent candidates for microwave absorption [69].

Panwar et al. (2024) M-type hexaferrites with the composition $Ca_{1-x}Bi_xFe_{12-x}Co_xO_{19}$ were synthesized through the sol-gel auto-combustion method to improve their structural, dielectric, and magnetic characteristics. The analysis through X-ray diffraction (XRD) validated the presence of a single-phase hexagonal structure, with

crystallite sizes measured between 42 and 49 nm. The findings indicated that higher levels of Bi and Co doping resulted in reduced bulk and X-ray densities, accompanied by an increase in porosity. Furthermore, the dielectric measurements indicated a significant dielectric constant at lower frequencies, which diminished as the frequency increased, alongside a decrease in dielectric loss due to doping. The magnetic analysis revealed that saturation magnetization varied between 15.51 and 38.27 emu/g, whereas coercivity exhibited a notable increase from 207.93 to 1359.69 Oe. The materials demonstrate significant potential for application in contemporary electronic devices, attributed to their enhanced dielectric and magnetic characteristics. [70].

Yang et al. (2024) the powders $Sr_{1-x}Ce_xFe_{12}O_{19}$ and $Sr_{1-x}Ce_xFe_{12-\gamma}O_{19-\delta}$ (where x = 0–0.2) were synthesized through the sol-gel auto-combustion method to investigate the influence of cerium doping and iron content on their structural and magnetic characteristics. The analysis via XRD validated the existence of M-phase ferrite, in addition to impurities such as CeO2 and Fe2O3. The analysis via SEM indicated that the introduction of cerium resulted in a decrease in grain size. The saturation magnetization for $Sr_{1-x}Ce_xFe_{12}O_{19}$ first rose to 77.73 emu/g before declining with additional cerium doping. The interplay between cerium doping and iron content modified the distribution of iron ions, influencing magnetic properties. The magnetic properties of $Sr_{1-x}Ce_xFe_{12-\gamma}O_{19-\delta}$ exhibited fluctuations in relation to iron content, underscoring the ability to modify magnetic behaviour through the adjustment of these parameters. [71].

Chen et al. (2024) Ho-doped strontium ferrite powders with different Fe/Sr ratios were successfully synthesized using the sol-gel auto-combustion method to investigate the effects of Ho doping on their structure and magnetic properties. XRD analysis showed changes in secondary phases like Fe_2O_3, $HoFeO_3$, and $SrFeO_{3-x}$ as the Fe/Sr ratio varied. SEM confirmed that Ho doping increased the grain size, and XPS indicated changes in iron's oxidation state. VSM measurements revealed that coercivity decreased from 5.26 to 4.78 kOe, and saturation magnetization decreased from 76.73 to 73.28 emu/g as the Ho doping level increased. The Fe/Sr ratio

influenced magnetic properties, with saturation magnetization first increasing and then decreasing, while coercivity exhibited the opposite trend [72].

Kayalvizhi et al. (2024) synthesized strontium ferrite and reduced graphene oxide (rGo) composites using the hydrothermal method. The microwave absorption analysis showed that particle size decreased from 55.60 to 41.55 nm with the inclusion of rGo. This non-magnetic inclusion also reduced the magnetic properties, with saturation magnetization decreasing from 53.3 to 35.89 emu/gm. Coercivity increased from 2679 to 3606 Oe with the addition of rGo, while RL values for ferrite and rGo composites were -28.49 dB and -23.78 dB, respectively [73].

Yang et al. (2024) explored the band gap, magnetic, and absorption properties of Zn^{2+} and Sn^{4+} doped barium hexaferrites synthesized by the auto-combustion method. The band gap increased from 1.80 to 1.97 eV with increasing doping levels. Doping also reduced magnetic saturation, coercivity, and anisotropy field. The absorption bandwidth was found to be 6 GHz, with an absorption band from 11.4 to 17.4 GHz. Carbon nanotube (CNT) composites, prepared via the hydrothermal method, showed improved microwave absorption, with a bandwidth of 7.1 GHz at similar thickness [74].

Wei et al. (2024) High-performance microwave absorbing coatings were developed using helical carbon nanotubes/doped barium ferrite composites with an epoxy resin matrix. The coating's concentration and thickness were optimized through numerical simulations and an adaptive genetic algorithm. The composites exhibited a porous structure with good conductivity and uniformity, leading to absorption bands in the 10–18 GHz range. The optimized coating achieved a reflection loss of -17.22 dB at 16.66 GHz and an absorption bandwidth of 9.16 GHz. These coatings showed strong potential for Ku-band microwave absorption applications [75].

Shu et al. (2024) Nitrogen-doped reduced graphene oxide/magnesium ferrite/polyaniline (NRGO/$MgFe_2O_4$/PANI) composite aerogel was successfully synthesized through solvothermal reaction, in situ chemical oxidation polymerization,

and hydrothermal self-assembly. The aerogel exhibited a 3D porous network structure with a low bulk density of 11.1–13.0 mg cm^{-3}. $MgFe_2O_4$ nanoparticles, coated with a thin PANI layer, were anchored onto the NRGO sheets. The composite aerogel showed significantly better microwave absorption performance than pure NRGO or NRGO/ $MgFe_2O_4$ composites. At a filling ratio of 11.5 wt.%, the aerogel achieved a maximum absorption bandwidth of 7.0 GHz and a minimum reflection loss of −42.9 dB [76].

Mudasar et al. (2024) cobalt/zinc-doped hexagonal ferrite flakes were successfully anchored on $Ti_3C_2T_x$ MXene through heterogeneous interface engineering to optimize electromagnetic parameters and microwave absorption properties. $Ti_3C_2T_x$ MXene was synthesized via hydrofluoric acid etching, and doped ferrite was prepared through solid-state sintering. SEM analysis revealed strong adhesion between ferrite particles and the MXene surface. The composite of doped ferrite@4% $Ti_3C_2T_x$ reached a peak reflection loss of -49 dB at 15.2 GHz, with a thickness of 1.9 mm and a noticeable absorption bandwidth of 8.3 GHz. Radar cross-section simulations showed a reduction of up to -47.8 dBsm at a 60° incident angle, highlighting its potential as an electromagnetic wave absorber [77].

Bala et al. (2024) nickel ferrite and activated carbon composites were developed using the mechanical alloying method, with nickel ferrite nanoparticles synthesized via the sol-gel auto-combustion technique. Various analytical methods confirmed the formation of the composite. Electromagnetic properties were assessed using a vector network analyzer to explore its potential for defence applications. The composite was applied as a coating on a metal sheet, and reflection coefficients were measured in the 2–18 GHz range. The NC-2 composite showed a reflection coefficient exceeding −10 dB, demonstrating its potential as a promising microwave absorber in the X-Band [78].

Yunasfi et al. (2024) Nickel ferrite, known for high permeability, was synthesized with La^{3+} ion substitution to increase permittivity, using co-precipitation techniques followed by sintering at 1200 °C for 5 hours. XRD analysis confirmed a single-phase

cubic spinel structure for $NiLa_xFe_{(2-x)}O_4$ samples. SEM images showed inconsistent particle sizes ranging from 100-800 nm. VSM analysis revealed ferromagnetic behaviour, with saturation magnetization decreasing from 35.89 to 21.54 emu/g and coercivity increasing from 249 to 416 Oe with higher La^{3+} content. Microwave absorption improved, with reflection loss increasing from 11.16 dB to 15.41 dB, reaching up to 97.11% absorption at x = 0.04 [79].

Kaur et al. (2024) A series of nickel and zirconium co-substituted zinc-cobalt spinel ferrites, with the formula $Zn_{0.25}Co_{0.75}(NiZr)_xFe_{2-2x}O_4$ ($0.05 \leq x \leq 0.25$), was successfully synthesized using the sol-gel citrate route to address electromagnetic pollution from 5G technologies. X-ray diffraction confirmed the formation of nanoparticles with a cubic spinel structure. The magnetic properties, such as saturation and remanent magnetization, exhibited a decline with the increasing substitution of Ni^{2+} and Zr^{4+}. Electromagnetic and absorption characteristics were studied in the Ka-band (26.5–40 GHz), with composition x = 0.10 achieving a reflection loss of −50.34 dB at 29.20 GHz and a thickness of 1.3 mm. These results indicate that the materials are effective microwave absorbers for next-generation applications [80].

Siddique et al. (2024) Nanoparticles of $Cd_{0.5-x}Zn_xCo_{0.5}Fe_2O_4$ (where x = 0.0, 0.1, 0.2, 0.3) were synthesized using the sol-gel auto-ignition technique. The XRD analysis validated the presence of a mono-phase cubic spinel structure, while IR spectroscopy revealed two absorption bands associated with tetrahedral and octahedral sites, which exhibited shifts with the increase in Zn content. The saturation magnetization exhibited an increase from 58.92 to 106.41 emu/g, whereas the coercivity showed a decrease from 246.47 to 192.10 Oe due to Zn^{2+} substitution. Among the samples, $Cd_{0.2}Zn_{0.3}Co_{0.5}Fe_2O_4$ showed a minimum reflection loss of −26.85 dB at 3.90 GHz, highlighting its potential as an effective electromagnetic wave absorber for high-frequency applications. [81].

Akhtar et al. (2024) Zr-In co-substituted Ni-Zn nano ferrites with the composition $Ni_{0.7}Zn_{0.3}(ZrIn)_xFe_{2-2x}O_4$ (x = 0 to 0.20, with 0.05 increments) were successfully

synthesized using the citrate-gel self-ignition method to address EMI issues. XRD, FESEM, FTIR, and VSM analyses confirmed the formation of spinel-based structures with circular and hexagonal particle shapes. FTIR verified the phase formation, while VNA measurements showed a minimum reflection loss of -61.5 dB at 2.43 GHz for the x = 0.20 sample. The x = 0.15 sample exhibited a reflection loss of -57.3 dB at 1.93 GHz and an absorption peak at 5.8 GHz. These Zr-In doped Ni-Zn meta-absorbers demonstrated excellent potential for high-frequency EMI shielding applications, particularly in the C band [82].

IjaZ M. (2024) examined the influence of cobalt on the magnetic and microstructural characteristics of sol-gel synthesized barium-strontium hexaferrite with the composition $Ba_{0.6}Sr_{0.3}Er_{0.1}Fe_{11.5-x}Al_{0.5}Co_xO_{19}$ ($0.0 \leq x \leq 2$). The analysis through X-ray diffraction (XRD) validated the emergence of a hexagonal phase, while scanning electron microscopy (SEM) illustrated a consistent particle distribution throughout all samples. The application of the hysteresis loop technique for magnetic measurements demonstrated that the incorporation of cobalt notably improved the magnetic properties. The saturation magnetization rose from 37.76 emu/g at x = 0.0 to 57.12 emu/g at x = 1.5. At x = 1.5, the anisotropy field (H_a) measured 1.303 kOe, while the coercivity (H_c) was recorded at 4.172 kOe. The findings indicate that these cobalt-doped samples hold significant potential for use in magnetic applications. [83].

Khan M. (2023) the sol-gel auto-combustion method was used to make Ba–Sr hexaferrite nanoparticles, and ultrasonication and in-situ polymerization were used to combine them with multi-walled carbon nanotubes (MWCNTs) and conductive polymers. X-ray diffraction and spectroscopy techniques confirmed the formation of the materials. Dielectric measurements revealed significant increases in losses in ternary composites, rising from 304 to 7861, indicating effective energy dissipation. The weakening of exchange coupling at the ferrite-MWCNT interface caused a shift in magnetic resonance to lower frequencies. The $Ba_{0.5}Sr_{0.5}Fe_{12}O_{19}$/MWCNTs/Polythiophene composite demonstrated a maximum shielding effectiveness of -34 dB at 8.1 GHz, with a reflection loss of -39 dB at 7.4 GHz, matching military radar frequencies [84].

Thanh T. (2023) MFe_2O_4 (M = Co, Fe, Mn) nanoparticles were synthesized using the chemical co-precipitation technique. $CoFe_2O_4$, Fe_3O_4, and $MnFe_2O_4$ were found to have distinct crystalline nanoparticles with grain sizes of 15 nm, 9 nm, and 34 nm, respectively, after structural characteristics were investigated using X-ray diffraction, scanning electron microscopy, and energy-dispersive X-ray analysis. Raman spectroscopy confirmed the spinel structure, while UV-visible spectroscopy estimated the direct bandgap energy to be around 2.59–2.64 eV. Photoluminescence spectra further supported these results. Magnetic property investigations showed that ion distribution and exchange interactions influenced the coercivity and squareness ratio, with $CoFe_2O_4$ displaying strong anisotropy and higher coercivity compared to Fe_3O_4 and $MnFe_2O_4$ [85].

Tian et al. (2023) Hexaferrites $Ba_2Co_2Mn_xFe_{12-x}O_{22}$ (x = 0.0 to 1.6) were synthesized through the solid-phase sintering method to investigate the impact of Mn substitution on their structural, magnetic, and microwave absorption characteristics. The introduction of Mn ions resulted in lattice distortion, leading to an initial increase followed by a decrease in the concentration of oxygen vacancies. The real component of the dielectric constant (ε') showed a decline as the Mn content increased, whereas the permeability (μ') exhibited an increase attributed to diminished magneto-crystalline anisotropy. The effective absorption bandwidth (EAB) increased from 5.5 GHz to 9.1 GHz with the rise in Mn substitution. The formulation with x = 1.2 reached an EAB of 8.74 GHz at a thickness of 1.57 mm, demonstrating effective absorption and a wide bandwidth, which can be ascribed to multiple reflections, resonance, and impedance matching. [86].

Liu X. (2023) Barium hexaferrite (BaM)/polyaniline (PANI) composites were enhanced through rare earth element doping to improve microwave absorption properties. Rare earth elements like La, Nd, and Ce were introduced into BaM particles, alleviating constraints on electric polarization in PANI near the BaM surfaces, which led to increased polarization at the Re-BaM and PANI interfaces. This method improved absorption efficiency, expanded the frequency range, and reduced

composite thickness. The La-BaM/PANI composite achieved a maximum reflection loss of -63.6 dB at 7.76 GHz with a thickness of 3.28 mm. The Nd-BaM/PANI composite had an effective absorption range of 4.72 GHz, while Ce-BaM/PANI provided a broad absorption range of 3.88 GHz at a thickness of 1.58 mm [87].

Verma et al. (2023) The solid-state reaction method was used to successfully make polycrystalline samples of M-type hexaferrite with the formula $BaZn_xZr_xFe_{12-2x}O_{19}$ (x = 0.1–0.7). The structural study showed that the phase was pure. As the dopant concentration went up, the crystallite size went down from 149 nm to 69 nm and the cell volume went up. The average grain size was between 0.61 and 0.79 µm, and as Zn^{2+} and Zr^{4+} doping levels went up, porosity went down. Magnetic studies showed that the saturation magnetization went up to 72.87 emu/g at x = 0.1, then went down. At the same time, the coercivity kept going down from 4118 Oe to 319 Oe. These features suggested that the material might be useful for magnetic data storage, microwave absorption, and spintronic devices. [88].

Khan K. (2023) Nanocomposites of $(MgFe_2O_4)_{100-x}/(BaFe_{12}O_{19})_x$ with varying hard ferrite ratios (x = 0, 25, 50, 75, and 100) were synthesized through the in-situ auto-combustion sol-gel method. The XRD analysis demonstrated the presence of both hexaferrite and spinel ferrite phases, free from impurities, with no notable variation in crystallite size detected. Magnetic measurements revealed a robust interphase exchange coupling, while a weaker coupling was noted for x = 50. Impedance analysis demonstrated that both grains and grain boundaries played a role in the overall conduction mechanism. The findings indicated that the elevated impedance values of the nanocomposites rendered them appropriate for applications in electromagnetic shielding and high band-pass filters. [89].

Gupta A. (2023) $SrFe_{8-x}Al_4Zn_xO_{19}$ ($0 \leq x \leq 1$) hexaferrites were synthesized using the sol-gel auto-combustion method to enhance the magnetic properties of strontium hexaferrite magnets. The impact of Zn substitution on the structural, magnetic, dielectric, and electrical properties was investigated. The energy density $(BH)_{max}$ was significantly improved to 19.15 MGOe, making this composition a cost-effective

alternative for permanent magnet applications. The dielectric properties exhibited typical hexaferrite behaviour, explained by the Maxwell-Wagner theory and Koop's model. This research provides an economical substitute for rare-earth-based permanent magnets [90].

Sahu et al. (2023) Sr^{2+} ion-doped nickel cobalt nano ferrite ($Ni_{0.5}Co_{0.45}Sr_{0.05}Fe_2O_4$) was synthesized using a high-energy ball mill. The composition NCFOS2 exhibited the highest saturation magnetization (M_s) of 60 emu/g. Magnetic properties such as remanent magnetization, coercivity, and anisotropy constant were found to increase up to NCFOS2, after which they decreased. The relationship between magnetic properties and induced lattice strain was established. Electromagnetic wave parameters were studied in the Ku band, with the highest reflection loss (RL) of -35.59 dB observed at 17.74 GHz for a thickness of 3 mm. These findings indicate that Sr-doped nano ferrite is a promising material for microwave absorption applications [91].

Caliskan S. (2023) Co-V co-substituted nano Sr-hexaferrites, $Sr_{0.5}Co_{0.5}V_xFe_{12-x}O_{19}$ (x = 0.00 to 0.08), were synthesized using the citrate combustion route. XRD analysis showed crystallite sizes ranging from 37 to 83 nm, and SEM, TEM, and EDX confirmed their hexagonal morphology and chemical composition. XPS revealed the oxidation states, while Mossbauer spectra indicated that V^{3+} content affected the electron density around Fe^{3+} ions. Magnetic properties, including M_s, M_r, and nB, peaked at x = 0.04, with all samples exhibiting hard magnetic behaviour. Microwave measurements in the 2–18 GHz range displayed non-linear properties, with reflection losses linked to dipole polarization processes [92].

Rana K. (2023) A pure M-type strontium hexaferrite ($SrFe_{12}O_{19}$) was synthesized using a modified citrate precursor method and sintered at 800 °C and 910 °C. XRD confirmed the formation of the M-phase with minor Fe_2O_3 impurities, supported by FTIR and Raman spectroscopy. FESEM revealed densely packed grains with hexagonal platelets. The saturation magnetization (M_s) increased from 81 emu/g to 92 emu/g with higher sintering temperatures, while the coercivity (H_c) rose from 107 Oe

to 262 Oe. The squareness ratio increased from 0.26 to 0.54, indicating a transition from multidomain to single-domain behaviour [93].

Gulbadan et al. (2023) $Ba_{0.6}Sr_{0.4-x}Yb_xFe_{12-y}Co_yO_{19}$ ($0.0 \leq x \leq 0.125$, $0.0 \leq y \leq 1.25$) M-type hexaferrites were synthesized using the auto combustion sol-gel method and sintered at 1200 °C for 5 hours. XRD analysis confirmed the pure single-phase structure of the Yb–Co co-substituted hexaferrites, with changes in Yb–Co concentration affecting lattice parameters and unit cell volume. FTIR and Raman spectroscopies revealed the formation of various absorption bands, while photoluminescence spectra showed emissions in the 630 nm–700 nm range. The bandgap for the pure sample ranged from 1.961 to 1.875 eV. Substitution improved dielectric losses and AC conductivity, making these materials suitable for microwave and high-frequency applications according to the Maxwell-Wagner theory [94].

Ramirez-Ayala M. (2023) The incorporation of neodymium (Nd) into strontium hexaferrite ($SrFe_{12}O_{19}$) using the sol-gel Pechini method significantly altered its microstructural, magnetic, and structural properties. Partial incorporation of neodymium into the hexaferrite structure led to the formation of neodymium orthoferrite as a secondary phase, which had a notable impact on the material's magnetic behaviour. X-ray diffraction (XRD) and Rietveld refinement were employed to investigate the structural modifications, while magnetic properties were analyzed using vibrating sample magnetometry (VSM). Microstructural analysis, conducted through electron microscopy, revealed changes in grain morphology due to Nd incorporation. The presence of up to 2.85 wt% neodymium orthoferrite resulted in a 35% increase in the maximum energy product (BH_{max}), which was attributed to enhanced magnetic interactions between the hexaferrite and neodymium orthoferrite phases [95].

Mironovich A. (2023) $BaFe_{12-2x}Ni_xO_{19}$ ($x = 0, 0.1, 0.3, 0.5$) hexaferrites were synthesized via the hydrothermal method followed by post-annealing. XRD and EDX analyses confirmed the successful incorporation of Ni ions into the barium hexaferrite crystal structure. Mossbauer spectroscopy and magnetic measurements indicated that

Ni^{2+} ions predominantly occupied the 12k sites, which resulted in a significant reduction in saturation magnetization (M_s) from 65.88 emu/g to 49.13 emu/g as the Ni content increased. The magnetic parameters, including saturation magnetization, coercivity, and remanence, decreased progressively with higher Ni concentrations, likely due to the creation of oxygen vacancies for charge compensation, adversely affecting the overall magnetic behaviour [96].

Gui et al. (2023) W-type $Ba_{1-x}La_xCo_2Fe_{16-y}Al_yO_{27}$ hexagonal ferrite was synthesized using the sol-gel auto-combustion method. XRD analysis confirmed the formation of the desired W-type magneto-plumbite structure, while SEM revealed a reduction in grain size with the introduction of La^{3+} and Al^{3+} ions. Electromagnetic wave absorption was significantly enhanced due to improved dielectric and magnetic losses, as well as better impedance matching. The sample with x = 0.05 and y = 0.5 exhibited a reflection loss of -50.13 dB at 11.9 GHz and 7.0 mm thickness, with an absorption bandwidth of -20 dB ranging from 11.6 to 12.2 GHz. These results highlight the potential of La–Al co-doped ferrites for effective microwave absorption applications [97].

Nishkala K. (2023) La-substituted barium hexaferrite, $Ba_{(1-x)}La_{(x)}Fe_{12}O_{19}$ (x = 0, 0.1, 0.15, 0.20), was synthesized via ball milling and subsequent heat treatment. Rietveld analysis of XRD patterns confirmed the formation of a single-phase magnetoplumbite structure across all samples. FESEM analysis showed hexagonal plate-like grains, with the grain size decreasing as La content increased. EDS verified that the elemental composition was within the expected range. Density measurements indicated a reduction in porosity up to x = 0.15, followed by a slight increase at x = 0.20. Mössbauer spectroscopy revealed no formation of Fe^{2+} ions, but electron delocalization occurred with La doping. The dielectric constant reached its maximum at x = 0.20, and P-E loop analysis demonstrated enhanced polarization with La substitution, showing both leaky and resistor circuit-type behaviour [98].

Fasate S. (2023) Manganese-substituted barium hexaferrite ($Ba_{1-x}Mn_xFe_{12}O_{19}$, x = 0.0 to 0.5) was synthesized using the sol-gel auto-combustion method with citric acid as a

chelating agent. The prepared powder was annealed at 950 °C for 12 hours to remove impurities and moisture. The study found that DC electrical resistance decreased with increasing temperature and Mn^{2+} concentration, exhibiting semiconductor behaviour. Dielectric constant, dielectric loss, and dielectric loss tangent decreased with increasing frequency and Mn^{2+} substitution. Magnetic properties showed a decrease in saturation magnetization with higher levels of Mn substitution [99].

Chagas P. (2023) Analyze the effect of Sn-substitution on the electrical conductivity of $SrFe_{12}O_{19}$ hexaferrite, synthesized using the solid-state reaction method. Impedance analysis showed two conductive processes, with grain boundary resistance significantly higher than grain resistance, aligning with the Koop model. Conductivity increased with higher Sn^{4+} content, revealing a DC-conductivity process at low frequency and a frequency-dependent process at high frequency. Activation energy analysis indicated a small polaron tunnelling mechanism with negative activation energy at low frequency and an electron hopping mechanism with activation energies ranging from 0.135 to 0.355 eV [100].

Bilovol V. (2023) $SrFe_{12}O_{19}/CoFe_2O_4$ composites were fabricated with varying weight fractions (x = 10, 20, 30, 40 wt%) of hexagonal and cubic ferrite powders through ball milling, followed by annealing at 900 °C for 3 hours. Structural analysis using X-ray diffraction confirmed the composite phases, and energy dispersive X-ray analysis verified the elemental composition. Magnetic properties, measured through various techniques, showed that magnetic interactions were affected by the proportions of each component. The composite containing 10 wt% $CoFe_2O_4$ exhibited the highest energy product $(BH)_{max}$ of 10.9 kJ/m^3, which was approximately 20% higher than pristine $SrFe_{12}O_{19}$. This enhancement was attributed to the exchange coupling effect observed in Henkel plots [101].

Zhang et al. (2022) M-type $Sr_{0.7}La_{0.3}Zn_{0.3}Fe_{11.7-x}Al_xO_{19}$ hexaferrites were synthesized using the conventional solid-state reaction method at 1240 °C. XRD analysis confirmed the presence of a single magnetoplumbite phase in all samples, with no secondary phases detected. FT-IR and Raman spectra indicated that Al^{3+} ions

entered the lattice structure. FE-SEM revealed platelet-like grains, and EDS confirmed the presence of predetermined elements. The dielectric properties were optimized with varying Al content, consistent with hexaferrite characteristics. VSM analysis showed a 96.4% increase in coercivity (H_c), reaching 4576.8 Oe at x = 1.5, compared to undoped samples [102].

Akthar et al. (2022) Rare-earth (RE) doped graphene-based $NiFe_2O_4$ nanocomposites were synthesized using the sol-gel auto-combustion method and hydrothermal technique. The structural, magnetic, and thermal properties were determined using TGA/DTA, FESEM, UV-Vis, and VSM. The optical band gap of the nanocomposites decreased from 2.66 to 1.65 eV with RE doping. Magnetic saturation increased from 11.552 emu/g to 46.243 emu/g due to the incorporation of Yb^{3+}, Gd^{3+}, and Sm^{3+} ions. DC conductivity values ranged from 1.75×10^{-3} to 4.24×10^{-3} S cm^{-1}, while activation energy in the paramagnetic region varied between 0.0171 and 0.1890 eV [103].

Zareef Khan M. (2022) $BaFe_{12}O_{19}/NiFe_2O_4$ nanocomposites with different concentrations (x = 0, 0.3, 0.5, 0.7, and 1) were synthesized, with average crystallite sizes ranging between 27–34 nm. The merging of ZFC/FC magnetization curves for x = 0.7 indicated strong magnetic interactions due to spring exchange coupling between hard and soft magnetic phases. A sharp increase in coercivity and saturation magnetization for x = 0.7 and x = 0.5 further supported the presence of this coupling. The smallest Bloch's constant for x = 0.7 and a single peak in the dM/dH vs. H plot for x = 0.5 provided additional evidence of strong exchange coupling. These findings suggest that magnetic interactions in these nanocomposites are strongly dependent on the concentration of hard and soft ferrite phases [104].

Karnajit Singh H. (2022) Al^{3+}- substituted polycrystalline $Ba_{0.4}La_{0.1}Sr_{0.5}Al_xFe_{12-x}O_{19}$ ($0 \leq x \leq 1$) hexaferrites were prepared using the solid-state method. XRD and Rietveld refinement confirmed the formation of a magneto-plumbite hexaferrite structure with decreased lattice parameters as Al^{3+} content increased. The complex permittivity values (ε' and ε") decreased with increasing Al^{3+} concentration, while

coercivity and anisotropy field increased. The saturation magnetization deviated from Bloch's T3/2 law but fit well with Dyson's approximation up to the T5/2 term. Magnetic anisotropy constant K1 (T) was linearly fitted with cubic saturation magnetization, confirming uniaxial hexagonal crystal symmetry in all samples [105].

Hassan et al. (2022) β-type hexagonal ferrite $KCe_xFe_{11-x}O_{17}$ (x = 0, 0.02, 0.06, and 0.1) was synthesized using the sol-gel auto-combustion method. XRD analysis confirmed the formation of a single-phase structure for all samples. The Williamson-Hall (W-H) technique indicated that both pure and Ce-substituted samples exhibited positive tensile microstrain. The dielectric properties, such as dielectric constant and loss, decreased with increasing frequency, while AC conductivity increased. The M-H loops revealed changes in saturation magnetization and coercivity with Ce^{3+} substitution, and one sample uniquely showed both ferromagnetic and diamagnetic behaviour [106].

Shakir H. (2022) Polypyrrole was successfully coated on barium ferrites using in-situ polymerization. The average particle size achieved for both barium ferrites and polypyrrole was approximately 50 nm. Barium hexaferrite-polypyrrole (BHF-Ppy) nanoparticles were synthesized, and the resulting films demonstrated high electromagnetic interference (EMI) shielding effectiveness of up to 60 dB in the microwave region. Characterization techniques such as SEM, XRD, and VSM confirmed the properties of the materials. Less than 1% transmission was observed in the near-infrared region, indicating excellent shielding performance [107].

Chauhan C. (2022) $SrFe_{12}O_{19}/NiFe_2O_4$ nanocomposites with varying weight ratios were synthesized using crown flower extract. XRD and FTIR analysis confirmed the coexistence of M-type hexagonal and spinel phases, with hexagonal platelets representing the M-phase and spherical particles for the S-phase. Magnetic measurements revealed a decrease in coercivity and saturation magnetization as the spinel phase content increased. Composites with ratios of 9:1, 8:2, 7:3, and 6:4 exhibited hard ferrite characteristics, while the 5:5 ratios displayed soft magnetic

behaviour. Exchange coupling interactions were found to be weak in 9:1 and 8:2 ratios, partial in 7:3 and 6:4, and perfect in the 5:5 composite [108].

Singh et al. (2022) analyze the microwave absorption properties of Co-Y doped Ba-Sr hexaferrites within the 8.2–12.4 GHz range. X-ray analysis confirmed the M-phase at low doping levels, while a spinel phase appeared at higher doping concentrations. The composition with x = 0.2 exhibited a reflection loss of −28.72 dB at 11.64 GHz with a thickness of 1.5 mm, while the x = 0.8 composition showed a bandwidth-to-thickness ratio of 3.6 at 10.55 GHz. The absorption characteristics were influenced by magnetic and dielectric losses, as well as impedance matching. These results indicated the potential use of the compositions for lightweight and wide-bandwidth electromagnetic absorbers [109].

Dilshad et al. (2022) Aluminium-substituted M-type hexaferrites with the composition $SrAl_{2x}Fe_{12-2x}O_{19}$ (x = 0.0 to 1.0) were successfully synthesized using the sol-gel auto combustion method. XRD analysis confirmed the formation of M-type hexagonal ferrites with high purity. The lattice parameters, cell volume, and crystallite size were calculated, with 'a' ranging from 5.86 to 5.88 Å, 'c' from 22.87 to 23.08 Å, and crystallite sizes between 39 and 61 nm. The optical bandgap decreased with increasing aluminium substitution, ranging from 1.74 to 2.80 eV. The dielectric constant reached a maximum of 15.5 for x = 1.0 at 2.5 GHz, and the dielectric parameters were explained using space charge polarization and electron hopping models. These materials are suitable for use in high-frequency devices like modulators, sensors, and energy storage systems [110].

Godara S. (2022) Calcium-substituted barium hexaferrites, $Ba_{1-x}Ca_xFe_{12}O_{19}$ (x = 0.0–0.5), were synthesized using the sol-gel auto-combustion method. XRD analysis showed that the samples remained in a pure phase up to x = 0.20, with a secondary phase (α-Fe_2O_3) appearing beyond this concentration. FESEM revealed that the average grain size increased from 140 nm to 276 nm with increasing Ca^{2+} substitution. Raman spectroscopy indicated improved crystallinity with calcium substitution up to x = 0.20. The saturation magnetization (M_s) peaked at 72.38 emu/g

for x = 0.20, and the coercivity (H_c) ranged from 5043 to 5290 Oe. The dielectric constant also improved with calcium substitution up to x = 0.3, highlighting the potential of these materials for permanent magnet applications [111].

Basha et al. (2022) $Sr_{1-x}La_xFe_{12}O_{19}$ (x = 0.2–0.8) nanoparticles were synthesized using the hydrothermal technique and characterized for their structural, electrical, and magnetic properties. X-ray diffraction confirmed the formation of hexagonal peaks, with lattice constants increasing from 0.58801 to 0.58825 nm (a = b) and from 2.30309 to 2.30341 nm (c) as the dopant content increased. Morphological studies showed that the nanoparticles exhibited a nearly spherical shape. The optical bandgap (E_g) was observed to increase from 1.866 to 2.118 eV with higher La doping. Electrical properties were analyzed as a function of temperature and frequency, with dielectric modulus and impedance spectroscopy used to explore space charge polarization and conduction mechanisms. The magnetic analysis revealed a decrease in magnetization from 36.34 to 7.17 emu/g as La content increased [112].

Yousaf et al. (2022) $BiNd_xCr_xFe_{1-2x}O_3$ (x = 0, 0.05, 0.10, 0.15) nanoparticles were synthesized to explore their tunable microwave absorption characteristics. The incorporation of Nd and Cr into the bismuth ferrite (BFO) structure was found to reduce dielectric losses and enhance magnetization by introducing interfacial defects. Nd and Cr co-doping helped improve the ordering of the BFO crystal structure, leading to enhanced microwave absorption properties. The $BiNd_{0.10}Cr_{0.10}Fe_{1.8}O_3$ (BNCF2) sample demonstrated a reflection loss of −37.7 dB at a 3 mm thickness within the 10.15 GHz-10.30 GHz frequency range. This work suggests that Nd and Cr doping in BFO nanoparticles offers a promising approach for developing efficient materials for microwave absorber applications [113].

Zahid et al. (2022) Hexaferrites of $Sr_{1-x}Cr_xFe_{12}O_{19}$ (x = 0.0 to 0.5) were synthesized using the citrate sol-gel method. X-ray diffraction confirmed the formation of a single-phase M-type hexaferrite structure, with lattice parameters increasing as the Cr^{3+} content increased. Scanning electron microscopy revealed a reduction in grain size with higher Cr^{3+} substitution. The dielectric constant and AC conductivity

increased with Cr^{3+} content, while dielectric loss and tangent loss decreased with increasing frequency. Saturation magnetization varied due to the different site occupancy of iron ions, and coercivity values ranged from 6.64 to 6.72 kOe, making the materials suitable for high-frequency applications [114].

Purnama et al. (2022) Strontium-substituted cobalt ferrite nanoparticles were synthesized using the co-precipitation method. Thermogravimetric analysis revealed that the reduction in mass was influenced by the presence of strontium cations. X-ray diffraction confirmed the formation of single-phase nanoparticles, indicating that strontium cations replaced metal cations in the cobalt ferrite structure. The crystallite size increased with higher annealing temperatures, while crystalline stress decreased. Saturation magnetization declined as the annealing temperature increased. The highest coercive field, 2.76 kOe, was observed for Sr-substituted nanoparticles annealed at 1000°C, with Sr cations contributing to the anisotropic magnetic behaviour [115].

Singh et al. (2021) M-type barium strontium hexagonal ferrite was synthesized with Co^{2+} and Sn^{4+} doping. X-ray diffraction (XRD) analysis confirmed the presence of the M-phase in the prepared samples. The microwave absorption characteristics were investigated using a vector network analyzer, and it was found that the electromagnetic parameters, including permeability and dielectric constant, increased with CoSn doping. Microwave absorption improved significantly, with absorption increasing from −15.2 dB in the undoped sample to −51.09 dB in the composition with x = 0.6. A bandwidth of 2.43 GHz was observed for the x = 1.0 composition at 1.7 mm thickness. The mechanism of microwave absorption was governed by input impedance and the λ/4 criterion, making these materials suitable for applications in wireless communication, such as isolators, circulators, and radar systems [116].

Kumar et al. (2021) Ultrahigh efficient electromagnetic interference (EMI) shielding composites were fabricated using a combination of polyaniline (PANI) and zinc-cobalt ferrites ($Co_{1-x}Zn_xFe_2O_4$, $0.1 \leq x \leq 0.4$). The ferrite nanoparticles, synthesized via the sol-gel method, were functionalized with PANI through in situ polymerization. The average crystallite sizes of the nanoparticles were found to be between 20-30 nm,

as estimated by the Debye-Scherrer and Rietveld methods. FTIR spectra confirmed interactions between PANI molecules and the ferrite nanoparticles. The substitution of nonmagnetic Zn ions significantly altered the magnetic properties of cobalt ferrites. The EMI shielding performance of the composites increased with thickness, achieving ~100 dB shielding effectiveness at 3.0 mm thickness for the $Co_{0.7}Zn_{0.3}Fe_2O_4$-PANI composite. Additionally, PANI-ferrite nanocomposites were incorporated into cotton fabrics, demonstrating an EMI shielding effectiveness of 40-45 dB at just 0.30 mm thickness [117].

Bozorgmehr M. (2021) $SrZn_{2-x}(MnCa)_{x/2}Fe_{16}O_{27}$ hexaferrite nanoparticles were successfully synthesized using the co-precipitation method and composited with single-walled carbon nanotubes (SWCNTs). The saturation magnetization of the powdered samples gradually decreased with the substitution of divalent cations. The substitution also significantly impacted the resonance frequency of the W-type hexaferrite. A nanocomposite sample containing x = 0.4 exhibited the highest magnetization (70 emu/g) and coercivity (605 Oe). The microwave absorption study revealed a maximum reflection loss of −42 dB at 10.2 GHz and a frequency bandwidth of 4 GHz for the nanocomposite sample [118].

Fang G. (2021) $Ba(Zr–Ni)_{0.6}Fe_{10.8}O_{19}/Fe_3O_4$ hard/soft magnetic composites were synthesized to achieve broad microwave absorption over the 2–18 GHz range. The results indicated that increasing the heat treatment temperature caused more Fe_3O_4 particles to attach to $Ba(Zr–Ni)_{0.6}Fe_{10.8}O_{19}$, enhancing the exchange coupling effect between the hard and soft magnetic phases. The sample heat-treated at 400°C demonstrated the widest magnetic loss range ($\mu'' > 0.2$) of 12.4 GHz, contributing to an effective absorption bandwidth of 6.68 GHz at a thickness of 1.9 mm. This performance surpassed many contemporary microwave absorbers [119].

Tran N. (2021) $Ba_{1-x}La_xFe_{12}O_{19}$/polyaniline composites were successfully synthesized using a co-precipitation method. The microwave absorption performance of the composites remained consistent across different thicknesses, maintaining reflection loss (RL) values for all measured thicknesses. The $Ba_{0.9}La_{0.1}Fe_{12}O_{19}$/PANI

composite absorbed over 90% of the incident wave for thicknesses between 1.75 and 3.50 mm. Additionally, the effective bandwidth increased as the thickness decreased, with a maximum of 2.52 GHz observed for thicknesses of 1.75 and 2.00 mm. The La-doping and polyaniline compositing enhanced the electromagnetic properties and microwave absorption efficiency [120].

Rostami M. (2021) Co–Al–Ti doped barium hexaferrite-MWCNT-epoxy resin nanocomposites were synthesized using the sol-gel auto combustion method. XRD and Rietveld analysis were utilized to characterize the crystalline nanoparticles, confirming their structure. The microwave absorption properties were investigated across a frequency range of 1–18 GHz, showing that the reflection loss minimum (RL_{min}) reached −47.40 dB for the sample with x = 0.3. The nanocomposite with x = 0.2 exhibited a bandwidth of 4.59 GHz at a thickness of 1.5 mm. All nanocomposites demonstrated effective microwave absorption with more than 99.9% absorption at a matching thickness of less than 1.75 mm [121].

Aggarwal N. (2021) Mg–Zr-doped Ni–Zn spinel ferrites, $Ni_{0.6}Zn_{0.4}(MgZr)_xFe_{2-2x}O_4$ (x = 0.05–0.20), were successfully synthesized using the sol-gel citrate precursor method. Structural characterization through X-ray diffraction (XRD) and morphological analysis using scanning electron microscopy (SEM) confirmed the enhancement of structural and electromagnetic properties upon doping with Mg and Zr. The sample with x = 0.10 exhibited a reflection loss of −35.10 dB at a matching frequency of 10.552 GHz and a thickness of 4 mm. This composition also demonstrated a −10 dB absorption bandwidth of 2.8 GHz. The x = 0.10 sample was found to be most suitable for microwave-absorbing applications [122].

Widanarto W. (2020) Barium ferrite composites activated with Nd^{3+} ions was synthesized using a modified mechanical alloying technique. The effects of varying Nd^{3+} concentrations (0, 1, and 2 mol %) on the morphology, microstructure, and magnetic properties of the composites were thoroughly investigated. The inclusion of Nd^{3+} strongly influenced the complex relative permeability, permittivity, and microwave reflection loss in the X-band frequency range (8.2–12.4 GHz). The

evaluation of these properties was performed using the Nicholson-Ross-Weir (NRW) method. Nd^{3+} doping significantly enhanced the microwave absorption characteristics of the composites [123].

Feng G. (2020) the effects of La doping in $Ba_{0.4}Ca_{0.6}Fe_{11.4}Co_{0.6}O_{19}$ ferrites were investigated to examine their absorption properties. XRD analysis confirmed the formation of standard hexagonal $BaFe_{12}O_{19}$ crystalline phases. Magnetic properties, including saturation magnetization (M_s), remnant magnetization (M_r), and coercivity (H_c), were determined from hysteresis loops, revealing a decrease in M_s from 80 emu/g to 50 emu/g with increasing La concentration, while H_c and H_a gradually increased. Measurements using a vector network analyzer (VNA) showed higher complex permittivity (ε') and permeability (ε") values for La-substituted ceramics compared to undoped samples in the frequency ranges of 21.5–34.9 GHz and 6.6–44.3 GHz, respectively. The minimum reflection loss (RL) of -5 dB was observed at 8.6–12.9 GHz at a thickness of 1.5 mm, and the maximum RL of -28.3 dB was recorded at 10.6 GHz, demonstrating enhanced absorption properties due to La doping [124].

Phan T. L. (2020) Hexagonal $BaCo_{1-x}Mn_xFe_{11}O_{19}$ (x = 0-1) mixture were successfully synthesized via the co-precipitation method. Morphological analyses showed that particle size increased with the rise in Mn content, accompanied by changes in lattice constants. This was attributed to the substitution of Mn^{3+} and Mn^{4+} for Co^{2+} and/or Fe^{3+} in the host lattice, along with Jahn-Teller distortions. Magnetization data revealed that all compounds exhibited hard-magnetic properties, with saturation magnetization (M_s) decreasing and coercivity (H_c) significantly increasing as x increased. Additionally, the squareness ratio (M_r/M_s) and energy product $(BH)_{max}$ also improved, indicating enhanced hard-magnetic characteristics for $BaCo_{1-x}Mn_xFe_{11}O_{19}$ with higher Mn content [125].

Guan G. (2020) a double-layer microwave absorber based on carbon nanofibers (CNFs) and hollow $Ba_2Co_2Fe_{12}O_{22}$ microfibers (Co_2Y MFs) was successfully designed. The study demonstrated that the double-layer absorbers had significantly

better absorption properties than single-layer ones due to improved impedance matching and synergistic effects between layers. The optimized structure, with an absorbing layer of 1.15 mm filled with 5 wt% CNFs and a matching layer of 0.85 mm filled with 67 wt% Co_2Y MFs, achieved a minimum reflection loss (RL) of −85.5 dB at 16.1 GHz and an effective bandwidth of 10 GHz. The study also revealed that the absorption properties could be tuned by adjusting the thickness and stacking order of the layers, showing high potential for practical applications [126].

Anand S. (2020) PVDF/RGO/$BaZrFe_{11}O_{19}$ composites were developed using a simple solvent casting approach. The synthesized samples were analyzed with XRD, FTIR, Raman Spectroscopy, HRSEM, EDX, XPS, and VSM. The flexible films exhibited excellent electromagnetic interference (EMI) shielding effectiveness (SE) of 48.59 dB at 11.1 GHz with the addition of 10 wt% $BaZrFe_{11}O_{19}$ in the polymer composite at a 0.2 mm thickness. The combination of high dielectric loss ($\varepsilon' = 1.95$) and magnetic loss ($\mu' = 0.26$) contributed to over 99% absorption attenuation, dominated by an absorption mechanism. These results demonstrated that RGO and $BaZrFe_{11}O_{19}$ nanofillers in PVDF composites hold promise for radar and military applications [127].

Jing Z. (2020) a new microwave absorber was developed using Sr-hexaferrite, FeCo nanoparticles, and polyaniline (PANI) as magnetodielectric components. The absorber was characterized using X-ray diffraction and scanning electron microscopy, while its magnetic properties were studied with a vibrating sample magnetometer. Electromagnetic analysis revealed excellent microwave absorption performance in the X-band, with a minimum reflection loss of −22.1 dB at 8.5 GHz and a bandwidth of 2.6 GHz at a thickness of 2 mm and 30 wt% filler loading. The presence of polar Si-O groups in the silicon resin matrix improved the absorber's reflection loss and reduced the matching frequency [128].

Tao Ma et al. (2020) Porous MnZn ferrite was successfully anchored on reduced graphene oxide (rGO) to create lightweight microwave absorbers. The addition of varying amounts of rGO effectively adjusted the morphology and microwave

absorption performance of the composites. The maximum reflection loss (RL) achieved was −60.9 dB at 12.4 GHz with a thickness of 2.75 mm. The effective absorption bandwidth (EAB) reached 5.6 GHz in the range of 12.4−18.0 GHz at a thickness of 2.38 mm. The study demonstrated that rGO/MnZn ferrite composites offer excellent microwave absorption properties and have potential applications as efficient microwave absorbers [129].

Zhang et al. (2020) Zr^{4+} - Ni^{2+} co-doped barium ferrites, $BaFe_{12-2x}(ZrNi)_xO_{19}$, were successfully synthesized using a sol-gel process followed by sintering in Ar to achieve enhanced microwave absorption properties in the 2–18 GHz frequency range. The resonance frequency of $BaFe_{12}O_{19}$ was effectively shifted by the Zr^{4+}-Ni^{2+} doping, resulting in a broadened bandwidth of around 6.9 GHz and a strong microwave absorption of −59.3 dB for the composition with x = 0.6. The improved microwave absorption was attributed to the shifting of resonance peaks and the increased dielectric loss caused by lattice vacancies generated during oxygen-deficient sintering. This work provided insights into regulating resonance behaviour to improve the efficiency of ferrite absorbers [130].

Jiao et al. (2020) $Ni_{0.5}Zn_{0.5}Nd_{0.04}Fe_{1.96}O_4$ ferrite (NZNF)/polyaniline (PANI) nanocomposites were synthesized using interfacial polymerization. The crystal structure and microstructure analyses revealed that PANI uniformly coated the ferrite particles in a coral-like form. Electromagnetic parameter testing showed that the inclusion of PANI improved both the real and imaginary parts of the dielectric constant, influencing impedance matching and attenuation performance. While PANI negatively affected impedance matching, it enhanced attenuation capacity. The NZNF/PANI composite with 25 wt % aniline exhibited the best balance between impedance matching and attenuation, with a maximum reflection loss of −37.4 dB at 8.4 GHz and an effective absorption bandwidth of 4.9 GHz at 4.0 mm thickness [131].

Shu et al. (2020) a nitrogen-doped reduced graphene oxide (NRGO)/$Ni_{0.5}Zn_{0.5}Fe_2O_4$ composite was successfully fabricated using a two-step strategy with graphene oxide as the template. The composite exhibited a well-designed entangled structure of

$Ni_{0.5}Zn_{0.5}Fe_2O_4$ microspheres and crumpled NRGO. The incorporation of NRGO significantly enhanced the microwave absorption properties of the ferrite. The composite achieved a minimum reflection loss of −63.2 dB at a matching thickness of 2.91 mm in the X-band, with an effective absorption bandwidth of 5.4 GHz (12.0–17.4 GHz) at a thin thickness of 2.0 mm. Additionally, the relationship between filler loading and reflection loss was clarified, providing insights into the design of efficient microwave absorbers [132].

Khadour et al. (2020) flexible nanocomposite sheets made from spinel MnNiZn ferrite ($Mn_{0.1}Ni_{0.45}Zn_{0.45}Fe_2O_4$) and thermoset polyurethane (PU) matrix were synthesized as efficient microwave absorbers. Different ferrite loading ratios (70%, 75%, and 80 wt%) were used, and the absorption properties were characterized in the S- and C-band frequency ranges (2–8 GHz). The nanocomposite with 80 wt% ferrite loading at a thickness of 5 mm showed the best absorption performance, with a reflection loss of −29.7 dB at 5.86 GHz and an effective absorption bandwidth of 4.28 GHz. Structural and mechanical properties were examined using XRD, FTIR, and SEM, and the results indicated improved microwave absorption due to polar–polar interactions between the matrix and the filler. The lightweight and flexible composite was identified as a promising material for microwave absorption applications [133].

Moradnia et al. (2020) Nano-crystalline ferrites ($BaFe_{12}O_{19}$, $Ba_4MnZnFe_{36}O_{60}$, and $NiFe_2O_4$) were successfully synthesized using co-precipitation and high-energy reactive milling methods. The materials underwent heat treatment at 1100°C for 4 hours and were sintered at 1200°C for 4 hours. XRD, SEM, VSM, and VNA were used to examine the microstructural, magnetic, and microwave absorption properties. It was observed that the saturation magnetization and coercivity varied depending on the type of ferrite. Ba-ferrites showed lower saturation magnetization (300 G) and higher coercivity (1.8 kOe) compared to Ni-ferrite. $NiFe_2O_4$ exhibited the highest reflection loss of −35 dB, indicating its potential for microwave absorption applications [134].

Yu He et al. (2020) Co_2Y ferrite was synthesized using the sol-gel method, and its morphology, phase structure, magnetic, and electromagnetic properties were studied. The results indicated that the saturation magnetization decreased from 54.46 to 48.04 emu/g as the sintering temperature increased. The microwave absorption peaks shifted to higher frequencies with rising temperatures, with a minimum reflection loss of −24.82 dB at 11.68 GHz at a thickness of 8.0 mm. Additionally, when nickel powder was added, the microwave absorption peaks shifted to lower frequencies, with a mixture of 40% nickel and 60% Co_2Y ferrite achieving a minimum reflection loss of −33.75 dB at 4.88 GHz and a thickness of 2.5 mm. This combination improved the reflection loss at lower thicknesses [135].

Handoko E. (2019) used a conventional ceramic method and planetary ball mill technique to synthesize Barium hexaferrite ($BaFe_{12}O_{19}$) and Fe_3O_4 powders for studying multilayer absorbers in the X-band frequency region. The XRD pattern confirmed a single phase of both $BaFe_{12}O_{19}$ and Fe_3O_4. Magnetic properties were evaluated using the hysteresis loop technique, revealing a saturation magnetization (M_s) of approximately 0.25 Tesla for both samples. $BaFe_{12}O_{19}$ exhibited a significantly larger coercive field (H_c) compared to Fe_3O_4. Absorption parameters, measured using the transmission line theory method, demonstrated effective reflection loss at a 10 mm thickness with a bandwidth below -10 dB, emphasizing the importance of layer count and sample thickness for enhanced electromagnetic absorption capacity [136].

Shooshtary Veisi S. (2019) studied $Ba_{0.5}Sr_{0.5}Cu_xZr_xFe_{12-2x}O_{19}$ hexaferrite nanoparticles to analyze their microwave and magnetic properties. Using VSM, it was observed that the saturation magnetization increased from x = 0.0 to x = 0.4 and then decreased to a minimum of 48.6 emu/g at x = 0.8. Coercivity also declined from 5010 Oe to 301.180 Oe with increasing Cu-Zr doping. Microwave properties, evaluated via vector network analysis, showed non-linear reflection loss behaviour, with a maximum reflection loss of -15.2 dB at 11.1 GHz for x = 0.4 [137].

Arora et al. (2019) investigated the microwave absorption characteristics of La^{3+}-Na^{+} substituted barium hexaferrites with chemical compositions $Ba_{(1-2x)}La_xNa_xFe_{10}CoTiO_{19}$ and $Ba_{(1-2x)}La_xNa_xFe_{10}Co_{0.5}TiMn_{0.5}O_{19}$ $(0.00 \leq x \leq 0.25)$ in the Ka-band frequency range. The electromagnetic properties, including complex permittivity, permeability, and microwave absorption, were examined using a Vector Network Analyzer in the 26.5–40.0 GHz frequency range. Dielectric properties remained relatively constant with increasing frequency, while magnetic permeability showed wavy variations. The Co–Ti–Mn series exhibited higher electromagnetic properties than the Co–Ti series. The best performance was observed for composition x = 0.15 of the $Ba_{(1-2x)}La_xNa_xFe_{10}Co_{0.5}TiMn_{0.5}O_{19}$ series, achieving a reflection loss of −55.33 dB at 30 GHz with a −10 dB absorption bandwidth of 3.51 GHz, making these materials effective for Ka-band microwave absorption [138].

Mansour S. (2018) Nanoferrites $BaFe_{11.7}Al_{0.15}Zn_{0.15}O_{19}$ and $Mn_{0.8}Mg_{0.2}Fe_2O_4$ were synthesized using the citrate combustion method. X-ray diffraction and FESEM analyses confirmed that the nanocomposite structure remained intact without any structural deformation. The addition of the hard ferrite $BaFe_{11.7}Al_{0.15}Zn_{0.15}O_{19}$ phase resulted in a doubling of remanent magnetization and a 2.5-fold increase in coercivity. Cole-Cole plots for the nanocomposite with x = 0.4 at different temperatures exhibited two semicircles, representing grain boundary and grain contributions to the conduction process. These nanocomposites show promise for use in exchange spring magnet applications [139].

Tyagi S. (2018) A RADAR-absorbing medium was developed by dispersing carbon nanotubes (CNTs) in a composite of barium hexaferrite and zinc spinel ferrite nanoparticles. The composite, $BaFe_{12}O_{19}/ZnFe_2O_4$, was synthesized via the auto-combustion method and heat-treated at 700 °C, leading to an increase in saturation magnetization from 24.10 to 53.49 emu/g. CNTs were synthesized separately using thermal decomposition of acetylene gas. By incorporating 20 wt% CNTs into the ferrite nanoparticles, the microwave absorption properties were enhanced, achieving a maximum reflection loss of −43.22 dB at 10.30 GHz and a −10 dB bandwidth of 2.95

GHz for a 2 mm thick composite. This method provides an efficient route for mass production of nanosized RADAR absorbing materials [140].

Patel C. K. (2017) $CoFe_2O_4$ (S: Y-1:0) and $Sr_2Co_2Fe_{12}O_{22}$ (S: Y-0:1) ferrites were synthesized using the chemical co-precipitation technique and calcined at 1000 °C for 5 hours. Mixed ferrite composites with different weight ratios (S: Y-3:7, 4:6, 5:5, 6:4, and 7:3) were prepared by mixing the ferrite powders, followed by heating at 1150°C. XRD analysis confirmed the presence of M and Y-type hexagonal phases in $Sr_2Co_2Fe_{12}O_{22}$ and both spinel and Y-type phases in the composites. FTIR spectra validated Fe–O stretching vibrations. VSM analysis revealed saturation magnetization values ranging from 50.44 emu/g to 31.21 emu/g, with remanent magnetization between 11.18 emu/g and 3.70 emu/g. The highest coercivity of 562 emu/g was observed for the composite S: Y-3:7, and dielectric properties were interpreted using Maxwell–Wegner interfacial polarization and N. Rezlescu's model [141].

Malana et al. (2016) Molybdenum-doped strontium calcium hexagonal ferrites were successfully synthesized using the sol-gel combustion method. The structural and morphological properties were analyzed using X-ray diffraction (XRD) and scanning electron microscopy (SEM), revealing a single magnetoplumbite phase with particle sizes ranging from 34 to 47 nm. The magnetic studies showed a decrease in remanent magnetization as the dopant concentration increased, while the coercivity values increased with molybdenum content, making these materials suitable for use in longitudinal magnetic recording media. The dielectric properties exhibited relaxation behaviour at higher frequencies, with the dielectric constant increasing with Mo content. These characteristics suggest that the synthesized ferrites are promising candidates for miniaturization in microwave devices [142].

Z. Mosleh et al. **(2016)** Polycrystalline samples of $Ba_{1-x}Ce_xFe_{12}O_{19}$ (x = 0.0, 0.05, 0.1, 0.15, and 0.2) were synthesized using the sol-gel method. The magnetization initially increased and then decreased with higher Ce content, with a maximum value of 53 emu/g observed for x = 0.1. The coercivity did not show a regular trend but reached 5088 Oe at x = 0.1. XRD analysis confirmed a near-single magnetoplumbite

phase for all samples, and the average particle size decreased with increasing Ce content. The microwave absorption measurements showed a maximum reflection loss of −20.47 dB at 16.22 GHz for the x = 0.2 sample, making Ce-doped barium hexaferrite a potential material for microwave absorption applications [143].

Zheng He et al. (2015) PANI/Ag/$SrFe_{12}O_{19}$ composites were successfully synthesized through a three-step process involving the co-precipitation of $SrFe_{12}O_{19}$, chemical plating of Ag on $SrFe_{12}O_{19}$, and in-situ polymerization of polyaniline (PANI) with Ag/$SrFe_{12}O_{19}$ particles. The structural and morphological characterizations confirmed the successful synthesis of $SrFe_{12}O_{19}$ and Ag/$SrFe_{12}O_{19}$. The addition of Ag reduced the saturation magnetization from 117.22 emu/g to 70.54 emu/g. The composites exhibited improved thermal stability, electrical, and magnetic properties compared to pure PANI. Microwave absorption measurements showed a minimum reflection loss of −14.86 dB at 9.98 GHz, with absorption below −10 dB over the 8.7 to 12.1 GHz range, making the composites promising candidates for microwave absorption applications [144].

Durmus Z. (2015) graphene sheets were successfully decorated with $SrFe_{12}O_{19}$ nanoparticles, forming novel carbon/ferrite nanocomposites synthesized via the citrate sol-gel combustion method. The structural and morphological features of the nanocomposites were characterized using techniques such as XRD, SEM, TEM, and AFM. The analysis confirmed that $SrFe_{12}O_{19}$ nanoparticles were successfully attached to the graphene surface, forming well-structured composites. Magnetic measurements using a vibrating sample magnetometer (VSM) showed that the nanocomposites exhibited significantly high magnetic saturation values, even though they contained a lower proportion of active magnetic components compared to bulk hexaferrite. The synthesized nanocomposites demonstrated strong potential as microwave absorbing materials [145].

Table 2.1. Literature Review Summary: Hexaferrite Properties and Their Applications

Sr. No.	Authors (Year)	Composition/Material System	Synthesis Method	Key Structural/Morphological Findings	Key Magnetic Properties	Key Dielectric/EM Absorption Properties (RL, BW, Thickness)	Key Application/Insights	Research Gap/Contribution Not Fully Addressed
1	Jing et al. (2024) [66]	Pr & Dy doped $SrFe_{12}O_{19}$	Sol-gel	M-type phase + heterophase; decreased grain size with doping.	Saturation magnetization decreased, coercivity increased.	Max RL: -52.51 dB; BW: 4.81 GHz	EM wave absorber	Synergistic effects of multi-rare-earth doping on combined EM properties.
2	Wang et al. (2024) [67]	Lu-La-$SrFe_{12}O_{19}$	Co-precipitation	Hexagonal single-phase magnetoplumbite; regular hexagonal grains.	Hard magnetic; coercivity decreased (2065.3 to 910.3 Oe).	Relative dielectric constant increased significantly ($6.71x10^3$ to $1.28x10^5$).	Electromagnetic shielding	Detailed correlation between specific rare-earth site occupancy and enhanced dielectric loss mechanisms.
3	Jin et al. (2024) [68]	Ce^{3+}-doped $BaFe_{12}O_{19}$	Sol-gel	Stable M-type crystal structure; constant micrometer grain size.	Enhanced magnetic and dielectric losses.	Min RL: -58 dB; EAB: 9.44 GHz @ 2.3 mm	Efficient EM wave absorber, EMI shielding	Impact of Ce^{3+} on impedance matching across a broad frequency range for varying thicknesses.
4	Wei et al. (2024) [69]	Nd^{3+}-M^{5+} (M=Nb^{5+}, Ta^{5+}) substituted Ba-ferrites	Solid-state reaction	Reduced anisotropic field.	Multiple natural resonances, improved	RL: -35 to -50 dB; BW: ~13.5 GHz;	Ultrabroadband microwave absorption	Detailed analysis of interface polarization contributio

					impedance matching.	thickness < 0.75 mm (26.5–40 GHz); <1.5 mm (2–18 GHz)		ns from multi-site substitution on bandwidth.
5	Panwar et al. (2024) [70]	Ca-Bi-Co substituted M-type hexaferrites	Sol-gel auto-combustion	Single-phase hexagonal; crystallite size 42-49 nm; reduced density, increased porosity.	Saturation magnetization 15.51-38.27 emu/g; coercivity increased (207.93 to 1359.69 Oe).	Significant dielectric constant at low freq., decreased dielectric loss.	Contemporary electronic devices (enhanced dielectric/magnetic)	Specific role of porosity on microwave absorption mechanisms beyond just density.
6	Yang et al. (2024) [71]	Ce-doped $SrFe_{12}O_{19}$	Sol-gel auto-combustion	M-phase ferrite + impurities (CeO_2, Fe_2O_3); decreased grain size with Ce.	Saturation magnetization first rose then declined; fluctuations with iron content.	Not explicitly focused on MA properties.	Modifying magnetic behavior through composition	Quantitative impact of impurity phases on primary magnetic and dielectric properties relevant for MA.
7	Chen et al. (2024) [72]	Ho-doped Sr-ferrite	Sol-gel auto-combustion	Changes in secondary phases (Fe_2O_3, $HoFeO_3$, $SrFeO_{3-x}$); increased grain size with Ho.	Coercivity decreased (5.26 to 4.78 kOe); saturation magnetization decreased (76.73 to 73.28 emu/g).	Not explicitly focused on MA properties.	Understanding Ho doping effects on structure and magnetism	Direct correlation between specific secondary phases and their role in EM wave interaction.
8	Kayalvizhi et al.	Sr-ferrite/rGO composites	Hydrothermal	Particle size decreased with rGO (55.60 to	Saturation magneti	RL: -28.49 dB	Microwave absorption	Optimizing rGO loading to

	(2024) [73]			41.55 nm).	zation decreased (53.3 to 35.89 emu/gm); coercivity increased (2679 to 3606 Oe).	(ferrite), -23.78 dB (composites).		balance magnetic property degradation with improved dielectric loss for MA.
9	Yang et al. (2024) [74]	Zn^{2+} & Sn^{4+} doped Ba-hexaferrites / CNT composites	Auto-combustion (ferrite), Hydrothermal (CNT comp.)	Band gap increased.	Reduced magnetic saturation, coercivity, anisotropy field.	BW: 6 GHz (11.4-17.4 GHz for ferrite); BW: 7.1 GHz (CNT comp.)	Microwave absorption	Detailed mechanism of how CNTs interact at the interface with doped ferrites for enhanced absorption.
10	Wei et al. (2024) [75]	Helical CNTs/doped Ba-ferrite/epoxy coatings	Optimized with numerical simulations/genetic algorithm	Porous structure; good conductivity and uniformity.	Not primary focus.	RL: -17.22 dB @ 16.66 GHz; BW: 9.16 GHz (10-18 GHz).	High-performance Ku-band microwave absorbing coatings	Scalability and long-term stability of such complex composite coatings under various environmental conditions.
11	Shu et al. (2024) [76]	NRGO/$MgFe_2O_4$/PANI composite aerogel	Solvothermal, chemical oxidation polymerization, hydrothermal self-assembly	3D porous network; low bulk density (11.1–13.0 mg cm^{-3}); $MgFe_2O_4$ coated with PANI.	Not primary focus on magnetic values.	Max BW: 7.0 GHz; Min RL: −42.9 dB @ 11.5 wt.% filling ratio.	Microwave absorption (lightweight)	Practical manufacturing feasibility and cost-effectiveness of these multi-component aerogel systems.
12	Mudasar et al. (2024) [77]	Co/Zn-doped hexaferrite flakes on Ti_3C_2Tx MXene	HF etching (MXene), solid-state sintering	Strong adhesion between ferrite and MXene; flakes.	Optimized electromagnetic paramet	Peak RL: -49 dB @ 15.2 GHz;	High-performance EM wave absorber	Long-term stability and environmental

			(ferrite)		ers.	BW: 8.3 GHz @ 1.9 mm. RCS reduction up to -47.8 dBsm.		resilience of ferrite-MXene interfaces in practical applications.
13	Bala et al. (2024) [78]	Ni-ferrite/activated carbon composites	Mechanical alloying (composite), sol-gel auto-combustion (Ni-ferrite NP)	Confirmed composite formation.	Electromagnetic properties assessed.	Reflection coefficient > -10 dB (X-Band).	Microwave absorber for defense applications	Detailed investigation into the synergistic effect of activated carbon and ferrite for tunable absorption.
14	Yunasfi et al. (2024) [79]	La^{3+}-substituted Ni-ferrite ($NiLa_xFe_{2-x}O_4$)	Co-precipitation, sintering (1200 °C, 5h)	Single-phase cubic spinel; particle size 100-800 nm.	Saturation magnetization decreased (35.89 to 21.54 emu/g); coercivity increased (249 to 416 Oe).	RL increased (11.16 to 15.41 dB); up to 97.11% absorption @ x=0.04.	Microwave absorption	Impact of sintering conditions on La^{3+} substitution uniformity and resulting EM properties.
15	Kaur et al. (2024) [80]	Ni & Zr co-substituted Zn-Co spinel ferrites	Sol-gel citrate route	Cubic spinel nanoparticles.	Saturation and remanent magnetization declined.	RL: −50.34 dB @ 29.20 GHz; thickness 1.3 mm (Ka-band).	Microwave absorbers for 5G technologies	Deeper insight into the specific roles of Ni^{2+} and Zr^{4+} in altering spin configurations and anisotropy for Ka-band performance.
16	Siddique et al. (2024) [81]	Cd-Zn-Co ferrites ($Cd_{0.5-x}Zn_xCo_{0.5}Fe_2O_4$)	Sol-gel auto-ignition	Mono-phase cubic spinel; IR bands shifted with Zn.	Saturation magnetization increased (58.92	Min RL: −26.85 dB @ 3.90 GHz.	Effective EM wave absorber for high-frequency application	Broader bandwidth optimization through impedance matching

					to 106.41 emu/g); coercivity decreased (246.47 to 192.10 Oe).		s	for high-frequency applications.
17	Akhtar et al. (2024) [82]	Zr-In co-substituted Ni-Zn nano ferrites	Citrate-gel self-ignition	Spinel-based, circular & hexagonal particles.	Min RL: -61.5 dB @ 2.43 GHz (x=0.20); -57.3 dB @ 1.93 GHz (x=0.15); peak @ 5.8 GHz.	Excellent potential for high-frequency EMI shielding (C band).	Role of mixed valence states and defect chemistry in achieving such extreme reflection losses.	
18	IjaZ M. (2024) [83]	Co-doped Ba-Sr-Er-Al hexaferrite	Sol-gel	Hexagonal phase; consistent particle distribution.	Saturation magnetization increased (37.76 to 57.12 emu/g); H_a: 1.303 kOe; Hc: 4.172 kOe.	Not explicitly focused on MA properties.	Magnetic applications	Comprehensive analysis of dielectric properties and microwave absorption performance for these complex co-doped systems.
19	Khan M. (2023) [84]	Ba-Sr hexaferrite/MWCNTs/Polythiophene	Sol-gel auto-combustion, ultrasonication, in-situ polymerization	Confirmed material formation.	Weakening of exchange coupling at ferrite-MWCNT interface; magnetic resonance shifted to lower frequenc	Max shielding effectiveness: -34 dB @ 8.1 GHz; RL: -39 dB @ 7.4 GHz.	Military radar frequencies, effective energy dissipation	Stability and degradation mechanisms of polymer-ferrite-CNT composites in harsh environments.

					ies.			
20	Thanh T. (2023) [85]	MFe_2O_4 (M=Co, Fe, Mn) nanoparticles	Chemical co-precipitation	Distinct crystalline NPs (15 nm Co, 9 nm Fe, 34 nm Mn).	Ion distribution & exchange interactions influenced coercivity & squareness ratio. $CoFe_2O_4$ showed strong anisotropy.	Direct bandgap 2.59–2.64 eV.	Fundamental properties, potentially sensing/catalysis	Integration of these spinel ferrites into composite structures for MA, and the resulting performance.
21	Tian et al. (2023) [86]	Mn-substituted $Ba_2Co_2Mn_xFe_{12-x}O_{22}$	Solid-phase sintering	Lattice distortion, initial increase then decrease in oxygen vacancies.	Permeability (μ') increased; dielectric constant (ε') declined.	EAB increased from 5.5 GHz to 9.1 GHz; x=1.2 achieved EAB of 8.74 GHz @ 1.57 mm.	Effective absorption, wide bandwidth	Precise control over oxygen vacancy concentration and its direct impact on specific loss mechanisms for MA.
22	Liu X. (2023) [87]	Rare earth (La, Nd, Ce) doped BaM/PANI composites	Not specified for composite method	Increased polarization at Re-BaM and PANI interfaces.	Improved absorption efficiency.	La-BaM/PANI: Max RL: -63.6 dB @ 7.76 GHz @ 3.28 mm; Nd-BaM/PANI: EAB 4.72 GHz; Ce-BaM/PANI: EAB 3.88 GHz @	Enhanced microwave absorption, EMI shielding	Scalability and long-term stability of these high-performance, multi-component composites.

						1.58 mm.		
23	Verma et al. (2023) [88]	Zn & Zr co-substituted Ba-hexaferrite	Solid-state reaction	Pure M-type phase; crystallite size 149 to 69 nm; cell volume increased; porosity decreased.	Saturation magnetization up to 72.87 emu/g @ x=0.1; coercivity decreased (4118 to 319 Oe).	Not explicitly focused on MA properties.	Magnetic data storage, microwave absorption, spintronic devices	Direct microwave absorption measurement results for the studied compositions.
24	Khan K. (2023) [89]	$(MgFe_2O_4)_{100-x}/(BaFe_{12}O_{19})_x$ nanocomposites	In-situ auto-combustion sol-gel	Hexaferrite & spinel ferrite phases; no notable crystallite size variation.	Robust interphase exchange coupling (stronger at x=0.7); weaker at x=50.	Elevated impedance values.	Electromagnetic shielding, high band-pass filters	Detailed analysis of the impedance matching performance and reflection loss for specific microwave bands.
25	Gupta A. (2023) [90]	Zn-substituted $SrFe_{8-x}Al_4Zn_xO_{19}$	Sol-gel auto-combustion	Confirmed structural changes with Zn.	Energy density $(BH)_{max}$ improved to 19.15 MGOe.	Typical hexaferrite dielectric behavior.	Cost-effective permanent magnets	Direct microwave absorption properties as related to the enhanced magnetic properties.
26	Sahu et al. (2023) [91]	Sr^{2+}-doped Ni-Co nano ferrite	High-energy ball mill	Not explicitly focused on structural.	Max saturation magnetization (Ms) of 60 emu/g; remanent magnetization, coercivity, anisotropy	Highest RL: -35.59 dB @ 17.74 GHz @ 3 mm.	Promisinmicrowave absorber	Detailed impedance matching analysis to explain the observed reflection loss.

					constant increased then decreased.			
27	Caliskan S. (2023) [92]	Co-V co-substituted nano Sr-hexaferrites	Citrate combustion	Crystallite size 37-83 nm; hexagonal morphology.	Ms, Mr, nB peaked at x=0.04; hard magnetic behavior.	Non-linear properties; reflection losses linked to dipole polarization.	Microwave measurements	Comprehensive analysis of the multiple loss mechanisms contributing to MA in these co-substituted systems.
28	Rana K. (2023) [93]	Pure M-type $SrFe_{12}O_{19}$	Modified citrate precursor method	M-phase + minor Fe_2O_3 impurities; densely packed hexagonal grains.	Ms increased (81 to 92 emu/g); Hc rose (107 to 262 Oe); squareness ratio increased (0.26 to 0.54).	Not explicitly focused on MA properties.	Fundamental magnetic properties	Direct microwave absorption performance of the synthesized pure phase and its correlation with magnetic domain behavior.
29	Gulbadan et al. (2023) [94]	Yb-Co co-substituted M-type hexaferrites	Auto combustion sol-gel	Pure single-phase; lattice parameters/unit cell volume changed.	Not primary focus on magnetic values.	Improved dielectric losses & AC conductivity; bandgap 1.961 to 1.875 eV.	Microwave & high-frequency applications	Quantitative assessment of microwave absorption performance, including RL and bandwidth.
30	Ramirez-Ayala M. (2023) [95]	Nd-incorporated $SrFe_{12}O_{19}$	Sol-gel Pechini method	Nd orthoferrite as secondary phase; changes in grain morphology.	BHmax increased by 35% due to enhanced magnetic	Not explicitly focused on MA properties.	Enhanced permanent magnets	Direct impact of the secondary orthoferrite phase on microwave absorption

					interactions.			characteristics.
31	Mironovich A. (2023) [96]	Ni-substituted $BaFe_{12}O_{19}$	Hydrothermal, post-annealing	Ni ions incorporated; Ni^{2+} in 12k sites.	Saturation magnetization (Ms) reduced (65.88 to 49.13 emu/g); magnetic parameters decreased.	Not explicitly focused on MA properties.	Fundamental magnetic property alteration	Detailed study on the link between oxygen vacancies, magnetic property degradation, and EM wave interaction.
32	Gui et al. (2023) [97]	La-Al co-doped W-type Ba-Co-Fe hexagonal ferrite	Sol-gel auto-combustion	W-type magnetoplumbite; reduced grain size.	Enhanced dielectric & magnetic losses; improved impedance matching.	RL: -50.13 dB @ 11.9 GHz @ 7.0 mm; BW: -20 dB from 11.6 to 12.2 GHz.	Effective microwave absorption	Optimization of multi-doping for simultaneous reduction in thickness and broadened absorption bandwidth.
33	Nishkala K. (2023) [98]	La-substituted $BaFe_{12}O_{19}$	Ball milling, heat treatment	Single-phase magnetoplumbite; decreased grain size; reduced porosity.	Electron delocalization with La doping.	Dielectric constant max at x=0.20; enhanced polarization.	Fundamental electrical properties	Direct measurement of microwave absorption properties and their correlation with observed polarization behavior.
34	Fasate S. (2023) [99]	Mn-substituted $BaFe_{12}O_{19}$	Sol-gel auto-combustion	Not primary focus on structural.	Saturation magnetization decreased with Mn.	DC electrical resistance decreased with temp/Mn^{2+}; dielectri	Semiconductor behavior, dielectric properties	Detailed analysis of microwave absorption characteristics (RL, BW) for these Mn-substituted

						c constant/loss decreased with freq/Mn^{2+}.		ferrites.
35	Chagas P. (2023) [100]	Sn-substitution in $SrFe_{12}O_{19}$	Solid-state reaction	Not primary focus on structural.	Not primary focus on magnetic.	Conductivity increased with Sn^{4+}; two conductive processes (grain/grain boundary).	Electrical conductivity	Correlation between enhanced electrical conductivity due to Sn-substitution and the resulting microwave absorption performance.
36	Bilovol V. (2023) [101]	$SrFe_{12}O_{19}/CoFe_2O_4$ composites	Ball milling, annealing (900 °C, 3h)	Composite phases confirmed.	Highest (BH)max of 10.9 kJ/m³ (10 wt% $CoFe_2O_4$); exchange coupling effect.	Not explicitly focused on MA properties.	Permanent magnets (enhanced energy product)	Microwave absorption performance of these hard/soft exchange-coupled composites.
37	Zhang et al. (2022) [102]	Al-substituted Sr-La-Zn hexaferrites	Solid-state reaction	Single magnetoplumbite phase; platelet-like grains.	96.4% increase in coercivity (Hc), reaching 4576.8 Oe.	Optimized dielectric properties.	Enhanced coercivity, potentially MA	Direct microwave absorption measurements and optimization for the specific composition.
38	Akthar et al. (2022) [103]	RE-doped graphene-based $NiFe_2O_4$ nanocomposites	Sol-gel auto-combustion, hydrothermal	Confirmed nanocomposite formation.	Saturation magnetization increased (11.552 to 46.243 emu/g).	Optical band gap decreased (2.66 to 1.65 eV); DC conductivity 1.75x10	Multifunctional nanocomposites	Comprehensive microwave absorption study including impedance matching and bandwidth

						$^{-3}$ to 4.24x10 $^{-3}$ S cm^{-1}.		for these graphene composites.
39	Zareef Khan M. (2022) [104]	$BaFe_{12}O_{19}/NiFe_2O_4$ nanocomposites	Not specified for composite method	Crystallite size 27-34 nm.	Strong magnetic interactions due to spring exchange coupling.	Not explicitly focused on MA properties.	Magnetic interactions, potentially MA/EMI	Detailed microwave absorption characteristics driven by the observed exchange coupling.
40	Karnajit Singh H. (2022) [105]	Al^{3+}-substituted Ba-La-Sr hexaferrites	Solid-state method	Decreased lattice parameters.	Increased coercivity and anisotropy field; Ms deviated from Bloch's law.	Complex permittivity (ε', ε") decreased.	Fundamental magnetic and dielectric properties	Direct microwave absorption properties and how the decreasing permittivity impacts performance.
41	Hassan et al. (2022) [106]	Ce-substituted β-type hexagonal ferrite	Sol-gel auto-combustion	Single-phase structure; positive tensile microstrain.	Not primary focus on magnetic.	Dielectric constant/loss decreased with frequency; AC conductivity influenced by Ce.	Dielectric properties	Direct microwave absorption measurements and performance evaluation of these β-type ferrites.

2.2. Research Gaps

Following the study of the literature, there are a few research gaps that are listed below:

- **Gap 1 - Optimizing Properties and Cost-Effectiveness through Hybrid Magnetic Composites:** High-performance hard magnetic materials frequently rely on expensive rare-earth elements, limiting their commercial viability. Conversely, soft magnetic materials offer better stability and are more economical. Combining these, such as integrating ferrite with hexaferrites,

could yield composites with enhanced magnetic, electrical, and absorption properties while remaining cost-effective.

- **Gap 2 - Understanding Morphology's Role in Substituted Ferrites and Composites:** There's a notable lack of comprehensive research exploring how the physical form and structure (morphology) of substituted M-type hexaferrites and their composites directly influence their electrical, magnetic, and electromagnetic (EM) absorption characteristics.

- **Gap 3 - Under-Investigated Specific Composite Formulations:** Research on microwave-absorbing composites that combine rare-earth or transition metal-doped M-type hexaferrites with ferrites and conductive polymers (like polyaniline) remains limited. This area presents a significant opportunity for further exploration.
- **Gap 4 - Prioritizing Bandwidth-to-Thickness Ratio for Practical Absorber Design:** While much research focuses on achieving high reflection loss and broad bandwidth, practical applications, especially in compact electronic devices, demand consideration for the absorber's dimensions and cost. An absorber might offer excellent reflection loss but be impractical due to excessive thickness. Therefore, the bandwidth-to-thickness ratio is a critical, yet often overlooked, parameter in designing effective absorbers, highlighting a clear need for more dedicated research.

2.3. Objective of this study

The objective of this research is to make divalent and trivalent improved M-type hexaferrite material and a combination of it that can absorb electromagnetic energy in the GHz frequency range.

1. Synthesis and electrical characterization of Barium nano-ferrite composites.
    - Directly addresses: Gap 1 (cost-effectiveness, combination of materials), Gap 3 (scarce composite systems).
    - Enables: Data for Gap 2 (morphology-property correlation), Gap 4 (foundational material for lightweight/adjustable absorber).

2. Measurement and analysis of S-parameters and reflection loss characteristics of nano-ferrite composites.
    - Directly addresses: Gap 2 (correlation of properties), Gap 4 (quantifying reflection loss and bandwidth for practical applications).
    - Enables: Data for Objective 3 (enhancement).
3. Enhancement of tunable reflection loss and absorption bandwidth in nano-ferrite composites.
    - Directly addresses: Gap 4 (achieving desired RL and BW while considering thickness and tunability).

Conclusion

The chapter establishes the necessity of exploring innovative approaches to improve the structural, magnetic, and dielectric properties of hexaferrites for EMI shielding and microwave absorption. By addressing identified research gaps—such as morphology-property correlations, the bandwidth-to-thickness ratio, and material adaptability—this study aims to develop advanced hexaferrite composites that are not only high-performing but also commercially viable. The objectives are well-aligned with addressing practical challenges in contemporary electronic and communication technologies.

CHAPTER-3
RESEARCH METHODOLOGY AND CHARACTERIZATION

The objective of our current study is to utilize the sol-gel technique to synthesizing both pure barium hexaferrite and doped variations. The selected synthesis method significantly influences the fundamental attributes of hexaferrite, such as its structural features, morphology, and electrical and magnetic properties. However, these qualities are not only determined by the process of synthesis. They are also greatly influenced by parameters like as the composition, dopant type, doping concentrations, and the calcination temperature of the resulting material. This chapter details the methodology employed for synthesizing pure and doped M-type barium hexaferrites, as well as their composites with Polyaniline (PANI). The chosen synthesis and characterization parameters are critical for tailoring the structural, morphological, electrical, magnetic, and microwave absorption properties to meet specific application requirements.

3.1. Method of Synthesis

3.1.1. Sol-gel Auto Combustion Methodology

The sol-gel auto-combustion method is a wet chemical procedure extensively employed in the synthesis of nanomaterials. The sol-gel auto-combustion technique has gained popularity and widespread acceptance among various methods used to synthesize hexaferrites. This is due to its unique advantages compared to other synthesis approaches such as chemical co-precipitation, solid-state reaction, ceramic routes, and microemulsion. This approach provides advantages such as precise control over particle sizes, production of particles at the nanoscale, cost efficiency, and consistency in material characteristics. In the sol-gel auto-combustion process, the raw materials, including metal nitrates or alkoxides, are dissolved in a liquid medium like water, ethylene glycol, or an appropriate acid to create a colloidal suspension known as a sol. This solution undergoes a process of aging prior to being heated, resulting in the formation of a solid structure commonly referred to as a "gel." When the gel is heated or dried at high temperatures, the liquid medium evaporates, causing

the development of a "precursor." A sol is a colloidal suspension within a liquid medium, while a gel is a suspension that retains its shape, which is reflected in the term "sol-gel." [146-148].

Sol-gel auto combustion was used to synthesized M-type hexaferrites, which have the chemical formula $BaCo_xCe_xFe_{12-2x}O_{19}$ (x = 0.0-1.0), $BaCo_xCr_xFe_{12-2x}O_{19}$ (x = 0.0-1.0), $BaCo_xCd_xFe_{12-2x}O_{19}$ (x = 0.0-1.0), $BaCo_xAl_xFe_{12-2x}O_{19}$ (x = 0.0-1.0) and are co-substituted with Co^{2+} and Ce^{3+}, Cr^{3+} , Cd^{2+} , Al^{3+} respectively . The process employed analytical-grade (99%, Loba Chemie Pvt. Ltd.) nitrates of Barium ($Ba(NO_3)_2$) - Molecular Weight 261.32, Cobalt ($Co(NO_3)_2 \cdot 6H_2O$) - Molecular Weight: 291.03, Cerium ($Ce(NO_3)_3 \cdot 6H_2O$) - Molecular Weight: 434.23, chromium nitrate nonahydrate (Cr(NO3)3·9H2O – Molecular Weight: 400.15, Cadmium nitrate tetrahydrate $Cd(NO_3)_20.4H_2O$ – molecular Weight; 308.47, Aluminum ($Al(NO_3)_3 \bullet 9H_2O$) – Molecular Weight 375.13 and Iron ($Fe(NO_3)_3 \cdot 9H_2O$) - Molecular Weight: 404 were employed as precursors due to their high solubility and ease of achieving precise stoichiometry. Citric acid from Loba Chemie Pvt. Ltd. ($C_6H_8O_7$) - Molecular Weight: 210.14 acted as the chelating agent, facilitating the formation of a homogeneous solution and influencing the final particle morphology. Stoichiometric calculations guided the precursor weight ratios, maintaining a consistent 1:1.5 cation-to-citric acid molar ratio.

Precursor Preparation:

- Aqueous Solution: We dissolved cation nitrates in deionized water while continuously stirring. We then adjusted the pH to 7 using an ammonium hydroxide (NH_4OH) solution.
    - Gelation: The solution was agitated constantly at 80°C for around 4 hours, promoting water evaporation and resulting in a dark brown viscous gel.
    - Auto-Combustion: We subjected the gel to a temperature ramp (200-250°C) in a hot plate for 1 hour, triggering an auto-combustion process that yielded a mixed-metal oxide precursor.
- Fine Powder: The auto-combustion precursor was then ground into a powder using a mortar and pestle.

- Calcination and Sintering: The powder was sintered at 900°C for 5 hours in a muffle furnace. Finally, we crushed the sintered powder into pellets using a 2% polyvinyl alcohol (PVA) solution.

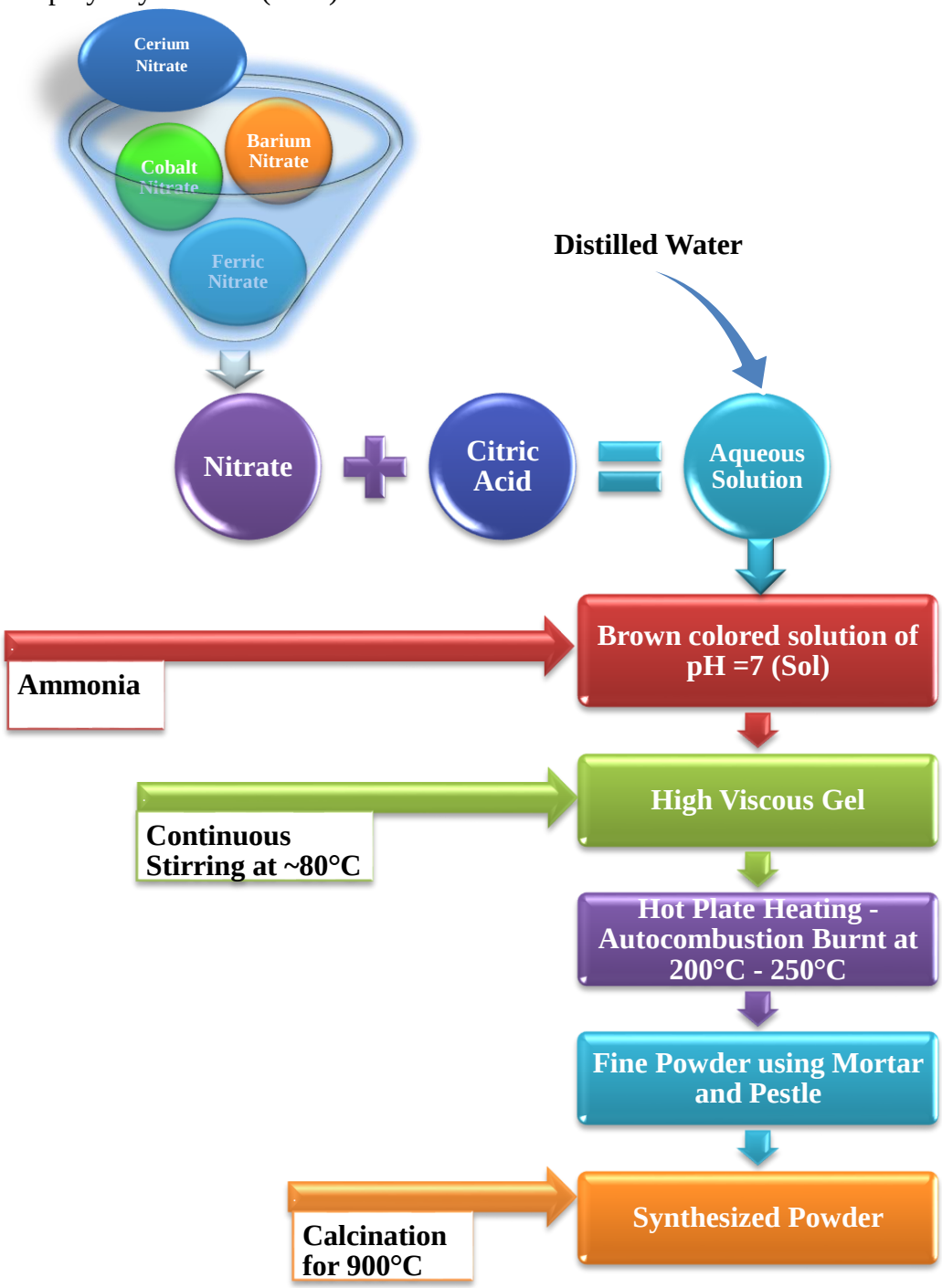

Figure 3.1. Synthesis Flowchart for Sol-Gel Auto-Combustion

3.1.2. Polyaniline (PANI) synthesis method

Following the process outlined in Figure 3.1, ferrite samples were prepared. Because ferrites are naturally rigid, filler materials were added to enhance their flexibility and formability. These fillers also served to improve the electrical and magnetic characteristics of the composite. Polyaniline (PANI), a conductive polymer, was then integrated into the ferrite composites to significantly boost their electromagnetic performance. The PANI itself was created through a chemical polymerization reaction of aniline, using ammonium persulfate as the oxidizing agent, with the temperature carefully maintained between 0–5°C. After drying, the resulting PANI powder was blended with the ferrite powder at a 20% PANI to 80% ferrite ratio to create the final composites.

3.1.3. Pellet formation and sintering

To prepare for electromagnetic (EM) property testing using a Vector Network Analyzer (VNA) with a rectangular waveguide, the synthesized materials were formed into rectangular pellets. A hydraulic press compacted the powder into a rectangular die under a uniaxial pressure of 2–3 tons/cm² for 2 minutes. These shaped pellets then underwent sintering at 900 °C for 2 hours to increase their hardness. After cooling to room temperature, these hexagonal ferrite compositions were ready for VNA analysis.

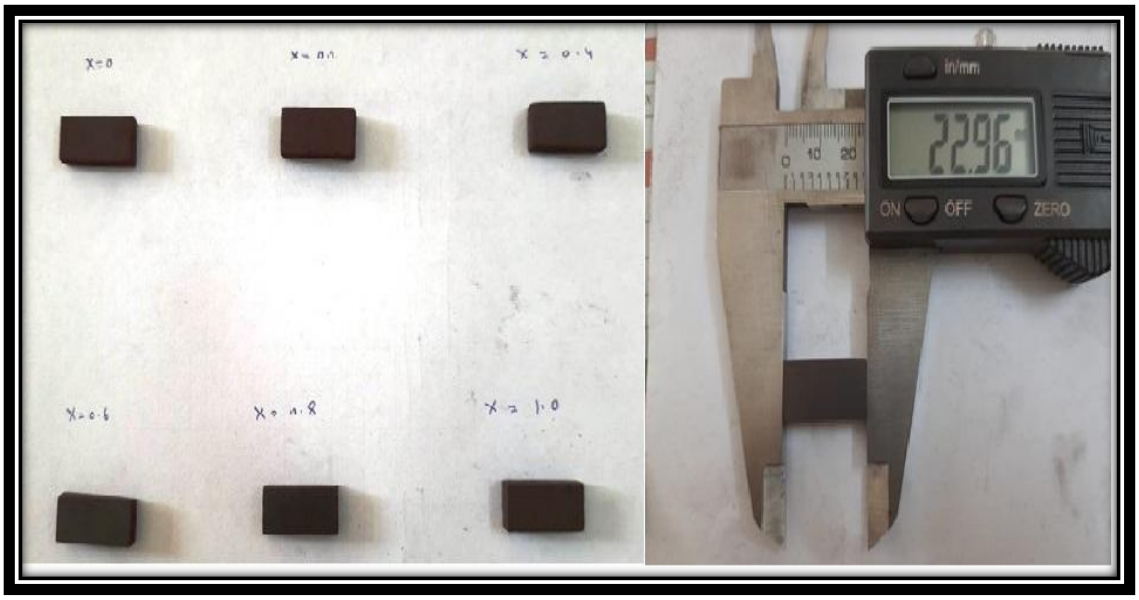

Figure 3.2. Rectangular pellets prepared for VNA measurement

3.2. Synthesis of Co^{2+} and Al^{3+} substituted BaM hexaferrite with composition $BaCo_xAl_xFe_{12-2x}O_{19}$

The combustion reaction can be represented by the following equation:

$$Ba(NO_3)_2 + xCo(NO_3)_2.6H_2O + xAl(NO_3)_3.9H_2O + (12-2x)Fe(NO_3)_3.9H_2O + yNH_4OH + zC_6H_8O_7 + H_2O + \text{heat} \rightarrow BaCo_xAl_xFe_{(12-2x)}O_{19} + mH_2O + nCo_2 + pNO \quad (3.1)$$

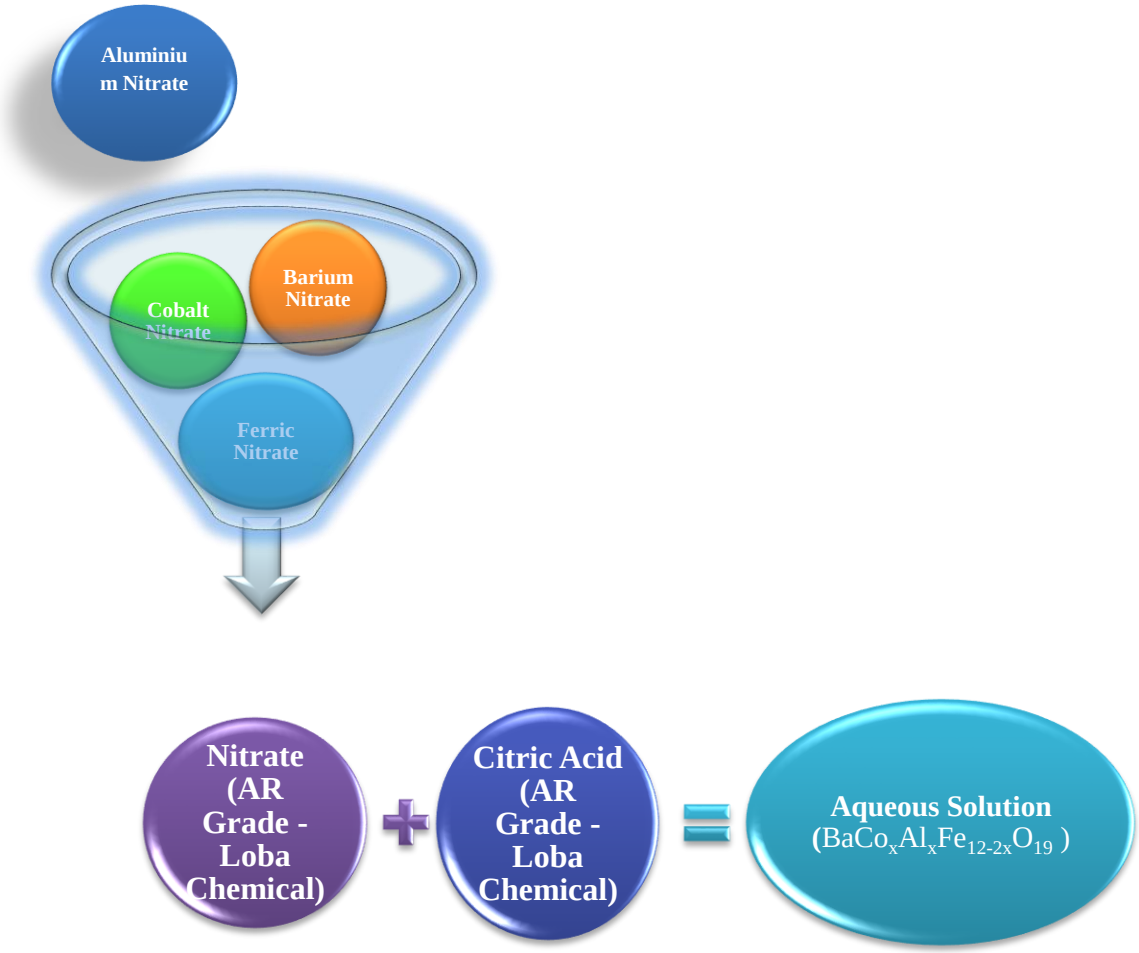

Figure 3.3. Chemicals along with their company for the preparation of $BaCo_xAl_xFe_{12-2x}O_{19}$.

Figure 3.3 depicts the chemicals of analytical reagent (AR) grade, together with the manufacturer's name, that were used to prepare the $BaCo_xAl_xFe_{12-2x}O_{19}$ ($0.0 \leq x \leq 1.0$) hexaferrite. The comprehensive information regarding the compounds utilized in specific quantities (grams), together with their properties analyzed by various characterization methods, is provided in Table 3.1.

Table 3.1. Detailed description of chemicals used in quantity (g) and performed characterization of $BaCo_xAl_xFe_{12-2x}O_{19}$

Synthesis Material: Cobalt and Aluminium doped Barium hexaferrite ($BaCo_xAl_xFe_{12-2x}O_{19}$)						
Method of Synthesis: Sol-gel Method						
Doping Concentration: x = 0.0, 0.2, 0.4, 0.6, 0.8, 1.0						
Cations to citric acid ratio: 1:1.5						
Chemicals used with Mol. Wt. (g)		$Ba(NO_3)_2$	**x** $Co(NO_3)_2.6H_2O$	**x** $Al(NO_3)_3.9H_2O$	**(12-2x)** $Fe(NO_3)_3.9H_2O$	$C_6H_8O_7$
Amount of chemicals used (In g)	x = 0.0	6.533	-	-	121.2	102.443
	x = 0.2	6.533	1.455	1.875	117.16	102.443
	x = 0.4	6.533	2.9103	3.7513	113.12	102.443
	x = 0.6	6.533	4.365	5.6269	109.08	102.443
	x = 0.8	6.533	5.8206	7.50	105.04	102.443
	x = 1.0	6.533	7.275	9.378	101	102.443

3.3. Synthesis of Co^{2+} and Ce^{3+} substituted BaM hexaferrite with composition $BaCo_xCe_xFe_{12-2x}O_{19}$

The combustion reaction can be represented by the following equation:

$$Ba(NO_3)_2 + xCo(NO_3)_2.6H_2O + xCe(NO_3)_3.6H_2O + (12-2x)Fe(NO_3)_3.9H_2O + yNH_4OH + zC_6H_8O_7 + H_2O + \text{heat} \rightarrow BaCo_xCe_xFe_{(12-2x)}O_{19} + mH_2O + nCo_2 + pNO \quad (3.2)$$

Figure 3.4 depicts the chemicals of analytical reagent (AR) grade, together with the manufacturer's name, that were used to prepare the $BaCo_xCe_xFe_{12-2x}O_{19}$ ($0.0 \leq x \leq 1.0$) hexaferrite. The comprehensive information regarding the compounds utilized in specific quantities (grams), together with their properties analyzed by various characterization methods, is provided in Table 3.2.

Table 3.2. Detailed description of chemicals used in quantity (g) and performed characterization of $BaCo_xCe_xFe_{12-2x}O_{19}$

Synthesis Material: Cobalt and Aluminium doped Barium hexaferrite ($BaCo_xCe_xFe_{12-2x}O_{19}$)
Method of Synthesis: Sol-gel Method
Doping Concentration: x = 0.0, 0.2, 0.4, 0.6, 0.8, 1.0
Cations to citric acid ratio: 1:1.5

Chemicals used with Mol. Wt. (g)		$Ba(NO_3$	x $Co(NO_3)_2.6H_2O$	x $Ce(NO_3)_3.6H_2O$	(12-2x) $Fe(NO_3)_3.9H_2O$	$C_6H_8O_7$
Amount of chemicals used (In g)	x = 0.0	6.533	-	-	121.2	102.443
	x = 0.2	6.533	1.455	2.17115	117.16	102.443
	x = 0.4	6.533	2.9103	4.3423	113.12	102.443
	x = 0.6	6.533	4.365	6.51345	109.08	102.443
	x = 0.8	6.533	5.8206	8.6846	105.04	102.443
	x = 1.0	6.533	7.275	10.85575	101	102.443

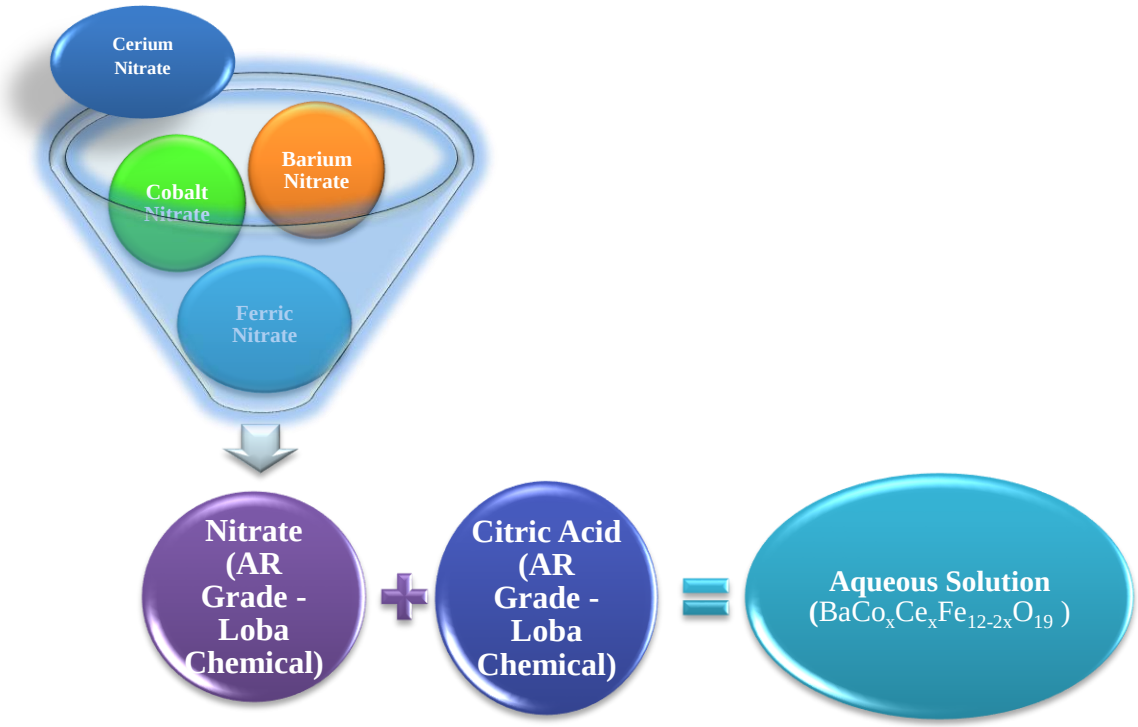

Figure 3.4. Chemicals along with their company for the preparation of $BaCo_xCe_xFe_{12-2x}O_{19}$

3.4. Synthesis of Co^{2+} and Cd^{2+} substituted BaM hexaferrite with composition $BaCo_xCd_xFe_{12-2x}O_{19}$

The combustion reaction can be represented by the following equation:

$$Ba(NO_3)_2 + xCo(NO_3)_2.6H_2O + xCd(NO_3)_2.4H_2O + (12-2x)Fe(NO_3)_3.9H_2O + yNH_4OH + zC_6H_8O_7 + H_2O + \text{heat} \rightarrow BaCo_xCd_xFe_{(12-2x)}O_{19} + mH_2O + nCo_2 + pNO \quad (3.3)$$

Figure 3.5 depicts the chemicals of analytical reagent (AR) grade, together with the manufacturer's name, that were used to prepare the $BaCo_xCd_xFe_{12-2x}O_{19}$ ($0.0 \leq x \leq 1.0$) hexaferrite. The comprehensive information regarding the compounds utilized in

specific quantities (grams), together with their properties analyzed by various characterization methods, is provided in Table 3.3.

Table 3.3. Detailed description of chemicals used in quantity (g) and performed characterization of $BaCo_xCd_xFe_{12-2x}O_{19}$

Synthesis Material: Cobalt and Aluminium doped Barium hexaferrite ($BaCo_xCd_xFe_{12-2x}O_{19}$)						
Method of Synthesis: Sol-gel Method						
Doping Concentration: x = 0.0, 0.2, 0.4, 0.6, 0.8, 1.0						
Cations to citric acid ratio: 1:1.5						
Chemicals used with Mol. Wt. (g)		**$Ba(NO_3)_2$**	**x $Co(NO_3)_2.6H_2O$**	**x $Cd(NO_3)_2.4H_2O$**	**(12-2x) $Fe(NO_3)_3.9H_2O$**	**$C_6H_8O_7$**
Amount of chemicals used (In g)	x = 0.0	6.533	-	-	121.2	102.443
	x = 0.2	6.533	1.455	1.54235	117.16	102.443
	x = 0.4	6.533	2.9103	3.0847	113.12	102.443
	x = 0.6	6.533	4.365	4.62705	109.08	102.443
	x = 0.8	6.533	5.8206	6.1694	105.04	102.443
	x = 1.0	6.533	7.275	7.71175	101	102.443

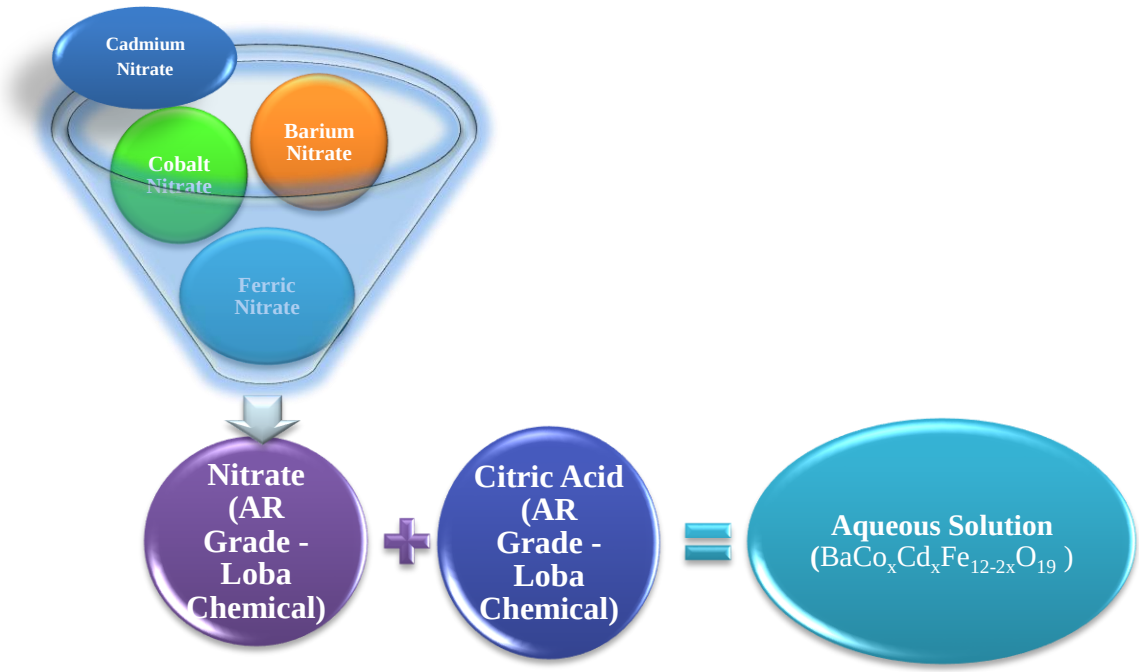

Figure 3.5. Chemicals along with their company for the preparation of $BaCo_xCd_xFe_{12-2x}O_{19}$

3.5. Synthesis of Co^{2+} and Cr^{3+} substituted BaM hexaferrite with composition $BaCo_xCr_xFe_{12-2x}O_{19}$

The combustion reaction can be represented by the following equation:

$$Ba(NO_3)_2 + xCo(NO_3)_2.6H_2O + xCr(NO_3)_3.9H_2O + (12-2x)Fe(NO_3)_3.9H_2O + yNH_4OH + zC_6H_8O_7 + H_2O + \text{heat} \rightarrow BaCo_xCr_xFe_{(12-2x)}O_{19} + mH_2O + nCo_2 + pNO \quad (3.4)$$

Figure 3.6 depicts the chemicals of analytical reagent (AR) grade, together with the manufacturer's name, that were used to prepare the $BaCo_xCr_xFe_{12-2x}O_{19}$ ($0.0 \leq x \leq 1.0$) hexaferrite. The comprehensive information regarding the compounds utilized in specific quantities (grams), together with their properties analyzed by various characterization methods, is provided in Table 3.4.

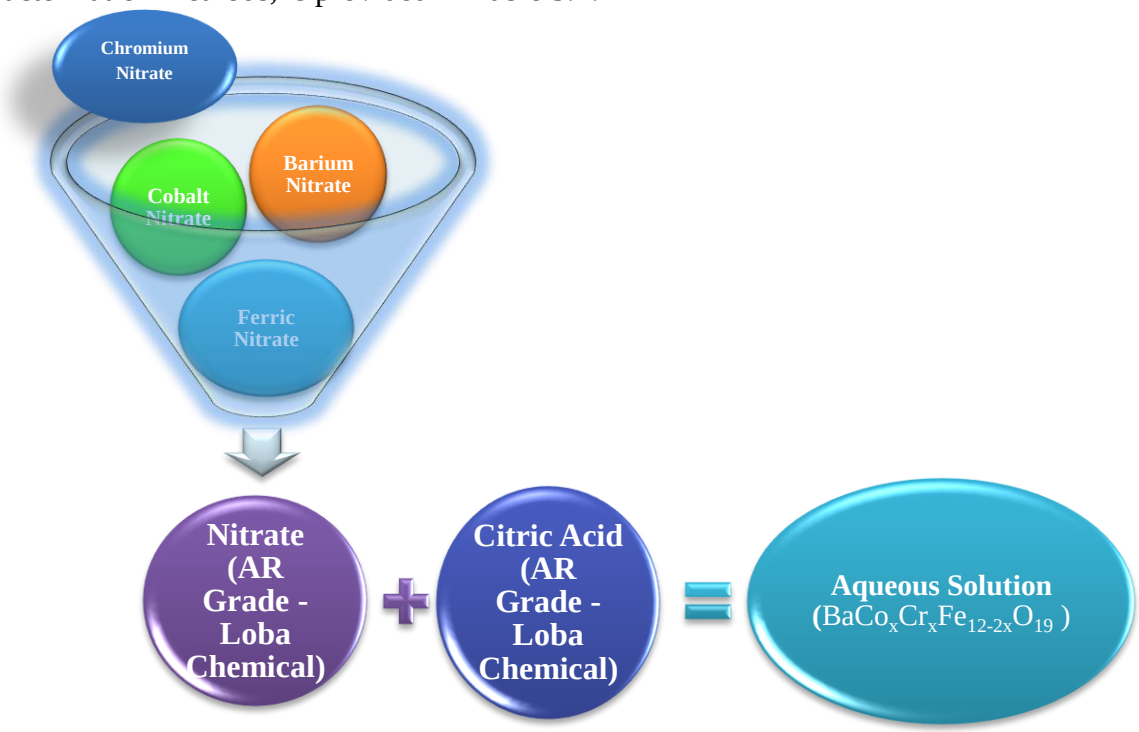

Figure 3.6. Chemicals along with their company for the preparation of $BaCo_xCr_xFe_{12-2x}O_{19}$

Table 3.4 Detailed description of chemicals used in quantity (g) and performed characterization of $BaCo_xCr_xFe_{12-2x}O_{19}$

Synthesis Material: Cobalt and Aluminium doped Barium hexaferrite ($BaCo_xCr_xFe_{12-2x}O_{19}$)
Method of Synthesis: Sol-gel Method
Doping Concentration: x = 0.0, 0.2, 0.4, 0.6, 0.8, 1.0
Cations to citric acid ratio: 1:1.5

Chemicals used with Mol. Wt. (g)		$Ba(NO_3)_2$	x $Co(NO_3)_2.6H_2O$	x $Cr(NO_3)_3.9H_2O$	(12-2x) $Fe(NO_3)_3.9H_2O$	$C_6H_8O_7$
Amount of chemicals used (In g)	x = 0.0	6.533	-	-	121.2	102.443
	x = 0.2	6.533	1.455	2.00075	117.16	102.443
	x = 0.4	6.533	2.9103	4.0015	113.12	102.443
	x = 0.6	6.533	4.365	6.00225	109.08	102.443
	x = 0.8	6.533	5.8206	8.003	105.04	102.443
	x = 1.0	6.533	7.275	10.00375	101	102.443

3.6. Structural Characterization

3.6.1. X-ray diffraction analysis

X-ray diffraction (XRD) is our main tool for checking the structure of solid materials. It tells us about things like their unit cell, lattice parameters, crystal size, how well-ordered they are (crystallinity), if they're pure, and their overall crystal shape. It works for most solid materials. You can see our Rigaku Miniflex-II XRD setup in Figure 3.7.

We shine a focused beam of X-rays onto the material. When these X-rays hit the atoms arranged in a crystal, they bounce off. At certain angles, these bounced X-rays line up perfectly, creating a unique pattern. This pattern acts like a fingerprint, showing us how the atoms are arranged. The Bragg equation helps us understand this:

$$n\lambda = 2d_{hkl}Sin\theta \quad (3.5)$$

Figure 3.7. X-ray Diffraction Setup: Rigaku Miniflex-II System.

The symbols n, d_{hkl}, λ, and θ represent the order of reflection, interplanar spacing, wavelength of X-ray (1.54 Å), and diffraction angle, respectively. We identify each

peak in the pattern using Miller indices. We can do this by looking at the data directly, using graphs, or comparing it to standard ICDD cards [160]. Figure 3.8 shows a basic diagram of an XRD setup.

For our M-type hexaferrite samples, we scanned them from 20° to 80° (2θ) in steps of 0.02° at a speed of 1° per minute. We used settings of 30 kilovolts and 15 milliamperes [149–153].

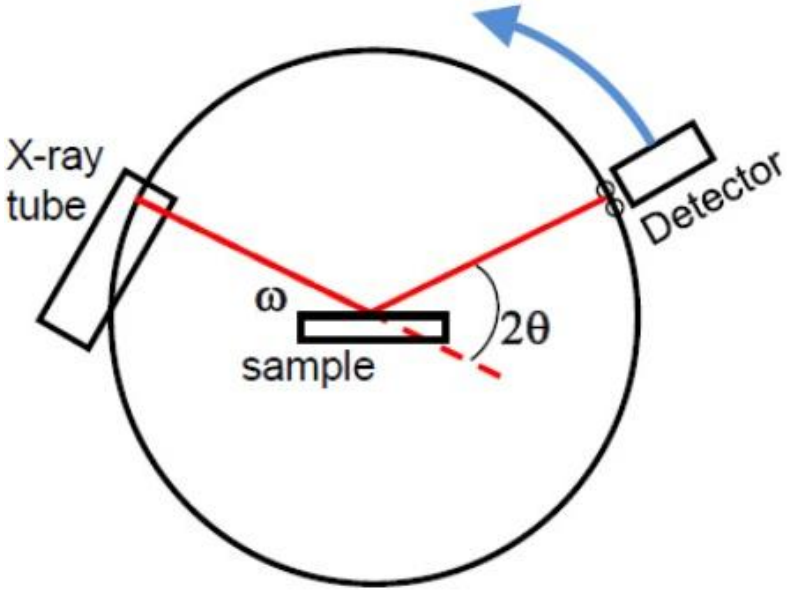

Figure 3.8. X-ray Diffractometer: Schematic Overview.

The basic formula for determining the lattice constants (a and c) from X-ray data is given by equation 3.6.

$$\frac{1}{d_{hkl}^2} = \frac{4}{3}\left[\frac{h^2+hk+k^2}{a^2}\right] + \frac{l^2}{c^2} \tag{3.6}$$

The cell's volume has been computed using equation 3.7:

$$V_{cell} = 0.8666a^2c \tag{3.7}$$

Equation 3.8's expression has been used to calculate the X-ray density.

$$D_x = \frac{ZM}{N_A V_{cell}} \tag{3.8}$$

The number of molecules in each unit cell is denoted by Z. The letters M, NA, and V_{cell} stand for molecular weight, Avogadro's number (6.023 x 10^{23}), and cell volume, respectively. The porosity (P) of the sample is determined using equations 3.8, 3.9, and 3.10 [154].

$$P = \left(\frac{D_x - D_b}{D_x}\right) \times 10 \tag{3.9}$$

$$D_b = \frac{m}{\pi r^2 d} \tag{3.10}$$

In these, D_b is the bulk density, and 'm', 'r', and 'd' are the mass, radius, and thickness of the pellet, respectively. The crystallite size (D) was estimated using the Scherer formula.

$$D = \frac{k\lambda}{\beta \cos\theta} \tag{3.11}$$

The symbol λ represents the wavelength of X-rays, which is equal to 1.54 Å. The symbol β represents the full width at half maximum, measured in radians. The symbol θ represents the Bragg's angle. The symbol k represents the shape factor, which has a value of 1 for a hexagonal structure.

3.7. Field Emission Scanning Electron Microscopy

Standard light microscopes can't zoom in enough or show fine details because they use longer light waves [155]. To see much smaller things, we use Field Emission Scanning Electron Microscopy (FESEM) (as seen with HR-TEM in Figure 3.9 from JEOL Instruments).

Figure 3.9. Morphological Analysis via FESEM and HR-TEM (JEOL Instruments)

FESEM is a powerful tool. It can magnify things up to 600,000 times and show details as tiny as 10 nanometers. This lets us study the surface, grain size, how porous a material is, its shape, and what it's made of at a super small scale [156]. FESEM works by sending out electrons and catching the signals that bounce back. These signals help us see the material's surface very clearly. Because our M-type hexagonal ferrites don't conduct electricity, we had to put a thin layer of a conductive material

(like carbon, gold, or silver) on them to get good images. We did all this analysis using a JEOL FESEM machine.

3.8. Vibrating Sample Magnetometer (VSM)

The Vibrating Sample Magnetometer (VSM) is a crucial tool for understanding the magnetic behavior of our M-type hexagonal ferrites. It works by making the sample, which is attached to a quartz rod, vibrate rapidly (80 times per second) between two strong electromagnets. As the magnetic field around the sample changes, the VSM measures a tiny electrical signal that tells us about the material's magnetization (M). This is then plotted against the applied magnetic field (H) to create a graph called a hysteresis loop. Figure 3.10 shows the Microsense EV-90 VSM setup.

We used a Microsense EV-90 VSM from the USA, applying magnetic fields from -20,000 to +20,000 Oersted (Oe) at room temperature. From the resulting M-H loops, we find important magnetic values like coercivity (H_c), saturation magnetization (M_s), anisotropy field (H_a), squareness ratio (SQR), and remanent magnetization (M_r).

The equation [157] is utilized to derive the M_s and H_a of prepared specimens through the application of the saturation law [158].

$$M = M_s(1 - A/H - B/H^2) + \chi_p H \quad (3.12)$$

The designation "M_s" indicates saturation magnetization, "χ_p" signifies susceptibility at high field, "A" stands for an inhomogeneity parameter, and "B" represents the anisotropy parameter.

The value of B in the crystal's hexagonal symmetry can be determined using the expression shown below [159]:

$$B = H_a^2 / 15 = 4K_1^2 / 15M_s^2 \quad (3.13)$$

In this context, K_1 represents a fixed value that represents anisotropy, while H_a refers to the field that causes anisotropy.

The squareness ratio (SQR) is characterized as the proportion of the remanent magnetization (M_r) to the saturation magnetization (M_s). This factor plays a crucial role in assessing the hardness of magnetic materials and the existence of inter-grain clusters in the synthesized samples. The M_r/M_s ratio in M-type hexaferrite often exhibits a high value within the range of 0 to 1. Materials with a squareness ratio more than 0.5 and less than 1 ($0.5<M_r/M_s<1$) exhibit higher levels of anisotropy, consist of a single domain, and are harder. On the other hand, materials with a

squareness ratio greater than 0.05 and less than 0.5 ($0.05<M_r/M_s<0.5$) have randomly oriented multiple magnetic domains. The Stoner-Wohlfarth model of ferromagnetism is a fundamental model that can well explain the magnetic properties of grains that are tiny enough to have only one domain [160].

Figure 3.10. Magnetic Characterization using Microsense EV-90 Vibrating Sample Magnetometer

3.9. Impedance Analyzer

An impedance analyzer helps us measure a system's impedance (total resistance to an alternating current, or AC signal) and its opposite, admittance. Figure 3.11 presents a picture of the universal impedance analyzer. Impedance has both a "real" part (Z') and an "imaginary" part (Z"). When the connection is made in series, the impedance can be represented as follows [161]:

$$Z = R + jX \tag{3.14}$$

$$Z^* = Z' - jZ'' \tag{3.15}$$

The impedance measuring plane is illustrated by graphing resistance along the x-axis and reactance along the y-axis. Furthermore, the obtained parameters can be utilized to determine the dielectric characteristics of the material, including the loss tangent (tan δ), dielectric constant (ε), AC conductivity (σ), and complex electric modulus (M*). [162].

We took these measurements at room temperature using an Agilent E4980A LCR meter, covering frequencies from 20 Hz to 2 MHz. To prepare the samples, we pressed the powder into disc-shaped pellets using 4 wt% PVA (polyvinyl alcohol) as a binder and 2 tons of pressure. Then, we polished the sides of the pellets and applied silver paste to create parallel plate capacitors for testing. We carefully recorded their

thickness and diameter. Finally, we gently placed the pellets into the measurement cell, making sure the electrodes touched without applying too much force, and noted the micrometer calibration and electrometer settings.

Figure 3.11. LCR meter used for electrical characterization

3.10. Vector Network Analyzer

A Vector Network Analyzer (VNA) is a key tool for checking how well high-frequency electrical parts work in radio and microwave systems [165]. Figure 3.12 shows our setup with the Agilent E8361C VNA, which we use to measure how signals reflect and pass through a material. This helps us understand its behavior at different frequencies [166]. The normalized input impedance (Z_{in}) – basically, how much a material resists an incoming signal – is calculated using this formula, based on how signals travel through lines [167]:

$$Z_{in} = Z_0(\mu_r/\varepsilon_r)^{1/2}\tanh\left[j\frac{2\pi ft(\mu_r/\varepsilon_r)^{1/2}}{c}\right] \quad (3.17)$$

Z_0 represents the characteristic impedance, which has a value of 377Ω. f represents the frequency of the electromagnetic wave, t represents the thickness of the pellet, c represents the velocity of the electromagnetic wave in a vacuum, and ε_0 is equal to 8.854× 10^{-7} F/m wand $\mu_0 = 4\pi \times 10^{-7}$ H/m. The values represent the permittivity and permeability of the vacuum, respectively. According to the theory of absorbing walls, the reflection loss can be written as [168]:

$$\text{REL (dB)} = 20\log\left|\frac{Z_{in}-Z_0}{Z_{in}+Z_0}\right| \quad (3.18)$$

3.11. Application / Design-specific parameters

The complex dielectric constant is composed of two components: the real part (ε') and the imaginary part (ε").

3.11.1. Dielectric Analysis - Complex permittivity

Permittivity is a characteristic of materials that indicates their capacity to store electrical energy when exposed to an electric field. The dielectric constant is a multifaceted quantity defined by the ratio of a capacitor's capacitance when placed in a dielectric material compared to its capacitance in a vacuum. The real part (ε') of the material represents its capacity to store electrical energy, the imaginary component (ε'') signifies its tendency to absorb electrical energy, leading to energy dissipation as heat. A high dielectric loss indicates significant wave attenuation as it passes through the material [17-18].

$$\varepsilon_r = \varepsilon' - i * \varepsilon'' \tag{3.19}$$

It has been computed using the formulae [163].

$$\varepsilon' = \frac{Cd}{\varepsilon_o A} \tag{3.20}$$

In this context, the symbols C, A, d, and ε_o stand for the round pellet's capacitance, cross-sectional area, thickness, and permittivity constant, respectively, in Farads and meters, respectively.

The dielectric loss is obtained from the subsequent equation:

$$\varepsilon'' = \varepsilon' tan\delta \tag{3.21}$$

3.11.2. Complex permeability

Permeability is a characteristic that indicates the extent to which a material can facilitate the establishment of a magnetic field within its structure. It is a complex quantity and has a real part (μ') which indicates how well the material supports a magnetic field (magnetic storage) and an imaginary part (μ'') which represents how much energy is lost as the magnetic field is applied (magnetic energy loss) [19-20].

$$\mu_r = \mu' - i * \mu'' \tag{3.22}$$

3.11.3. Loss tangent

It is denoted by $tan\delta$ it may be dielectric loss tangent and magnetic loss tangent. This quantifies the energy lost as heat relative to the energy that is retained. Dielectric loss tangent is the ratio of ε' and ε'' and similarly magnetic loss tangent is the ratio of μ' and μ''[20].

$$tan\delta_\varepsilon = \frac{\varepsilon''}{\varepsilon'} \tag{3.23}$$

$$tan\delta_\mu = \frac{\mu''}{\mu'} \tag{3.24}$$

The following equation can be utilized to approximate the dielectric loss tangent:

$$tan\ \delta = \frac{1}{2\pi f C_p R_p} \tag{3.25}$$

The symbol δ represents the loss angle, f denotes the frequency, and C_p and R_p represent the analogous parallel capacitance and resistance, respectively.

The subsequent equation is employed to approximate the AC conductivity:

$$\sigma = 2\pi f \varepsilon_0 \varepsilon' \tag{3.26}$$

3.11.4. Complex Electric Modulus

Electric modulus spectroscopy offers a thorough comprehension of charge transport mechanisms, including ion kinetics, conductivity relaxation, and the mechanism of electrical transport. Furthermore, it can be employed to distinguish between grain boundary conduction and electrode polarization mechanisms. The electric modulus can be mathematically represented using an equation. [164].

$$\begin{aligned} M^* &= (\varepsilon^*)^{-1} = (\varepsilon' - i\varepsilon'')^{-1} \\ &= \frac{\varepsilon'}{\varepsilon'^2 + \varepsilon''^2} + i\frac{\varepsilon''}{\varepsilon'^2 + \varepsilon''^2} \\ &= M' + iM'' \end{aligned} \tag{3.27}$$

Here, M' represents the real component and M" represents the imaginary part of the complex modulus.

3.11.5. Complex Impedance Modulus

Complex impedance (Z^*) essentially tells us how much a material resists the flow of AC electricity, and how it handles electrical energy at different frequencies. Think of it as a total "AC resistance" that changes depending on the speed of the electrical signal. This total opposition is broken down into two components:

Z' (the real part): This is the actual resistance that causes energy to be lost, often as heat. It's about how much the material fights the current.

Z'' (the imaginary part): This represents reactance, which is about storing electrical energy. It can be like a capacitor (storing charge) or an inductor (storing magnetic energy).

You can visualize these characteristics using Nyquist plots (also called Cole-Cole plots). These graphs plot Z'' against Z' across a range of frequencies. They usually form semicircles, with each arc revealing a different electrical process happening inside the material.

3.11.6. Uniaxial Magnetocrystalline Anisotropy

This is a key feature. Imagine a magnet that really wants to point in one specific direction. That's what these ferrites do; their internal magnetism strongly prefers to line up along a particular axis in their hexagonal structure (the "c-axis"). This strong preference is why they're "hard" magnets – it's tough to get their magnetism to switch or get rid of it. We measure how much they resist this change with something called the anisotropy field (H_a). M-type ferrites have very high H_a values (like 17 kOe for barium ferrite), making them awesome for strong, stable magnets.

3.11.7. Coercivity - H_c

When you magnetize these materials, they stay magnetized, even if you try to push them with another magnetic field. The strength of the field needed to "un-magnetize" them is called coercivity. Because they have that strong internal "preferred" direction, M-type hexaferrites have high coercivity at room temperature. This makes them perfect for things like permanent magnets. How big their tiny magnetic particles are, their shape, and the boundaries between them all play a role in how high this coercivity is. You can even tweak it by adding different elements (doping).

3.11.8. Saturation Magnetization - M_s

This property refers to the maximum magnetic punch the material can deliver when fully magnetized. M-type hexaferrites generally have good saturation magnetization, which is vital for any device needing strong magnetic action. While they might not be as powerful as some metal magnets, their combo of good magnetic strength, resistance to demagnetization, and their electrical properties (which we'll touch on next) makes them incredibly useful. Scientists can even fine-tune this strength by swapping out some of the atoms in their structure.

3.11.9. Eddy Current Loss

The magnetic loss is characterized by the resonance peaks, which are indicative of the influence of eddy currents. This relationship is described by the following equation:

$$C_o = \mu"(\mu')^{-2} f^{-1} = 2\pi\mu_0\sigma t \qquad (3.28)$$

Where σ implies conductivity.

3.11.10. Reflection loss (Microwave Absorber)

The reflection loss (REL) may be used to examine the frequency-dependent microwave absorption characteristics of synthetic material. Reflection loss occurs when there is a difference in impedance between the surface of a material and the

electromagnetic waves it encounters. The capacity of an electromagnetic wave to be absorbed can be determined through the application of transmission line theory, represented by the subsequent equation. [21].

$$Z_{in} = Z_o \sqrt{\frac{\mu_r}{\varepsilon_r}} \tan h \left[j \frac{2\pi f t}{c} \sqrt{\mu_r \varepsilon_r} \right] \quad (3.29)$$

Where, $Z_{in} = 3\ 77 ohm$, impedance of composite / impedance of air

t – Thickness, ε_r - Complex permittivity, μ_r - Complex permeability, f - Frequency of electromagnetic wave

$$R_L = 20 \log \left| \frac{Z_{in} - Z_o}{Z_{in} + Z_o} \right| \quad (3.30)$$

3.11.11. S (scattering) – Parameter

The S-parameter is fundamentally a complex matrix represented as S = x + i*y, which includes both real and imaginary components, and magnitude and phase elements, within the frequency domain. This is a square matrix that represents all possible combinations of power relationships among the different input and output ports of a microwave junction. At higher frequencies, such as those in the microwave range, it is not feasible to have both an open circuit and a short circuit simultaneously. Additionally, there is currently no instrument available on the market capable of measuring total voltage and current in the GHz frequency range. To address this issue, we employed S parameters. The VNA (Vector Network Analyzer) is the most frequently utilized instrument for calculating the S parameter matrix [22].

3.11.12. Impedance Characteristics

For a material to effectively absorb incoming electromagnetic waves without reflection, its impedance must perfectly match that of free space. This ideal scenario, where the ratio of the material's input impedance (Z_{in}) to the impedance of free space (Z_0) is equal to 1 ($Z_{in}/Z_0 = 1$), ensures that all incident waves are absorbed.

As explained by transmission line theory, any mismatch in impedance leads to reflection loss, meaning some of the waves bounce back instead of being absorbed. Therefore, achieving good impedance matching is crucial for optimizing microwave absorption. Even if a material has excellent dielectric or magnetic loss properties, its absorption efficiency will be limited if impedance matching is poor.

Ideally, for perfect absorption, the real part of the impedance (Z_{real}) should be 1 and the imaginary part (Z_{img}) should be 0. However, this perfect condition is rarely met in

real-world applications, which invariably leads to some reduction in absorption performance.

3.11.13. Quarter Wavelength Mechanism

The Quarter Wavelength Mechanism states that maximum signal attenuation in an absorber occurs when its thickness is one-fourth of the microwave wavelength (λ/4) [23].

This phenomenon happens when a microwave interacts with a ferrite layer placed on a metal surface. A portion of the wave is reflected from the front surface of the ferrite. The remaining part passes through the ferrite, reflects off the underlying metal, and then travels back through the ferrite. If these two reflected waves (one from the ferrite's front surface and one that traveled through the ferrite and bounced off the metal) have equal intensity but are 180° out of phase, they cancel each other out. This cancellation results in minimal reflection and maximum absorption of the incident microwave. This optimal cancellation effect is achieved when the ferrite's thickness is an odd multiple of a quarter-wavelength (e.g., nλ/4, where n=1,3,5,…). This can be mathematically represented as

$$t_m = \frac{n.c}{4\, f_m \sqrt{|\mu_r \varepsilon_r|}} \tag{3.31}$$

Where t_m is matching thickness and f_m is matching frequency.

3.11.14. Bandwidth to thickness ratio and percentage bandwidth

It has been reported that REL = -10 dB results in 90% attenuation, while REL = -20 dB achieves 99% attenuation [24].

The subsequent formulas are employed to assess the Bandwidth to Thickness Ratio (BTR) and the Percentage Bandwidth (PBW):

$$BTR = \frac{\lambda_2 - \lambda_1}{t} \tag{3.32}$$

$$PBW = \frac{f_2 - f_1}{f_o} \tag{3.33}$$

Analysis of tunable frequency and bandwidth to thickness ratio in hexagonal ferrite composites

In order to grasp this concept, we will create a graph illustrating the relationship between REL and frequency across various thicknesses, dopants, and doping percentages. The graph is analyzed, revealing enhancements in microwave absorption samples across various doping levels and percentages.

Calculation of Bandwidth $= Highest\ obtained\ frequency\ at\ R_L$

$< -10dB\ - Lowest\ obtained\ frequency\ at\ R_L < -10dB$

Measurement of Bandwidth to thickness ratio $= \frac{\text{Bandwidth obtained}}{Minimum\ thickness\ noted}$ (3.34)

Figure 3.12. Vector network analyzer (VNA).

Table 3.5 Application-Specific Parameters for Electromagnetic Ferrite Materials

General Material Characteristic	Application-Specific Parameter / Design Specification	Why it Matters for Applications
Complex Permittivity ($\epsilon*=\epsilon'-j\epsilon''$)	Target ϵ' and ϵ'' values over a specific frequency range.	For microwave absorption or EMI shielding, a balanced ϵ'' is crucial for dissipating electromagnetic waves. Too high, and impedance matching suffers; too low, and absorption is weak.
Complex Permeability ($\mu*=\mu'-j\mu''$)	Target μ' and μ'' values over a specific frequency range.	Like permittivity, a balanced μ'' is vital for microwave absorption and EMI shielding to dissipate magnetic energy effectively.
Dielectric Loss Tangent ($\tan\delta_e=\epsilon''/\epsilon'$)	Maximum allowable $\tan\delta_e$ at operating frequency for low-loss applications; optimal range for high-loss applications.	For low-loss applications (e.g., substrates for high-frequency circuits), you'd specify a very low $\tan\delta_e$. For microwave absorbers, an optimized $\tan\delta_e$ value helps in energy dissipation, often alongside magnetic losses.
Magnetic Loss Tangent ($\tan\delta_m =\mu''/\mu'$)	Maximum allowable $\tan\delta_m$ at operating frequency for low-loss applications; optimal range for high-loss applications.	For microwave absorbers, a suitable $\tan\delta_m$ is critical for dissipating magnetic energy from the incident waves. For magnetic cores in inductors or transformers, you'd specify a low $\tan\delta_m$ to minimize energy waste.

AC Conductivity (σac)	Target conductivity range for specific conduction mechanisms.	For EMI shielding, some conductivity might be desired, but excessive conductivity can lead to reflection. For microwave absorption, controlled conductivity can enhance absorption through mechanisms like interfacial polarization.
Complex Electric Modulus ($M*=M'+jM''$)	Frequency range where specific relaxation peaks (M' or M") occur, indicative of grain/grain boundary effects.	For materials where charge transport mechanisms need to be precisely controlled (e.g., certain sensors or ionic conductors), defining the behaviour of M' and M'' at specific frequencies is crucial for optimizing charge mobility and minimizing undesirable effects.
Complex Impedance Modulus ($Z*=Z'-jZ''$)	Target Impedance (Z', Z'') profiles (e.g., Nyquist plot shape) for specific charge transport behavior.	For low-loss applications, you'd aim for high resistance and minimal frequency-dependent reactance. For microwave absorbers, controlling Z' and Z'' is essential for achieving good impedance matching with free space.
Uniaxial Magnetocrystalline Anisotropy (H_a)	Required Anisotropy Field (H_a) for specific magnetic stability or resonance frequency.	A high Ha means the material's magnetism is strongly "locked" in a preferred direction. For permanent magnets, a high Ha ensures stability. For high-frequency microwave devices (e.g., circulators, isolators), anisotropy dictates the ferromagnetic resonance frequency, which needs to be precisely controlled for device operation.
Coercivity (H_c)	Required Coercivity value for magnetic permanence.	High H_c is a key specification for permanent magnets to ensure they resist demagnetization from external fields. For magnetic recording media, the H_c must be optimized to allow for stable data storage while still being writable.
Saturation Magnetization (M_s)	Minimum Saturation Magnetization for desired magnetic strength.	A higher M_s means the material can achieve a stronger magnetic field. For permanent magnets in motors or sensors, a specific Ms is needed to deliver the required magnetic force.
Eddy Current Loss	Maximum allowable eddy current loss at operating frequencies.	High electrical resistivity minimizes eddy currents, which cause energy loss (heat). For high-frequency magnetic cores (e.g., in power electronics, RF inductors), the specification would be

		to minimize eddy current losses to improve efficiency.
Reflection Loss (REL)	Target REL value (e.g., < -10 dB, < -20 dB) over a specific frequency band.	This is a primary metric for microwave absorbers and EMI shielding. An application might specify "REL < -20 dB from 8 GHz to 12 GHz" for X-band radar stealth, or "REL < -10 dB for 2.4 GHz Wi-Fi interference."
Impedance Characteristics (Impedance Matching)	Target impedance ratio ($Z_{in}/Z_0 \approx 1$) over the operating frequency range.	For microwave absorbers, the most critical design parameter. The material's impedance must closely match that of free space to minimize reflection and maximize absorption. A specification would be to achieve this match across the desired bandwidth.
Quarter Wavelength Mechanism ($t_m = n\lambda/4$)	Optimal matching thickness (tm) at specific matching frequencies (fm) for maximum absorption.	This principle guides the design of microwave absorber layer thickness. An application might specify an optimal thickness like "2.5 mm for maximum absorption at 10 GHz" to ensure the reflected waves cancel out.
Bandwidth to Thickness Ratio (BTR) & Percentage Bandwidth (PBW)	Minimum BTR or PBW for broadband applications.	For broadband microwave absorbers or wide-spectrum EMI shields, applications would demand a high BTR (meaning a wide absorption band for a given thickness) or a high PBW (indicating effective absorption across a large percentage of the target frequency range).

Conclusion:

The research methodology effectively combines advanced synthesis and characterization techniques to explore the properties of M-type hexaferrites and their composites. The sol-gel auto-combustion method proves to be a versatile and precise approach for synthesizing high-purity nanostructured materials with tailored properties. The addition of PANI enhances the flexibility and electromagnetic properties of the composites, addressing practical challenges such as mechanical rigidity. The characterization techniques provide comprehensive insights into the structural, morphological, magnetic, and dielectric properties of the synthesized materials, enabling a detailed understanding of their performance in electromagnetic interference (EMI) shielding and microwave absorption. This chapter establishes a

robust framework for evaluating the correlation between synthesis parameters, material properties, and application-specific performance metrics.

CHAPTER-4

RESULTS AND DISCUSSION

4.1. Co^{2+}- Al^{3+} substituted $BaCo_xAl_xFe_{12-2x}O_{19}$ hexaferrite.

In this section, we will be utilizing the sol-gel combustion method to synthesize a hexaferrite with Co and Al substitutions. The composition of this hexaferrite will be $BaCo_xAl_xFe_{12-2x}O_{19}$. Displayed in Table 4.1 are the sample names/codes for various levels of substitution in $BaCo_xAl_xFe_{12-2x}O_{19}$.

Table 4.1. Presents the assignment of sample names corresponding to various substitution levels in $BaCo_xAl_xFe_{12-2x}O_{19}$ hexaferrite.

Sample Composition **$BaCo_xAl_xFe_{12-2x}O_{19}$**	Sample Code Name	Sample Code (W-series)
x= 0.0	**$BaFe_{12}O_{19}$**	W0
x = 0.2	**$BaCo_{0.2}Al_{0.2}Fe_{11.6}O_{19}$**	W1
x = 0.4	**$BaCo_{0.4}Al_{0.4}Fe_{11.2}O_{19}$**	W2
x = 0.6	**$BaCo_{0.6}Al_{0.6}Fe_{10.8}O_{19}$**	W3
x = 0.8	**$BaCo_{0.8}Al_{0.8}Fe_{10.4}O_{19}$**	W4
x = 1.0	**$BaCoAlFe_{10}O_{19}$**	W5

4.1.1 Structural Analysis

4.1.1.1 X-ray Analysis

Figure 4.1 presents the X-ray diffraction (XRD) patterns of $BaCo_xAl_xFe_{12-2x}O_{19}$ hexaferrite samples with varying Co-Al dopant concentrations (W0 (x = 0.0), W1 (x = 0.2), W2 (x = 0.4), W3 (x = 0.6), W4 (x = 0.8), W5 (x = 1.0)). The patterns exhibit well-defined Bragg peaks, which were analyzed using powder-X software. These peaks closely match the reference pattern of Barium hexaferrite ($BaFe_{12}O_{19}$) belonging to the P63/mmc space group (JCPDS card no. 96-100-8842). The XRD analysis confirms the formation of a predominantly hexagonal M-type phase in the synthesized samples[170]. The calculated values for the lattice parameters are presented in Table 4.2.All samples exhibit significant changes in lattice parameters compared to the undoped sample (W0) and lattice parameters decrease with increasing the doping level. The c/a ratio remains constant at 3.94 for all samples [171]. As evident from Table 4.2, the unit cell volume steadily decreases with increasing Co-Al doping concentration (W0 to W5). This phenomenon can be attributed to the difference in ionic radii between the dopants (Co^{2+}: 0.72 Å, Al^{3+}: 0.51 Å) and the substituted Fe^{3+} ion (0.64 Å) [170-171]. The crystallite size, determined

using the Scherrer equation, decreases with increasing doping level (except for W3), ranging from 37.31 nm to 43.40 nm.

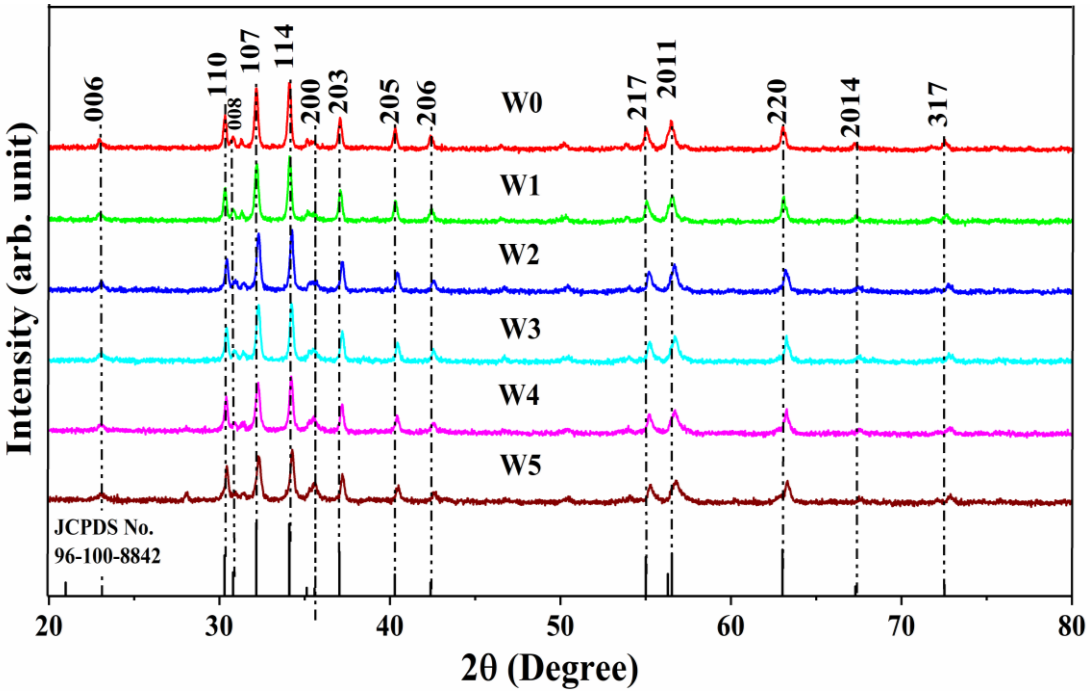

Figure 4.1. X-ray Diffraction Analysis of M-type $BaCo_xAl_xFe_{12-2x}O_{19}$ Hexaferrites

Table 4.2. Effect of Co-Al Doping on Structural Parameters of $BaCo_xAl_xFe_{12-2x}O_{19}$ Ferrites (W0 (x = 0.0), W1 (x = 0.2), W2 (x = 0.4), W3 (x = 0.6), W4 (x = 0.8), W5 (x = 1.0)).

Parameter	W0 (x = 0.0)	W1 (x = 0.2)	W2 (x = 0.4)	W3 (x = 0.6)	W4 (x = 0.8)	W5 (x = 1.0)
a = b (Å)	5.8937	5.8894	5.8829	5.8777	5.8737	5.8725
c (Å)	23.2261	23.2041	23.1773	23.1602	23.1453	23.13331
c/a	3.9408	3.9399	3.9397	3.9403	3.9404	3.9392
Vol /10^6 pm^3	698.6767	697.0137	694.6554	692.9166	691.5248	690.8899
Crystallite Size D_{xrd} (nm)	43.3961	41.5085	39.8247	38.4650	39.1389	37.3097

An EDX analysis was conducted to determine the elemental composition of the synthesized $BaCo_xAl_xFe_{12-2x}O_{19}$ compounds. Figure 4.2 displays the EDX spectra acquired for compositions W0 and W2. As observed in the spectra, the elemental composition of W0 consists solely of Barium (Ba), Oxygen (O), and Iron (Fe). Conversely, the composition of W2 additionally includes Cobalt (Co) and Aluminum

(Al) alongside Ba, O, and Fe. The weight and atomic percentages of all elements present in the final compositions are provided in Table 4.3.

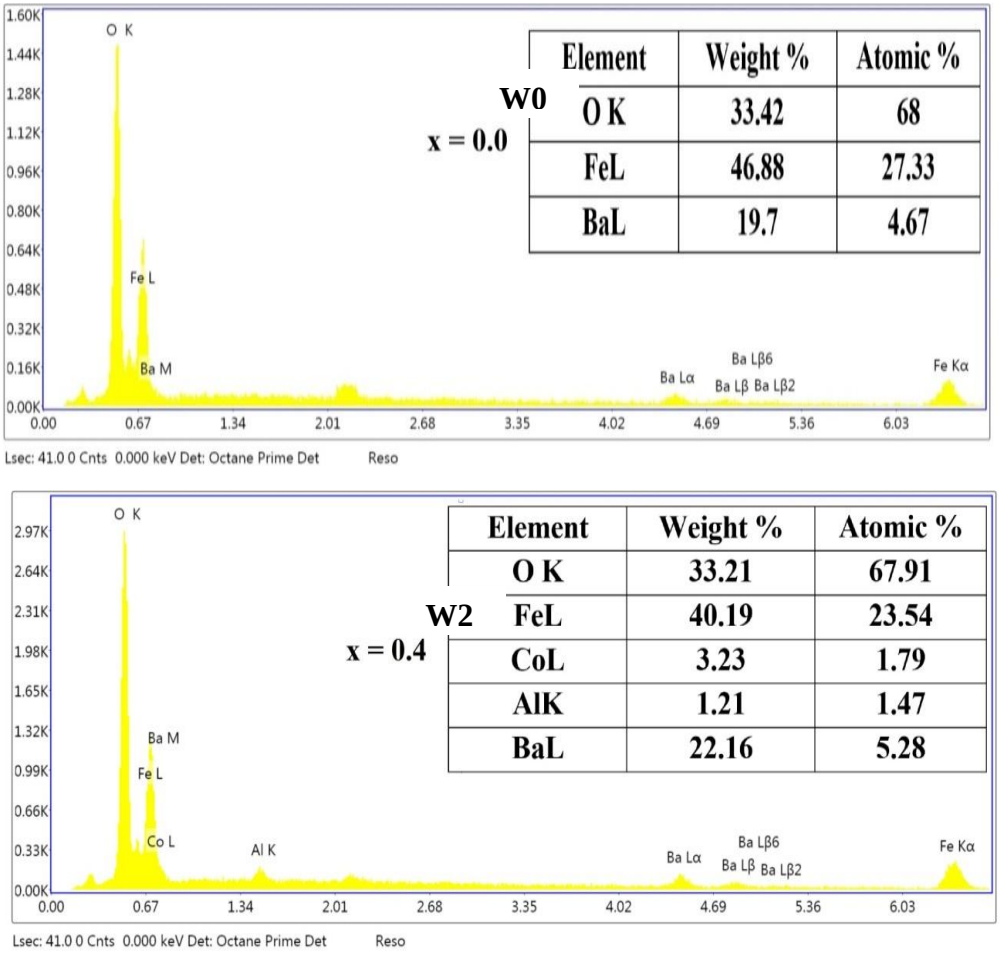

Figure 4.2. Energy-Dispersive X-ray Spectroscopy (EDX) Analysis of $BaCo_xAl_xFe_{12-2x}O_{19}$ Hexaferrites (W0 and W2)

Table 4.3. Elemental Composition of $BaCo_xAl_xFe_{12-2x}O_{19}$ Determined by EDX Analysis (W0 (x = 0.0), W1 (x = 0.2), W2 (x = 0.4), W3 (x = 0.6), W4 (x = 0.8), W5 (x = 1.0)).

Element	W0 (x = 0.0)		W1 (x = 0.2)		W2 (x = 0.4)		W3 (x = 0.6)		W4 (x = 0.8)		W5 (x = 1.0)	
	W %	A %	W %	A %	W %	A %	W %	A %	W %	A %	W %	A %
O K	33.4	68	30.5	67.7	33.2	67.9	20.5	49.2	31.9	67.2	24.5	54.2
FeL	46.8	27.3	35.3	22.4	40.2	23.6	62.1	42.8	33.5	20.2	56.9	36.2
BaL	19.7	4.6	32.1	8.3	22.2	5.3	11.6	3.2	27.8	6.8	10.5	2.7
CoL	-	-	1.6	0.9	3.2	1.8	4.6	3	3.9	2.3	5.2	3.1
AlK	-	-	0.52	0.7	1.2	1.5	1.3	1.8	2.8	3.5	2.9	3.9

4.1.2 Field Emission Scanning Electron Microscopy

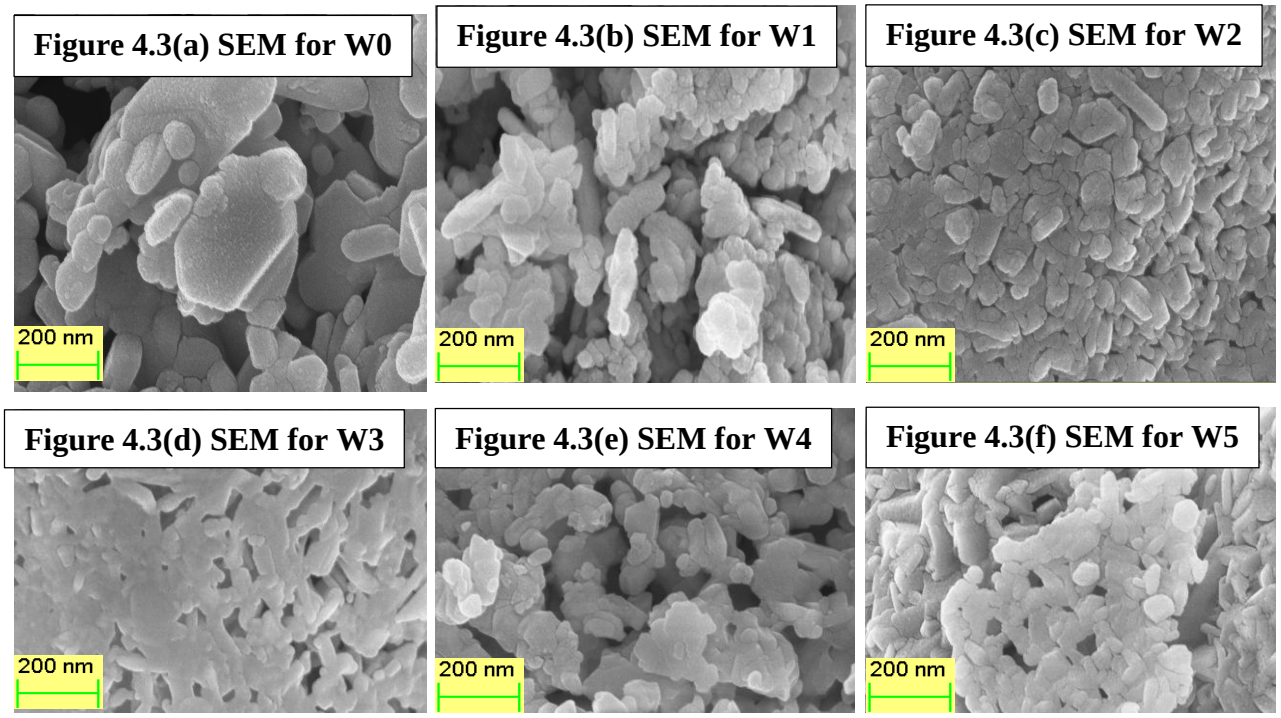

Figure 4.3. SEM Micrographs of $BaCo_xAl_xFe_{12-2x}O_{19}$ Ferrites (W0 (x = 0.0), W1 (x = 0.2), W2 (x = 0.4), W3 (x = 0.6), W4 (x = 0.8), W5 (x = 1.0)).

Formulation of nanoferrites composite

The micrographs in Figures 4.3(a-f) reveal the structure of the samples at different magnifications. In the undoped sample (W0), individual grains fuse together to form a single, giant grain. When Co-Al is added (W3), the grains clump together. Interestingly, as the doping level increases from W0 to W5, the grain size shrinks and transforms into needle-shaped platelets. Additionally, nanoferrites, sized between 1 and 100 nanometers, appear.

Tiny pockets of empty space, called voids, exist between the grains. These act as grain roadblocks for charge carriers, making it harder for them to flow. The smaller the grains, the more numerous these roadblocks become, creating even more resistance to the electric field and altering how charges move through the material.

Grain size may have an impact on two types of electrical resistance: intragranular resistance (R_g) and boundary resistance (R_{gb}). Typically, the intragranular resistance of a material increases and the boundary resistance decreases as the grain size grows. The methods by which charge carriers flow through a substance provide an

explanation for this connection. Charge carriers must traverse both the bulk grains and the grain boundaries in a polycrystalline material like M-type hexagonal ferrites. As the grain size grows, there are fewer grain boundaries for the charge carriers to traverse through, which leads to a decrease in boundary resistance. On the other hand, in materials with smaller grain sizes, there are more grain boundaries that the charge carriers must travel through, resulting in higher boundary resistance. Meanwhile, the intragranular resistance tends to decrease as the grain size grows because there is less likelihood of impurities or defects that may cause resistance within the grains themselves. Therefore, in general, larger grain sizes result in lower boundary resistance and higher intragranular resistance, while smaller grain sizes result in higher boundary resistance and lower intragranular resistance.

4.1.3 Electrical Characterization

4.1.3.1 Dielectric constant

Measurements were conducted at room temperature across a broad frequency range (100 Hz to 2 MHz) using disc-shaped samples with varying thicknesses (1.5-4.5 mm) and a diameter of approximately 5 mm. To measure how these materials respond to electrical fields, made discs (pellets) from the samples and sandwiched them between copper plates. Then sent an electric signal, varying in frequency from 100 Hz to 2 MHz, through the pellets. By measuring how much the materials stored and resisted this electricity, could calculate their key electrical properties, known as the real and imaginary parts of the dielectric constant.

Figure 4.4 shows how the material's ability to store and lose electrical energy changes with frequency. At lower frequencies, these abilities (represented by the real and imaginary parts of the dielectric constant) decrease as the frequency increases. This is due to how the material responds to the changing electric field. However, when the frequency gets high enough, the material's behaviour stabilizes and no longer depends on the frequency. While the ε' value of pure Ba hexaferrite (W0) is 83.48 at 100 Hz and decreases to 12.38 at 2 MHz, the ε' value of W1 is 107.31 at 100 Hz and decreases to 5.60 at 2 MHz as shown in Figure 4.4(a). This trend holds true for W2, where the ε' value is 52.79 and decreases to 5.01, and for W3, where it is 57.90 and decreases to 4.00. The asymmetric nature of grain boundaries, voids, dislocations, etc. causes these greater values in the lower frequency range. Alternatively, decreasing

space charge polarization may cause a smaller ε′ at higher frequencies. The observed change in the material's electrical response with frequency (dielectric dispersion) is better explained by a model called "Maxwell-Wagner interfacial polarization"[171-172]. This model imagines the material as having two layers: one more conductive and one less so. These layers interact in a way that affects how the material stores and releases electrical energy at different frequencies. Imagine the material as tiny conducting islands connected by less conductive bridges. At low frequencies, the bridges act like capacitors, readily storing charge and creating a strong "dielectric field" (a measure of energy storage). But at high frequencies, the charges can't move across the bridges quickly enough, so the field weakens and the energy storage drops. Doping (adding other elements) also reduces the bridges' ability to store charge, leading to a lower dielectric constant overall. The drop in electrical storage (dielectric constant) might be caused by fewer positive iron ions (Fe^{3+}) in the material after adding other elements (doping). This matters because these iron ions help move electrons and store energy in this specific material (ferrite). When we add other elements, they might affect the number of these iron ions available, making it harder to store energy, as seen in Figure 4.4.

4.1.3.2 Analysis of Dielectric Loss and Loss Tangent in $BaCo_xAl_xFe_{12-2x}O_{19}$ Ferrites

Figures 4.4(b) and 4.4(c) depict the frequency dependence of both dielectric loss and loss tangent for the investigated materials. The behaviour of ε" in Figure 4.4(b) is similar to that of ε′ except for W1. At low frequency, interfacial polarization of the Maxwell-Wagner type increases, leading to maximum ε". [173].

The ability of a material to dissipate energy loss, which is represented by loss tangent, changes with frequency (100 Hz – 2 MHz) as shown in Figure 4.4(c). For samples W1, W2, and W3, the loss tangent first increases, then peaks at specific frequencies (5636.77 Hz, 26670.40 Hz, and 16827.90 Hz, respectively), and decreases afterward. This behaviour can be explained by resonance. The peaks in the Figure 4.4 (c) suggest that these materials exhibit maximum energy dissipation at their natural resonant frequencies. When an external alternating field with changing frequency interacts with the material, resonance occurs when the frequency of the external field matches the material’s natural resonant frequency. At this point, the material reaches

maximum energy loss, as indicated by the peak in the loss tangent, which reflects the material's ability to dissipate energy.

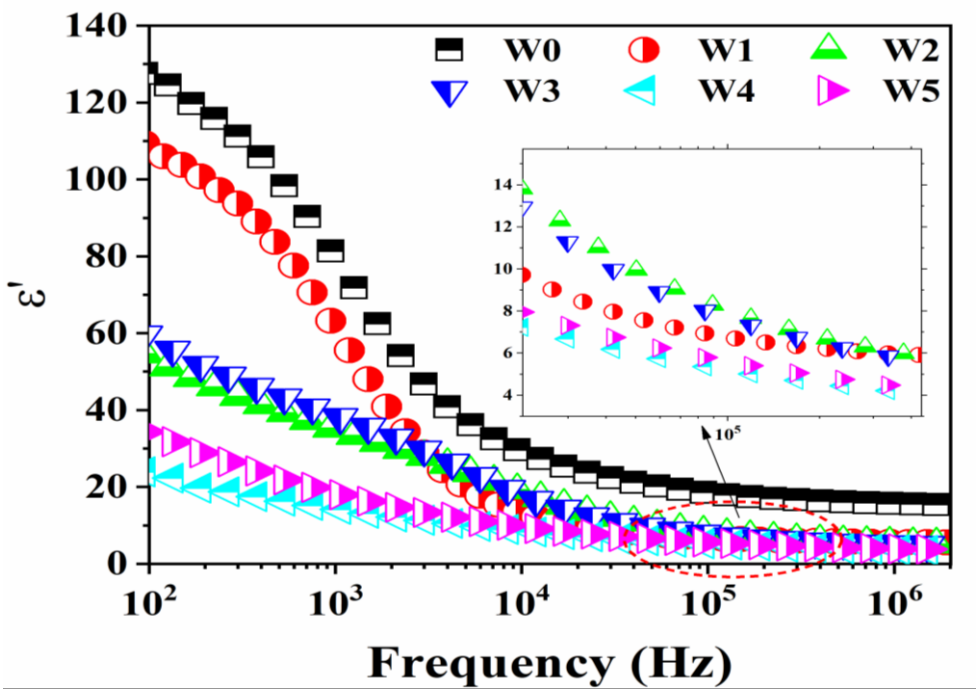

Figure 4.4(a). Dielectric Constant Dependence on Frequency in $BaCo_xAl_xFe_{12-2x}O_{19}$ (W0 (x = 0.0), W1 (x = 0.2), W2 (x = 0.4), W3 (x = 0.6), W4 (x = 0.8) and W5 (x = 1.0)) Hexaferrites

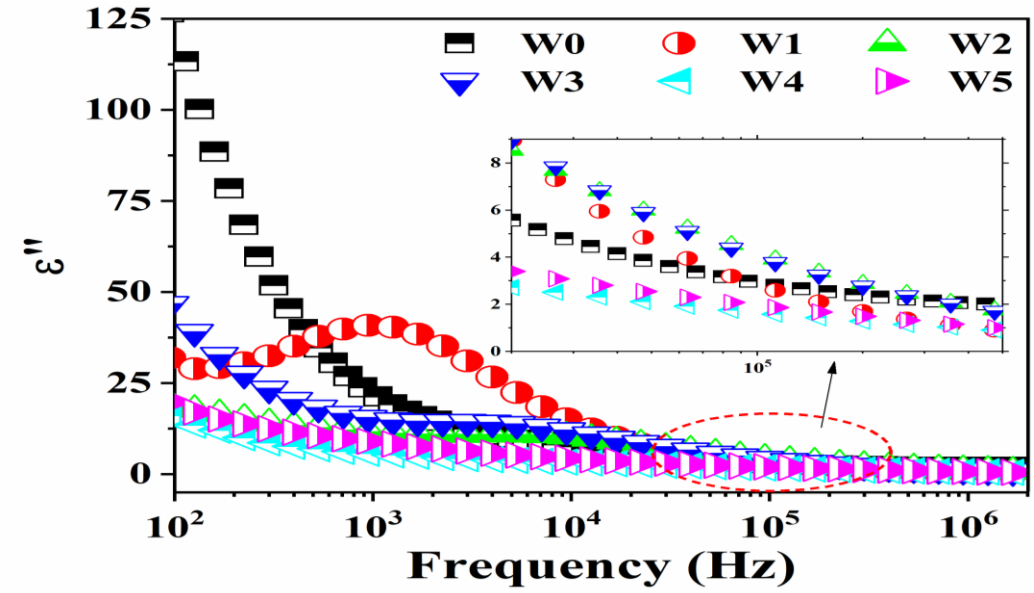

Figure 4.4(b). Dielectric Loss Dependence on Frequency in $BaCo_xAl_xFe_{12-2x}O_{19}$ (W0 (x = 0.0), W1 (x = 0.2), W2 (x = 0.4), W3 (x = 0.6), W4 (x = 0.8) and W5 (x = 1.0)) Hexaferrites

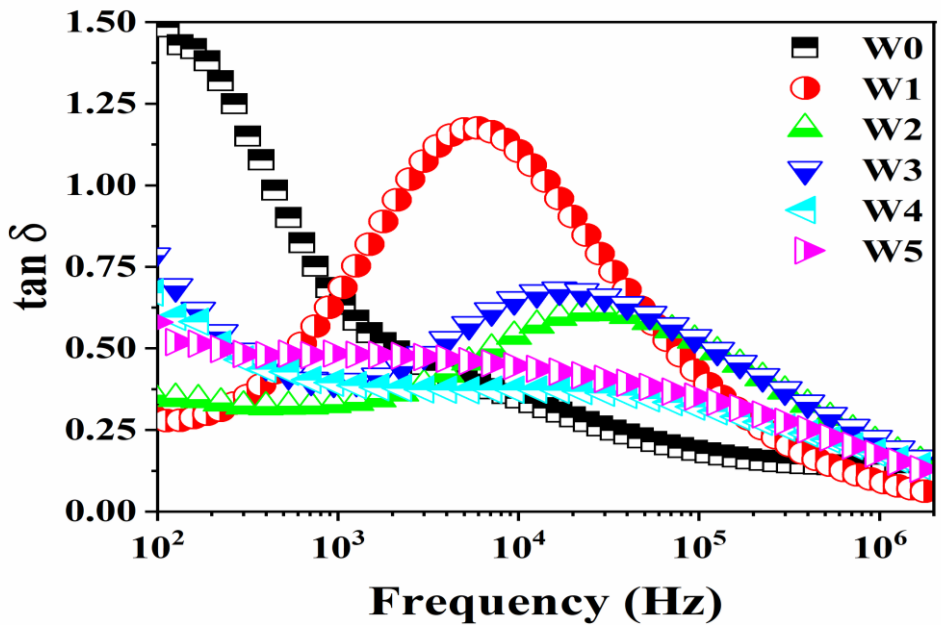

Figure 4.4(c) Dielectric Loss Tangent Dependence on Frequency in $BaCo_xAl_xFe_{12-2x}O_{19}$ (W0 (x = 0.0), W1 (x = 0.2), W2 (x = 0.4), W3 (x = 0.6), W4 (x = 0.8) and W5 (x = 1.0)) Hexaferrites

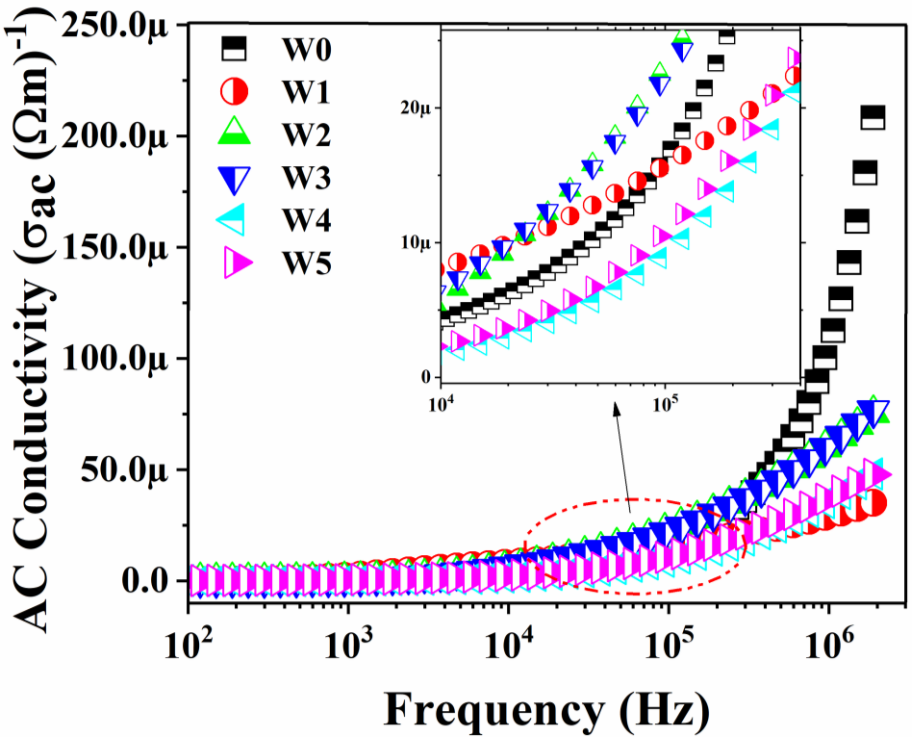

Figure 4.4(d) AC Conductivity Dependence on Frequency in $BaCo_xAl_xFe_{12-2x}O_{19}$ (W0 (x = 0.0), W1 (x = 0.2), W2 (x = 0.4), W3 (x = 0.6), W4 (x = 0.8) and W5 (x = 1.0)) Hexaferrites

The absence of a peak in the dielectric loss for W4 and W5 is due to the limited mobility of ions in the crystal lattice, resulting in a dominance of crystal lattice polarization. This leads to a decrease in dielectric loss with increasing frequency, without any peak. The dielectric loss factor generally decreases as frequency increases, except for W1, W2 and W3, which show an initial increase followed by a decrease. At lower frequencies, sample W1 exhibits the lowest loss tangent because Fe^{3+} ions were reduced, which are responsible for conductivity [174–176]. The Substitution of Fe^{3+} ions with dopant causes decrease in electron hopping between Fe^{3+} and Fe^{2+} ions and thus loss decreases.

The graph depicts the variation of the loss tangent (tan δ) as a function of frequency for different doping concentrations (x = 0.0 to x = 1.0).

1. Trend with Frequency:
    - The tan δ initially increases, reaches a peak at a specific frequency, and then decreases as the frequency increases further.
2. Peak Heights:
    - The peak height is most pronounced for the sample with x = 0.2, which exhibits the highest tan δ at around 10^3 - 10^4 Hz.
    - As the doping concentration increases from x = 0.4 to x = 1.0, the peak heights progressively decrease, with the sample at x = 1.0 having the smallest peak height.
3. Peak Shift with Frequency:
    - The peaks for all samples shift to lower frequencies as doping concentration increases.
    - For x = 0.2, the peak shifts slightly to the right towards 10^3 Hz, indicating a peak at a lower frequency.
    - For higher doping levels (x = 0.4 to x = 1.0), the peaks gradually shift further to the right, toward lower frequencies.
4. Width of the Peaks:
    - The peak for x = 0.2 is the broadest, indicating a wider frequency range over which tan δ remains high.

- As doping increases (x = 0.4 to x = 1.0), the peaks become narrower, suggesting a more concentrated tan δ response over a specific frequency range.

5. Doping Impact:
    - Doping initially increases the loss tangent significantly, as seen by the large peak at x = 0.2.
    - However, further increases in doping concentration beyond x = 0.2 reduce the tan δ peak and shift the response to lower frequencies, suggesting that excessive doping may hinder the material's ability to sustain high energy loss over a broad frequency range.

4.1.3.3 AC Conductivity

Electrons in ferrites primarily move by jumping between iron ions (Fe^{2+} and Fe^{3+}) within the material. This phenomenon occurs more often as the frequency of an electric field increases, resulting in heightened electron mobility. The concept of "polaron hopping" provides a comprehensive understanding of electron motion. [177]. Charge transport in this material is governed by a hopping mechanism, with its frequency dependence captured by Johnscher's universal power law [178-179]. This is expressed as follows:

$$\sigma_{ac} = \sigma_{dc} + A\omega^{n} \quad (4.1)$$

Where n represents the frequency exponent and satisfying 0 < n < 1, in addition with A and n, which are thermally activated, have been previously discussed in the literature [180].

The exponent n, as depicted in Figure 4.5, typically represents the power law relationship between two variables:

AC Conductivity (σ_{ac}): This signifies the material's ability to conduct alternating current (AC) at a specific frequency.

ω: This variable usually represents a compositional or microstructural parameter that can influence the conductivity.

The power law relationship between σ_{ac} and ω can be expressed as follows:

$$\sigma_{ac} \alpha\ \omega^{n} \quad (4.2)$$

The value of n provides valuable insights into the conduction mechanism within the material:

n = 1: This indicates a linear relationship between conductivity and the compositional/microstructural parameter. This behaviour might suggest Ohmic conduction, where current flow is directly proportional to the applied electric field.

n < 1: This signifies a sub-linear relationship, implying a weaker dependence of conductivity on the parameter.

n > 1: This suggests a super-linear relationship, indicating a stronger than proportional dependence of conductivity on the parameter.

The material's ability to conduct AC electricity (σ_{ac}) depends on both frequency and how well charges move between specific points (octahedral sites). Figure 4.4(d) shows that at low frequencies, σ_{ac} doesn't change. But as the frequency gets higher, it increases for all the materials tested. Within the high-frequency range, all synthesized materials demonstrate a rise in AC conductivity, ranging from 0.000036 Ωm^{-1} to 0.000078 Ωm^{-1}. Verwey's hopping mechanism, as described in reference [181], offers an explanation for the universally observed increase in AC conductivity at higher frequencies for hexaferrites.

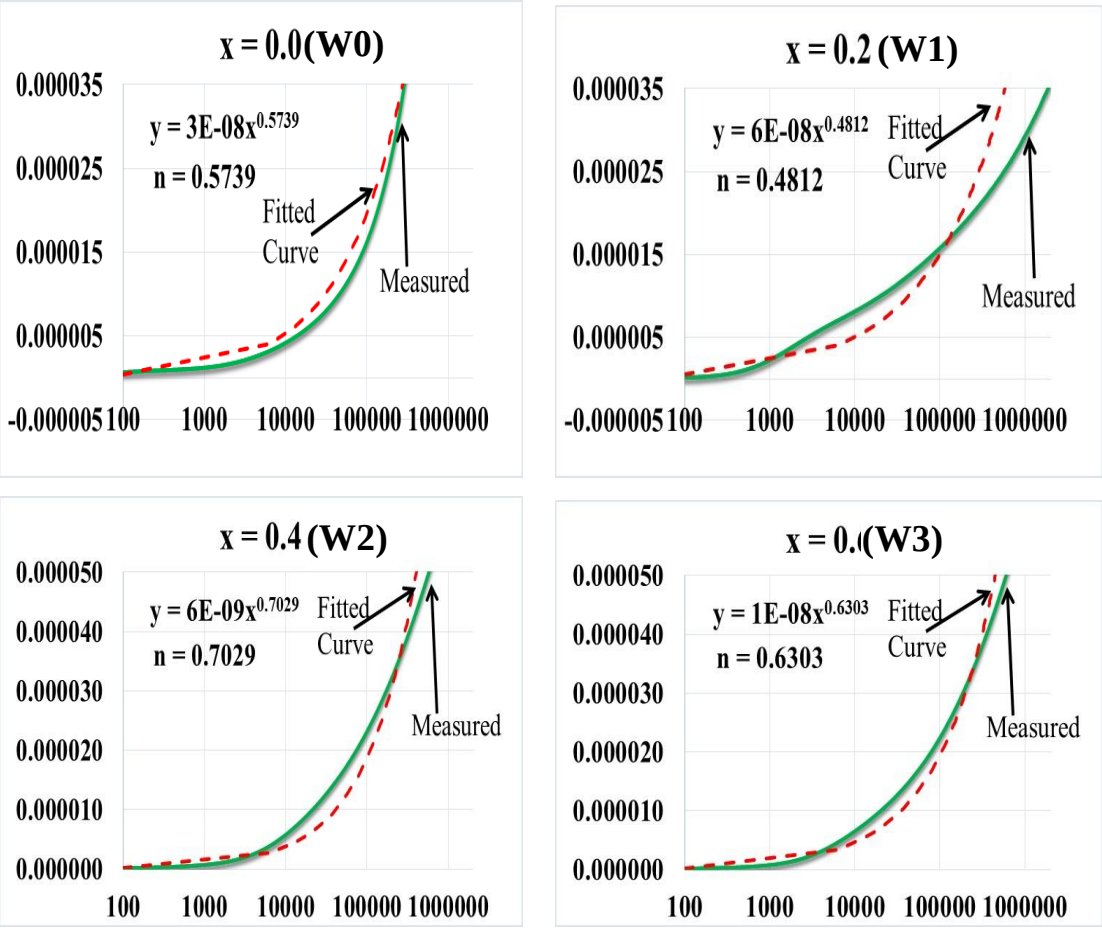

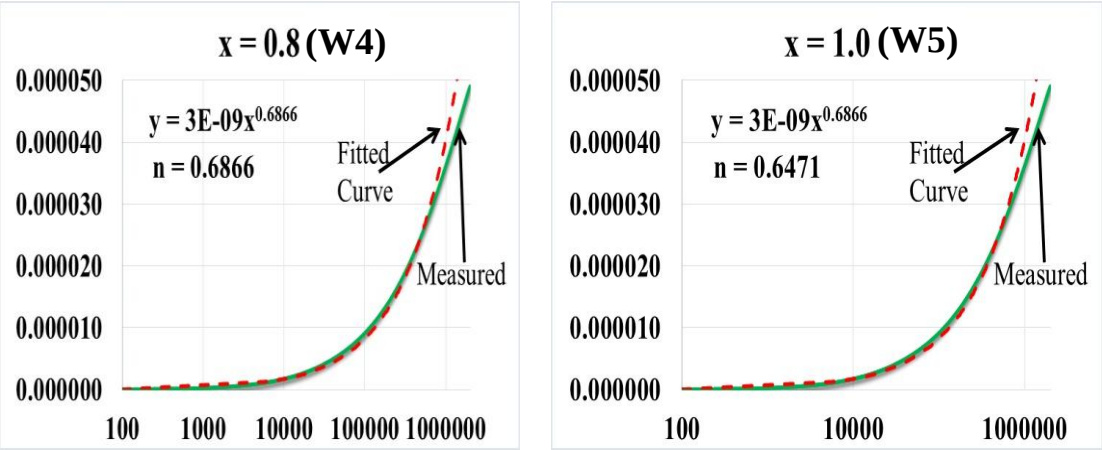

Figure 4.5. n-Value Analysis of AC Conductivity in $BaCo_xAl_xFe_{12-2x}O_{19}$ Ferrites (W0 (x = 0.0), W1 (x = 0.2), W2 (x = 0.4), W3 (x = 0.6), W4 (x = 0.8) and W5 (x = 1.0)).

Enhanced electrical conduction in hexaferrites at higher frequencies might be caused by electrons successfully transitioning between the two valence states of t1he same element, namely iron (Fe^{2+} and Fe^{3+}). At low frequencies, boundaries within the material act like roadblocks, hindering the movement of electrons (charge hopping) and leading to high polarization (energy storage). This is because many electrons get trapped at these boundaries. However, at higher frequencies, the material's structure helps electrons bypass these grain roadblocks, releasing the trapped charges and boosting conductivity.

4.1.3.4 Electric modulus analysis

Figure 4.6(a) presents the frequency dependence of the real part of the dielectric modulus (M') for all samples at room temperature. The electric modulus, calculated using the formula described in [182-183], reflects the material's ability to store electrical energy. Low-frequency behaviour: At lower frequencies, the real part of the modulus (M') starts low for all samples and gradually increases with rising frequency, reaching a maximum at 2 MHz. Near-zero M' at low frequencies: All samples exhibit a tendency for M' to approach near-zero values in the low-frequency range. This suggests maximized restoring force dipolarization, implying minimal conductivity and negligible electrode polarization spread. Suppressed electrode polarization: The low M' values at low frequencies for W0, W1 and W2 indicate suppressed electrode polarization. Increased electrode polarization with doping: Doping seems to enhance the electrode polarization effect. This is observed as the M' value in the low-

frequency region increases with increasing concentrations of Co-Al dopants, reaching significantly higher values for samples W4 and W5.

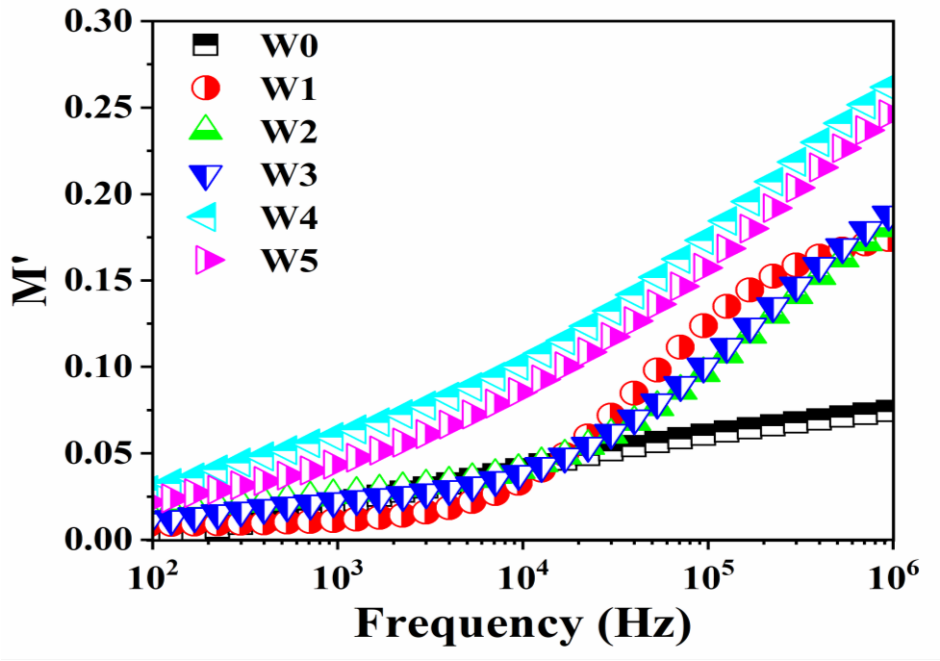

Figure 4.6(a). Real Modulus (M′) Dependence on Frequency in $BaCo_xAl_xFe_{12-2x}O_{19}$ (W0 (x = 0.0), W1 (x = 0.2), W2 (x = 0.4), W3 (x = 0.6), W4 (x = 0.8) and W5 (x = 1.0)) Hexaferrites

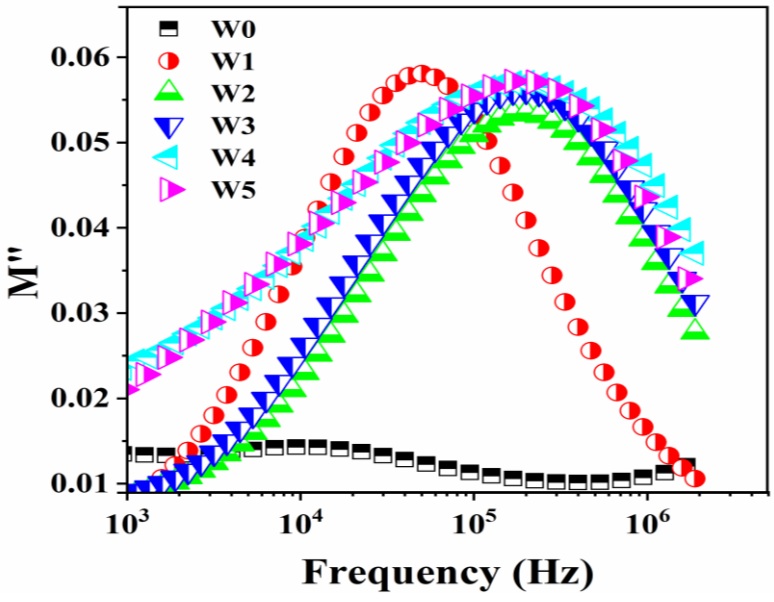

Figure 4.6(b) Imaginary Modulus (M") Dependence on Frequency in $BaCo_xAl_xFe_{12-2x}O_{19}$ (W0 (x = 0.0), W1 (x = 0.2), W2 (x = 0.4), W3 (x = 0.6), W4 (x = 0.8) and W5 (x = 1.0)) Hexaferrites

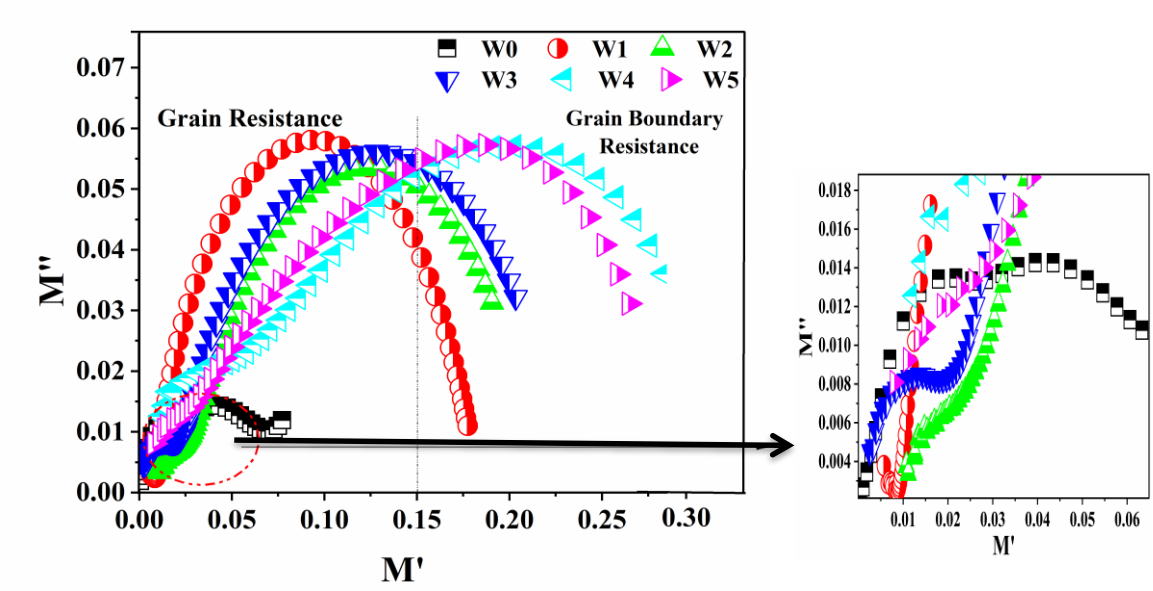

Figure 4.6(c) Cole-Cole Impedance Plots of $BaCo_xAl_xFe_{12-2x}O_{19}$ (W0 (x = 0.0), W1 (x = 0.2), W2 (x = 0.4), W3 (x = 0.6), W4 (x = 0.8) and W5 (x = 1.0)) Hexaferrites at 900°C, 5h.

Figure 4.6(b): The imaginary part of the complex modulus (M'') reveals crucial information about charge transport in conductivity domain, relaxation phenomena, and their dependence on grain boundaries, defects, and compositional variations. M'' exhibits an initial rise, peaks, and then declines with increasing frequency. The observed spectrum can be interpreted based on:

Asymmetrical peak maxima (f_{max}): These indicate the presence of conductivity relaxation mechanisms.

Peak broadening with increasing Co-Al content: This suggests diverse conductivity relaxation mechanisms in the ferrites.

Peak shift towards higher frequencies with increasing x: This signifies faster conductivity relaxation processes with higher dopant concentrations.

Increasing peak height with increasing Co-Al content: This indicates enhanced conductivity relaxation.

The pre-peak region represents the range of charge carriers capable of long-range mobility due to hopping between octahedral sites. Conversely, the post-peak region signifies the confinement of charge carriers within their potential wells within the grains. The transition from long-range to short-range mobility and the associated relaxation time dispersion occur beneath the asymmetrical peaks.

Figure 4.6(c): The diameter of the semicircles in the Cole-Cole plots (M'' vs. M') corresponds to the conductivity relaxation time, which increases with increasing doping concentration. The movement of the semicircles toward the high frequency region indicates the reduction in relaxation time with doping. Cole-Cole plots reveal the influence of grains and grain boundaries:

Left side of the semicircle (lower frequency): Represents grain resistance.

Intermediate frequency region beneath the curve: Represents grain boundary contribution.

Right side of the semicircle (higher frequency): Represents grain and grain boundary resistance.

Co-Al doping induces a shift towards the high-frequency domain, indicating faster conductivity relaxation processes. The distribution of conductivity relaxation times is reflected by the shift in the high-frequency intercept of the semicircle with doping, further supporting the non-Debye relaxation.

4.1.3.5 Impedance spectroscopy

As evident in Figures 4.7(a) and 4.7(b), both the real (Z') and imaginary (Z'') components of impedance exhibit high values at low frequencies. However, with increasing frequency, both Z' and Z'' decrease, while AC electrical conductivity increases. This behaviour can be primarily attributed to electron hopping. At low frequencies, the high Z' and Z'' suggest space charge polarization. This phenomenon involves the accumulation of charge carriers at grain boundaries [46], leading to significant polarization, often termed interfacial polarization. The Maxwell-Wagner theory provides a framework for understanding this type of polarization.

High-Frequency Behaviour: As frequency increases, the contribution of grain boundaries diminishes, resulting in lower Z' and Z'' values. This behaviour aligns with the Koop's double-layer model, where the impedance response is dominated by the bulk material at higher frequencies.

When an electric field is applied, the dipoles within the ferrite material, attempt to align themselves with the field. In an ideal scenario, the dipoles would flip simultaneously, displaying a remarkable level of coordination. This phenomenon is known as Debye relaxation. However, the truth is far more complicated. Some dipoles in these ferrites may exhibit slower behaviour as a result of their surrounding

environment or interactions with neighbouring elements. Instead of a single rapid flip, you will experience a range of response times. There is a variation in the speed at which dipoles flip, with some doing so quickly while others take a longer time. This spread is non-Debye relaxation. Additionally, the presence of two relaxation peaks for W0 suggests distinct relaxation processes: a slower one within the bulk and a faster one near grain boundaries. The Cole-Cole plot (Figure 4.7(c)), derived from plotting the real (Z') vs. imaginary (Z'') impedance components, offers valuable insights into the electrical response of the material. This plot, based on a two-layer model, exhibits two overlapping semicircles.

Low-frequency semicircle: This represents the grain boundary resistance (R_{gb}), attributed to the accumulation of charge carriers at grain boundaries, leading to interfacial polarization [184]. High-frequency semicircle: This corresponds to the grain or bulk resistance (R_g), reflecting the intrinsic conduction properties of the material [185-186].

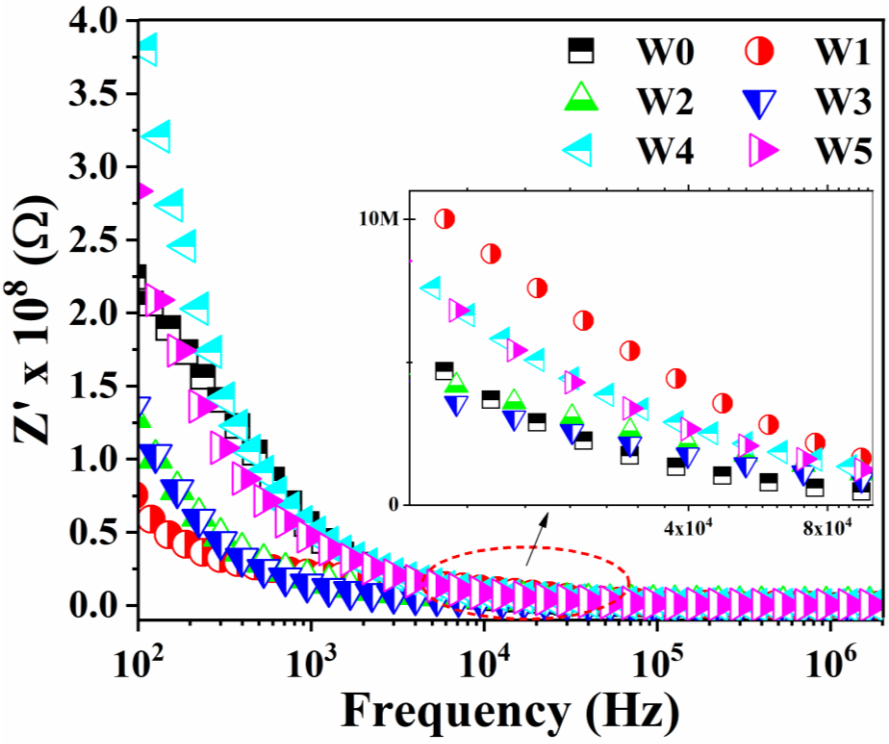

Figure 4.7(a) Real Impedance (Z′) Dependence on Frequency in BaCoxAlxFe12-2xO19 (W0 (x = 0.0), W1 (x = 0.2), W2 (x = 0.4), W3 (x = 0.6), W4 (x = 0.8) and W5 (x = 1.0)) Hexaferrites

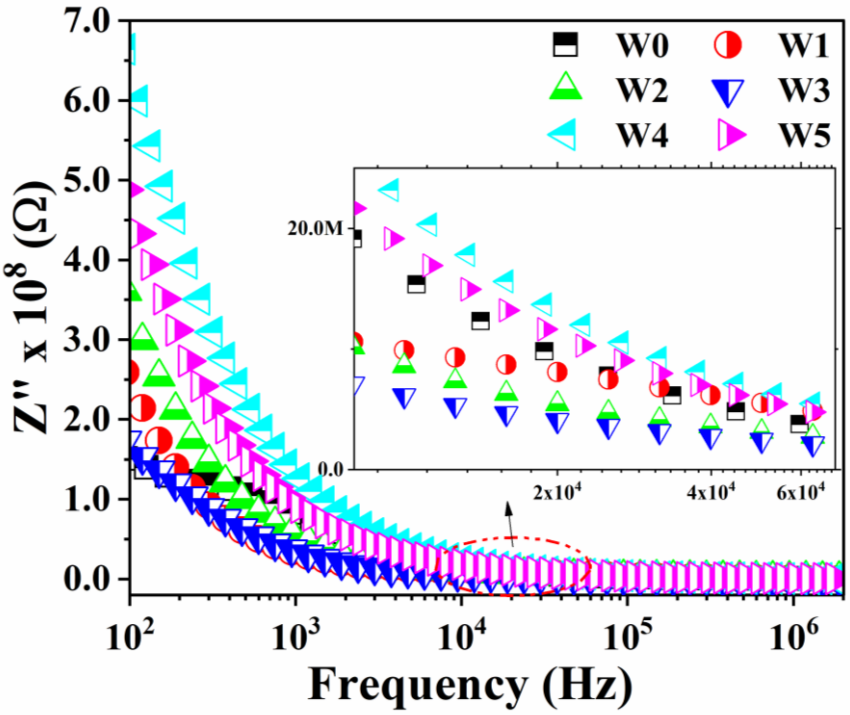

Figure 4.7(b) Imaginary Impedance (Z′) Dependence on Frequency in BaCoxAlxFe12-2xO19 (W0 (x = 0.0), W1 (x = 0.2), W2 (x = 0.4), W3 (x = 0.6), W4 (x = 0.8) and W5 (x = 1.0)) Hexaferrites

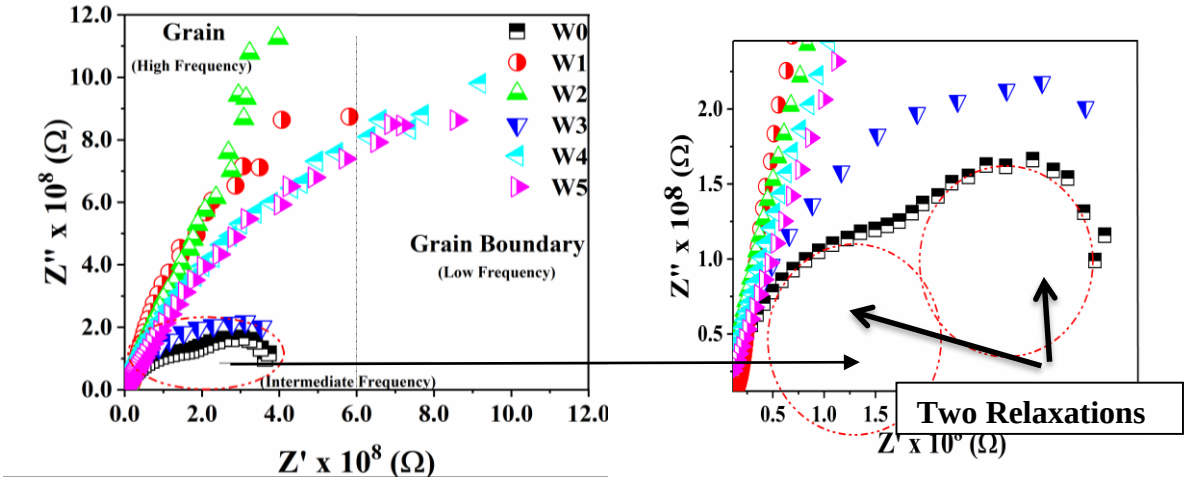

Figure 4.7(c) Cole-Cole Impedance Plots of BaCoxAlxFe12-2xO19 (W0 (x = 0.0), W1 (x = 0.2), W2 (x = 0.4), W3 (x = 0.6), W4 (x = 0.8) and W5 (x = 1.0)) Hexaferrites after Heat Treatment at 900°C for 5 Hours.

This observed behaviour is a consequence of the distribution of relaxation times within the material. Different relaxation times, associated with varying charge carrier

mobility across grain boundaries and bulk regions, contribute to the distinctive shape of the Cole-Cole plot. This overlap is further influenced by grain size:

Smaller grains: Exhibit only one semicircle as the grain and grain boundary responses merge due to their similar time constants.

Larger grains: Display two distinct semicircles, clearly separating the contributions from grain boundary and grain resistance.

Room-temperature Cole-Cole plots for all compositions revealed only single, incomplete semicircles (except for W0), suggesting:

High grain boundary resistance: The grain contribution is not well-resolved, indicating a dominant influence of grain boundaries on conduction.

Factors contributing to high R_{gb}: Decreased Fe^{3+} concentration, increased surface-to-volume ratio, porosity, and disordered atomic arrangements near grain boundaries [187].

4.1.3.6 Computational Impedance Simulation and Validation

Figure 4.8 presents the outcome of an equivalent circuit analysis applied to complex impedance data obtained through Electrochemical Impedance Spectroscopy (EIS) software [188]. The equivalent circuit comprises a series connection of two parallel sub-circuits:

First sub-circuit: Models the individual grains' resistance and capacitance (R_g & C_g).

Second sub-circuit: Represents the resistance and capacitance of individual grain boundaries (R_{gb} & C_{gb}).

The observed non-ideal (depressed) semicircle necessitated replacing the ideal capacitor in the model with a constant phase element (CPE). This substitution accounts for the non-Debye type behaviour exhibited by the composition under study. The following equation was used to calculate capacitance:

$$C_{CPE} = (P.R^{-(n-1)})^{1/n} \quad (4.3)$$

The equivalent circuit model utilizes CPE (constant phase element) values denoted as "P" and resistance values denoted as "R", along with a phase offset "n" ranging from 0 to 1 for the capacitor. This model accurately captures the behaviour observed in the mixtures, as evidenced by the high agreement between measured and simulated/fitted curves in the Figure 4.8. Table 4.4 presents the relaxation time, resistance, and capacitance values extracted from the EIS data for both grains and grain boundaries.

These parameters quantify the electrical response of these microstructural features within the mixtures.

Table 4.4. Extracted Grain and Grain Boundary Parameters from EIS Modelling

X	R_g (MΩ)	R_{gb} (MΩ)	C_g (μF)	C_{gb} (μF)
0.0 (W0)	324.550	166.580	1872.274	20.484
0.2 (W1)	20.781	1000.000	81.426	10.472
0.4 (W2)	825.390	72.803	3.955	244966.636
0.6 (W3)	505.400	3.078	75.950	6.983
0.8 (W4)	1000.000	903.130	3.307	749.281
1.0 (W5)	104.230	1000.000	681.505	2.581

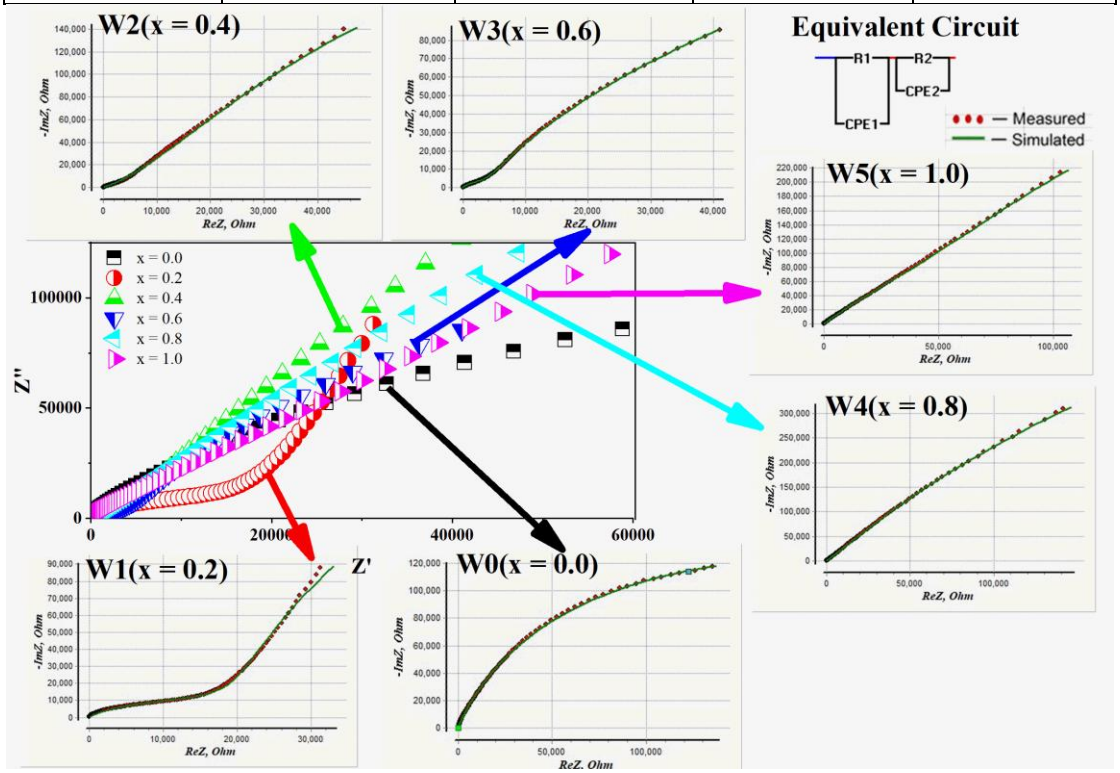

Figure 4.8. Measured and Fitted Impedance Data with Equivalent Circuit (W0 to W5)

4.1.3.7 Investigating the Relationship between EIS Data and Microstructure

Micrographs of W0 (Figures 4.3(a) and 4.9(a)) reveal significant grain agglomeration, where individual grains cluster together to form larger structures. This phenomenon can facilitate the development of larger grains, potentially increasing their intragranular resistance. Consequently, the effective grain size is perceived as larger,

leading to an increased grain capacitance (C_g = 1872.270 µF), as observed in the equivalent circuit analysis.

This leads to a relatively small capacitance value at the grain boundaries, C_{gb} =20.484 µF (Table 4.4). Large, fused, agglomerated, or clustered grains are also visible in this section of the micrographs (Figures 4.3 and 4.9); their polarization is enhanced, leading to the highest simulated C_g =1872.274 µF. For sample W1, grain size reduction renders a fall in C_g to 81.426 µF from 1872.270 µF. When the grain size is small, there will be a large number of the grains and thus a large number of the grain boundaries in the material, which makes for a large resistance of the grain boundaries. In sample W1, grain size is small, which causes an increase in the resistance of grain boundaries (R_{gb} = 1000 MΩ) and the lowest grain resistance (R_g = 20.781 MΩ), as seen in Table 4.4. Figure 4.3(c) and Figure 4.9(c) display the composition with W2 and it is clear that the inter-grain connection is considerably improved. Figure 4.9(c) demonstrates how the nearness of grain boundaries and relatively good grain size distribution give rise to considerable polarization, which in turn increases C_{gb}, in agreement with the maximum simulated C_{gb} of 244966.636 µF indicated in Table 4.4. This polarisation may originate from the development of a dipole moment across a boundary caused by the build-up of charges at the interfaces of neighbouring grain boundaries [189].

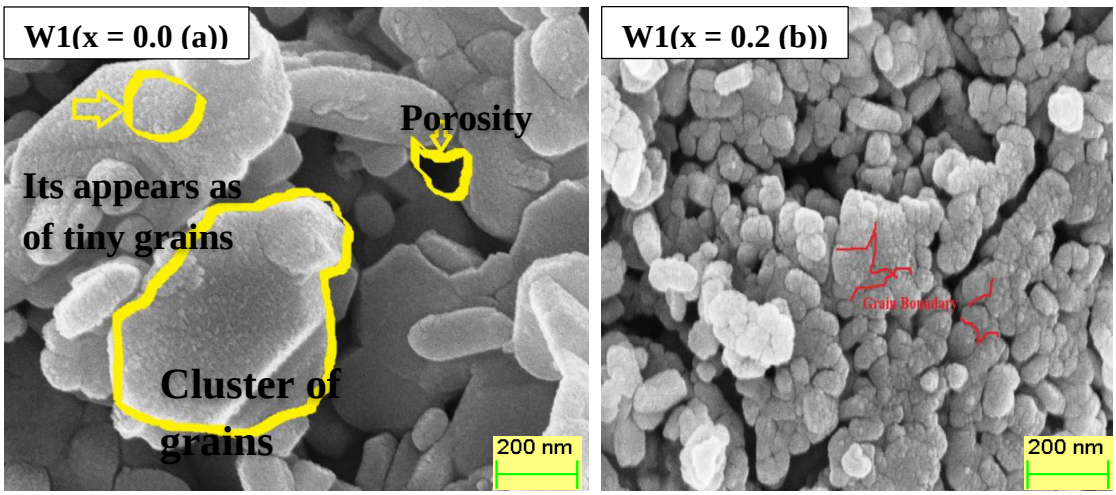

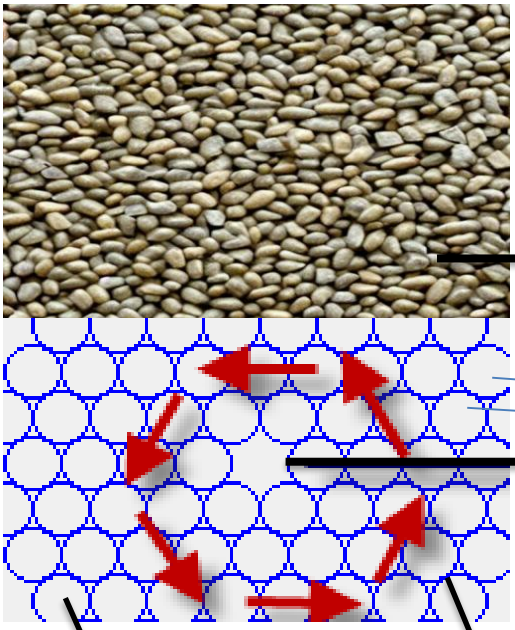

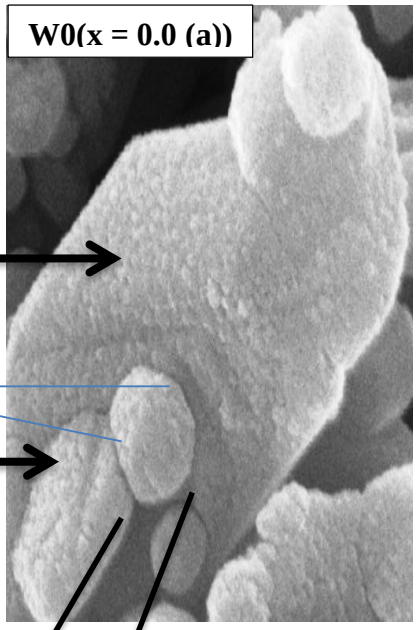

Good Grain Conductivity

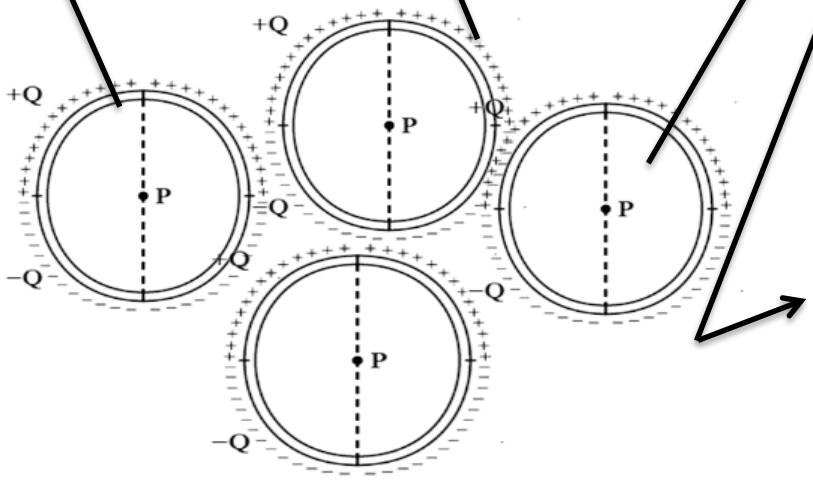

Large Grains = surface of grains appears as of tiny grains that enhanced polarization and lead to maximum dielectric constant as reflect in the Figure 4.3 (a)

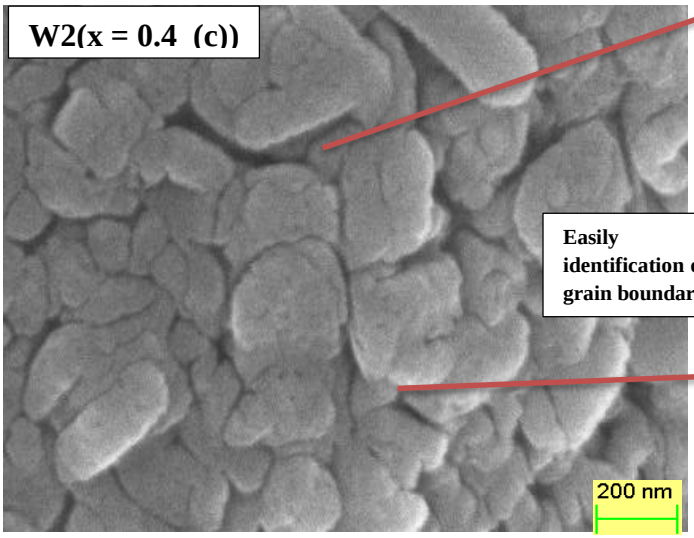

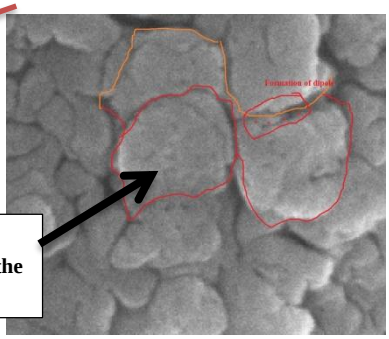

Easily identification of the grain boundaries

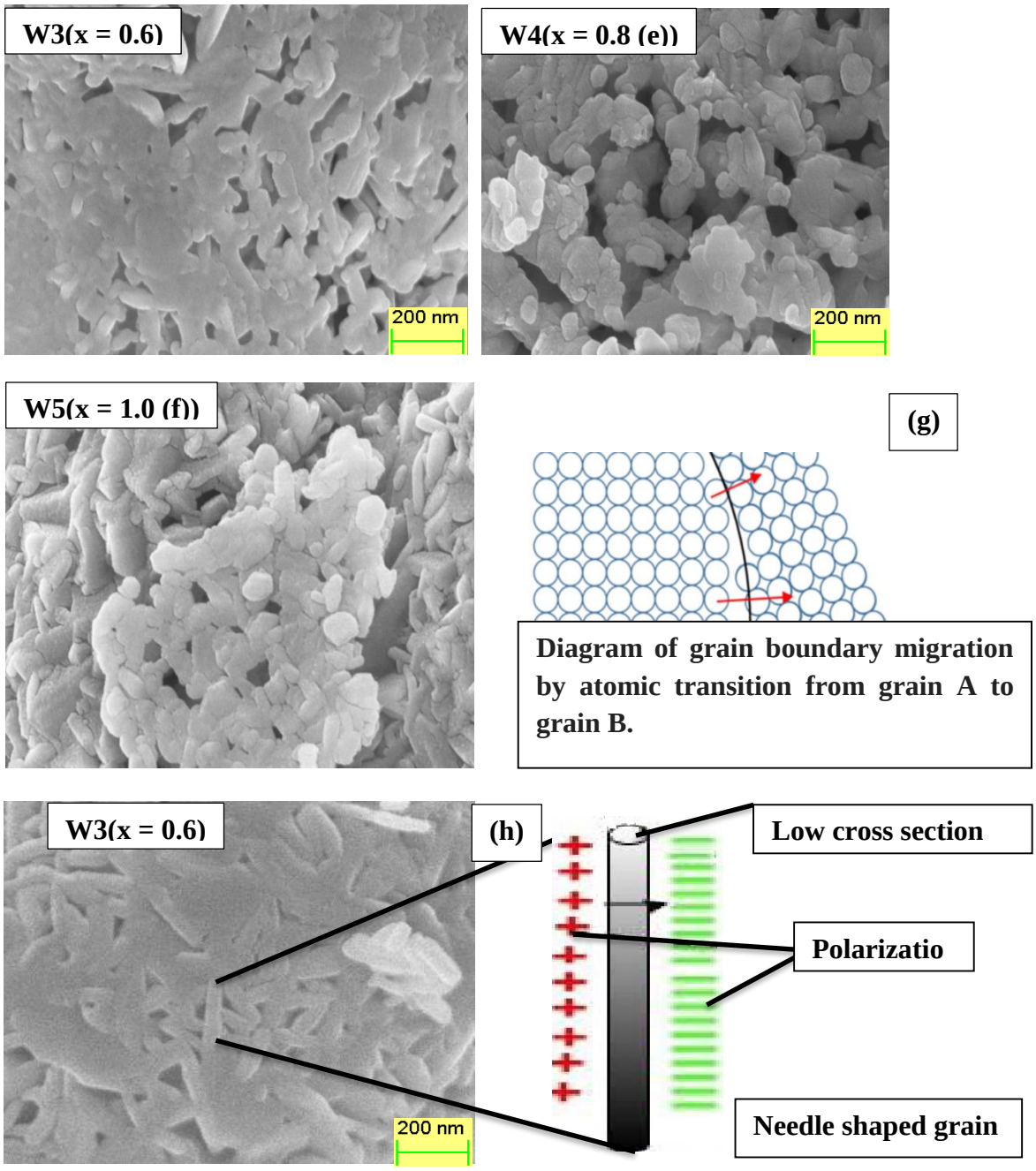

Figure 4.9. SEM Characterization of $BaCo_xAl_xFe_{12-2x}O_{19}$ Ferrites (x = 0.0-1.0 (W0 to W5))

The polarisation that forms as a consequence might increase the resistance at the grain boundary from 20.78 MΩ to 825.39 MΩ. For W3, grains started fusing with each other, and due to that, grain boundaries reduced, R_{gb} reached its lowest value of 3.08 MΩ and fused grains increased grain capacitance C_g = 75.95 µF as shown in Figures 4.3(d) and 4.9(d). In W4, small regions of grain fusing can be seen with easy identification of individual grain boundaries. It increases the capacitance of grain

boundary C_{gb} to 749.28 µF and due to multilayer grain boundaries, R_{gb} is increased to 903.13 MΩ as shown in Figures 4.3(e) and 4.9(e). In W5, maximum grain boundary resistance reached 1000 MΩ and C_g = 681.505 µF has been observed. This sample has three regions of grain agglomeration, as shown in Figure 4.9 (g). This causes an increase in C_g and a fall in C_{gb} since agglomerates discourage polarization at grain boundaries. However, the geometry or grain size distribution of agglomerates also depicts individual grains in all regions, which causes a larger R_{gb} than R_g. When the grain size is large and the number of grain boundaries is low, as shown in Figures 4.9(a) and 4.9(g). However, the intragranular resistance may decrease when the grain size is small and the number of grain boundaries is high. As the resistance at the grain boundary increases, it acts as a barrier to the passage of charge carriers, making the material stiffer and more resistive, and so it decreases the ε′. Similar responses were observed in Figure 4.4 and Table 4.4 for W4 grain boundary resistance (R_{gb}) of 903.13 MΩ and also ε′ = 39.80, which is the lowest in doped samples.

Understanding these relationships can be crucial for enhancing the performance of these materials in electronic applications because the morphology and microstructure of M-type hexagonal ferrites affect their dielectric constant overall.

The grain size and morphology of a material significantly impact its dielectric loss. Materials with smaller and more uniformly distributed grains (e.g., W2, W4 and W5 in Figure 4.3) exhibit lower dielectric losses due to their increased surface area to volume ratio. This reduces the contribution of interfacial losses arising from grain boundaries and other interfaces within the material. Conversely, materials with larger grains or non-uniform distribution (e.g., W0 in Figure 4.3) experience higher dielectric losses (highest for W0 with 499.95). The larger volume in such cases contributes more significantly to bulk losses.

Figure 4.4(c) illustrates the highest loss tangent (3.68) for W0. This can be attributed to the heterogeneous morphology observed, where the non-uniform distribution of grains creates additional interfacial losses. Interfaces can lead to increased energy dissipation due to phenomena like interfacial polarization.

Interestingly, for W3, smaller grain sizes exhibit higher loss tangent compared to other doped samples. This suggests increased electron hopping at grain boundaries due to the higher concentration of dopants, leading to additional energy dissipation. In

contrast, samples with more homogeneous morphology (W2 and W5) exhibit lower loss tangent (0.61 and 0.99) due to the combined effects of reduced interfacial losses and a more uniform distribution of charged species throughout the material.

The pronounced relaxation peak observed for W1 suggests a strong correlation with the concentration and distribution of charged species, likely Fe^{3+} ions due to their abundance in the material. A homogeneous microstructure with uniform particle shapes often contributes to a well-defined and higher relaxation peak. This is because a more uniform distribution of charged species allows for a larger collective response to the applied electric field, resulting in greater energy dissipation and a consequently higher peak.

The lower peak heights observed for W2 and W3 compared to W1 could be attributed to either a reduced concentration or a less uniform distribution of charged species. This non-uniformity hinders the collective reorientation of these species in response to the field, leading to lower energy dissipation and a weaker peak.

4.1.3.8 Impact of Microstructure on Dielectric Loss

Loss tangent (tan δ): Figure 4.4(c) shows the highest value (3.68) for W0, attributed to its heterogeneous morphology:

Non-uniform grain distribution: Creates interfaces between regions, causing enhanced energy dissipation through interfacial polarization.

W3(x = 0.6): Doped sample with smaller grains exhibits higher tan δ due to increased electron hopping at grain boundaries, leading to more energy loss.

W2(x = 0.4) & W5(x = 1.0): Homogeneous morphology results in lower tan δ (0.61 & 0.99) due to reduced interfacial losses and uniform distribution of charged species

W1(x = 0.2): Highest peak height: Correlation with charged species concentration and distribution (Fe^{3+} ions): A higher peak at W1 signifies a greater concentration and/or a more even distribution of charged species, likely Fe^{3+} ions, within the material.

Homogeneous structure and efficient energy dissipation: This peak likely corresponds to a more homogeneous microstructure in the material at this doping level. A well-defined and higher peak reflects efficient energy dissipation as the charged species reorient themselves in response to the applied electric field.

Reduced concentration or non-uniform distribution (W2 and W3) lowers peak height.

Investigating the Impact of Simulated Microstructure on AC Conductivity

4.1.3.9 Impact of Microstructure on AC Conductivity

Grain size, boundaries, and porosity: These influence AC conductivity by affecting charge carrier movement.

High porosity: Air gaps disrupt charge flow, leading to reduced conductivity (e.g., W1).

Dense materials: Higher carrier density can enhance conductivity.

Heterogeneous microstructure: Pores, cracks, and grain boundaries act as barriers, lowering conductivity.

W0(x = 0.0) vs. W1(x = 0.2):

W0(x = 0.0): Highest conductivity (0.00022 Ωm^{-1}) due to Fused small grains: Increased cluster polarization enhances dielectric constant (low frequency).

More homogeneous structure: Facilitates easy charge carrier movement.

W1(x = 0.2): Lowest conductivity: Heterogeneous structure: Pores and boundaries hinder charge flow.

4.1.3.10 Investigating the Influence of Simulated Grain Boundaries on Electric Modulus Responses

Impact of Composition on Relaxation Behaviour: At W0, the prominent semicircle observed in the Cole-Cole plot (Figure 4.6) suggests a dominant contribution from grain boundaries. This is further supported by the concentration of the relaxation phenomenon in the low-frequency regime.

W2: Doping alters the behaviour, shifting the semicircle towards higher frequencies, suggesting a transition towards grain-dominated relaxation.

For W4 and W5, the influence of grain boundaries increases further. This is evident by the re-emergence of the semicircle in the low-frequency region of the impedance spectra and its significantly reduced diameter.

For W4, small cluster of grains can be seen in micrograph and are oriented in different planes which trends to enhance the conductivity their by leading to height electric modules

Microstructural and relaxation behaviour

W0(x = 0.0): The double peak in the Cole-Cole plot suggests coexistent conductive and dielectric relaxation. Grain agglomeration increases grain boundaries, contributing to enhanced polarization and low-frequency conductivity.

At W3(x = 0.6), the presence of two distinct peaks in the impedance spectra suggests the simultaneous contribution of two relaxation mechanisms. The peak at lower frequencies likely originates from low-frequency conductivity relaxation. The higher-frequency peak, extending into the intermediate frequency range, coincides with the observed high grain resistance (R_g = 505.402 MΩ) and potentially reflects dielectric relaxation phenomena.

W1, W2 and W4: Narrower and closer peaks, indicative of a more uniform distribution of relaxation times, arise from a more uniform grain size distribution. At W4, the behaviour gradually shifts towards higher frequencies, with combined grain and grain boundary contributions.

W5: Extensive grain agglomeration (refer to Figure 4.9) leads to a drastic increase in grain boundary resistance (1000 MΩ) and cluster formation, emphasizing grain resistance contribution.

W1: While promoting conductivity, the large porosity in grain boundaries limits their polarization contribution.

4.1.3.11 Incorporating Simulated Grain Boundaries into Impedance Spectroscopy Analysis

The Cole-Cole plot (Figure 4.7(c)) for W0 exhibits two distinct relaxation peaks, suggesting the presence of concurrent conductive and dielectric relaxation mechanisms. At high frequencies, the initial semicircle represents the combined influence of dielectric relaxation and grain resistance. The subsequent, incomplete semicircle at intermediate frequencies signifies contributions from both grain and grain boundary resistance ($R_{gb} < R_g$). As the level of dopant (x) increases to 0.8 and 1.0 (W4 and W5), the entire semi-circular feature shifts towards lower frequencies, implying combined contributions from both resistances across the frequency spectrum. Notably, at W3, grain merging occurs, leading to a significant increase in grain resistance (R_g) reaching 505.40 MΩ.

4.1.4 Magnetic Analysis

By replacing cations with different electronegativity, magnetic moment, and d-configuration, it is possible to tune the magnetic properties of the sample that have been created [190]. It has been shown that ions with a higher electronegativity tend to occupy octahedral sites in the crystal lattice more often than they do tetrahedral places

[191]. This phenomenon occurs due to the enhanced electrostatic interaction between the positively charged cation and the negatively charged oxygen anions in its vicinity.

The aluminium ion (Al^{3+}) in the $BaCo_xAl_xFe_{12-2x}O_{19}$ has a lower electronegativity (1.61) compared to Cobalt ion (Co^{2+}) with an electronegativity of 1.88. As a result, Al^{3+} can occupy tetrahedral sites $4f_1$, whereas Co^{2+} can occupy octahedral sites. The Fe^{3+} atoms in M-type barium hexagonal ferrites are spread out among five distinct sites: two tetrahedral sites (2b and $4f_1$) and three octahedral sites (2a, 12k, and $4f_2$). Among these sites, 2a, 2b, and 12k have spin up, while $4f_1$ and $4f_2$ have spin down [4].

In accordance with the ligand field theory, Al^{3+} ions do not exhibit any site preference because of their d^0 configuration. On the other hand, Co^{2+} ions, which have a d^7 configuration [192-193].

If the substituted ion has a greater ionic radius than the host ion, it selectively occupies octahedral sites located at the edges of the unit cell. According to earlier findings, Co^{2+} ions may be found in both the octahedral ($4f_2$) and tetrahedral ($4f_1$) crystallographic sites [194-195]. Conversely, Al^{3+} ions (0.51 Å), because of their lower ionic radius, tend to occupy octahedral positions in the crystal structure, resulting in enhanced electrostatic stability [196].

Figure 4.10 demonstrates the hysteresis loops of all $BaCo_xAl_xFe_{12-2x}O_{19}$ samples at room temperature. The metrics derived from the M-H loop are shown in Table 4.5. It consist of the saturation magnetization (M_s), the remanence magnetization (M_r), the coercivity (H_c), the anisotropy field (H_a), and the remanence ratio (M_r/M_s).

The magnetic moment of the specimen may be elucidated by examining the arrangement of host and substituted cations across five crystallographic sites inside a hexagonal crystal structure, as described by the equation [197].

$$b\ (4f_1 + 4f_2)\ (\downarrow) \tag{4.4}$$

By replacing non-magnetic ions or ions with lower magnetic properties at the ($4f_1\downarrow$ + $4f_2\downarrow$) lattice site, the total magnetization rises. However, when these ions are substituted at the ($2a\uparrow$ + $12k\uparrow$ + $2b\uparrow$) lattice sites, the magnetization exhibits a drop in behaviour [198]. Table demonstrates a non-monotonic drop in M_s as the quantity of substitution increases from W0 to W5. The drop in magnetization (M_s) may be attributed to many mechanisms, including spin canting, transition from a high to low

spin valence state, site occupancy, and exchange interaction [199]. There is a clear 42% decline in the M_s value at lower degrees of substitution, namely from W0 to W1. The replacement of Fe^{3+} (5 μB) with Co^{2+} (3 μB) and Al^{3+} (0 μB) can leads to a drop in M_s. This decrease occurs because it lowers the quantity of Fe^{3+} ions at magnetic sites. The subsequent rise of 16%, 8%, and 14% in M_s from W2 to W4 may be attributed to a decrease in porosity. Porosity functions as a non-magnetic empty space that reduces magnetization and at the same time generates demagnetizing forces. Nevertheless, the rise in M_s is not as significant as the decline in porosity. The rise in M_s may be attributed to the occupancy of both the $4f_2$ and $4f_1$ locations of crystallographic sites [200]. Finally, from W4 to W5, the M_s Value decreased by 18%. Replacing a significant quantity of Fe^{3+} with Co^{2+} and Al^{3+} (W5(x = 1.0)) has the potential to disturb the integrity of the crystal lattice. This disturbance has the potential to diminish the collective magnetic superexchange interactions among the remaining Fe^{3+} ions, leading to a reduction in M_s [x].

The mechanism of coercivity relies on both intrinsic and external factors. The intrinsic impact is related to the occupation of certain sites, where the parameter H_a is directly connected to H_c. H_a is primarily affected by the $4f_2$ and 2b sites. The extrinsic impact includes the characteristics of grain size and porosity. The coercivity (H_c) is directly proportional to porosity and inversely proportional to grain size. The coercivity (H_c) decreases with increasing doping level. The trend can be noticed as the H_c decreases from an initial value of 4671 Oe in the undoped sample to a value of 2826.384 Oe when x = 1.0(W5). The pure sample of barium hexaferrite (W0) exhibits the greatest values of coercivity (4671 Oe) and remanent magnetization (45.687 emu/g). The decrease in H_c from W0 (4671 Oe) to W3 (3099.795 Oe) due to rising substitution levels is attributed to H_a. A greater anisotropic field results in an increased coercivity, meaning that a greater amount of energy is necessary to reverse the magnetic moment of the hexaferrite. However, with further substitution at W3 and W4, gradually increase to 3468.90 Oe and H_a from 16.23 kOe to 17.50 kOe. The replacement of Co^{2+} and Al^{3+} may have a complicated impact on the grain size of the material. At x = 0.6 (W3), there is a possibility that the grain size approaches a threshold where it decreases H_c. Nevertheless, when x = 0.8 (W4), the grain size may change to a range that promotes a little rise in H_c. We observe a decrease in coercivity

from 0.8 to 1.0 (W4 to W5) and around 18% decrease the value from 3468.90 Oe to 2826.38 Oe. An Al substitution with a high concentration (x = 1.0 (W5)) might greatly disturb the crystal structure and diminish the magnetic anisotropy of the material. Magnetic anisotropy refers to the tendency of magnetization to align in a certain direction inside a material. A decrease in anisotropy might facilitate the movement of magnetic domain walls when subjected to an external field, hence reducing the required external field (H_c) to overcome this resistance and accomplish magnetization reversal. The remanent magnetization (M_r) of the samples shows a declining pattern as the amount of Co^{2+} and Al^{3+} substitution (x) increases in $BaCo_xAl_xFe_{12-2x}O_{19}$. The reduction in magnetization, seen from M_r(W0(x = 0)) = 45.687 emu/g to M_r(W5(x = 1.0)) = 31.589 emu/g (Table 4.5), may be ascribed to the action of Co^{2+} and Al^{3+} on the alignment of magnetic moments inside the material. When Co^{2+} and Al^{3+} replaces Fe^{3+}, it may disturb the exchange interactions that are essential for aligning these magnetic moments. This disruption results in a reduced total magnetization that remains weaker even after removing an applied magnetic field. The remanence ratio (M_r/M_s) is a critical characteristic that signifies the material's capacity to preserve magnetization.

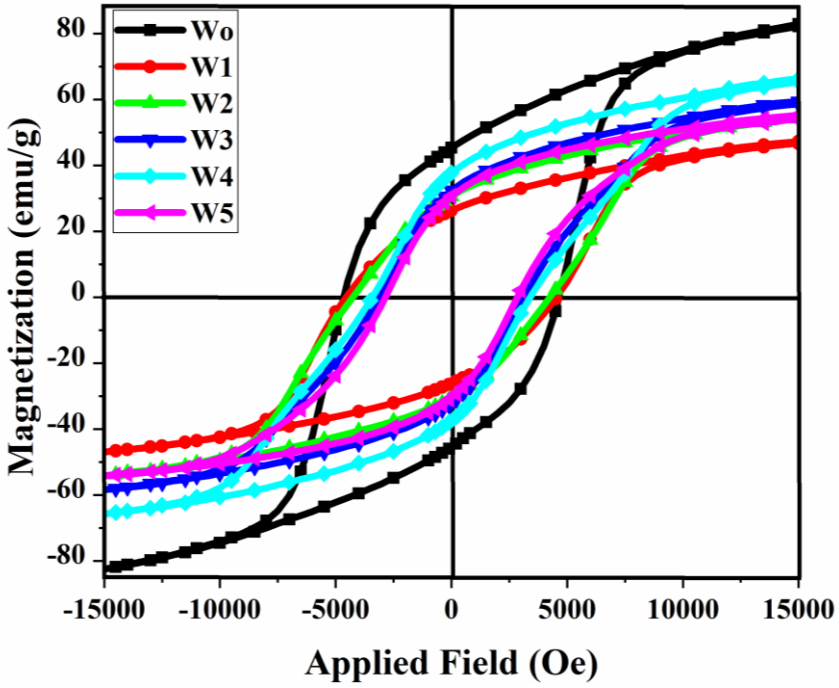

Figure 4.10. Hysteresis loops of W0, W1, W2, W3, W4 and W5 hexaferrite.

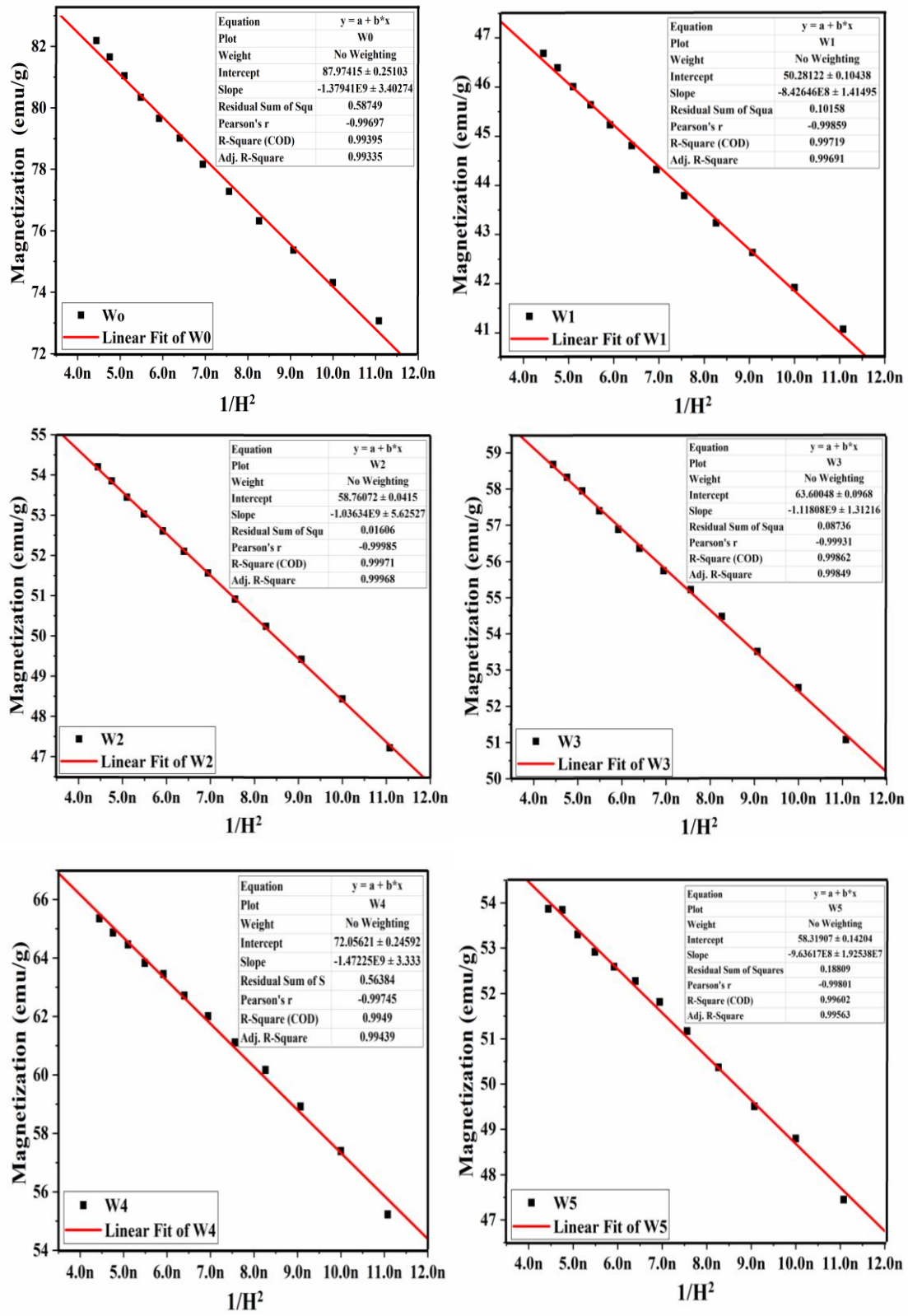

Figure 4.11. M_s versus 1/ H^2 plots for all hexaferrite samples.

Table 4.5. Magnetic parameters determined from M-H curves

sample	M_s	H_c	H_a = sqrt(-15B)	H_a (kOe)	M_r	M_r/M_s
W0 (x = 0.0)	87.97	4671.00	15336.09	15.34	45.69	0.519
W1 (x = 0.2)	50.28	4507.86	15854.97	15.85	26.34	0.524
W2 (x = 0.4)	58.76	4179.77	16264.97	16.26	30.43	0.518
W3 (x = 0.6)	63.60	3099.79	16238.72	16.24	33.08	0.520
W4 (x = 0.8)	72.06	3468.90	17506.56	17.51	38.33	0.532
W5 (x = 1.0)	58.32	2826.38	15743.18	15.74	31.59	0.542

Generally, M-type hexaferrites have large remanence ratios M_r/M_s as a result of their intrinsic magnetic characteristics. Nevertheless, the remanence ratio is also highly responsive to the microstructure of the material, namely the existence of inter-granular areas. The remanence ratio range, as defined in reference [201], spans from 0 to 1. Values between 0.05 and 0.5 are considered suggestive of randomly oriented multi-domain particles, according to reference [202]. Upon analyzing Table 4.5, it is evident that all the produced samples have remanence ratios that are either less than or equal to 0.5. The finding indicates the formation of particles with multi domains inside the Al-series samples. The existence of these particles with multiple domains may be ascribed to the impact of Co^{2+} and Al^{3+} substitution on the microstructure, possibly influencing the distribution of grain sizes and creating inter-granular areas that impede the alignment of magnetic moments throughout the material.

4.1.5 Electromagnetic Characteristics

4.1.5.1 Complex permeability and complex permittivity

The Figure 4.12 displays plots of (ε'),(ε''), (μ'), and (μ'') against frequency. The dielectric constant and loss exhibited non-monotonically variations due to the Co-Al doping. Except for W2, ε' decreases as frequency increases and the value of ε' increases as the doping value increases. When compared to the other compositions, W2 exhibits a notable decrease followed by increase at low frequencies. At mid-frequency, W4 exhibits a significant decrease. Throughout the samples, it is observed that the W1 sample exhibits the lowest ε' with the value of 4.55 at 12.4 GHz, whereas the W4 sample demonstrates the highest value of 7.46 at 8.2 GHz. This indicates that the substitution leads to an increase in the capacity for charge storage.

The dielectric loss values of all the doped compositions show minimal variation. The peak of relaxation for W1, W3, W4 and W5 is observed in ε'' between 9 and 10 GHz. The W4 sample has the highest value of ε'' among the others at 9.96 GHz with value

of 1.38. In contrast to the other compositions, W2 exhibits a noticeable decrease at low frequencies.

The permeability of the compositions is influenced in a non-linear manner by the Co-Al doping. All values of μ′ increase in proportion to the frequency increase, except for W2. The compositions of W1 and W4 stable even with doping, while the compositions of W2, W3, and W5 do undergo significant increment in the value of μ′. In contrast to the other compositions, W2 exhibits a significant reduction in low frequencies.

The electron spin, dipole polarization at the microwave region, porosity, and grain size distribution all have an impact on the complex permittivity and permeability. The dielectric polarization [82] is attributed to the electron hopping in Fe^{2+}/ Fe^{3+}. The significant porosity restricts the flow in the field and reduces polarization. The permeability is affected by ferromagnetic resonance and exchange resonance between Fe^{3+}/ Fe^{2+} [83–84]. When Co-Al is doped, it leads to a reduction in the amount of Fe^{3+}, causing an effect on resonance and polarization. The micrographs of the developed compositions display pores that serve as non-magnetic voids, causing changes in magnetization that are linked to permittivity and permeability.

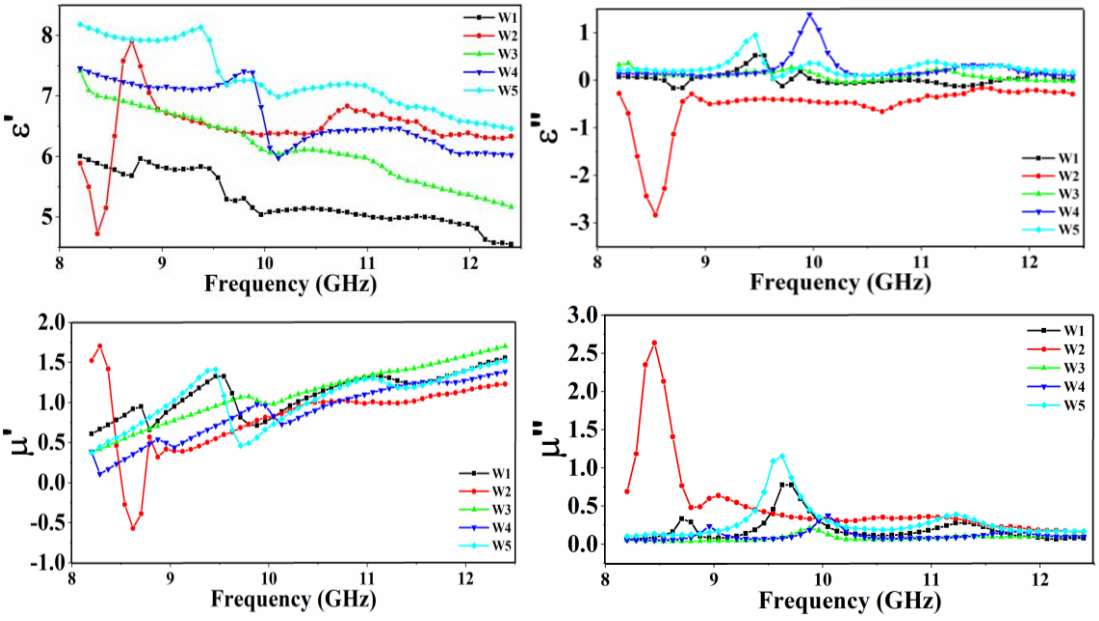

Figure 4.12. Complex permittivity and permeability versus frequency plots for $BaCo_xAl_xFe_{12-2x}O_{19}$.

Electron hopping is more efficient in larger grains, whereas the presence of grain boundaries restricts the movement of electrons. Polarization is promoted by the accumulation of charges at grain borders; conversely, permeability increases as larger grains enhance electron spin. Due to the small size of the grains and their porous nature, the exchange resonance is reduced, resulting in an increase in magnetic loss. The peaks in the prepared compositions are caused by dielectric relaxation and ferromagnetic resonance, respectively.

4.1.5.2 Microwave absorption in $BaCo_xAl_xFe_{12-2x}O_{19}$

One way to evaluate the microwave absorption capacity of a material is by examining its reflection loss. The calculation involves considering the electrical properties of the material (input impedance) and the electrical properties of air (impedance of air) using equations 1.5 and 1.6. In the upcoming sections, we will delve into the impact of various factors on the absorption of microwaves by different materials. These factors include material thickness (λ/4), impedance matching, and the extent of reflection loss.

4.1.5.3 Quarter Wavelength Mechanism

We analyzed graphs that illustrate the reflection loss of various materials at different thicknesses and frequencies, showcasing the amount of microwave energy reflected by each material. These graphs provided crucial insights into the microwave absorption properties of the ferrites we synthesized. Figures 4.13 and subsequent Figures present the detailed results for these ferrites. By carefully examining these graphs, we were able to quantify several key characteristics of the materials, such as their reflection loss performance, frequency ranges, and thicknesses for optimal microwave absorption. A summary of these properties is provided in Table 4.6.

Composition W1 demonstrates a wide range of reflection loss values across varying thicknesses. At a thickness of 3.4 mm, the maximum REL is -24.63 dB at a frequency of 9.88 GHz, with a bandwidth of 0.44 GHz for REL > -10 dB and 0.1 GHz for REL > -20 dB. As the thickness increases to 3.5 mm, the REL improves to -30.31 dB at the same frequency, but with a slightly reduced bandwidth of 0.42 GHz for REL > -10 dB. Further increases in thickness continue to show a decrease in REL, indicating a shift in peak absorption. For instance, at 3.6 mm, the REL reaches -26.10 dB with a 0.37 GHz

bandwidth for REL > -10 dB. At 3.7 mm, the REL decreases to -21.07 dB, and the bandwidth narrows further to 0.34 GHz.

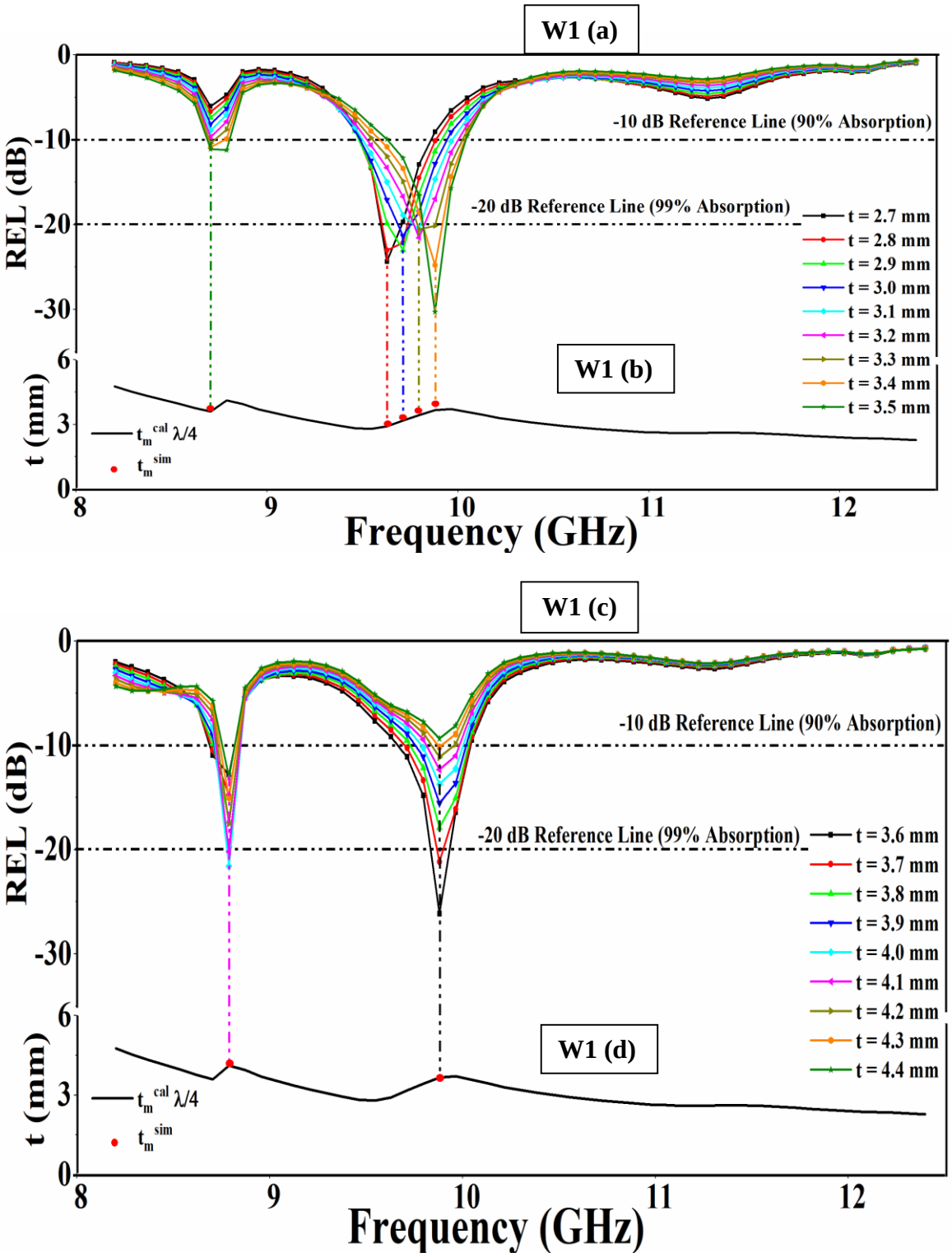

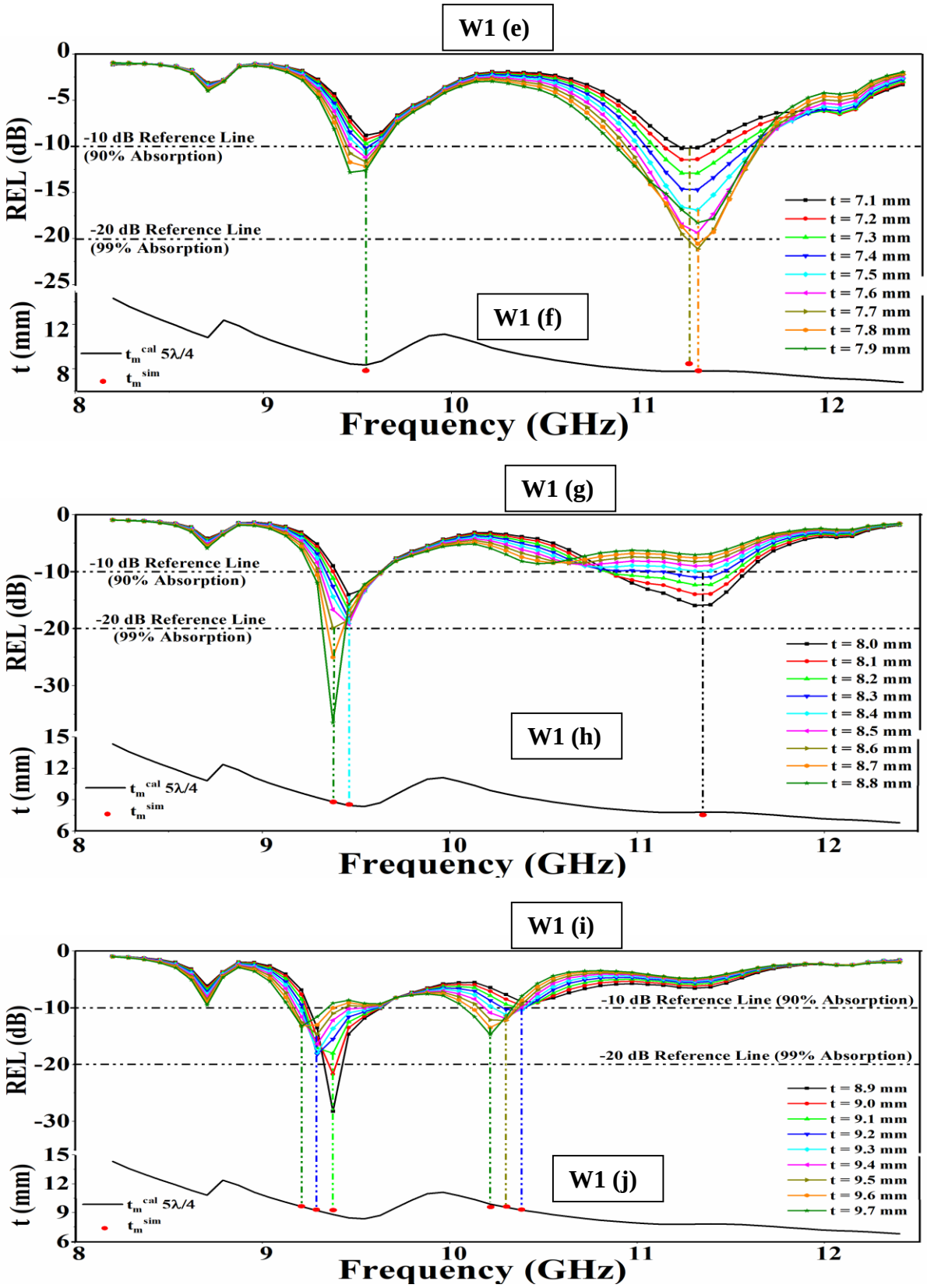

Figure 4.13. REL versus frequency for different thickness (W1) and calculate thickness versus frequency for $BaCo_xAl_xFe_{12-2x}O_{19}$

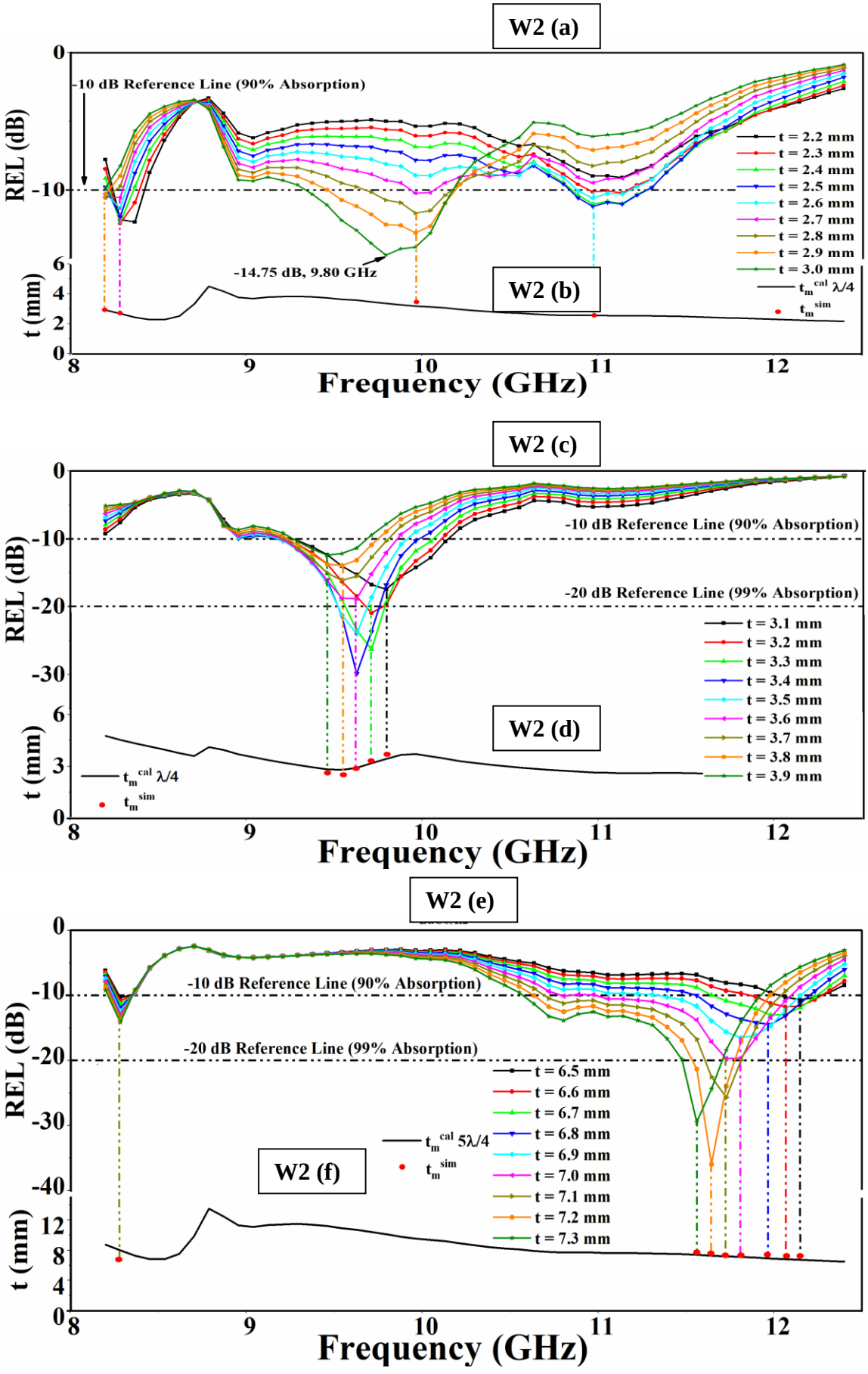
W2 (a)
-10 dB Reference Line (90% Absorption)
REL (dB)
-14.75 dB, 9.80 GHz
t = 2.2 mm
t = 2.3 mm
t = 2.4 mm
t = 2.5 mm
t = 2.6 mm
t = 2.7 mm
t = 2.8 mm
t = 2.9 mm
t = 3.0 mm
t_m^{cal} λ/4
t_m^{sim}
W2 (b)
t (mm)
Frequency (GHz)
W2 (c)
-10 dB Reference Line (90% Absorption)
-20 dB Reference Line (99% Absorption)
t = 3.1 mm
t = 3.2 mm
t = 3.3 mm
t = 3.4 mm
t = 3.5 mm
t = 3.6 mm
t = 3.7 mm
t = 3.8 mm
t = 3.9 mm
W2 (d)
W2 (e)
t = 6.5 mm
t = 6.6 mm
t = 6.7 mm
t = 6.8 mm
t = 6.9 mm
t = 7.0 mm
t = 7.1 mm
t = 7.2 mm
t = 7.3 mm
t_m^{cal} 5λ/4
W2 (f)

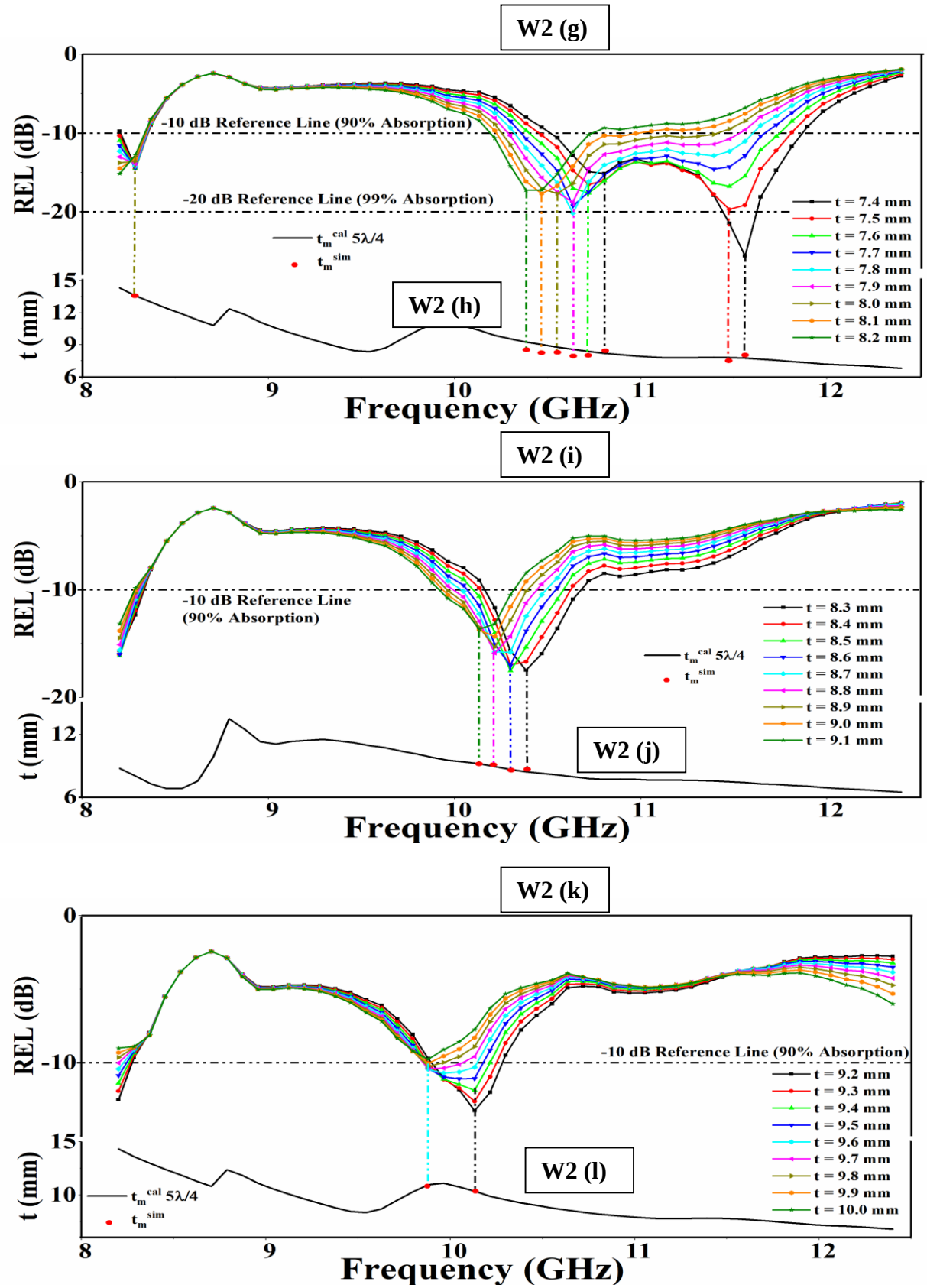

Figure 4.14. REL versus frequency for different thickness (W2) and calculate thickness versus frequency for $BaCo_xAl_xFe_{12-2x}O_{19}$

For thicker samples, such as 8.8 mm, W1 exhibits a maximum REL of -36.73 dB at 9.37 GHz, with a 0.37 GHz bandwidth for REL > -10 dB and 0.12 GHz for REL > -20 dB. The absorption band for REL > -10 dB is quite broad at this thickness, confirming effective absorption over a wide frequency range.

In composition W2, the maximum REL performance is observed at a thickness of 7.2 mm, where the REL reaches -35.98 dB at 11.64 GHz. The bandwidth for REL > -10 dB is 1.34 GHz, demonstrating broadband absorption, and the bandwidth for REL > -20 dB is 0.25 GHz, making W2 a suitable candidate for broadband applications.

At thinner thicknesses, such as 2.8 mm, the REL is -11.66 dB at 9.96 GHz, with a bandwidth of 0.49 GHz for REL > -10 dB. The bandwidth expands significantly as thickness increases, with 2.9 mm and 3 mm showing RELs of -13.12 dB and -14.75 dB, respectively, at the same frequency.

For W3, absorption is observed across a range of thicknesses, with the best REL occurring at 8.7 mm, reaching -28.07 dB at 9.79 GHz. The bandwidth for REL > -10 dB is 0.45 GHz, and the bandwidth for REL > -20 dB is 0.13 GHz, indicating moderate absorption properties.

At 8.6 mm, the REL is -19.88 dB with a 0.54 GHz bandwidth, showing good broadband absorption at a slightly lower thickness. As thickness increases to 9.1 mm, the REL improves to -24.49 dB with a 0.58 GHz bandwidth for REL > -10 dB and 0.13 GHz for REL > -20 dB.

Composition W4 demonstrates strong absorption characteristics, particularly at thinner thicknesses. At 3.4 mm, the REL reaches -33.53 dB at 10.13 GHz, with a 0.31 GHz bandwidth for REL > -10 dB and a 0.12 GHz bandwidth for REL > -20 dB. This indicates that W4 is effective at thin thicknesses, offering strong reflection loss over a relatively broad range.

At 4.4 mm, the REL reaches -25.5 dB at 9.04 GHz, with a 0.39 GHz bandwidth for REL > -10 dB and a 0.08 GHz bandwidth for REL > -20 dB, showing that the material continues to perform well at higher thicknesses. As thickness increases to 6.7 mm, the REL improves to -33.3 dB at 8.46 GHz with a 0.15 GHz bandwidth for REL > -20 dB, confirming the wide absorption range of W4.

The composition W5 demonstrates high reflection loss across various thicknesses. At 3.1 mm, the maximum REL is -46.55 dB at 10.05 GHz, with a bandwidth of 0.42 GHz

for REL > -10 dB and 0.16 GHz for REL > -20 dB, making W5 one of the strongest absorbers. The high absorption efficiency is retained even at thinner thicknesses, as seen with the 2.2 mm sample, where the REL is -30.06 dB at 9.46 GHz.

At thicker samples, such as 7.1 mm, the REL reaches -32.79 dB at 10.72 GHz, with a 1.14 GHz bandwidth for REL > -10 dB, indicating broadband absorption. W5 remains highly effective even at larger thicknesses, with 9.7 mm achieving -30.98 dB at 12.32 GHz.

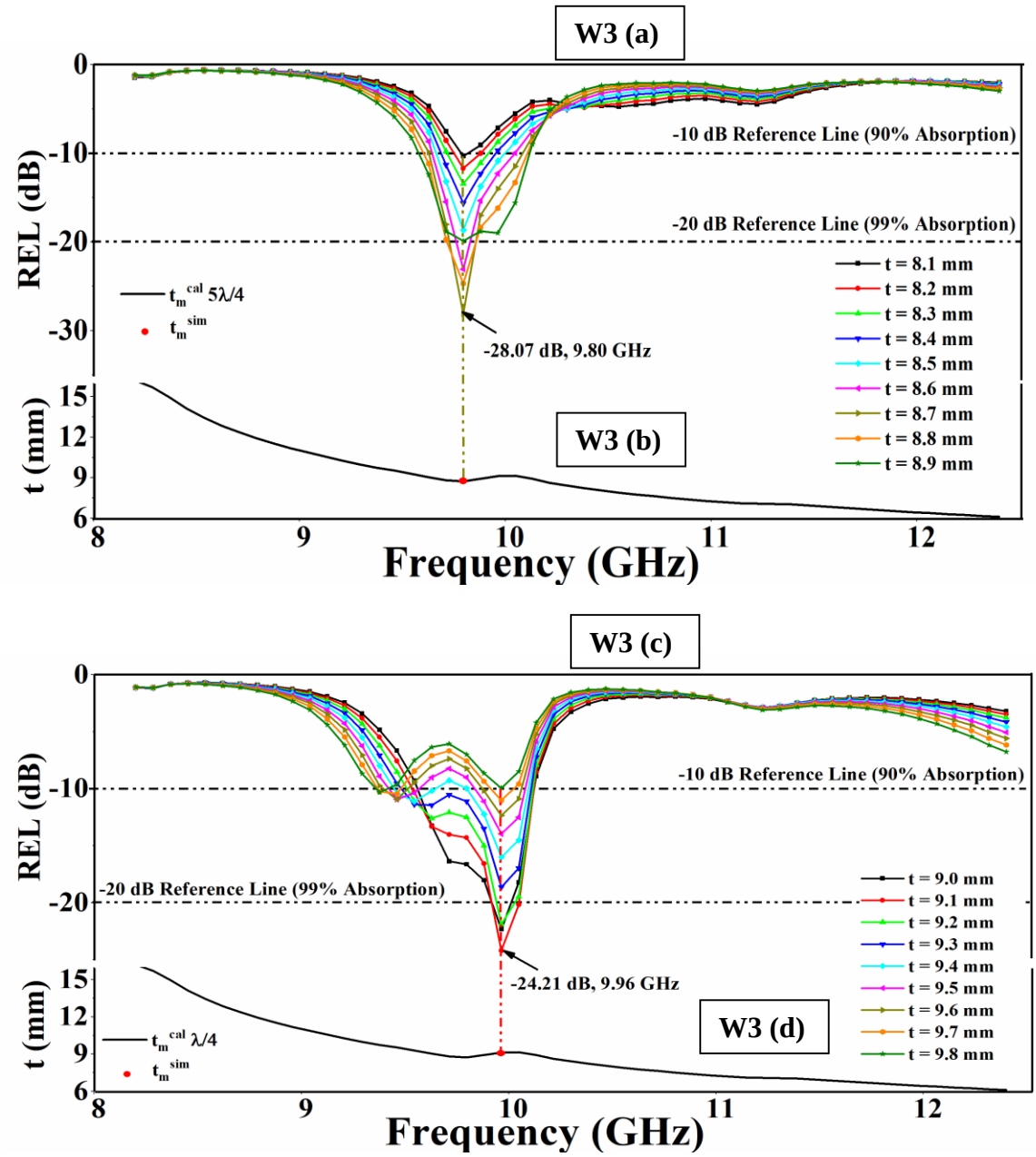

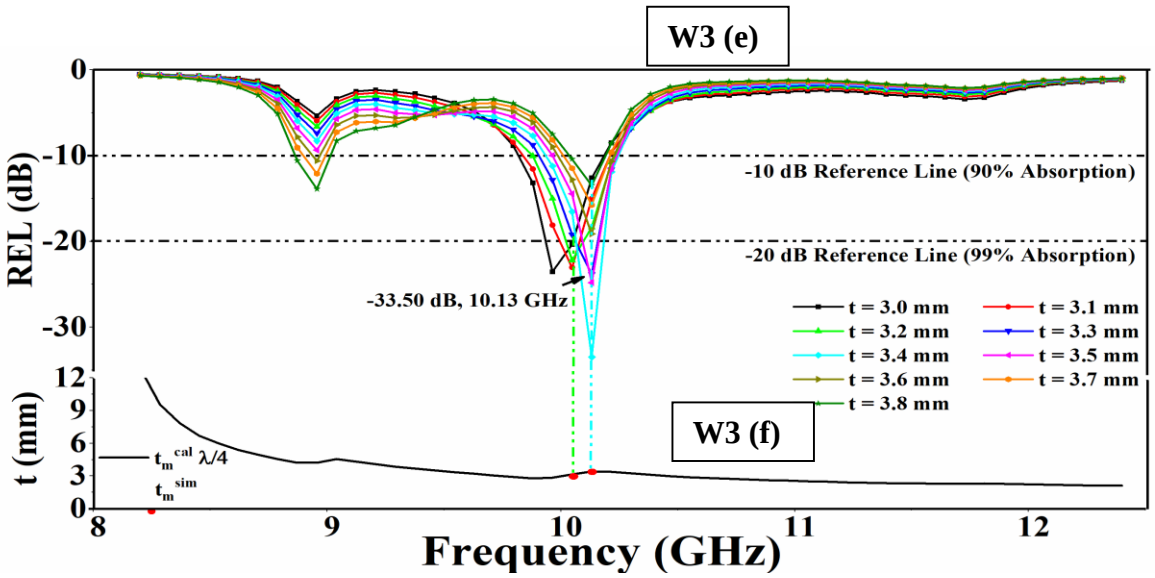

Figure 4.15. REL versus frequency for different thickness (W3) and calculate thickness versus frequency for $BaCo_xAl_xFe_{12-2x}O_{19v}$

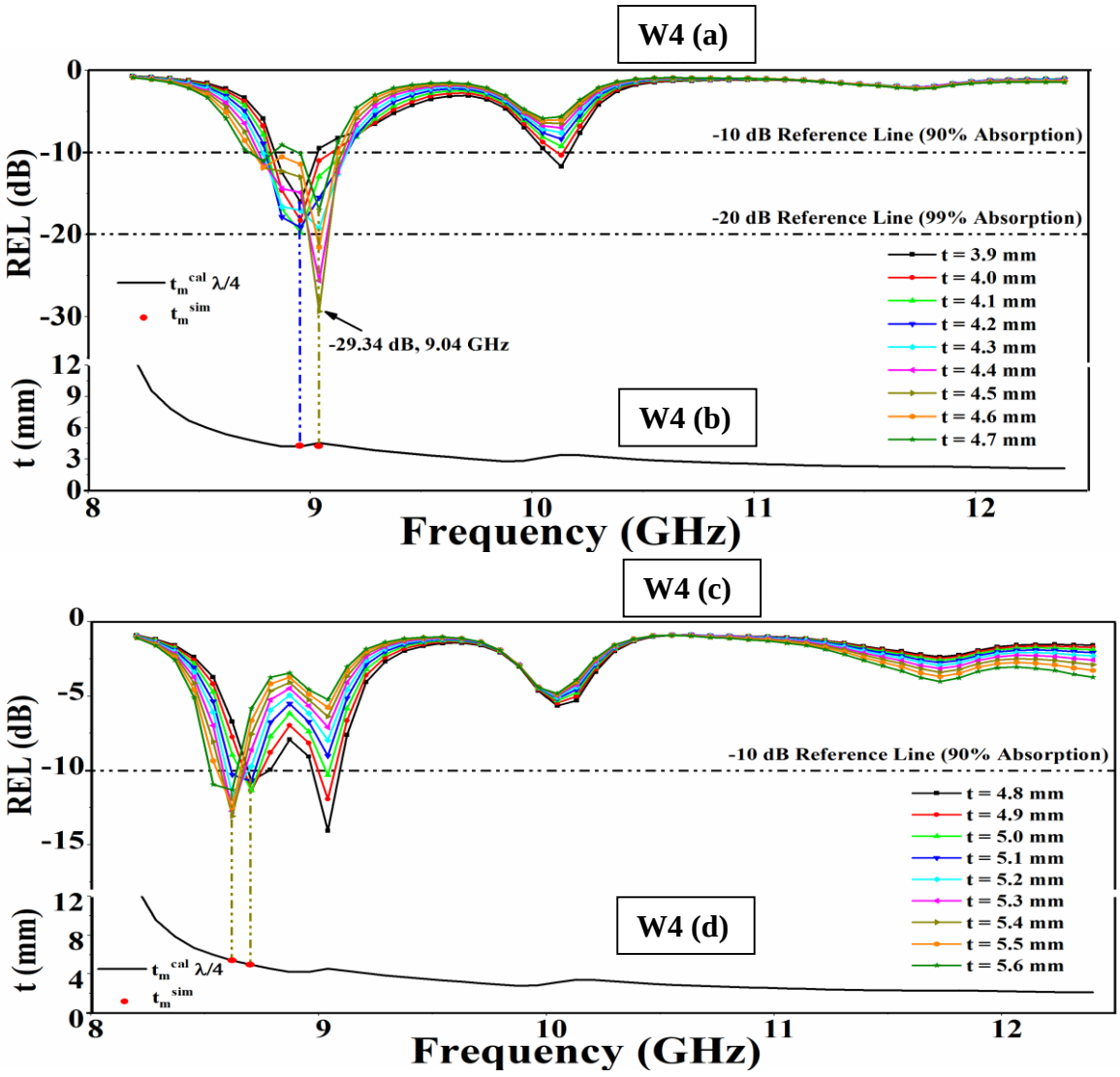

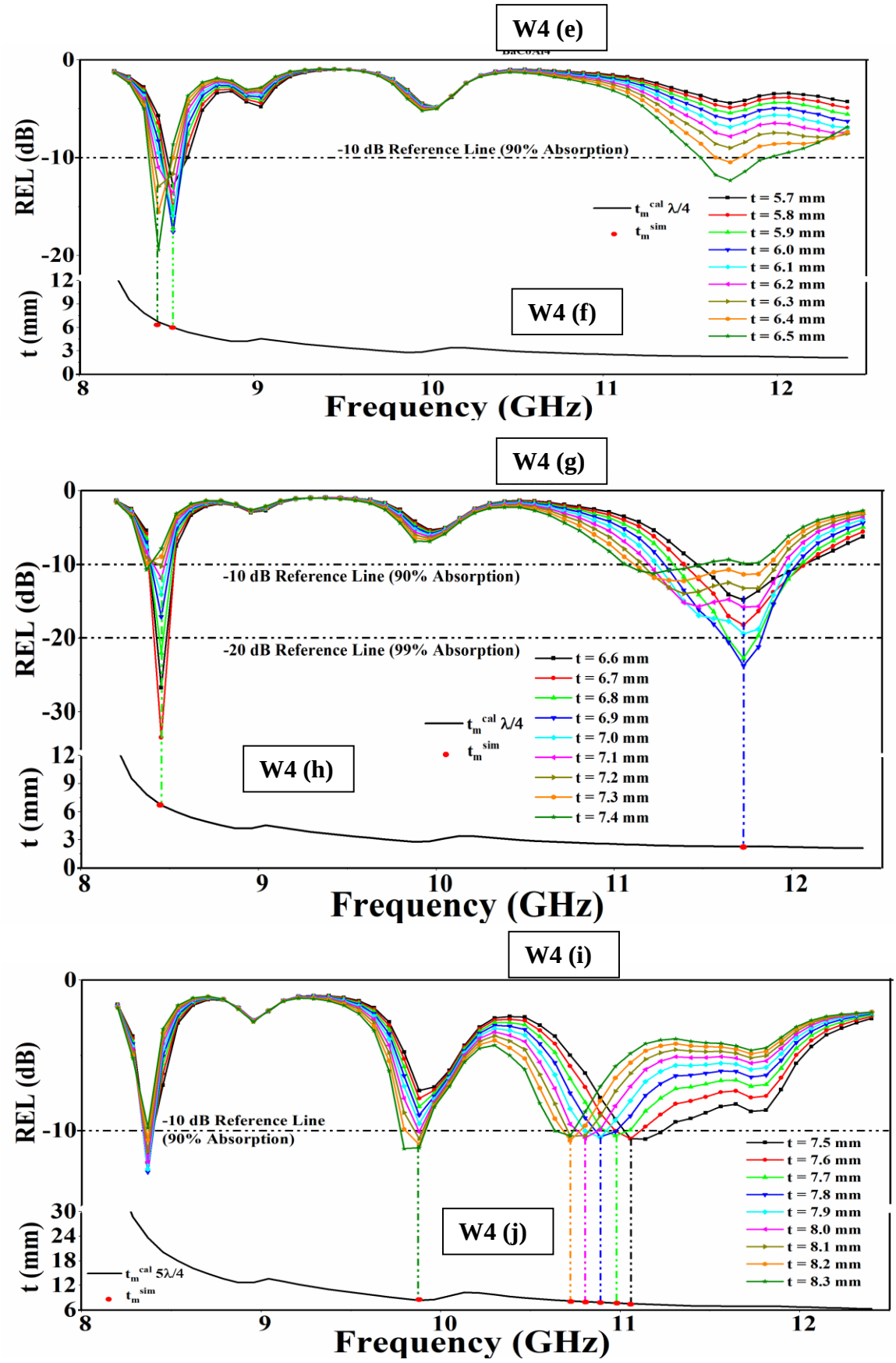
W4 (e)
REL (dB)
-10 dB Reference Line (90% Absorption)
t = 5.7 mm
t = 5.8 mm
t = 5.9 mm
t = 6.0 mm
t = 6.1 mm
t = 6.2 mm
t = 6.3 mm
t = 6.4 mm
t = 6.5 mm
W4 (f)
t (mm)
Frequency (GHz)
W4 (g)
REL (dB)
-10 dB Reference Line (90% Absorption)
-20 dB Reference Line (99% Absorption)
t = 6.6 mm
t = 6.7 mm
t = 6.8 mm
t = 6.9 mm
t = 7.0 mm
t = 7.1 mm
t = 7.2 mm
t = 7.3 mm
t = 7.4 mm
W4 (h)
t (mm)
Frequency (GHz)
W4 (i)
REL (dB)
-10 dB Reference Line
(90% Absorption)
t = 7.5 mm
t = 7.6 mm
t = 7.7 mm
t = 7.8 mm
t = 7.9 mm
t = 8.0 mm
t = 8.1 mm
t = 8.2 mm
t = 8.3 mm
W4 (j)
t (mm)
Frequency (GHz)

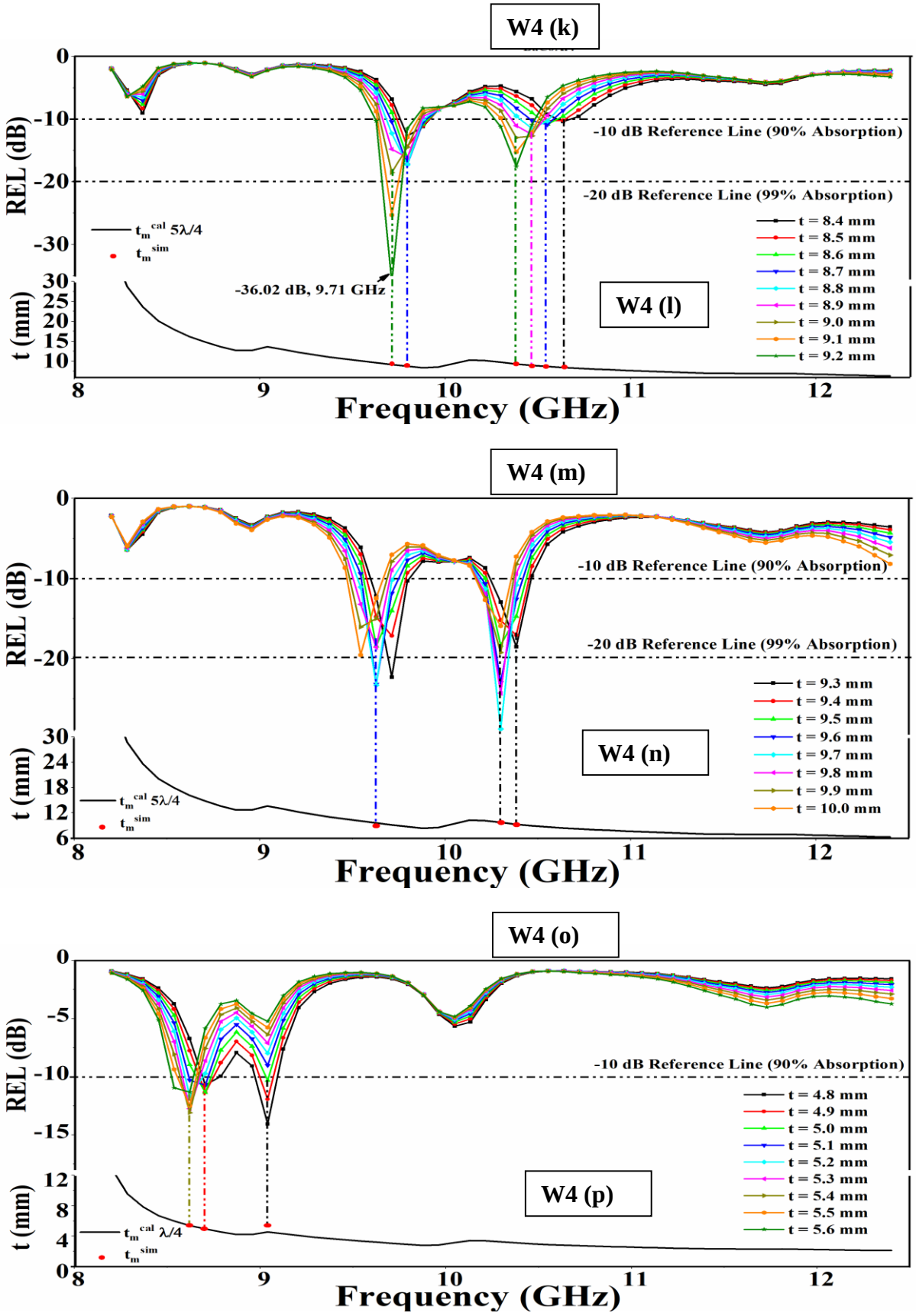

Figure 4.16. REL versus frequency for different thickness (W4) and calculate thickness versus frequency for $BaCo_xAl_xFe_{12-2x}O_{19}$

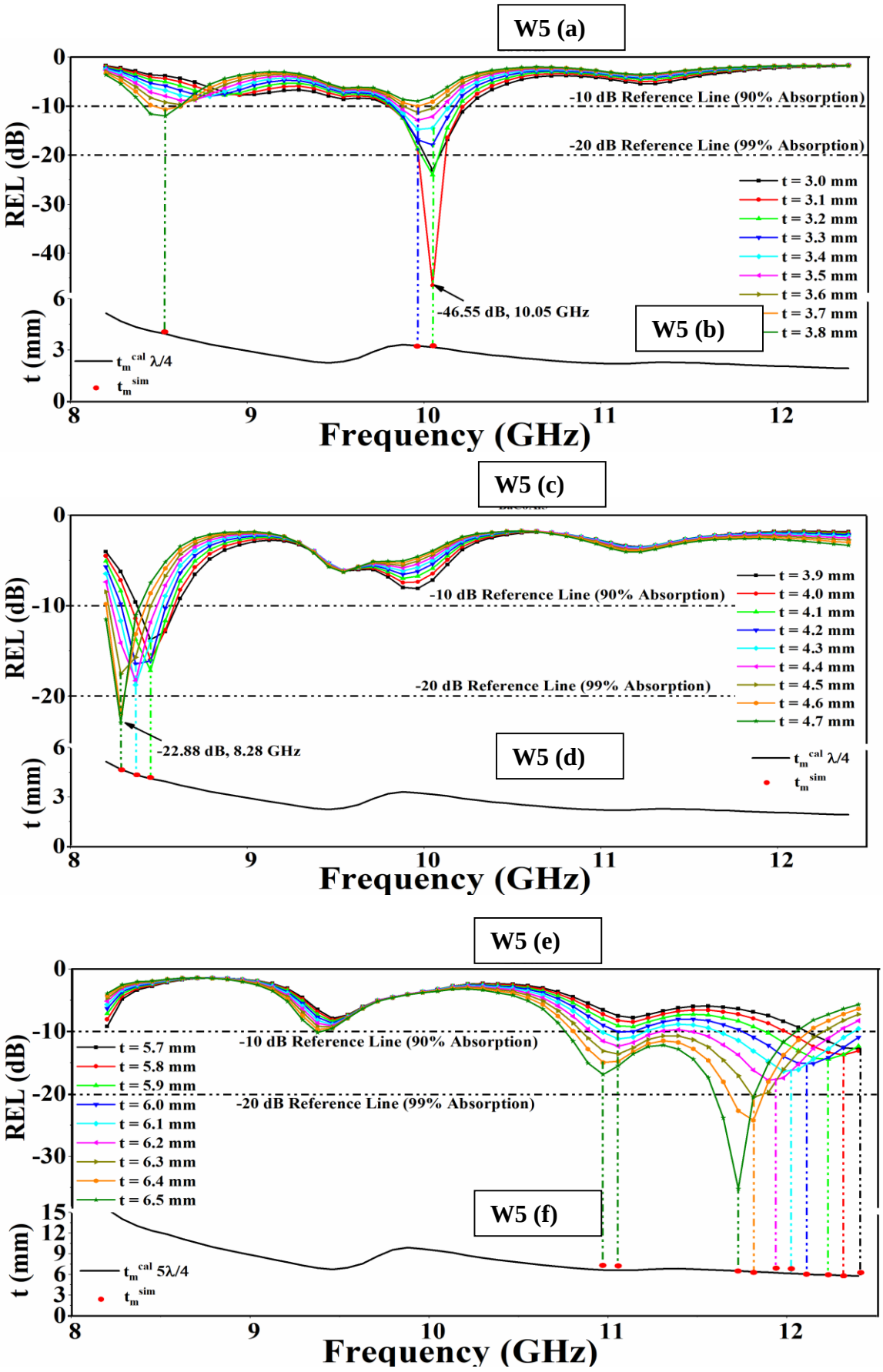
W5 (a)
REL (dB)
-10 dB Reference Line (90% Absorption)
-20 dB Reference Line (99% Absorption)
t = 3.0 mm
t = 3.1 mm
t = 3.2 mm
t = 3.3 mm
t = 3.4 mm
t = 3.5 mm
t = 3.6 mm
t = 3.7 mm
t = 3.8 mm
-46.55 dB, 10.05 GHz
W5 (b)
t (mm)
t_m^{cal} λ/4
t_m^{sim}
Frequency (GHz)
W5 (c)
REL (dB)
-10 dB Reference Line (90% Absorption)
-20 dB Reference Line (99% Absorption)
t = 3.9 mm
t = 4.0 mm
t = 4.1 mm
t = 4.2 mm
t = 4.3 mm
t = 4.4 mm
t = 4.5 mm
t = 4.6 mm
t = 4.7 mm
-22.88 dB, 8.28 GHz
W5 (d)
t (mm)
t_m^{cal} λ/4
t_m^{sim}
Frequency (GHz)
W5 (e)
REL (dB)
-10 dB Reference Line (90% Absorption)
-20 dB Reference Line (99% Absorption)
t = 5.7 mm
t = 5.8 mm
t = 5.9 mm
t = 6.0 mm
t = 6.1 mm
t = 6.2 mm
t = 6.3 mm
t = 6.4 mm
t = 6.5 mm
W5 (f)
t (mm)
t_m^{cal} 5λ/4
t_m^{sim}
Frequency (GHz)

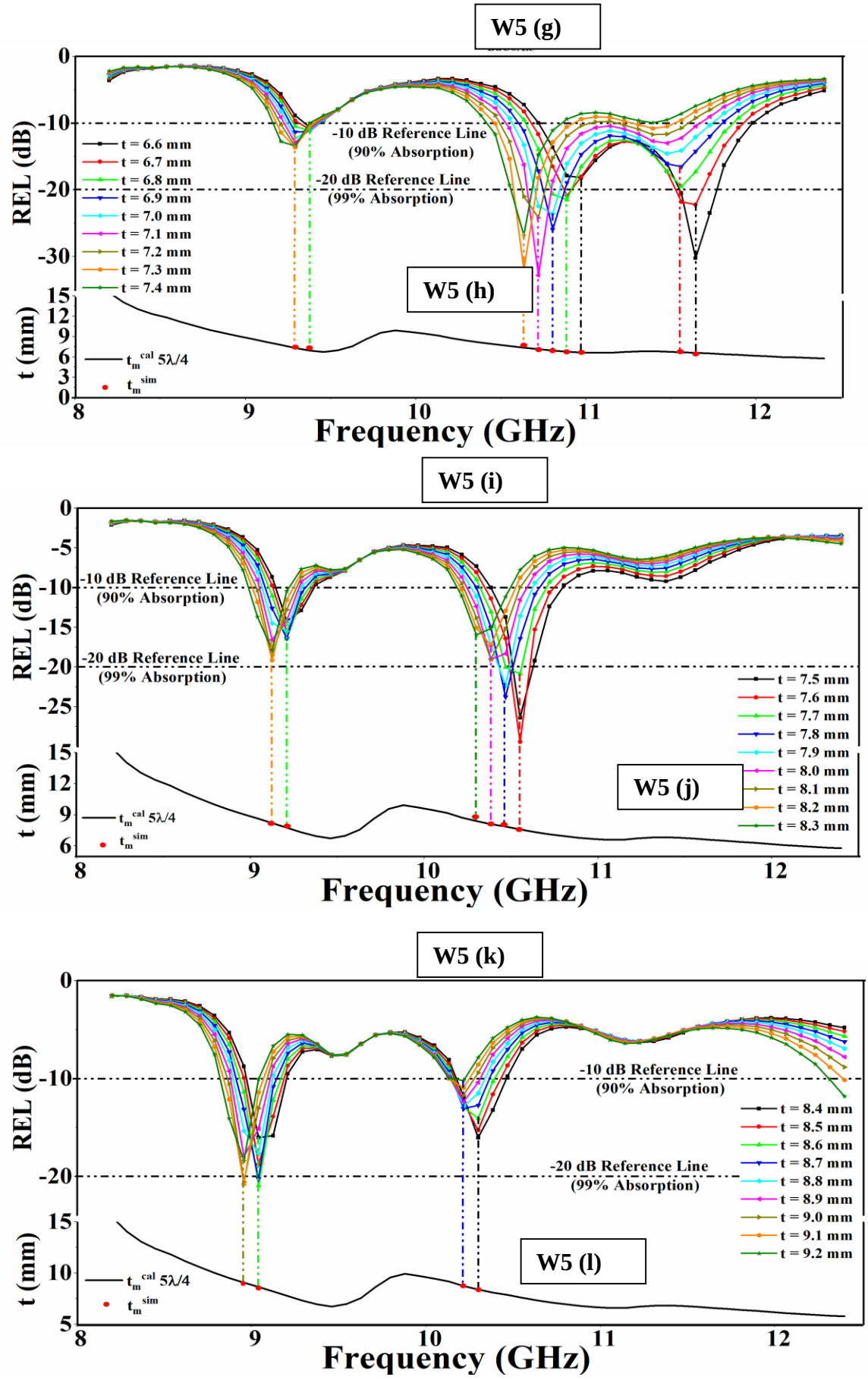
W5 (g)
REL (dB)
t (mm)
Frequency (GHz)
-10 dB Reference Line
(90% Absorption)
-20 dB Reference Line
(99% Absorption)
t = 6.6 mm
t = 6.7 mm
t = 6.8 mm
t = 6.9 mm
t = 7.0 mm
t = 7.1 mm
t = 7.2 mm
t = 7.3 mm
t = 7.4 mm
W5 (h)
W5 (i)
W5 (j)
t = 7.5 mm
t = 7.6 mm
t = 7.7 mm
t = 7.8 mm
t = 7.9 mm
t = 8.0 mm
t = 8.1 mm
t = 8.2 mm
t = 8.3 mm
W5 (k)
W5 (l)
t = 8.4 mm
t = 8.5 mm
t = 8.6 mm
t = 8.7 mm
t = 8.8 mm
t = 8.9 mm
t = 9.0 mm
t = 9.1 mm
t = 9.2 mm

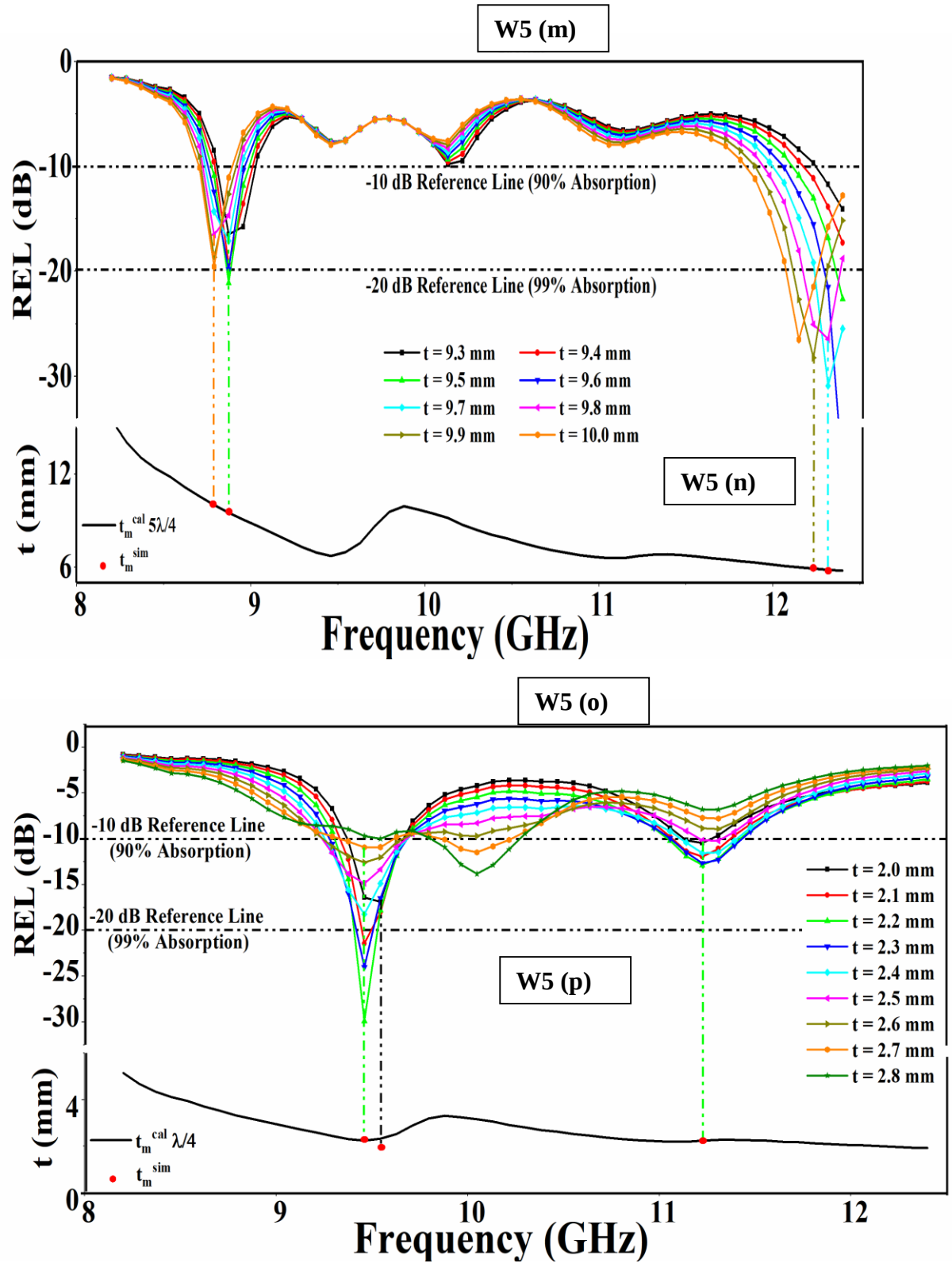

Figure 4.17. REL versus frequency for different thickness (W5) and calculate thickness versus frequency for $BaCo_xAl_xFe_{12-2x}O_{19}$

Table 4.6. REL with matching thickness/frequency, BW, and PBW for $BaCo_xAl_xFe_{12-2x}O_{19}$ (W1 to W5).

Sample Name	Matching Thickness (mm)	Maximum REL (dB)	Matching frequency (GHz)	Frequency Band for REL > -10 dB (GHz)	Bandwidth for REL > -10 dB (GHz)	Frequency Band REL > -20 dB (GHz)	Band width for REL > -20 dB (GHz)	BTR	PBW (%)
W1	3.4	-24.63	9.88	9.59-10.03	0.44	9.82-9.92	0.1	4.04 E-04	4.45
	3.5	-30.31	9.88	9.62-10.04	0.42	9.82-9.94	0.12	3.73 E-04	4.25
	3.6	-26.106	9.88	9.67-10.04	0.37	9.83-9.93	0.1	3.18 E-04	3.74
	3.7	-21.07	9.88	9.7-10.04	0.34	9.86-9.9	0.04	2.83 E-04	3.44
	4.1	-20.16	8.79	8.72-8.85	0.13	-	-	1.23 E-04	1.48
	7.6	-19.57	11.3	10.96-11.64	0.68	-	-	2.10 E-04	6.02
	7.7	-20.96	11.31	10.93-11.65	0.72	11.26-11.36	0.1	2.20 E-04	6.37
	7.8	-20.48	11.3	10.89-11.65	0.76	11.28-11.35	0.07	2.30 E-04	6.73
	8.6	-19.91	9.37	9.3-9.64	0.34	-	-	1.32 E-04	3.63
	8.7	-25.07	9.37	9.28-9.63	0.35	9.35-9.43	0.08	1.35 E-04	3.74
	8.8	-36.73	9.37	9.26-9.63	0.37	9.32-9.44	0.12	1.41 E-04	3.95
	8.9	-27.92	9.37	9.24-9.64	0.4	9.33-9.43	0.1	1.51 E-04	4.27
	9	-21.79	9.37	9.23-	0.4	9.35-	0.04	1.50	4.27

				9.63		9.39		E-04	
	9.1	-18.11	9.37	9.22-9.62	0.4	-	-	1.49 E-04	4.27
	9.2	-21.79	9.29	9.22-9.62	0.4	-	-	1.47 E-04	4.31
W2	2.8	-11.66	9.96	9.68-10.17	0.49	-	-	5.33 E-04	4.92
	2.9	-13.125	9.96	9.46-10.19	0.73	-	-	7.83 E-04	7.33
	3	-14.75	9.8	9.34-10.17	0.83	-	-	8.74 E-04	8.47
	3.3	-26.24	9.71	9.19-10.06	0.87	9.56-9.79	0.23	8.55 E-04	8.96
	3.4	-29.73	9.62	9.19-9.98	0.79	9.52-9.76	0.24	7.60 E-04	8.21
	7	-19.8	11.76	10.98-12.09	1.11	-	-	3.58 E-04	9.44
	7.2	-35.98	11.64	10.63-11.97	1.34	11.53-11.78	0.25	4.39 E-04	11.51
	7.3	-29.49	11.51	10.57-11.92	1.35	11.47-11.71	0.24	4.40 E-04	11.73
	7.4	-25.53	11.56	10.52-11.87	1.35	11.44-11.63	0.19	4.38 E-04	11.68
	7.5	-19.66	11.47	10.45-11.81	1.36	-	-	4.41 E-04	11.86
	7.8	-20.14	10.64	10.33-11.61	1.28	-	-	4.10 E-04	12.03
	8.3	-17.41	10.39	10.16-10.69	0.53	-	-	1.76 E-04	5.10
	9.2	-13.092	10.14	9.89-10.29	0.4	-	-	1.28 E-04	3.94
W3	8.6	-19.88	9.79	9.58-10.12	0.54	-	-	1.94 E-04	5.52
	8.7	-28.07	9.79	9.63-	0.45	9.73-	0.13	1.60	4.60

				10.08		9.86		E-04	
	8.8	-24.43	9.79	9.6-10.11	0.51	9.72-9.86	0.14	1.79 E-04	5.21
	9	-22.41	9.96	9.56-10.12	0.56	9.92-10.01	0.09	1.93 E-04	5.62
	9.1	-24.49	9.96	9.54-10.12	0.58	9.92-10.05	0.13	1.98 E-04	5.82
	9.2	-21.75	9.96	9.51-10.12	0.61	9.94-10.03	0.09	2.07 E-04	6.12
W4	3.4	-33.53	10.13	9.93-10.24	0.31	10.06-10.18	0.12	2.69 E-04	3.06
	3.5	-24.9	10.13	9.97-10.24	0.27	10.09-10.16	0.07	2.27 E-04	2.67
	4.4	-25.5	9.04	8.77-9.16	0.39	8.99-9.07	0.08	3.31 E-04	4.31
	4.5	-29.37	9.03	8.75-9.14	0.39	8.99-9.08	0.09	3.25 E-04	4.32
	4.8	-13.95	9.04	8.97-9.09	0.12	-	-	9.20 E-05	1.33
	5.5	-12.99	8.62	8.57-8.67	0.1	-	-	7.34 E-05	1.16
	6	-17.45	8.54	8.47-8.59	0.12	-	-	8.25 E-05	1.41
	6.5	-19.48	8.45	8.39-8.52	0.13	-	-	8.39 E-05	1.54
	6.6	-26.74	8.46	8.38-8.53	0.15	8.43-8.48	0.05	9.54 E-05	1.77
	6.7	-33.3	8.46	8.38-8.53	0.15	8.41-8.49	0.08	9.40 E-05	1.77
	7.8	-12.72	8.37	8.34-8.4	0.06	-	-	3.29 E-05	0.72
	9.1	-25.25	9.71	9.63-9.86	0.23	9.69-9.75	0.06	7.99 E-05	2.37
	9.2	-36.02	9.71	9.62-	0.22	9.67-	0.1	7.58	2.27

				9.84		9.77		E-05	
	9.7	-28.92	10.3	10.18-10.4	0.22	10.26-10.34	0.08	6.43 E-05	2.14
	9.8	-24.27	10.3	10.17-10.38	0.21	10.27-10.33	0.06	6.09 E-05	2.04
W5	2.2	-30.06	9.46	9.31-9.68	0.37	9.4-9.53	0.13	5.60 E-04	3.91
	2.3	-23.85	9.46	9.27-9.66	0.39	9.42-9.51	0.09	5.68 E-04	4.12
	3.1	-46.55	10.05	9.79-10.21	0.42	9.97-10.13	0.16	4.07 E-04	4.18
	3.2	-24.09	10.05	9.81-10.2	0.39	9.98-10.08	0.1	3.65 E-04	3.88
	4.6	-21.93	8.28	8.2-8.43	0.23	8.27-8.31	0.04	2.17 E-04	2.78
	4.7	-22.83	8.28	8.19-8.39	0.2	8.28-8.31	0.03	1.86 E-04	2.42
	6.4	-24.26	11.82	10.81-12.12	1.31	11.68-11.87	0.19	4.69 E-04	11.08
	6.5	-35.19	11.73	10.76-12.05	1.29	11.59-11.82	0.23	4.59 E-04	11.00
	7.1	-32.79	10.72	10.53-11.67	1.14	10.65-10.8	0.15	3.92 E-04	10.63
	7.3	-32	10.64	10.47-10.92	0.45	10.58-10.71	0.13	1.62 E-04	4.23
	7.5	-26.21	10.55	10.38-10.79	0.41	10.51-10.63	0.12	1.46 E-04	3.89
	7.6	-29.37	10.55	10.35-10.75	0.4	10.49-10.6	0.11	1.42 E-04	3.79
	8.6	-21	9.04	8.93-9.17	0.24	9.03-9.05	0.02	1.02 E-04	2.65
	9.1	-20.71	8.96	8.84-9.07	0.23	8.95-8.97	0.02	9.46 E-05	2.57
	9.5	-21.03	8.87	8.77-	0.22	8.86-	0.02	8.81	2.48

				8.99		8.88		E-05	
	9.7	-30.98	12.32	-	-	-	-	-	-
	9.9	-28.15	12.23	-	-	-	-	-	-
	10	-19.5	8.79	8.7-8.89	0.19	-	-	-	-

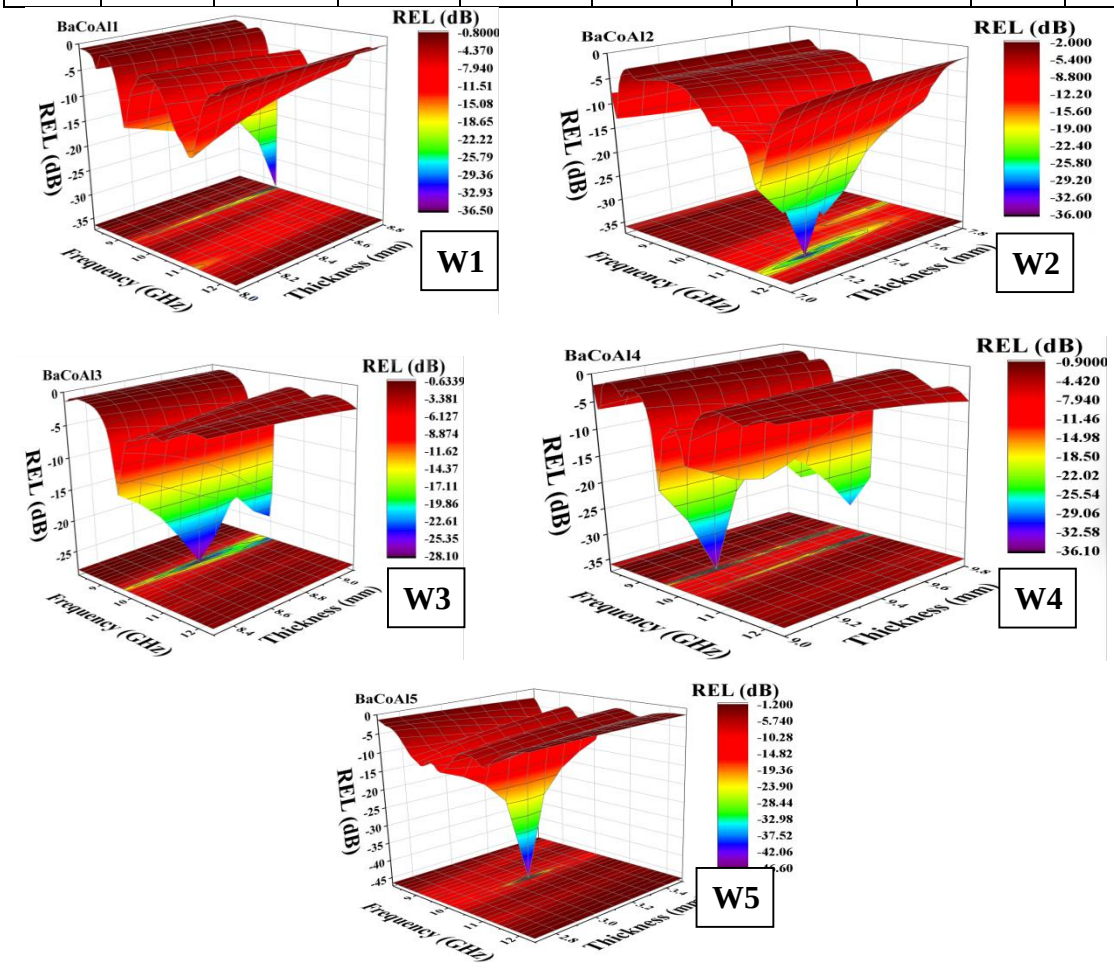

Figure 4.18. Three-dimensional (3D) plots of reflection loss at various frequencies and thicknesses for all samples of BaCoAl-series.

According to Table, the quarter wavelength criterion for composition W1 originates at thicknesses ranging from 3.4 mm to 9.2 mm and a -10 dB bandwidth of 0.13 GHz to 0.76 GHz. REL = -21.07 dB to REL = -36.73 dB are reported within the -20 dB bandwidth of 40 MHz to 120 MHz respectively. As shown in Figure 4.13 W1(a), the reflection loss peaks with composition W1 are at the same frequency at 8.70 GHz for t = 3.4 mm, 3.5 mm, and 3.6 mm. Similar peaks may be seen at 8.78 GHz and 9.88 GHz for 3.6 mm to 4.4 mm. As can be seen in Figures 4.13 W1(c) and W1(e), the peak height decreases as thickness increases at 9.88 GHz and 9.46 GHz, respectively.

At 11.31 GHz, it is seen that the thickness increases with peak height for 7.1 mm to 7.9 mm. However, as Figure 4.13 W1(g) illustrates, for 8.0 mm to 8.3 mm, the height of peak decreases with an increase in thickness at 11.31 GHz. As thickness increase from 8.0 mm to 8.8 mm, Figure 4.13 W1(g) again demonstrates that peaks shift into the narrow frequency range of 9.46 GHz to 9.21 GHz, and that peak height likewise increases with thickness. In a similar vein, for 8.9 to 9.7 mm, it is evident that as thickness grows, peaks shift into the narrow frequency band of 10.38 GHz to 10.05 GHz, and that peak height likewise decreases as thickness increases. This behaviour is tied to the quarter-wavelength mechanism, where frequency and thickness are inversely related. Subsequently, in order to determine the relationship between quarter wavelength mechanism and REL, the estimated thickness (t_{cal}) is evaluated using equation 1.7 and compared to a simulated thickness (t_{sim}), from which REL may be computed using equation 1.6. The frequency-related calculated thickness or $n\lambda/4$ graphs are shown in Figure 4.13 to Figure 4.17. Equation (1.7) uses n = 1 and n = 5 to construct the estimated thickness curves. Lines in vertical form are drawn across the greatest values of reflection loss to computed thickness graphs in order to compare the calculated thickness and simulated thickness for peaks of reflection loss. Bubbles show the simulated thickness on graphs for levels of reflection loss. It is evident from Figure 4.13 to Figure 4.17 that the predicted thickness, shown on the $n\lambda/4$ curve, is close to the bubble with a vertical line drag by maximum reflection loss peaks for the stated simulated thickness.

For composition W2, the -10 dB bandwidth ranges from 0.40 GHz to 1.36 GHz, observed across thicknesses of 2.8 mm to 9.2 mm. Maximum REL values of -25.53 dB to -35.98 dB are recorded, with -20 dB bandwidths between 190 MHz and 250 MHz. As shown in Figure 4.14 W2(a), the REL peaks shift to lower frequencies as thickness increases, particularly between 2.7 mm to 3.9 mm, 6.5 mm to 7.3 mm, and 8.3 mm to 10.0 mm. Additionally, a W-shaped curve is observed between 10.00 GHz and 12.00 GHz in Figure 4.14 W2(g), indicating broad absorption that is ideal for electromagnetic interference (EMI) shielding.

In the case of composition W3, REL values range between -22.41 dB and -24.43 dB for thicknesses between 8.6 mm and 9.2 mm. The bandwidth of this composition varies from 0.45 GHz to 0.58 GHz at corresponding frequencies of 9.79 GHz and 9.96

GHz, with -20 dB bandwidths between 90 MHz and 140 MHz. Figures 4.15 W3(a) and W3(c) show that as thickness increases from 8.1 mm to 8.8 mm, peak height increases at the same frequency, but for 9.0 mm to 9.7 mm, peak height decreases with increasing thickness.

For composition W4, the -10 dB bandwidth is 0.06 GHz at a thickness of 7.8 mm, covering the frequency range 8.34 GHz to 8.4 GHz, while at 4.4 mm and 4.5 mm, it is 0.39 GHz. Maximum REL values range between -26.74 dB and -33.53 dB for a -20 dB bandwidth of 50 MHz to 120 MHz. As thickness increases from 6.6 mm to 7.4 mm and from 4.8 mm to 5.6 mm, the reflection loss peaks occur at consistent frequencies, as seen in Figure 4.16 W4(o). Additionally, peaks shift towards lower frequencies as thickness increases from 7.5 mm to 9.2 mm.

For composition W5, the -10 dB bandwidth of 0.19 GHz occurs at 10 mm thickness, with a broader 1.31 GHz bandwidth noted at 6.4 mm thickness. At 8.6 mm and 9.1 mm, the -20 dB bandwidth is 20 MHz, occurring within the frequency range 9.03 GHz to 9.05 GHz and 8.95 GHz to 8.97 GHz. Figures 4.17 W5(c) and W5(i) show that as thickness increases from 3.9 mm to 8.3 mm, the REL peaks shift toward lower frequencies. The W-shaped curve observed between 10.00 GHz to 12.00 GHz in Figures 4.17 W5(e) and W5(g) further suggests broad absorption, which is typical of materials used in EMI shielding.

The results for all compositions indicate that both -10 dB and -20 dB REL bands are influenced by the quarter-wavelength mechanism, with calculated and simulated thicknesses demonstrating good agreement with reflection loss peaks.

4.1.5.4 Impedance matching mechanism

The impedance of a material varies due to differences in its permittivity and permeability compared to free space. This variation affects the material's absorption properties. When these properties are mismatched, most of the incident signal is reflected, while only a small portion penetrates the material. However, if the permittivity and permeability are closely matched, more of the signal enters the material and is absorbed. Therefore, impedance matching is crucial for designing an efficient absorber. Figures 4.19 show the reflection loss (REL) and $|Z_{in}|$ versus frequency for the prepared samples, while Table 4.7 lists the corresponding Z_{in} values

at the maximum REL for each composition. Across all compositions (W1 to W5), the highest REL peaks align with the impedance matching principle.

For composition W1, with a thickness of 8.8 mm, the peak REL of -36.73 dB at 9.37 GHz corresponds to Z_{in} = 386.39 Ω, which is close to the characteristic impedance of free space (Z_0 = 377 Ω)**.** Similarly, for W2, at 11.64 GHz**,** the peak REL of -35.98 dB corresponds to Z_{in} = 387.26 Ω, which is also near 377 Ω. In the case of W3**,** a peak REL of -28.07 dB at 9.79 GHz is observed with Z_{in} = 348.82 Ω, which deviates from the desired value of 377 Ω. However, no REL peaks are detected at 10.048 GHz with Z_{in} = 381.18 Ω or at 9.54 GHz with Z_{in} = 390.03 Ω, both of which are closer to 377 Ω than the value at 9.79 GHz.

For W4, a peak REL of -36.02 dB at 9.71 GHz corresponds to Z_{in} = 368.65 Ω, which is further from 377 Ω compared to Z_{in} = 385.39 Ω at 10.55 GHz, where no REL peak is observed.

Finally, for W5**,** the maximum REL of -46.55 dB at 10.05 GHz corresponds to Z_{in} = 379.49 Ω, which is very close to the characteristic impedance of free space.

The complex nature of Z_{in}, with both real and imaginary components (Z_{real} & Z_{img}), explains this behaviour. For successful impedance matching, the real part of the impedance (Z_{real}) should approach 377 Ω and the imaginary part (Z_{img}) should approach zero. For instance, in W5, the peak REL of -46.55 dB at 10.05 GHz meets these criteria with Z_{real} = 379.48 Ω and Z_{img} = 2.55 Ω. Similarly, in W1, the peak REL of -36.73 dB at 9.37 GHz satisfies these requirements with Z_{real} = 386.33 Ω and Z_{img} = 6.60 Ω.

However, in W3, no REL peaks are observed at 10.05 GHz because Z_{real} = 330.49 Ω and Z_{img} = 189.94 Ω deviate significantly from the target values of 377 Ω and zero. This indicates that the differences in absorption properties are caused by the mismatch between Z_{real}, Z_{img}, and the ideal values.

The absorption properties of the prepared compositions are influenced by both the λ/4 resonance and impedance matching. The non-monotonic behaviour of Z_{in} (both Z_{real} and Z_{img}) when doped with Co-Al further confirms this.

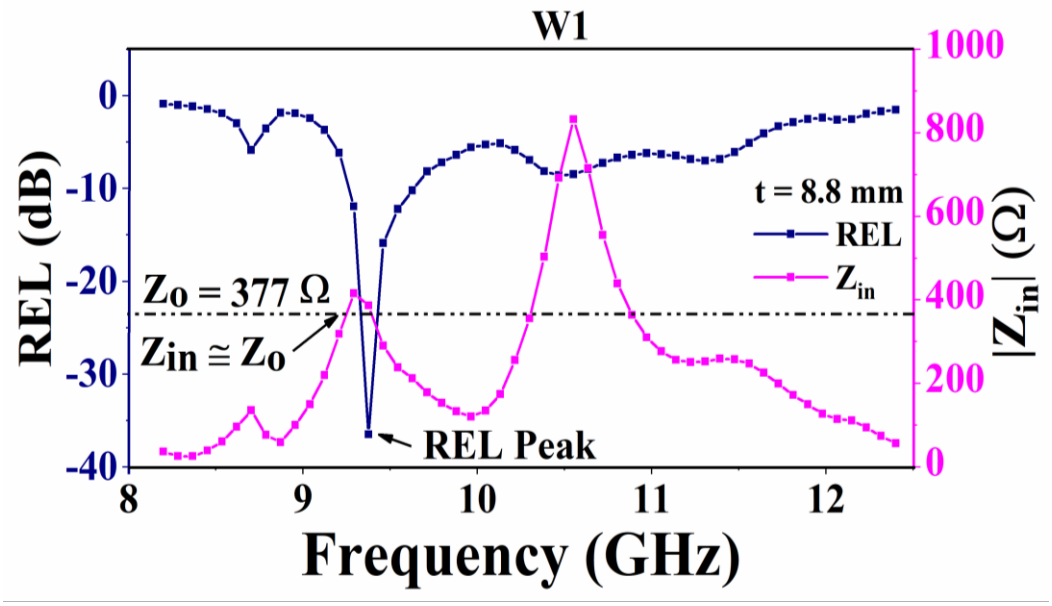
W1
REL (dB)
|Zin| (Ω)
Frequency (GHz)
t = 8.8 mm
REL
Zin
Zo = 377 Ω
Zin ≅ Zo
REL Peak

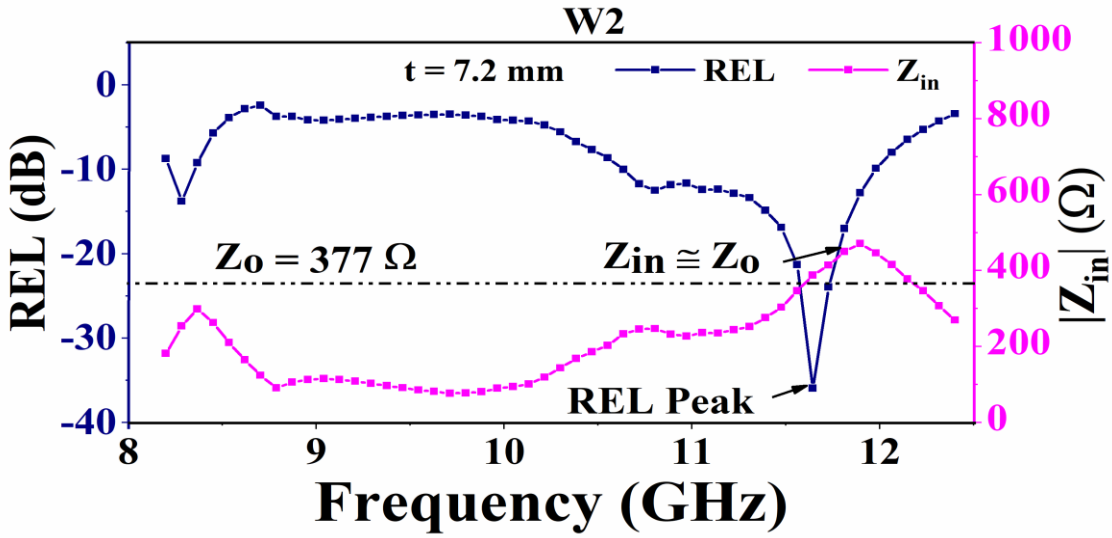
W2
REL (dB)
|Zin| (Ω)
Frequency (GHz)
t = 7.2 mm
REL
Zin
Zo = 377 Ω
Zin ≅ Zo
REL Peak

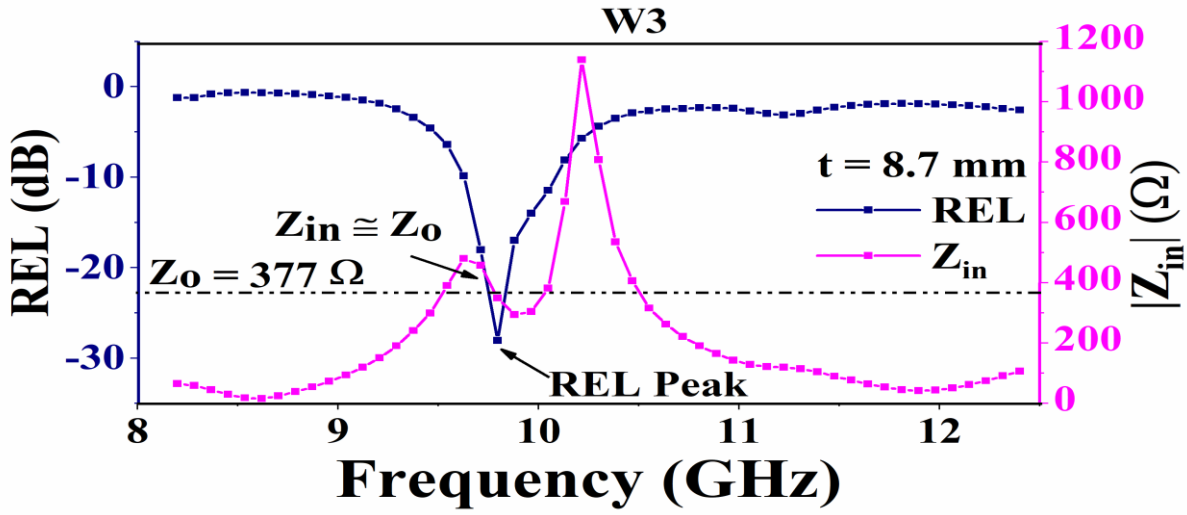
W3
REL (dB)
|Zin| (Ω)
Frequency (GHz)
t = 8.7 mm
REL
Zin
Zin ≅ Zo
Zo = 377 Ω
REL Peak

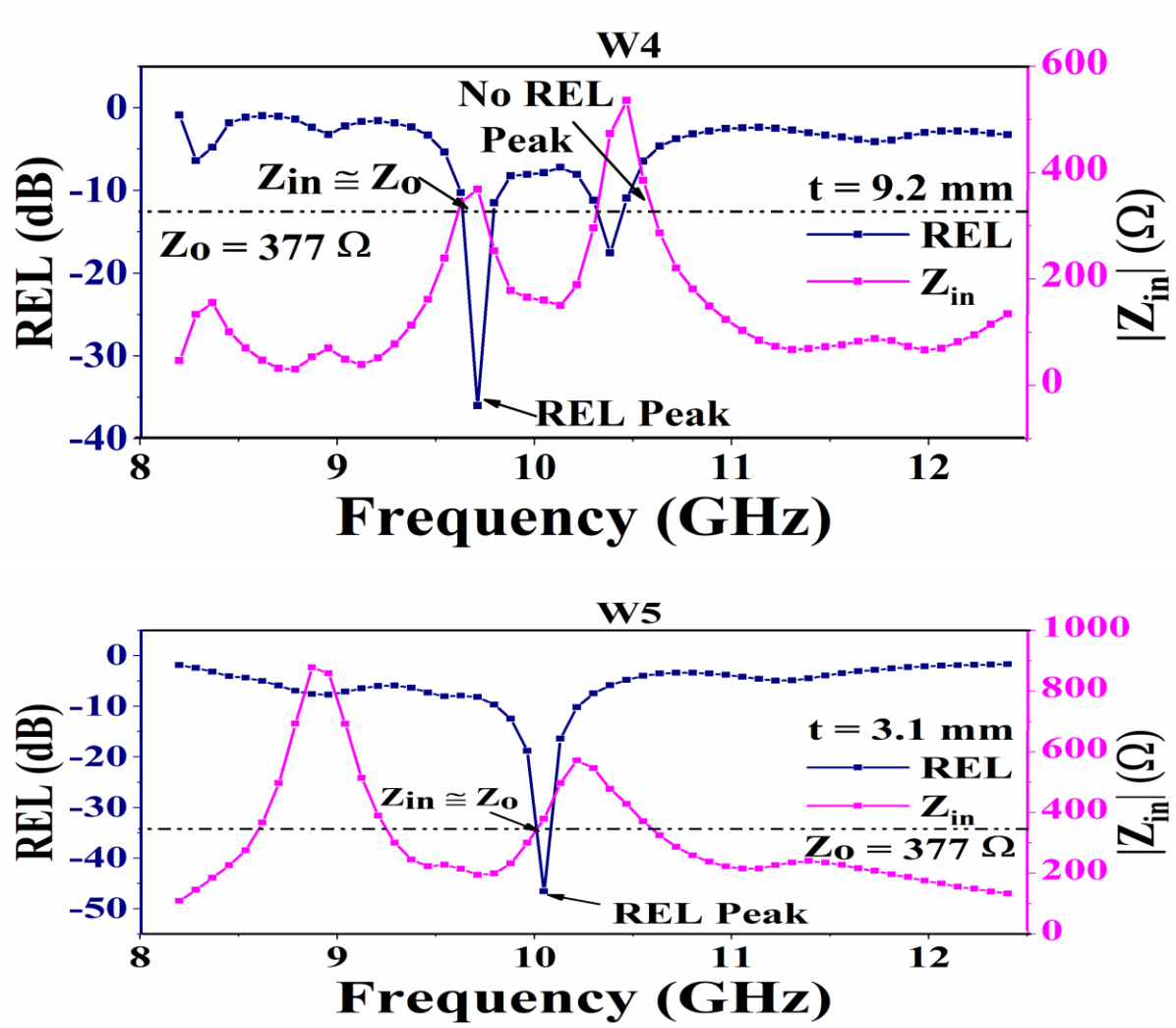

Figure 4.19. Zin and REL curve against frequency for $BaCo_xAl_xFe_{12-2x}O_{19}$.

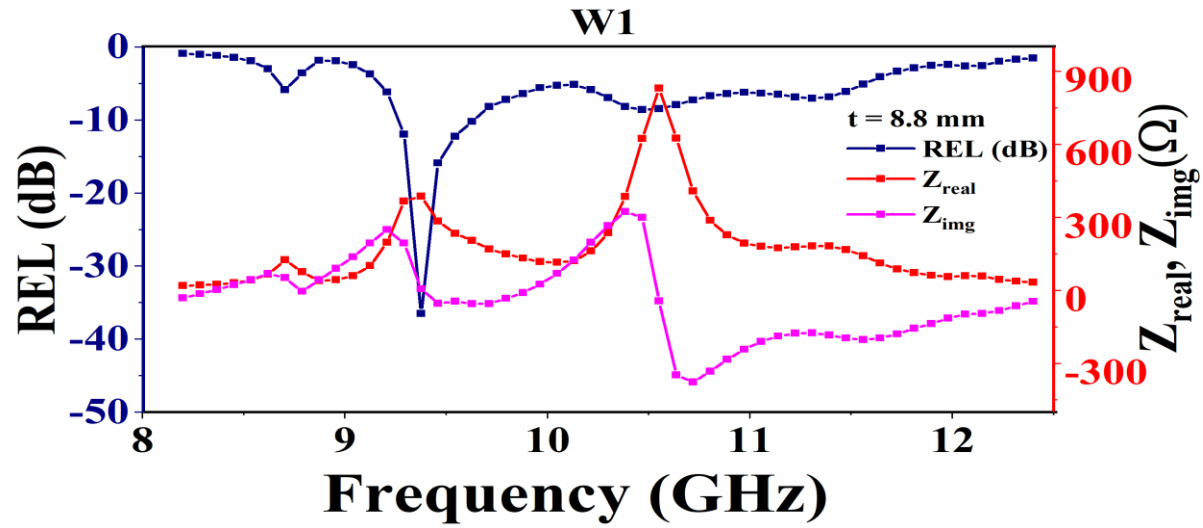

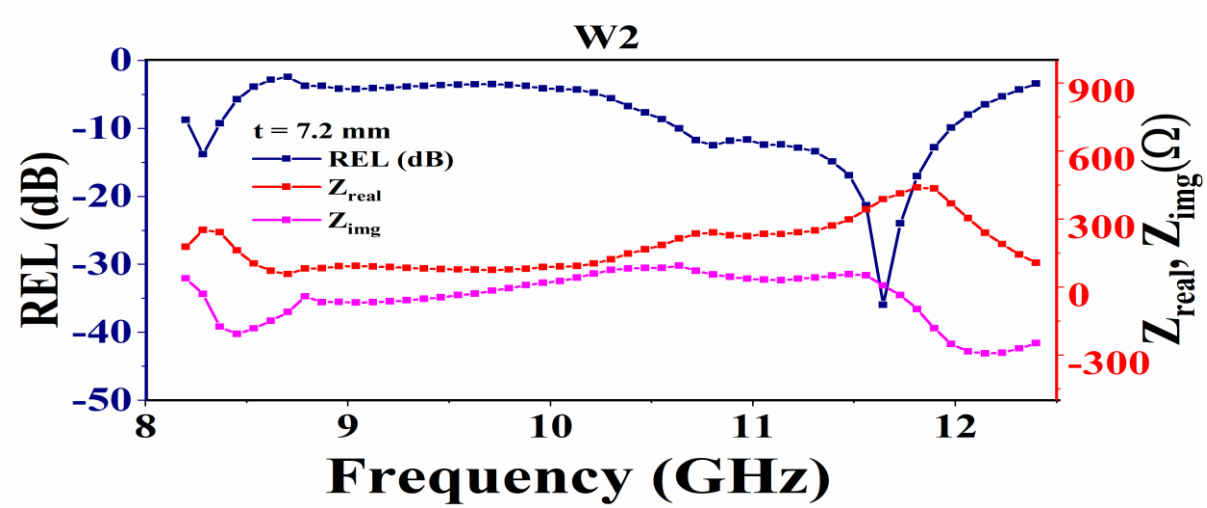
W2
t = 7.2 mm
REL (dB)
Z_{real}
Z_{img}
REL (dB)
Z_{real}, Z_{img}(Ω)
Frequency (GHz)

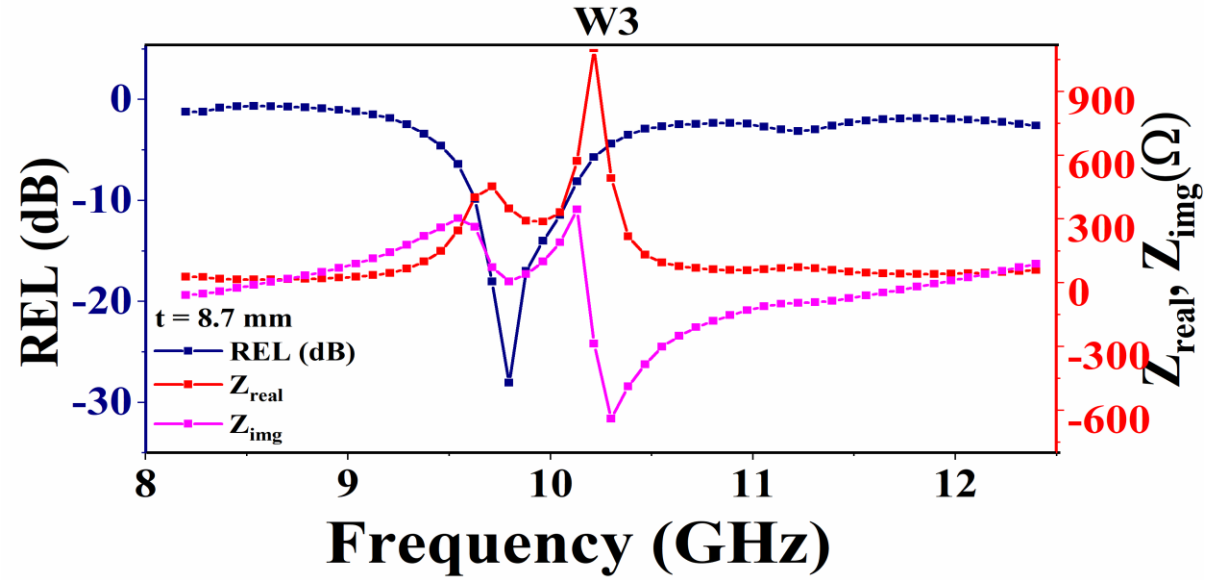
W3
t = 8.7 mm
REL (dB)
Z_{real}
Z_{img}
REL (dB)
Z_{real}, Z_{img}(Ω)
Frequency (GHz)

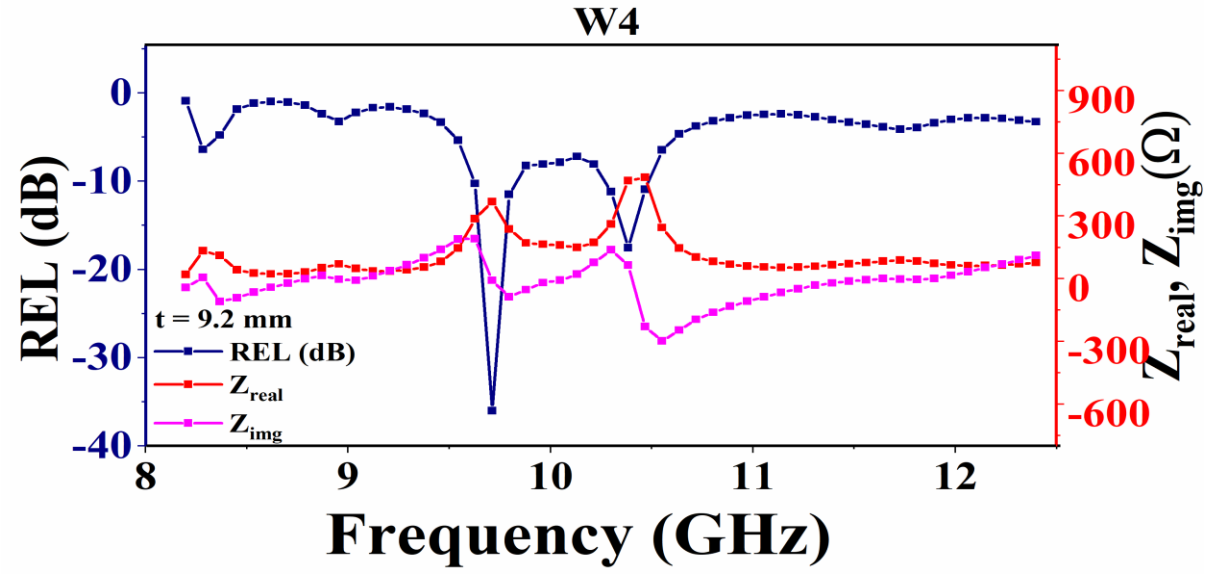
W4
t = 9.2 mm
REL (dB)
Z_{real}
Z_{img}
REL (dB)
Z_{real}, Z_{img}(Ω)
Frequency (GHz)

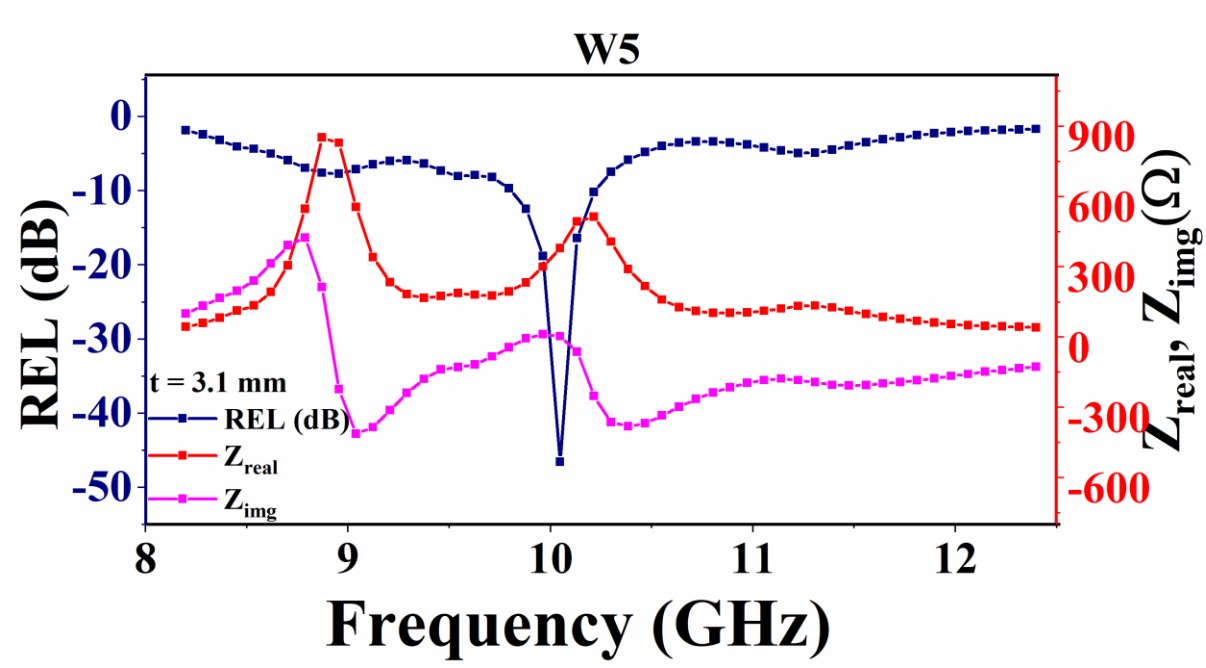

Figure 4.20. Z_{real}, Z_{imag}, and REL v/s frequency for $BaCo_xAl_xFe_{12-2x}O_{19}$.

Table 4.7. Z_{in}, Z_{real}, and Z_{imag} values corresponding to REL for $BaCo_xAl_xFe_{12-2x}O_{19}$.

Sample Name	Matching Thickness(mm)	Maximum REL (dB)	Matching frequency(GHz)	Z_{real} (Ω)	Z_{img} (Ω)	$\|Z_{in}\|$ (Ω)
W1	8.8	-36.73	9.37	386.33	6.60	386.39
W2	7.2	-35.98	11.64	387.20	6.63	387.26
W3	8.7	-28.07	9.79	348.82	5.21	348.86
W4	9.2	-36.02	9.71	368.56	-8.23	368.65
W5	3.1	-46.55	10.05	379.48	2.55	379.49

4.1.5.5 Eddy Current Loss

In ferrites, the presence of eddy currents results in magnetic loss. The formula for calculating eddy current loss can be expressed as

$$C_0 = \frac{\mu''(\mu')^{-2}}{f} \quad (4.5)$$

Where C_0 is a constant and the remaining parameters remain unchanged, as previously discussed. W1 shows a very stable and low C_0 value across the entire frequency range. W1 has two minor peaks, one around 9.04 GHz and another around 9.71 GHz. At 9.71 GHz indicate the REL = -13.39 dB at 3.4 mm thickness. W2 shows a dramatic response at lower frequencies. A significant peak occurs at 8.54 GHz, where C_0 reaches 33.53 ns**;** there will be an impact on the eddy current loss. After this

peak, the value drops off sharply. W2 shows a very strong interaction at the frequency around 8.5 GHz and then stabilizes quickly at higher frequencies. For W3, A small peak occurs at 8.28 GHz, where C_0 reaches 0.49 ns, but otherwise, the values remain low and stable. W3 behaves relatively stably, with low C_0 values across the frequency range. W4 shows a clear peak in the lower range but stabilizes afterward. A prominent peak occurs at 8.45 GHz, with C_0 reaching 14.56 ns. After this, the values drop rapidly. W5 shows the most prominent peak among all materials. The peak occurs at 9.71 GHz, where C_0 reaches 4.21 ns. After the peak, C_0 decreases gradually. W5 is highly responsive around 9.7 GHz, showing the strongest interaction among the materials in this frequency range.

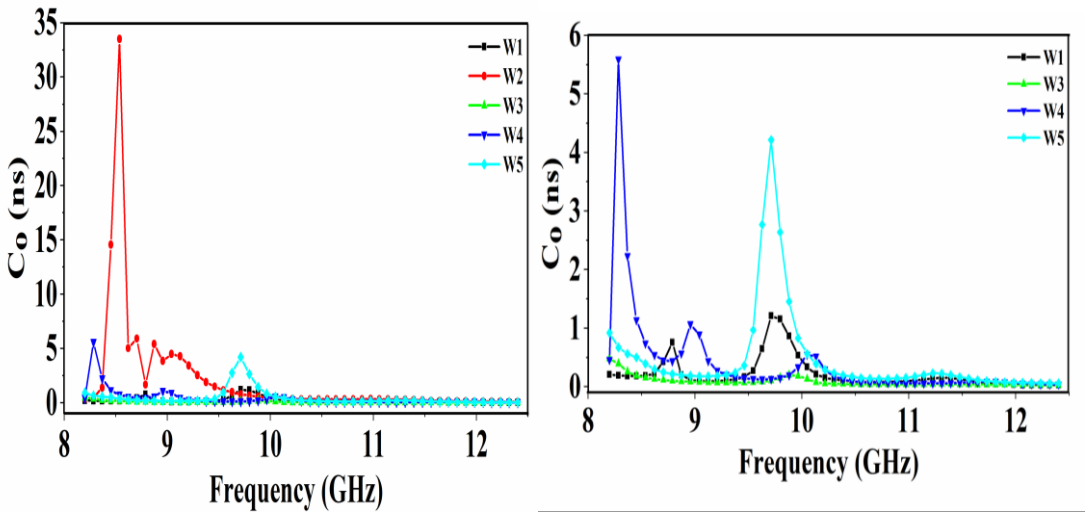

Figure 4.21. C_0 versus frequency curve for $BaCo_xAl_xFe_{12-2x}O_{19}$.

4.1.5.6 Bandwidth to Thickness Ratio

Wide bandwidths with reduced thickness play a crucial role in the characterization and design of an absorber. Instead of focusing just on raising REL values, one should strive for a low thickness after reaching the REL≥-10 dB. This makes figuring out the bandwidth to thickness ratio (BTR) and percentage bandwidth (PBW) crucial [86-88]

The thickness corresponding to the REL peak is shown by t, while the bandwidth is represented by BW. The high, low, and canter frequencies of the frequency band are indicated by f_2, f_1, and f_0.

The BTR (Bandwidth to Thickness Ratio) and PBW (Percentage Bandwidth) values for the prepared compositions are summarized in the Table 4.6. Among the samples, W2 shows the highest BTR of 8.74E-04 and PBW of 8.47% at 9.8 GHz with a

reflection loss (REL) of -14.75 dB at a thickness of 3.0 mm. notably, while W4 achieves a significantly higher REL of -46.55 dB, its BTR is lower than that of the W2 sample. For W1, the BTR ranges from 1.23E-04 to 4.04E-04, and the PBW spans from 1.48% to 4.45%, covering frequencies between 9.88 GHz and 11.31 GHz for thicknesses between 3.4 and 9.2 mm.

The composition W2 demonstrates a BTR between 1.28E-04 and 8.74E-04 and a PBW ranging from 3.94% to 12.03% for thicknesses of 2.8 to 9.2 mm across frequencies from 9.62 to 11.76 GHz.

For W3, at thicknesses from 8.6 to 9.2 mm, the BTR varies from 1.60E-04 to 2.07E-04, with a PBW range of 4.60% to 6.12% over the frequency range of 9.79 to 9.96 GHz.

The composition W4 displays a BTR between 9.54E-05 and 3.31E-04 and a PBW from 0.72% to 4.32%, covering frequencies from 8.37 to 10.3 GHz for thicknesses between 3.4 and 9.8 mm.

Lastly, W5 shows a BTR between 9.46E-05 and 5.68E-04, with a PBW of 2.42% to 11.00% for thicknesses ranging from 2.2 to 10.00 mm across frequencies from 8.28 to 11.82 GHz.

4.1.5.7 S – Parameter

When the input signal is applied at input port 1 of the test waveguide from VNA, the two-port S_{11} parameter accounts for the reflected signal from the same input port 1 from the sample fitted in the test waveguide of the VNA. S_{21} accompanies the attenuation in the signal traveling from input port 1 to output port 2. The values for W1 begin at around -1.25 dB at 8.2 GHz and reach a deeper minimum of around -6.8 dB at 9.7 GHz. Afterward, S_{11} increases slightly, reaching about -4.26 dB at 12.4 GHz. W1 demonstrates an initial dip in S_{11}, indicating higher reflection or less transmission around the 9.7 GHz region, followed by a recovery. W2 shows a sharp dip in S_{11} at around 8.3 GHz, reaching -7.67 dB, and then gradually increasing until it stabilizes around -1.9 dB at 9.6 GHz. It remains relatively flat after that, with minor variations up to 12.4 GHz. For W3, the values start at around -0.85 dB at 8.2 GHz and dip to approximately -3.49 dB around 10 GHz. Afterward, S_{11}increases and stays at around -4.17 dB at 12.4 GHz. W4 starts at around -0.99 dB at 8.2 GHz and reaches a deeper dip of around -6.6 dB at 9.46 GHz. It then follows a slight recovery; stabilizing

around -2.34 dB at 12.4 GHz. W5 shows significant dips at around 9.3 GHz, reaching about -4.8 dB. At 12.4 GHz, S_{11} is around -2.7 dB.

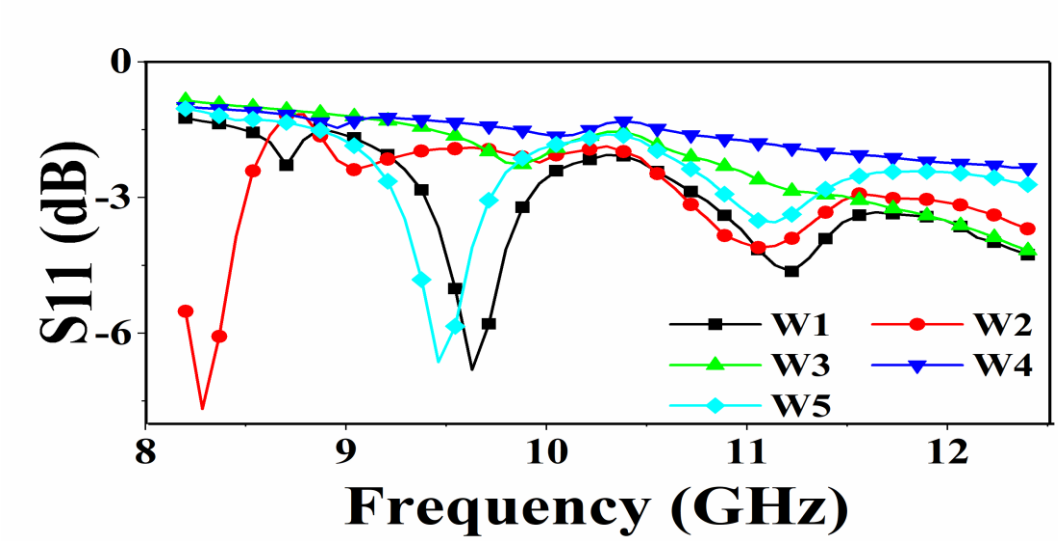

Figure 4.22. S_{11} versus frequency curve for $BaCo_xAl_xFe_{12-2x}O_{19}$.

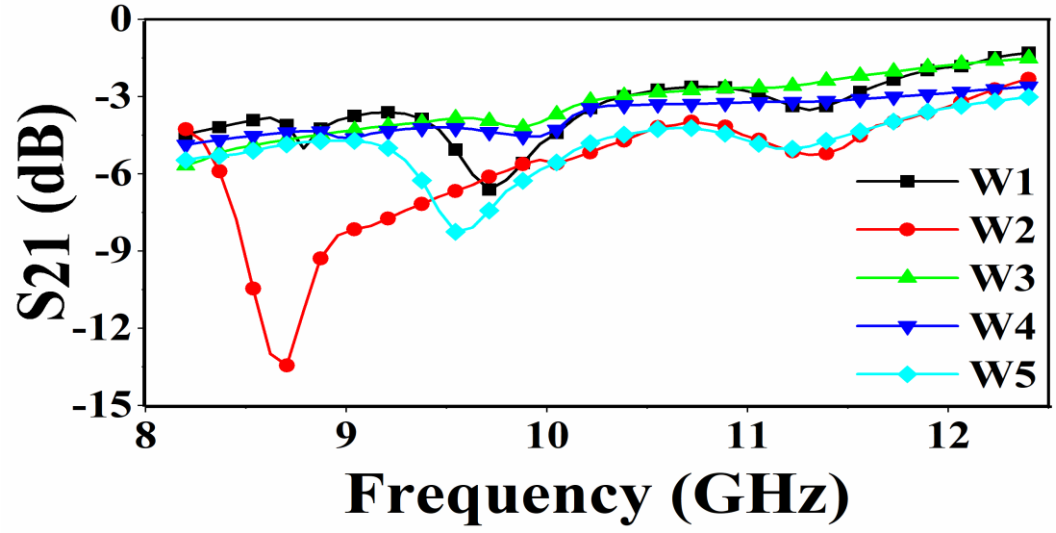

Figure 4.23. S_{21} versus frequency curve for $BaCo_xAl_xFe_{12-2x}O_{19}$.

For W1, From 8.2 GHz to about 9.8 GHz, the S_{21} value decreases from around -2.24 dB to -3.31 dB (showing more attenuation). After 9.8 GHz, the trend reverses and S_{21} increases, with attenuation gradually reducing until it reaches around -0.65 dB at 12.4 GHz (showing less attenuation). W2 shows a significantly deeper attenuation, starting at around -2.13 dB at 8.2 GHz and reaching a minimum of -6.72 dB at 8.70 GHz. After this, the attenuation starts to recover, reducing to -1.15 dB at 12.4 GHz. The

values for W3 start at around -2.83 dB at 8.2 GHz and gradually improve (less negative) to about -0.76 dB at 12.4 GHz. Similarly to W3, W4, the data shows that S_{21} starts at around -2.44 dB at 8.2 GHz and improves to about -1.3 dB at 12.4 GHz. In the case of W5, the data shows that S_{21} starts at -2.74 dB at 8.2 GHz and improves to around -1.51 dB at 12.4 GHz.

4.2 Co^{2+}- Ce^{3+} substituted $BaCo_xCe_xFe_{12-2x}O_{19}$ hexaferrite.

In this section, we will be utilizing the sol-gel combustion method to synthesize a hexaferrite with Co and Ce substitutions. The composition of this hexaferrite will be $BaCo_xCe_xFe_{12-2x}O_{19}$. Displayed in Table 4.8 are the sample names/codes for various levels of substitution in $BaCo_xCe_xFe_{12-2x}O_{19}$.

Table 4.8. Presents the assignment of sample names corresponding to various substitution levels in $BaCo_xCe_xFe_{12-2x}O_{19}$ hexaferrite.

Sample Composition **$BaCo_xCe_xFe_{12-2x}O_{19}$**	Sample Code Name	Sample Code (X-series)
x= 0.0	**$BaFe_{12}O_{19}$**	X0
x = 0.2	**$BaCo_{0.2}Ce_{0.2}Fe_{11.6}O_{19}$**	X1
x = 0.4	**$BaCo_{0.4}Ce_{0.4}Fe_{11.2}O_{19}$**	X2
x = 0.6	**$BaCo_{0.6}Ce_{0.6}Fe_{10.8}O_{19}$**	X3
x = 0.8	**$BaCo_{0.8}Ce_{0.8}Fe_{10.4}O_{19}$**	X4
x = 1.0	**$BaCoCeFe_{10}O_{19}$**	X5

4.2.1. X-ray diffraction analysis

Figure 4.24 presents the XRD patterns of $BaCo_xCe_xFe_{12-2x}O_{19}$ hexaferrites (X0 to X5). PowderX software identified the peaks, with (0027) and (1112) matching PDF# 96-153-4314 (barium iron oxide, secondary phase) and (006), (008), (110), etc. matching PDF# 96-100-8842 (hexagonal phase, major phase). The strongest peak shifts from (114) for X0 to X3 to (0027) for X4 and X5, indicating a potential structural change at higher doping levels. Table 4.9 summarizes these values. Notably, the c/a ratio remains close to 3.94 (as expected) and the average crystallite size decreases with increasing doping except for X4, suggesting limited grain growth at this specific composition [170]. As demonstrated in Figure 4.24 and Table 4.9, Co-Ce doping has a minimal impact on the sample lattice parameters, unit cell volume, and c/a ratio. The lattice parameter 'a' exhibits a minor variation between 5.8937 Å and 5.8898 Å. Similarly, the 'c' parameter shows a limited change from 23.1998 Å to 23.2261 Å

[162-163]. Interestingly, the unit cell volume slightly decreases from 698.68 Å^3 to 696.97 Å^3. Notably, the c/a ratio remains within a narrow range of 3.9390 to 3.9408, consistent with the expected value of 3.94[29].

Table 4.9. Effect of Co-Ce Doping on Lattice Parameters and Unit Cell Volume of $BaCo_xCe_xFe_{12-2x}O_{19}$ (X0 to X5)

Parameter	X0 (x = 0.0)	X1 (x = 0.2)	X2 (x = 0.4)	X3 (x = 0.6)	X4 (x = 0.8)	X5 (x = 1.0)
a = b (Å)	5.8937	5.893	5.8921	5.8915	5.8903	5.8898
c (Å)	23.2261	23.2211	23.2174	23.2125	23.2025	23.1998
c/a	3.9408	3.9405	3.9404	3.9400	3.9391	3.9390
Vol /10^6 pm^3	698.6875	698.3712	698.0466	697.7572	697.1725	696.9730
Crystallite Size D_{xrd} (nm)	43.3961	40.6701	39.8334	36.4659	33.0873	33.7306

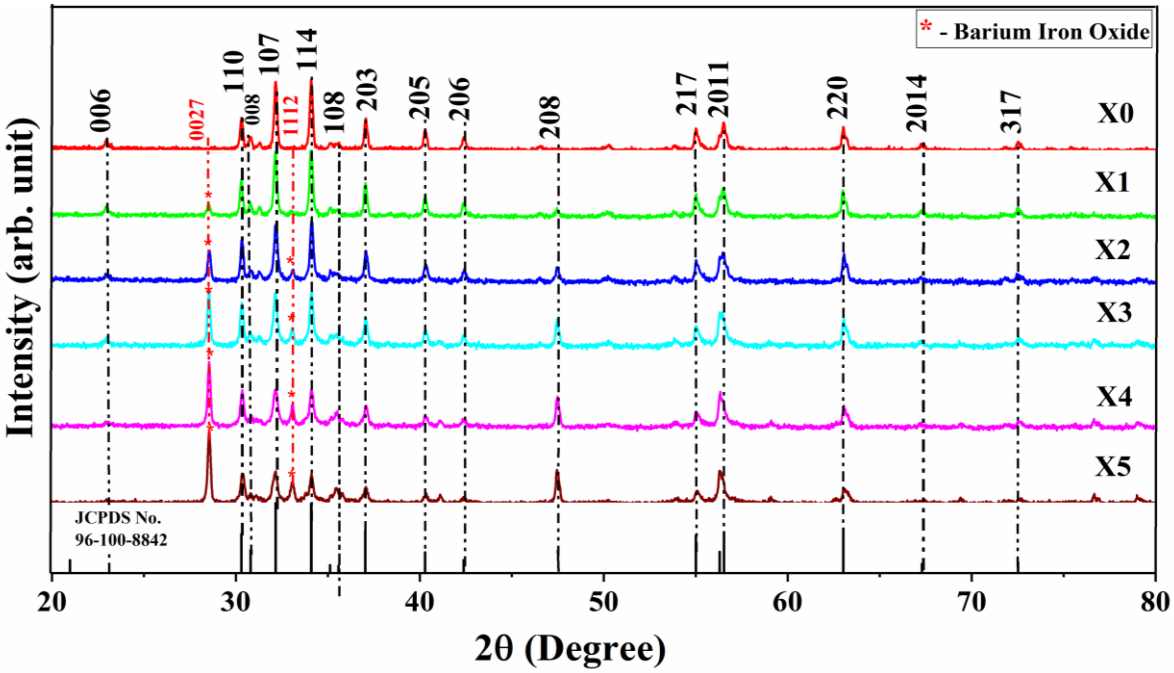

Figure 4.24. XRD Patterns of Co^{2+} and Ce^{3+} Doped M-type Ba Hexaferrites

The most significant observation is the decrease in crystallite size with increasing Co-Ce doping (x). This trend is evident in all compositions except X4, where the crystallite size falls within the range of 43.3961 nm and 30.9368 nm. This suggests that the Co-Ce substitution might have an effect on how crystal growth, with smaller crystallites appearing as the doping levels rises.

Figure 4.25 presents EDX spectra for samples with x = 0.0 (X0) (undoped) and x = 0.4 (X2) (doped). The spectra confirm the presence of the expected elements (Ba, O, and Fe) in the undoped sample. The doped sample (X2) also shows peaks that correspond to the dopant elements (Co and Ce), which shows that they were successful added to the material. Table 4.10 further quantifies the elemental composition by providing the weight and atomic percentages of all detected elements across all compositions studied. There are a few reasons why peaks in an EDX spectrum might not be identified:

Low Peak Intensity: Weak peaks from minor elements or background noise might not be distinguished from the baseline signal.

Peak Overlap: Peaks from different elements can overlap significantly, making it difficult to identify them individually.

Database Limitations: The reference database used by the EDX software might not have a record for a specific element or compound that is present in the sample.

Same Peak Identifying Two or Three Elements: EDX identifies elements based on the energy of the emitted X-rays. However, sometimes X-rays with similar energies can be emitted by different elements. This can lead to peak overlap, where a single peak in the spectrum might correspond to multiple elements.

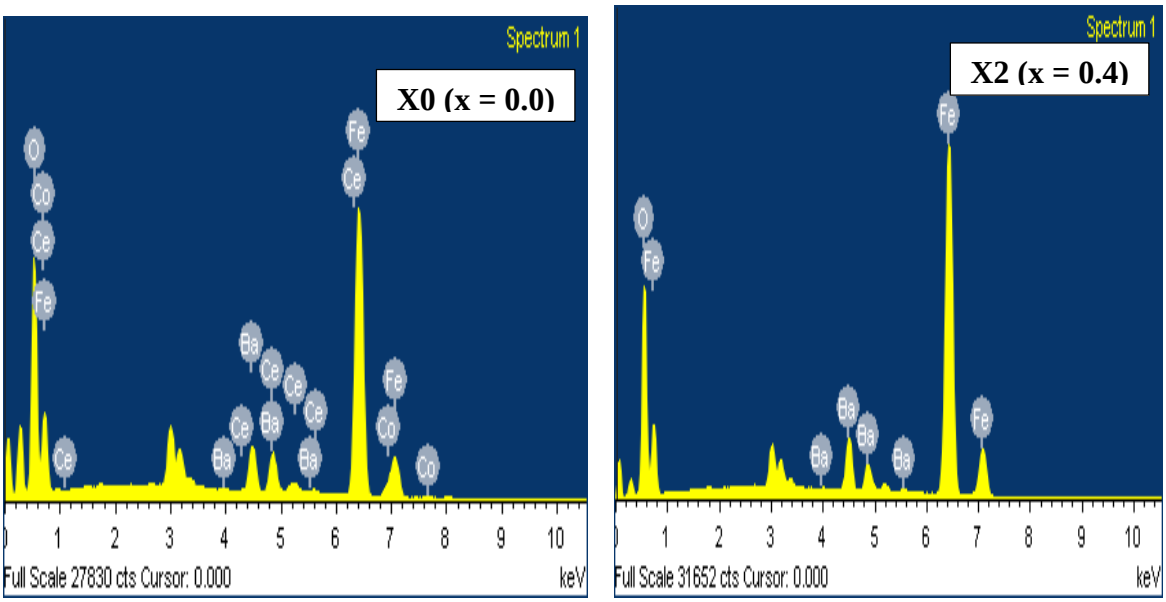

Figure 4.25. EDX Spectra of Barium Hexaferrite ($BaCo_xCe_xFe_{12-2x}O_{19}$) with Varying Doping Levels (X0 and X2)

Table 4.10. Elemental Composition (Weight % and Atomic %) of $BaCo_xCe_xFe_{12-2x}O_{19}$ (x = X0 to X5, 0.0-1.0) determined by EDX Analysis

Element	x = 0.0		x = 0.2		x = 0.4		x = 0.6		x = 0.8		x = 1.0	
	W %	A %	W %	A %	W %	A %	W %	A %	W %	A %	W %	A %
O K	21.2	51.1	27.6	62.2	27.5	60.6	21.5	53.3	26.2	59.8	22.4	53.5
Fe K	65.3	45.1	45.2	29.1	53.8	33.9	53.6	38.2	49.2	32.2	60.6	41.4
Ba L	13.5	3.8	11.1	2.9	11.7	3.0	13.4	3.	11.2	2.9	13.0	3.6
Co K	-	-	4.8	2.9	2.3	1.4	3.5	2.3	4.1	2.6	1.3	0.8
Ce L	-	-	11.3	2.9	4.7	1.2	8.1	2.3	9.4	2.4	2.6	0.7

4.2.2 Field Formulation and Morphological Analysis of Nanoferrite Composites via FESEM Characterization

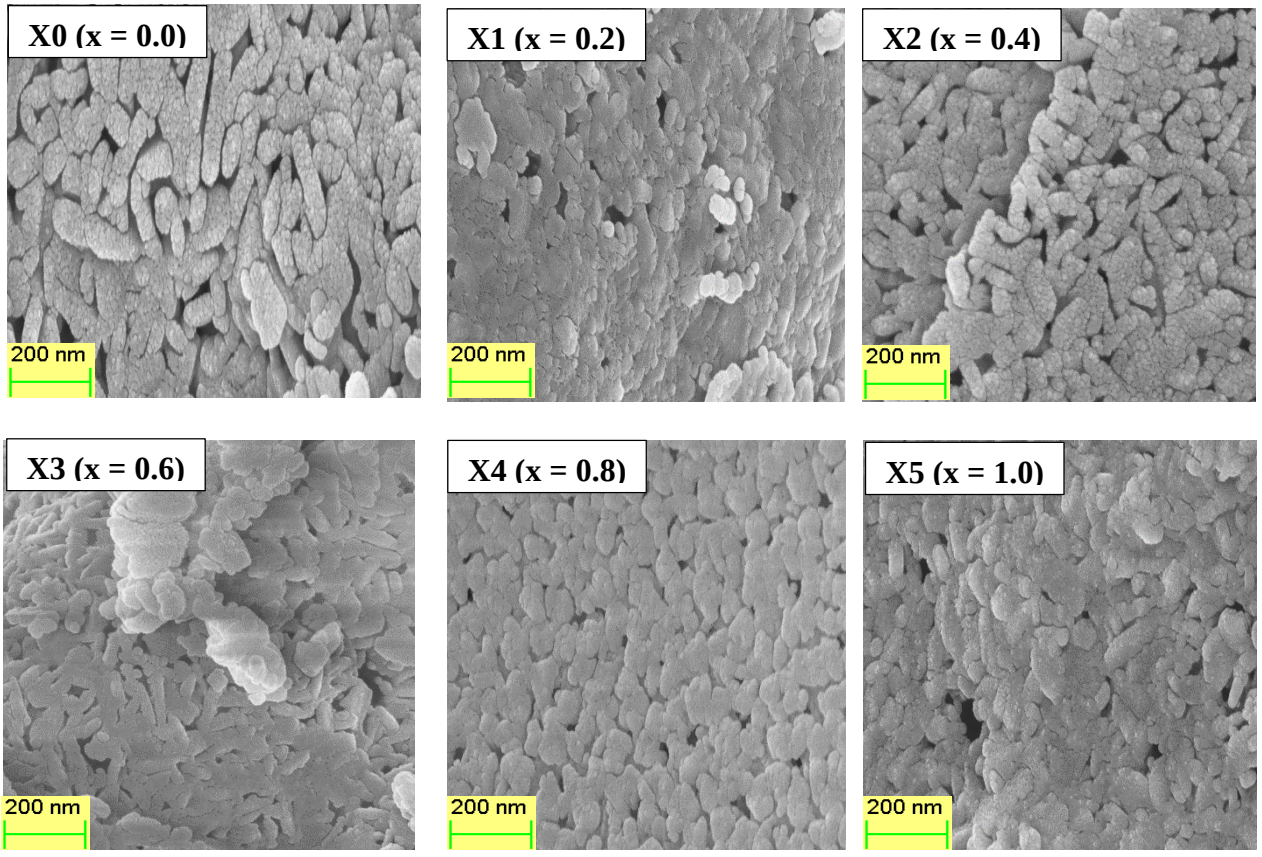

Figure 4.26. Microstructure Analysis: SEM Images of Co-Doped $BaFe_{12}O_{19}$ (x = 0.0-1.0 (X0 to X5))

The scanning electron microscopy (SEM) images in Figure 4.26 show the grain structure of the $BaCo_xCe_xFe_{12-2x}O_{19}$ hexaferrites. At x = 0.2 (X1), a fusion of individual grains leads to the formation of a significantly more prominent, "colossal" grain. Additionally, smaller individual grains are visible in other compositions. Co-Ce doping induces grain agglomeration, leading to a non-uniform grain size distribution

across the different samples. Based on this behaviour, it seems that the electrostatic and magnetic interactions between ferrite particles help create non-uniform grain aggregates and smaller individual grains within these clusters. Observations reveal void spaces within the grain configuration, which could potentially impede the movement of charge carriers. Furthermore, we expect the smaller grain size and increased presence of grain boundaries to contribute to higher impedance or resistance to applied fields, thereby affecting the overall charge transport mechanism of these materials.

4.2.3 Electrical Characterization

4.2.3.1 Dielectric constant

Figure 4.27 displays the variations of ε' and ε'' with frequency. At lower frequencies, both components exhibit a decrease with increasing frequency due to dielectric relaxation and dispersion phenomena. At higher frequencies, however, they become independent of frequency. Pure Ba hexaferrite (X0) starts with an ε' value of 83.48 at 100 Hz, dropping to 12.38 at 2 MHz. Similar trends are observed for other compositions, with ε' values decreasing from 94.92 (X2) to 4.28, 14.48 (X3) to 3.69, 96.67 (X4) to 3.97, and 130.03 (X5) to 4.13 [175-176].

The higher ε' values observed at lower frequencies can be attributed to defects, voids, and dislocations within grain boundaries [177]. As frequency increases, ε' decreases due to the diminishing contribution of space charge polarization. The two-layer Maxwell-Wagner model of interfacial polarization, in line with Koop's theory [39-41], further explains the dielectric dispersion..

4.2.3.2 Dielectric Loss and Tangent Loss factor

Figure 4.27(b) illustrates the frequency dependence of the dielectric loss (ε''). Like ε', the ε'' curves exhibit higher values at lower frequencies due to increased contributions from relaxation processes. These relaxation mechanisms become less effective as frequency increases, resulting in a frequency-independent plateau at higher frequencies. This behaviour happens because of persistent interfacial polarization at lower frequencies. This is because the material is made up of highly conductive grains that are separated by less conductive grain boundaries [41]. Electrons hop within the grains, accumulating at the grain boundaries due to their high resistance, inducing polarization. But as the applied field frequency raises, space charge carriers have a

harder time keeping up with the field reversals. This means that interfacial polarization decreases at higher frequencies [179].

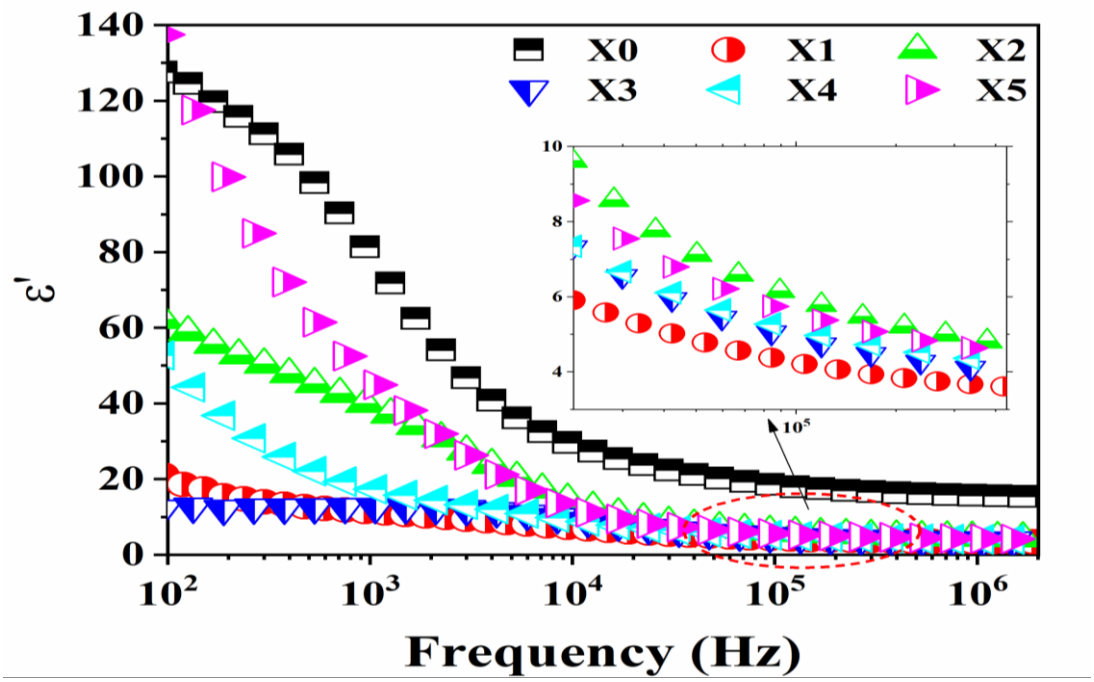

Figure 4.27(a). Frequency Dependence of Dielectric Constant for Co-Ce Doped $BaFe_{12}O_{19}$ (X0 to X5 (x = 0.0-1.0))

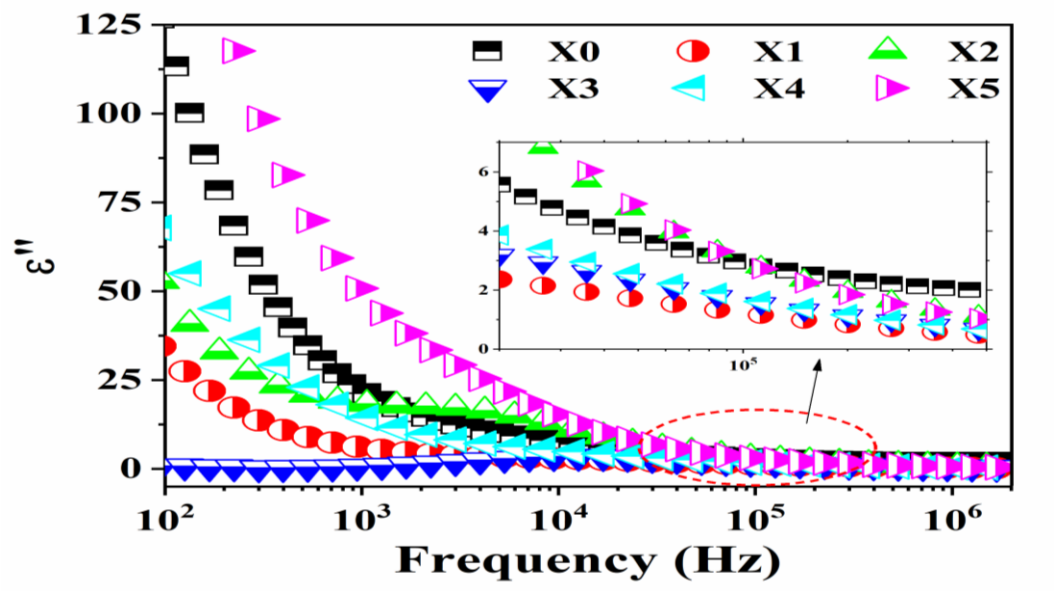

Figure 4. 27(b) Frequency Dependence of Dielectric Loss in $BaCo_xCe_xFe_{12-2x}O_{19}$ (X0 to X5 (x = 0.0-1.0)) Hexaferrites

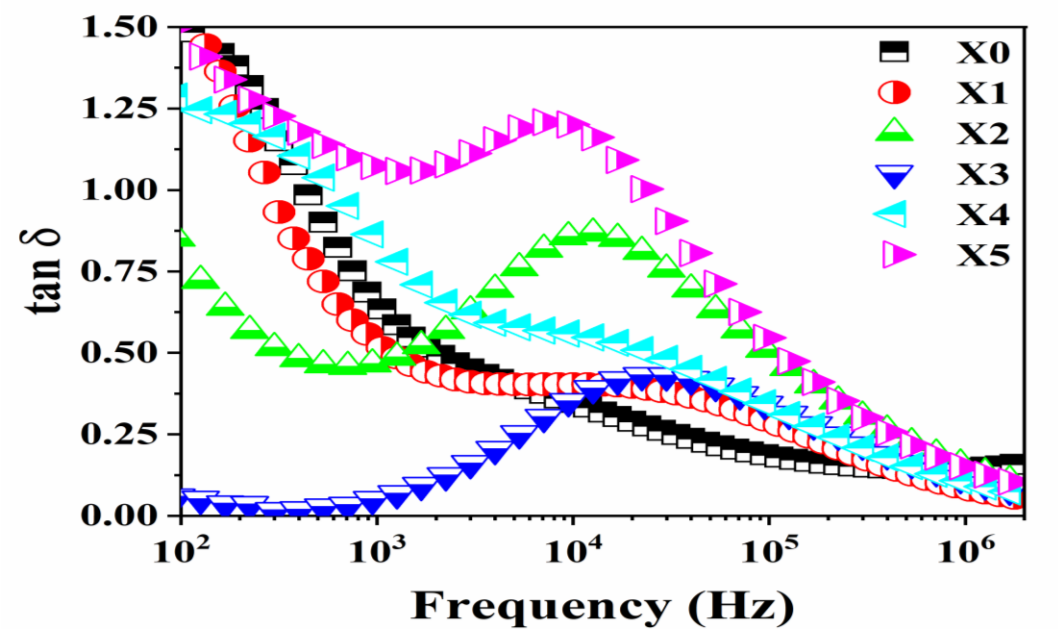

Figure 4.27(c) Frequency Dependence of Tan δ for $BaCo_xCe_xFe_{12-2x}O_{19}$ Hexaferrites (X0 to X5 (x = 0.0-1.0)).

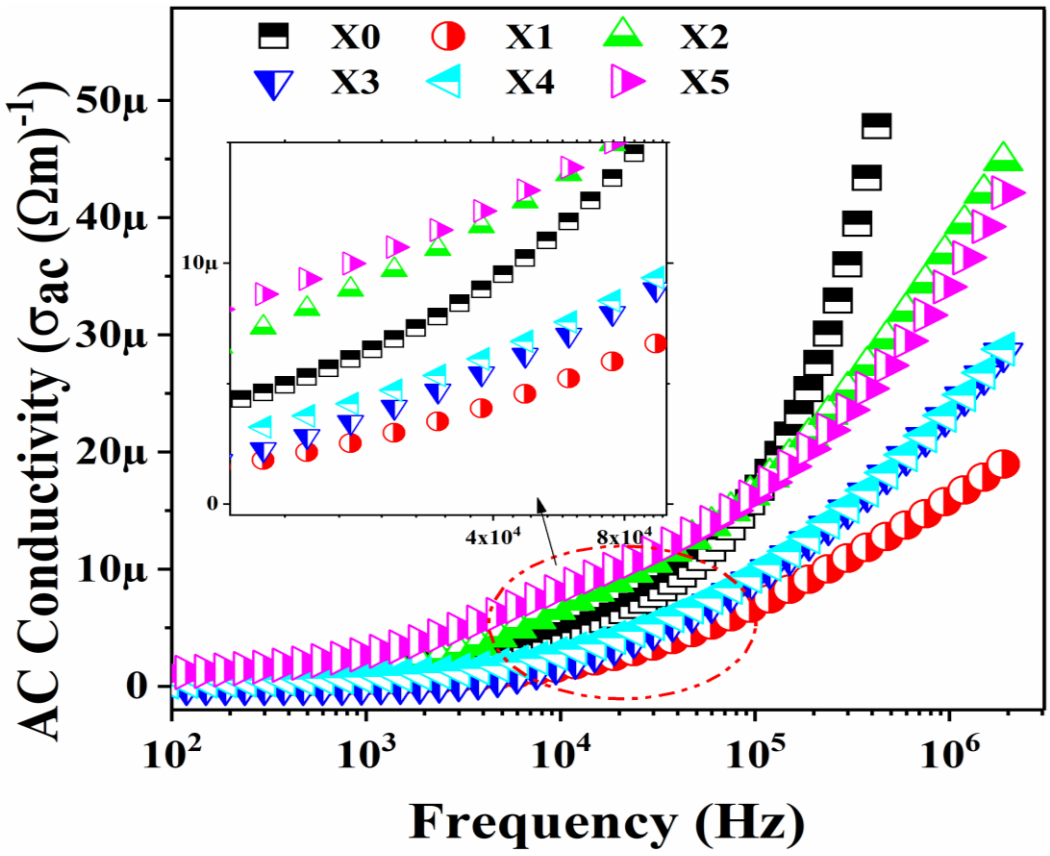

Figure 4.27 (d) Frequency Dependence of AC Conductivity in Co- Ce Doped $BaFe_{12}O_{19}$ (X0 to X5 (x = 0.0-1.0))

At higher frequencies, the decrease in dielectric constant (ε') can be attributed to the limitations of dipolar polarization. As the frequency of the applied electric field increases, dipole reorientation becomes progressively challenging, hindering their alignment with the field beyond a certain threshold. This results in a diminished net polarization and, consequently, a reduction in ε'. The dielectric loss tangent (tan δ) reflects the energy dissipation within the material under an applied electric field. As shown in Figure 4.27(c), tan δ initially exhibits an increasing trend with frequency until a critical point is reached. This behaviour is followed by a decrease at even higher frequencies. This "resonance-like" phenomenon is frequently observed in various dielectric materials [180] and arises when the hopping frequency of electrons between Fe^{2+} and Fe^{3+} ions aligns with the applied field frequency. At lower frequencies, conduction losses or ion migration losses become dominant, contributing significantly to the observed high tan δ values. This works because ions hop back and forth between two places at different frequencies. The most energy is lost when the hopping frequency lines up with the applied field [19, 20]. Conversely, atomic jumps become unlikely when the applied frequency surpasses the hopping frequency, resulting in negligible losses.

4.2.3.3 AC Conductivity

Figure 4.27(d) depicts the frequency dependence of AC conductivity (σ_{ac}) for all samples. This data aligns with the observed dielectric behaviour. At low frequencies, the grain boundaries exhibit higher conductivity than the grains. This suggests that grain boundary volume dominates this regime's conduction mechanism. Their lower conductivity hinders the movement of charge carriers, impacting the dielectric response at low frequencies.

As the frequency goes up, the dielectric behaviour changes and gets closer to the frequency at which electron hop Fe^{2+} and Fe^{3+} ions. This is because the hopping frequency becomes comparable to the applied field, leading to a plateauing of the dielectric constant at higher frequencies.

Johscher's universal power law (Equation 4.6) governs the hopping process facilitating electrical conduction [182-183]. The parameters A and n are thermally activated, with n being the frequency exponent ($0 < n < 1$) as shown in Figure 4.28 [184].

$$\sigma_{ac} = \sigma_{dc} + A\,\omega_n \quad (4.6)$$

Within the frequency range where ε' is constant and tangent loss variation is minimal (except for x = 0.2), Equation (4.6) reveals a direct relationship between conductivity and frequency. Consequently, AC conductivity increases with increasing frequency. Notably, x = 0.2 exhibits the highest AC conductivity. This high value, along with the appearance of a loss peak at higher frequencies, might be attributed to increased electron hopping frequency. Additionally, high-frequency AC conductivity enhancements have been associated with contributions from grains.

Dependence of Compositional Variation on Electrical Properties:

Dielectric Constant (ε′) and Dielectric Loss (ε″): In Co-Ce doping, ε′ and ε″ both decrease with frequency due to factors like defect creation or interfacial polarization. Doping might introduce additional defects or influence grain boundaries, potentially impacting ε′ and ε″ at lower frequencies. However, the specific effect would depend on the dopant type, concentration, and its interaction with the material's structure.

Tan δ (Loss Tangent): Tan δ is directly related to ε′ and ε″ (tan δ = ε″/ε′). All compositions (X0 to X5, x = 0.0 to x = 1.0) exhibit a peak in tan δ at a certain frequency, followed by a decrease at higher frequencies. This "resonance-like" peak is a common feature in dielectric materials. The peak in tan δ corresponds to the alignment of the hopping frequency of electrons between Fe^{2+} and Fe^{3+} ions with the applied electric field frequency. Doping can potentially influence the concentration or mobility of these ions is as:

Increased Concentration: If doping introduces more Fe^{2+} or Fe^{3+} ions, it could lead to a higher concentration of participating electrons, potentially amplifying the peak magnitude of tan δ.

Decreased Mobility: Doping might introduce defects or other factors that hinder the movement of these ions. This could lead to a broader peak (lower peak frequency) as a wider range of frequencies might be needed to achieve the alignment with the applied field.

Conductivity: The conductivity of the material increases with increasing frequency for all compositions (X0 to X5). This is likely because higher frequencies correspond to a rapidly changing electric field. As the frequency increases, the ions or electrons in the material have less time to respond to the field and overcome potential energy barriers.

This can lead to increased hopping or movement of these charged particles, resulting in higher conductivity.

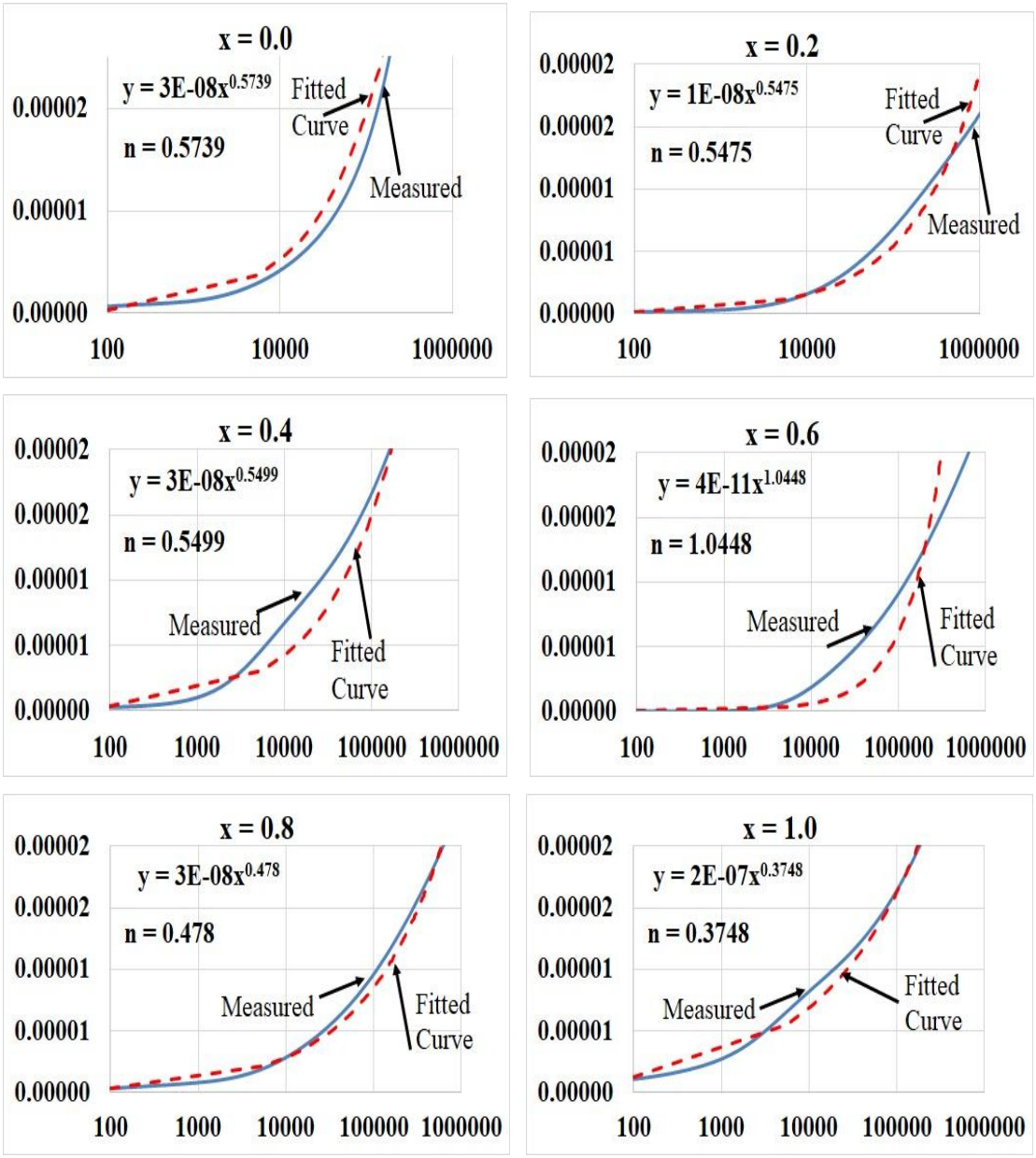

Figure 4.28. Frequency Dependence of AC Exponent (n) for $BaCo_xCe_xFe_{12-2x}O_{19}$ (X0 to X5 (x = 0.0-1.0)).

4.2.3.4 Electric modulus analysis

Figure 4.27 shows how the real part of the modulus (M′) changes with frequency for all samples at room temperature. It was calculated using a formula from reference [49]. We see that M′ values first decrease at low frequencies, then rise with increasing frequency, reaching a peak around 2 MHz for all samples. It is Interesting that all the

samples move toward M′ = 0 at low frequencies, which means that the dipolar polarization has the most restoring force. This means that there is little conductivity and electrode polarization influence [185-186].

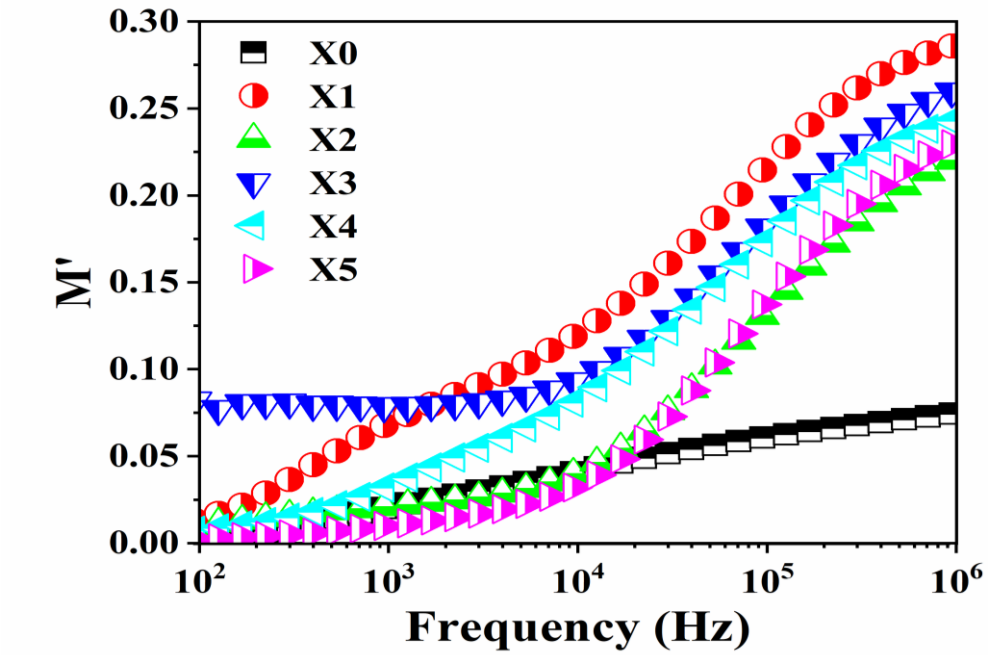

Figure 4. 29(a) M' vs. Frequency of Co- Ce Doped $BaFe_{12}O_{19}$ (X0 to X5, x = 0.0-1.0) Hexaferrites (900°C, 5h)

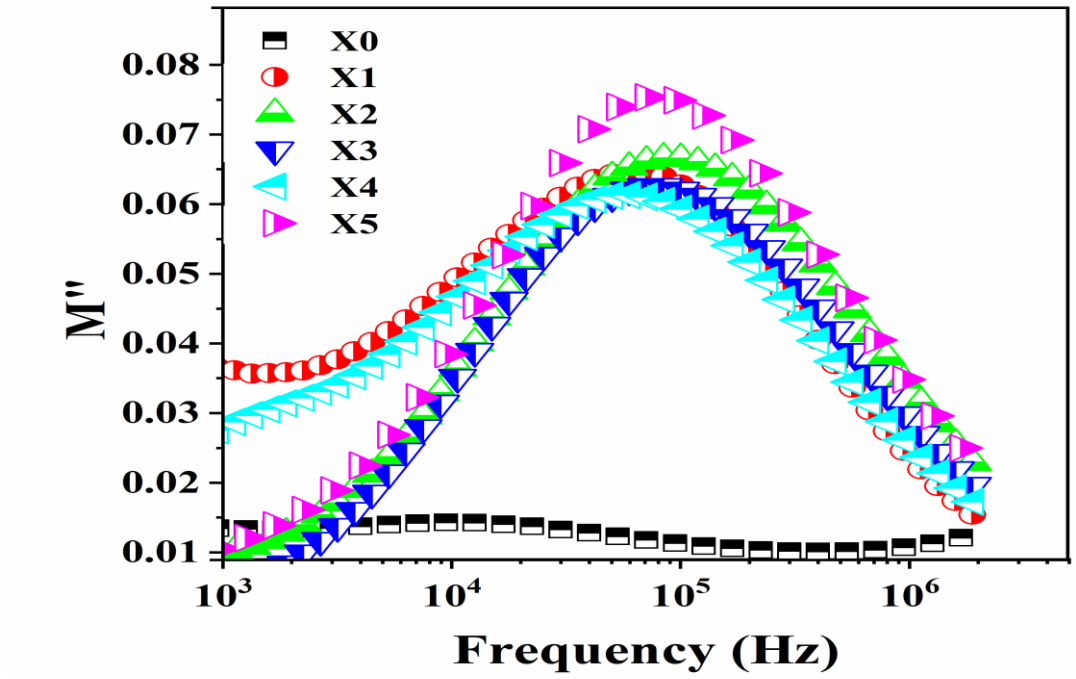

Figure 4.29(b) M″ vs. Frequency of Co-Ce Doped $BaFe_{12}O_{19}$ (X0 to X5, x = 0.0-1.0) Hexaferrites (900°C, 5h)

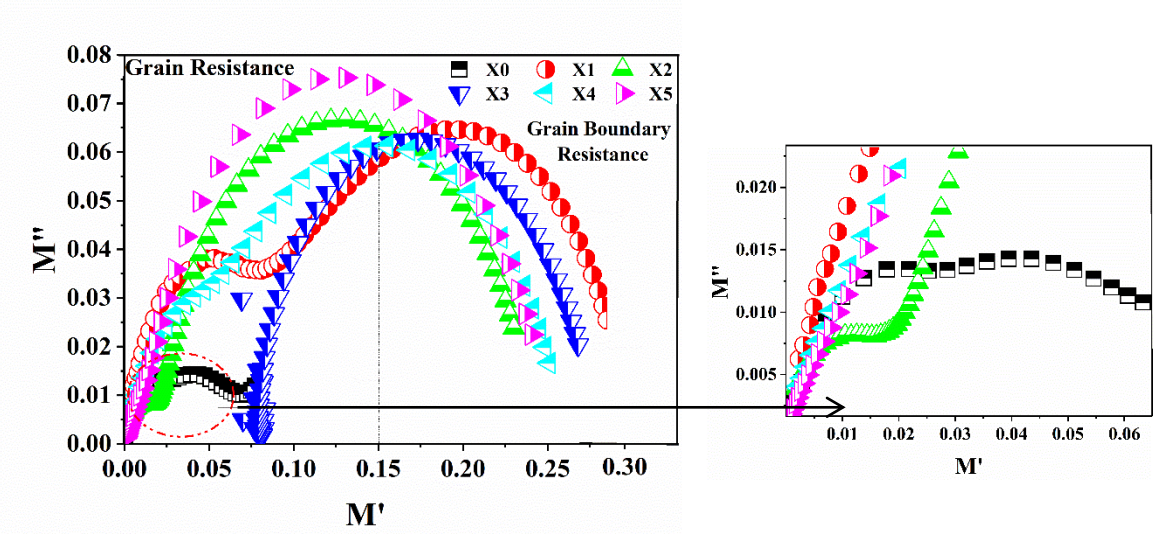

Figure 4.29(c) Cole-Cole Impedance Plots of $BaCo_xCe_xFe_{12-2x}O_{19}$ (X0 to X5, x = 0.0-1.0) Hexaferrites at 900°C

The low frequencies, this low M′ indicates suppressed electrode polarization. The low-frequency M′ goes up as the iron doping concentration goes up. This suggests that the electrode polarization effect is stronger because charge carrier can move around more easily. This aligns with previous research showing that higher applied frequencies lead to higher real modulus, confirming that conduction is linked to short-range charge carrier mobility. Doping with iron significantly increases M' values. Figure 4.29(b) depicts the frequency dependence of the imaginary component of the electric modulus (M″), which provides information on charge transport, relaxation phenomena, and how they are affected by grain boundaries, grains, defects, composition variations, and cation distribution. We see a peak in M″ that decreases with increasing frequency. The specific features of the M″ spectrum are important for analysis:

- Asymmetrical peak maxima at characteristic frequencies (f_{max}) suggest diverse relaxation mechanisms.
- Peak broadening with increasing Co-Ce content indicates different relaxation mechanisms in different compositions.
- With increasing Co-Ce content, the peak shifts towards higher frequencies.

Grain boundaries dominate long-range mobility in the frequency range before the peak, which represents mobile charge carriers hopping between adjacent sites. Beyond the peak, charge carriers become confined within their local grains. The

observed transition between distinct regions in the electric modulus spectra reflects a shift from long-range to short-range order in mobility and relaxation time distribution. This transition is likely due to carrier heterogeneity within the material. Crystal defects can introduce such heterogeneity, leading to a non-Debye relaxation mechanism. This mechanism involves ionic interactions alongside electronic processes.

To assess the individual contributions of grains and grain boundaries to conductivity, the study used Cole-Cole plots (M'' vs. M') as depicted in Figure 4.29(c). All compositions except X0, X1, and X2 exhibit a single, well-defined semicircular arc in the Cole-Cole plot. Following established literature [187], the low-frequency intercept of the semicircle on the real axis (M') corresponds to the bulk resistance of the grains within the material. The intermediate frequency range under the curve reflects the contribution of grain boundaries, as reported in [188]. Finally, the high-frequency region on the right side corresponds to the combined resistance of both grains and grain boundaries.

Overall, the Cole-Cole analysis confirms the influence of both grains and grain boundaries on the overall conductivity of the samples. Additionally, it reveals that Co-Ce doping modifies the conduction behaviour by reducing resistance and introducing non-Debye relaxation mechanisms.

4.2.3.5 Impedance spectroscopy

Figures 4.30(a) and 4.30(b) display the frequency dependence of Z' and Z'' for all samples. Both components exhibit high values at low frequencies, decreasing with increasing frequency, and eventually reaching a frequency-independent plateau at high frequencies. This behaviour reflects the dominant resistive nature of grain boundaries at low frequencies. The decreasing Z' with increasing frequency indicates rising AC conductivity due to hopping events. The frequency-independent behaviour at high frequencies aligns with the Maxwell-Wagner theory and suggests the absence of space charge polarization.

Except for x = 0.2, the increasing impedance with higher dopant concentration is attributed to an increase in the composite's resistive character with increasing Co-Cd content. The decreasing Z' and Z'' values at higher frequencies stem from the

diminishing contribution of grain boundaries, as explained by the Koop double layer model.

For further analysis of grain and grain boundary contributions to transport behaviour, Cole-Cole or Nyquist plots (Z" vs. Z') are employed (Figure 4.30(c)). The presence of semicircles in these plots depends on the degree of relaxation and the frequency range investigated. Small-grain samples typically exhibit a single semicircle representing both grain boundary and grain resistance, while large-grain samples may show two distinct semicircles. The semicircles observed in samples with X0, X1, X2, X3, and X5 indicate a dominant contribution from grain boundaries compared to grains. Increasing the Co-Ce concentration leads to larger circle radii, signifying decreasing capacitance or conductivity.

Impedance (Z') and Imaginary Impedance (Z"): General trend of decreasing Z' with increasing doping level (x-axis) across the entire frequency range. This suggests that the materials become more conductive as the doping level increases (except for X1). At lower frequencies, Z" seems to generally decrease with increasing doping level (except for X1). This aligns somewhat with the trend observed for Z'. At higher frequencies, the differences in Z" between compositions become smaller.

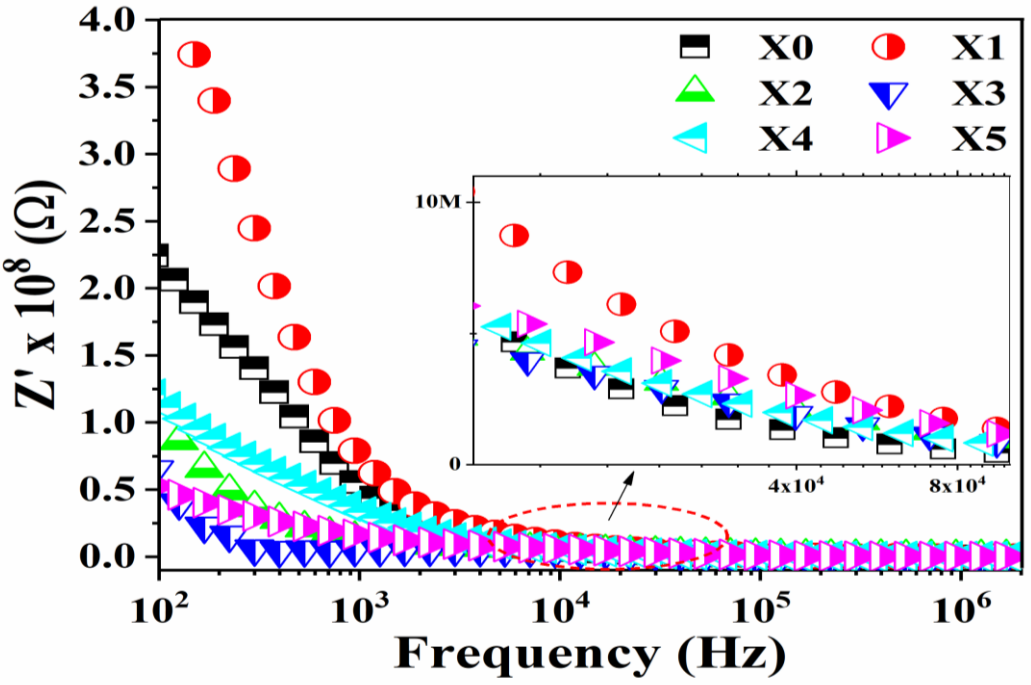

Figure 4.30(a) Frequency Dependence of Real Impedance (Z') in $BaCo_xCe_xFe_{12-2x}O_{19}$ (x = 0.0-1.0) Hexaferrites (900°C, 5h)

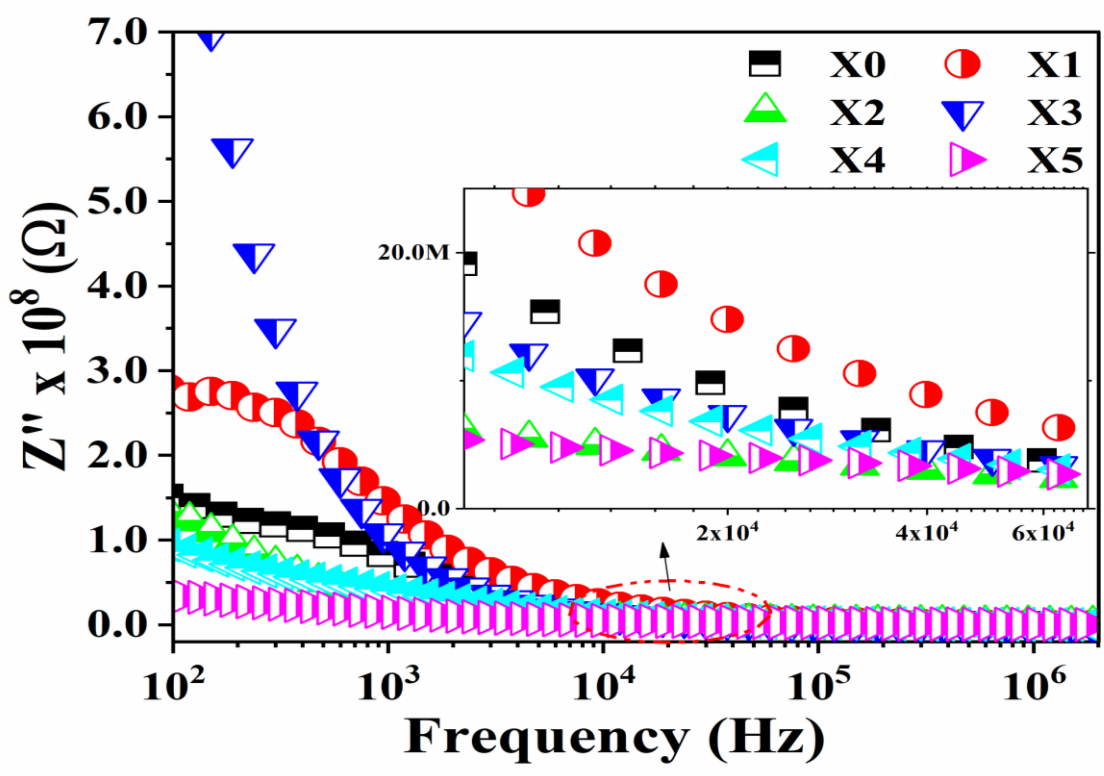

Figure 4.30(b) Imaginary Impedance (Z") vs. Frequency for $BaCo_xCe_xFe_{12-2x}O_{19}$ (x = 0.0-1.0) Hexaferrites (900°C, 5h)

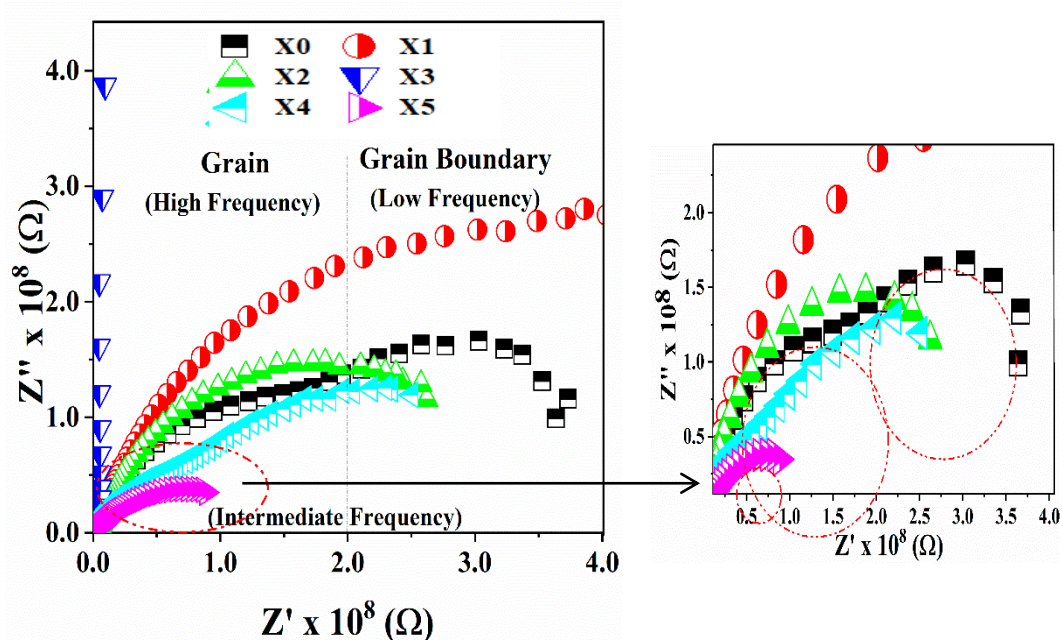

Figure 4.30(c) Cole-Cole Impedance Plots of $BaCo_xCe_xFe_{12-2x}O_{19}$ (X0 to X5, x = 0.0-1.0) Hexaferrites.

4.2.3.6 Software-based Impedance Simulation and Validation

Complex impedance data obtained from the samples were analyzed using EIS software. The resulting equivalent circuit model, depicted in Figure 4.31, consists of two parallel circuits connected in series. These circuits represent the individual contributions of grains (R_g and C_g) and grain boundaries (R_{gb} and C_{gb}) to the overall impedance response. To account for the non-Debye relaxation behaviour observed in some compositions, a constant phase element (CPE) was incorporated to replace the capacitor in the depressed semicircle region [190-191]. The CPE capacitance (CPE) was calculated using the following equation:

$$C_{CPE} = (P.R^{-(n-1)})^{1/n} \quad (4.7)$$

Figure 4.31 demonstrates good agreement between the measured and simulated/fitted curves for all compositions. Additionally, Table 4.11 summarizes the resistance, and capacitance values estimated by EIS for both grains and grain boundaries.

Table 4.11 Extracted Grain and Grain Boundary Parameters (EIS)

X	R_g (MΩ)	R_{gb} (MΩ)	C_g (µF)	C_{gb} (µF)
X0 (0.0)	993.75	66.58	10.4125	20.44
X1 (0.2)	795.45	120.79	1818.32	81.32
X2 (0.4)	94.56	642.13	7.72	3301492.46
X3 (0.6)	22.83	870.19	1835590599	13.19
X4 (0.8)	172.15	1000	1333.54	644.60
X5 (1.0)	104.15	1000	684.05	2.5797

Correlation between EIS Parameters and Microstructure

- **Impact of Porosity:**
  - Porosity generally reduces the effective grain size by hindering grain growth during sintering. Smaller grains contribute to more numerous grain boundaries, potentially affecting R_{gb}, C_g, and C_{gb}.
  - Interconnected pores can lead to irregular grain shapes, complicating Rg measurement due to non-spherical geometries.
- **Impact of Grain Size:**
  - Smaller grain sizes typically correlate with smaller R_g values. However, porosity influences accurate grain size measurements, impacting R_g determination.

- Smaller grains may have large relative grain boundaries (higher R_{gb}/D ratio), as observed in X5 with the smallest R_g and highest R_{gb} (Table 3). This aligns with the reported decrease in crystallite size with increased doping.

- **Impact of Grain Shape:**
  - Irregular grain shapes due to porosity can complicate the interpretation of R_g measurements.

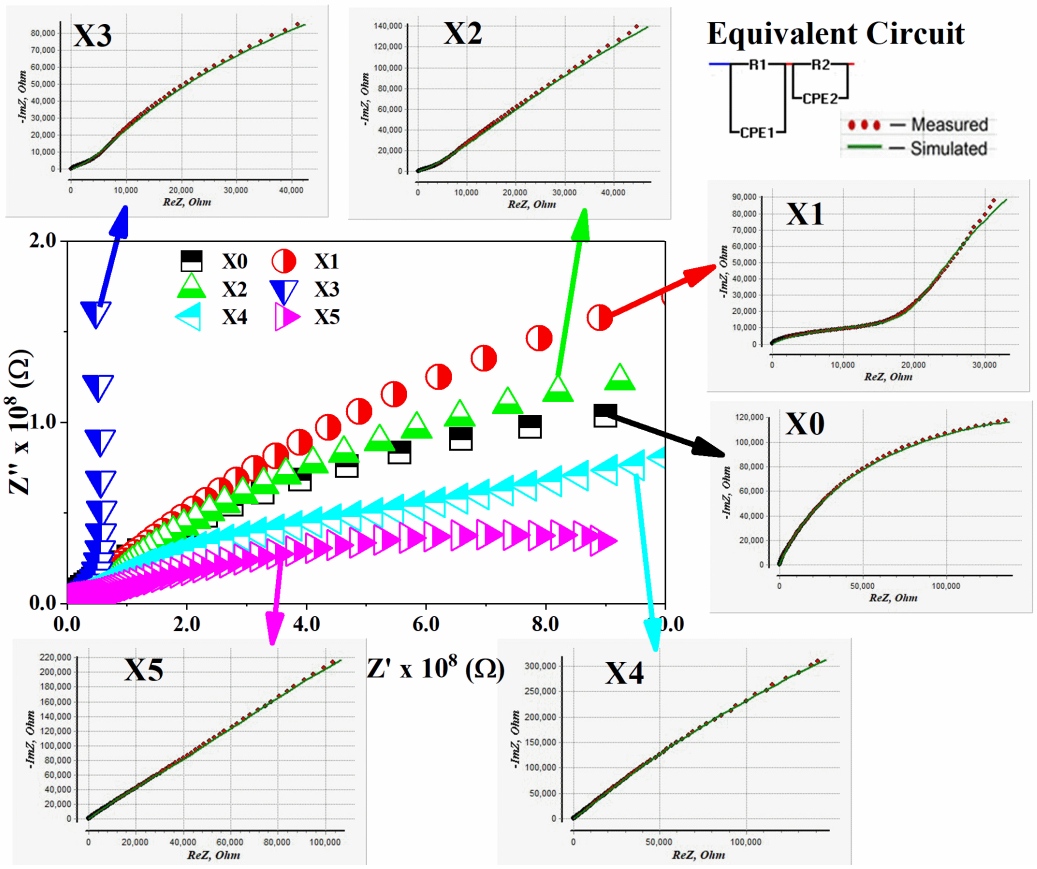

Figure 4.31 Complex Impedance Plots: Measured vs. Fitted Data (Equivalent Circuit Included), Where X0 = 0.0, X1 = 0.2, X2 = 0.4, X3 = 0.6, X4 = 0.8 and X5 = 1.0.

Relationships between EIS and Morphological Parameters:

- The R_g value that is lowest is shown in Table 4.11 for X5. This is because SEM images (Figure 4.26) show small grains with a clear two-layer microstructure.
- Higher grain capacitance (C_g) might lead to higher M′ (real part of electric modulus) due to increased charge storage capacity. Table 4.11 and Figure

4.29 (a) suggest a correlation between high C_g for X3 and high M′ values across different doping levels.

- Larger grain sizes (R_g) might imply fewer grain boundaries, potentially reducing the contribution of relaxation processes and leading to lower M''. Figure 4.29(b) shows X0 with the lowest peak relaxation and highest R_g (Table 4.11), supporting this connection.

4.2.4 Magnetic Analysis

The Cerium ion (Ce^{3+}) in the $BaCo_xCe_xFe_{12-2x}O_{19}$ compound has a lower electronegativity value of 1.12, in contrast to the Cobalt ion (Co^{2+}) which has a higher electronegativity value of 1.88. Consequently, Ce^{3+} can occupy tetrahedral sites with a $4f_1$ configuration, whereas Co^{2+} can occupy octahedral sites. The Fe^{3+} ions in M-type barium hexagonal ferrites are distributed among five specific locations: two tetrahedral sites (2b and $4f_1$) and three octahedral sites (2a, 12k, and $4f_2$). Out of these locations, 2a, 2b, and 12k exhibit spin up, while $4f_1$ and $4f_2$ display spin down [4].

Co^{2+} ions prefer to occupy octahedral sites because of their d^7 configuration, which helps them stabilize in a high-spin state. Reports indicate that Co^{2+} ions tend to favour the $4f_1$, $4f_2$, and 2b sites. In addition, it is important to mention that the Co^{2+} ions have a larger ionic radius of 0.72 Å compared to the host Fe^{3+} ions, which have a radius of 0.64 Å. Due to their larger ionic size and the nature of their 4f orbitals, Ce^{3+} ions with a [Xe] $4f_1$ configuration have a tendency to occupy octahedral sites. Ce^{3+} ions possess a greater ionic radius in comparison to Fe^{3+} ions, enabling them to occupy octahedral positions that offer more ample space. [183-184].

Figure demonstrates the hysteresis loops of all $BaCo_xCe_xFe_{12-2x}O_{19}$ samples at room temperature. The values obtained from the M-H loop are presented in the Table. The values include the saturation magnetization (M_s), the remanence magnetization (M_r), the coercivity (H_c), the anisotropy field (H_a), and the remanence ratio (M_r/M_s).

The distribution of host and substituted cations across five crystallographic sites within a hexagonal crystal structure, as given by the equation, may be used to determine the specimen's magnetic moment [185].

$$M_s = M_a(2a + 12k + 2b)\,(\uparrow) - M_b\,(4f_1 + 4f_2)\,(\downarrow) \qquad (4.8)$$

The overall magnetization increases by substituting non-magnetic ions or ions with weaker magnetic characteristics at the ($4f_1\downarrow + 4f_2\downarrow$) lattice location. Nevertheless,

when these ions are replaced at the (2a↑ + 12k↑ + 2b↑) lattice locations, the magnetization shows a decrease in behaviour [186].

Table 4.12 shows a non-monotonic decline in M_s from X0 to X5 as the amount of substitution rises. Numerous processes, such as spin canting, the shift from a high to a low spin valence state, site occupancy, and exchange contact, can be responsible for the decrease in magnetization (M_s). There is a clear 26.5% decline in the M_s Value at lower degrees of substitution, namely from Xo to X2. The replacement of Fe^{3+} (5 μB) with Co^{2+} (3 μB) and Ce^{3+} (0 μB) can leads to a drop in M_s. This decrease occurs because it lowers the quantity of Fe^{3+} ions at magnetic sites. The abrupt increase in M_s from 77.26 to 139.41 (X2 to X3) may be attributed to a reduction in porosity. Porosity is a non-magnetic vacant space that simultaneously generates demagnetizing forces and reduces magnetization. However, the increase in M_s is not as substantial as the decrease in porosity. The occupancy of both the $4f_2$ and $4f_1$ locations of crystallographic sites may be responsible for the increase in M_s[187]. At last, the M_s Value dropped significantly from X3 to X5, going from 139.41 to 65.36. Introducing a considerable amount of Ce^{3+} (X5) instead of Fe^{3+} could potentially disrupt the structure of the crystal lattice. This disruption has the ability to weaken the overall magnetic superxchange interactions between the remaining Fe^{3+} ions, resulting in a decrease in M_s. There is a phenomenon Ce ions take up positions that are typically occupied by Fe ions [x]. There is a possibility of negative magnetic interactions occurring, which could result in a reduction in magnetization saturation (M_s).

The coercivity (H_c) of a material is determined by a combination of internal (intrinsic) and external (extrinsic) factors. The arrangement of atoms within the crystal lattice is of utmost importance in Intrinsic. The parameter H_a, which represents the material's resistance to magnetic reversal, is closely connected to H_c. The connection between these sites within the lattice is greatly influenced by their occupation, specifically the $4f_2$ and 2b sites. The presence of iron ions in these sites has a significant impact on H_a and, as a result, H_c. The significance lies in the role of extrinsic factors such as grain size and porosity. Higher H_c values are typically associated with larger grains. The reason behind this phenomenon is that larger grains create a smoother pathway for magnetic domains, which are regions with aligned magnetic moments, to travel

through. As a result, it becomes more difficult to demagnetize the material. Pores, those empty spaces, have a rather disruptive effect. They diminish the magnetic volume and weaken the resistance to demagnetization. As a result, materials that possess greater porosity generally exhibit decreased H_c values. Introducing foreign atoms (dopants) through doping typically decreases the coercivity (H_c) of the material. The data clearly shows a noticeable trend, as the H_c value decreases from 5382.78 Oe in the undoped sample (X0) to 2511.96 Oe when fully doped (X5). The undoped sample (X0) demonstrates the highest values for coercivity (5382.775 Oe). The remarkable success of this performance can be credited to the lack of any foreign atoms that disturb the crystal lattice and the ideal arrangement of iron ions, especially at the $4f_2$ and 2b sites. The decrease in H_c observed with increasing Ce substitution (X0 to X5) can be attributed to the variation in anisotropy field (H_a). The energy needed to change the orientation of the magnetic moments of the material is represented by H_a. A higher H_a value indicates a greater ability to resist magnetic reversal. As a result, the material requires more energy to overcome its resistance and become demagnetized, leading to a higher coercivity (H_c). The anisotropy field (H_a) is mainly influenced by the magnetic moments of iron ions found in the $4f_2$ and 2b sites of the crystal lattice.

The remanent magnetization (M_r) of the samples exhibits a decreasing trend with the increase in Ce^{3+} substitution (x) in $BaCo_xCe_xFe_{12-2x}O_{19}$. The decrease in magnetization, observed from M_r (X0) = 54.486 emu/g to M_r(X5) = 34.198 emu/g (Table 4.12), can be attributed to the influence of Ce^{3+} on the orientation of magnetic moments within the material. When Ce^{3+} replaces Fe^{3+}, it can potentially disrupt the exchange interactions that play a crucial role in aligning these magnetic moments.

Table 4.12. Magnetic parameters determined from M-H curves

Sample	M_s (emu/g)	H_c (Oe)	H_a(kOe)	M_r (emu/g)	M_r/M_s
X0	105.2912	5382.775	15.97572	54.486	0.517479
X1	86.49667	4596.719	15.56777	44.817	0.518136
X2	77.26088	4425.837	15.22391	41.489	0.536999
X3	139.4149	3680.793	14.42702	72.318	0.518725
X4	65.36006	3010.936	13.81055	34.198	0.523225
X5	68.99048	2511.962	13.32308	35.149	0.509476

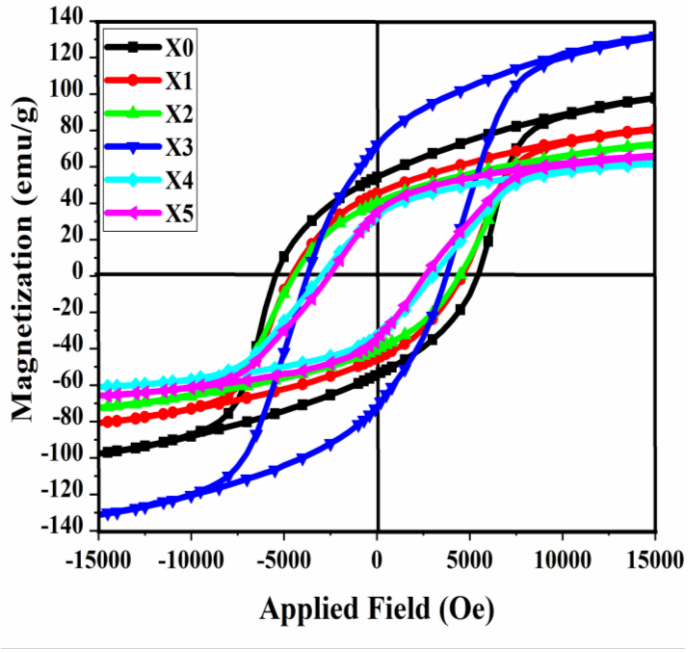

Figure 4.32. Hysteresis loops of X0, X1, X2, X3, X4 and X5 hexaferrite.

This disturbance leads to a decrease in the overall magnetization, which remains diminished even after the removal of a magnetic field. The remanence ratio (M_r/M_s) is a crucial indicator of the material's ability to retain magnetization. In general, M-type hexaferrites exhibit significant remanence ratios due to their inherent magnetic properties. However, the remanence ratio is greatly influenced by the microstructure of the material, specifically the presence of inter-granular areas. The range of remanence ratios spans from 0 to 1[187]. It suggests that values between 0.05 and 0.5 indicate the presence of randomly oriented multi-domain particles [188].

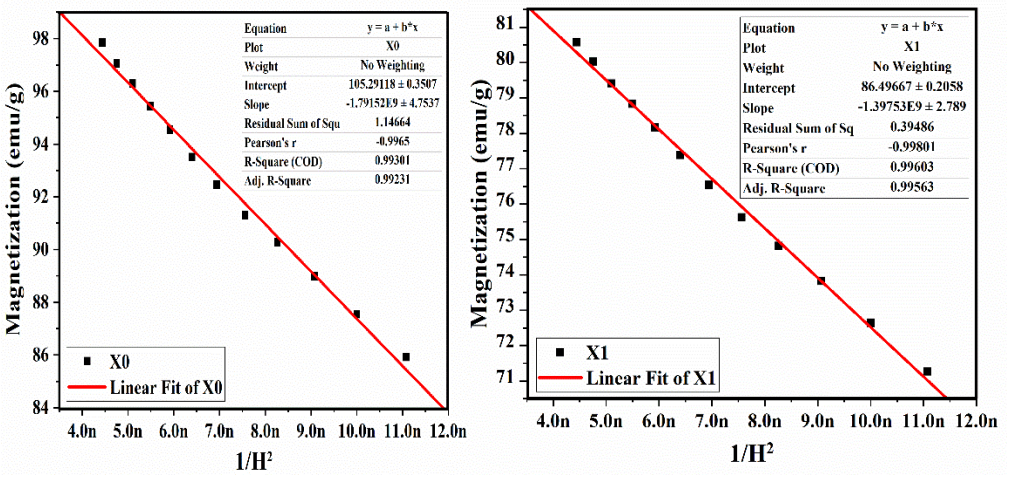

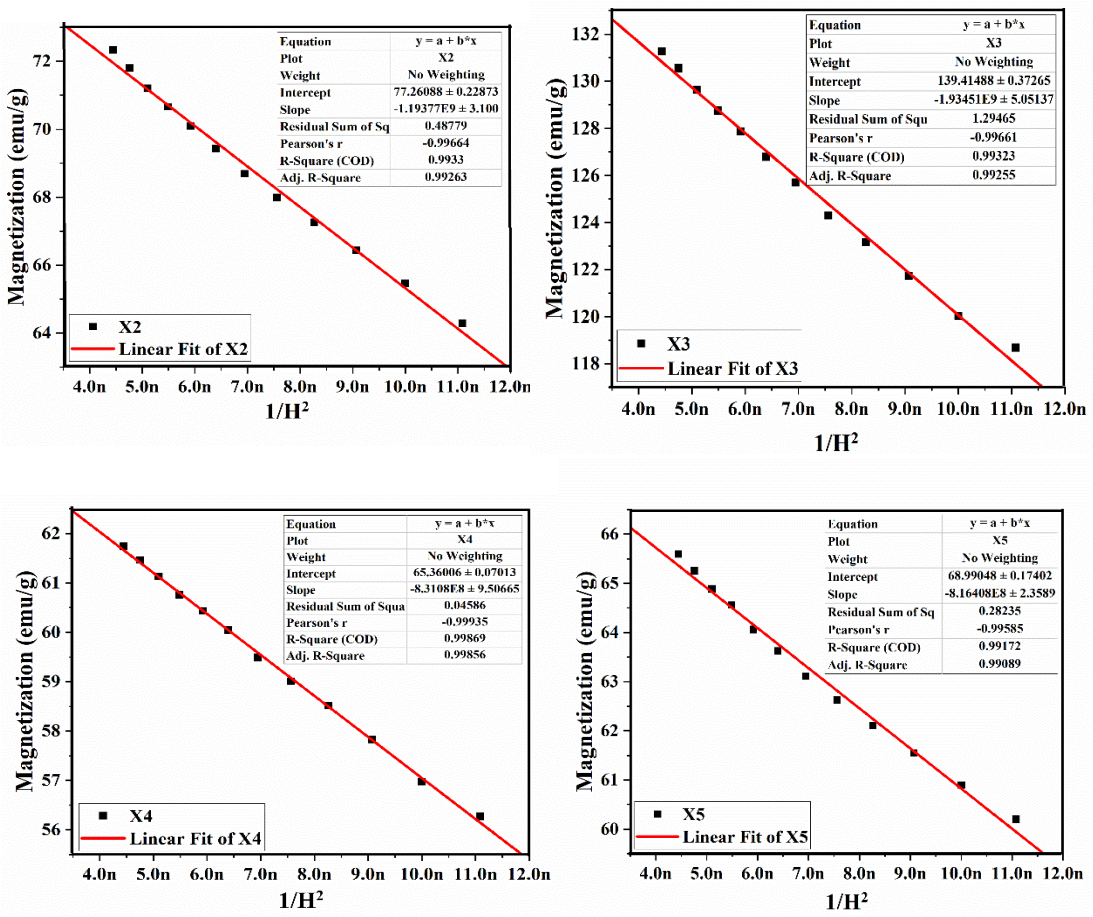

Figure 4.33 M_s versus 1/ H^2 plots for all hexaferrite samples.

4.2.5 Electromagnetic Characteristics

4.2.5.1 Complex permeability and complex permittivity

The Figure 4.34 illustrates the relationship between the dielectric constant (ε') of $BaCo_xCe_xFe_{12-2x}O_{19}$ and frequency for various values of x (0.2, 0.4, 0.6, 0.8, 1.0 says X1, X2, X3, X4 and X5 respectively). The curves X1, X2, X3, X4, and X5 all have an oscillating pattern, alternating between 0 to 15 values of ε' and μ′. The magnitude of these oscillations increases with larger values of x and also with increase in frequency. The existence of resonance phenomena, which may be associated with interfacial polarization or structural relaxation processes, is indicated by the oscillatory behaviour.

X1: Exhibits an initial rapid decrease of ε' from 10.09 to -0.62 and increase μ′ from -0.61 to 10.42, followed by oscillations characterized by diminishing magnitude, ultimately converging towards zero with highest peak of ε' 21.14 at 11.98 GHz and μ′ 19.78 at 11.31 GHz.

X2: exhibits a similar pattern to X1 and the value of ε' decrease from 8.07 to 0.27 and increase μ′ from 0.19 to 7.85, however with a postponed initiation of oscillations and a little lesser peak amplitude of ε' 14.82 compare to 17.05 at 10.30 GHz and μ′ 13.38 compare to 19.78.

X3: Maintains a reasonably constant level with few fluctuations above zero and settle around the value of ε' is 9.73 and μ′ is 1.08.

X4: exhibits a similar pattern to X1 and X2 and the value of ε' decrease from 7.42 to 0.62 and increase μ′ from 0.52 to 6.87, however with a postponed initiation of oscillations and a little lesser peak amplitude of 9.28 at 10.05 GHz then others but in high frequency range its shows different oscillation behaviour than X1 and X2.

X5: exhibits a similar pattern to X3, however its value decrease than X3 but curve follows and settle down nearly around the value of ε' is 7.96 and μ′ is 0.95.

The ε" and μ" values exhibit an upward trend as the doping concentration increases, ε" transitioning from a negative value (-2.92) to a positive value (0.43). At greater doping levels (shown by X3 and X5), the ε" and μ" reaches a stable state with little variations. In dielectric loss, X3 has minor peaks at around 9.71 GHz, whereas X5 displays modest peaks at roughly 10.30 GHz.

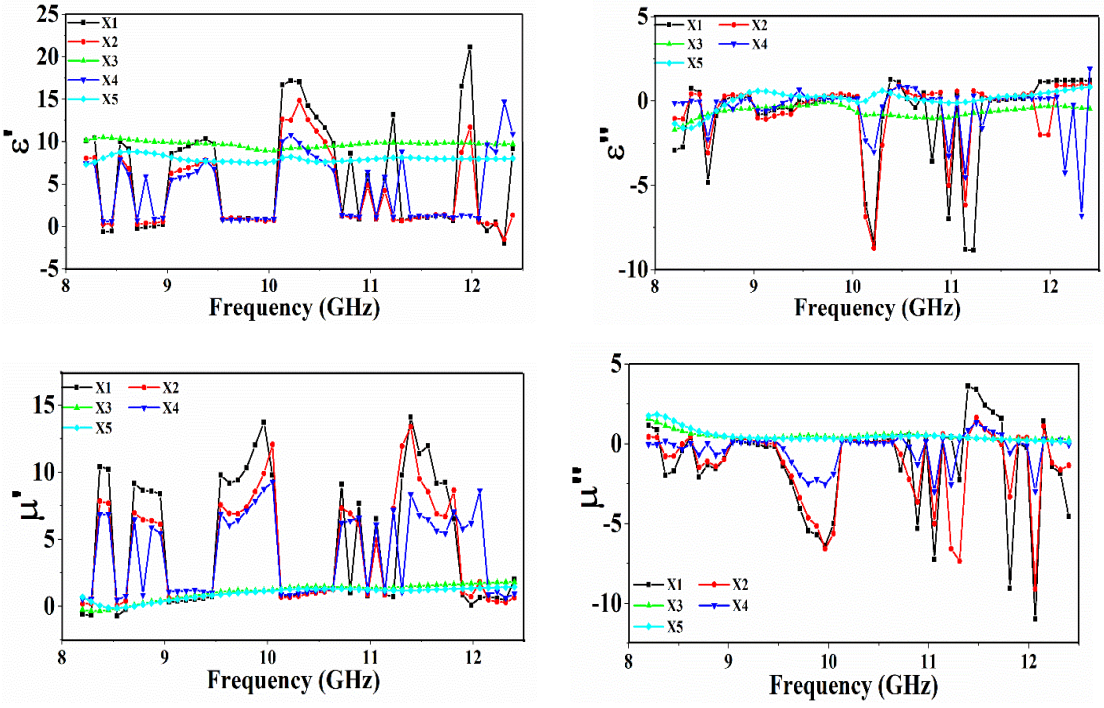

Figure 4.34 Complex permittivity and permeability versus frequency plots for $BaCo_xCe_xFe_{12-2x}O_{19}$.

4.2.5.2 Microwave absorption in $BaCo_xCe_xFe_{12-2x}O_{19}$

4.2.5.3 Quarter Wavelength Mechanism

We analyzed graphs depicting the reflection loss of several materials at varying thicknesses and frequencies, demonstrating the extent to which they reflected microwave radiation. The plots provided useful information about the absorption of microwaves by the materials. Figures 4.35 and subsequent figures illustrate the outcomes of the ferrites we manufactured. By conducting a meticulous analysis of these graphs, we were able to ascertain and measure many attributes of the materials. Table 4.13 provides a concise overview of these qualities.

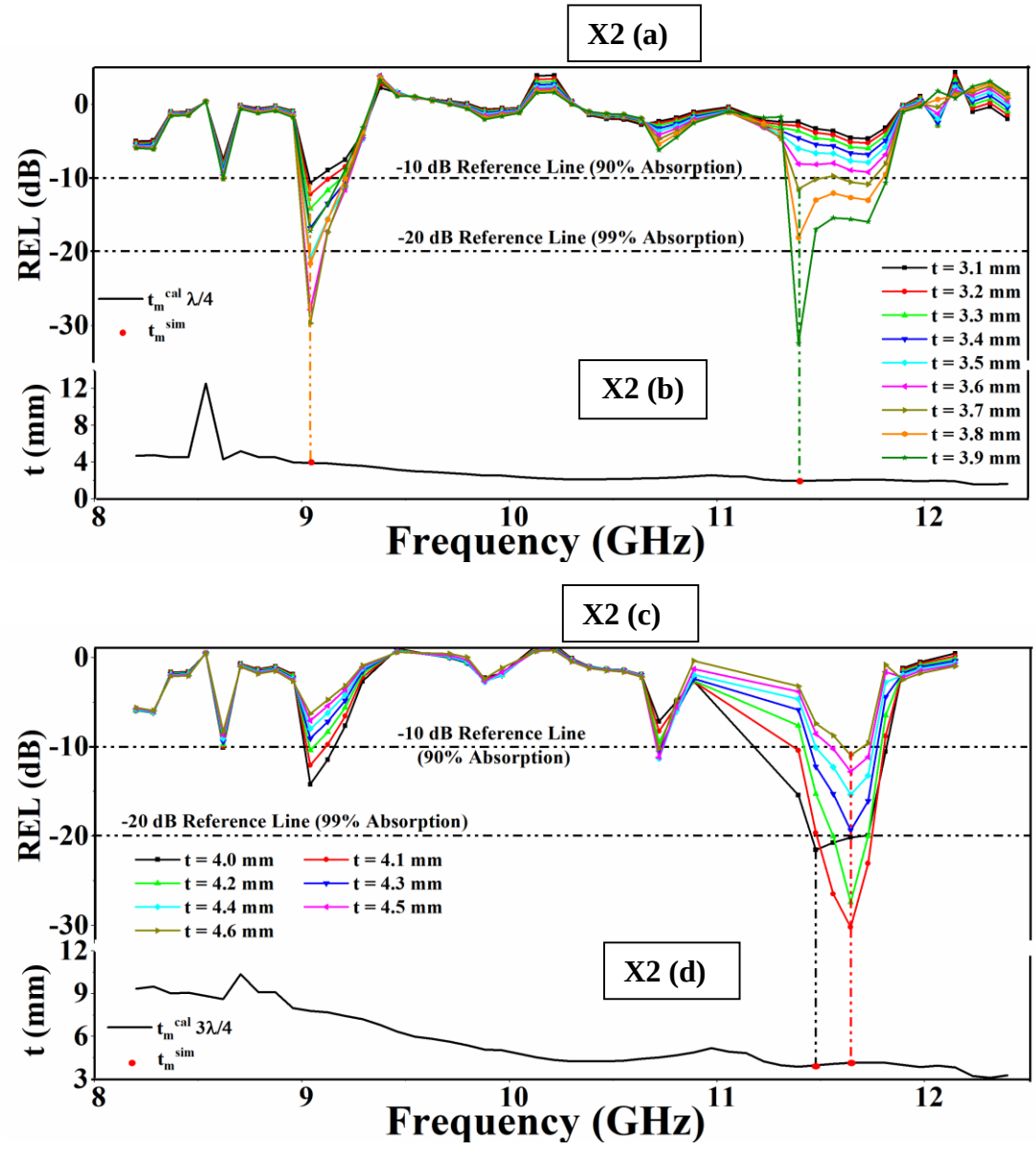

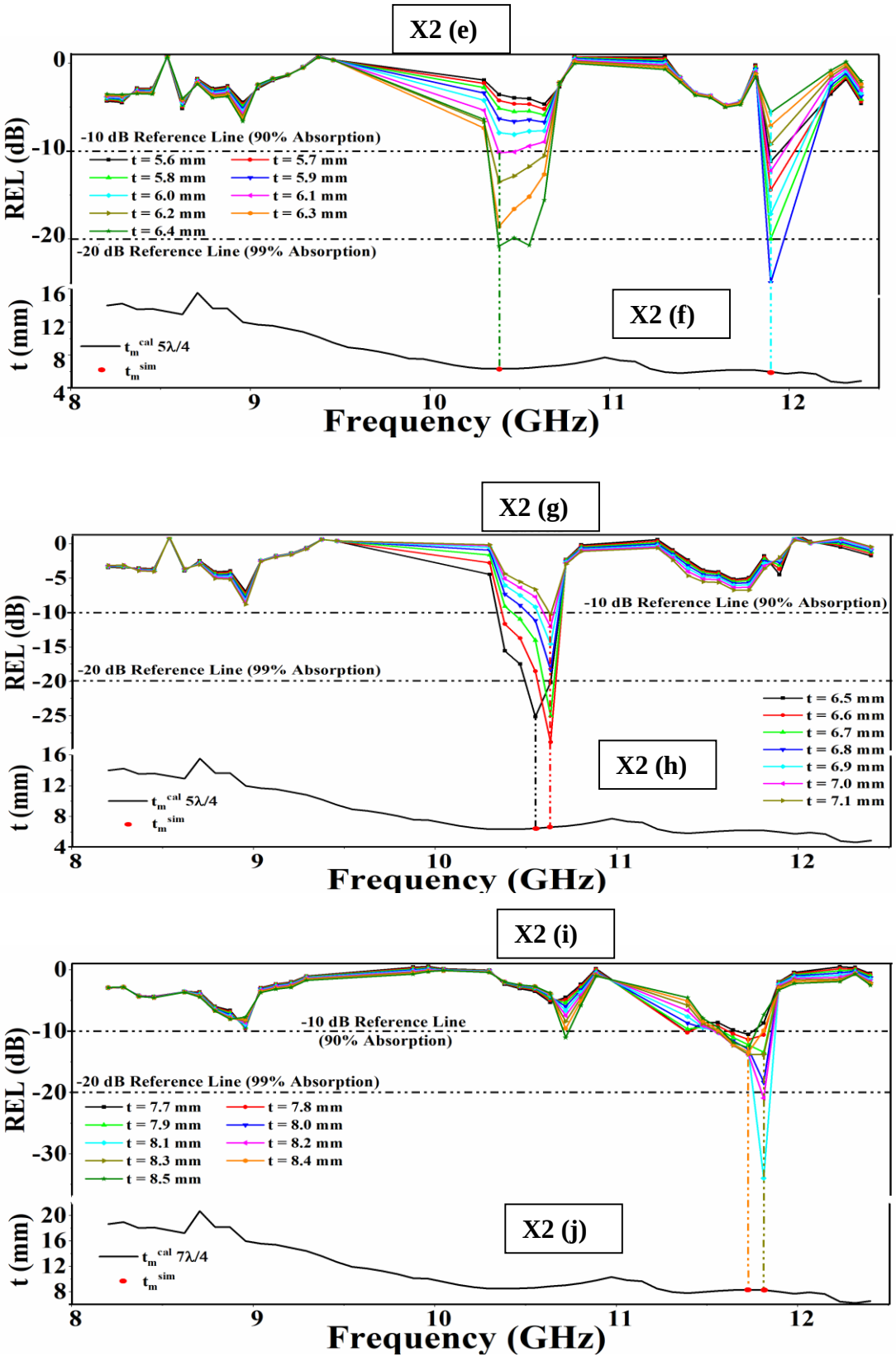
X2 (e)
REL (dB)
-10 dB Reference Line (90% Absorption)
t = 5.6 mm
t = 5.7 mm
t = 5.8 mm
t = 5.9 mm
t = 6.0 mm
t = 6.1 mm
t = 6.2 mm
t = 6.3 mm
t = 6.4 mm
-20 dB Reference Line (99% Absorption)
X2 (f)
t (mm)
t_m^{cal} 5λ/4
t_m^{sim}
Frequency (GHz)
X2 (g)
REL (dB)
-10 dB Reference Line (90% Absorption)
-20 dB Reference Line (99% Absorption)
t = 6.5 mm
t = 6.6 mm
t = 6.7 mm
t = 6.8 mm
t = 6.9 mm
t = 7.0 mm
t = 7.1 mm
X2 (h)
t (mm)
t_m^{cal} 5λ/4
t_m^{sim}
Frequency (GHz)
X2 (i)
REL (dB)
-10 dB Reference Line
(90% Absorption)
-20 dB Reference Line (99% Absorption)
t = 7.7 mm
t = 7.8 mm
t = 7.9 mm
t = 8.0 mm
t = 8.1 mm
t = 8.2 mm
t = 8.3 mm
t = 8.4 mm
t = 8.5 mm
X2 (j)
t (mm)
t_m^{cal} 7λ/4
t_m^{sim}
Frequency (GHz)

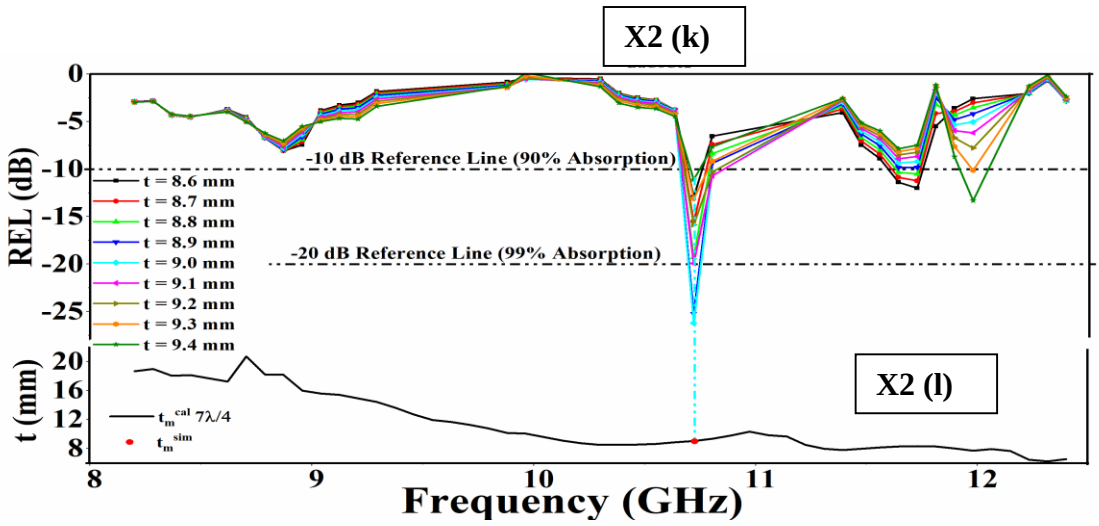

Figure 4.35 REL versus frequency for different thickness (X2) and calculate thickness versus frequency for $Ba_{1-x}Co_xTi_xFe_{12-2x}O_{19}$

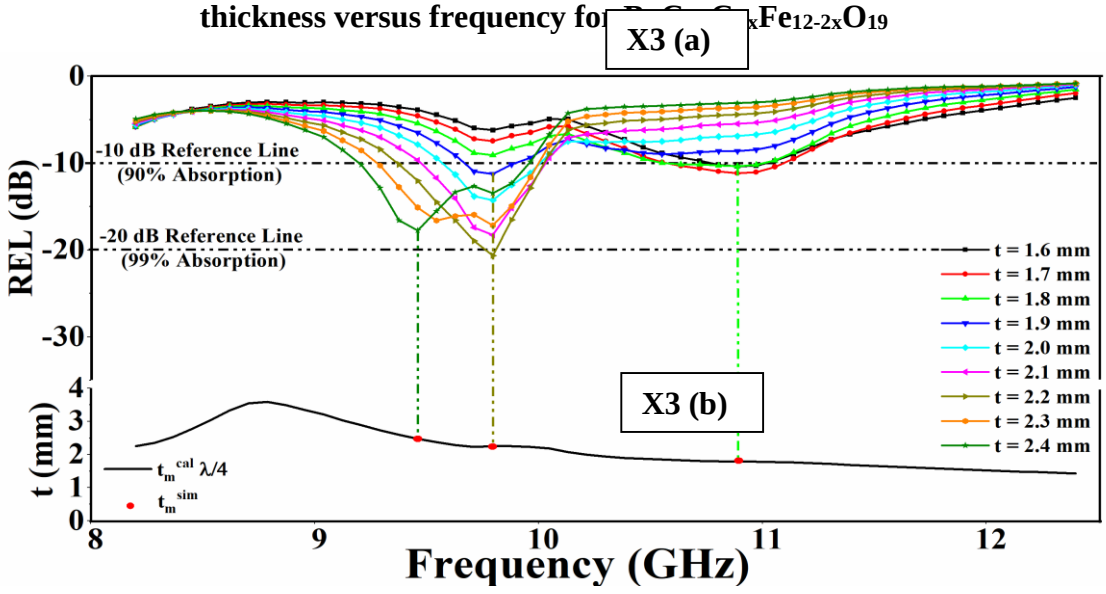

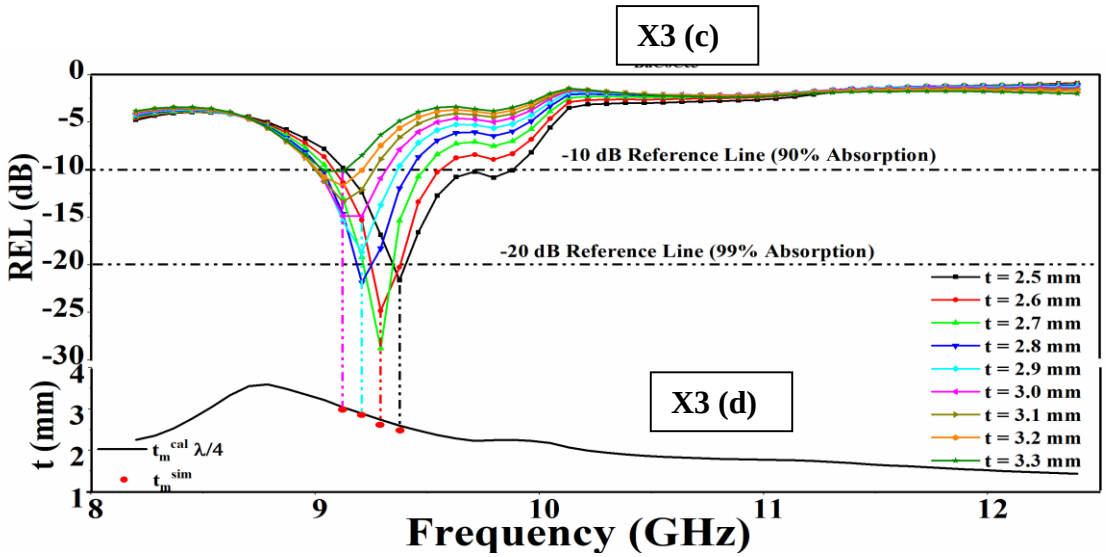

X3 (e)

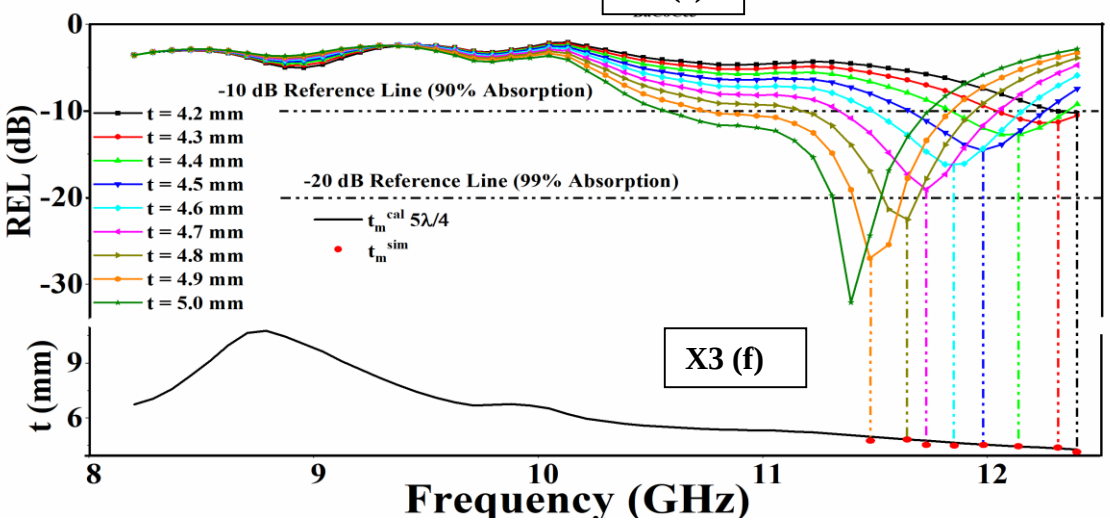

X3 (f)

X3 (g)

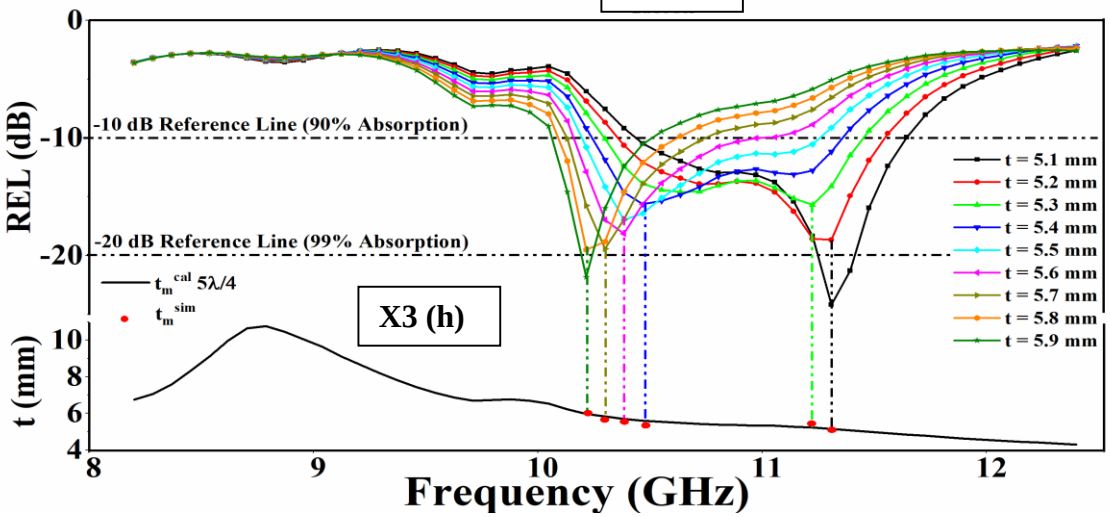

X3 (h)

X3 (i)

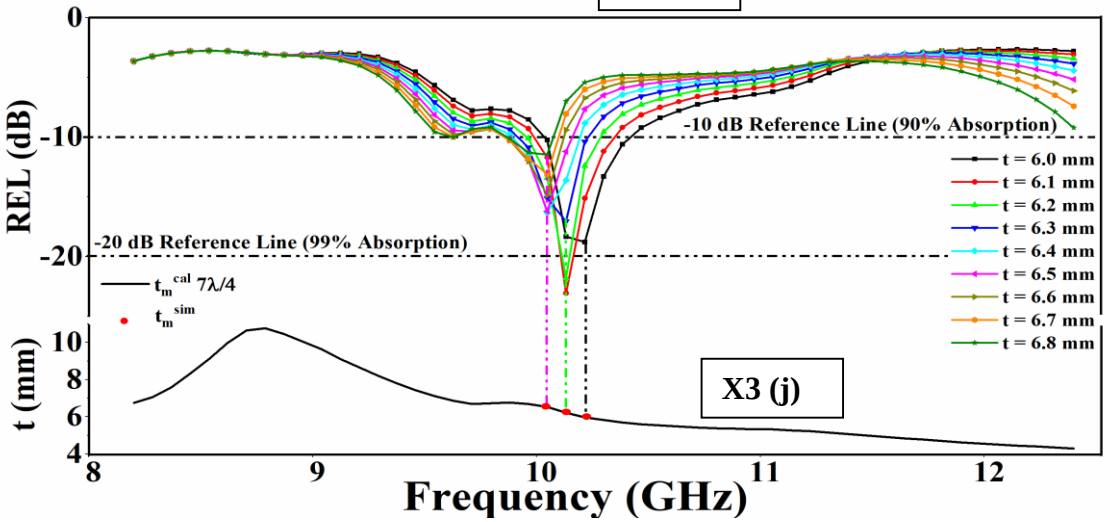

X3 (j)

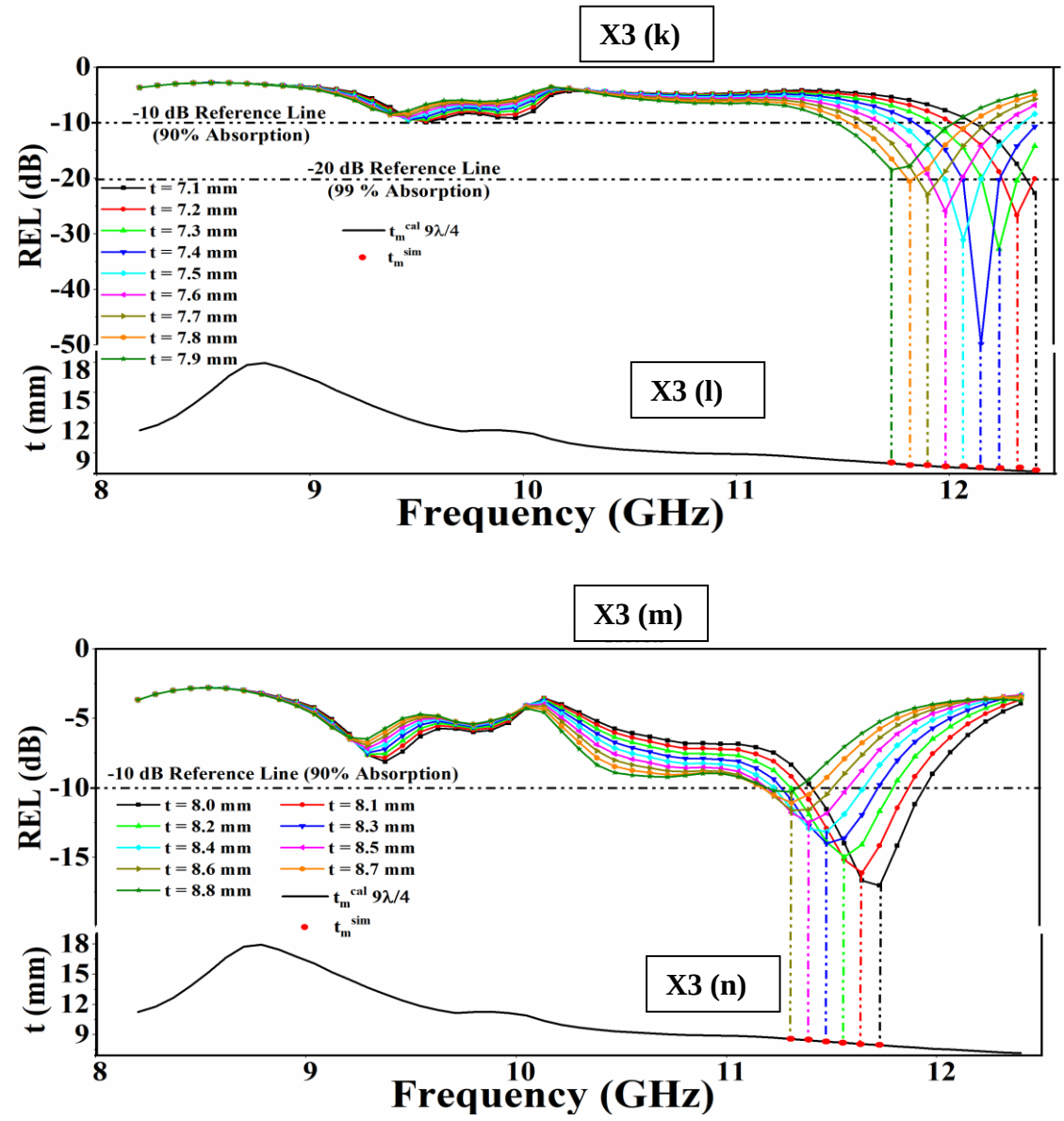

Figure 4.36 REL versus frequency for different thickness (X3) and calculate thickness versus frequency for $BaCo_xCe_xFe_{12-2x}O_{19}$

At 12.15 GHz and thickness of 7.4 mm, composition X3 yields the maximum REL of -49.46 dB. For thicknesses of 5.5 mm, 8.1 mm, 4.7 mm and 5.4 mm, the REL is -41.09 at 10.30 GHz, -34.06 at 11.81 GHz, -30.85 at 11.56 GHz and -34.05 at 12.32 GHz for X1, X2, X4 and X5 respectively.

At a thickness of 5.5 mm, the composition X1 has an REL = -41.09 dB for 10.30 GHz. For thickness of 8.1 mm, the composition X2 has an REL = -34.06 dB for 11.81 GHz. Thicknesses ranging from 3.7 mm to 9.0 mm in this composition X2 exhibit REL ≥ -10

dB in Figure 4.35. For thicknesses of 3.7 mm, 3.9 mm, 4.00 mm, 4.1 mm, 5.9 mm, 6.4 mm, 6.5 mm, 6.6 mm, 8.1 mm and 9 mm, the REL -29.65 dB at 9.04 GHz, -32.32 at 11.39 GHz, -21.58 at 11.48 GHz, -30.18 at 11.64 GHz, -24.85 at 11.90 GHz, -20.97 at 10.39 GHz, -25.12 at 10.55 GHz, -29.49 at 10.63 GHz, -34.06 at 11.81 GHz and -26.13 at 10.64 GHz are found respectively, which correspond to the REL ≥ -20 dB bands. At 12.15 GHz, the composition X3 exhibits highest REL of -49.46 dB at a thickness of 7.4 mm, Thicknesses ranging from 2.2 mm to 8.0 mm in this composition X3 exhibit with REL ≥ -10 dB in Figure 4.36. For thicknesses of 2.5 mm, 2.7 mm, 4.9 mm, 6.1 mm and 7.4 mm, the REL -21.78 at 9.38 GHz, -28.97 at 9.29 GHz, -27.05 at 11.48 GHz, -22.94 at 10.13 GHz and -49.46 at 12.15 GHz are obtained respectively, which correspond to the REL ≥ -20 dB bands.

With a matching frequency of 11.56 GHz and a thickness of 4.7 mm, the composition X4 yields a highest REL = -30.85 dB, Thicknesses ranging from 3.0 mm to 9.6 mm in this composition X4 exhibit with REL ≥ -10 dB in Figure 4.37. For thicknesses of 7.1 mm, 7.3 mm and 9.1 mm, the REL ≥ -20 dB bands are obtained, with the REL –27.57 dB at 10.47 GHz, -20.34 at 10.64 GHz and -22.33 dB at 11.90 GHz respectively. The composition with X5 has a maximum REL peak of -34.05 dB at 12.32 GHz at 5.4 mm, Thicknesses ranging from 2.3 mm to 7.7 mm in this composition X5 exhibit with REL ≥ -10 dB in Figure 4.38. For thicknesses of 5.4 mm, the REL -34.05 dB at 12.32 GHz is obtained, which correspond to the REL ≥ -20 dB bands.

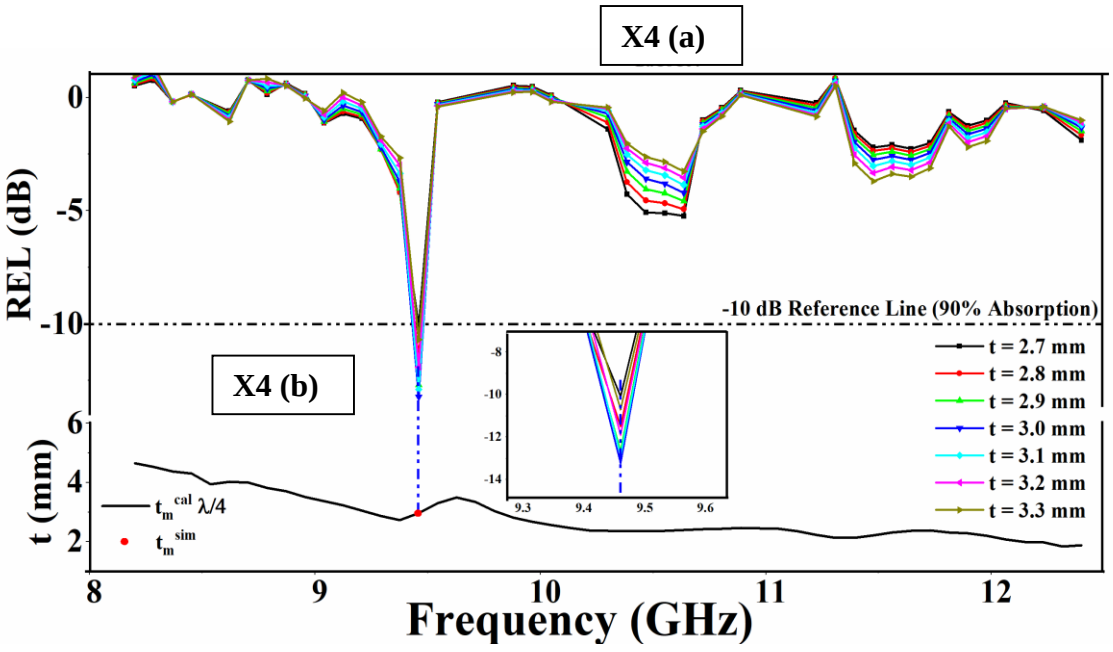

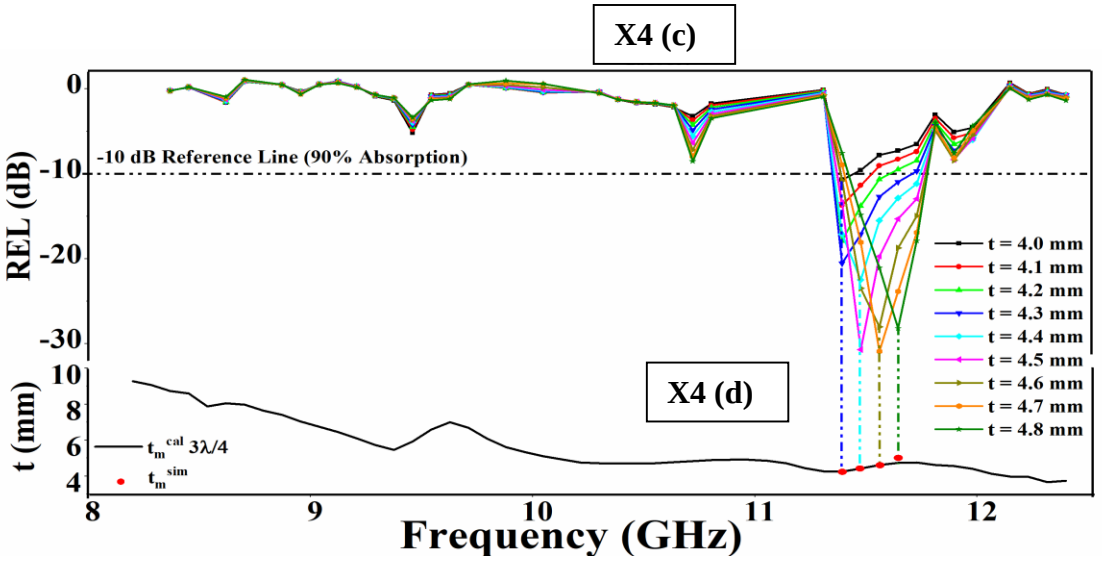
X4 (c)
-10 dB Reference Line (90% Absorption)
REL (dB)
t = 4.0 mm
t = 4.1 mm
t = 4.2 mm
t = 4.3 mm
t = 4.4 mm
t = 4.5 mm
t = 4.6 mm
t = 4.7 mm
t = 4.8 mm
X4 (d)
t (mm)
t_m^{cal} 3λ/4
t_m^{sim}
Frequency (GHz)

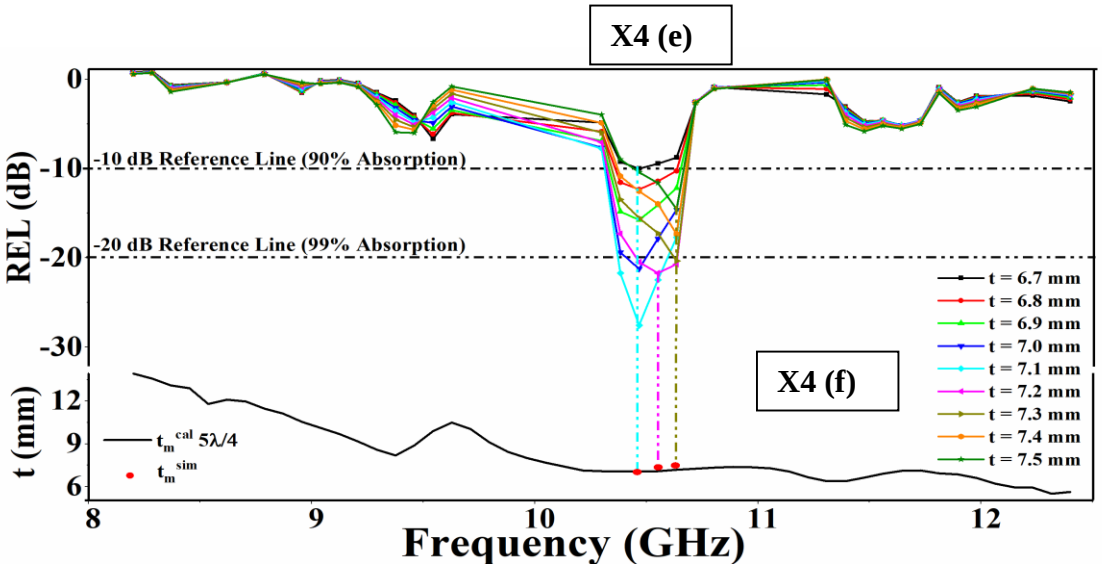
X4 (e)
-10 dB Reference Line (90% Absorption)
-20 dB Reference Line (99% Absorption)
REL (dB)
t = 6.7 mm
t = 6.8 mm
t = 6.9 mm
t = 7.0 mm
t = 7.1 mm
t = 7.2 mm
t = 7.3 mm
t = 7.4 mm
t = 7.5 mm
X4 (f)
t (mm)
t_m^{cal} 5λ/4
t_m^{sim}
Frequency (GHz)

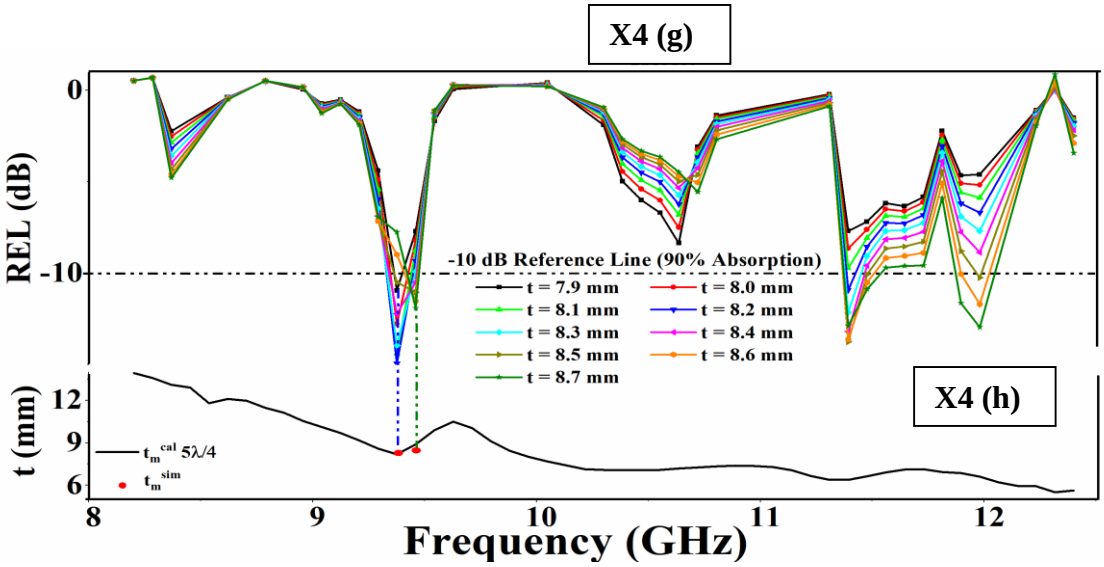
X4 (g)
-10 dB Reference Line (90% Absorption)
REL (dB)
t = 7.9 mm
t = 8.0 mm
t = 8.1 mm
t = 8.2 mm
t = 8.3 mm
t = 8.4 mm
t = 8.5 mm
t = 8.6 mm
t = 8.7 mm
X4 (h)
t (mm)
t_m^{cal} 5λ/4
t_m^{sim}
Frequency (GHz)

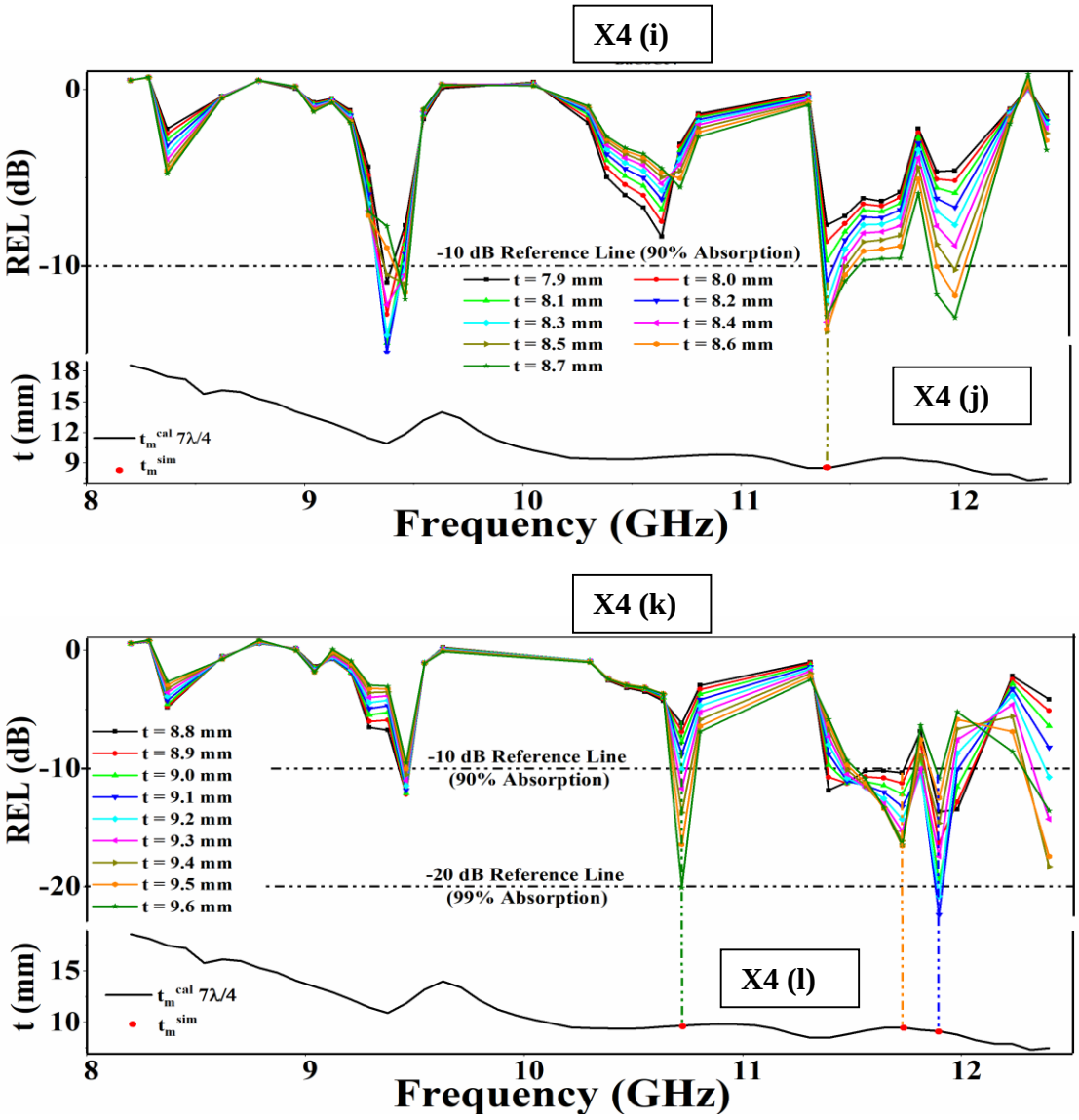

Figure 4.37 REL versus frequency for different thickness (X4) and calculate thickness versus frequency for $BaCo_xCe_xFe_{12-2x}O_{19}$

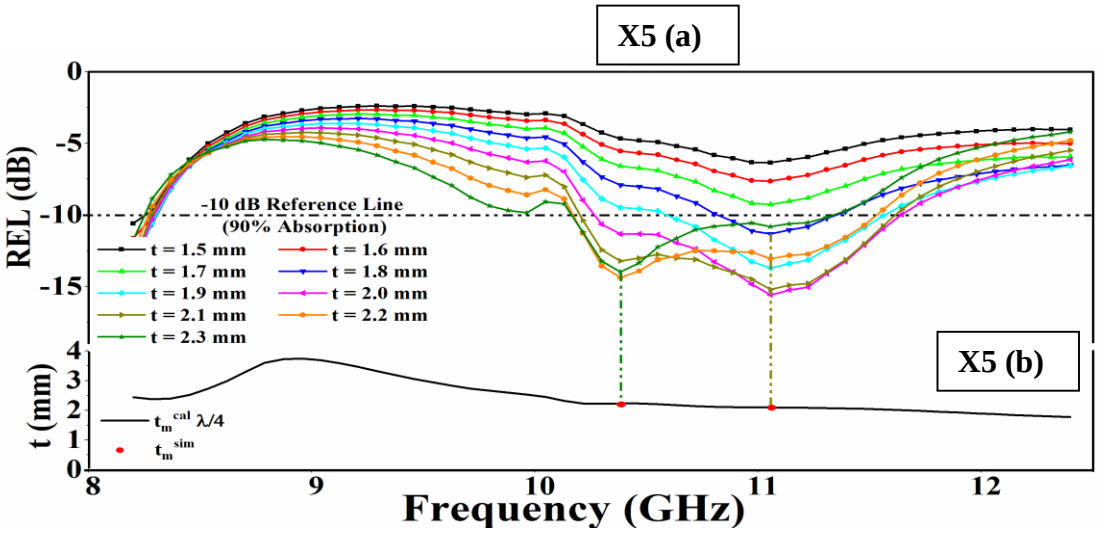

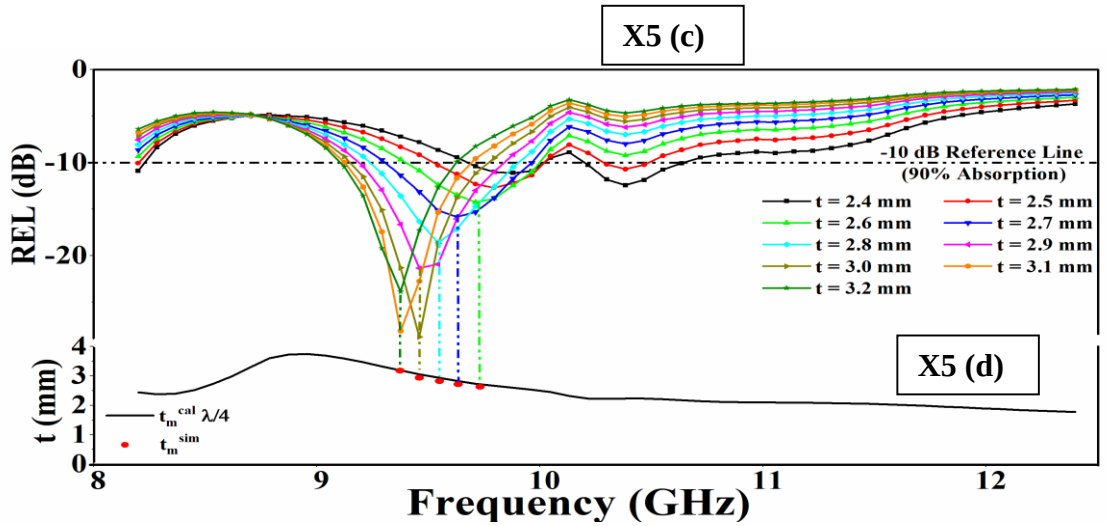
X5 (c)
REL (dB)
-10 dB Reference Line
(90% Absorption)
t = 2.4 mm
t = 2.5 mm
t = 2.6 mm
t = 2.7 mm
t = 2.8 mm
t = 2.9 mm
t = 3.0 mm
t = 3.1 mm
t = 3.2 mm
X5 (d)
t (mm)
t_m^{cal} λ/4
t_m^{sim}
Frequency (GHz)

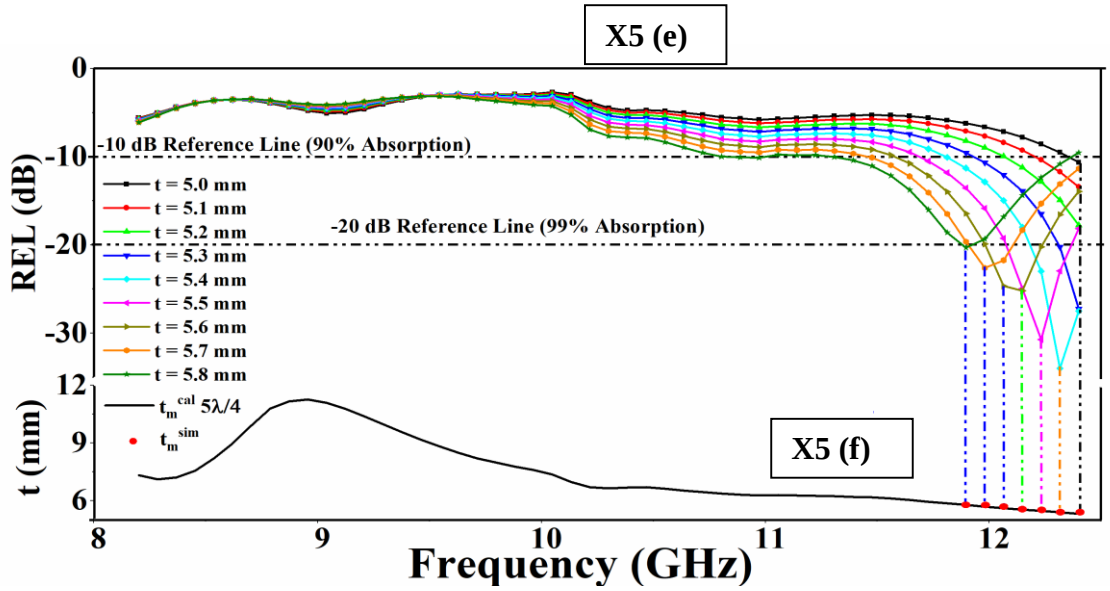
X5 (e)
REL (dB)
-10 dB Reference Line (90% Absorption)
-20 dB Reference Line (99% Absorption)
t = 5.0 mm
t = 5.1 mm
t = 5.2 mm
t = 5.3 mm
t = 5.4 mm
t = 5.5 mm
t = 5.6 mm
t = 5.7 mm
t = 5.8 mm
X5 (f)
t (mm)
t_m^{cal} 5λ/4
t_m^{sim}
Frequency (GHz)

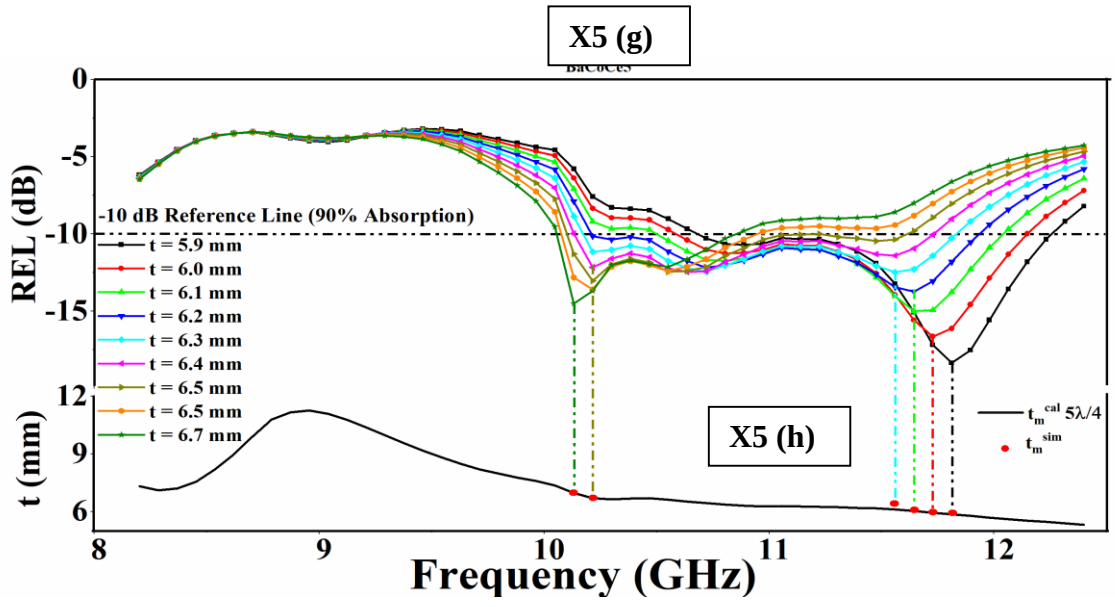
X5 (g)
REL (dB)
-10 dB Reference Line (90% Absorption)
t = 5.9 mm
t = 6.0 mm
t = 6.1 mm
t = 6.2 mm
t = 6.3 mm
t = 6.4 mm
t = 6.5 mm
t = 6.5 mm
t = 6.7 mm
X5 (h)
t (mm)
t_m^{cal} 5λ/4
t_m^{sim}
Frequency (GHz)

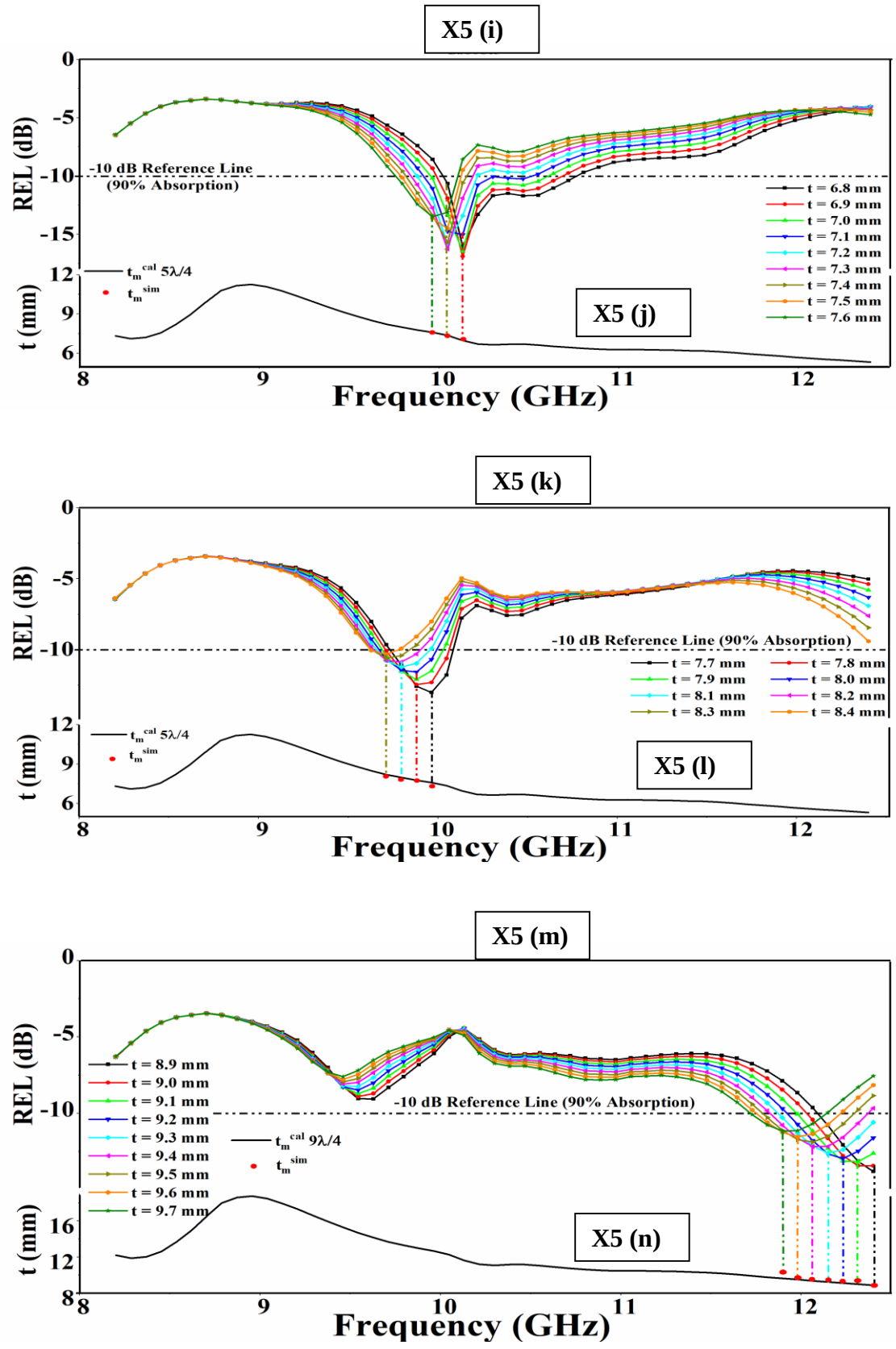

Figure 4.38 REL versus frequency for different thickness (X5) and calculate thickness versus frequency for $BaCo_xCe_xFe_{12-2x}O_{19}$

An analysis was conducted to compare the computed thickness (t_m^{cal}) and simulated thickness (t_m^{sim}) in order to explore the possible correlation between REL peaks and the λ/4 mechanism. The graphs depicting the relationship between calculated thickness and frequency are shown in Figure 4.35 to Figure 4.38. The REL peaks are included in the thickness-frequency charts to facilitate the comparison between the calculated and simulated thickness lines. The compositions X2 and X4 with a calculated thickness of λ/4, 3λ/4, 5λ/4 and 7λ/4 and refractive indices of 1, 3, 5 and 7. For X3 with a calculated thickness of λ/4, 5λ/4, 7λ/4 and 9λ/4 and refractive indices of 1, 5, 7 and 9. For X5 with a calculated thickness of λ/4, 5λ/4 and 9λ/4 and refractive indices of 1, 5 and 9.

Table 4.13 REL with matching thickness/frequency, BW, and PBW for $BaCo_xCe_xFe_{12-2x}O_{19}$ (X1 to X5).

Sample Name	Matching Thickness (mm)	Maximum REL (dB)	Matching frequency (GHz)	Frequency Band for REL > -10 dB (GHz)	Bandwidth for RL > -10 dB (GHz)	Frequency Band REL > -20 dB (GHz)	Bandwidth for REL > -20 dB (GHz)	BTR	PBW (%)
X2	3.7	-29.65	9.04	8.981-9.22	0.239	9.01-9.11	0.1	2.34E-04	2.64
	3.9	-32.32	11.39	11.33-11.82	0.49	11.36-11.46	0.1	2.81E-04	4.30
	4	-21.58	11.48	11.18-11.82	0.64	11.45-11.73	0.28	3.63E-04	5.57
	4.1	-30.18	11.64	11.37-11.8	0.43	11.48-11.75	0.27	2.35E-04	3.69
	5.9	-24.85	11.9	11.84-12.12	0.28	11.88-11.97	0.09	9.92E-05	2.35
	6.4	-20.97	10.39	10.32-10.67	0.35	10.38-10.56	0.18	1.49E-04	3.37
	6.5	-25.12	10.55	10.34-10.68	0.34	10.49-10.64	0.15	1.42E-04	3.22
	6.6	-29.49	10.63	10.37-10.7	0.33	10.56-10.66	0.1	1.35E-04	3.10
	8.1	-34.06	11.81	11.54-	0.34	11.76-11.85	0.09	9.19E-05	2.88

				11.88					
	8.4	-13.41	11.73	11.57 - 11.81	0.24	-	-	6.27E -05	2.05
	9	-26.13	10.64	10.66 - 10.83	0.17	10.7- 10.75	0.05	4.91E -05	1.60
X3	2.2	-20.58	9.79	9.37- 10.03	0.66	9.76-9.81	0.05	9.58E -04	6.74
	2.4	-17.74	9.46	9.2- 9.96	0.76	-	-	1.04E -03	8.03
	2.5	-21.78	9.38	9.13- 9.87	0.74	9.35-9.4	0.05	9.85E -04	7.89
	2.7	-28.97	9.29	9.05- 9.48	0.43	9.21-9.35	0.14	5.57E -04	4.63
	2.9	-18.66	9.21	9- 9.37	0.37	-	-	4.54E -04	4.02
	3	-14.93	9.12	9.02- 9.31	0.29	-	-	3.45E -04	3.18
	4.3	-11.43	12.32	12.05 - 12.41	0.36	-	-	1.68E -04	2.92
	4.4	-12.73	12.14	11.83 - 12.34	0.51	-	-	2.38E -04	4.20
	4.5	-14.46	11.98	11.64 - 12.25	0.61	-	-	2.85E -04	5.09
	4.9	-27.05	11.48	10.73 - 11.83	1.1	11.4- 11.62	0.22	5.31E -04	9.58
	6	-18.88	10.22	10.04 - 10.41	0.37	-	-	1.77E -04	3.62
	6.1	-22.94	10.13	9.99- 10.35	0.36	10.11- 10.16	0.05	1.71E -04	3.55
	7.4	-49.46	12.15	11.83 -12.4	0.57	12.06- 12.23	0.17	1.58E -04	4.69
	7.9	-18.56	11.73	11.48 - 12.02	0.54	-	-	1.49E -04	4.60
	8	-17.02	11.73	11.41 - 11.94	0.53	-	-	1.46E -04	4.52
X4	3	-13.24	9.46	9.43- 9.48	0.05	-	-	5.59E -05	0.53
	4.7	-30.85	11.56	11.4- 11.78	0.38	-	-	1.81E -04	3.29
	7.1	-27.57	10.47	10.31 - 10.68	0.37	10.37- 10.6	0.23	1.42E -04	3.53

	7.3	-20.34	10.64	10.35 - 10.69	0.34	10.61-10.63	0.02	1.26E-04	3.20
	8.5	-13.8	11.39	11.37 - 11.48	0.11	-	-	2.97E-05	0.97
	9.1	-22.33	11.9	11.81 - 11.98	0.17	11.88-11.91	0.03	3.96E-05	1.43
	9.5	-16.54	11.73	11.49 - 11.79	0.3	-	-	6.99E-05	2.56
	9.6	-20.00	10.72	10.67 - 10.78	0.11	-	-	2.99E-05	1.03
X5	2.3	-13.97	10.38	10.17 - 11.34	1.17	-	-	1.32E-03	11.27
	3.3	-18.88	9.29	9.09-9.57	0.48	-	-	5.02E-04	5.17
	5.4	-34.05	12.32	11.8-12.5	0.7	12.18-12.5	0.32	2.64E-04	5.68
	5.8	-19.98	11.9	11.31 - 12.37	1.06	-	-	3.92E-04	8.91
	5.9	-18.48	11.82	10.69 - 12.26	1.57	-	-	6.09E-04	13.28
	6.9	-16.91	10.13	9.98-10.68	0.7	-	-	2.86E-04	6.91
	7.7	-12.99	9.97	9.74-10.08	0.34	-	-	1.35E-04	3.41

According to Table 4.13, the quarter wavelength criterion for composition X2 originates at thicknesses ranging from 3.7 mm to 9.0 mm and a -10 dB bandwidth of 0.17 GHz to 0.64 GHz. REL = -20.97 dB to REL = -34.06 dB is reported within the -20 dB bandwidth of 0.05 GHz to 0.28 GHz respectively. As shown in Figure 4.35 X2(a), the reflection loss peaks with composition X2 are at the same frequency 9.04 GHz for t = 3.1 mm to 3.9 mm. Similar peaks may be seen at 11.392 GHz for same thickness. As can be seen in Figures 4.35 X2(a), X2(e), X2(i) and X2(k), the peak height increase as thickness increases at 9.04 GHz, 10.39 GHz, 11.81 GHz and 10.64 GHz respectively. However, in Figure 4.35 X2(c) and X2(g) illustrates, the height of peak decreases with an increase in thickness at 11.48 GHz and 10.55 GHz respectively.

As shown in Figure 4.36 X3(a), the reflection loss peaks with composition X3 are at the same frequency 9.79 GHz for t = 1.6 mm to 2.3 mm. As thickness increase from 2.5 mm to 3.3 mm and 4.2 to 5.0 mm, Figure 4.36 X3(c) and X3(e) demonstrates that peaks shift into the narrow frequency range of 9.38 GHz to 9.12 GHz and 12.5 GHz to 11.48 GHz, and peak height increases with increase in thickness. In a similar vein, for 5.1 mm to 5.9 mm and 8.0 mm to 8.8 mm, it is evident that as thickness grows, peaks shift into the narrow frequency band of 10.552 GHz to 10.216 GHz and 11.812 GHz to 11.392 GHz respectively and that peak height likewise decreases as thickness increases.

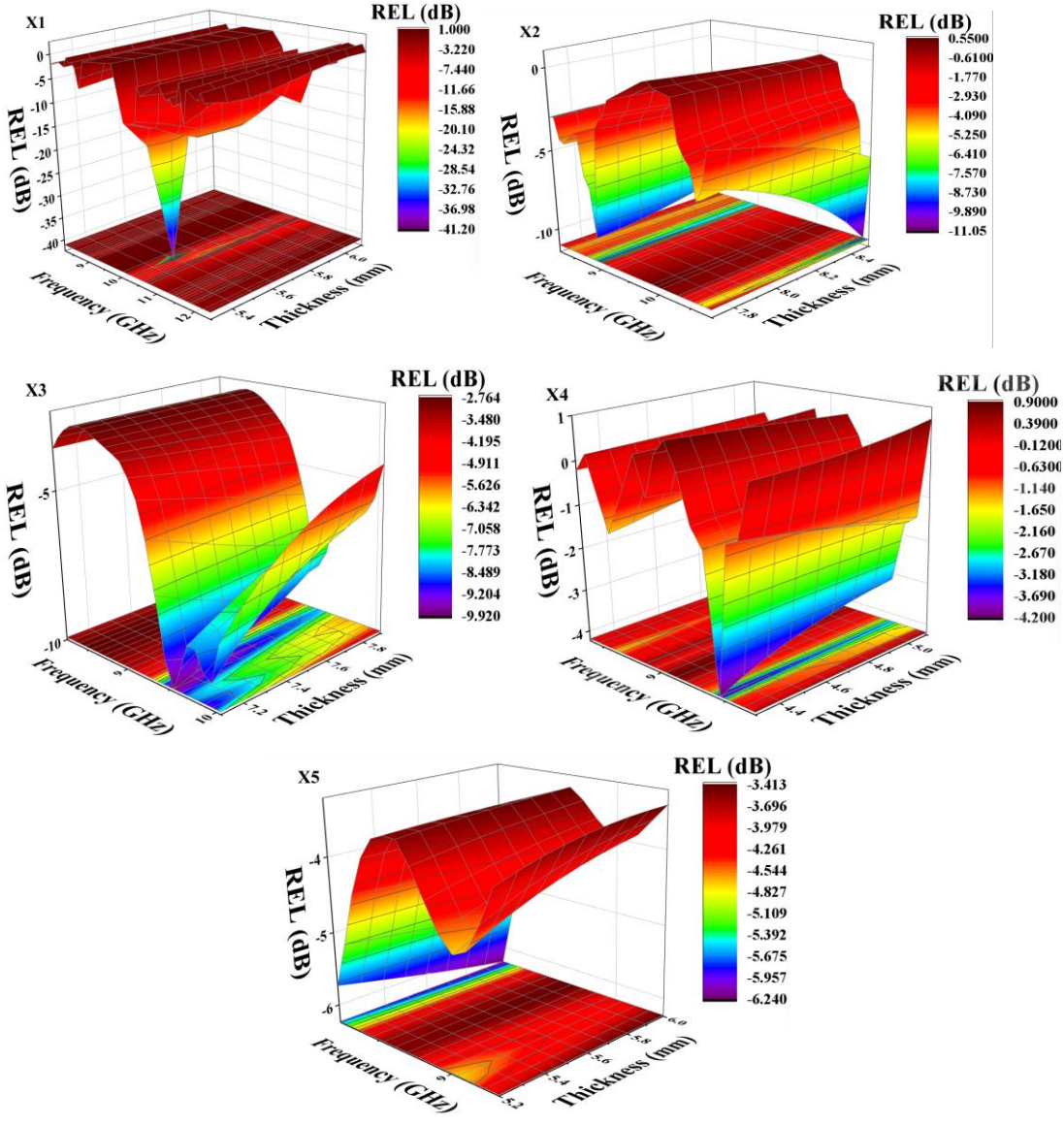

Figure 4.39 Three-dimensional (3D) plots of reflection loss at various frequencies and thicknesses for all samples of BaCoCe-series.

This has to do with the quarter-wavelength process described in equation 1.7, which shows how frequency and material thickness are inversely connected. Subsequently, in order to determine the relationship between quarter wavelength mechanism and REL, the estimated thickness (t_{cal}) is evaluated using equation 1.7 and compared to a simulated thickness (t_{sim}), from which REL may be computed using equation 1.7. The frequency-related calculated thickness or $n\lambda/4$ graphs are shown in Figure 4.35 to Figure 4.38. Equation (1.7) uses n = 1, n = 3, n = 5, n = 7 and n = 9 to construct the estimated thickness curves. Lines in vertical form are drawn across the greatest values of reflection loss to computed thickness graphs in order to compare the calculated thickness and simulated thickness for peaks of reflection loss. Bubbles show the simulated thickness on graphs for levels of reflection loss. It is evident from Figure 4.35 to Figure 4.38 that the predicted thickness, shown on the $n\lambda/4$ curve, is close to the bubble with a vertical line drag by maximum reflection loss peaks for the stated simulated thickness.

In Figure 4.36 X3(g), a W shaped is observed between 10.00 GHz to 10.50 GHz and Materials that exhibit W-shaped curves are commonly favoured for applications that require broad absorption, such as electromagnetic interference (EMI) shielding. In Figure 4.36 X3(k), V Shaped is observed or symmetry around the thickness t = 7.4 mm.

As shown in Figure 4.37 X4(a), the reflection loss peaks with composition X4 is at the same frequency 9.46 GHz for t = 2.7 mm to 3.3 mm and as increase the thickness, there is no change in the height of peak. As can be seen in Figures 4.37 X4(c), the peak height increase as thickness increases from 4.0 mm to 4.8 mm and peak shift right side. As shown in Figure 4.37 X4(i), X4(k) and X4(m), the reflection loss peaks with composition X4 is at the same frequency 9.376 GHz, 11.39 GHz for t = 7.9 mm to 8.7 mm and 10.72 GHz, 11.9 GHz for t = 8.8 mm to 9.6 mm.

The composition X5 yields bandwidths of 0.7 GHz at 5.4 mm for the 11.8 GHz – 12.5 GHz frequency. REL = -34.05 dB is observed for the -20 dB bandwidth of 0.32 GHz. As shown in Figure 4.38 X5(a), X5(i) and X5(k), the reflection loss peaks with composition X5 are at the same frequency for t = 1.5 mm to 2.1 mm, 6.8 mm to 7.6 mm and t = 7.7 mm to 8.4 mm respectively. As shown in Figure 4.38 X5(c), X5(e) and X5(g), the REL peaks shift toward left in lower frequency region as thickness

increase for 2.4 mm to 3.0 mm, 5.0 mm to 5.8 mm and 5.9 mm to 6.7 mm respectively. Therefore, reflection loss values greater than -10 dB and -20 dB with compositions of X2, X3, X4 and X5 indicate a quarter wavelength mechanisms with computed thickness and simulated thickness.

4.2.5.4 Impedance matching mechanism

The material's impedance changes due to its different permittivity/permeability compared to free space. The difference between these two factors affects the material's ability to absorb. A smaller portion of the incident signal passes through the material while the majority is reflected off the surface due to their misalignment. However, if there are similarities, a portion of it permeates the material and becomes absorbed. Researching impedance matching is crucial to develop an effective absorber.

Figure 4.40 displays the plots of reflection loss and $|Z_{in}|$ versus frequency for the prepared samples. The Z_{in} values that correspond to the maximum reflection loss of the different compositions can be found in Table 4.14. In each composition (X1 to X5), the impedance matching technique consistently produces the highest REL peaks. For a 7.4 mm thickness in composition X3, the REL peak of -49.46 dB at 12.15 GHz equates to Z_{in} = 375.26 Ω, or roughly 377 Ω. At 10.30 GHz, there is an REL peak measuring -41.09 dB, and Z_{in} = 372.76 Ω in X1 corresponds to the value of Z_o = 377 Ω. For composition X2, an REL peak of -34.06 at 11.81 GHz with Z_{in} = 380.23 Ω is detected. For X3, at 12.316 GHz no REL peaks are observed with Z_{in} = 379.79 Ω which is near to Z_o = 377 Ω. There is an REL peak of -30.85 at 11.56 GHz with Z_{in} = 389.59 Ω in composition X4, but no REL peaks at 8.788 GHz with Z_{in} = 375.42 Ω. Z_{in} = 389.59 Ω is less similar to Z_o = 377 Ω than Z_{in} = 375.42 Ω. Z_{in} = 366.22 Ω corresponds to the composition X5 REL peak of -34.05 at 12.32 GHz. Due to the presence of both real and imaginary components, Z_{in} exhibits a complex nature, which is associated with its unique behavior (Z_{real} & Z_{img}). As a result, Z_{real} and Z_{img} are calculated, and the resulting graphs are depicted as shown in the Figure. The values corresponding to Z_{real} and Z_{img} are listed in Table 4.14. For successful implementation of impedance matching, it is crucial that the real and imaginary impedances of the material meet the specified requirements of 377 Ω and/or 0. The maximum REL of -49.46 dB at 12.15 GHz for X3 fulfills this requirement, with Z_{real} = 375.26 Ω and Z_{img}

= 1.69 Ω. The peak at 10.30 GHz, which has a value of -41.09 dB for X1, meets the requirement due to the values of Z_{real} = 372.73 Ω and Z_{img} = -5.05 Ω. Similar at 11.81 GHz, 11.56 GHz, 12.32 GHz which has value of –34.06 dB, -30.85 dB and -34.05 dB for X2, X4 and X5 respectively.

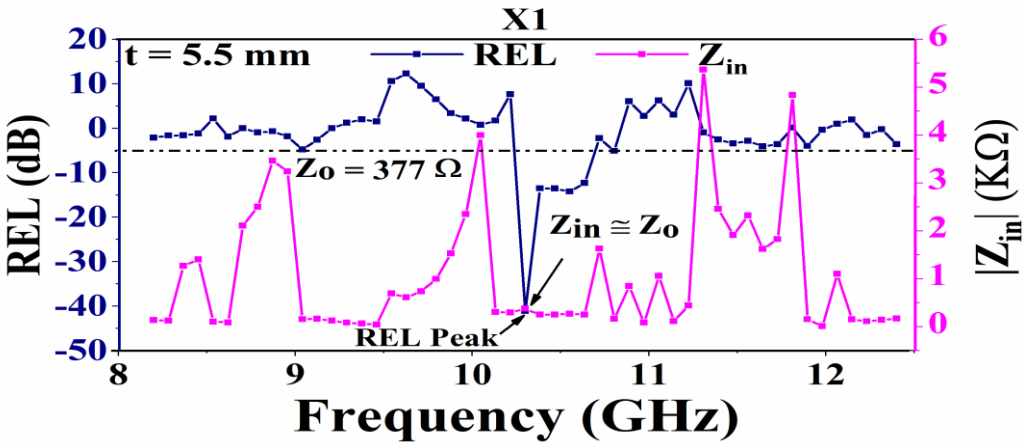

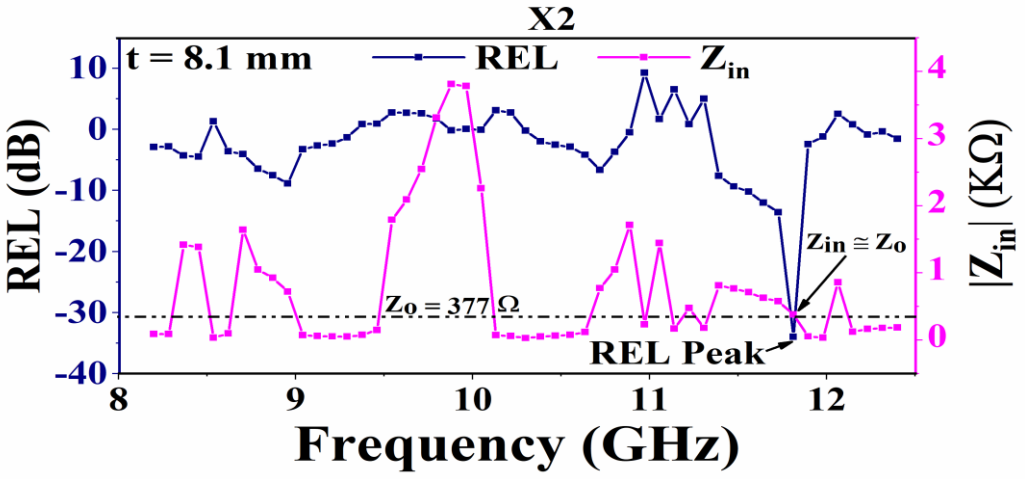

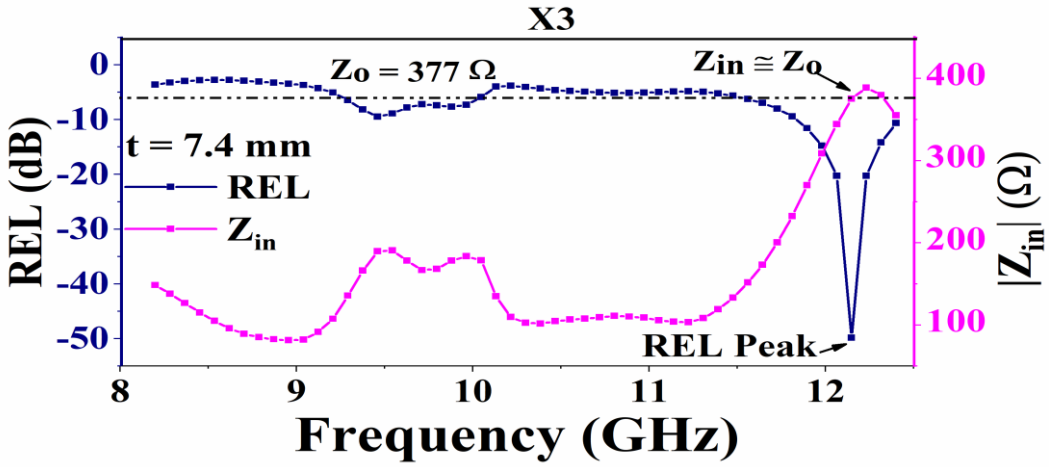

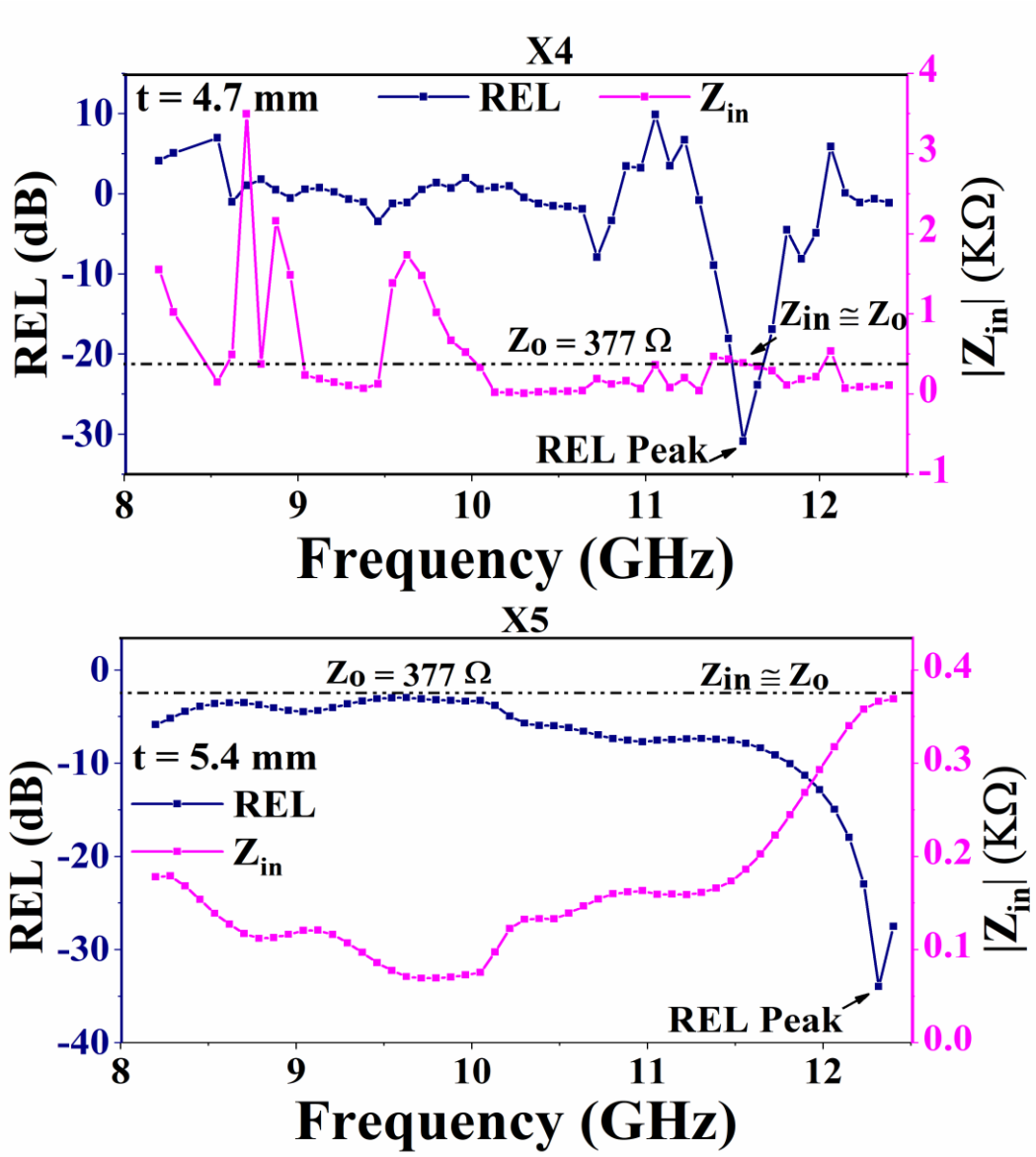

Figure 4.40 Zin and REL curve against frequency for $BaCo_xCe_xFe_{12-2x}O_{19}$.

Table 4.14 Z_{in}, Z_{real}, and Z_{imag} values corresponding to REL_{max} for $BaCo_xCe_xFe_{12-2x}O_{19}$.

Sample Name	Matching Thickness (mm)	Maximum REL (dB)	Matching frequency (GHz)	Z_{real} (Ω)	Z_{img} (Ω)	$\|Z_{in}\|$ (Ω)
X1	5.5	-41.09	10.30	372.73	-5.05	372.76
X2	8.1	-34.06	11.81	380.23	-14.82	380.51
X3	7.4	-49.46	12.15	375.26	1.69	375.26
X4	4.7	-30.85	11.56	389.17	18.18	389.59
X5	5.4	-34.05	12.32	366.08	10.09	366.22

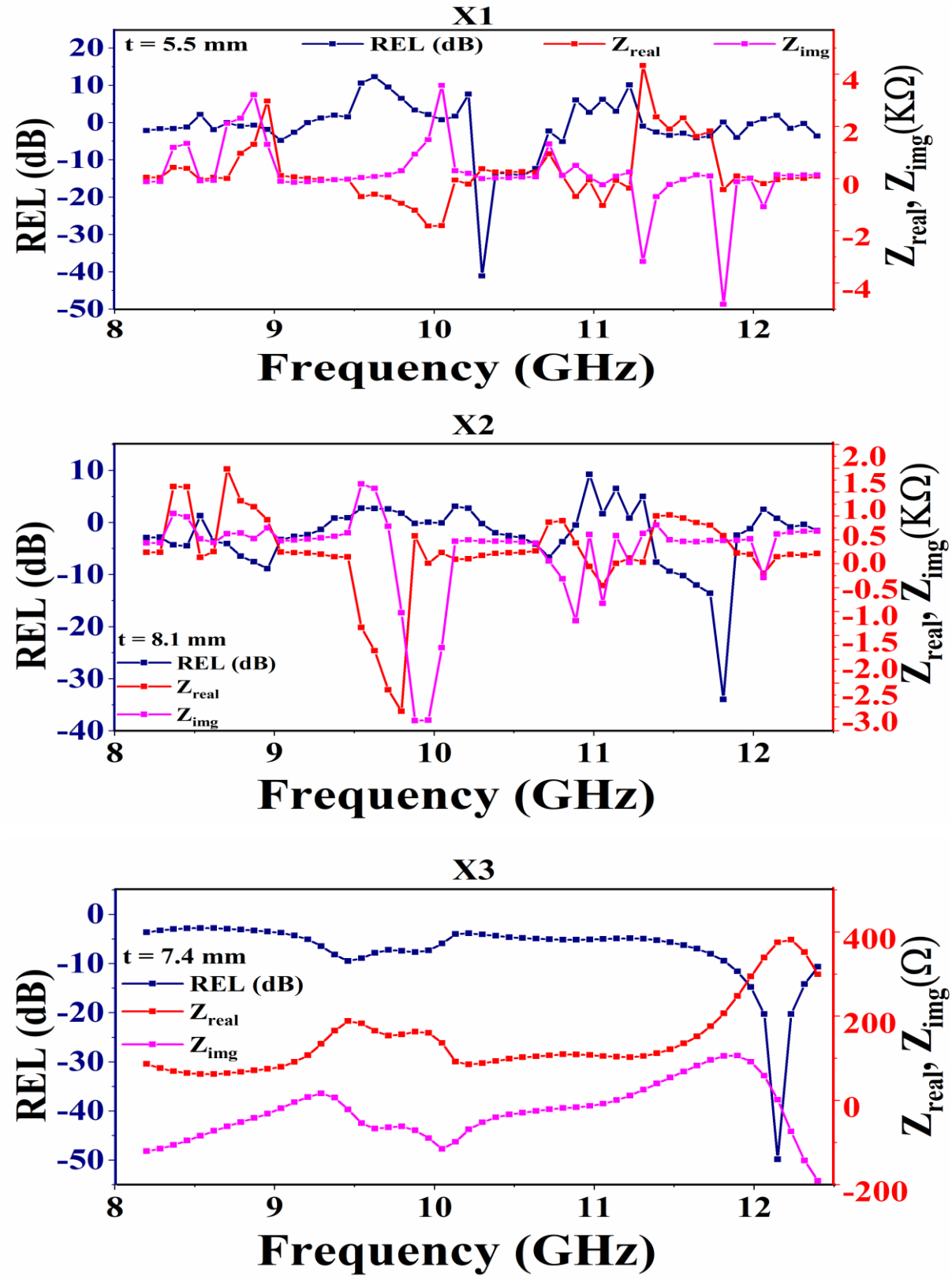
X1
t = 5.5 mm
REL (dB)
Z_{real}
Z_{img}
REL (dB)
Z_{real}, Z_{img}(KΩ)
Frequency (GHz)
X2
t = 8.1 mm
REL (dB)
Z_{real}
Z_{img}
REL (dB)
Z_{real}, Z_{img}(KΩ)
Frequency (GHz)
X3
t = 7.4 mm
REL (dB)
Z_{real}
Z_{img}
REL (dB)
Z_{real}, Z_{img}(Ω)
Frequency (GHz)

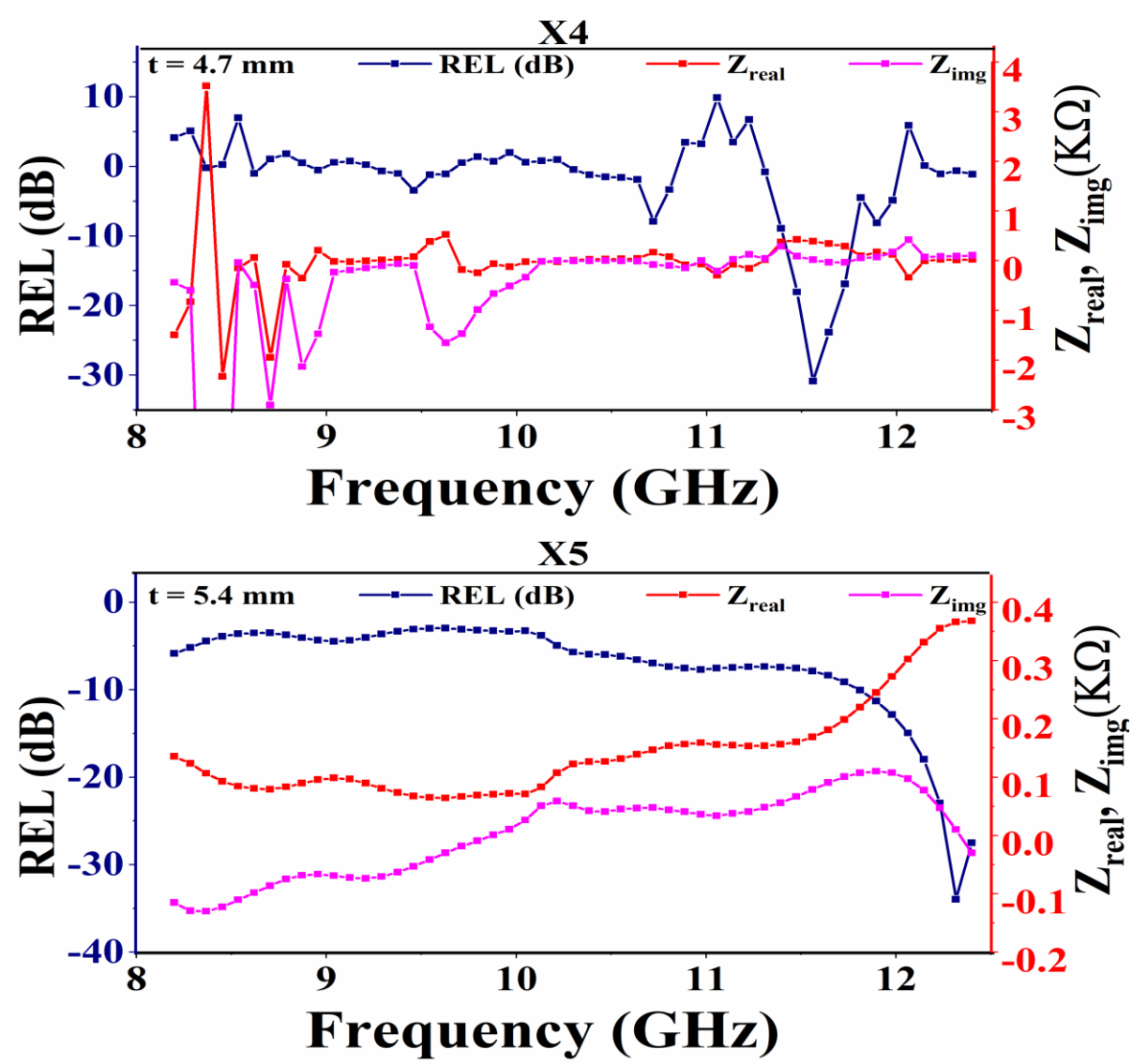

Figure 4.41 Z_{real}, Z_{imag}, and REL v/s frequency for $BaCo_xCe_xFe_{12-2x}O_{19}$.

4.2.5.5 Eddy Current Loss

The plot illustrates the relationship between the compositions C_0 and frequency. It becomes evident that the plots of all the compositions remain consistent beyond 8.78 GHz, suggesting that the absorption of ferrite compositions is influenced by eddy current loss.

4.2.5.6 Bandwidth to Thickness Ratio

The BTR and PBW values found for the prepared compositions are listed in Table 4.13. The X5 sample exhibits the highest BTR, with values of 1.32E-03 and PBW (11.27%) at 10.38 GHz and REL = -13.97 dB at 2.3 mm thickness. Remarkably, the X3 sample showed a substantially higher REL of -49.46 dB and a lower BTR than the

X5 sample. In addition, the composition X2 has a BTR ranging from 1.35E-04 to 9.92E-05 and a PBW ranging from 1.60% to 5.57% for frequencies between 9.04 GHz and 11.81 GHz for thicknesses between 3.7 mm and 9.0 mm. For thicknesses ranging from 2.2 mm to 8.0 mm, the composition X3 has a BTR in the range of 1.04E-03 to 9.85E-04 and a PBW in the range of 2.92% to 9.58% from 9.12 GHz to 12.32 GHz. For thicknesses of 3.0 mm to 9.6 mm, the composition X4 has a BTR in the range of 1.81E-04 to 6.99E-05 and a PBW in the range of 0.53% to 3.53% from 9.46 GHz to 11.90 GHz. For thicknesses ranging from 2.3 mm to 7.7 mm, the composition X5 has a BTR in the range of 1.32E-03 to 6.09E-04 and a PBW in the range of 3.41% to 13.28% from 9.29 GHz to 12.32 GHz.

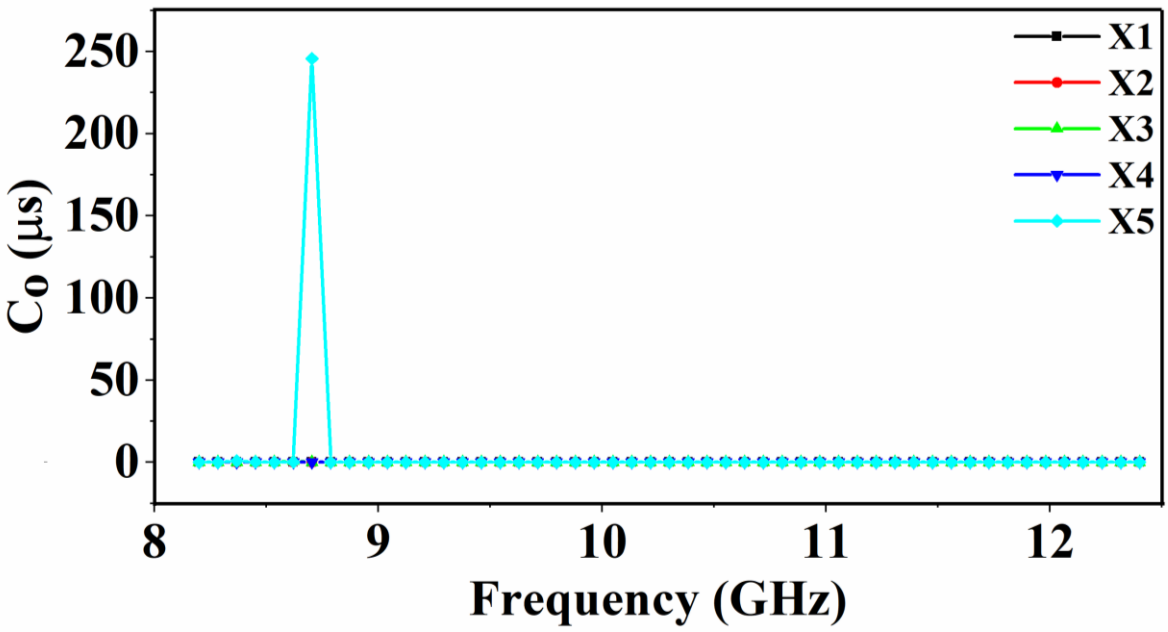

Figure 4.42 C_0 versus frequency curve for $BaCo_xAl_xFe_{12-2x}O_{19}$.

4.2.5.7 S – Parameter

When the input signal is applied at input port 1 of the test waveguide from VNA, the two-port S_{11} parameter accounts for the reflected signal from the same input port 1 from the sample fitted in the test waveguide of the VNA. S_{21} accompanies the attenuation in the signal traveling from input port 1 to output port 2.

S_{11} values fluctuate significantly across the frequency range, with instances of positive values around 8.2 GHz and other points, such as 9.21 GHz and 9.29 GHz, where values reach around 0.5 dB. However, at higher frequencies, beyond 10 GHz, the reflection worsens, with S_{11} values becoming more negative (as low as -5.89 dB),

indicating better matching. X2 and X4 follows a similar pattern to X1, with high values (positive S_{11}) at low frequencies (around 0.77 dB at 8.28 GHz and around 0.6 dB at 8.2 GHz respectively). As frequency increases, the reflection worsens, with S_{11} values reaching as low as -6.44 dB around 10.9 GHz and -7.63 dB around 10.9 GHz respectively, implying significant improvements in impedance matching at higher frequencies. X3 shows a consistent negative trend across the frequency range, with no positive S_{11} values. This suggests better impedance matching compared to X1 and X2 throughout. At lower frequencies, S_{11} is approximately -1.45 dB at 8.2 GHz, and it gradually worsens (becomes more negative), reaching around -4.12 dB by 12.4 GHz. This consistent downward trend reflects improved impedance matching as frequency increases. X5 at lower frequencies, with S_{11} as low as -3.91 dB at 8.2 GHz, indicating relatively better performance than the others at lower frequencies. The trend stays relatively negative across the frequency range, reaching values as low as -4.28 dB at 12.4 GHz, showing improved matching as frequency increases.

For X1, at lower frequencies (around 8.2 GHz), the value of S_{21} is high around -4.7 dB. As the frequency increases, the value of S_{21} decreases and approaching -2.2 dB around 12.4 GHz, indicating improved. X2 shows similar behaviour to X1 but with less value. At lower frequencies, S_{21} starts around -4.1 dB and reduces to about -1.78 dB at 12.4 GHz.X3 starting at about -4.23 dB at lower frequencies and ends with about -1.35 dB at 12.4 GHz. X4 Starts at a higher value around -3.15 dB at lower frequencies and shows steady improvement, reaching around -1.53 dB at 12.4 GHz. X5 begins with S_{21} values around -4.04 dB at 8.2 GHz and ends with -1.73 dB at 12.4 GHz.

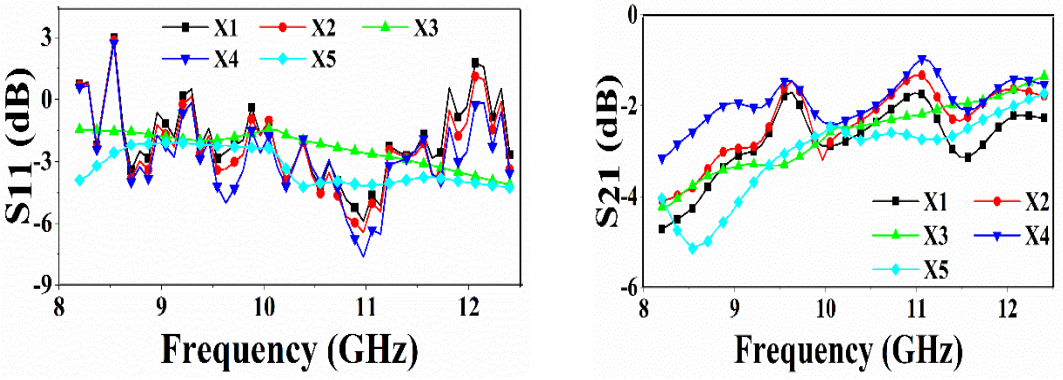

Figure 4.43 S_{11} and S_{21} versus frequency curve for $BaCo_xCe_xFe_{12-2x}O_{19}$.

4.3 Co^{2+}- Cd^{2+} substituted $BaCo_xCd_xFe_{12-2x}O_{19}$ hexaferrite.

This section will use the sol-gel combustion technique to produce a hexaferrite compound with replacements of Co and Cd. By composition, the hexaferrite will consist of $BaCo_xCd_xFe_{12-2x}O_{19}$. Table 4.15 presents the numerical values assigned to different degrees of substitution in $BaCo_xCd_xFe_{12-2x}O_{19}$.

Table 4.15. Presents the assignment of sample names corresponding to various substitution levels in $BaCo_xCd_xFe_{12-2x}O_{19}$ hexaferrite.

Sample Composition **$BaCo_xCd_xFe_{12-2x}O_{19}$**	Sample Code Name	Sample Code (Y-series)
x= 0.0	**$BaFe_{12}O_{19}$**	Y0
x = 0.2	**$BaCo_{0.2}Cd_{0.2}Fe_{11.6}O_{19}$**	Y1
x = 0.4	**$BaCo_{0.4}Cd_{0.4}Fe_{11.2}O_{19}$**	Y2
x = 0.6	**$BaCo_{0.6}Cd_{0.6}Fe_{10.8}O_{19}$**	Y3
x = 0.8	**$BaCo_{0.8}Cd_{0.8}Fe_{10.4}O_{19}$**	Y4
x = 1.0	**$BaCoCdFe_{10}O_{19}$**	Y5

4.3.1 X-ray diffraction analysis

Figure 4.44 displays the X-ray diffraction (XRD) pattern of $BaCo_xCd_xFe_{12-2x}O_{19}$ hexaferrite samples with the following values for Y0 to Y5. Powder-X was used to do an analysis on the data, which revealed the presence of clearly defined Bragg peaks. The peaks were compared to the conventional standard pattern for barium hexaferrite, which is $BaFe_{12}O_{19}$ and has the space group P63/mmc (JCPDS card no. 96-100-8842). According to the results of the XRD examination, the samples major peak matches with M-type (hexagonal), but two other peaks of barium iron oxide are also identify as minor.

The prepared samples computed values for the lattice parameters are reported in Table 4.16. It is clear from the table that both the lattice constants (a, c) and the cell volume decrease from 698.68 to 695.51 with increasing Co-Cd doping from samples with Y0 to Y5, although a substantial change in the lattice parameters is visible in all of the samples. It is plausible that this phenomenon is connected to the disparity in the ionic radii of the dopants Co2+ (0.72), Cd2+ (0.97), and the parent Fe3+ (0.64) [166-167]. The c/a ratio for all samples was found to be constant at 3.94 [168] and the size of the crystallites lies between 18.8459 and 43.3961 nm. As we increase the doping concentration level the secondary phase i.e barium iron oxide peak increasing as

shown in Figure 4.44. Doping of barium hexaferrite with Co^{2+} and Cd^{2+} ions can lead to the formation of a secondary phase of $BaFe_2O_4$. This can happen if the dopant ions are not fully incorporated into the barium hexaferrite lattice, or if the doping concentration is too high. The presence of a secondary phase of $BaFe_2O_4$ will give rise to two additional minor peaks in the XRD pattern. The intensity of the two peaks of $BaFe_2O_4$ will increase with increasing doped concentration. This is because the higher the dopant concentration, the more likely it is that the dopant ions will either substitute into the barium hexaferrite lattice or form a secondary phase of $BaFe_2O_4$. Co^{2+} ions have a preference for the hexagonal ring sites, while Cd^{2+} ions have a preference for the octahedral/tetrahedral sites. The distribution of Co^{2+} and Cd^{2+} ions between the two types of sites will affect the crystal structure and the XRD pattern of the barium hexaferrite. Co^{2+} and Cd^{2+} ions can interact with each other, forming pairs or clusters. The interaction between Co^{2+} and Cd^{2+} ions can also affect the crystal structure and the XRD pattern of the barium hexaferrite.

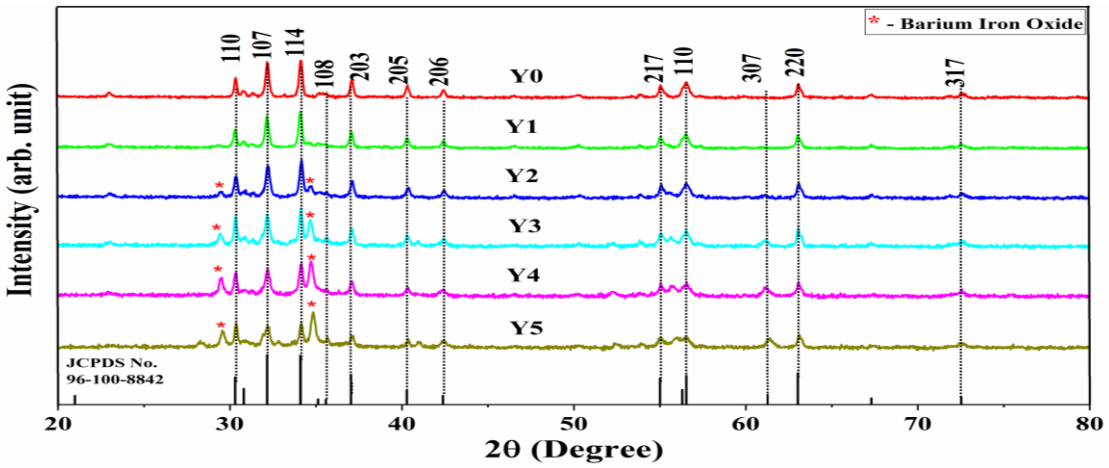

Figure 4.44 X-ray diffractions of M -type $BaCo_xCd_xFe_{12-2x}O_{19}$ (Y0 to Y5, x = 0.0, 0.2, 0.4, 0.6, 0.8, and 1.0) hexaferrites.

Table 4.16 Co-Cd content, Lattice constants, ratio c/a and unit cell volume of ferrite sample $BaCo_xCd_xFe_{12-2x}O_{19}$ (Y0 to Y5, x =0.0, 0.2, 0.4, 0.6, 0.8, and 1.0)

Parameter	Y0 (x = 0.0)	Y1 (x = 0.2)	Y2 (x = 0.4)	Y3 (x = 0.6)	Y4 (x = 0.8)	Y5 (x = 1.0)
a = b (Å)	5.8937	5.8935	5.891	5.8893	5.8874	5.8855
c (Å)	23.2261	23.2110	23.1981	23.1902	23.1873	23.1881
c/a	3.9408	3.9384	3.9379	3.9377	3.9385	3.9399
Vol /10^6 pm3	698.6875	698.1859	697.2060	696.5663	696.0299	695.6047

Crystallite Size D_{xrd} (nm)	43.3961	18.8459	23.3017	26.8323	25.3921	25.9485

In particular, the EDX analysis offers an assessment of the elemental presence in accordance with the requirements of mixed compounds during synthesis. Figure 4.45 shows the EDX spectra of samples Y0 and Y2 of $BaCo_xCd_xFe_{12-2x}O_{19}$. The Ba, O, and Fe elements are present in composition Y0, whereas the Ba, Fe, Co, and Cd elements are present in composition Y2, as can be observed from EDX spectra. Table 4.17 indicate weight % and atomic % of all the elements in the final compositions $BaCo_xCd_xFe_{12-2x}O_{19}$ (Y0 to Y5, x = 0.0, 0.2, 0.4, 0.6, 0.8, and 1.0) as evaluated from EDX analysis.

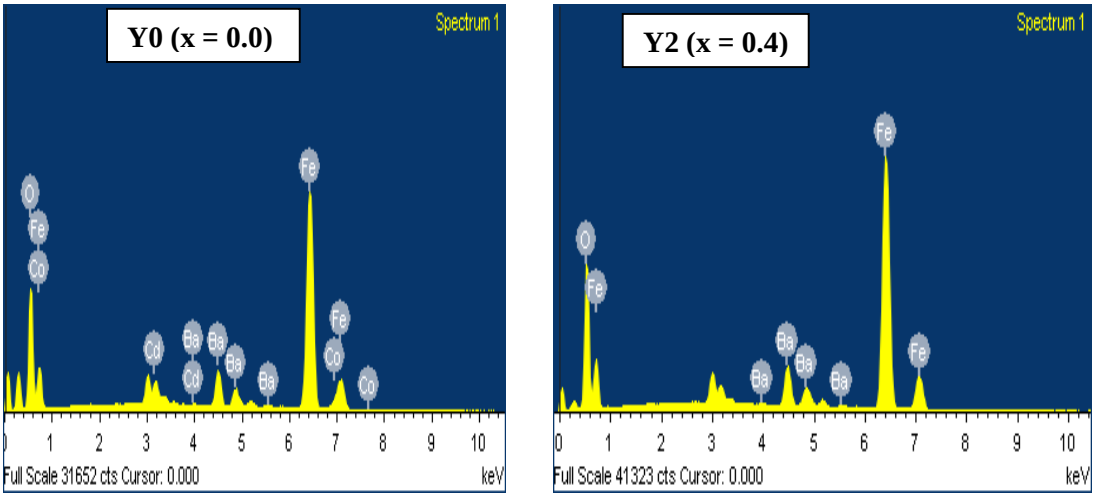

Figure 4.45 EDX spectra of $BaCo_xCd_xFe_{12-2x}O_{19}$ (Y0 to Y5, x =0.0, 0.2, 0.4, 0.6, 0.8, and 1.0) hexaferrite for samples Y0 and Y2.

Table 4.17 Weight % and Atomic % of all the elements in the final compositions $BaCo_xCd_xFe_{12-2x}O_{19}$ (Y0 to Y5, x =0.0, 0.2, 0.4, 0.6, 0.8, and 1.0) as evaluated from EDX analysis.

Element	Y0 (x = 0.0)		Y1 (x = 0.2)		Y2 (x = 0.4)		Y3 (x = 0.6)		Y4 (x = 0.8)		Y5 (x = 1.0)	
	W %	A %	W %	A %	W %	A %	W %	A %	W %	A %	W %	A %
O K	20.6	50.2	27.2	59.4	21.8	52.3	21.2	51.8	18.7	47.7	20.5	51.3
Fe K	65.6	45.9	58.4	36.5	60.6	41.7	58.4	40.9	59.9	43.7	54.0	38.6
Ba L	13.8	3.9	12.6	3.2	13.1	3.7	13.2	3.8	12.1	3.6	13.8	4.0
Co K	-	-	1.3	0.8	2.4	1.6	3.5	2.3	5.0	3.5	6.0	4.1
Cd L	-	-	0.5	0.2	2.1	0.7	3.6	1.3	4.3	1.6	5.6	2.0

4.3.2 Formulation and Morphological Analysis of Nanoferrite Composites via FESEM Characterization

Figure 4.46 displays the grain morphology of the samples. For Y0, small-size individual grains can be seen as shown in Figure 4.46 and also easily identify the boundaries of grains. In Figure 4.46 (Y1), a few empty spaces called porosity are also observed, along with the highest C_{gb}. For Y1, the presence of heterogeneities in the morphology can affect the connectivity and continuity of the grain boundaries. Discontinuities or variations in grain boundary connectivity can lead to higher overall grain boundary resistance in materials with a heterogeneous morphology. For Y2, fusion of grains occurs, which leads to an increase in grain size and can have a direct effect on grain capacitance C_g. Larger grains generally have a higher capacitance due to their increased surface area and larger volume for charge accumulation. For Y3, grain size reached its highest and also the highest C_g = 20231.43 occurred, and larger grain sizes typically result in slower grain time constants (Highest τ_g values).

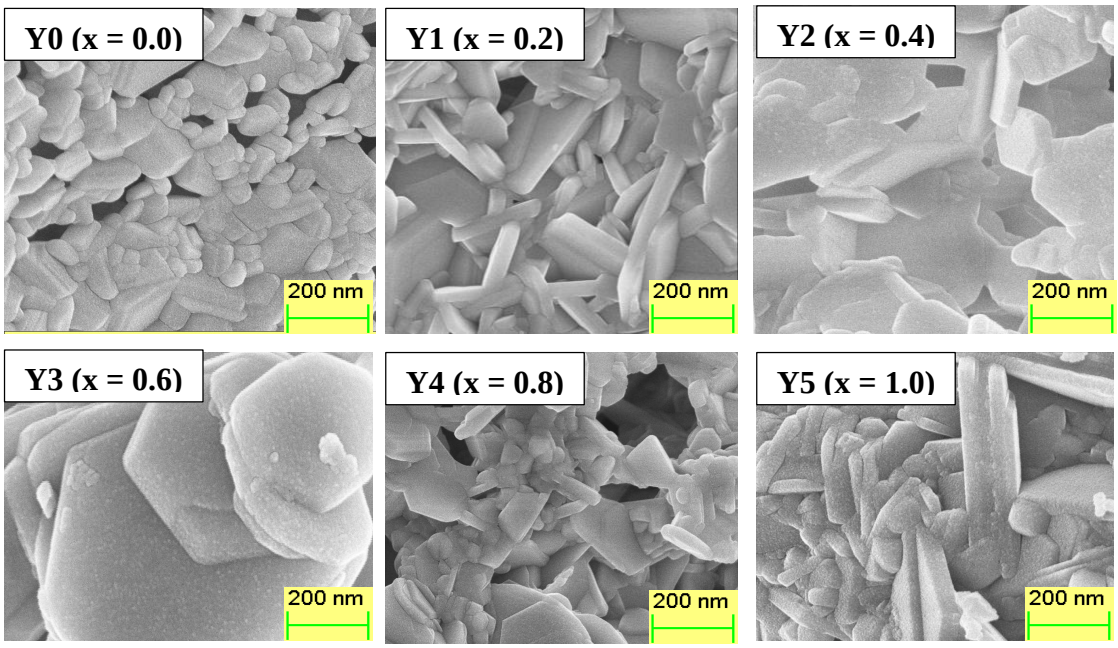

Figure 4.46 SEM micrographs of ferrite samples of $BaCo_xCd_xFe_{12-2x}O_{19}$ (Y0 to Y5, x =0.0, 0.2, 0.4, 0.6, 0.8, and 1.0)

This is because larger grains have a lower surface-to-volume ratio, leading to decreased surface effects, enhanced polarization, and more efficient charge carrier dynamics. Consequently, the relaxation processes within the higher grains occur very slowly, resulting in longer time constants. For Y4, grain fuses, but the size of the

grain is smaller, which again increases R_{gb} and reduces the time constant up to the lowest value. For Y5, R_{gb} reached maximum values, and due to the fusion of grain, R_g also increased again from 15.15 MΩ to 210.14 MΩ.

4.3.3 Electrical Characterization

4.3.3.1 Dielectric constant

Figure 4.47 depicts, separately, the ways in which the real and imaginary components of the dielectric constant change as a function of the frequency. Because of dielectric relaxation and dielectric dispersion in the lower frequency zone, the value of the dielectric constant drops with an increase in frequency as shown in Figure 4.47(a). On the other hand, the behaviour is independent of frequency in the higher frequency region. This is unambiguous evidence that both the real and imaginary portions of the dielectric constant fall with an increase in frequency. For pure Ba hexaferrite (Y0), the ε′ value is 83.48 at 100 Hz which reduces to 12.38 at 2 MHz, whereas for Y1, the ε′ value of 26.32 at 100 Hz reduces to 5.75 at 2 MHz. Similarly, for Y2, the value is 56.71 and reduces up to 4.43; for Y3, the value is 46.47 and reduces up to 5.98; for Y4, the value is 14.5 and reduces up to 4.10; and for Y5, the value is 36.31 and reduces up to 3.59 .The existence of grain boundary defects, voids, dislocations, and other imperfections contributed to these larger values in the lower frequency range [172]. whereas the decreasing magnitude of ε′ with the increasing frequency can be a result of the space charge polarization decreasing as a result of the increasing frequency. On the other hand, this kind of dielectric dispersion may be better described based on the two layer Maxwell-Wagner model of interfacial polarization, which is in good agreement with Koop's phenomenological theory [173-174]. The model postulates that a dielectric material will consist of conducting grains that will be physically separated from one another by resistive grain boundaries. When an electric field is produced, charge carriers are able to readily move between conducting grains and get collected at the grain boundaries, which produces polarization and a significant dielectric field. The effectiveness of grain boundaries is maximized at low frequency ranges, while the effectiveness of grains themselves is maximized at high frequency ranges. Charge carriers that have collected at grain boundaries are able to readily follow the direction of an applied electric field, which results in a high dielectric constant in the low frequency region. However, in the high frequency range,

charge carriers are unable to follow the applied field. This results in a decrease in the dielectric constant, which eventually becomes nearly constant at high frequencies [175-179].

4.3.3.2 Dielectric Loss and Tangent Loss factor

Figure 4.47(b) depicts the behaviour of the dielectric loss as a function of frequency. These depicted curves have a profile that is quite similar to the profile of ε′. It shows greater ε″ values in the lower frequency zone and then becomes frequency independent beyond a specific limiting frequency. Interfacial polarization may be seen at lower frequency ranges due to the fact that the dielectric structure is composed of good conducting grains that are separated by grain boundaries that are weakly conducting [13, 14]. The hopping causes the electrons to arrive at the grain boundary, and if the resistance of the grain boundary is high enough, then the electrons will accumulate at the grain boundary, which will result in polarization. Because it takes the space charge carriers a certain amount of time to align their axes in the same direction as an applied alternating field, the electrons are forced to change the direction in which they are moving more frequently when the frequency of the field that is being applied is increased. Because of this, the polarization of the interface is reduced at higher frequencies [15]. Beyond a certain frequency of an applied electric field, the particle exchange does not follow the electric field. As a result, it is nearly impossible for dipolar polarization to follow the electric field, and as a result, the dielectric constant decreases. This can be used to justify the negligible existence of dipolar polarization at higher frequencies.

In Figure 4.47(c) the frequency at which the peak occurs can be indicative of the relaxation process within the material. It also associated with the dielectric relaxation behaviour of the material. If there's a single peak in the Figure 4.47(c), it associated with a dominant dielectric relaxation process. This process could be related to the reorientation of dipoles, defects, or ionic motions in the material in response to the applied electric field. In some cases, the tan δ graph may exhibit multiple peaks. Each peak represents a different relaxation process with its own characteristic frequency and relaxation time. The height and width of the peak(s) provide information about the strength and broadness of the relaxation processes. A high peak indicates a

significant energy loss, while a wide peak suggests a broad distribution of relaxation times within the material.

Dielectric properties are often characterized by complex permittivity (ε*), which consists of both the real part (ε′) and the imaginary part (ε″). These two components are associated with different types of polarization in materials. The Maxwell-Wagner polarization is a phenomenon often observed in heterogeneous materials, and it can be related to ε′ and ε″ in dielectric spectroscopy.

ε′ (Real Part of Complex Permittivity):

Electronic Polarization: The real part of the complex permittivity (ε′) is primarily associated with electronic polarization. Electronic polarization occurs when charges within the material shift in response to an applied electric field (displacement of electrons within the crystal lattice).

ε″ (Imaginary Part of Complex Permittivity):

Ionic Polarization: The imaginary part of the complex permittivity (ε″) is often associated with ionic polarization. Ionic polarization involves the movement of charged ions, such as cations (e.g., Fe^{3+} ions), within the material in response to an applied electric field.

Interfacial Polarization: In addition to ionic polarization, the imaginary part of complex permittivity may also include contributions from interfacial polarization. This occurs at interfaces, grain boundaries, or phase boundaries within the material when charges accumulate due to the electric field.

Maxwell-Wagner Polarization:

The Maxwell-Wagner polarization, also known as interfacial polarization or Maxwell-Wagner-Sillars polarization, is a phenomenon observed in heterogeneous materials. It occurs when there are variations in the dielectric constant (permittivity) or conductivity within the material, leading to charge accumulation at interfaces or boundaries. This polarization is more prominent in materials with discontinuities, such as composites or materials containing different phases.

In dielectric spectroscopy, the Maxwell-Wagner polarization is related to the fact that the relaxation times of different regions within the material are not the same. When an alternating electric field is applied, charge carriers within regions with different

relaxation times respond differently, leading to charge accumulation and interfacial polarization.

Maxwell-Wagner polarization also associated with the interfacial regions between grains or phases, where variations in permittivity or conductivity exist. These variations can lead to charge accumulation and interfacial polarization, contributing to the dielectric response, especially the imaginary part of complex permittivity (ε″).

4.3.3.3 AC Conductivity

The relationship between frequency and AC conductivity (σ_{ac}) is seen in Figure 4.47(d). This relationship holds true for all of the samples. Figure 4.47(d) makes it very evident that an increase in frequency results in greater AC conductivity. According to what was covered in the section on the properties of the dielectric constant, the grain boundary is more effective than the grains themselves in the low frequency zone. This indicates that the volume of grain boundaries in the low frequency range controls the conduction processes in the material. As a result of the material's poor conductivity, the migration of charge carriers is influenced by the grain boundaries in the lower frequency range. Because grain boundaries have a higher resistance than other parts of the material, they can sometimes act as barriers to the conduction of material.

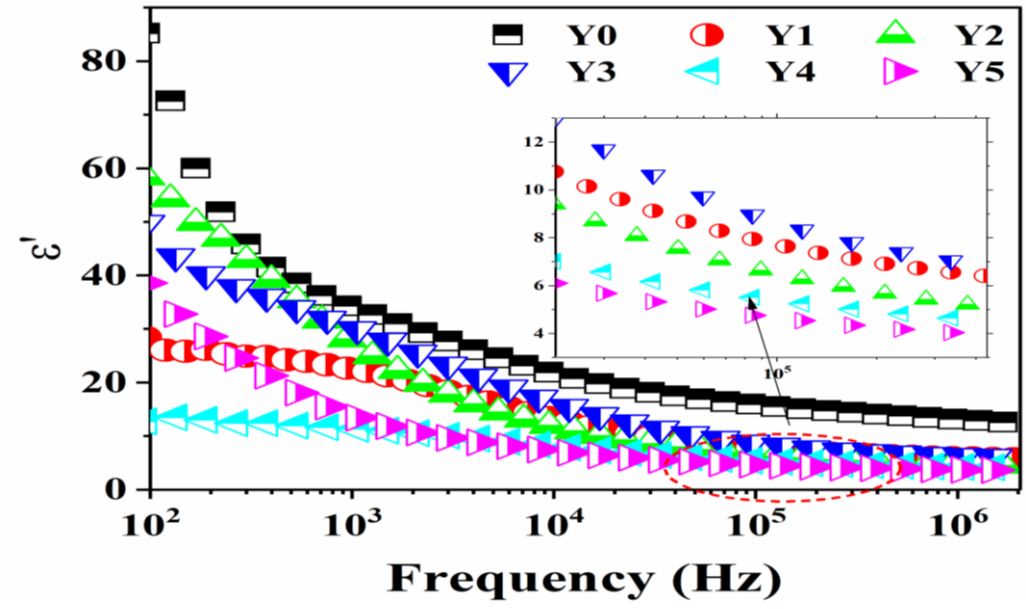

Figure 4.47(a) Variation of dielectric constant with frequency for $BaCo_xCd_xFe_{12-2x}O_{19}$ (Y0 to Y5, x = 0.0, 0.2, 0.4, 0.6, 0.8, and 1.0) hexaferrites samples heated at 900° C for 5 hours.

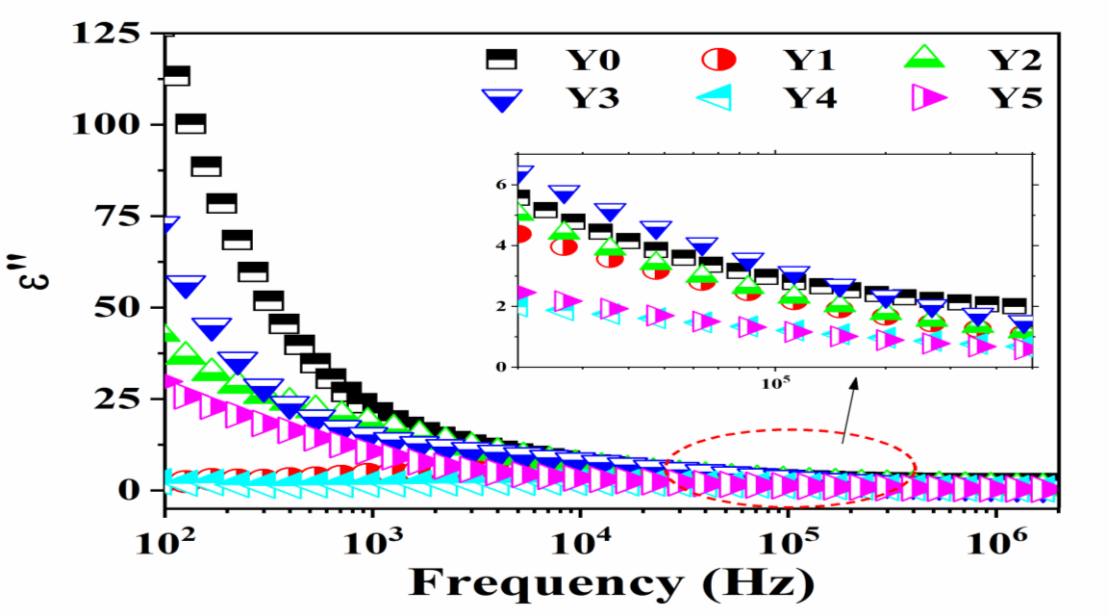

Figure 4.47(b) Variation of dielectric loss factor with frequency for $BaCo_xCd_xFe_{12-2x}O_{19}$ (Y0 to Y5, x = 0.0, 0.2, 0.4, 0.6, 0.8, and 1.0) hexaferrites samples heated at 900° C for 5 hours.

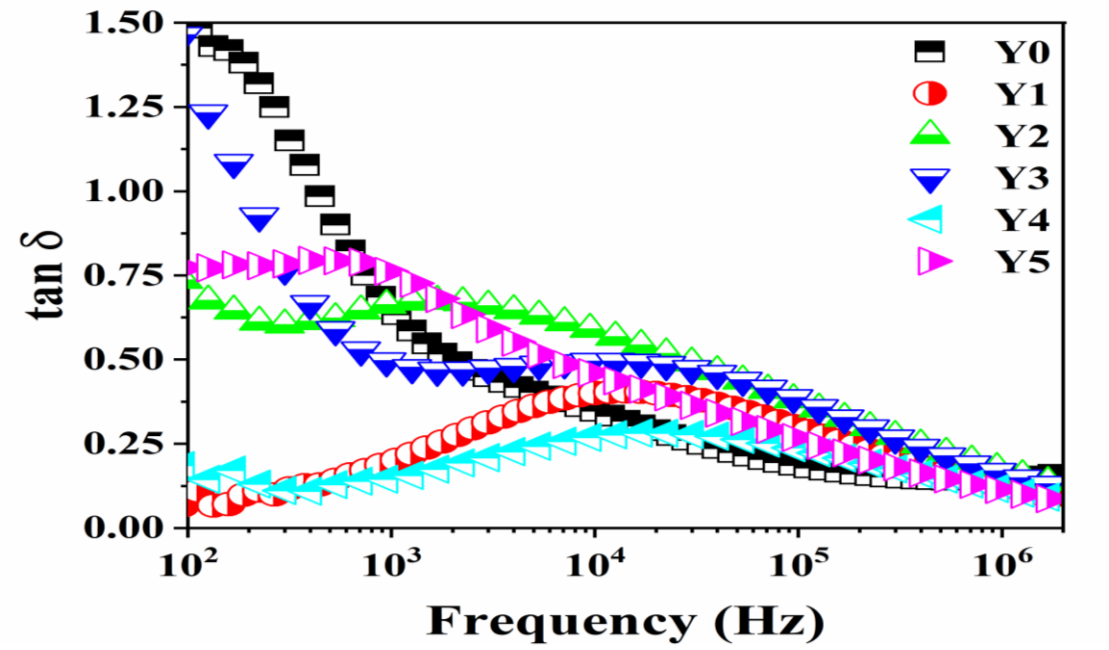

Figure 4.47(c) Variation of tangent loss with frequency for $BaCo_xCd_xFe_{12-2x}O_{19}$ (Y0 to Y5, x = 0.0, 0.2, 0.4, 0.6, 0.8, and 1.0) hexaferrites samples heated at 900° C for 5 hours.

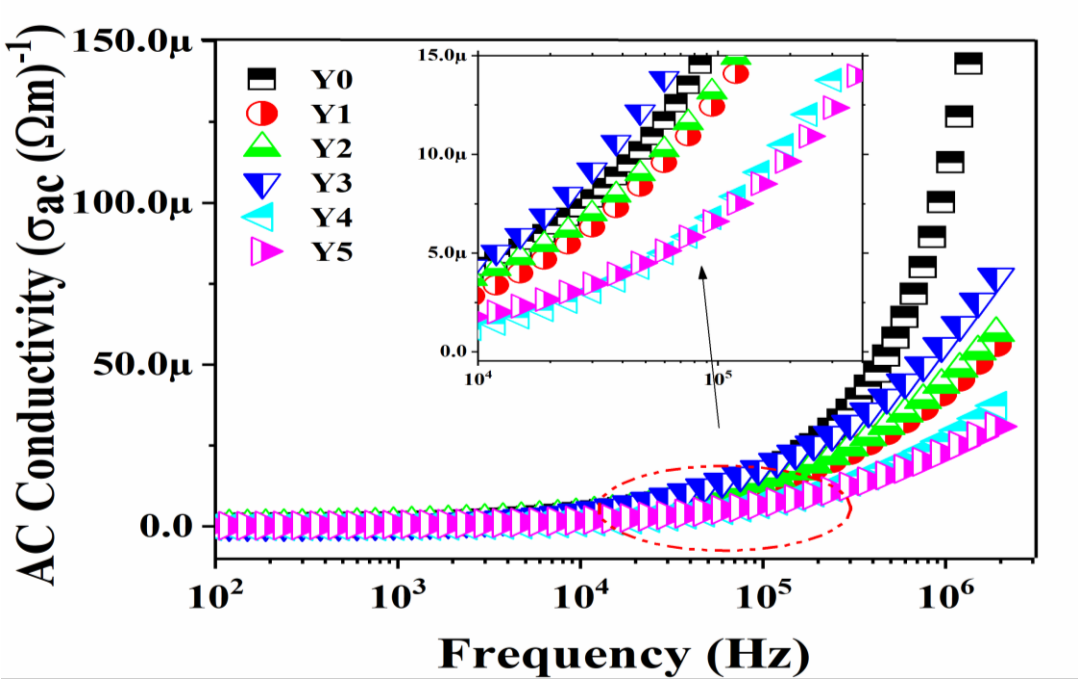

Figure 4.47(d) Variation of AC Conductivity as a function of frequency for $BaCo_xCd_xFe_{12-2x}O_{19}$ (Y0 to Y5, x =0.0, 0.2, 0.4, 0.6, 0.8, and 1.0) hexaferrites samples heated at 900° C for 5 hours.

The dielectric behaviour of the material will change when the frequency that is delivered becomes equal to the frequency that electrons hop at. When the frequency is increased, the dielectric constant of the material will become constant.

The hopping process that allows for electrical conduction in the material is regulated by Johnscher's universal power equation [179-180]:

$$\sigma_{ac} = \sigma_{dc} + A\,\omega_n \qquad (4.37)$$

In this equation, n represents the frequency exponent (0 < n < 1), and both A and n are thermally activated quantities [181].

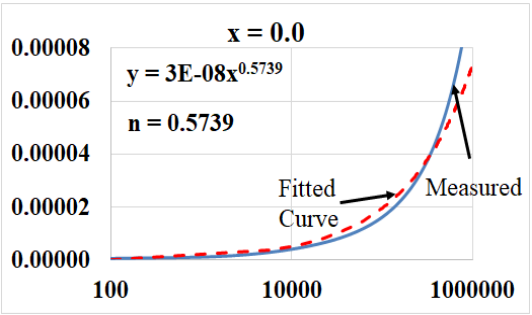

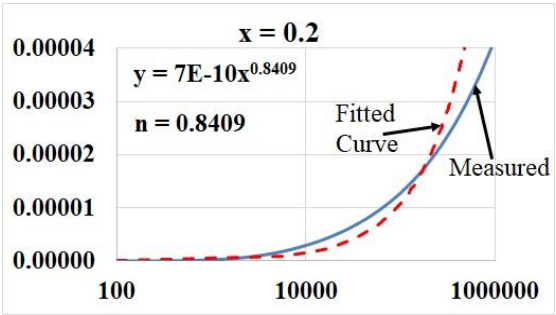

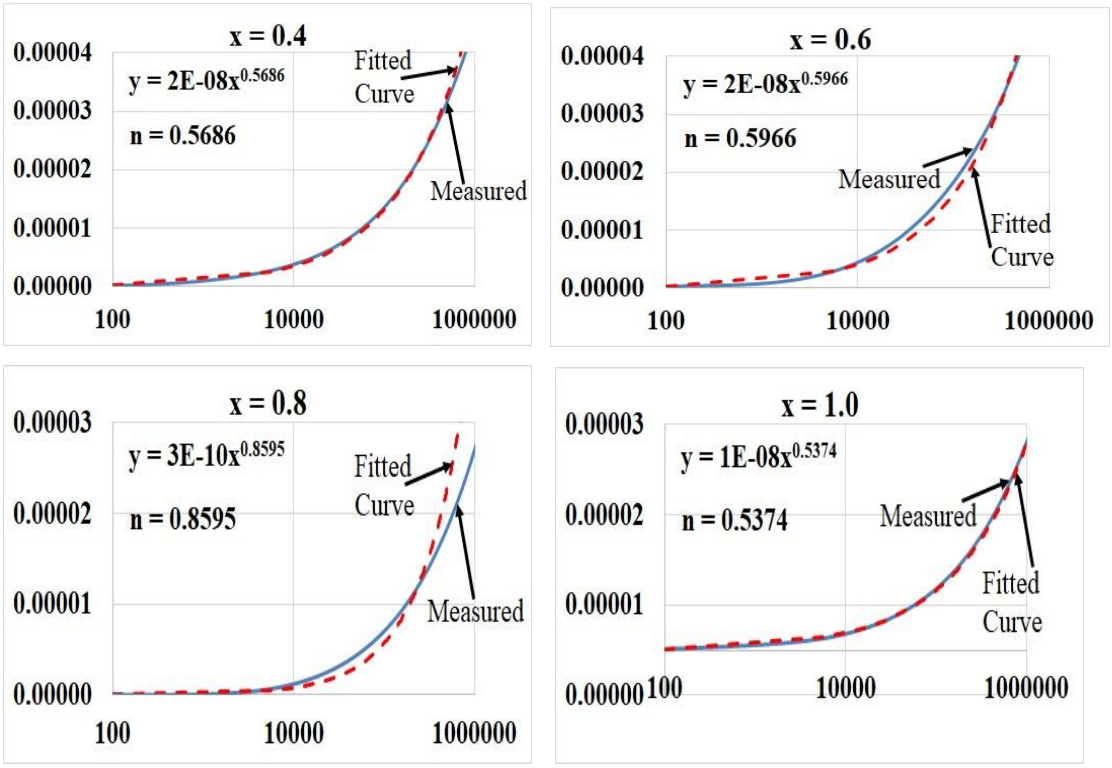

Figure 4.48 Calculation of n for AC conductivity with respect to frequency for ferrite sample $BaCo_xCd_xFe_{12-2x}O_{19}$ (Y0 to Y5, x =0.0, 0.2, 0.4, 0.6, 0.8, and 1.0) which is less than 1.

According to equation (4.37), conductivity is proportional to frequency if ε' is unchanging and there is only a small amount of change in the tangent loss (Y1). Therefore, an increase in frequency results in an increase in the conductivity of AC current. When Y1, AC conductivity is seen to be at its highest possible value. It is possible that the high values are caused by the occurrence of a loss peak at higher frequencies for Y1. This peak may be responsible for the rise in the jumping frequency of electrons. The contribution of grains is responsible for the rise in AC conductivity that occurs in the high frequency band. Figure 4.48 shown the Calculation of n for AC conductivity with respect to frequency for ferrite sample $BaCo_xCd_xFe_{12-2x}O_{19}$ (Y0 to Y5, x = 0.0, 0.2, 0.4, 0.6, 0.8, and 1.0) which is less than 1.

4.3.3.4 Electric modulus analysis

Figure 4.49(a) displays the frequency dependence of the real component of the modulus (M') for all samples of $BaCo_xCd_xFe_{12-2x}O_{19}$ (Y0 to Y5) measured at room temperature. Figure 4.49 shows that the sample standard deviation of M' is highest at

2 MHz, with decreasing values in the lower frequency area. In the low-frequency range, where all the synthesized samples overlap, the M' values exhibit a general tendency to approach zero. Such a standstill is indicative of an electrode polarization distribution with little conductivity and a very strong restoring force [44].The suppression of the electrode polarization phenomenon is reflected in the low frequency region's M' values. The M' value in the low frequency band rises and becomes quite high for samples as the Fe doping concentration rises, indicating that the electrode polarizations effect rises with doping. In the presence of an induced electric field, charge carriers exhibit long-range mobility due to the restoring force regulating their movement. This effect or phenomenon is known as electrode polarizations. Conduction is confirmed to be attributable to the short-range mobility of charge carriers by a rise in the real component of the modulus with an increase in applied frequency [179-180]. With Fe doping, M' values rise dramatically.

In Figure 4.49(b), we see the frequency dependence of the imaginary part of the complex modulus (M''), which provides insight into the relationship between grain boundaries and grains, defects, compositional variations, and cationic distribution, as well as the transport of electric charge and the relaxation phenomenon. Before M'' begins to decrease with increasing frequency, it initially grows to its maximum value.

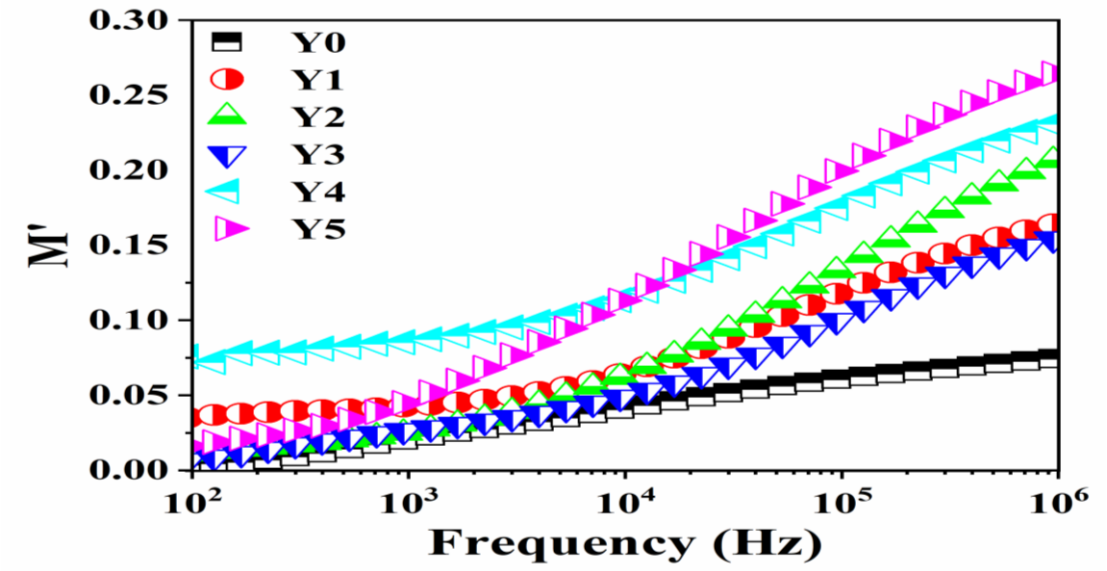

Figure 4.49(a) Variation of the real part of the electric modulus (M′) with frequency of $BaCo_xCd_xFe_{12-2x}O_{19}$ (Y0 to Y5, x =0.0, 0.2, 0.4, 0.6, 0.8, and 1.0) hexaferrite samples heated at 900° C for 5 hours.

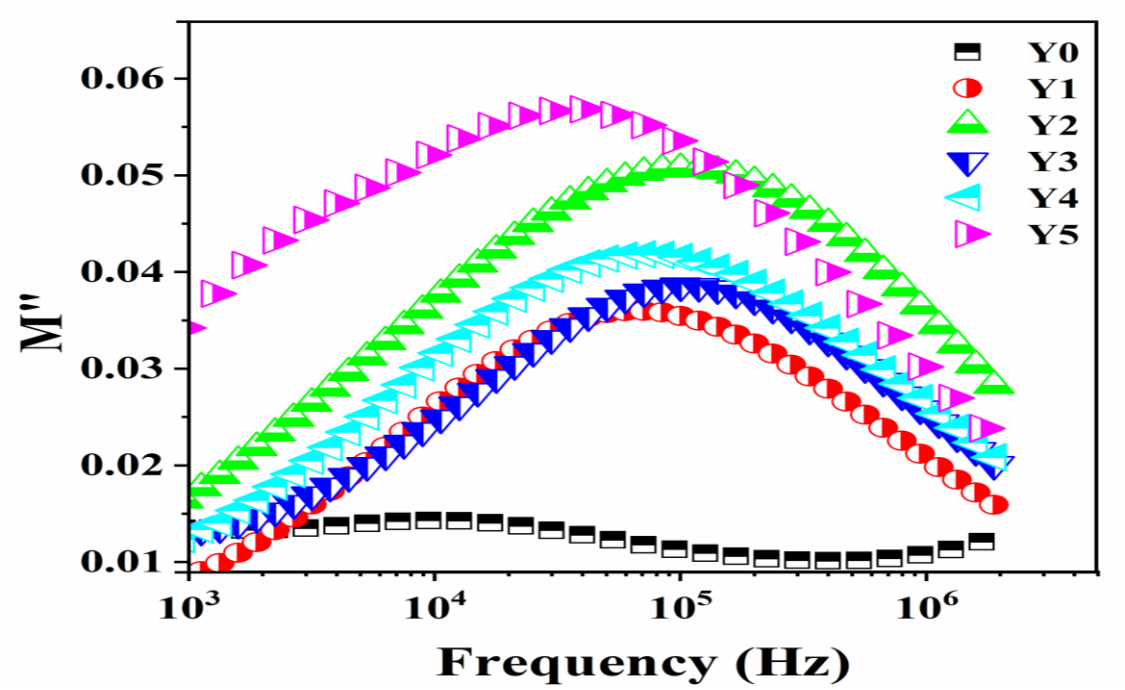

Figure 4.49(b) Variation of the imaginary part of the electric modulus (M″) with frequency of $BaCo_xCd_xFe_{12-2x}O_{19}$ (Y0 to Y5, x =0.0, 0.2, 0.4, 0.6, 0.8, and 1.0) hexaferrite samples heated at 900° C for 5 hours.

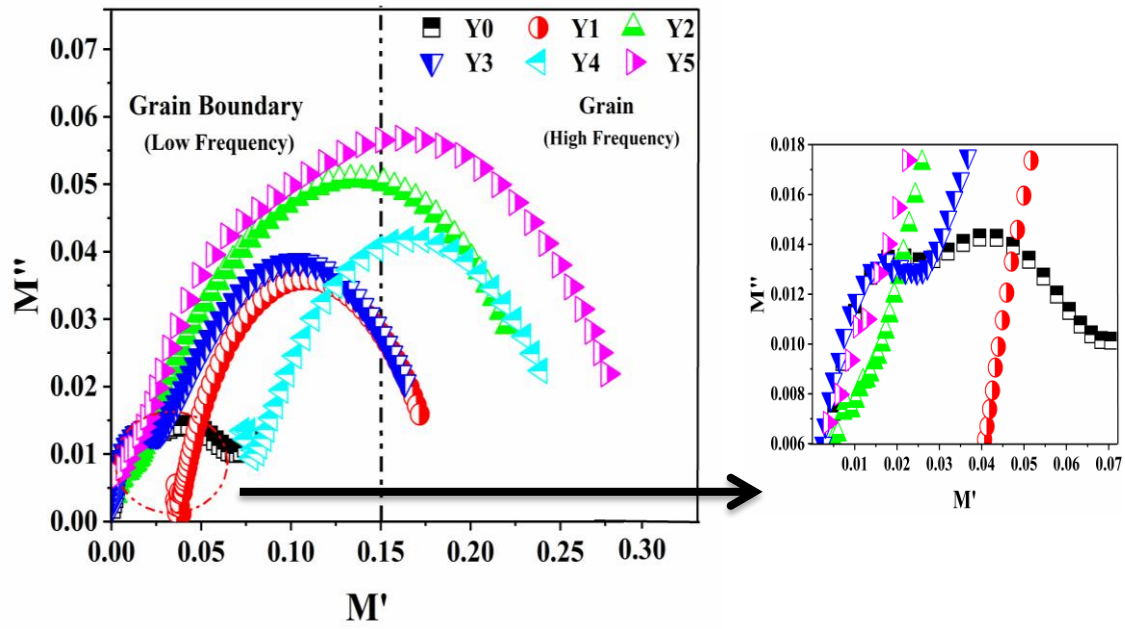

Figure 4.49 (c) Variation of the Cole-Cole type plot of $BaCo_xCd_xFe_{12-2x}O_{19}$ (Y0 to Y5, x =0.0, 0.2, 0.4, 0.6, 0.8, and 1.0) hexaferrite samples heated at 900° C for 5 hours.

As a result of (i) the appearance of asymmetrical peak maxima at characteristic frequency values (f_{max}), (ii) the broadening of peaks with increasing Co-Cd contents, indicating the existence of relaxation mechanisms for the hexagonal ferrites [181], and (iii) the shifting of these peaks towards high frequency with an increasing variation of x, the observed M'' spectrum of our synthesized compositions can be critically resolved. To what extent charge carriers are able to hop from one nearby octahedral site to another, sustaining their long-range mobility under the effect of grain boundary dominance, is shown by the frequency regime before the peak maxima. The spatial confinement of charge carriers to their potential wells of grains is represented by the higher frequency area on the far side of the peak [182]. The change from long-range to short-range order in mobility and relaxation time dispersion may be seen in the frequency band beneath the asymmetrical peaks. Carrier inhomogeneity due to crystalline defects causes this transition, which points to an interaction mechanism other than the Debye type and ionic contacts [183].

As shown in Figure 4.49(c), the produced hexagonal ferrites were analyzed using Cole-Cole plots (M'' versus M') to investigate the importance of grains and grain boundaries. Except for Y0 and Y3, all compositions have a single semi-circle on the Cole-Cole plot. The grain boundary contribution is seen by the area under the curve at intermediate frequencies [184], whereas the left side of the semicircle, towards the lower frequency zone, adds to the grain resistance [185]. Grain and boundary resistance may be seen in the higher frequency area on the far right [186]. When Co-Cd is doped, the arc moves to the high-frequency domain, and the intercept of the semicircular arc becomes larger. The distribution of relaxation time is shown by the shift in the maximum of the semicircle for the highest frequency as a function of doping. The non-Debye relaxation [187] is supported by this distribution.

The semicircular shape of the Cole-Cole plot is characteristic of materials with a single dielectric relaxation process. The centre of the semicircle represents the DC (direct current) conductivity, while the radius of the semicircle is related to the relaxation time of the material. The sharper the curvature of the semicircle, the more well-defined and single the relaxation process is. When multiple relaxation processes are present, the Cole-Cole plot may show multiple semicircles or deviations from the ideal semicircular shape. The absence of a semicircle in a Cole-Cole plot when

analyzing M-type Hexagonal Ferrites is likely due to the complex dielectric behaviour of these materials. The Cole-Cole plot is typically used to analyze dielectric spectra and determine the dielectric relaxation processes in materials. In some cases, the dielectric behaviour of materials, especially those with structural complexity, may not conform to the simple Debye or Cole-Cole model, resulting in deviations from the expected semicircular shape. Dielectric relaxation is a phenomenon where electric dipoles or charges in a material respond to an applied electric field. These dipoles or charges might need some time to align themselves with the changing field, and this time delay is frequency-dependent. Dielectric relaxation processes are common in materials with polarizable components.

4.3.3.5 Impedance spectroscopy

Figure 4.50(a) and Figure 4.50(b) showing the variation of real and imaginary part of impedance with frequency and by contrasting the real (Z') and imaginary (Z'') components, we get the Cole-Cole charts as shown in Figure 4.50(c), also known as complex impedance plots. Two overlapping semicircles make up the impedance in a Cole-Cole distribution based on a two-layer model. The low frequency semicircle represents the grain boundary resistance, whereas the high frequency semicircle indicates the grain or bulk property resistance [182-183]. The distribution of relaxation times is linked to this phenomenon. The impedance responses from the grain and grain border, however, will greatly overlap if the time constant of distinct processes vary by less than a factor of 100. Complex impedance plot behaviour is also grain size dependent. Whereas one semicircle represents both the grain boundary and grain resistance in small-grain samples, large-grain samples display two semicircles. The complex impedance, or Cole-Cole plot, was obtained at room temperature for all compositions in this investigation. Conduction owing to the grain boundary was observed to result in just a single, incomplete semicircle across all samples except for those with Y0.

This points to a strong resistance at the grain boundaries, and the grain's contribution was not clearly distinguished in these samples. A lower concentration of Fe^{3+}, a larger surface-to-volume ratio, increased porosity, and a disorganized atomic arrangement at the grain boundary are all possible causes of the increased value of grain boundary resistance [184].

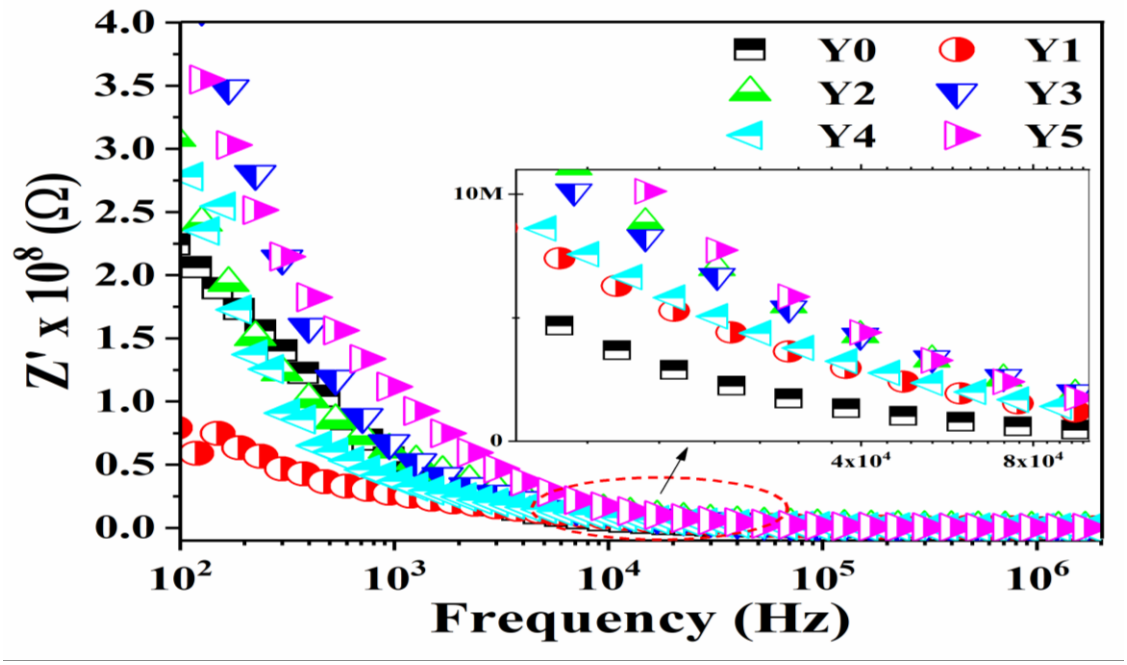

Figure 4.50(a) Variation of the real part of the Impedance (Z') with frequency of $BaCo_xCd_xFe_{12-2x}O_{19}$ (Y0 to Y5, x = 0.0, 0.2, 0.4, 0.6, 0.8, and 1.0) hexaferrite samples heated at 900° C for 5 hours.

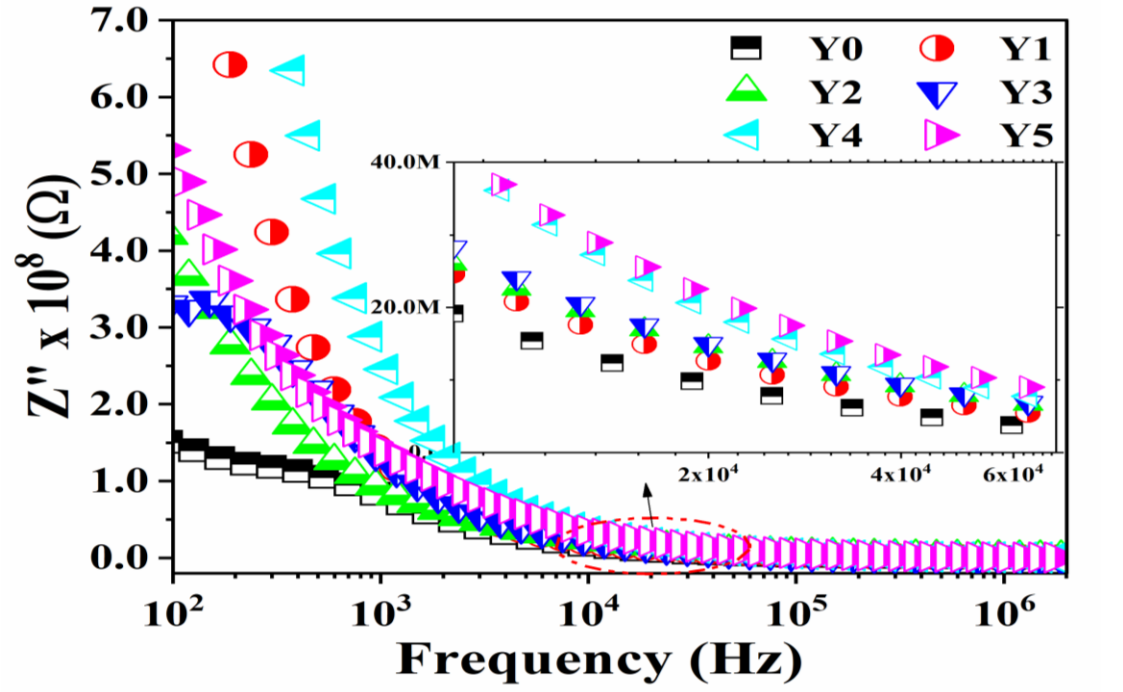

Figure 4.50(b) Variation of the imaginary part of the Impedance (Z") with frequency of $BaCo_xCd_xFe_{12-2x}O_{19}$ (Y0 to Y5, x = 0.0, 0.2, 0.4, 0.6, 0.8, and 1.0) hexaferrite samples heated at 900° C for 5 hours.

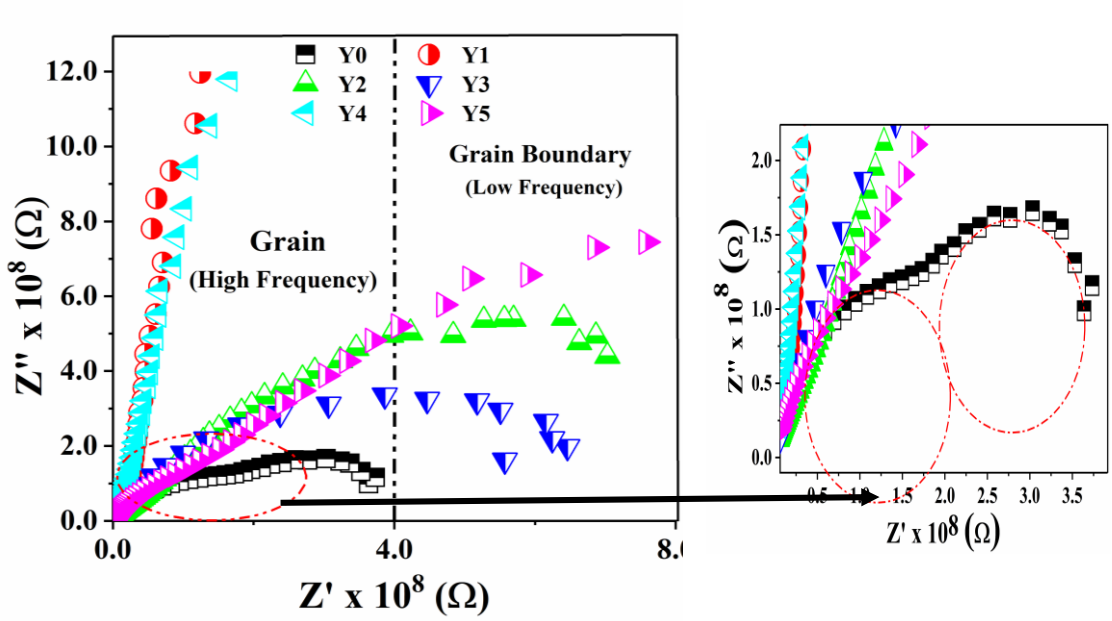

Figure 4.50(c) 51Variation of the Cole-Cole type plot of $BaCo_xCd_xFe_{12-2x}O_{19}$ (Y0 to Y5, x =0.0, 0.2, 0.4, 0.6, 0.8, and 1.0) hexaferrite samples heated at 900° C for 5 hours.

4.3.3.6 Software-based Impedance Simulation and Validation

The Figure 4.52 shows that there is a high degree of agreement between the observed curves and the simulated/fitted curves for all mixtures. Tables 4.18 show the expected relaxation time, resistance, and capacitance of grains and grain boundaries using EIS.

Table 4.18 Grain and Grain boundary parameters derived from EIS software

X	R_g (MΩ)	R_{gb} (MΩ)	C_g (μF)	C_{gb} (μF)	τ_g (Sec)	τ_{gb} (Sec)
Y0 (0.0)	207.060	239.480	20.827	8691.223	4.312E+03	2.081E+06
Y1 (0.2)	18.236	863.080	49.913	1.111	9.102E+02	9.591E+02
Y2 (0.4)	95.068	1029.200	746.594	5.802	7.098E+04	5.971E+03
Y3 (0.6)	314.130	498.650	20231.427	2.807	6.355E+06	1.400E+03
Y4 (0.8)	15.150	1081.000	16.102	0.560	2.439E+02	6.049E+02
Y5 (1.0)	210.140	1100.000	47.950	2.293	1.008E+04	2.522E+03

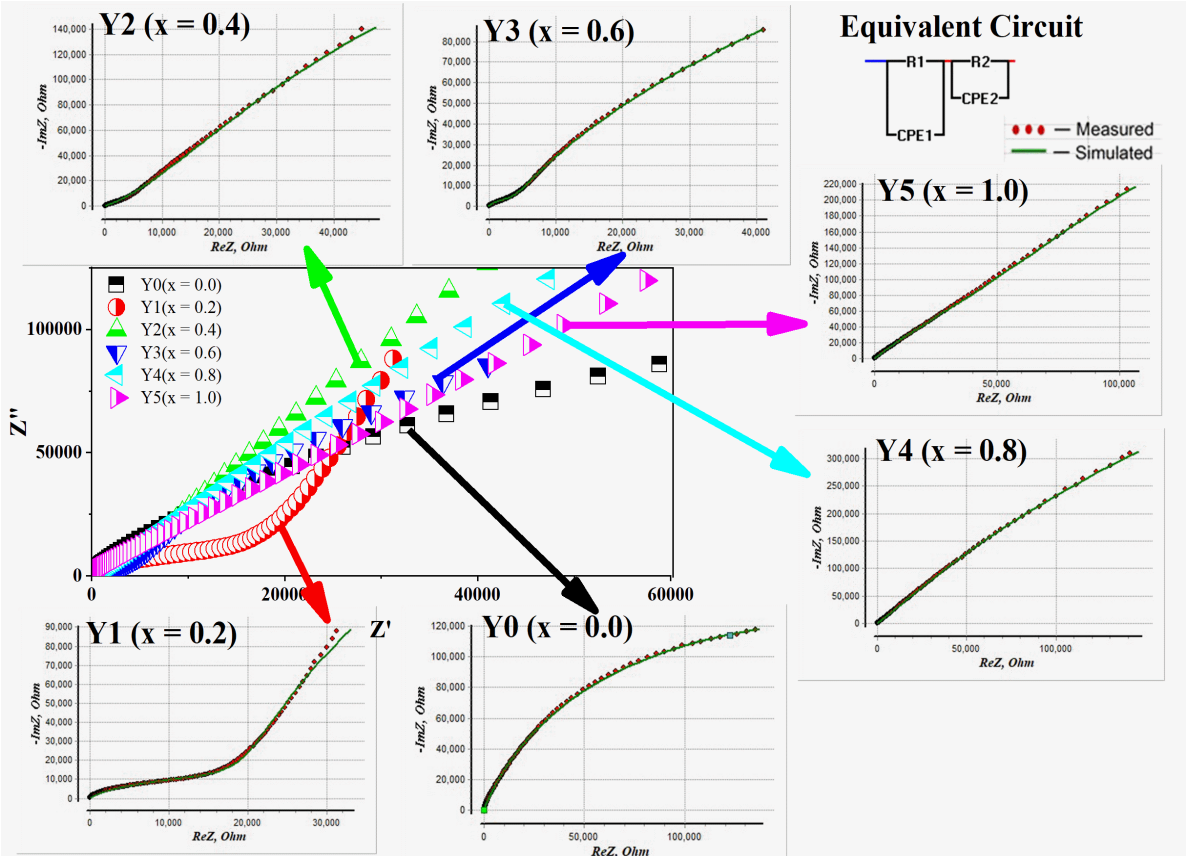

Figure 4.52 Complex impedance plots for ferrite samples (red points-measured values, green lines-fitted values) and an applied equivalent circuit.

4.3.3.7 Correlation between EIS parameters and Morphology

In Figure 4.46, it shows the sample Y0 having smaller grain sizes, which is associated with higher grain boundary density, which produces more grain boundaries per unit volume. Due to the enhanced dispersion of charge carriers at these interfaces, this higher density of grain boundaries may improve grain boundary resistance R_{gb} = 239.48 MΩ. Additionally, the higher surface area-to-volume ratio caused by smaller grain sizes might enhance (maximum) grain boundary capacitance C_{gb} up to 8691.22 µF. In a material's structure of Y0, porosity is the existence of voids or empty spaces. The introduction of porosity may cause the continuity of the grains to break down in M-type hexagonal ferrites, resulting in isolated patches. The movement of charge carriers through the material is impeded by these spaces, which serve as insulating barriers. Because there is less effective cross-sectional area available for charge transport, the porosity raises the grain resistance, R_g = 207.06 MΩ. For Y0, smaller grain sizes lead to quicker grain time constants (second, smaller τ_g values = 4.31E03

sec). This is because smaller grains have a higher ratio of surface area to volume, which makes surface effects stronger, polarisation stronger, and charge carrier dynamics work better. So, the processes of relaxation inside the smaller grains happen more quickly, leading to lower time constants. Lower grain boundary densities typically result in larger grain boundary time constants (largest τ_{gb} values = 2.081E+06 sec). This is because a lower density of grain boundaries provides fewer sites for charge carrier transport and trapping, leading to less rapid relaxation processes and larger time constants. For Y1, it is shown from Figures 4.46 and Figure 4.53 that materials have different grain size and crystal orientations, which increase the grain boundary resistance R_{gb} = 863.08 MΩ. The presence of heterogeneities in the morphology for Y1 can also affect the connectivity and continuity of the grain boundaries. Discontinuities or variations in grain boundary connectivity can lead to higher overall grain boundary resistance in materials with a heterogeneous morphology, as reflected in Table 4.18. For Y2, fusion of grains occurs, which leads to an increase in grain size and can have a direct effect on grain capacitance C_g. Larger grains generally have a higher capacitance due to their increased surface area and larger volume for charge accumulation. Therefore, fusing smaller grains into larger grains results in increased grain capacitance reached up to 746.59 μF. The fusion process introduces new defects, impurities, or structural changes at the fused grain boundaries. As a result, increase in the grain boundary resistance R_{gb} = 1029.20 MΩ from 746.59 MΩ. For example, if the fusion leads to the formation of disordered or structurally different regions at the grain boundaries, it can impede charge transport and increase resistance, as shown in Table 4.18.

For Y3, grain size reached its highest and also the highest C_g = 20231.427 μF occurred, and larger grain sizes typically result in slower grain time constants (Highest τ_g values = 6.355E+06 sec). This is because larger grains have a lower surface-to-volume ratio, leading to decreased surface effects, enhanced polarization, and more efficient charge carrier dynamics. Consequently, the relaxation processes within the higher grains occur very slowly, resulting in longer time constants. Also, increase grain resistance from 95.068 to 314.130 MΩ due to larger grain sizes. For Table 4.18, R_{gb} also equal 498.650 MΩ because of the multilayer grain structure as

shown in Figures 4.46 and 4.53. Multi-layer grains typically have more grain boundaries compared to single-layer grains.

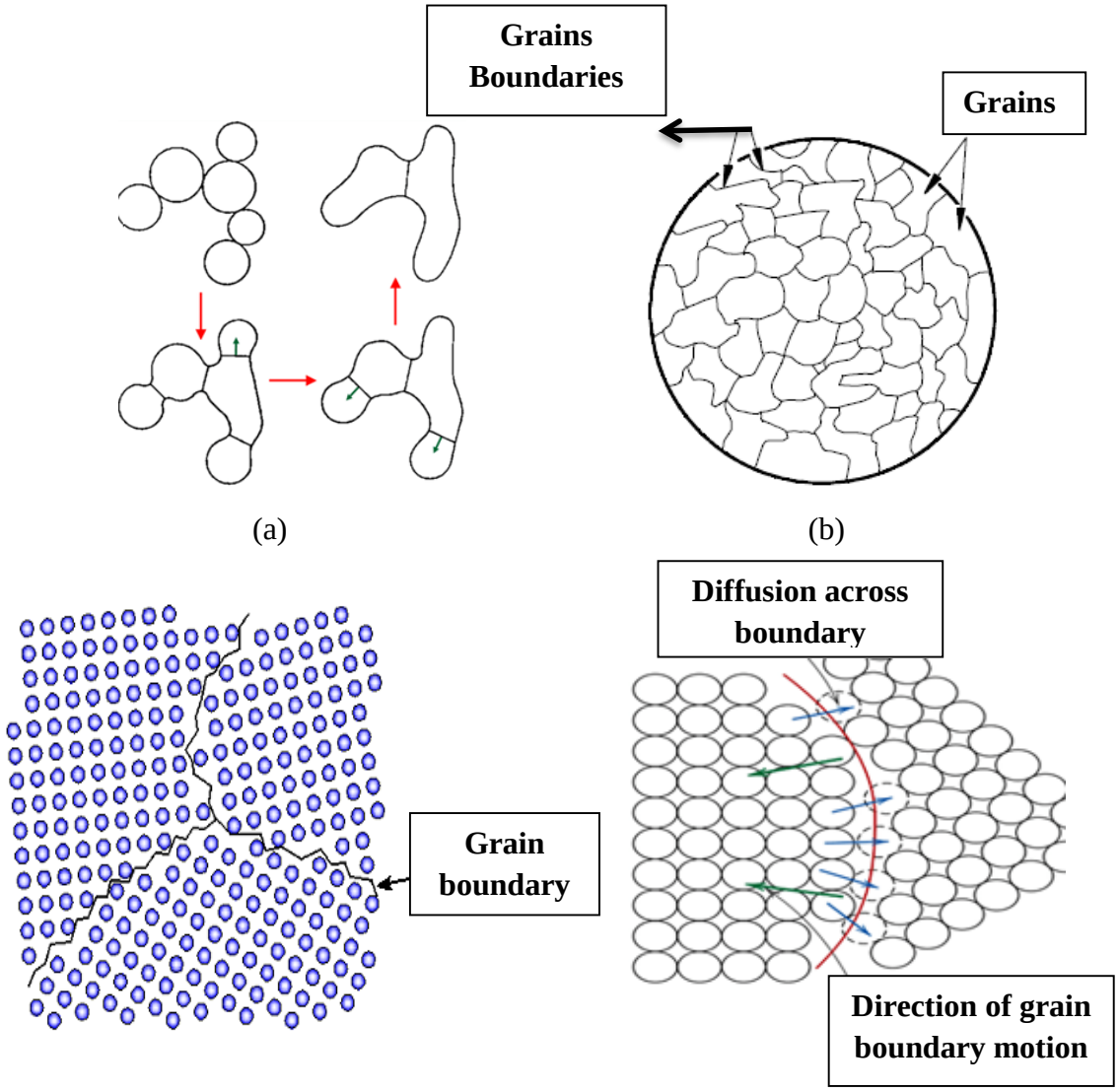

Figure 4. 53 (a) Migration of grain process; (b) Represent Grain and Grain Boundaries; (c) Separation of grain and identification of grain boundaries; (d) Diffusion across boundary for $BaCo_xCd_xFe_{12-2x}O_{19}$ (Y0 to Y5, x =0.0, 0.2, 0.4, 0.6, 0.8, and 1.0).

The additional layers result in an increased number of grain boundaries per grain volume. This increased grain boundary area can affect the electrical and mechanical properties of the material. For Y4, grain fuse but easily identify the grain boundary and lowest R_g = 15.150 MΩ because it is not able to form larger grains after fuse and R_{gb} increases and reaches up to 1081 MΩ and smaller grains have a higher surface-to-

volume ratio, leading to increased surface effects, enhanced polarization, and more efficient charge carrier dynamics. Consequently, the relaxation processes within the smaller grains occur more rapidly, resulting in shortest time constants = 2.439E+02 sec. For Y5, as grain fusion occurs, which raises the value of R_g from 15.15 to 210.014 (the second largest value), the size of the grain decreases, increasing grain boundary resistance, and reaching highest value of R_{gb} = 1100.00 MΩ.

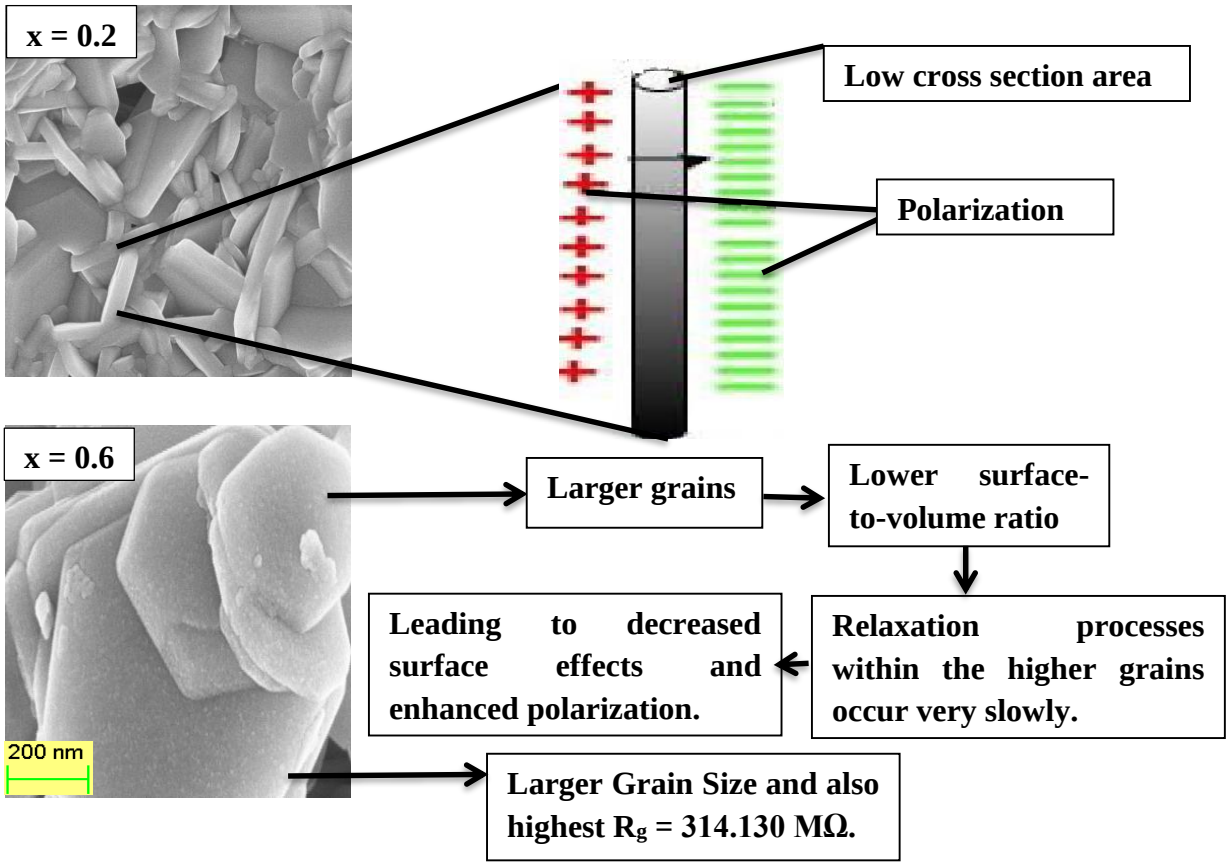

Figure 4.54 SEM micrographs of ferrite samples of $BaCo_xCd_xFe_{12-2x}O_{19}$ (Y1 and Y3)

The dielectric constant of a material is a measure of its ability to store electrical energy in an electric field. The correlation between dielectric constant and grain or grain boundary in a material can be influenced by several factors, like grain size as shown in Figure 4.53. In materials with smaller grain sizes, there is an increased grain boundary area per unit volume compared to materials with larger grain sizes. The grain boundaries can introduce interfacial effects that affect the dielectric behaviour. Therefore, materials with smaller grain sizes tend to exhibit higher dielectric constants due to the increased contribution from grain boundaries. The similar behaviour

observed in the Y0 is that it has the highest dielectric constant, i.e 135.94, and also has 239.8 MΩ grain boundary resistances. Grain boundaries often exhibit different dielectric properties compared to the grains themselves.

They can act as localized regions with distinct capacitance behaviour due to structural differences or impurity segregation. The presence of additional capacitance at the grain boundaries (C_{gb} = 8691.22 μF) can contribute to an increase in the overall dielectric constant of the material. For Y4 having the lowest dielectric constant, i.e 19.373 with the lowest capacitance values at the grain and grain boundary, i.e C_g = 16.10 μF and C_{gb} = 0.55 μF. This implies a reduced ability to store electrical energy and lower charge accumulation at the grain and grain boundary interfaces. In a doped sample, the highest dielectric constant is 116.97 for Y3 and also due to the fusion of grain, the larger grain size formed also has the highest capacitance, C_g = 20231.43 μF due to their larger surface area, which provides more space for charge accumulation. Additionally, the shape of the grain can affect its effective capacitance. Grains with irregular shapes or higher aspect ratios may have different capacitance values compared to more uniform or spherical grains.

The size and shape of the grains or particles in a material can also affect its dielectric loss. Materials with smaller grains or particles tend to have lower dielectric losses, as shown for Y1 and Y4 in Figure 4.46, because they have a larger surface area to volume ratio, which can reduce the contribution of interfacial losses. In contrast, materials with larger grains or particles may have higher dielectric losses, as seen in Y3, where the dielectric loss is 402.63 highest among all the doped samples.

In Figure 4.47(c), highest tangent loss is shown in the undoped sample for Y0, which is 3.67, because materials with a more heterogeneous morphology, where the distribution of grains is not uniform, can exhibit a higher loss tangent due to the presence of interfaces between different regions of the material. The interfaces can lead to additional energy dissipation due to interfacial polarization and other effects. The loss tangent can be influenced by the interfacial interactions between grains and grain boundaries. These interactions can contribute to energy dissipation and affect the overall loss tangent of the material. The nature of these interfacial effects depends on factors such as the grain boundary structure, charge accumulation, and polarization behaviour. For Y3, exhibit a higher loss tangent in doped samples. Variations in the

grain size, distribution, or orientation can impact the mobility of molecules or segments within the material. Changes in morphology can affect the extent and dynamics of molecular motion, resulting in shifts or modifications in the relaxation peak observed in the loss tangent curve.

For Y2, having the highest height of relaxation peaks is related to the concentration and distribution of charged species, such as Fe^{3+} ions, within the material. In general, materials with a more homogeneous and uniform morphology tend to have a more uniform distribution of charged species, leading to a more well-defined and higher relaxation peak. This is because the relaxation peak corresponds to the maximum energy dissipation that occurs as the charged species respond to the applied electric field by reorienting or moving within the material. For Y1 and Y4, the height of the relaxation peak may be lower due to the reduced concentration or non-uniform distribution of charged species.

4.3.3.8 Simulated Grain/Grain boundary parameters and AC Conductivity

The grain size and grain boundary features, as well as the porosity or density, of a material may affect its AC conductivity. For instance, the AC conductivity may drop in very porous materials because the air inside the pores disrupts the free movement of charge carriers. In contrast, a greater number of charge carriers might boost the AC conductivity of dense materials. Higher R_{gb} values result in increased resistance at the grain boundaries, leading to a decrease in AC conductivity. For Y5, R_{gb} is 1100 MΩ and the same sample has the lowest AC Conductivity (3.16E-05 Ωm^{-1}). Similarly, for Y0, R_{gb} is lowest (239.48 MΩ) and the same sample has the highest AC Conductivity (0.00022 Ωm^{-1})

$$R_{gb} \propto 1/(AC\ Conductivity)$$

The AC conductivity of a material is related to its ability to transport charge carriers, such as electrons or ions, in response to an applied electric field. In materials with a more uniform and homogeneous morphology, the charge carriers can move more freely and easily, leading to a higher conductivity at Y0 (0.00022Ωm^{-1}). Higher capacitance values, including both C_g and C_{gb}, indicate greater charge storage capabilities, which can enhance AC conductivity. Increased capacitance allows for a higher density of charge carriers and more efficient charge transport, leading to enhanced AC conductivity. For Y0, highest C_{gb} = 8691.22 μF corresponds to the

highest AC conductivity for the same sample (0.00022 Ωm^{-1}). For Y3, Highest Cg = 20231.42 μF correspond to second highest AC conductivity (7.91E-05 Ωm^{-1}).

4.3.3.9 Simulated Grain/Grain boundary parameters and Electric Modulus

Higher R_g values can result in a decrease in M′ at low frequencies, indicating reduced energy storage capabilities because higher grain resistance leads to increased energy dissipation and a reduced ability to store electrical energy. So from Table 4.18, for Y3, R_g is 314.13 MΩ is the highest grain resistance, but from Figure 4.49(a), the same sample has a lower M′ value equal to 0.17. Similarly, the lower the value of R_g = 15.15 MΩ higher the M′ value = 0.24.

$$\boldsymbol{Grain\ Resistance\ (R_g)\ \propto\ 1/(Real\ part\ of\ Electric\ Modulus\ (M'))}$$

Similarly, the imaginary portion of the electric modulus (M″), which characterizes the materials dissipative or loss qualities, may be influenced by variations in R_g, R_{gb}, C_g, and C_{gb}. An increase in either R_{gb} or C_{gb} may cause M″ to rise because of the enhanced dissipation of electric energy at the grain boundaries. From Table 4.18, it is clearly observed that R_{gb} is maximum at Y5 i.e. R_{gb} = 1100 MΩ but for the same sample, M″ is also highest, i.e M″ = 0.06 and lowest at Y0 i.e R_{gb} = 239.48 MΩ and M″ = 0.01.

$$\boldsymbol{Grain\ Boundary\ Resistance\ (R_{gb})} \propto \boldsymbol{Imaginary\ part\ of\ Electric\ Modulus\ (M')}$$

Composition Y0 (Figure 4.49) showed that grain boundaries had a more significant effect than grains themselves, with relaxation taking the shape of a semicircle whose area was concentrated in the low-frequency zone. Doping shifted the semicircle's role to that of grains in the Y2, Y4 and Y5 composition by moving it to the high-frequency region. For Y5, having smaller grain sizes can also lead to a higher density of charge within the material, which can increase the overall polarization and lead to the highest electric modulus value of 0.06.

In Figure 4.49(c), for Y0, the presence of two relaxation peaks in the Cole-Cole plot can indicate the two mechanisms of relaxation (conductivity and dielectric relaxation). In this sample, the grain gathering together of individual grains forms larger structures, due to which grain boundaries increase as larger grains are the summation of tiny grains and enhance the polarization and contribute to the conduction relaxation mechanism in the low frequency region. Higher values of R_g

and R_{gb} can shift the relaxation processes to higher frequencies or broaden the distribution of relaxation times. Higher capacitance values (C_g and C_{gb}) can lead to a steeper slope in the Cole-Cole plot at lower frequencies, indicating a higher degree of polarization and charge storage. Similarly, the pattern observed in Figure 4.49 and Table 4.18, R_g and R_{gb} equal to 210.14 MΩ and 1100 MΩ shift the graph in the high frequency region, as does the maximum diameter of the semicircle at Y5. Larger grains typically exhibit lower resistive contributions (M′) and a more linear frequency dependence of M″ due to enhanced charge transport. The presence of grain boundaries can lead to deviations from ideal behaviour and the appearance of semicircular arcs in the Cole-Cole plot. The semicircular arc in M″ indicates a relaxation process associated with the grain boundary effects, such as charge accumulation and relaxation at the interfaces.

$$\boldsymbol{Radius\ of\ Semicircle\ in\ the\ Cole\ Cole\ Plot} \propto (\boldsymbol{Sum\ of\ R_g\ and\ R_{gb}})$$

The highest sum of R_g and R_{gb} is 1310.14 MΩ for Y5 and the same sample has the highest diameter of a semicircle in the plot. For Y3, the presence of two relaxation peaks in the Cole-Cole plot can indicate the two mechanisms of relaxation (conductivity and dielectric relaxation). In this sample, the first relaxation peak is due to conductivity relaxation in the low frequency region, while the second peak crosses the intermediate frequency region, where grain resistance R_g = 314.13 MΩ is contributing and dielectric relaxation is also occurring. In the sample, Y2, Y4 and Y5, but moving towards the high frequency region and grain boundary contributed more. The presence of a semicircular arc in the Cole-Cole plot suggests the occurrence of a relaxation process involving charge accumulation and relaxation in the material.

4.3.3.10 Simulated Grain/Grain boundary parameters and Impedance spectroscopy

In Figure 4.50 (C), for Y0, the presence of two relaxation peaks in the Cole-Cole plot can indicate the two mechanisms of relaxation (conductivity and dielectric relaxation). In this sample for the high frequency region, the first semicircle is due to dielectric relaxation and grain resistance impact, and the second semicircle is reaching towards intermediate frequency and grain as well as grain boundary resistance contributing (R_{gb} is more than R_g). For Y2, Y3, and Y5, it moves from the low frequency region to the high frequency region, which means both resistances

contribute. For Y3, fusing of grain occurs, due to which grain resistance increases and reaches up to 498.65 MΩ. In a Cole-Cole plot, the position and shape of the semicircular arc can provide insights into the grain boundary properties, including resistance and capacitance.

- Position of the Semicircular Arc:
  - The position of the semicircular arc in the Cole-Cole plot is determined by the frequency at which the relaxation process associated with the grain boundaries occurs.
  - The relaxation process can be attributed to the charge accumulation and relaxation at the grain boundaries.
  - The lower the frequency at which the semicircular arc appears, the slower the relaxation process at the grain boundaries.
- Shape of the Semicircular Arc:
  - The shape of the semicircular arc in the Cole-Cole plot indicates the impedance response of the grain boundaries.
  - The curvature of the arc reflects the resistance and capacitance associated with the grain boundaries.
  - A smaller radius of the semicircular arc suggests lower grain boundary resistance and higher conductivity. For Y0, semicircular arc is smallest and same sample correspond lowest R_{gb} = 239.48 MΩ and highest conductivity (0.00022 Ωm^{-1}).

4.3.4 Magnetic Analysis

In the $BaCo_xCd_xFe_{12-2x}O_{19}$ compound, the Cadmium ion (Cd^{2+}) has a slightly lower electronegativity (1.69) in comparison to the Cobalt ion (Co^{2+}) which has an electronegativity of 1.88. Due to their different properties, Cd^{2+} can occupy tetrahedral sites $4f_1$ while Co^{2+} can occupy octahedral sites. In M-type barium hexagonal ferrites, the Fe^{3+} atoms are distributed across five different sites. These include two tetrahedral sites (2b and $4f_1$) and three octahedral sites (2a, 12k, and $4f_2$). Out of all these sites, 2a, 2b, and 12k have a spin up, while $4f_1$ and $4f_2$ have a spin down [4].

Co^{2+} ions have a tendency to occupy octahedral sites with a d^7 configuration, but Cd^{2+} ions do not have a preference for any specific site owing to their d^0 configuration.

According to reports, Co^{2+} ions have a preference for occupying the $4f_1$, $4f_2$, and 2b sites. Furthermore, it is worth noting that both Cd^{2+} (with an ionic radius of 0.96 Å) and Co^{2+} (with an ionic radius of 0.72 Å) ions have higher ionic radii compared to the host Fe^{3+} ions (with an ionic radius of 0.64 Å). As a result, both Cd^{2+} and Co^{2+} ions are capable of occupying octahedral positions at the borders of the unit cell [183].

Figure 4.55 demonstrates the hysteresis loops of all $BaCo_xCd_xFe_{12-2x}O_{19}$ samples at room temperature. The results obtained from the M-H loop are shown in Table 4.19. The values include saturation magnetization (M_s), remanence magnetization (M_r), coercivity (H_c), and anisotropy field (H_a), and remanence ratio (M_r/M_s). Through the examination of the arrangement of host and substituted cations across five crystallographic sites inside a hexagonal crystal structure, which is defined by the equation, it is possible to get insight into the magnetic moment of the specimen. [184].

$$M_s = M_a(2a + 12k + 2b)(\uparrow) - M_b(4f_1 + 4f_2)(\downarrow) \quad (4.9)$$

Through the substitution of ions that have weaker magnetic properties or are non-magnetic at the ($4f_1\downarrow + 4f_2\downarrow$) lattice site, there is an increase in the overall magnetization. Nevertheless, when these ions are replaced at the ($2a\uparrow + 12k\uparrow + 2b\uparrow$) lattice sites, the magnetization displays a decrease in behaviour [226]. Table demonstrates a non-monotonic drop in M_s as the quantity of substitution increases from Y0 to Y5. A gradual increase in the value of M_s from 87.98 to 101.60 as the Co-Cd ions are substituted in the Y0 to Y1 samples [284]. One possible explanation for this phenomenon is the presence of spin-down sites being occupied by these substituents. In addition, there is a decrease in the value of M_s upto 93.126 from Y1 to Y3, and it is then observed to slightly increase for Y4 and reached again 100.83. In addition, the densification of grains in the Y4 sample leads to a decrease in defects and grain boundaries within the material. It enhances the alignment of magnetic moments of atoms found within the grains. When a field is applied to the material, a significant number of magnetic moments effortlessly align themselves in a specific direction, enhancing the overall magnetization of the material and leading to a high M_s. Finally, there has been a decrease from 100.83 to 82.96 for Y5 (x = 1.0).

The coercivity (H_c) of a material is determined by several variables, including both internal and external influences. The precise structure arrangement of atoms inside the

crystal lattice is essential for intrinsic (internal) properties. The parameter H_a, which represents the material's magnetic reversal resistance, is closely associated with H_c. The interaction between these sites in the lattice is significantly influenced by their occupancy, namely the $4f_2$ and 2b sites. The presence of iron ions at these places has a significant impact on H_a and, as a result, H_c. The significance of the issue resides in the influence of extrinsic elements such as grain size and porosity. Greater grain size often correlates with elevated H_c levels. The reason for this phenomenon is that bigger grains provide a more efficient route for magnetic domains, which are regions with aligned magnetic moments, to traverse. As a result, the process of demagnetizing the material becomes progressively more difficult. Pores, which are vacant areas, may have a significantly disruptive impact. They diminish the magnetic volume and lessen the capacity to withstand demagnetization. Therefore, materials that have a greater amount of pores often exhibit lower values of H_c.

The coercivity (H_c) of the material is often decreased by the introduction of foreign atoms (dopants) via the process of doping. The data shows a noticeable trend, as the H_c value decreases from 4596.72 Oe in the undoped sample (Y0) to 228.98 Oe when completely doped (Y5). The sample without any doping (Y0) has the greatest values for coercivity, measuring at 4596.72 Oe. The remarkable success of this performance may be credited to the lack of any extraneous particles that disturb the crystal structure and the ideal arrangement of iron ions, namely at the $4f_2$ and 2b sites. The decline in H_c, which is seen when the Cd replacement increases from Y0 to Y5, may be related to the fluctuation in the anisotropy field (H_a). H_a is the amount of energy needed to modify the orientation of the magnetic moments in the substance. A greater H_a value indicates a more robust resistance to magnetic reversal. As a consequence, the material requires more energy to overcome its resistance and lose its magnetic, leading to an increase in coercivity (H_c). The anisotropy field (H_a) is mainly influenced by the magnetic moments of iron ions situated in the $4f_2$ and 2b positions of the crystal lattice.

The remanent magnetization (M_r) of the samples diminishes as the concentration of Cd^{2+} ions (x) in $BaCo_xCd_xFe_{12-2x}O_{19}$ increases. The observed decline in magnetization, from an initial magnitude of 46.29 emu/g to a final magnitude of 22.37 emu/g (Table 4.19), may be ascribed to the impact of Cd^{2+} on the alignment of magnetic moments

inside the substance. When Cd^{2+} replaces Fe^{3+}, it has the capacity to disrupt the exchange interactions that are crucial for aligning these magnetic moments.

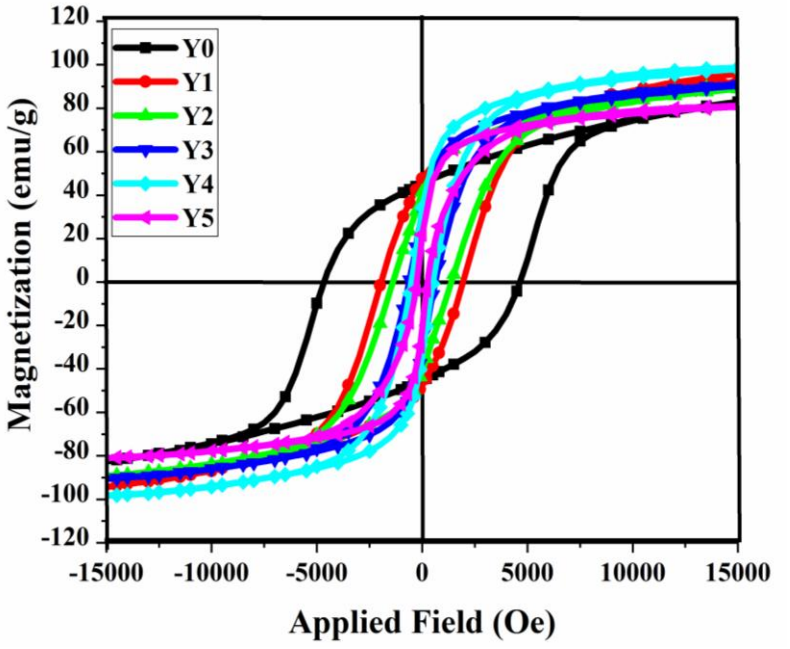

Figure 4.55. Hysteresis loops of Y0, Y1, Y2, Y3, Y4 and Y5 hexaferrite.

Table 4.19. Magnetic parameters determined from M-H curves

Sample	M_s (emu/g)	H_c (Oe)	H_a(kOe)	M_r (emu/g)	M_r/M_s
Y0	87.9783	4596.719	15.33462	44.59666	0.506905
Y1	101.6035	1930.964	14.21911	46.295	0.455644
Y2	93.12624	1349.966	12.80732	40.928	0.439489
Y3	93.37669	686.9446	11.11007	33.4559	0.35829
Y4	100.8321	475.0513	10.20625	34.27	0.339872
Y5	82.9612	228.9815	9.970796	22.37	0.269644

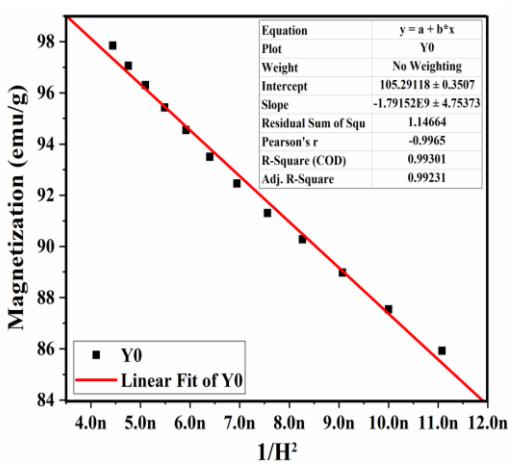

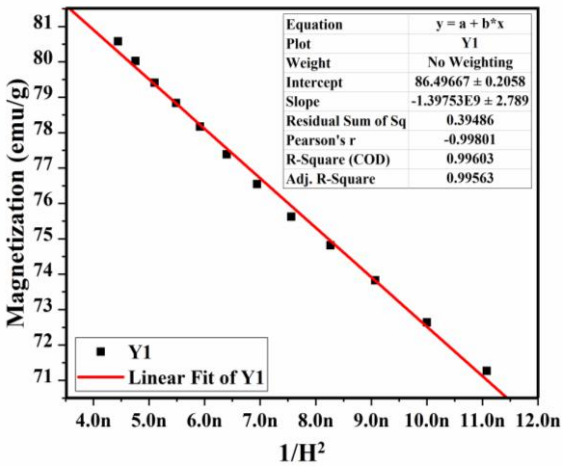

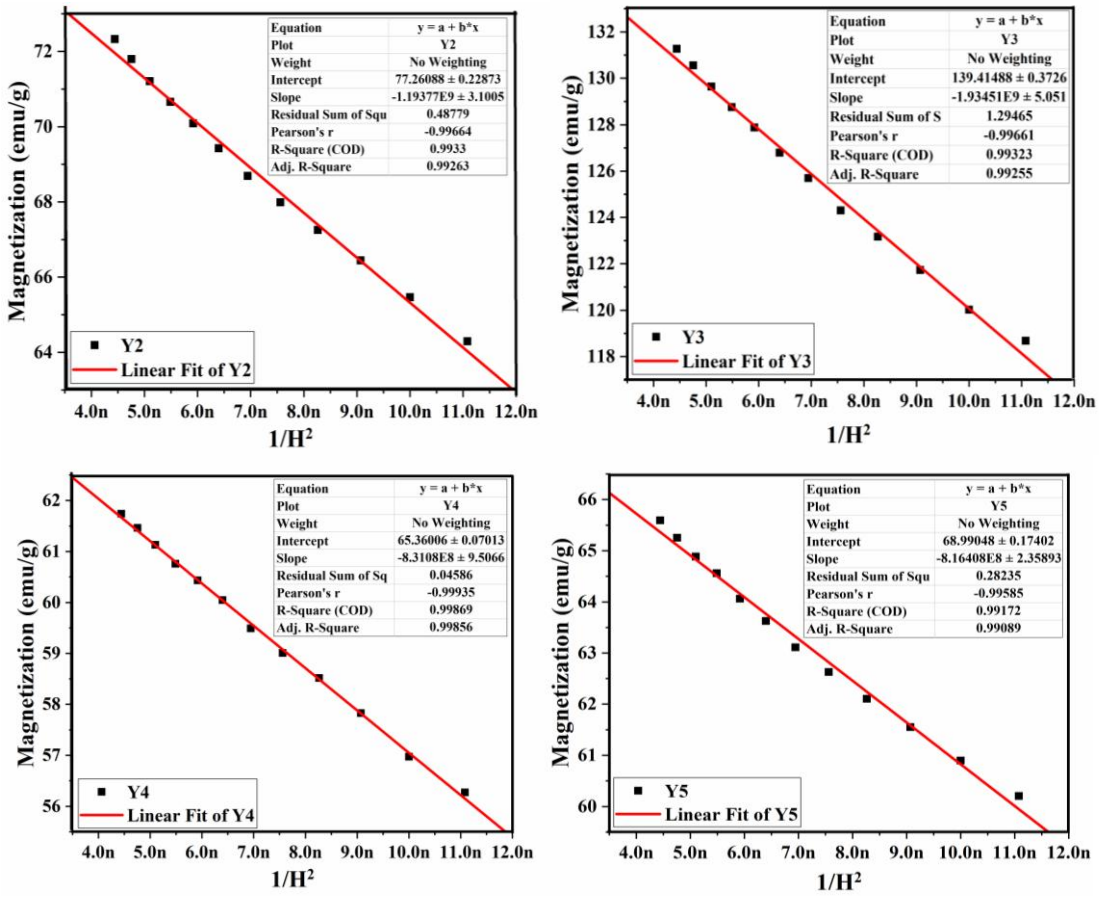

Figure 4.56 M_s versus 1/ H^2 plot for all hexaferrite samples.

This disturbance leads to a decrease in the total magnetization, which persists even when the magnetic field is no longer present. The remanence ratio (M_r/M_s) is a crucial determinant of a material's ability to sustain magnetization. M-type hexaferrites often exhibit significant remanence ratios due to their inherent magnetic characteristics. Conversely, the microstructure of the material, namely the spaces between the grains, greatly affects the remanence ratio. The remanence ratios span a broad spectrum, ranging from 0 to 1[185]. Research suggests that values between 0.05 and 0.5 indicate the presence of randomly oriented multi-domain particles [186]. After examining the data in the Table 4.19, it is clear that all of the samples produced had remanence ratios that are either less than or equal to 0.5. The Cd-series samples seem to consist of particles with numerous domains. The presence of these particles with many domains may be attributed to the influence of Cd^{2+} substitution on the microstructure. The replacement may affect the distribution of grain sizes, leading to the creation of areas between grains that hinder the alignment of magnetic moments in the material.

4.3.5 Electromagnetic Characteristics

4.3.5.1 Complex permeability and complex permittivity

The Figure 4.57 illustrate the frequency dependence of complex permittivity (ε′, ε″) and complex permeability (μ′, μ″) for the compositions Y1 to Y5. These variations are a direct result of Co-Cd doping in $BaCo_xCd_xFe_{12-2x}O_{19}$.

The dielectric constant (ε′) exhibits significant variation across the frequency range. Composition Y1 shows the highest peak in ε′, around 10.5 GHz reaching a maximum value of around 30, with a steep increase followed by a sharp drop. This behaviour is indicative of strong dielectric resonance. Y5 and Y3 also show a similar trend with a peak at around 11 GHz, but the increase is not as steep as Y1. The other compositions (Y2 and Y4) show more stable and consistent ε′ values over the frequency range, suggesting that their dielectric properties are less frequency-dependent.

The dielectric loss (ε″), representing the energy dissipation in the material, also exhibits non-monotonic trends. Y1, Y and Y5 display strong peaks in ε″ near 10.5 GHz, aligning with their respective ε′ peaks. This suggests significant energy loss due to dielectric relaxation at these frequencies. In contrast, Y2 and Y4 show relatively stable ε″ values, indicating lower energy dissipation across the measured frequency range.

The magnetic permeability (μ′) trends vary significantly among the samples. Y1 shows a rising μ′ up to around 12 GHz, indicating enhanced magnetic storage capabilities at higher frequencies. Y2 displays a peak in μ′ near 9 GHz, followed by a gradual decline. Y3, Y4, and Y5 show smoother, more gradual increases, with Y3 and Y5 having higher values of μ′ than Y2 and Y4. This indicates that Y3 and Y5 might have stronger magnetic properties in the measured frequency range.

The magnetic loss (μ″) trends reveal differences in how energy is dissipated magnetically across the samples. Y1 shows a sharp dip below zero, indicating significant magnetic losses while Y5 shows relatively higher μ″ values at mid and high frequencies, implying greater magnetic energy dissipation. Y2 shows a peak around 9 GHz, while Y3 and Y4 exhibit more consistent, gradual changes across the frequency range, indicating stable magnetic loss characteristics.

In summary, Co-Cd doping significantly affects both the dielectric and magnetic properties of the compositions. Y1, Y3 and Y5 exhibit more pronounced frequency-

dependent behaviour in both permittivity and permeability, particularly near 10.5 GHz. In contrast, Y2 and Y4 show more stable and gradual variations, making them less sensitive to frequency changes. This variation is due to the influence of factors like electron hopping, dipole polarization, and the grain boundary effect.

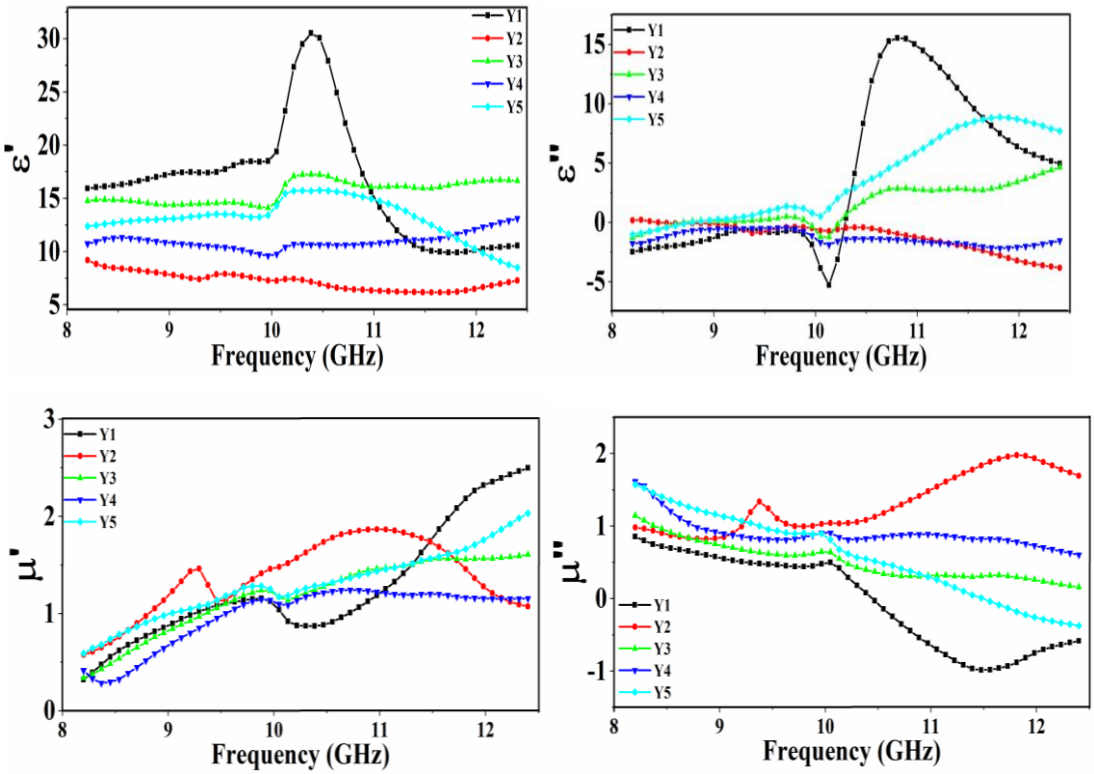

Figure 4.57 Complex permittivity and permeability versus frequency plots for $BaCo_xCd_xFe_{12-2x}O_{19}$.

4.3.5.2 Microwave absorption and Quarter Wavelength Mechanism in $BaCo_xCd_xFe_{12-2x}O_{19}$

The composite Y1 demonstrates its optimal absorption at a thickness of 1.6 mm, where a maximum REL of -38.17 dB is observed at a matching frequency of 9.72 GHz. As indicated in Figure 4.58 Y1, the quarter-wavelength mechanism contributes significantly to the reflection loss behaviour. The calculated thickness for Y1 matches well with the simulated thickness, showing that the REL peaks align with the predicted frequency range. The bandwidth for REL > -10 dB is 0.96 GHz (9.13–10.09 GHz), and for REL > -20 dB, the bandwidth is 0.35 GHz. At a slightly increased thickness of 1.8 mm, the REL value decreases to -18.77 dB, demonstrating how thickness influences the absorption characteristics. As the thickness increases from

1.6 mm to 1.8 mm, the height of the REL peak decreases. The peak frequency shifts slightly to the left as thickness increases.

In Y2, the optimal absorption is recorded at a thickness of 5.0 mm, with a maximum REL of -13.7 dB at a frequency of 10.88 GHz. The REL peaks are well-aligned with the calculated quarter-wavelength mechanism for this composition. The bandwidth for REL > -10 dB ranges from 10.3 GHz to 11.44 GHz, with a bandwidth of 1.14 GHz, demonstrating a relatively broad absorption band. As thickness increases to 5.6 mm, the REL decreases slightly to -12.37 dB at 10.64 GHz, and further increases in thickness reduce the absorption efficiency. As the thickness increases (e.g., from 5 mm to 9.3 mm), the peak REL continues to decrease. For example, at 5 mm thickness, the REL is -13.7 dB, while at 9.3 mm, it drops to -10.35 dB. The peaks shift right as the thickness increases. For example, at 5 mm, the peak occurs at 10.88 GHz, but for 9.3 mm, the peak moves to 10.68 GHz.

Composite Y3 shows its best absorption performance at a thickness of 1.4 mm, where the maximum REL reaches -36.64 dB at a matching frequency of 10.97 GHz. The bandwidth for REL > -10 dB is 2.23 GHz, which is one of the widest ranges among the materials tested. The quarter-wavelength mechanism is particularly pronounced in Y3, as the REL values show strong agreement with the calculated and simulated thickness values. As thickness increases from 1.5 mm to 1.9 mm, the REL decreases, confirming the role of the quarter-wavelength mechanism in determining the optimal thickness for absorption. The peak height decreases with increasing thickness. For example, the REL is -36.64 dB at 1.4 mm and reduces to -14.62 dB at 1.9 mm. The peak shifts left with increasing thickness. At 1.4 mm, the peak occurs at 10.97 GHz, and at 1.9 mm, it moves to 9.47 GHz.

For Y4, the quarter-wavelength mechanism also plays a significant role, as seen in the absorption performance at 1.7 mm thickness, where the maximum REL reaches -40.49 dB at a matching frequency of 10.39 GHz. This composition displays the highest absorption among all the samples, with a broad bandwidth for REL > -10 dB, ranging from 9.37 GHz to 11.69 GHz. The calculated and simulated thickness values match closely, validating the impact of the quarter-wavelength model. As thickness increases to 2.0 mm, the REL decreases to -19.91 dB, showing a shift in absorption properties. The peak REL decreases as thickness increases. For example, at 1.6 mm,

the peak is -38.8 dB, and at 2 mm, it reduces to -19.91 dB. The peaks shift left with increasing thickness. For instance, the peak shifts from 10.81 GHz at 1.6 mm to 9.75 GHz at 2 mm.

Composite Y5 exhibits its best performance at a thickness of 1.7 mm, where a maximum REL of -13.78 dB is observed at 9.87 GHz. The bandwidth for REL > -10 dB is 2.15 GHz, highlighting the ability of Y5 to absorb a wide range of frequencies. The calculated and simulated thicknesses for this composition follow the quarter-wavelength mechanism, with the REL peaks aligning with the expected frequencies. The performance of Y5 decreases as the thickness increases to 1.9 mm, with a corresponding reduction in REL to -10.54 dB at 9.46 GHz. The peak height decreases as thickness increases. At 1.7 mm, the peak REL is -13.78 dB, and at 1.9 mm, it drops to -10.54 dB. The peaks shift left slightly with increasing thickness. For example, at 1.7 mm, the peak occurs at 9.87 GHz, and at 1.9 mm, it moves to 9.46 GHz.

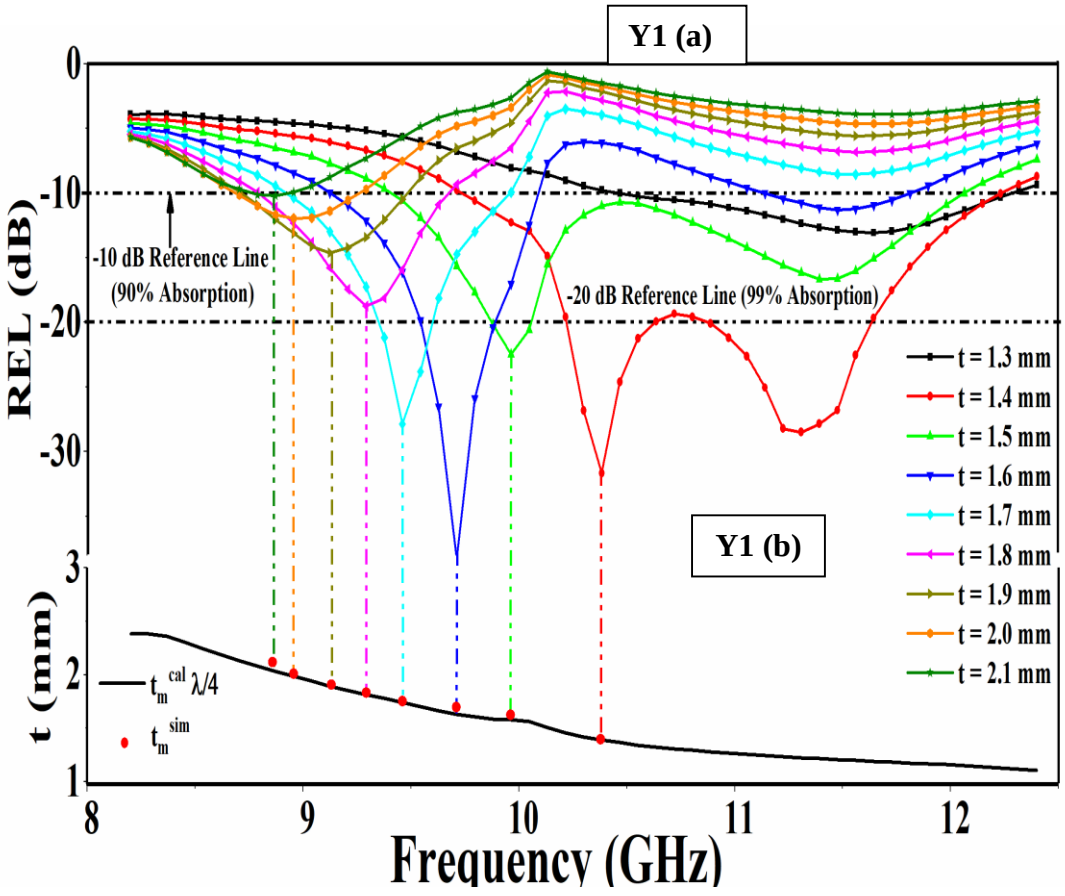

Figure 4.58 REL versus frequency for different thickness (Y1) and calculate thickness versus frequency for $BaCo_xCd_xFe_{12-2x}O_{19}$

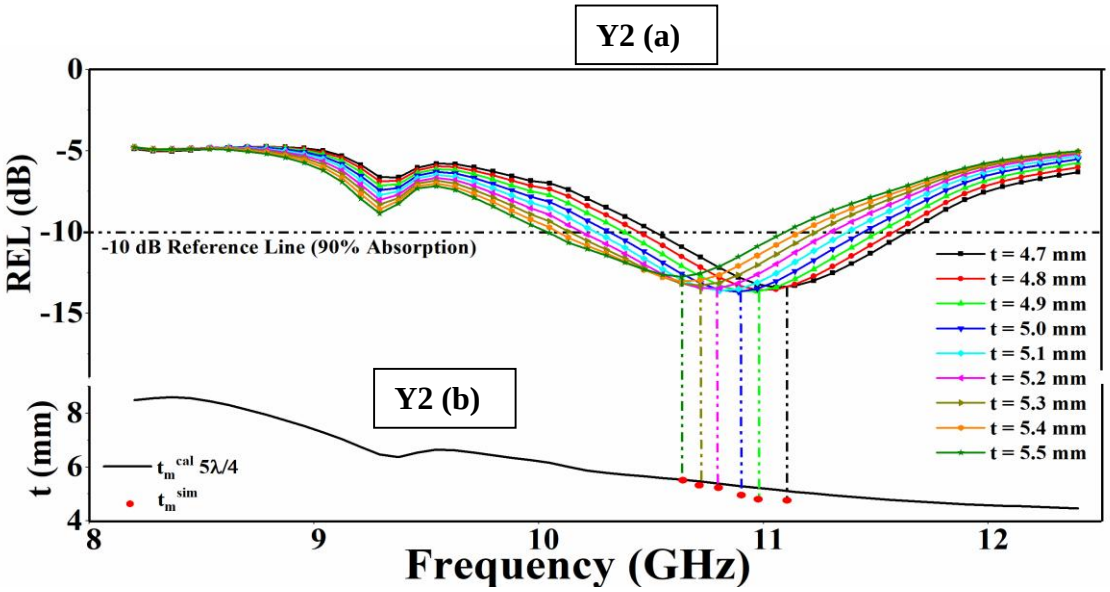
Y2 (a)
REL (dB)
-10 dB Reference Line (90% Absorption)
t = 4.7 mm
t = 4.8 mm
t = 4.9 mm
t = 5.0 mm
t = 5.1 mm
t = 5.2 mm
t = 5.3 mm
t = 5.4 mm
t = 5.5 mm
Y2 (b)
t (mm)
t_m^{cal} 5λ/4
t_m^{sim}
Frequency (GHz)

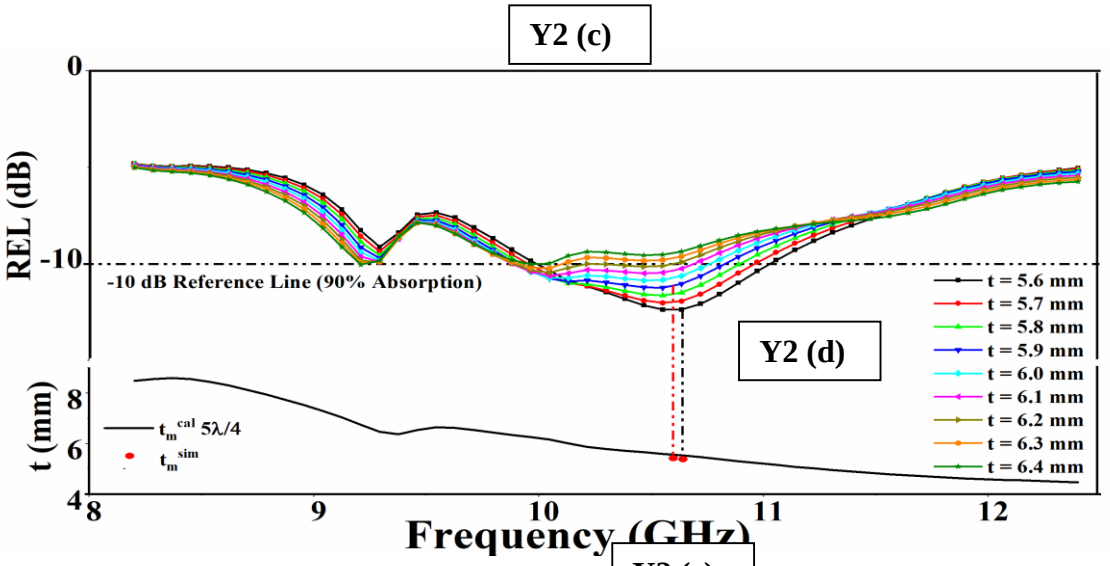
Y2 (c)
REL (dB)
-10 dB Reference Line (90% Absorption)
t = 5.6 mm
t = 5.7 mm
t = 5.8 mm
t = 5.9 mm
t = 6.0 mm
t = 6.1 mm
t = 6.2 mm
t = 6.3 mm
t = 6.4 mm
Y2 (d)
t (mm)
t_m^{cal} 5λ/4
t_m^{sim}
Frequency (GHz)

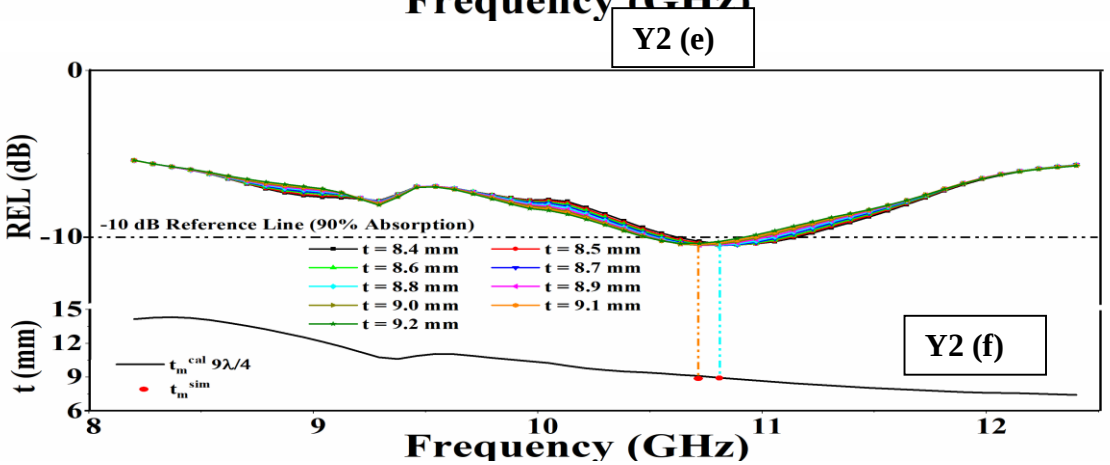
Y2 (e)
REL (dB)
-10 dB Reference Line (90% Absorption)
t = 8.4 mm
t = 8.5 mm
t = 8.6 mm
t = 8.7 mm
t = 8.8 mm
t = 8.9 mm
t = 9.0 mm
t = 9.1 mm
t = 9.2 mm
Y2 (f)
t (mm)
t_m^{cal} 9λ/4
t_m^{sim}
Frequency (GHz)

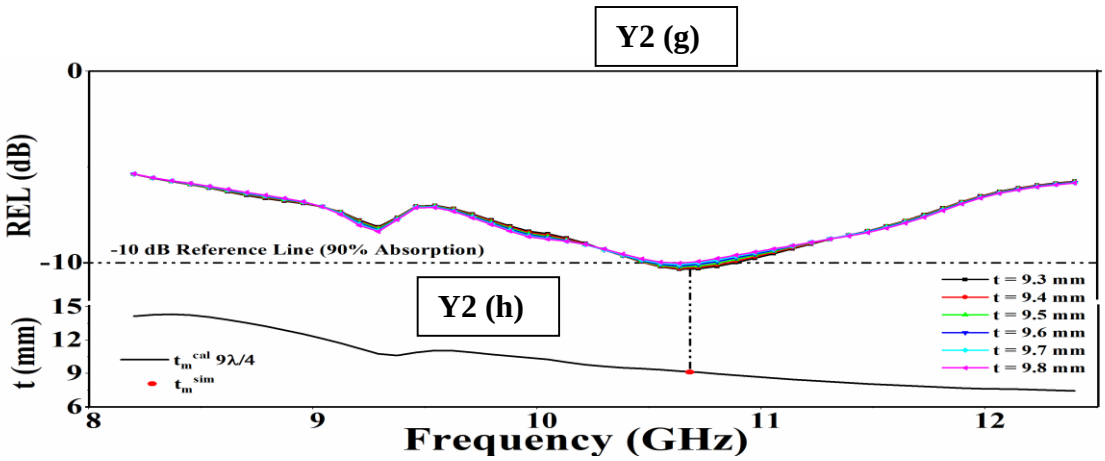

Figure 4.59 REL versus frequency for different thickness (Y2) and calculate thickness versus frequency for $BaCo_xCd_xFe_{12-2x}O_{19}$

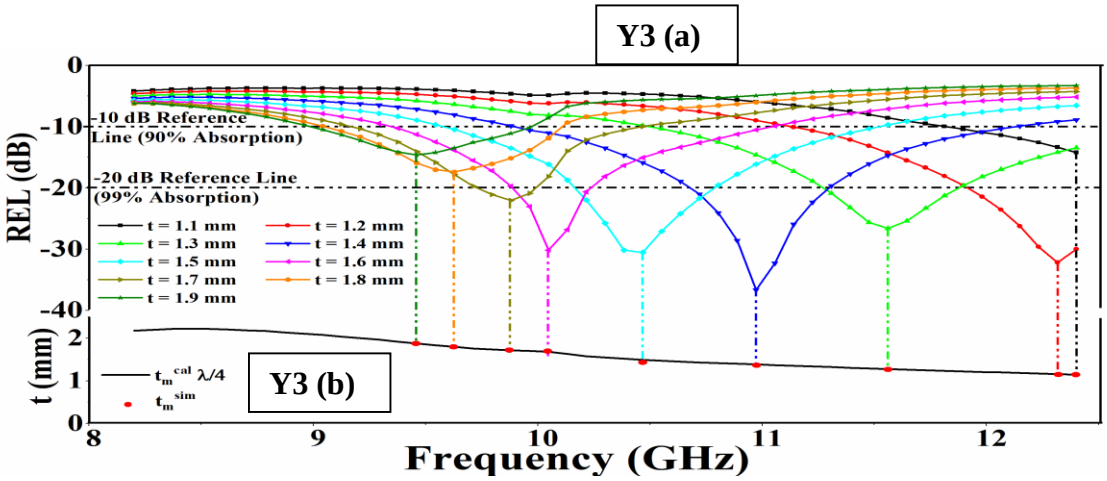

Figure 4.60 REL versus frequency for different thickness (Y3) and calculate thickness versus frequency for $BaCo_xCd_xFe_{12-2x}O_{19}$

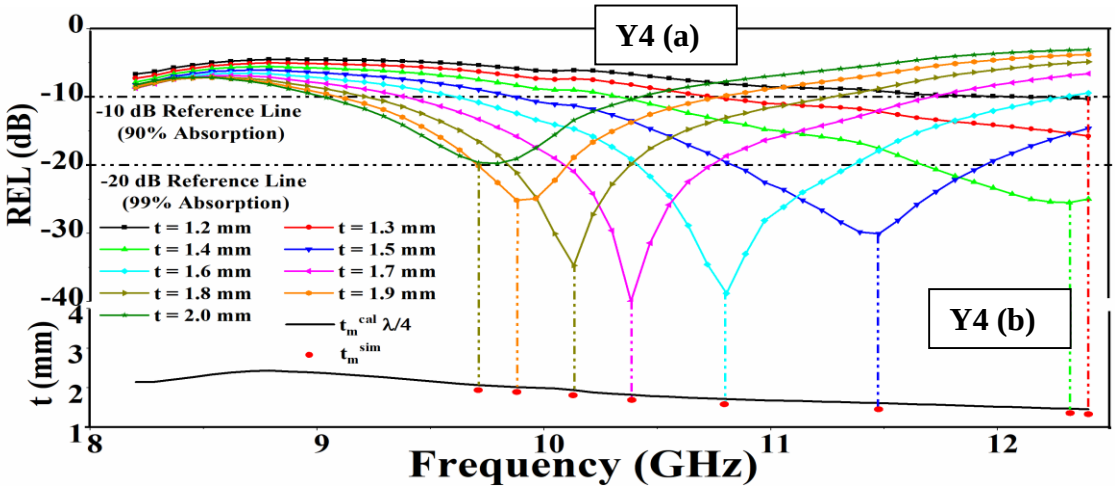

Figure 4.61 REL versus frequency for different thickness (Y4) and calculate thickness versus frequency for $BaCo_xCd_xFe_{12-2x}O_{19}$

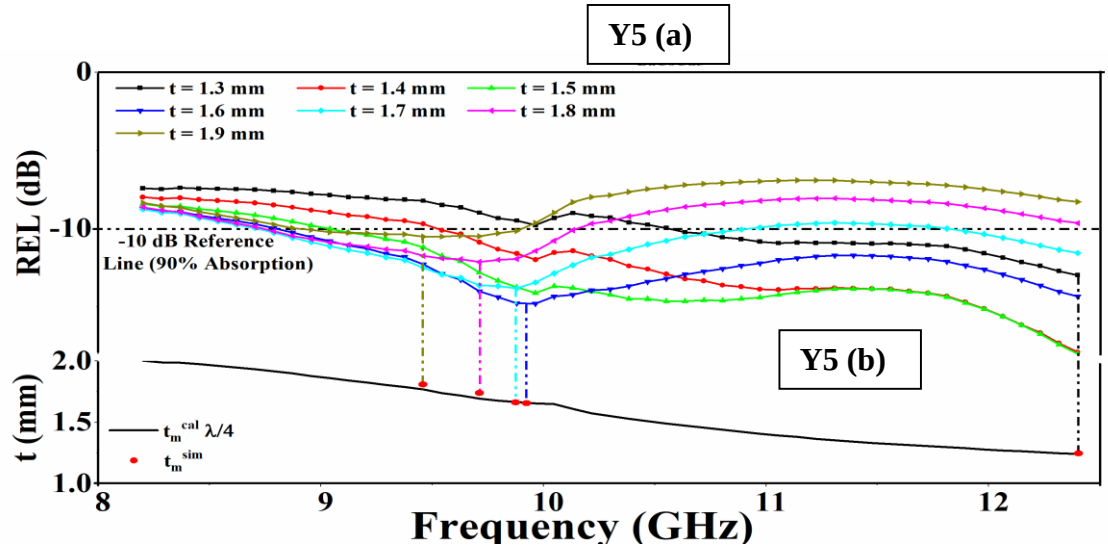

Figure 4.62 REL versus frequency for different thickness (Y5) and calculate thickness versus frequency for $BaCo_xCd_xFe_{12-2x}O_{19}$

Table 4.20 REL with matching thickness/frequency, BW, and PBW for $BaCo_xCd_xFe_{12-2x}O_{19}$ (Y1 to Y5).

Sample Name	Matching Thickness (mm)	Maximum REL (dB)	Matching frequency (GHz)	Frequency Band for REL > -10 dB (GHz)	Band width for RL > -10 dB (GHz)	Frequency Band REL > -20 dB (GHz)	Bandwidth for REL > -20 dB (GHz)	BTR	PBW (%)
Y1	1.6	-38.17	9.72	9.13-10.09	0.96	9.54-9.89	0.35	1.95E-03	9.88
	1.8	-18.77	9.29	8.8-9.67	0.87	-	-	1.70E-03	9.36
Y2	5	-13.7	10.88	10.3-11.44	1.14	-	-	5.80E-04	10.48
	5.6	-12.37	10.64	9.99-11.02	1.03	-	-	5.01E-04	9.68
	8.8	-10.58	10.81	10.61-11.13	0.52	-	-	1.50E-04	4.81
	9.3	-10.35	10.68	10.48-10.88	0.4	-	-	1.13E-04	3.75
Y3	1.4	-36.64	10.97	9.9-12.135	2.235	10.68-11.31	0.63	3.99E-03	20.37
	1.5	-30.52	10.47	9.58-12.11	2.53	10.17-10.79	0.62	4.36E-03	24.16
	1.6	-30.32	10.05	9.35-11.07	1.72	9.89-10.23	0.34	3.12E-03	17.11
	1.7	-22.13	9.88	9.16-10.49	1.33	9.72-9.99	0.27	2.44E-03	13.46
	1.8	-17.49	9.63	9.04-10.11	1.07	-	-	1.95E-03	11.11
	1.9	-14.62	9.47	8.99-9.97	0.98	-	-	1.73E-03	10.35
Y4	1.6	-38.8	10.81	9.62-12.26	2.64	10.41-11.36	0.95	4.20E-03	24.42
	1.7	-40.49	10.39	9.37-11.69	2.32	10.09-	0.64	3.74E-03	22.33

						10.73			
	1.8	-34.72	10.14	9.21-10.77	1.56	9.72-10.11	0.39	2.62E-03	15.38
	1.9	-25.23	9.88	9.1-10.76	1.66	9.71-10.11	0.4	2.68E-03	16.80
	2	-19.91	9.75	9.04-10.41	1.37	-	-	2.18E-03	14.05
Y5	1.7	-13.78	9.87	8.74-10.89	2.15	-	-	3.99E-03	21.78
	1.8	-12.18	9.72	8.77-10.16	1.39	-	-	2.60E-03	14.30
	1.9	-10.54	9.46	8.91-9.9	0.99	-	-	1.77E-03	10.47

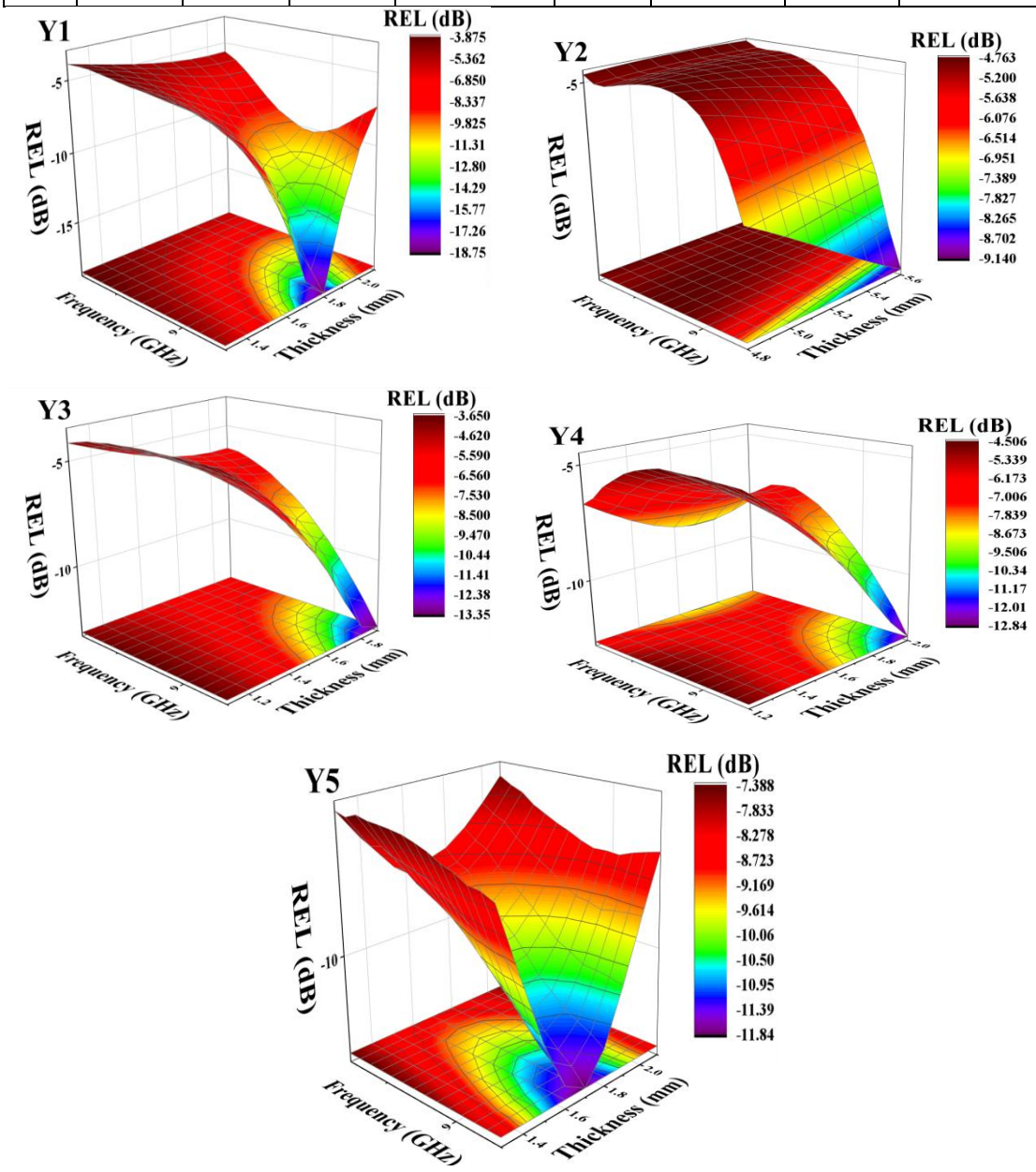

Figure 4.63 Three-dimensional (3D) plots of reflection loss at various frequencies and thicknesses for all samples of BaCoCd-series.

4.3.5.3 Impedance matching mechanism

The variation in the impedance of a material is primarily determined by its permittivity and permeability, which differ from that of free space. The reflection loss (REL) and impedance (Z_{in}) versus frequency plots for the prepared samples (Y1 to Y5) illustrate the relationship between these two factors. The highest REL peaks in each composition align with the impedance matching principle, wherein Z_{in} closely approaches the free-space impedance (Z_0 = 377 Ω).

For the Y1 sample, with a thickness of 1.6 mm, the maximum REL peak of -38.17 dB is observed at 9.72 GHz, where the impedance Z_{in} = 383.51 Ω, which is close to Z_0. Interestingly, no significant REL peak is noted at 9.63 GHz, even though Z_{in} = 373.78 Ω, which is closer to Z_0. This suggests that factors beyond exact impedance matching may also influence absorption efficiency, but proximity to Z_0 remains a strong determinant.

In Y2, with a thickness of 5.0 mm, a maximum REL of -13.7 dB is observed at 10.88 GHz, where the impedance Z_{in} = 267.58 Ω, deviating significantly from Z_0. This deviation explains the relatively lower absorption observed in Y2, as the mismatch between Z_{in} and Z_0 prevents efficient energy absorption.

The Y3 sample, with a thickness of 1.4 mm, exhibits a significant reflection loss of -36.64 dB at 10.97 GHz**,** with Z_{in} = 386.73 Ω, slightly higher than Z_0. Despite the proximity to Z_0, strong absorption is observed. However, at 10.80 GHz and 10.89 GHz**,** where Z_{in} values are closer to Z_0 (376.13 Ω and 382.85 Ω respectively), no REL peaks are detected; suggesting that even minor deviations in impedance can influence reflection loss.

In Y4, with a thickness of 1.7 mm, the maximum reflection loss is -40.49 dB at 10.39 GHz**,** with Z_{in} = 382.24 Ω, very close to Z_0, which confirms excellent impedance matching and high absorption efficiency. This sample performs exceptionally well, indicating that its impedance closely matches free space, allowing for significant absorption.

For Y5, with a thickness of 1.7 mm, the maximum REL is -13.78 dB at 9.87 GHz, where Z_{in} = 257.93 Ω, which is much lower than Z_0. This significant deviation from the free-space impedance leads to lower absorption efficiency compared to other

samples. The mismatch between Z_{in} and Z_0 causes a large portion of the incident wave to be reflected, leading to less effective absorption.

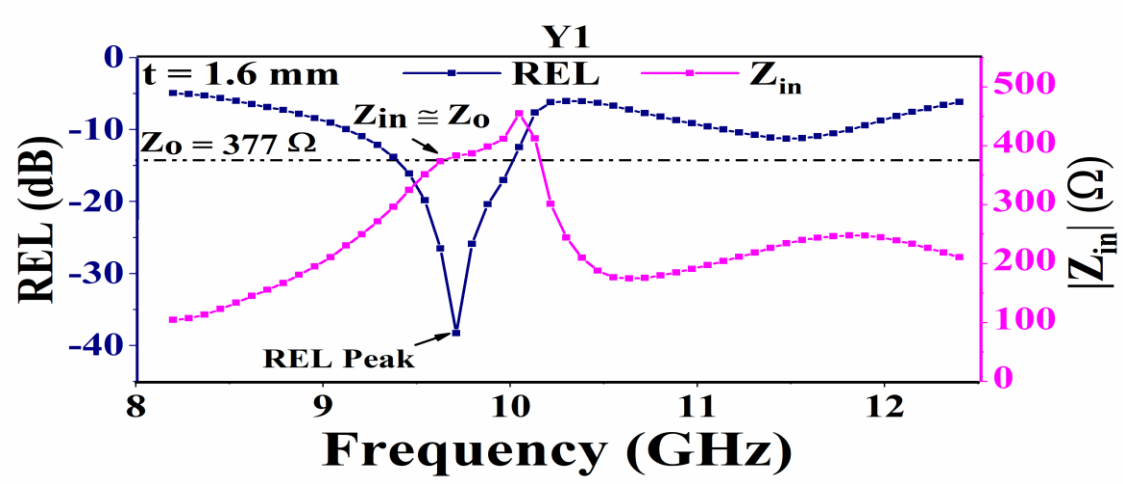

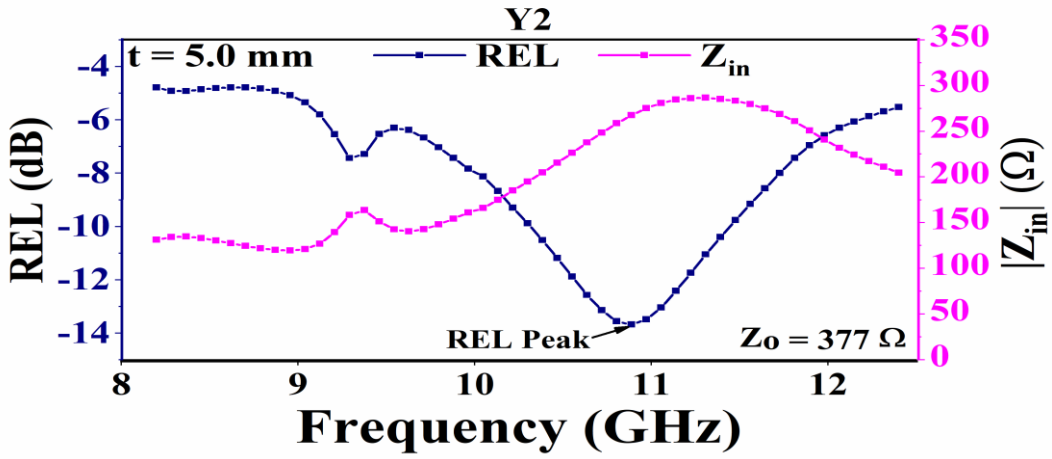

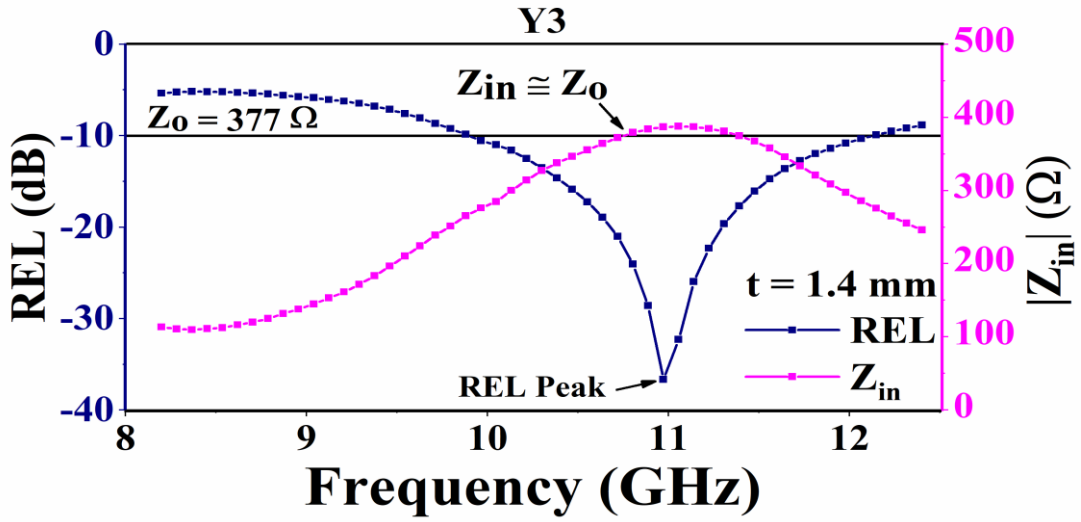

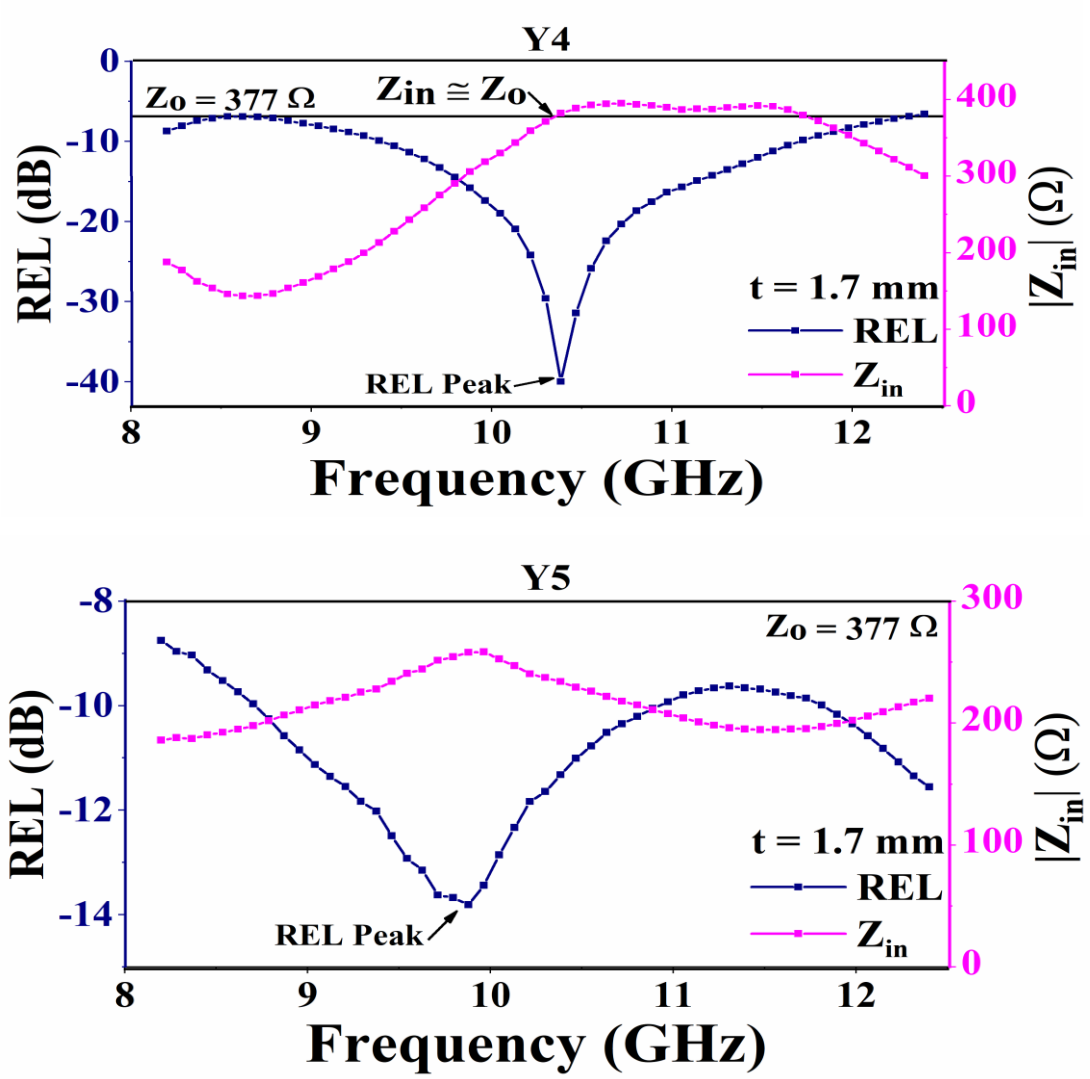

Figure 4.64 Z_{in} and REL curve against frequency for $BaCo_xCd_xFe_{12-2x}O_{19}$.

The input impedance (Z_{in}) consists of two components: real (Z_{real}) and imaginary (Z_{img}) parts. For effective impedance matching, Z_{real} should approach 377 Ω and Z_{img} should approach zero. In Y4, the peak REL at 10.39 GHz coincides with Z_{real} = 382.20 and Z_{img} = 5.55 Ω indicating nearly perfect matching conditions. Similarly, Y1 shows excellent impedance matching with Z_{real} = 383.45 Ω and Z_{img} = −6.62 Ω at 9.72 GHz. However, in Y3, no significant REL peak is observed at 11.31 GHz, where Z_{in} = 286.72 Ω, Z_{real} = 259.78 Ω and Z_{img} = −119.95 Ω deviate significantly from the ideal values for matching. This underscores the importance of both real and imaginary impedance components in achieving effective absorption.

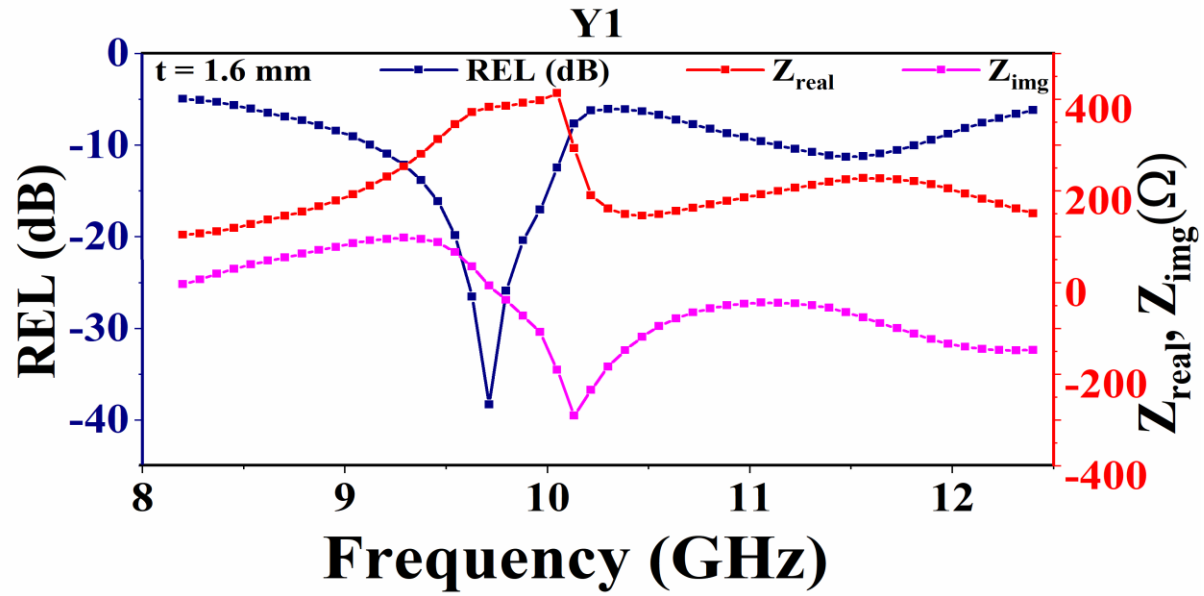
Y1
t = 1.6 mm
REL (dB)
Z_{real}
Z_{img}
REL (dB)
Z_{real}, Z_{img}(Ω)
Frequency (GHz)

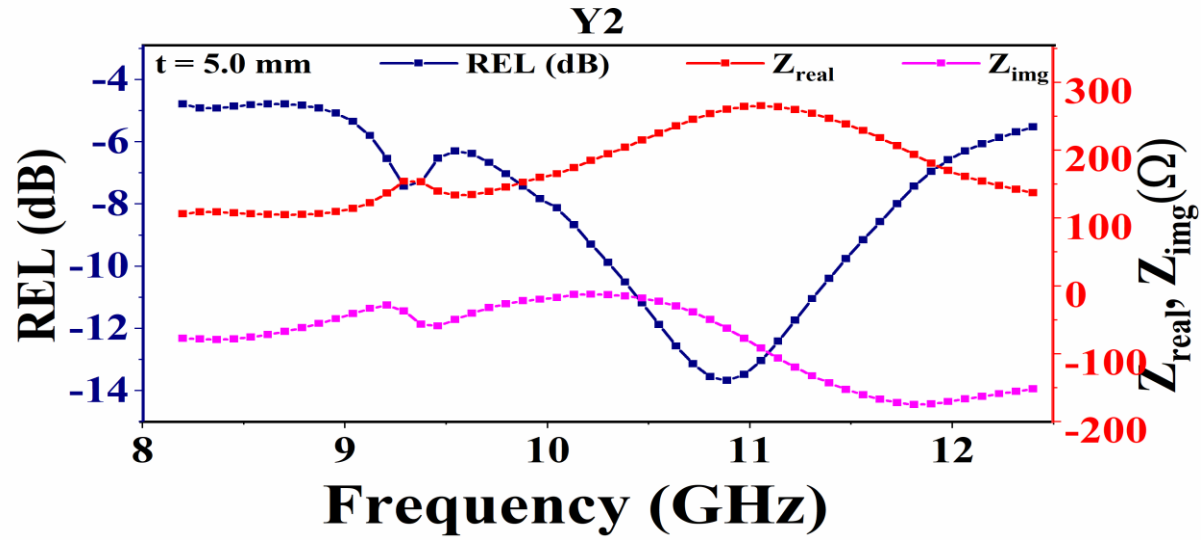
Y2
t = 5.0 mm
REL (dB)
Z_{real}
Z_{img}
REL (dB)
Z_{real}, Z_{img}(Ω)
Frequency (GHz)

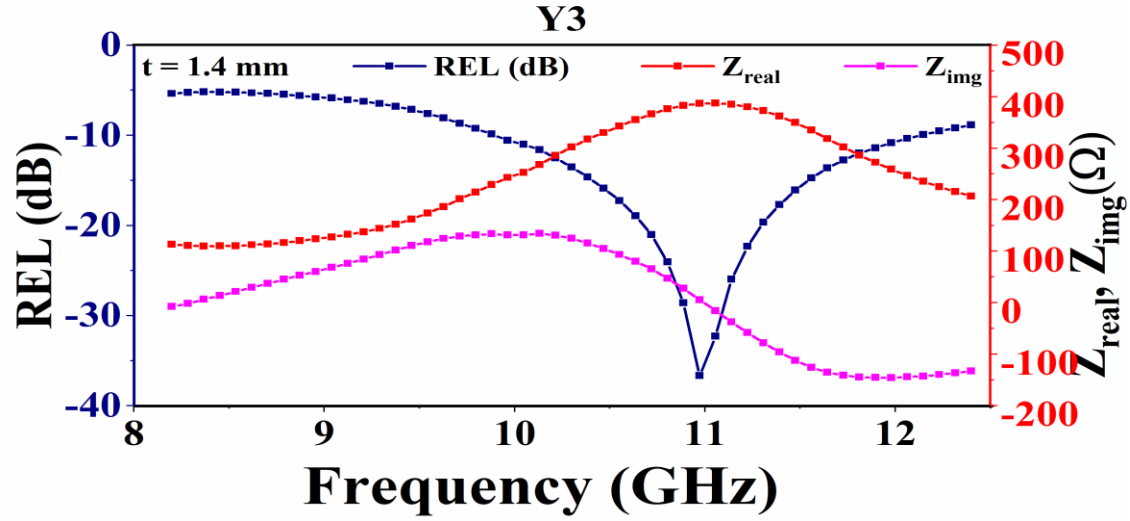
Y3
t = 1.4 mm
REL (dB)
Z_{real}
Z_{img}
REL (dB)
Z_{real}, Z_{img}(Ω)
Frequency (GHz)

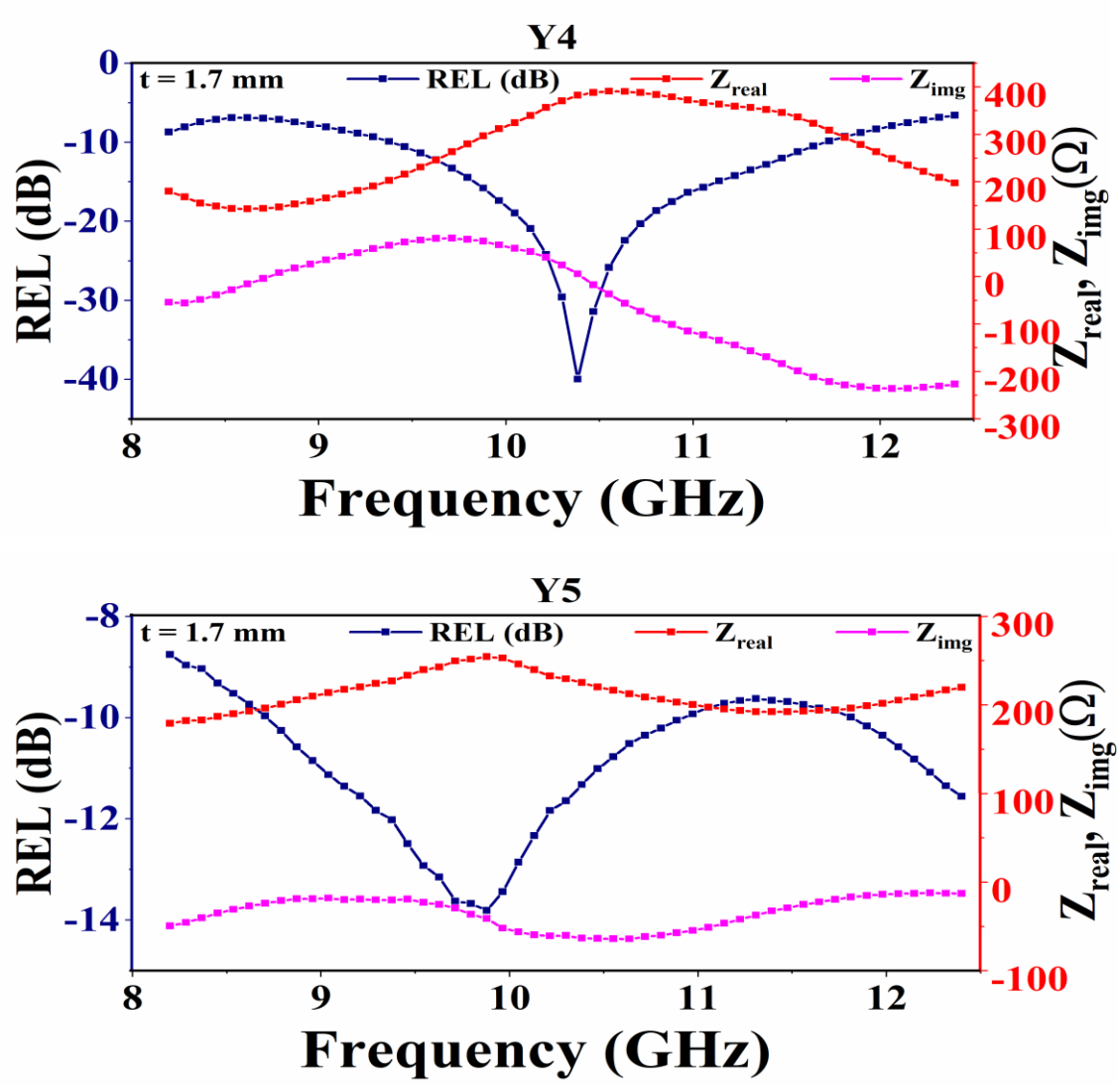

Figure 4.65 Z_{real}, Z_{imag}, and REL v/s frequency for $BaCo_xCd_xFe_{12-2x}O_{19}$.

Table 4.21 Z_{in}, Z_{real}, and Z_{imag} values corresponding to REL_{max} for $BaCo_xCd_xFe_{12-2x}O_{19}$.

Sample Name	Matching Thickness(mm)	Maximum REL (dB)	Matching frequency (GHz)	Z_{real} (Ω)	Z_{img} (Ω)	$\|Z_{in}\|$ (Ω)
Y1	1.6	-38.17	9.72	383.45	-6.62	383.51
Y2	5	-13.7	10.88	260.15	-62.64	267.58
Y3	1.4	-36.64	10.97	386.69	5.62	386.73
Y4	1.7	-40.49	10.39	382.20	5.55	382.24
Y5	1.7	-13.78	9.87	254.63	-41.15	257.93

4.3.5.4 Eddy Current Loss

It is important to consider that when the frequency increases and C_0 remains constant except in low frequency region. Each Composite (Y1 to Y5) exhibits a distinct peak at roughly 8 GHz, followed by a swift decrease in C_0. The Y4 exhibits the prominent

peak at around 20 ns, followed by Y3, Y5, Y2, and Y1.This indicates that at a frequency of 8 GHz, the system demonstrates a peak value for C_0, which rapidly decreases when the frequency beyond this threshold. All datasets reach a point of convergence and stability within the frequency range of 9 GHz to 12 GHz. The values of C_0 in this frequency range exhibit a notable decrease (ranging from 2 ns to 4 ns) in comparison to the maximum value observed at 8 GHz. This suggests that the response at higher frequencies is more uniform, with less variation in $C0$ across the different composition or datasets. The Y1 and Y2 peaks have the lowest magnitudes and are closely positioned, suggesting a comparable reaction throughout the whole frequency spectrum.

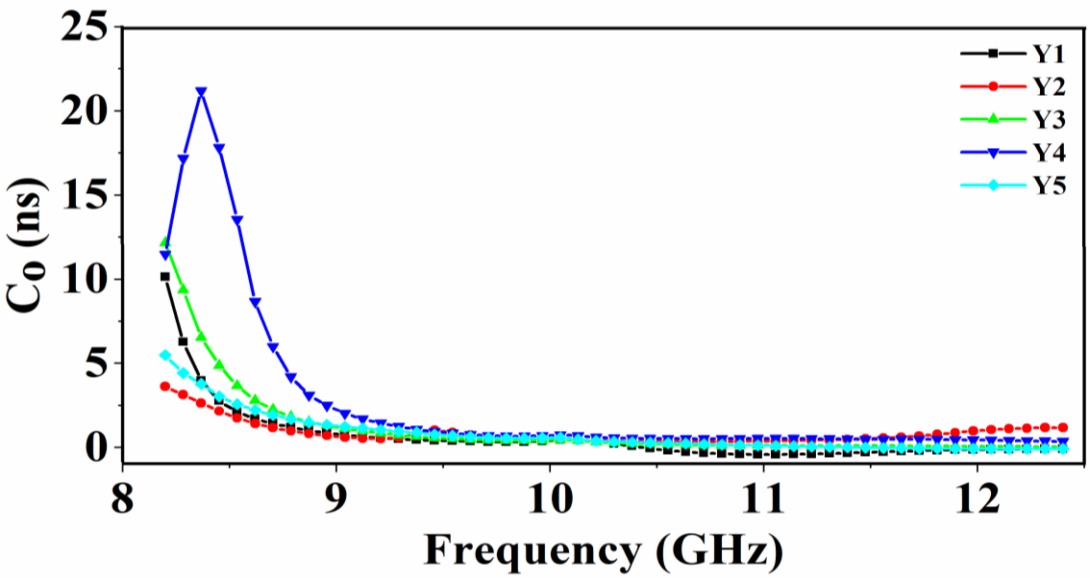

Figure 4.66 C_0 versus frequency curve for $BaCo_xCd_xFe_{12-2x}O_{19}$.

4.3.5.5 Bandwidth to Thickness Ratio

At a matching thickness of 1.6 mm, Y1 achieves a maximum reflection loss (REL) of -38.17 dB at a matching frequency of 9.72 GHz. The Bandwidth-to-Thickness Ratio (BTR) is 1.95E-03, and the Percentage Bandwidth (PBW) is 9.88%. With an increased thickness of 1.8 mm, the REL drops to -18.77 dB at 9.29 GHz. The BTR decreases to 1.70E-03, and PBW decreases to 9.36%.

At a 5 mm thickness, Y2 achieves an REL of -13.7 dB at 10.88 GHz. The BTR is 5.80E-04, and PBW is 10.48%. At 5.6 mm, Y2's REL slightly decreases to -12.37 dB at 10.64 GHz, with a bandwidth of 1.03 GHz for REL > -10 dB. The BTR reduces to 5.01E-04, and PBW is 9.68%. At 8.8 mm, Y2 shows a further decrease in REL to -

10.58 dB at 10.81 GHz, with a narrower bandwidth of 0.52 GHz for REL > -10 dB. The BTR is 1.50E-04, and PBW drops to 4.81%. At 9.3 mm, Y2's REL remains at -10.35 dB at 10.68 GHz, with a bandwidth of 0.4 GHz for REL > -10 dB. The BTR is 1.13E-04, and PBW is 3.75%.

At a 1.4 mm thickness, Y3 exhibits an impressive REL of -36.64 dB at 10.97 GHz, with a BTR of 3.99E-03 and a PBW of 20.37%. At 1.5 mm, the REL is -30.52 dB at 10.47 GHz, and the BTR increases to 4.36E-03, and PBW reaches 24.16%. As the thickness increases to 1.6 mm, the REL is -30.32 dB at 10.05 GHz, the BTR is 3.12E-03, and PBW is 17.11%. At 1.7 mm, Y3's REL decreases to -22.13 dB at 9.88 GHz, the BTR is 2.44E-03, and PBW is 13.46%. At 1.8 mm, the REL further decreases to -17.49 dB at 9.63 GHz, the BTR is 1.95E-03, and PBW is 11.11%. At 1.9 mm, the REL is -14.62 dB at 9.47 GHz, with BTR is 1.73E-03, and PBW is 10.35%.

At a 1.6 mm thickness, Y4 shows the highest performance with an REL of -38.8 dB at 10.81 GHz. The BTR is 4.20E-03, and PBW is 24.42%. At 1.7 mm, the REL improves further to -40.49 dB at 10.39 GHz, with BTR is 3.74E-03, and PBW is 22.33%. At 1.8 mm, the REL is -34.72 dB at 10.14 GHz, with BTR is 2.62E-03, and PBW is 15.38%. At 1.9 mm, Y4's REL decreases to -25.23 dB at 9.88 GHz with BTR are 2.68E-03, and PBW is 16.80%. At 2 mm, the REL drops to -19.91 dB at 9.75 GHz, with BTR are 2.18E-03, and PBW is 14.05%.

At 1.7 mm, Y5 has an REL of -13.78 dB at 9.87 GHz, with the BTR is 3.99E-03, and PBW is 21.78%. At 1.8 mm, the REL is -12.18 dB at 9.72 GHz, with the BTR is 2.60E-03, and PBW is 14.30%. At 1.9 mm, Y5 REL is -10.54 dB at 9.46 GHz, with the BTR is 1.77E-03, and PBW is 10.47%.

4.3.5.6 S – Parameter

For Y1: It starts at around -1.0 to -1.4 dB, gradually becoming more negative as frequency increases. It indicates moderate reflection and increasing absorption at higher frequencies. S_{11} continues to drop, reaching around -2.0 to -3.5 dB, showing an improvement in absorption between 9.8 GHz to 11 GHz. Y1 further improves absorption, reaching values of -3.96 dB at 12.4 GHz, showing good absorption with reduced reflection at higher frequencies.

For Y2: It starts at about -1.2 to -1.7 dB, indicating moderate absorption. As the frequency increases, Y2 absorption improves, especially around 9.7 GHz, where S_{11}

dips to -2.8 dB. Y2 experiences a significant drop in S_{11}, reaching its most negative value around -5.8 dB at 12 GHz, indicating excellent absorption in this region. After the drop around 11 GHz, Y2 maintains high absorption with S_{11} values of around -5.85 dB at 12.3 GHz, showing strong reflection loss.

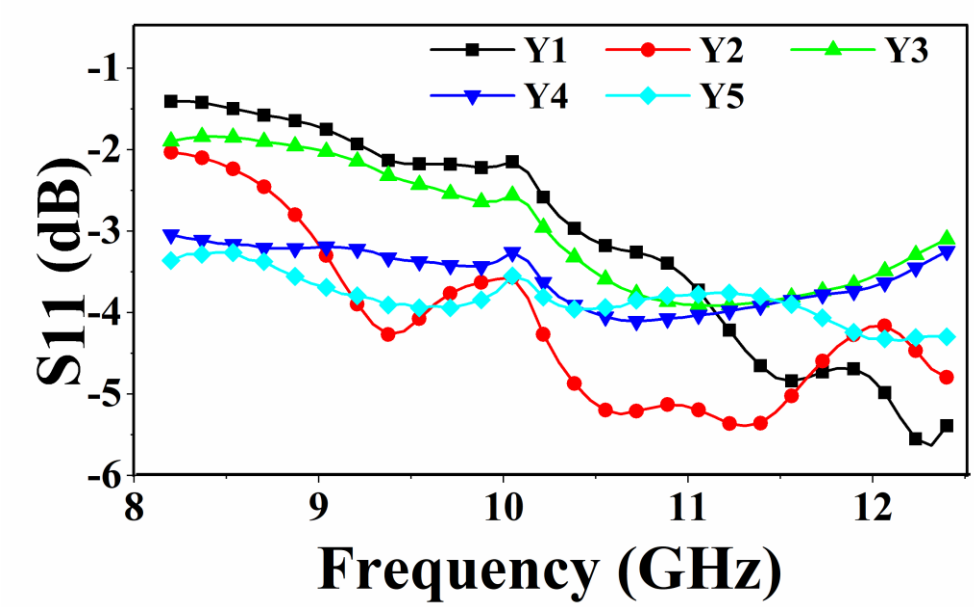

Figure 4.67 S_{11} versus frequency curve for $BaCo_xCd_xFe_{12-2x}O_{19}$.

Y3 starts with higher reflection, with S_{11} values of -1.7 to -2.3 dB at lower frequencies. However, as the frequency increases, its absorption improves. Y3 reaches S_{11} values of -2.5 to -3.5 dB, showing stable and good absorption in this region. Y3 continues to improve and maintain high absorption with S_{11} values of -4.39 dB at 12.4 GHz.

Y4 starts with moderate S_{11} values around -1.0 to -1.5 dB. There is steady improvement in absorption as frequency increases. Y4 reaches S_{11} values of -2.4 to -3.1 dB, showing good absorption across this frequency range. Y4 improves its absorption further, with S_{11} values reaching -3.26 dB at 12.4 GHz.

Y5 starts with relatively strong absorption, with S_{11} values around -3.0 to -3.5 dB, indicating good absorption at lower frequencies. Y5 maintains good performance, with S_{11} values reaching -4.3 dB, demonstrating continued strong absorption. Y5 shows consistent strong absorption, with S_{11}values reaching -3.26 dB at 12.4 GHz.

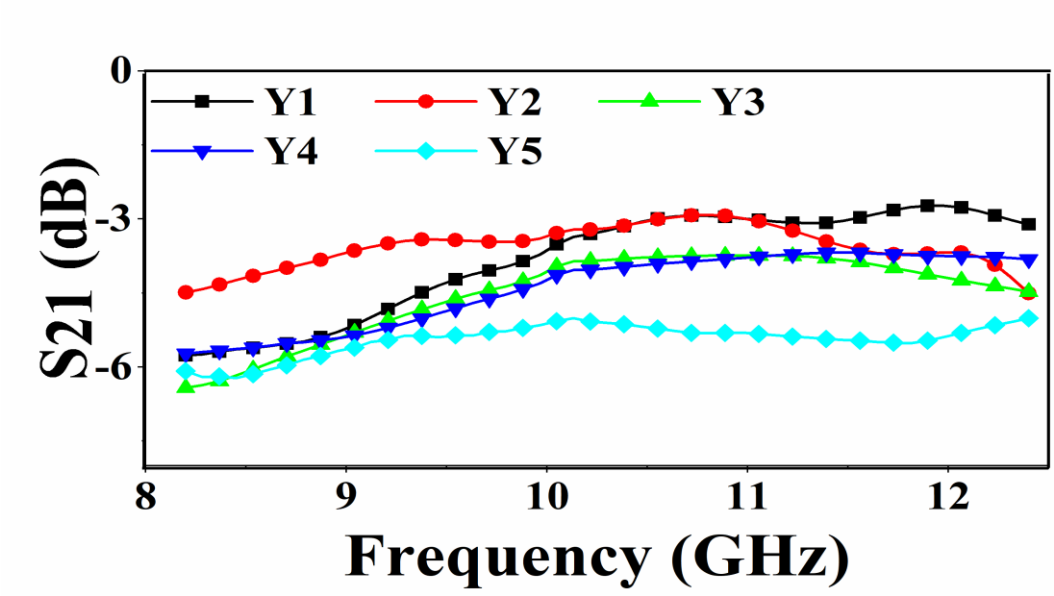

Figure 4.68 S_{21} versus frequency curve for $BaCo_xCd_xFe_{12-2x}O_{19}$.

Y1 starts with moderate transmission at -2.34 dB at 8.2 GHz and improves steadily as the frequency increases, reaching around -1.3 dB by 12.4 GHz. This consistent trend indicates that Y1 exhibits good transmission performance across the entire frequency range, with minimal variation, reflecting stable and efficient energy transmission.

Y2 begins with slightly lower transmission at -2.63 dB at 8.2 GHz and shows gradual improvement, reaching around -1.28 dB at 12.4 GHz. It follows a similar trend to Y1, with good transmission throughout the frequency range, especially as the frequency increases. Y2 performs steadily, with efficient energy transmission in higher frequencies.

Y3 starts with the weakest transmission among the composites, at -4.4 dB at 8.2 GHz, but improves significantly as the frequency increases. By 12.4 GHz, Y3 reaches -1.92 dB, reflecting a strong improvement in transmission performance.

Y4 shows stable and efficient transmission, starting at -2.69 dB at 8.2 GHz and improving to -1.31 dB at 12.4 GHz. The transmission trend is steady and consistent, indicating that Y4 performs well across the entire frequency spectrum, with no drastic changes or variations, making it a reliable performer

Y5 starts with relatively good transmission, at -1.22 dB at 8.2 GHz, but sees a slight decline as frequency increases, reaching -4.86 dB by 12.4 GHz. This indicates that Y5 performs better at lower frequencies and has weaker transmission at higher frequencies compared to the other composites.

4.4 Co^{2+}- Cr^{3+} substituted $BaCo_xCr_xFe_{12-2x}O_{19}$ hexaferrite.

In this section, we will utilize the sol-gel combustion method to fabricate a hexaferrite compound with Co and Cr substitutions. The composition of the hexaferrite will be $BaCo_xCr_xFe_{12-2x}O_{19}$. Table 4.22 displays the sample names/codes for various levels of substitution in $BaCo_xCr_xFe_{12-2x}O_{19}$.

Table 4.22. Presents the assignment of sample names corresponding to various substitution levels in $BaCo_xCr_xFe_{12-2x}O_{19}$ hexaferrite.

Sample Composition $BaCo_xCr_xFe_{12-2x}O_{19}$	Sample Code Name	Sample Code (Z-series)
x= 0.0	**$BaFe_{12}O_{19}$**	Z0
x = 0.2	**$BaCo_{0.2}Cr_{0.2}Fe_{11.6}O_{19}$**	Z1
x = 0.4	**$BaCo_{0.4}Cr_{0.4}Fe_{11.2}O_{19}$**	Z2
x = 0.6	**$BaCo_{0.6}Cr_{0.6}Fe_{10.8}O_{19}$**	Z3
x = 0.8	**$BaCo_{0.8}Cr_{0.8}Fe_{10.4}O_{19}$**	Z4
x = 1.0	**$BaCoCrFe_{10}O_{19}$**	Z5

4.4.1 X-ray diffraction analysis

The X-ray diffraction (XRD) patterns of $BaCo_xCr_xFe_{12-2x}O_{19}$ hexaferrite samples (Z0 to Z5, x = 0.0, 0.2, 0.4, 0.6, 0.8, and 1.0) are presented in Figure 4.69. The analysis using Powder-X software reveals well-defined Bragg peaks. These peaks were matched with the reference pattern for M-type barium hexaferrite ($BaFe_{12}O_{19}$, space group P63/mmc, JCPDS card no. 96-100-8842). The major peaks correspond to the M-type hexagonal phase, with one minor peak attributed to iron oxide impurities, which can have significant effects on both the electric and magnetic properties of the samples:

The presence of a minor peak, related to iron oxide, indicates a phase impurity. These impurities can lead to localized charge trapping, thus increasing the dielectric loss. The substitution of Co-Cr and the presence of iron oxide impurities can influence the magnetic saturation (M_s) of the hexaferrite. Iron oxide phases typically have lower magnetic saturation compared to M-type hexaferrites. Therefore, even a small amount of this secondary phase can decrease the overall magnetic moment of the material, leading to reduced magnetic saturation. Table 4.23 summarizes the calculated lattice parameters for the prepared samples. As Co-Cr doping increases (Z0 to Z4), both lattice constants (a and c) and unit cell volume decrease (699.0067 $Å^3$ to 695.7493 $Å^3$). This reduction can be attributed to the difference in ionic radii between the

dopants (Co^{2+}: 0.72 Å, Cr^{3+}: 0.63 Å) and the replaced Fe^{3+} (0.64 Å) [161-162]. The c/a ratio remains constant at around 3.93 [160] for all samples. The average crystallite size ranges from 20.39047 nm to 20.28484 nm.

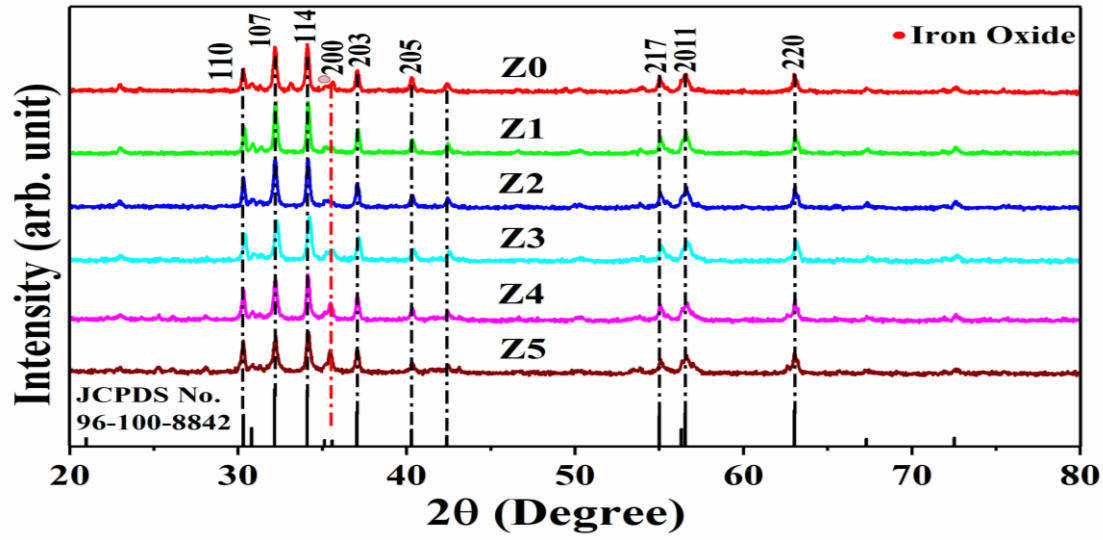

Figure 4.69 X-Ray Diffraction Analysis of M-Type $BaCo_xCr_xFe_{12-2x}O_{19}$ (Z0 (x = 0.0), Z1 (x = 0.2), Z2 (x = 0.4), Z3 (x = 0.6), Z4 (x = 0.8), Z5 (x = 1.0))

Table 4.23. Influence of Co-Cr Doping on the Lattice Parameters (a, c), c/a Ratio, and Unit Cell Volume of $BaCo_xCr_xFe_{12-2x}O_{19}$ Hexaferrites

Parameter	Z0 x = 0.0	Z1 x = 0.2	Z2 x = 0.4	Z3 x = 0.6	Z4 x = 0.8	Z5 x = 1.0
a = b (Å)	5.8945	5.8925	5.8915	5.8865	5.889	5.891
c (Å)	23.215	23.201	23.195	23.12	23.15	23.155
c/a	3.938417	3.937378	3.937028	3.927631	3.931058	3.930572
Vol /10^6 pm^3	699.0067	698.1111	697.6937	694.2579	695.7493	696.3723
Crystallite Size D_{xrd} (nm)	20.38479	20.28484	20.38632	20.39047	20.38599	20.38681

Energy-dispersive X-ray spectroscopy (EDX) was employed to qualitatively assess the elemental composition of the $BaCo_xCr_xFe_{12-2x}O_{19}$ samples, particularly verifying the presence of elements corresponding to the starting materials used during synthesis (Ba, Co, Cr, Fe, and O). Figure 4.70 presents the EDX spectra for samples with Z0 and Z2. The EDX spectra confirm the presence of barium (Ba), oxygen (O), and iron (Fe) in the sample with Z0, which aligns with the expected composition for undoped $BaFe_{12}O_{19}$. For the sample with Z2, the presence of barium (Ba), iron (Fe), cobalt

(Co), and Chromium (Cr) is observed, indicating successful incorporation of the dopant elements (Co and Cr) into the crystal structure.

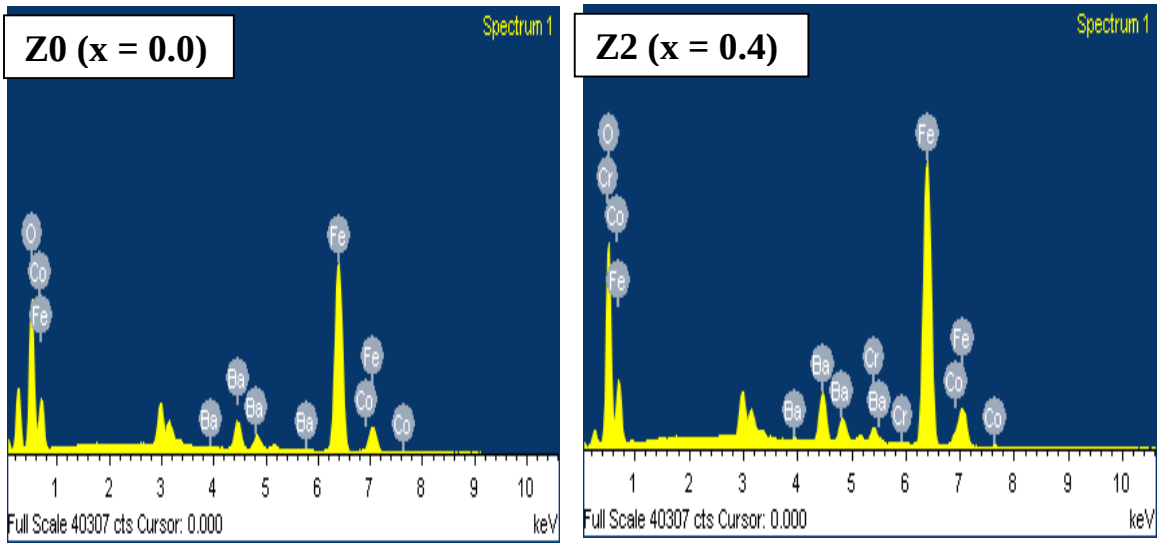

Figure 4.70 Focused EDX Analysis of $BaCo_xCr_xFe_{12-2x}O_{19}$ Hexaferrites for Z0 and Z2

Table 4.24 Qualitative Assessment of Elemental Presence in $BaCo_xCr_xFe_{12-2x}O_{19}$ using EDX Analysis

Element	Z0 x = 0.0		Z1 x = 0.2		Z2 x = 0.4		Z3 x = 0.6		Z4 x = 0.8		Z5 x = 1.0	
	W %	A %	W %	A %	W %	A %	W %	A %	W %	A %	W %	A %
O K	27.8	59.8	25.3	56.9	22.1	52.6	27.3	59.3	23.5	54.6	21.6	51.8
Fe K	60.0	37.1	59.3	38.2	59.6	40.6	54.9	34.1	54.2	36.0	53.	36.9
Ba L	11.9	3.0	13.2	3.5	13.9	3.8	12.3	3.1	13.7	3.7	13.7	3.8
Co K	0.3	0.1	1.2	0.7	2.4	1.5	3.1	1.8	4.4	2.8	5.7	3.7
Cr K	-	-	1.0	0.7	2.0	1.5	2.5	1.6	4.2	2.9	5.1	3.7

4.4.2 Formulation and Morphological Analysis of Nanoferrite Composites via FESEM Characterization

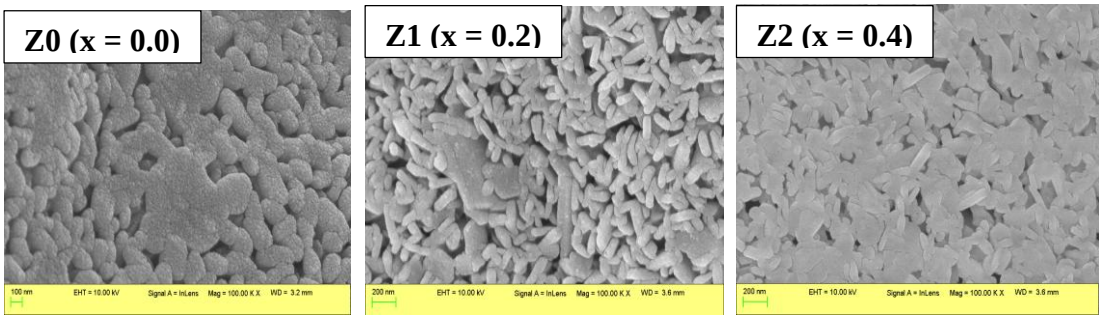

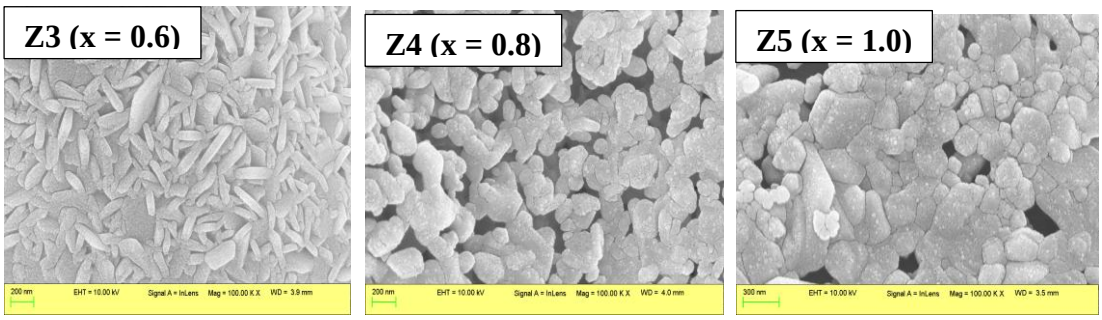

Figure 4.71 SEM micrographs of ferrite samples of $BaCo_xCr_xFe_{12-2x}O_{19}$ (Z0 (x = 0.0), Z1 (x = 0.2), Z2 (x = 0.4), Z3 (x = 0.6), Z4 (x = 0.8), Z5 (x = 1.0)).

The SEM micrographs for $BaCo_xCr_xFe_{12-2x}O_{19}$ samples with varying Co-Cr doping levels reveal interesting trends in grain morphology as shown in Figure 4.71.

Undoped (Z0): The image for the undoped sample shows a combination of large, fused grains and smaller individual grains, suggesting potential grain growth during the sintering process.

Doped Samples (x > 0.0): The micrographs for doped samples (x = 0.2, 0.4, 0.6, 0.8, and 1.0 – Z1 to Z5) are expected to exhibit:

Grain Agglomeration: Introduction of Co-Cr dopants is likely to lead to grain agglomeration compared to the undoped sample.

Non-uniform Grain Size Distribution: A non-uniform distribution of grain sizes was found across the doped samples.

Needle-Shaped Platelets: With increasing Co-Cr content (Z0 to Z5), the formation of needle-shaped platelets might become more prominent in the micrographs.

Influence of Doping: The observed changes in grain morphology with Co-Cr doping can be attributed to factors like: Electrostatic effects between the dopant ions and the host lattice and Magnetic interactions between the ferrite particles. Doping at higher levels (Z2 to Z5) might hinder grain growth, resulting in the presence of smaller individual grains within the agglomerates.

Implications for Electrical Properties: The presence of voids between the grains could potentially hinder the movement of charge carriers within the material. A higher concentration of grain boundaries due to smaller grain sizes (potentially observed at higher doping levels) can increase the resistivity and influence the overall charge transport mechanism.

The morphology of grains, including their size, shape, and orientation, plays a crucial role in determining the physical properties of a material. The grain structures resembling needles, as seen in FESEM images, possess distinct qualities that can have an influence on electrical and magnetic properties. The shape of needle-like grains can contribute to the overall magnetic anisotropy of the material. The anisotropy has the potential to impact various magnetic properties, including coercivity, remanence, and saturation magnetization. The shape of the grains can have a significant impact on the movement of domain walls, which plays a vital role in determining magnetic hysteresis behaviour. Needle-shaped grains possess a greater aspect ratio, resulting in an increased surface area-to-volume ratio when compared to grains that are more equiaxed. The increased surface area improves the chances of space charge accumulation at the grain interfaces or boundaries, leading to enhanced interfacial polarization. This can greatly contribute to improved interfacial polarization mechanisms.

4.4.3 Electrical Characterization

4.4.3.1 Dielectric constant

The graph (Figure 4.72) confirms the expected trend of a decreasing dielectric constant (ε′) with increasing frequency for $BaCo_xCr_xFe_{12-2x}O_{19}$ at all doping levels (Z0 to Z5). This behaviour is attributed to dielectric relaxation and dispersion phenomena occurring at lower frequencies. At lower frequencies, several factors contribute to the higher ε′ values observed that various relaxation mechanisms, such as Debye relaxation, might allow polarizable components within the material to align with the electric field, leading to higher polarization and ε′. Space charge polarization, where charges accumulate at interfaces between grains and grain boundaries, can also contribute to the overall polarization and a higher dielectric constant. Charge carriers can move within the conducting grains and accumulate at grain boundaries, generating an additional polarization effect. This effect is most prominent at lower frequencies.

As the frequency increases, these relaxation processes become less effective. The charge carriers cannot follow the rapidly changing electric field at high frequencies. Consequently, the contribution of these mechanisms to polarization diminishes, resulting in a decrease in the dielectric constant. Eventually, at very high frequencies,

ε' becomes nearly constant due to these limitations. This behaviour aligns with the two-layer Maxwell-Wagner model for interfacial polarization, which is consistent with Koop's theory [41, 42]. This model suggests that the material can be visualized as conducting grains separated by resistive grain boundaries. At low frequencies, charge carriers accumulate at the grain boundaries, leading to a high dielectric constant. However, at high frequencies, these charges cannot follow the field as effectively, resulting in a decrease in ε′.

The data reveals a significant decrease in the dielectric constant (ε′) with increasing frequency for all $BaCo_xCr_xFe_{12-2x}O_{19}$ samples (Z0 to Z5). Pure Ba Hexaferrite (Z0): The ε′ value starts high at 83.48 at 100 Hz and reduces to 12.38 at a higher frequency of 2 MHz.

Doped Samples (Z1 to Z5): Similar trends are observed for all doping levels. The initial ε′ values at 100 Hz vary depending on the dopant concentration (x) but exhibit a decrease at 2 MHz. Here are the specific maximum/minimum values in compositions:

Z1 (x = 0.2): ε′ (100 Hz) = 16.68, ε′ (2 MHz) = 4.13

Z2 (x = 0.4): ε′ (100 Hz) = 55.38, ε′ (2 MHz) = 5.66

Z3 (x = 0.6): ε′ (100 Hz) = 53.34, ε′ (2 MHz) = 5.06

Z4 (x = 0.8): ε′ (100 Hz) = 73.56, ε′ (2 MHz) = 3.93

Z5 (x = 1.0): ε′ (100 Hz) = 25.50, ε′ (2 MHz) = 3.52

4.4.3.2 Dielectric Loss and Tangent Loss factor

The dielectric loss (ε″) curves in Figure 4.72(b) exhibit a trend similar to the dielectric constant (ε′) curves, with higher values at lower frequencies and a decrease towards a constant value at higher frequencies. This behaviour suggests that the mechanisms responsible for dielectric loss are also influenced by the frequency of the applied electric field.

Interfacial Polarization at Lower Frequencies: At lower frequencies, interfacial polarization is likely a dominant contributor to dielectric loss. This phenomenon occurs because the material is composed of well-conducting grains separated by less conductive grain boundaries. Electrons can hop between these grains and accumulate at the grain boundaries if the resistance is high enough. This accumulation of charge carriers (space charge) contributes to polarization and energy loss (ε″).

Frequency Dependence of Polarization Mechanisms: As the frequency of the applied field increases, the ability of these polarization mechanisms to respond effectively diminishes. This is because the space charge carriers (electrons) need to change direction more frequently to follow the rapidly oscillating electric field. This hinders their ability to accumulate at grain boundaries, reducing interfacial polarization and consequently, dielectric loss (ε″).

Limited Response at High Frequencies: Beyond a certain critical frequency, the hopping of electrons or other relaxation processes cannot keep up with the rapidly changing field. This limits not only interfacial polarization but also other potential contributors to dielectric loss. This explains the decrease in ε″ towards a constant value at high frequencies [13-15].

The data reveals a significant decrease in the dielectric loss (ε″) with increasing frequency for all $BaCo_xCr_xFe_{12-2x}O_{19}$ samples (Z0 to Z5). Pure Ba Hexaferrite (Z0): The ε″ value starts high at 121.68 at 100 Hz and reduces significantly to 1.9 at a higher frequency of 2 MHz. Doped Samples (Z1 to Z5): Similar trends are observed for all doping levels. The initial ε″ values at 100 Hz vary depending on the dopant concentration (x) but exhibit a decrease at 2 MHz. Here are the specific maximum/minimum values in compositions:

Z1 (x = 0.2): ε″ (100 Hz) = 30.00, ε″ (2 MHz) = 0.32

Z2 (x = 0.4): ε″ (100 Hz) = 20.08, ε″ (2 MHz) = 0.60

Z3 (x = 0.6): ε″ (100 Hz) = 44.75, ε″ (2 MHz) = 0.70

Z4 (x = 0.8): ε″ (100 Hz) = 15.59, ε″ (2MHz) = 0.44

Z5 (x = 1.0): ε″ (100 Hz) = 19.48, ε″ (2 MHz) = 0.43

The tangent loss (tan δ) curves likely exhibit a peak at a specific frequency, followed by a decrease at higher frequencies. This peak behaviour is commonly observed in various dielectric materials and is referred to as relaxation/resonance behaviour [40-41]. Since tan δ is the ratio of dielectric loss to dielectric constant, the peak in tan δ suggests a corresponding peak in ε″. This peak in ε″ could be attributed to specific relaxation processes within the material, such as the hopping of electrons between Fe^{2+} and Fe^{3+} ions [16-20].

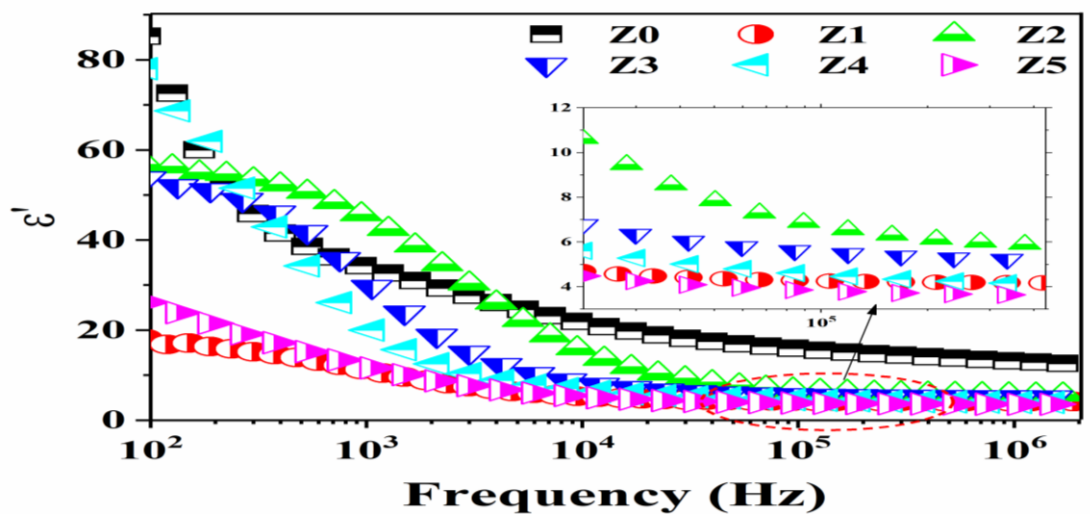

Figure 4.72(a) Frequency Dependence of Dielectric Constant in $BaCo_xCr_xFe_{12-2x}O_{19}$ (Z0 (x = 0.0), Z1 (x = 0.2), Z2 (x = 0.4), Z3 (x = 0.6), Z4 (x = 0.8), Z5 (x = 1.0)) Hexaferrites

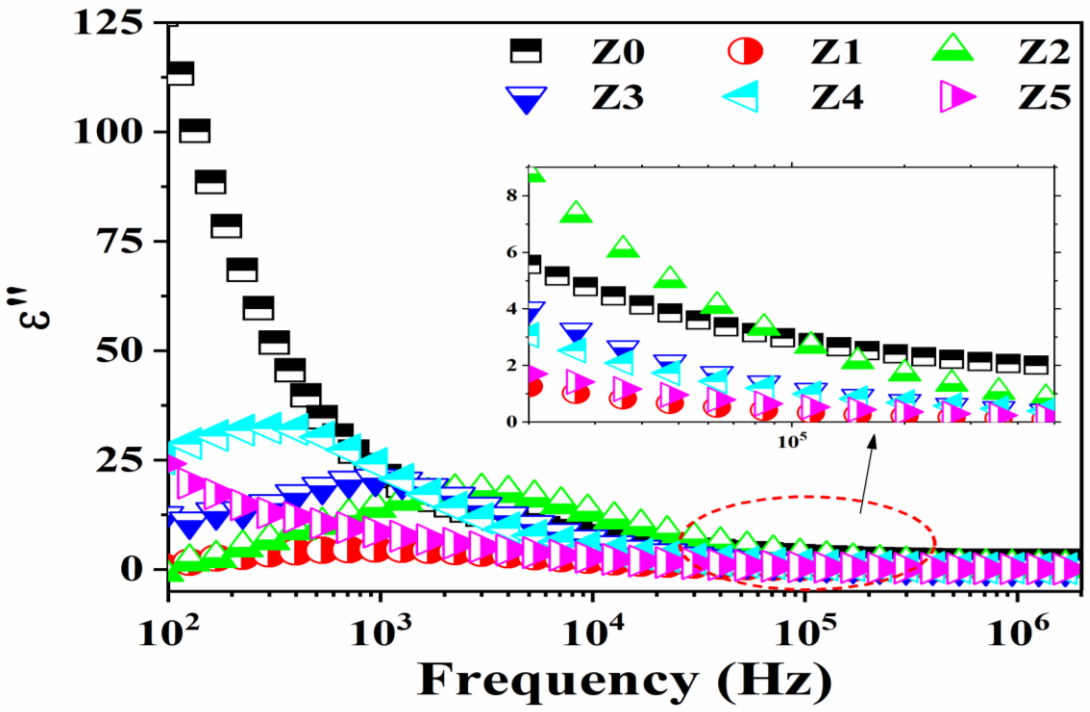

Figure 4.72(b) Frequency Dependence of Dielectric Loss in $BaCo_xCr_xFe_{12-2x}O_{19}$ Hexaferrites (Z0 (x = 0.0), Z1 (x = 0.2), Z2 (x = 0.4), Z3 (x = 0.6), Z4 (x = 0.8), Z5 (x = 1.0)).

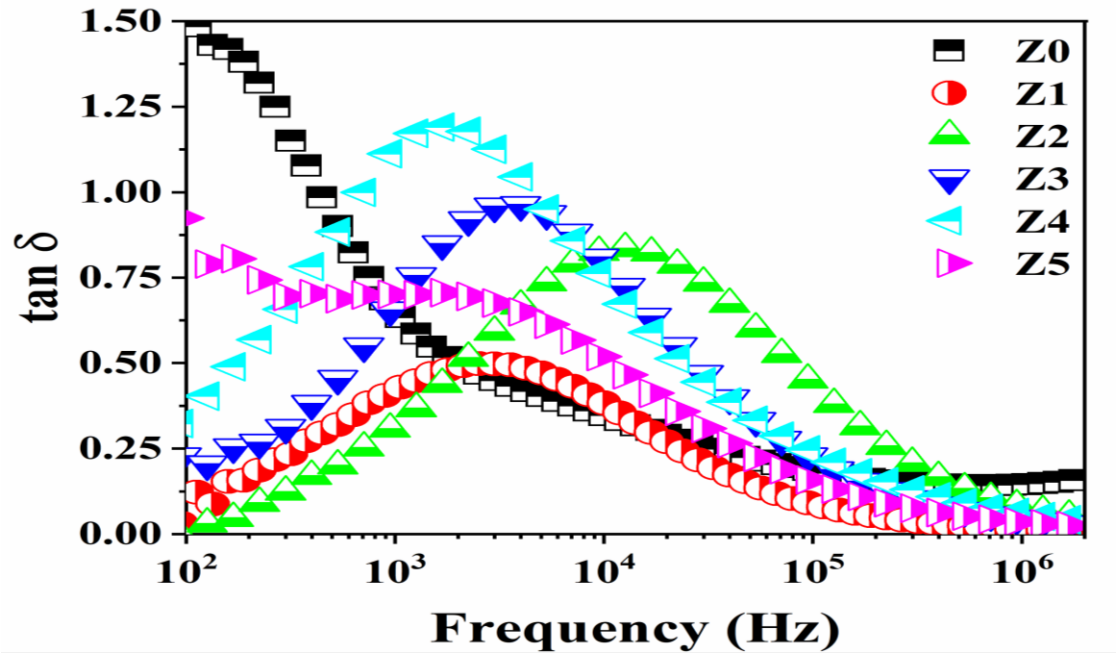

Figure 4.72(c) Frequency Dependence of tangent loss in $BaCo_xCr_xFe_{12-2x}O_{19}$ Hexaferrites (Z0 (x = 0.0), Z1 (x = 0.2), Z2 (x = 0.4), Z3 (x = 0.6), Z4 (x = 0.8), Z5 (x = 1.0)).

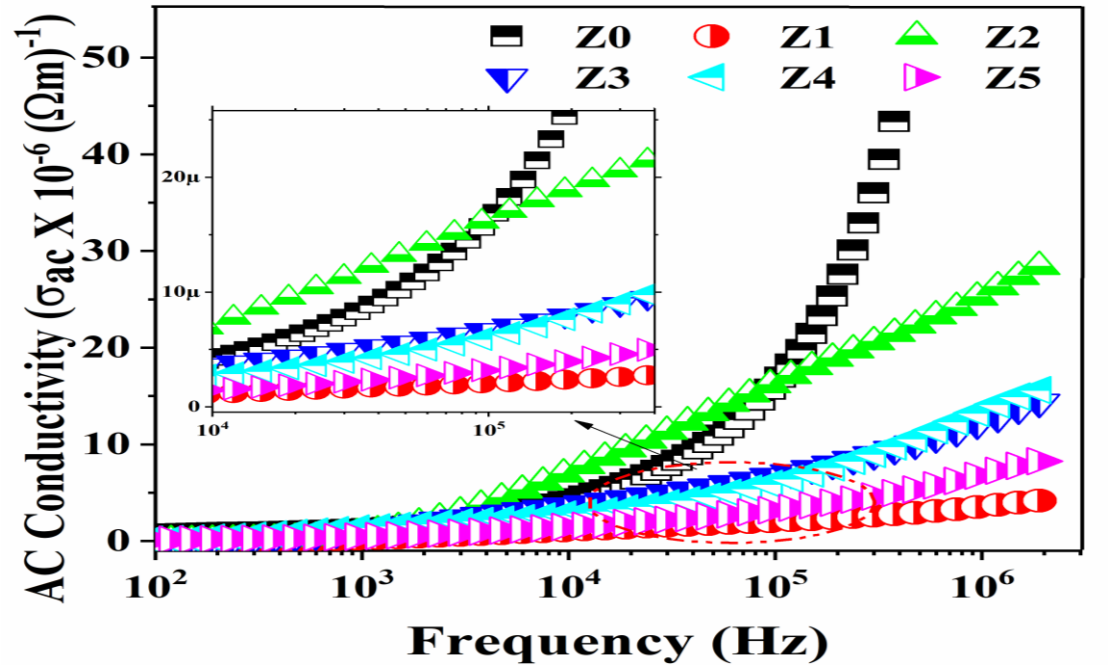

Figure 4.72(d) Frequency Dependence of AC Conductivity in $BaCo_xCr_xFe_{12-2x}O_{19}$ Hexaferrites (Z0 (x = 0.0), Z1 (x = 0.2), Z2 (x = 0.4), Z3 (x = 0.6), Z4 (x = 0.8), Z5 (x = 1.0)).

Competing Loss Mechanisms at Lower Frequencies: The conduction losses and ion migration losses becoming more dominant at lower frequencies. While these contribute to energy dissipation, they might not exhibit strong frequency dependence. Therefore, their contribution to tan δ might be overshadowed by the peak due to relaxation processes.

The observed peak in the tangent loss response suggests the presence of a dominant relaxation mechanism in $BaCo_xCr_xFe_{12-2x}O_{19}$, potentially involving electron hopping between Fe^{2+} and Fe^{3+} ions. The decrease in tan δ at higher frequencies indicates limitations in these relaxation processes as the field changes rapidly. It's important to consider the interplay between various loss mechanisms, especially at lower frequencies, for a complete understanding.

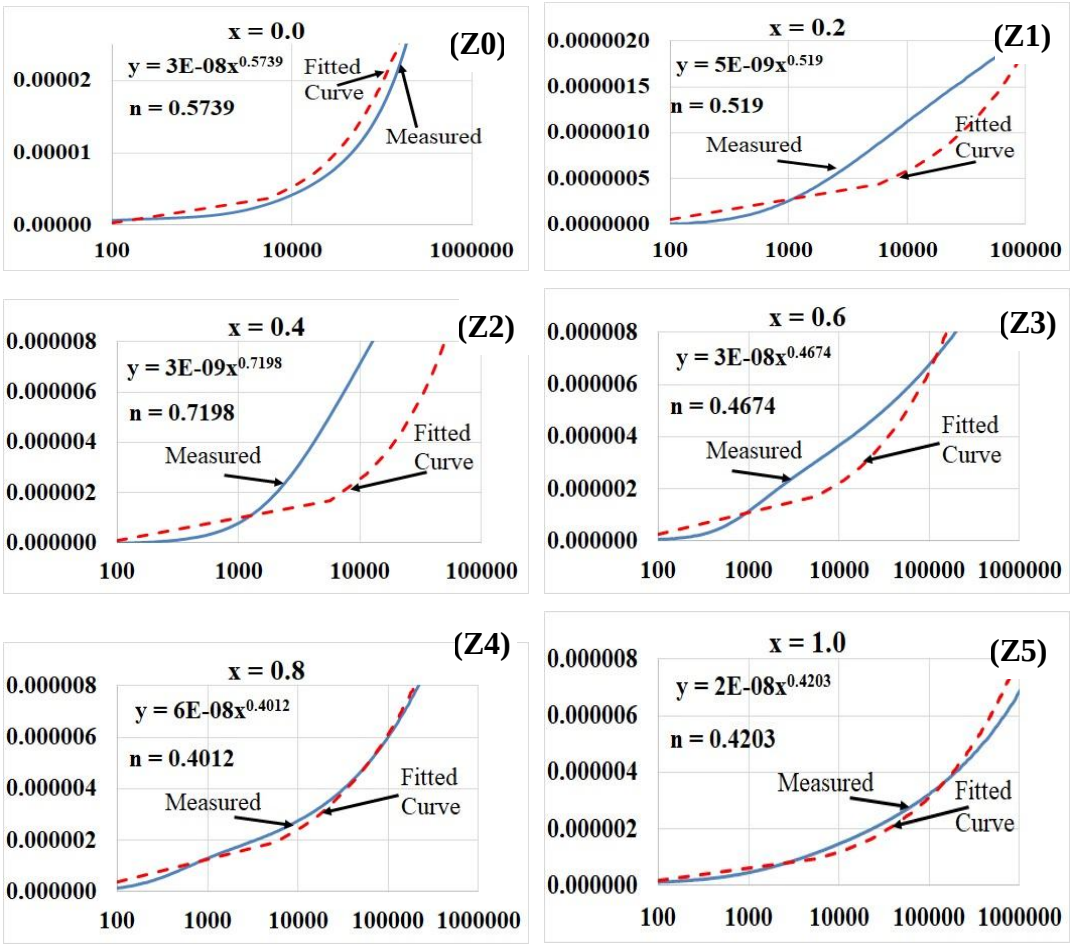

Figure 4.73 Frequency Exponent (n) of AC Conductivity in $BaCo_xCr_xFe_{12-2x}O_{19}$ (Z0 (x = 0.0), Z1 (x = 0.2), Z2 (x = 0.4), Z3 (x = 0.6), Z4 (x = 0.8), Z5 (x = 1.0)).

4.4.3.3 AC Conductivity

The observed increase in AC conductivity with frequency in Figure 4.72(d) aligns with the dominance of electronic conduction at lower frequencies and the growing influence of ionic conduction at higher frequencies.

The grain boundaries play a significant role in the material's conduction behaviour, particularly at lower frequencies. Due to their higher resistivity compared to the grains themselves, grain boundaries can act as barriers to the movement of charge carriers. This might explain why the volume of grain boundaries seems to control the conduction processes in the low-frequency regime.

The electrical conduction within the material is attributed to a hopping process described by Johnscher's universal power law equation [30, 31]:

$$\sigma_{ac} = \sigma_{dc} + A\,\omega^{n} \tag{4.10}$$

Both A and n are thermally activated quantities, meaning their values depend on the temperature of the material [33]. This implies that the hopping process and, consequently, the AC conductivity are influenced by temperature. The value of n provides valuable insights into the conduction mechanism within the material:

n = 1: This indicates a linear relationship between conductivity and the compositional/microstructural parameter. This behaviour might suggest Ohmic conduction, where current flow is directly proportional to the applied electric field.

n < 1: This signifies a sub-linear relationship, implying a weaker dependence of conductivity on the parameter.

n > 1: This suggests a super-linear relationship, indicating a stronger than proportional dependence of conductivity on the parameter.

Equation (4.53 & 4.54) suggests that AC conductivity (σ_{ac}) is proportional to frequency (ω) when the dielectric constant (ε') remains relatively constant and the tangent loss ($\tan\delta$) exhibits minimal change (except for Z1). This implies that for most doping levels (Z0, Z2, Z3, Z4 and Z5), increasing frequency leads to an increase in AC conductivity. For Z2, the AC conductivity appears to be the highest. This could potentially be attributed to a loss peak observed at higher frequencies for this specific doping level. This peak might be linked to an enhanced hopping frequency of electrons within the material. At higher frequencies, the contribution from the grains is believed to be responsible for the further rise in AC conductivity. Figure 4.73

illustrates the calculation of the frequency exponent (n) for AC conductivity in $BaCo_xCr_xFe_{12-2x}O_{19}$ samples with varying Co/Cr ratios (Z0 to Z5). As mentioned previously, the value of n is consistently less than 1, which aligns with the theoretical predictions from Johnscher's universal power law equation [26-38].

4.4.3.4 Electric modulus analysis

The graph (Figure 4.74(a)) depicts the dependence of the real modulus component (M′) on frequency for various $BaCo_xCr_xFe_{12-2x}O_{19}$ samples (with x ranging from 0.0 to 1.0) at room temperature. The real component of the dielectric modulus, M′, can be determined using the formula mentioned in reference [48]. The standard deviation of M′ appears to be highest at around 2 MHz, and it decreases at lower frequencies. In the low-frequency region (where all the curves appear to overlap), the M′ values tend towards zero. This indicates minimal conductivity and a strong restoring force, possibly due to high dielectric constant (Figure 4.74(a)) and electrode polarization effects [49].

At lower frequencies, the M′ values seem to increase with increasing Cr concentration. This suggests that the influence of electrode polarization becomes more pronounced with higher doping levels. Electrode polarization refers to the limitation of long-range mobility of charge carriers caused by the hindrance of their reorientation under an applied electric field [50, 51]. The rise in M′ with increasing frequency across all samples signifies that conduction is primarily dominated by the short-range motion of charge carriers facilitated by the restoring force within the material [50, 51]. Interestingly, the M′ values show a noticeable increase with Cr doping, suggesting a potential impact of dopant concentration on charge carrier mobility.

Figure 4.74(b) depicts the variation of the imaginary modulus component (M″) with frequency for $BaCo_xCr_xFe_{12-2x}O_{19}$ samples (Z0 to Z5). As emphasized earlier, M″ offers valuable insights into the interplay between grain boundaries, grains, defects, compositional variations, cationic distribution, and the dynamics of charge transport and conductivity relaxation [48]. M″ exhibits a well-defined peak at a characteristic frequency (f_{max}) for all samples, followed by a decrease with increasing frequency. This trend indicates a greater conductive loss at higher frequencies. The presence of these peaks suggests distinct conductivity relaxation mechanisms within the

hexagonal ferrites, as reported in [52]. The position of the peak (f_{max}) and its broadening with increasing Cr concentration provide valuable information about these mechanisms. The initial increase in M″ with frequency reflects the growing contribution of various conductivity relaxation processes within the material. These processes might involve the movement of charge carriers across grain boundaries or between different defect sites. The subsequent decrease in M″ at higher frequencies suggests a diminishing influence of these conductivity relaxation mechanisms. This could be due to the inability of charge carriers to follow the rapidly changing electric field at high frequencies.

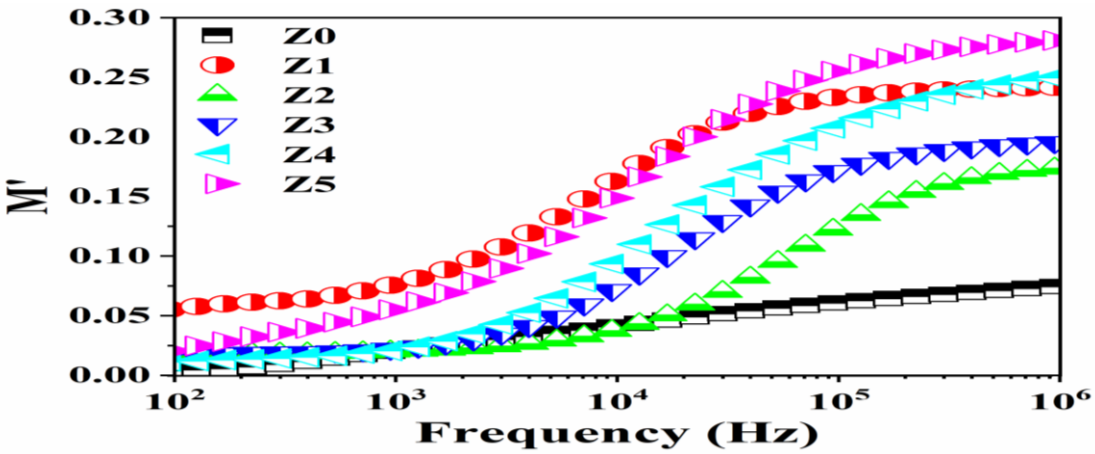

Figure 4.74(a) Frequency Dependence of Real Electric Modulus (M′) in Co-Cr Doped of $BaCo_xCr_xFe_{12-2x}O_{19}$ hexaferrite.

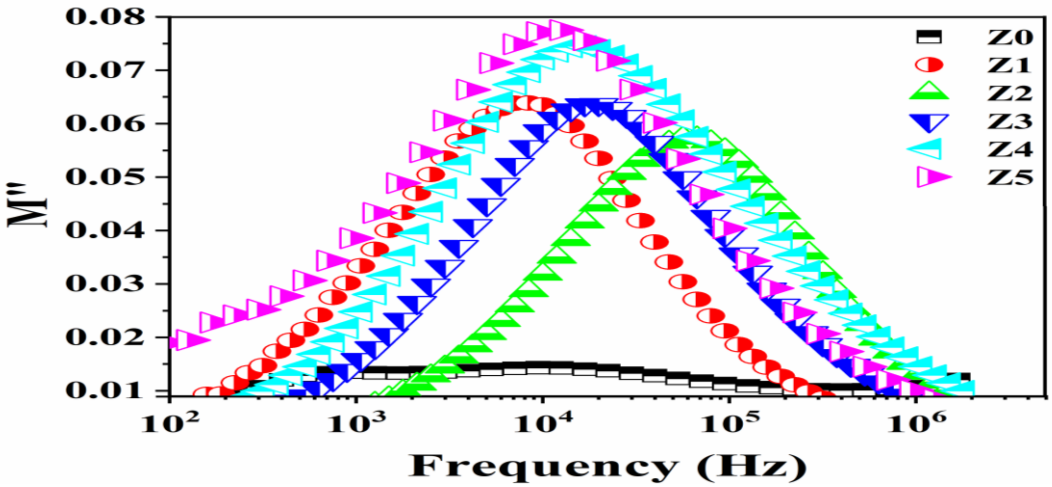

Figure 4.74(b). Frequency Dependence of Imaginary Electric Modulus (M″) in Co-Cr Doped of $BaCo_xCr_xFe_{12-2x}O_{19}$ hexaferrite

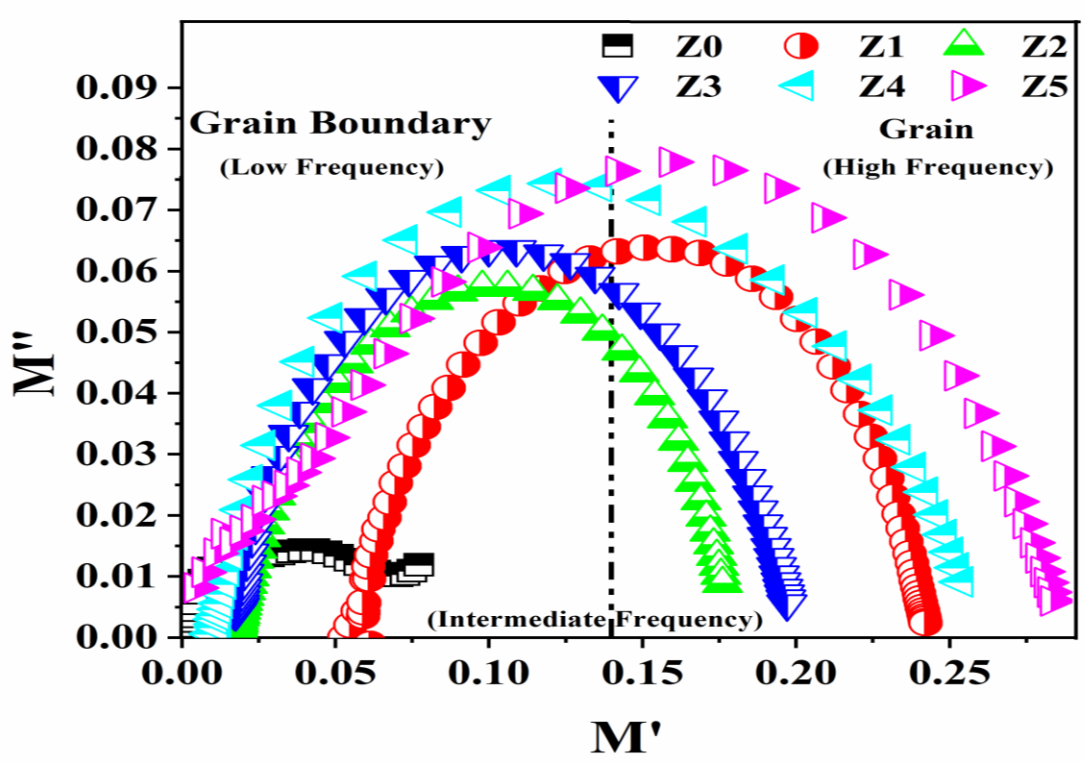

Figure 4.74(c) Frequency Dependence of Cole-Cole plot in Co-Cr Doped of $BaCo_xCr_xFe_{12-2x}O_{19}$ (Z0 (x = 0.0), Z1 (x = 0.2), Z2 (x = 0.4), Z3 (x = 0.6), Z4 (x = 0.8), Z5 (x = 1.0)) hexaferrite.

Figure 4.74(c) presents Cole-Cole plots (M″ vs. M′) for the synthesized $BaCo_xCr_xFe_{12-2x}O_{19}$ samples (Z0 to Z5) measured at room temperature. This graphical technique offers valuable insights into the influence of grain boundaries and grains on the electrical response of the material. All compositions except Z0 exhibit a single semicircle on the Cole-Cole plot. This suggests a dominant conductivity relaxation process within these samples. The plot typically displays two separate regions:

a. The lower frequency region is influenced by the presence of grain boundaries. In this region, there is a noticeable depressed semicircle, suggesting a broader range of conductivity relaxation times for grain boundaries.

b. The data points in the high-frequency region are associated with contributions from grains. In this particular region, there is a noticeable semicircle that appears to be less depressed, indicating that the grains have a more concentrated range of conductivity relaxation times.

The semicircles undergo variations in their position and shape as the doping level (x) increases. It appears that the size of the semicircles changes with doping, suggesting alterations in the resistance of grains and grain boundaries.

The semicircles with larger diameters in the low-frequency region indicate that grain boundary effects play a more significant role in these materials. It is clear that the grain boundaries have a significant impact on the electrical properties.

Observing the semicircles, it becomes evident that there is a clear indication of a distribution of conductivity relaxation times for both grains and grain boundaries, which contributes to their depressed nature. The observed deviation from Debye behaviour can be attributed to the intricate microstructure and defect structure of the material.

The Cole-Cole plots undergo changes when doping is introduced, indicating that the substitution of Co-Cr alters the properties of the grains and grain boundaries, thereby impacting the conductivity relaxation behaviour.

The area under the curve at intermediate frequencies is generally attributed to the contribution of grain boundaries to the overall impedance [55]. The left side of the semicircle towards the lower frequencies corresponds to the grain boundary resistance [56]. The higher frequency region on the right side of the plot reflects the combined influence of grain resistance [57]. Doping with Co-Cr leads to a shift of the semicircle towards the high-frequency domain. This indicates a faster conductivity relaxation process at higher frequencies with increasing Cr concentration, implying a significant contribution of grains. The increased diameter of the semicircle with doping suggests a higher overall conductivity for the Co-Cr doped samples. The shift in the maximum of the semicircle towards higher frequencies with increasing dopant concentration (x) signifies a distribution of conductivity relaxation times within the material dominated by grains. This observation supports a non-Debye relaxation mechanism, where relaxation processes occur with a spectrum of time constants rather than a single time constant [58].

Non-Debye relaxation strays from the ideal Debye model, where relaxation takes place with a single relaxation time. Relaxation times in real materials, particularly complex ones such as doped barium hexaferrites, tend to exhibit a distribution. This is a result of the natural diversity of the material, which includes:

a. Microstructural variations play a significant role in the presence of multiple relaxation environments, stemming from disparities in grain size, grain boundaries, and porosity.
b. Defects such as vacancies, interstitials, and dopant ions can have an impact on the mobility and relaxation behavior of charge carriers by introducing localized energy levels.

Co and Cr doping add additional complexity to the relaxation behaviour:

a. The crystal lattice is distorted due to the substitution of Fe ions with Co and Cr, which have different ionic radii. This distortion creates local electric fields and alters the potential energy landscape for charge carriers.
b. The presence of d-electrons from Co and Cr can significantly impact the electronic band structure, leading to changes in the availability of energy states for charge carriers and their mobility.
c. Doping has the potential to introduce extra defects, like oxygen vacancies, that can function as charge traps and impact relaxation processes.

Exploring the Impact of Co-Cr Doping:

a. At lower doping levels (Z0 to Z1), the material shows reduced grain sizes and increased porosity. Charge carriers face additional obstacles at grain boundaries, resulting in a broad range of conductivity relaxation times.
b. At intermediate doping levels (Z2 to Z3), grain growth and fusion take place, resulting in a decrease in grain boundary density and porosity. As a result, the distribution of conductivity relaxation times becomes somewhat narrower, although it still shows non-Debye behaviour because of remaining defects and inconsistencies.
c. At high levels of doping, there is a noticeable fusion of grains and a decrease in the area of grain boundaries. Nevertheless, the existence of sizable grains or clusters brings about fresh conductivity relaxation mechanisms, which uphold non-Debye characteristics.

4.4.3.5 Impedance spectroscopy

5 Across all compositions, the impedance (Z' and Z'') decreases significantly as the frequency increases from low to high frequencies. This is typical of dielectric materials where resistive components dominate at low frequencies, and at higher

frequencies, capacitive effects start to dominate, reducing impedance. As the frequency increases beyond 10^4 Hz, the impedance values for all compositions tend to converge. This behaviour suggests that at higher frequencies, the impedance becomes less sensitive to the level of doping. The decrease in Z' and Z'' flattens out for all samples, indicating that the material behaves more capacitive at these frequencies, with less influence from resistive components.

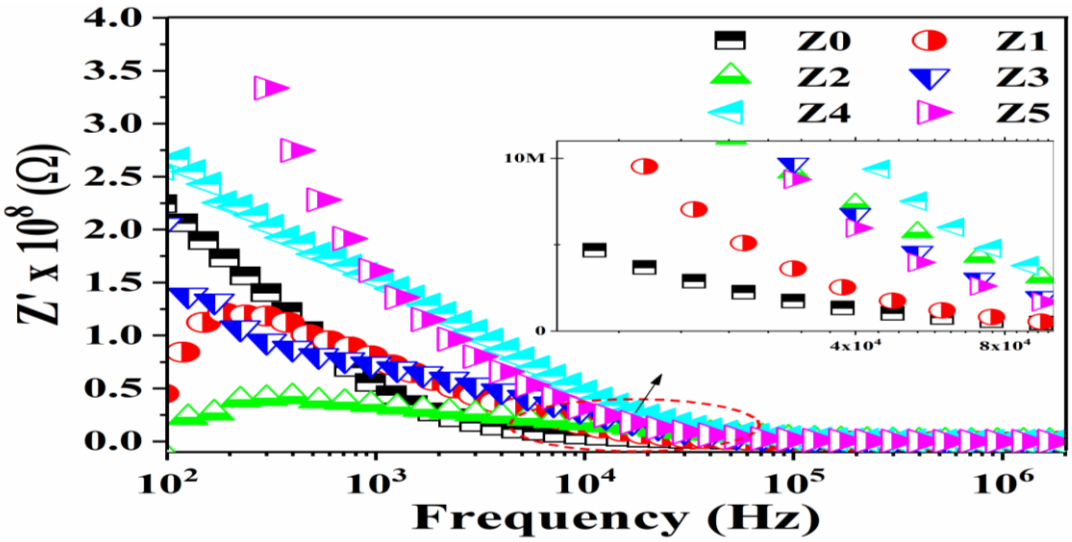

Figure 4.75(a) Frequency Dependence of Real Impedance (Z') in Co-Cr Doped $BaCo_xCd_xFe_{12-2x}O_{19}$ (Z0 (x = 0.0), Z1 (x = 0.2), Z2 (x = 0.4), Z3 (x = 0.6), Z4 (x = 0.8), Z5 (x = 1.0)) hexaferrite.

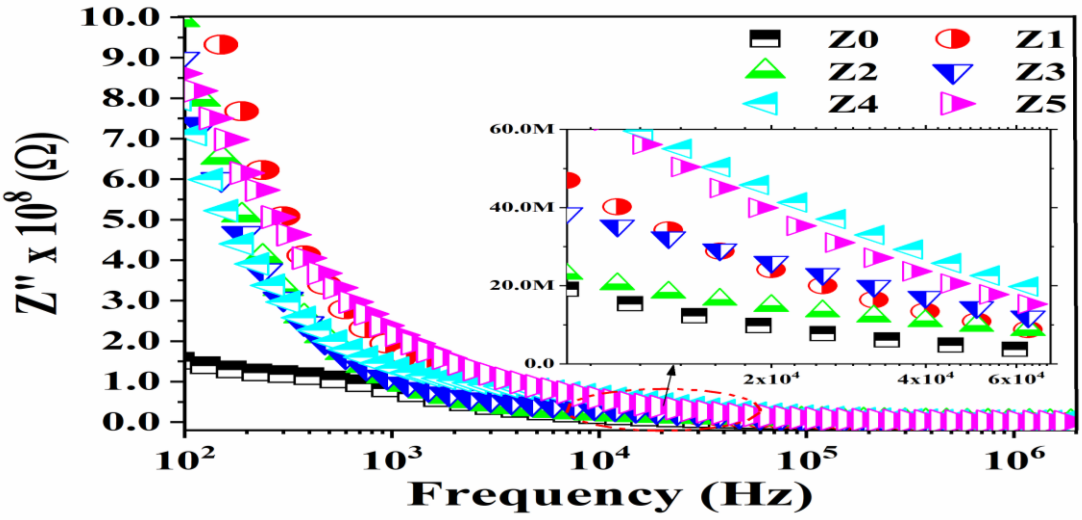

Figure 4.76(b) Frequency Dependence of Imaginary Impedance (Z″) in Co-Cr Doped $BaCo_xCd_xFe_{12-2x}O_{19}$ (Z0 (x = 0.0), Z1 (x = 0.2), Z2 (x = 0.4), Z3 (x = 0.6), Z4 (x = 0.8), Z5 (x = 1.0)) hexaferrite.

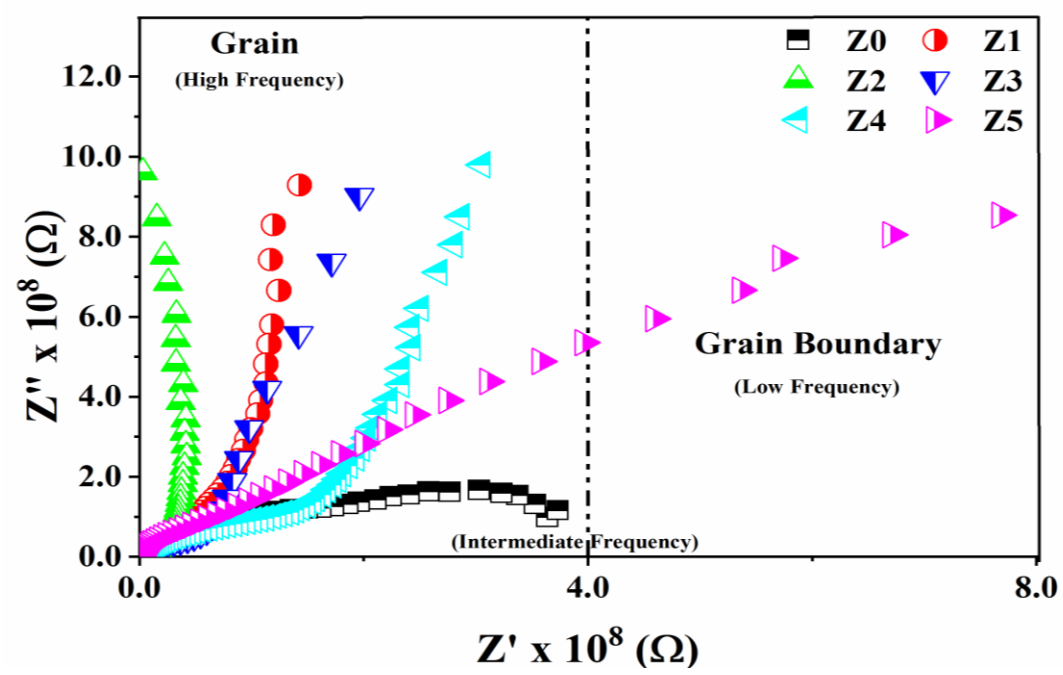

Figure 4.76(c) Frequency Dependence of Cole-Cole Plot in Co-Cr Doped $BaCo_xCd_xFe_{12-2x}O_{19}$ (Z0 (x = 0.0), Z1 (x = 0.2), Z2 (x = 0.4), Z3 (x = 0.6), Z4 (x = 0.8), Z5 (x = 1.0)) hexaferrite.

Models are used to fit experimental data in order to quantitatively analyze non-Debye relaxation. Here are some commonly used models:

The Cole-Cole model: This empirical model incorporates a distribution parameter (α) to consider the range of relaxation times. The equation for the complex permittivity (ε*) is as follows:

$$\varepsilon^* = \varepsilon^{\infty} + (\varepsilon^s - \varepsilon^{\infty})/[1 + (i\omega\tau)^{-1} - \alpha] \quad (4.59)$$

The equation represents the relationship between two variables, ε* and ω, in a mathematical expression. It involves various parameters such as ε^{∞}, ε^s, τ, and α. The equation allows for the calculation of ε* based on these parameters. The equation includes several variables such as the high-frequency permittivity, static permittivity, angular frequency, characteristic relaxation time, and the Cole-Cole parameter.

Figures 4.76(a) and 4.76(b) depict the dependence of the real (Z′) and imaginary (Z″) parts of the impedance on frequency for $BaCo_xCr_xFe_{12-2x}O_{19}$ samples. By plotting Z′ vs. Z″, Cole-Cole impedance plots, as illustrated in Figure 4.76(c). These plots offer a comprehensive view of the material's electrical response across a frequency range. The observed semi-circular arcs in the Cole-Cole plots can be interpreted using a two-

layer model, where two overlapping semicircles contribute to the overall impedance response [54-56]. The low-frequency semicircle is generally attributed to the resistance at grain boundaries within the material. The high-frequency semicircle is associated with the resistance of the grain interiors or bulk properties. The presence of these two semicircles suggests a distribution of relaxation times within the material. Relaxation time refers to the time constant associated with various polarization processes. However, it's important to note that if the relaxation time constants of the grain and grain boundary processes differ by less than a factor of 100, their corresponding semicircles in the Cole-Cole plot will exhibit significant overlap, making it challenging to distinguish them clearly. The influence of grain size on the complex impedance response is well documented. In small-grain materials, a single semicircle is often observed in Cole-Cole plots, encompassing both grain boundary and grain resistance contributions. In contrast, larger-grain materials may exhibit two distinct semicircles, allowing for a clearer separation of these effects. Our investigation employed Cole-Cole impedance spectroscopy at room temperature for all synthesized $BaCo_xCr_xFe_{12-2x}O_{19}$ samples (Z0 to Z5). The observed impedance response suggests that grain boundary conduction dominates the behaviour, as evidenced by the presence of a single, incomplete semicircle in most samples (except Z0). Possible explanations for the high grain boundary resistance and the absence of a distinct grain contribution in some samples (Z0) include strong resistive character of the grain boundaries; increased surface-to-volume ratio associated with smaller grains, enhanced porosity within the material and disorganized atomic arrangement at the grain boundaries.

5.3.1.1 Software-based Impedance Simulation and Validation

Parameters Utilized in Impedance Simulations and Calibration. As stated, the equivalent circuit model commonly uses a mix of resistors, capacitors, and constant phase elements to depict the electrical characteristics of the material. These components are utilized to simulate different aspects of the material's response, including:

a. Grain resistance (R_g) refers to the resistance that exists within the grains.
b. Grain boundary resistance (R_{gb}) is a measure of the resistance that occurs at the boundaries between grains.

c. The grain capacitance (C_g) represents the capacitance that is related to the grains.
d. The grain boundary capacitance (C_{gb}) represents the capacitance related to the grain boundaries.

The constant phase element (CPE) is used to model non-ideal capacitive behaviour, commonly observed in grain boundaries and interfaces.

Calibrating these parameters requires matching the simulated impedance spectra to the experimental data. This is usually accomplished by utilizing optimization algorithms that fine-tune the parameter values in order to minimize the discrepancy between the simulated and experimental data.

Important steps in parameter calibration:

a. The circuit parameters are estimated using the material's properties and the anticipated behavior.
b. The selected equivalent circuit model is simulated using the initial parameter values.
c. The simulated impedance spectra are compared to the experimental data.
d. Parameter optimization involves using an optimization algorithm to iteratively adjust parameter values until the simulated and experimental data are in the best possible agreement.
e. Statistical metrics like chi-square or mean squared error are used to determine how well the data fits.

The least squares method aims to minimize the sum of squared differences between simulated and experimental data.

Genetic algorithms are an effective optimization technique that utilizes a population-based approach to explore a diverse set of parameter values.

Simulated annealing is a powerful probabilistic optimization method that effectively avoids getting stuck in local minima.

Equivalent circuit modelling of the complex impedance data was conducted using dedicated EIS software. The results are presented in Figure 4.77. Our analysis reveals a good concordance between the observed and simulated/fitted impedance curves for all material compositions (shown in the Figure 4.77). Additionally, Table 4.25

summarizes the resistances, and capacitances of both grains and grain boundaries as extracted from the EIS measurements.

In the low frequency region, the impedance spectra are primarily influenced by grain boundary effects. These effects result in noticeable resistance and capacitance due to the presence of multiple interfaces and defects.

In the high frequency region, the characteristics of the grains become more noticeable. In this region, the resistance and capacitance values are lower, indicating that the grains are more conductive than the grain boundaries.

The modulus spectra display broad peaks, suggesting a diverse range of relaxation times and supporting the non-Debye behaviour. The peaks' position and width vary with doping, indicating alterations in the microstructure and defect landscape.

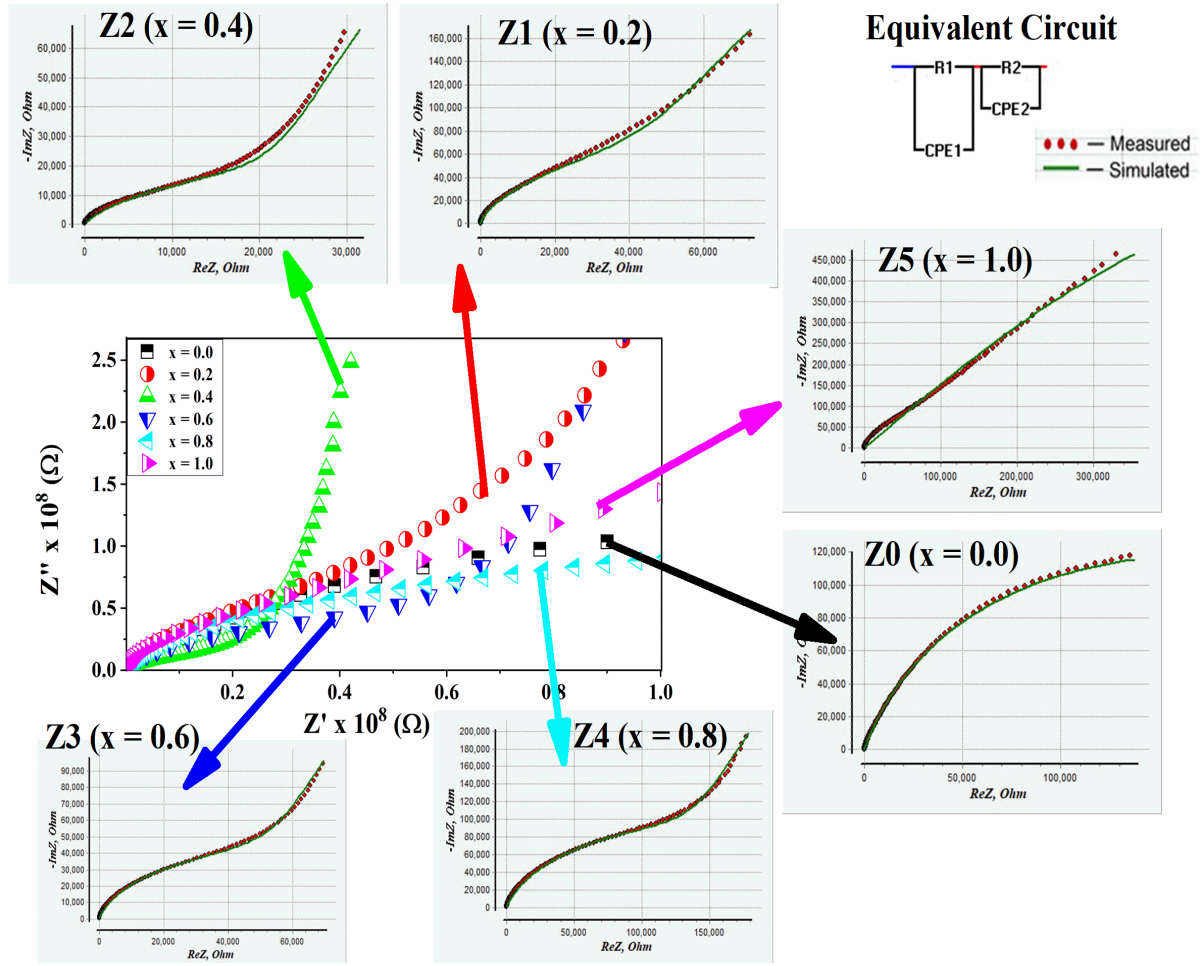

Figure 4.77 Complex Impedance Spectroscopy of Ferrite Samples: Measured Data (Red Points) and Equivalent Circuit Fitting (Green Lines) where Z0 = 0.0, Z1 = 0.2, Z2 = 0.4, Z3 = 0.6, Z4 = 0.8 and Z5 = 1.0

Table 4.25 Extracted Grain and Grain Boundary Parameters from Electrical Impedance Spectroscopy

x	R_g (MΩ)	R_{gb} (MΩ)	C_g (μF)	C_{gb} (μF)
Z0 (0.0)	190.090	480.660	19.431	11815.577
Z1 (0.2)	57.427	1205.000	2.079	0.848
Z2 (0.4)	24.942	802.730	11.849	2.331
Z3 (0.6)	57.843	1012.000	2.396	3.815
Z4 (0.8)	163.620	1122.500	5.306	1.595
Z5 (1.0)	1010.000	850.110	1.793	7652.563

Looking at the table, we can observe some general trends are as follows:

R_g: Seems to show a complex relationship with doping level. It's low for Z1 and increases for both lower (Z0) and higher doping levels (Z3, Z4 and Z5).

R_{gb}: Generally remains high across all doping levels, with a possible peak at Z1.

C_g: Appears to decrease with increasing doping level.

C_{gb}: Shows a significant decrease from Z0 to Z1, followed by a slight increase or remains relatively constant at higher doping levels.

5.3.1.2 Correlation between EIS parameters and Morphology

Figure 4.71 reveals smaller grain sizes for Z0. This translates to a higher density of grain boundaries per unit volume. These numerous interfaces can enhance the dispersion of charge carriers, potentially contributing to a higher grain boundary resistance (R_{gb}) of 480.66 MΩ. The increased surface area associated with smaller grains (Z0) might lead to a larger grain boundary capacitance (C_{gb}) of up to 11815.57 μF. This can be attributed to the increased interfacial capacitance at these boundaries. The presence of voids or empty spaces (porosity) observed in the Z0 sample can disrupt the continuity of the grains. These insulating spaces act as barriers, hindering the movement of charge carriers and potentially increasing the grain resistance (R_g) to 190.09 MΩ due to the reduced effective cross-sectional area for conduction. Smaller grain sizes (Z0) are associated with faster grain time constants (τ_g). This is because the higher surface area to volume ratio in smaller grains strengthens surface effects, leading to more efficient polarization and charge carrier dynamics. The Figure 4.71 shows a microstructure with relatively small and uniformly sized grains. This aligns with the expectation of a higher grain boundary area for Z0, which could contribute to the following in the electrical properties data:

Higher grain boundary resistance (R_{gb}): A larger grain boundary area can provide more resistance to current flow across grain boundaries, potentially explaining the high value of R_{gb} (480.66 MΩ) observed in the table 4.25.

Higher grain boundary capacitance (C_{gb}): The increased interfacial area associated with smaller grains might contribute to a higher capacitance for grain boundaries, reflected in the high value of C_{gb} (11815.58 µF) in the table 4.25.

Analysis of Figures 4.71 and 4.77 indicates variations in grain size and crystallographic orientation for Z1. These microstructural heterogeneities can influence grain boundary characteristics, potentially increasing the overall grain boundary resistance (R_{gb}) observed in Table 4.25 (1205.00 MΩ). The presence of heterogeneous grain morphology can disrupt the connectivity and continuity of grain boundaries. Such discontinuities or variations in grain boundary connectivity might contribute to higher R_{gb} values. The Figure 4.71 shows a microstructure with a wider distribution of grain sizes compared to Z0. There are some larger grains visible alongside smaller grains. The grain morphology appears more irregular compared to the uniform rounder grains seen for Z0. The presence of some larger grains might contribute to an increase in R_g compared to Z0. However, the overall distribution of grain sizes could also lead to a lower average value of R_g due to the presence of smaller grains. The table 4.25 shows a decrease in R_g (57.43 MΩ) compared to Z0, which aligns with this possibility. The observed variation in grain size and more irregular morphology suggest a complex grain boundary network for Z1. This could lead to a higher R_{gb} compared to Z0 with its more uniform grain boundaries. The above table 4.25 shows an increase in R_{gb} (1205.00 MΩ) compared to Z0. The presence of some larger grains might suggest a slightly higher overall C_g compared to Z0. However, the reduced volume fraction of large grains compared to Z2 might limit a significant increase. The table 4.25 shows a significant decrease in C_g (2.08 µF) compared to Z0, which could be due to the dominance of smaller grains in the microstructure. The complex grain boundary network with potentially lower connectivity (due to the irregular morphology) could lead to a decrease in C_{gb} compared to Z0. The table 4.25 shows a significant decrease in C_{gb} (0.85 µF) compared to Z0.

Doping at Z2 promotes grain fusion, leading to an increase in average grain size. This directly affects grain capacitance (C_g) as larger grains offer more surface area and volume for charge accumulation. Consequently, the fusion process can enhance C_g, as reflected in the data (up to 11.85 μF). While grain fusion increases grain size and potentially C_g, it can also introduce new defects, impurities, or structural changes at the fused grain boundaries. These alterations, as seen in Table 4.25 (continued high R_{gb} of 1205.00 MΩ), may impede charge carrier transport and elevate grain boundary resistance. For instance, if the fusion process creates disordered or structurally distinct regions at the grain boundaries, it can act as a barrier, hindering charge transport and contributing to the observed high R_{gb}. The Figure 4.71 shows a significant difference compared to Z0 and Z1. There is evidence of grain growth and fusion, resulting in a larger average grain size. The distinct rounder shapes of individual grains observed in Z0 are less evident. The Figure 4.71 shows a more interconnected network of grains with some irregular boundaries, suggesting some fusion events might not have been perfect. The presence of larger grains due to fusion is expected to increase R_g compared to Z0 and Z1. The table 4.25 shows a moderate increase in R_g (24.94 MΩ) compared to Z1. Grain fusion can lead to a reduction in grain boundary area. However, the presence of some irregular grain boundaries in the image suggests that the fusion process might not have been complete, leaving behind some higher resistance boundaries. The table 4.25 shows a decrease in R_{gb} (802.73 MΩ) compared to Z1, indicating a reduction in overall grain boundary area despite potentially higher resistance at some remaining boundaries. The larger grain size observed due to fusion is expected to increase the overall grain capacitance (C_g) compared to Z0 and Z1. The table 4.25 shows an increase in C_g (11.85 μF) compared to Z1. The reduction in grain boundary area due to fusion suggests a decrease in C_{gb} compared to Z0 and Z1. However, the presence of some residual grain boundaries and potentially imperfect fusion might contribute slightly to C_{gb}. The table 4.25 shows a small increase in C_{gb} (2.33 μF) compared to Z1.

The Figure 4.71 shows a continuation of the grain growth trend observed at Z2. The average grain size appears larger compared to previous doping levels. There's evidence of significant grain fusion, resulting in a more interconnected network of large grains. Distinct individual grain boundaries are less visible compared to lower

doping levels. The overall morphology suggests extensive fusion events, creating a more uniform network of large grains. The continued presence of larger grains due to fusion is expected to further increase R_g compared to lower doping levels. The table 4.25 shows a moderate increase in R_g (57.84 MΩ) compared to Z2. The increase might be due to the overall larger grain size, but it's important to consider other factors like porosity that can also influence R_g. The extensive grain fusion observed in the image suggests a significant reduction in overall grain boundary area compared to lower doping levels. This would lead to a decrease in R_{gb}. The table 4.25 shows a decrease in R_{gb} (1012.00 MΩ) compared to Z2. The larger average grain size due to fusion is expected to further increase the overall grain capacitance (C_g) compared to lower doping levels. The table 4.25 shows a slight increase in C_g (2.39 µF) compared to Z2. The significant reduction in grain boundary area due to fusion suggests a further decrease in C_{gb} compared to lower doping levels. The table 4.25 shows a decrease in C_{gb} (3.82 µF) compared to Z2, aligning with this expectation.

The Figure 4.71 shows a microstructure dominated by large grains, consistent with the trend of grain growth observed at higher doping levels. The average grain size appears larger compared to Z3. Distinct individual grain boundaries are almost invisible, suggesting extensive grain fusion events, resulting in a highly interconnected network of large equiaxed grains. The continued presence of very large grains is expected to further increase R_g compared to lower doping levels. The table 4.25 shows a significant increase in R_g (163.62 MΩ) compared to Z3. This increase aligns with the expectation of higher resistance associated with larger grains. The presence of even larger grains due to fusion suggests a further increase in the overall grain capacitance (C_g) compared to lower doping levels. The table 4.25 shows a moderate increase in C_g (5.31 µF) compared to Z3. This increase aligns with the expectation of higher capacitance for larger grains. The significant reduction in grain boundary area due to fusion suggests a further decrease in C_{gb} compared to lower doping levels. The table 4.25 shows a decrease in C_{gb} (1.59 µF) compared to Z3. The Figure 4.71 showcases a microstructure dominated by very large, equiaxed grains. This aligns with the trend of grain growth observed at higher doping levels (Z3 to Z4). Individual grain boundaries are practically invisible, indicating extensive grain fusion events, resulting in a highly interconnected network of large grains. The presence of exceptionally large grains is

expected to further elevate R_g compared to lower doping levels. The data shows a very high R_g value (1010.00 MΩ) for Z5, which aligns with the expectation of increased resistance associated with these large grains.

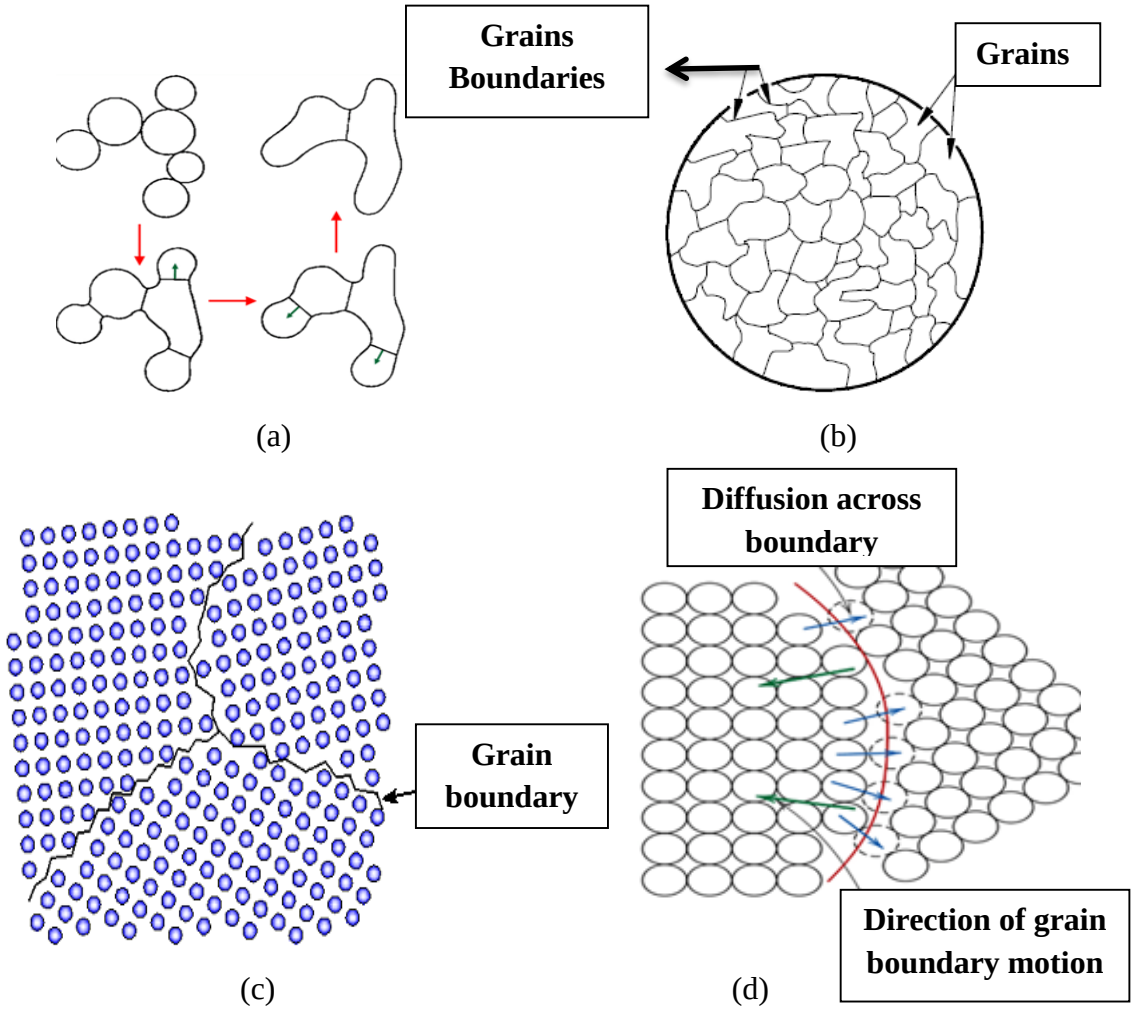

Figure 4.78 (a) Migration of grain process; (b) Represent Grain and Grain Boundaries; (c) Separation of grain and identification of grain boundaries; (d) Diffusion across boundary for $BaCo_xCr_xFe_{12-2x}O_{19}$ (Z0 (x = 0.0), Z1 (x = 0.2), Z2 (x = 0.4), Z3 (x = 0.6), Z4 (x = 0.8), Z5 (x = 1.0)).

The extensive grain fusion observed in the image suggests a significant reduction in overall grain boundary area compared to lower doping levels. This would generally lead to a decrease in R_{gb}. The table 4.25 shows a surprisingly high value for R_{gb} (850.11 MΩ) at Z5. This deviation from the expected trend might be due to a few reasons as electrical impedance spectroscopy might not perfectly separate the contributions from grains and grain boundaries, especially in materials with minimal

grain boundaries, like the one observed here for Z5, although the overall image shows extensive fusion, there might be some localized areas with less perfect fusion, leading to higher resistance grain boundaries and if the material has any porosity (voids or empty spaces), it can act as insulating barriers and elevate the overall resistance, including grain boundary resistance. While not directly visible in the FESEM image, porosity can be present within the material. The FESEM image for Z5 confirms the continuation of grain growth and fusion observed with increasing doping level. This aligns with the presence of very large grains, which likely contribute to the high grain resistance (R_g) seen in the electrical properties data. However, the high value of grain boundary resistance (R_{gb}) might be due to limitations in measurement techniques or the presence of porosity. The low grain capacitance (C_g) observed could be due to limitations of grain growth or the influence of porosity. The decrease in grain boundary capacitance (C_{gb}) is consistent with the reduction in grain boundary area due to fusion.

5.3.2 Magnetic Analysis

The chromium ion (Cr^{3+}) in the $BaCo_xCr_xFe_{12-2x}O_{19}$ compound has a lower electronegativity value of 1.66, while the cobalt ion (Co^{2+}) has a higher electronegativity value of 1.88. Therefore, Cr^{3+} can occupy tetrahedral sites with a $4f_1$ structure, whereas Co^{2+} can occupy octahedral sites. The Fe^{3+} ions in M-type barium hexagonal ferrites are scattered in five distinct locations: three octahedral sites (2a, 12k, and $4f_2$) and two tetrahedral sites (2b and $4f_1$). 2a, 2b, and 12k show spin up, while $4f_1$ and $4f_2$ exhibit spin down [4].

Co^{2+} ions preferentially occupy octahedral sites because of their d^7 electron configuration, which is stabilized by a high-spin state. Reports indicate that Co^{2+} ions have a predilection for occupying the $4f_1$, $4f_2$, and 2b locations. Cr^{3+} ions, characterized by a d^3 electron configuration, have a preference for occupying tetrahedral positions ($4f_1$). It is important to mention that the Co^{2+} (0.72 Å) ions have greater ionic radii in comparison to the Fe^{3+} (0.64 Å) ions in the host material. The increased dimensions allow for the accommodation of both Cr^{3+} and Co^{2+} ions, which may have an impact on the magnetic and structural characteristics of the unit cell. [183-184].

Figure 4.79 demonstrates the hysteresis loops of all $BaCo_xCr_xFe_{12-2x}O_{19}$ samples at room temperature. The values obtained from the M-H loop are shown in the Table. The values include the saturation magnetization (M_s), the remanence magnetization (M_r), the coercivity (H_c), the anisotropy field (H_a), and the remanence ratio (M_r/M_s).

As the amount of substitution grows from Z0 to Z5, the table illustrates that there is a non-monotonic reduction in M_s. There are a number of possible explanations for the decrease in magnetization (M_s), some of which include spin canting, the shift from a high to a low spin valence state, site occupancy, and exchange interaction.

The table 4.26 illustrates a decrease in M_s from Z0 to Z5 that is not consistently linear as the level of substitution increases. There are several factors that can contribute to the reduction in magnetization (M_s), including spin canting, transition from a high to a low spin valence state, changes in site occupancy, and exchange contact. At lower degrees of substitution, specifically from Z0 to Z2, there has been a noticeable 44% decrease in the M_s Value. When Fe^{3+} (5 μB) is replaced by weak magnetic Co^{2+} (3 μB) and Cr^{3+} (3 μB), there is a decrease in M_s. This decrease happens because it reduces the number of Fe^{3+} ions at magnetic sites. The increase in M_s from 44.43 to 64.47 from Z2 to Z3 could potentially be linked to a decrease in porosity. Porosity is a vacant space that generates demagnetizing forces and reduces magnetization, without any magnetic properties. Nevertheless, the rise in M_s is not as significant as the decline in porosity. It is possible that the increase in M_s [188] is due to the occupancy of both the $4f_2$ and $4f_1$ locations of crystallographic sites. Finally, the M_s Value experienced a significant decrease from Z3 to Z5, dropping from 64.465 to 24.173. Replacing Fe^{3+} with a significant amount of Cr^{3+} (Z5) has the potential to disturb the integrity of the crystal lattice. In Z5, the substitution of weak magnetic ions with Fe^{3+} ions weakens the superexchange interaction at high doping level which decreases the M_s. This disturbance has the potential to diminish the overall magnetic superexchange interactions among the remaining Fe^{3+} ions, leading to a reduction in M_s. It is possible for certain interactions to occur that may lead to a decrease in magnetization saturation (M_s).

Table 4.26. Magnetic parameters determined from M-H curves

Sample	M_s (emu/g)	H_c (Oe)	H_a(kOe)	M_r (emu/g)	M_r/M_s
Z0	79.99935	5341.764	15.69861	39.96	0.499504

Z1	74.0807	3844.839	14.42977	39.37	0.531447
Z2	44.42534	2641.832	14.01935	22.8474	0.514288
Z3	64.46483	2552.973	13.21776	33.626	0.521618
Z4	63.36949	2183.869	13.27192	33.3541	0.526343
Z5	24.17329	1514.021	10.89705	12.11435	0.501146

The coercivity (H_c) of a material is influenced by a variety of factors, both internal and external in nature. The structured arrangement of atoms within the crystal lattice is crucial in Intrinsic (Internal). The parameter H_a, which characterizes the material's resistance to magnetic reversal, is strongly linked to H_c. The relationship between these sites in the lattice is heavily impacted by their occupation, particularly the $4f_2$ and 2b sites. The presence of iron ions in these sites greatly affects H_a and consequently, H_c. The importance of the matter lies in the impact of external factors like grain size and porosity. Larger grains provide a more continuous pathway for magnetic domains (regions with aligned magnetic moments) to move through, making it easier for the material to demagnetize. Conversely, pores or voids within the material can disrupt the magnetic structure, reducing the effective magnetic volume and increasing resistance to domain movement. As a result, materials with higher porosity tend to exhibit higher coercivity (H_c) values due to the increased difficulty in aligning magnetic domains. By introducing foreign atoms (dopants) through doping, the coercivity (H_c) of the material is reduced. There is a clear trend in the data, with the H_c value decreasing from 5341.76 Oe in the undoped sample (Z0) to 1514.02 Oe when fully doped (Z5). The undoped sample (Z0) exhibits the highest values for both coercivity (5341.76 Oe) and M_r (39.96). The exceptional performance can be attributed to the absence of any structural disruptions and the optimal positioning of iron ions, particularly at the $4f_2$ and 2b sites. The decrease in H_c observed with the increasing Cr substitution (Z0 to Z5) can be attributed to the variation in the anisotropy field (H_a). H_a represents the energy required to alter the alignment of the magnetic moments in the material. A higher H_a value suggests a stronger resistance to magnetic reversal. Consequently, the material demands additional energy to overcome its resistance and lose its magnetism, resulting in an increased coercivity (H_c). The anisotropy field (H_a) is primarily affected by the magnetic moments of iron ions located in the $4f_2$ and 2b sites of the crystal lattice.

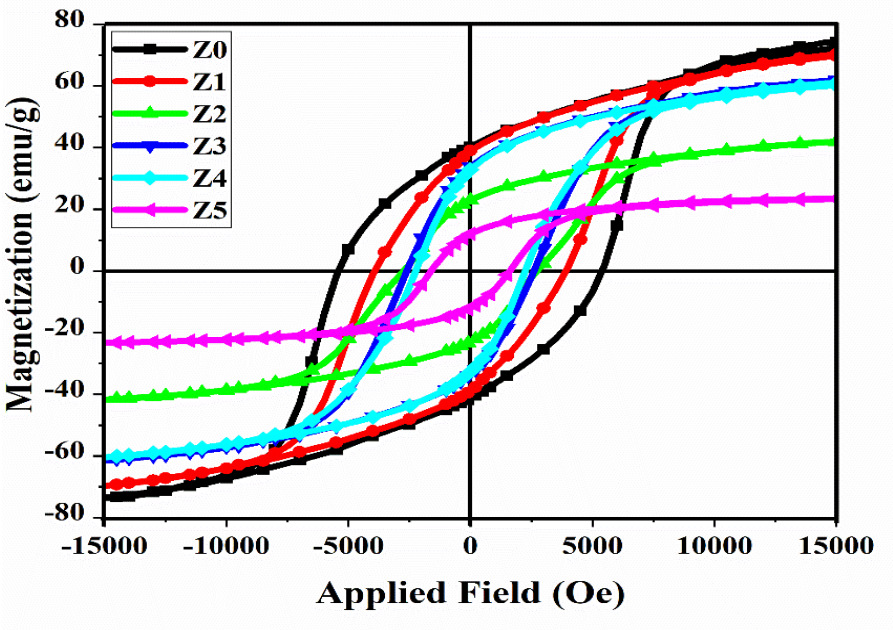

Figure 4.79. Hysteresis loops of Z0, Z1, Z2, Z3, Z4 and Z5 hexaferrite.

The samples remanent magnetization (M_r) shows a decline as the amount of Cr^{3+} substitution (x) in $BaCo_xCr_xFe_{12-2x}O_{19}$ increases. The observed decrease in magnetization, from an initial value of 39.96 emu/g to a final value of 12.114 emu/g (Table 4.26), can be attributed to the influence of Cr^{3+} on the orientation of magnetic moments within the material. When Cr^{3+} substitutes Fe^{3+}, it has the potential to disturb the exchange interactions that are vital for aligning these magnetic moments. This disruption results in a reduction in the overall magnetization, which continues to be diminished even after the magnetic field is removed.

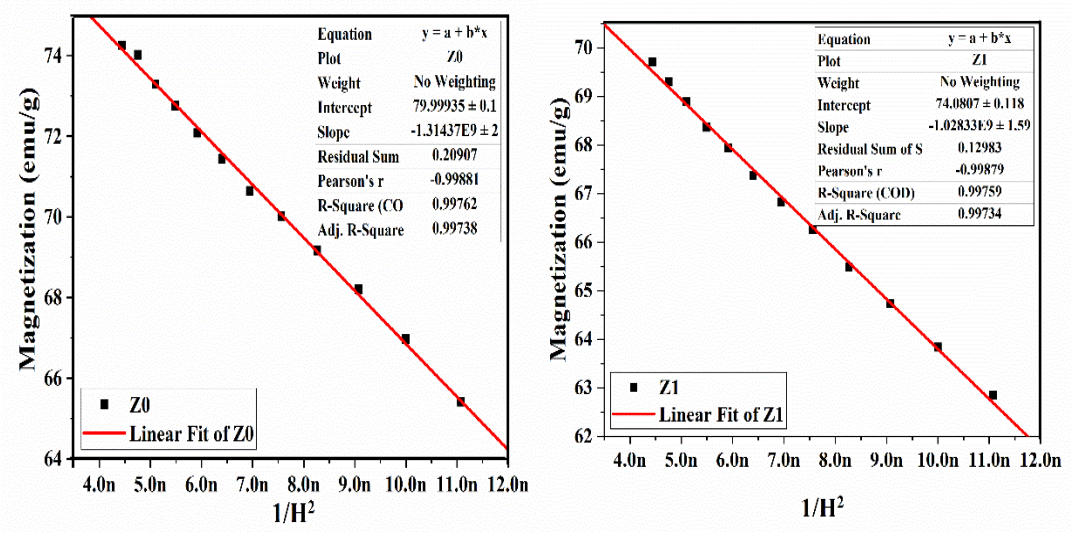

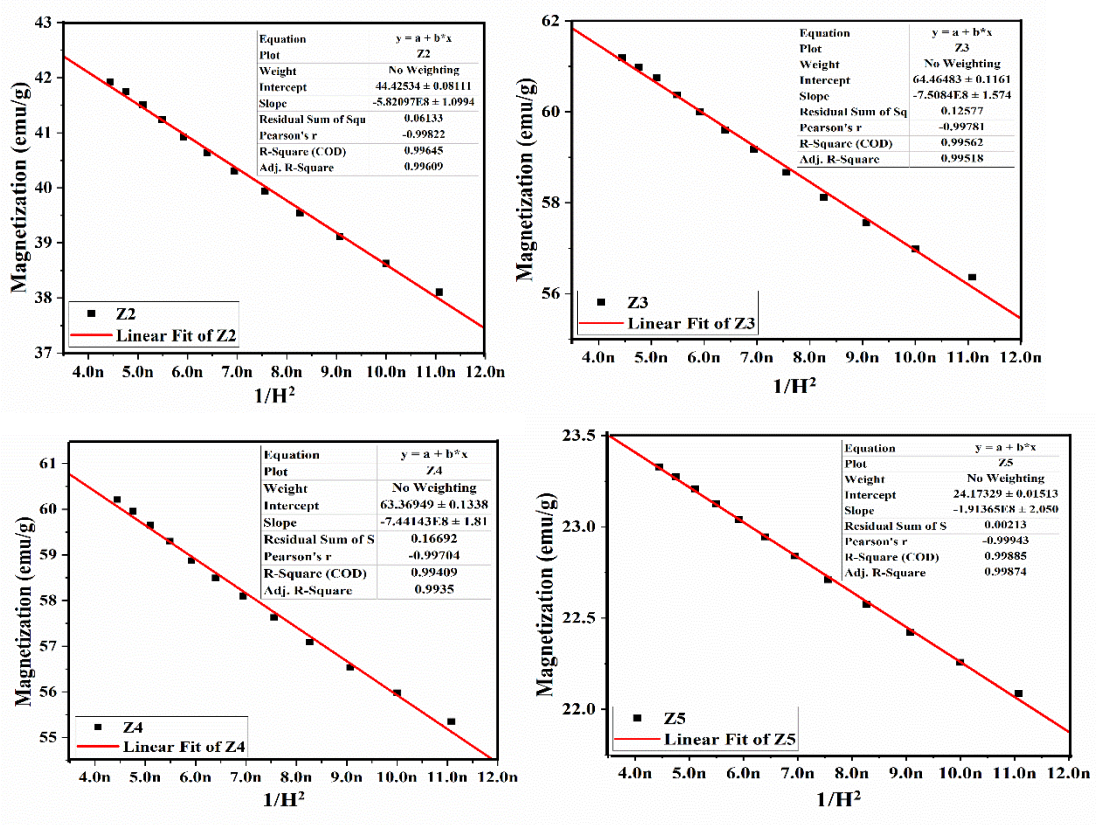

Figure 4.80 M_s versus 1/ H^2 plot for all hexaferrite samples.

The remanence ratio (M_r/M_s) is an important factor in determining the material's capacity to maintain magnetization. Typically, M-type hexaferrites display notable remanence ratios as a result of their intrinsic magnetic properties. On the other hand, the microstructure of the material, particularly the inter-granular areas, has a significant impact on the remanence ratio. The remanence ratios cover a wide range, from 0 to 1[189]. According to the research, values ranging from 0.05 to 0.5 are an indication of the existence of randomly oriented multi-domain particles [190]. Upon analyzing the data in Table 4.26, it is evident that all of the samples generated exhibit remanence ratios that are either less than or equal to 0.53. It appears that the Cr-series samples contain particles with multiple domains. The existence of these particles with multiple domains can be ascribed to the impact of Cr^{3+} substitution on the microstructure. The substitution could potentially impact the distribution of grain sizes, resulting in the formation of inter-granular regions that impede the alignment of magnetic moments within the material.

5.3.3 Electromagnetic Characteristics

5.3.3.1 Complex permeability and complex permittivity

The Figure 4.81 displays plots of the real (ε′) and imaginary (ε″) parts of permittivity and permeability (μ′ and μ″) as functions of frequency, showcasing the impact of Co-Cr doping. The dielectric constant (ε′) and dielectric loss (ε″) for the samples exhibit non-monotonic variations across the frequency range due to the complex interactions introduced by the Co-Cr doping. Z1 the real permittivity ε′ remains constant around 6 up to 9 GHz. After 9 GHz, there is a dramatic decrease in ε′, dropping close to zero around 10 GHz and remaining low throughout the higher frequency range. Z2 maintains a fairly constant ε′ around 6 to 6.5 up to approximately 9.5 GHz. After 9.5 GHz, ε′ undergoes a steep drop to near-zero values, similar to Z1, and remains low for the rest of the frequency range. Z3 exhibits a more stable ε′ curve, remaining around 8 to 8.5 throughout the entire frequency range from 8 GHz to 12 GHz. There are small fluctuations, but overall, Z3 demonstrates the most stable behaviour in terms of permittivity compared to Z1, Z2, and Z4. Z4 follows a similar trend to Z1 and Z2, remaining stable (around ε′ = 6.5) up to 10 GHz before dropping sharply to near-zero values, where it remains constant beyond 10 GHz.

ε″ for Z1 remains relatively close to zero across the frequency range, with only slight fluctuations around zero. Z2 shows a sharp peak in ε″ around 10 GHz, reaching a maximum value of approximately 1.5. After this peak, ε″ quickly declines back towards zero. Z3 shows noticeable fluctuations in ε″, with multiple peaks at frequencies around 9 GHz and again between 10 and 11 GHz. Z4 displays a series of peaks, especially around 9 GHz and 11 GHz, indicating variable dielectric loss in these regions.

μ′ remains below 1 until about 9 GHz, where there is a sudden and steep rise, reaching values near 5.9. After the sharp rise at 9 GHz, μ′ stabilizes at around 5.9 and remains relatively constant up to 12 GHz. There is a slight drop after 12 GHz, but the values remain stable and high. Like Z1, Z2 exhibits a sharp rise around 9.5 GHz, increasing from a low value below 1 to around 5.8. After the sharp increase, μ′ remains stable in the 5.5 to 5.8 range up to 12 GHz, following a similar trend as Z1, but with slightly lower values. Z3 shows a slower, more gradual increase in μ′ compared to Z1 and Z2. Starting at around 0.5 at 8 GHz, μ′ increases steadily, reaching about 2 by 12 GHz.

Unlike Z1 and Z2, Z3 does not exhibit a sudden spike; instead, it shows a smoother and slower rise, indicating more gradual magnetic permeability changes. Z4, like Z1 and Z2, shows a steep increase in μ′ around 9.5 GHz, with values rising from around 0.5 to 6.1. After reaching a peak value around 6.1, μ′ stabilizes and remains constant in the higher frequency range (9.5 GHz to 12 GHz), with only slight fluctuations.

μ″ remains close to zero across the entire frequency range (8 GHz to 12 GHz), there are only slight fluctuations around zero, with one slight peaks around 10 GHz. Z2 shows a sharp peak at around 10 GHz, where μ″ rises upto 1.0. Apart from the peak near 10 GHz, μ″ remains relatively stable and low at other frequencies. Z3 exhibits a broad peak between 8 GHz and 9 GHz, with μ″ reaching values close to 1.5. After 10 GHz, μ″ decreases steadily, with only one more minor fluctuations around 11 GHz. Z4 shows a sharp increase in μ″ around 10 GHz, with a peak close to 0.75. Beyond 10 GHz, μ″ decreases and remains relatively stable with minor fluctuations.

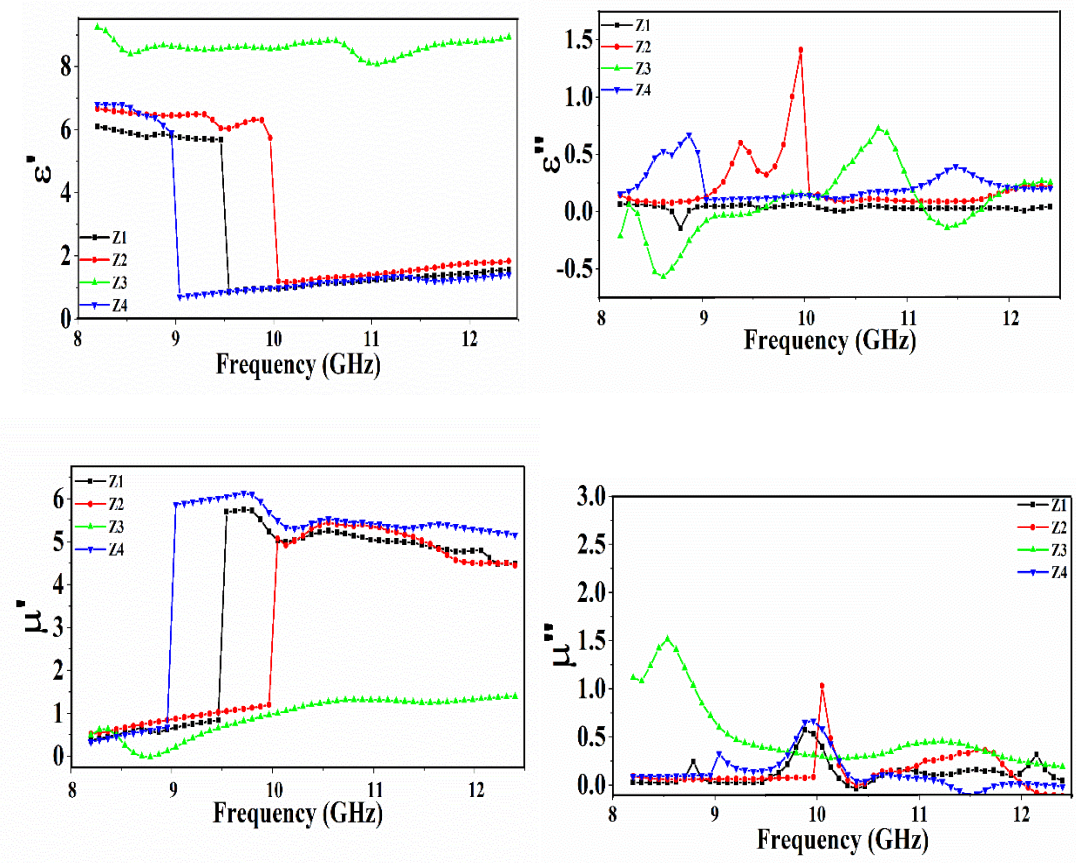

Figure 4.81 Complex permittivity and permeability versus frequency plots for $BaCo_xCr_xFe_{12-2x}O_{19}$ (Z0 to Z4).

5.3.3.2 Microwave absorption in $BaCo_xCr_xFe_{12-2x}O_{19}$

5.3.3.3 Quarter Wavelength Mechanism

By analyzing the graphs depicting reflection loss (REL) at varying thicknesses and frequencies, the microwave absorption characteristics of these materials were investigated. Figures related to REL versus frequency for various thicknesses (Z1 to Z4) provide significant insights into the absorption behaviour of each composition.

For each composition, the REL data is reported alongside the matching thicknesses and corresponding frequencies. A detailed analysis of these graphs reveals crucial information about the microwave absorption properties of the materials. The findings are summarized in Table 4.28, which offers a clear comparison of the bandwidths and REL values for different sample compositions.

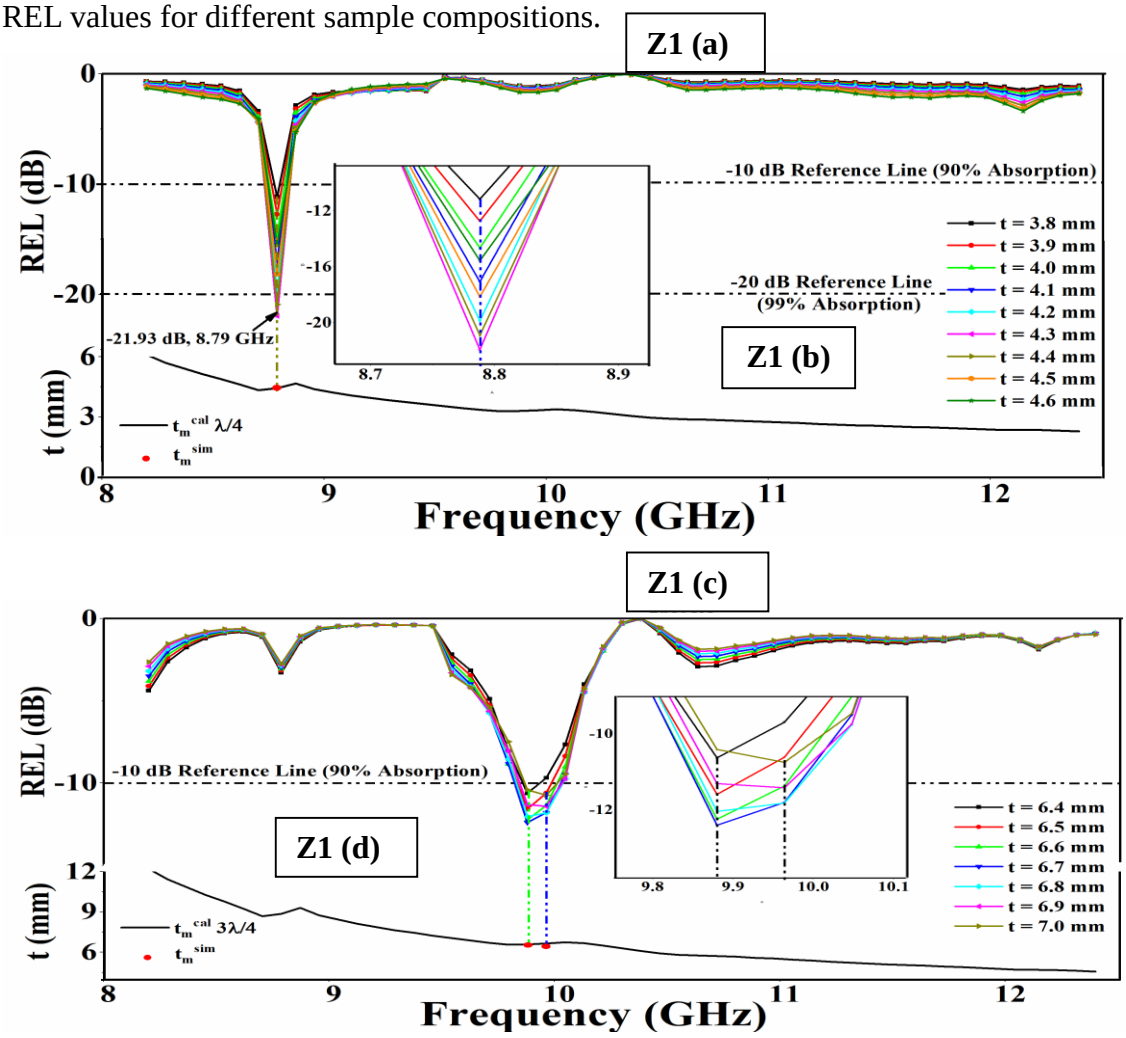

Figure 4.82 REL versus frequency for different thickness (Z1) and calculate thickness versus frequency for $BaCo_xCr_xFe_{12-2x}O_{19}$

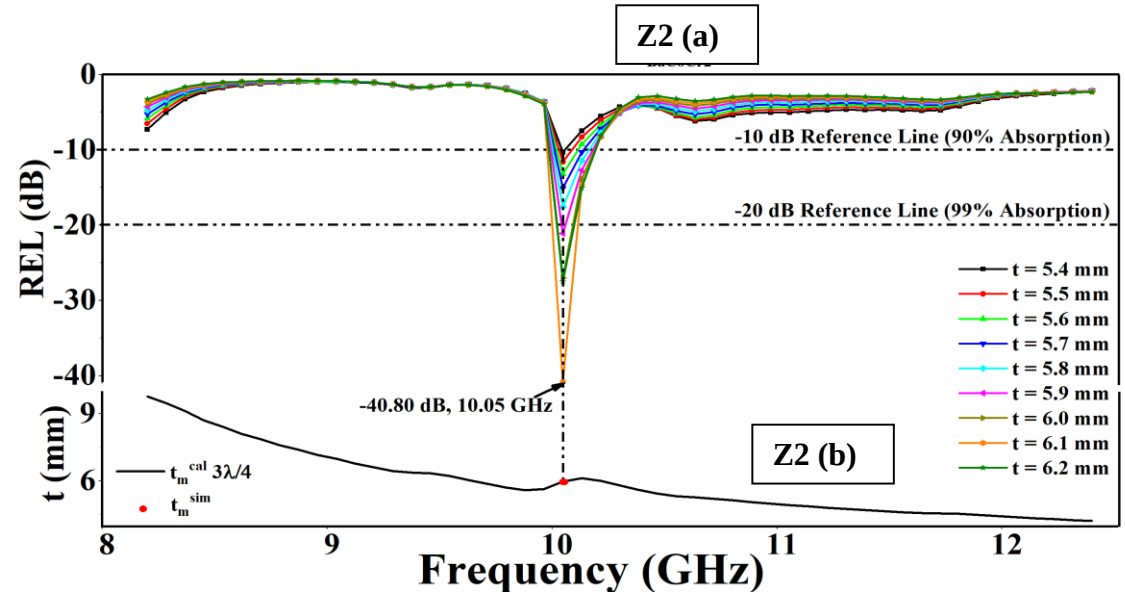
Z2 (a)
REL (dB)
-10 dB Reference Line (90% Absorption)
-20 dB Reference Line (99% Absorption)
t = 5.4 mm
t = 5.5 mm
t = 5.6 mm
t = 5.7 mm
t = 5.8 mm
t = 5.9 mm
t = 6.0 mm
t = 6.1 mm
t = 6.2 mm
-40.80 dB, 10.05 GHz
Z2 (b)
t (mm)
t_m^{cal} 3λ/4
t_m^{sim}
Frequency (GHz)

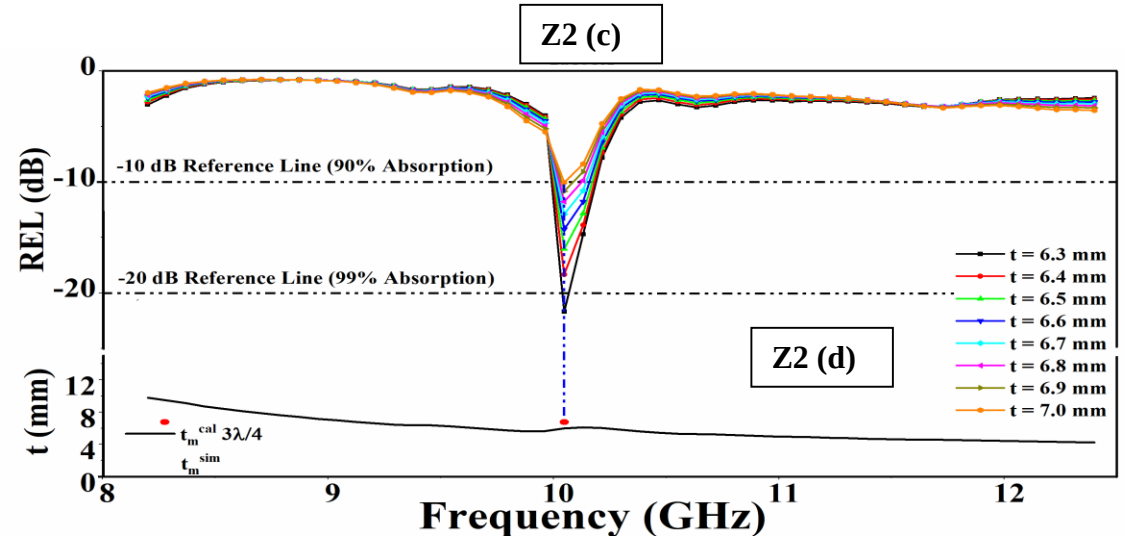
Z2 (c)
REL (dB)
-10 dB Reference Line (90% Absorption)
-20 dB Reference Line (99% Absorption)
t = 6.3 mm
t = 6.4 mm
t = 6.5 mm
t = 6.6 mm
t = 6.7 mm
t = 6.8 mm
t = 6.9 mm
t = 7.0 mm
Z2 (d)
t (mm)
t_m^{cal} 3λ/4
t_m^{sim}
Frequency (GHz)

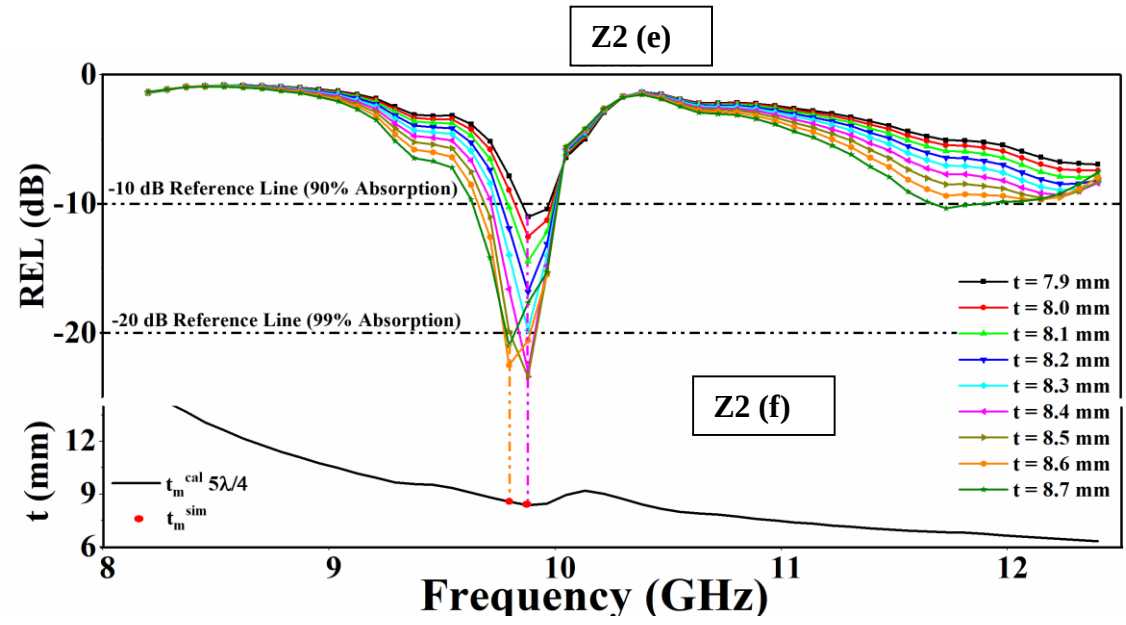
Z2 (e)
REL (dB)
-10 dB Reference Line (90% Absorption)
-20 dB Reference Line (99% Absorption)
t = 7.9 mm
t = 8.0 mm
t = 8.1 mm
t = 8.2 mm
t = 8.3 mm
t = 8.4 mm
t = 8.5 mm
t = 8.6 mm
t = 8.7 mm
Z2 (f)
t (mm)
t_m^{cal} 5λ/4
t_m^{sim}
Frequency (GHz)

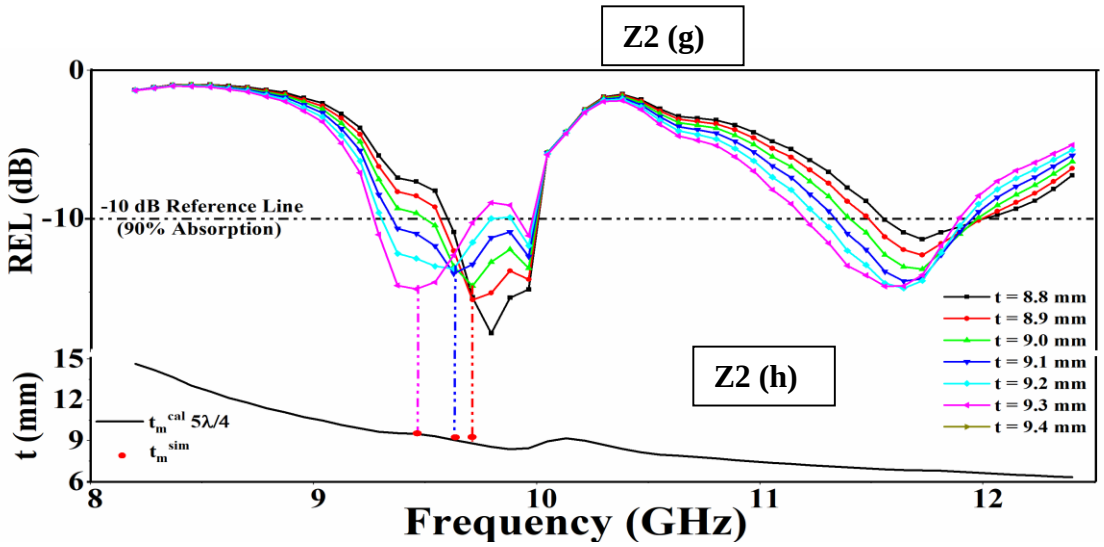
Z2 (g)
REL (dB)
-10 dB Reference Line
(90% Absorption)
t = 8.8 mm
t = 8.9 mm
t = 9.0 mm
t = 9.1 mm
t = 9.2 mm
t = 9.3 mm
t = 9.4 mm
Z2 (h)
t (mm)
t_m^{cal} 5λ/4
t_m^{sim}
Frequency (GHz)

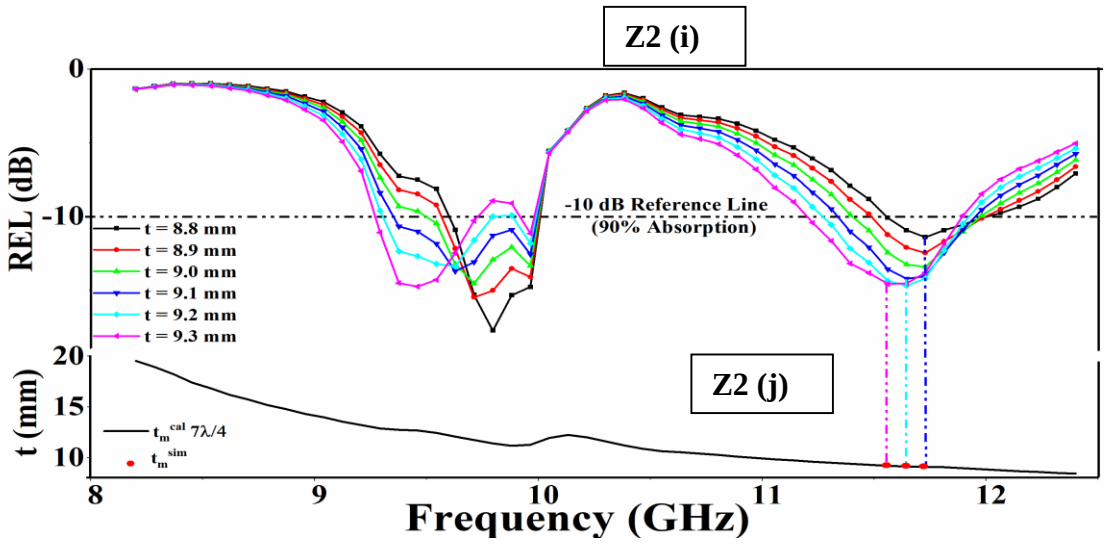
Z2 (i)
REL (dB)
-10 dB Reference Line
(90% Absorption)
t = 8.8 mm
t = 8.9 mm
t = 9.0 mm
t = 9.1 mm
t = 9.2 mm
t = 9.3 mm
Z2 (j)
t (mm)
t_m^{cal} 7λ/4
t_m^{sim}
Frequency (GHz)

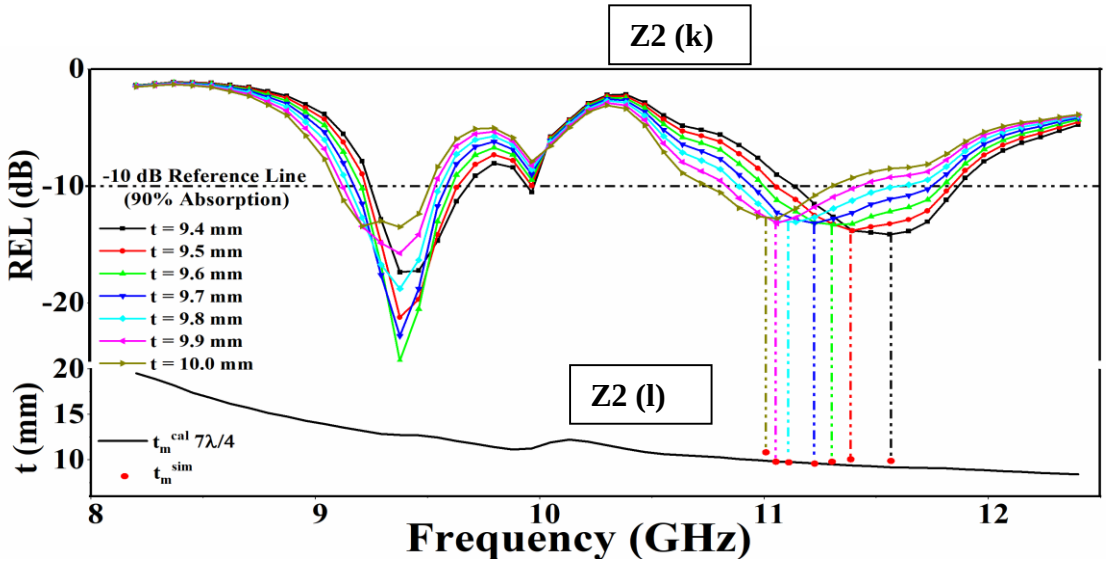
Z2 (k)
REL (dB)
-10 dB Reference Line
(90% Absorption)
t = 9.4 mm
t = 9.5 mm
t = 9.6 mm
t = 9.7 mm
t = 9.8 mm
t = 9.9 mm
t = 10.0 mm
Z2 (l)
t (mm)
t_m^{cal} 7λ/4
t_m^{sim}
Frequency (GHz)

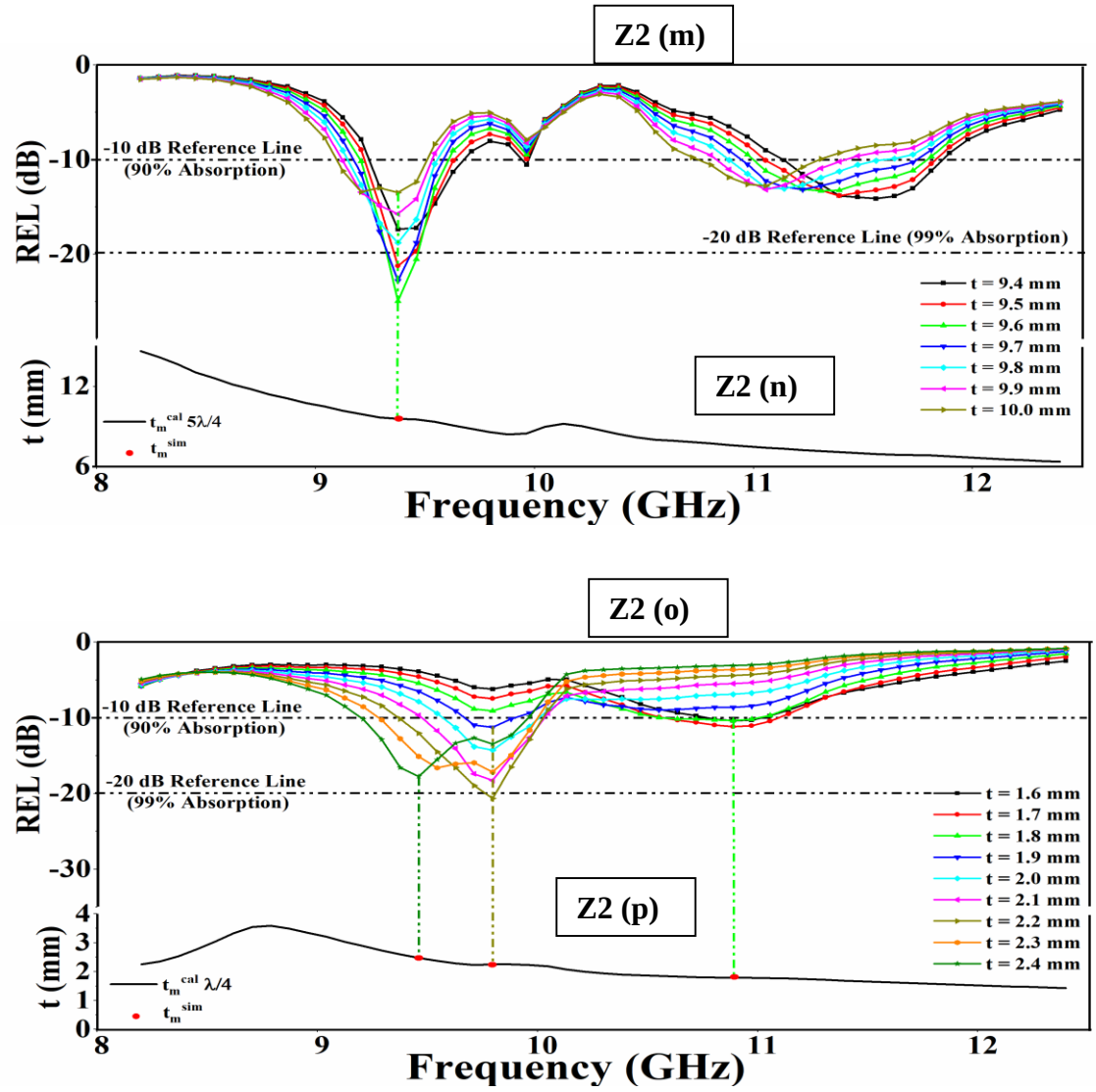

Figure 4.83 REL versus frequency for different thickness (Z2) and calculate thickness versus frequency for $BaCo_xCr_xFe_{12-2x}O_{19}$

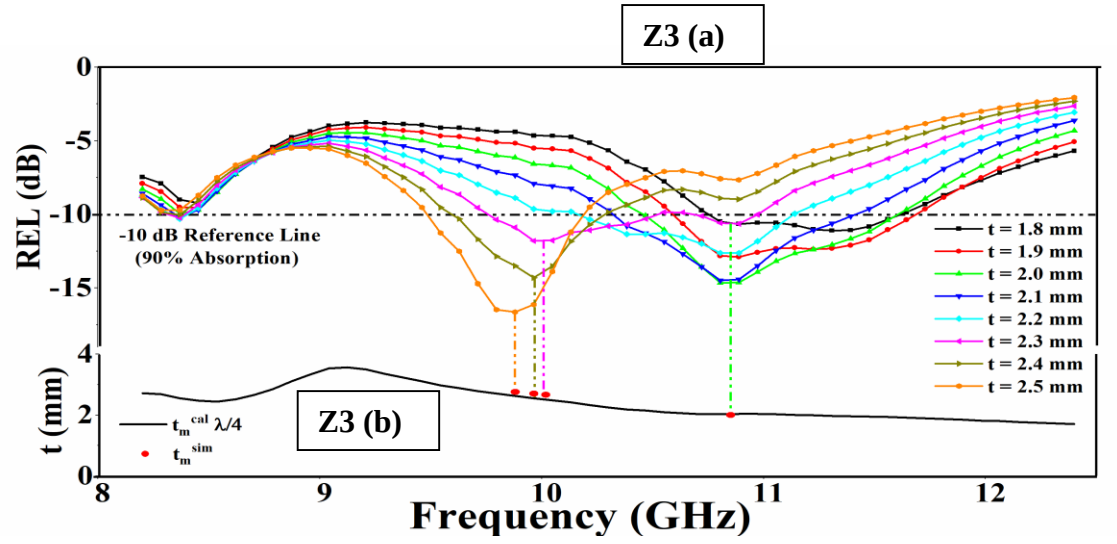

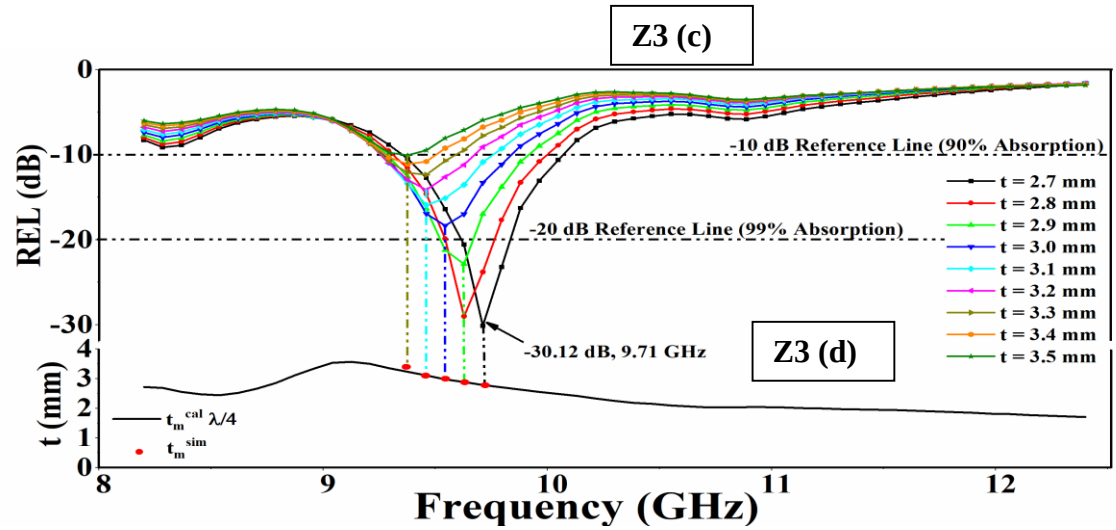
Z3 (c)
REL (dB)
-10 dB Reference Line (90% Absorption)
-20 dB Reference Line (99% Absorption)
t = 2.7 mm
t = 2.8 mm
t = 2.9 mm
t = 3.0 mm
t = 3.1 mm
t = 3.2 mm
t = 3.3 mm
t = 3.4 mm
t = 3.5 mm
-30.12 dB, 9.71 GHz
Z3 (d)
t (mm)
t_m^{cal} λ/4
t_m^{sim}
Frequency (GHz)

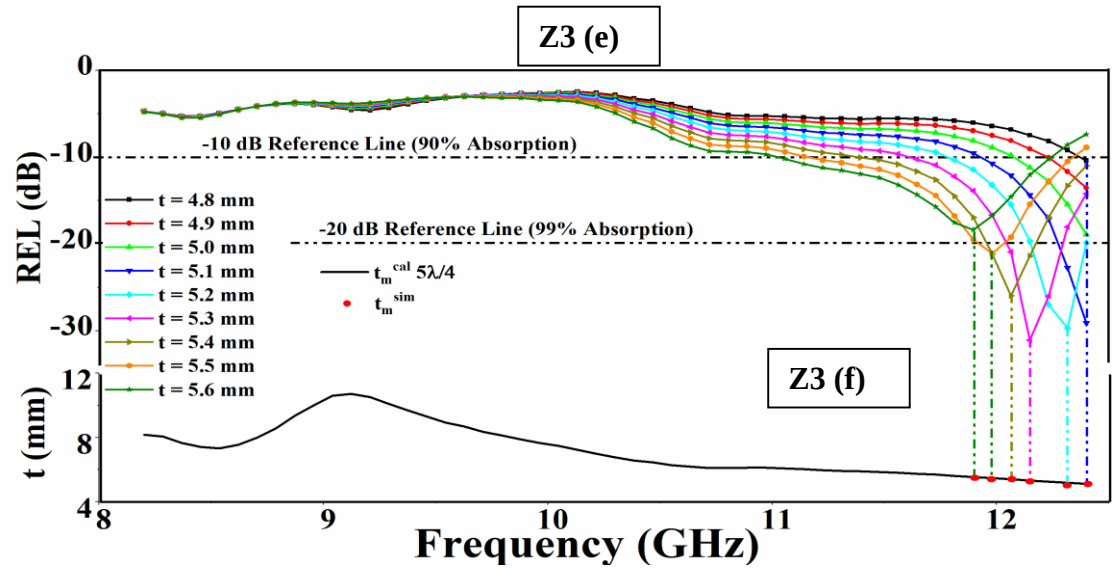
Z3 (e)
REL (dB)
-10 dB Reference Line (90% Absorption)
-20 dB Reference Line (99% Absorption)
t = 4.8 mm
t = 4.9 mm
t = 5.0 mm
t = 5.1 mm
t = 5.2 mm
t = 5.3 mm
t = 5.4 mm
t = 5.5 mm
t = 5.6 mm
t_m^{cal} 5λ/4
t_m^{sim}
Z3 (f)
t (mm)
Frequency (GHz)

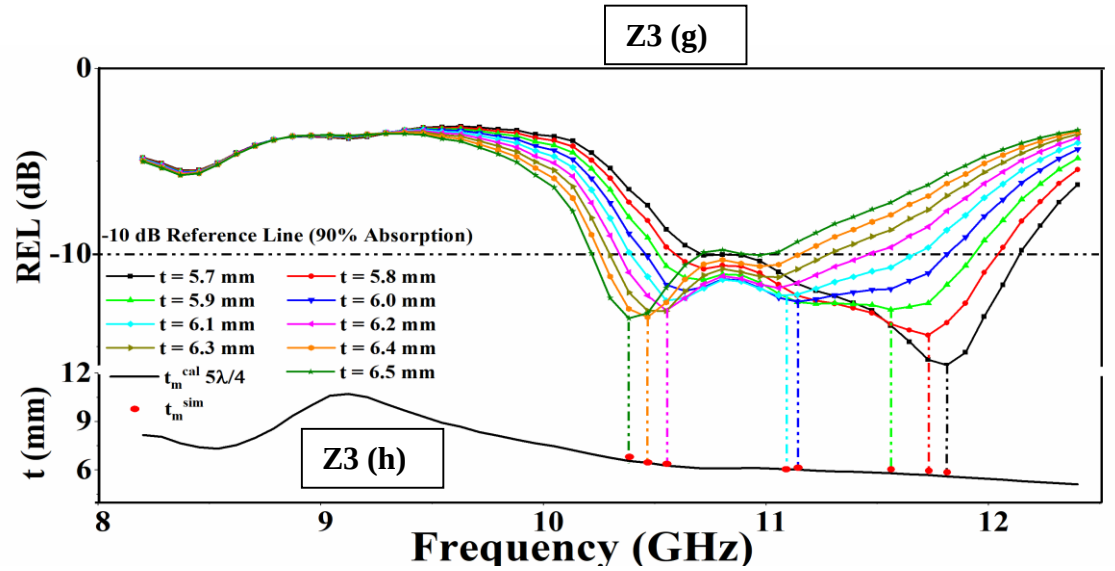
Z3 (g)
REL (dB)
-10 dB Reference Line (90% Absorption)
t = 5.7 mm
t = 5.8 mm
t = 5.9 mm
t = 6.0 mm
t = 6.1 mm
t = 6.2 mm
t = 6.3 mm
t = 6.4 mm
t = 6.5 mm
t_m^{cal} 5λ/4
t_m^{sim}
Z3 (h)
t (mm)
Frequency (GHz)

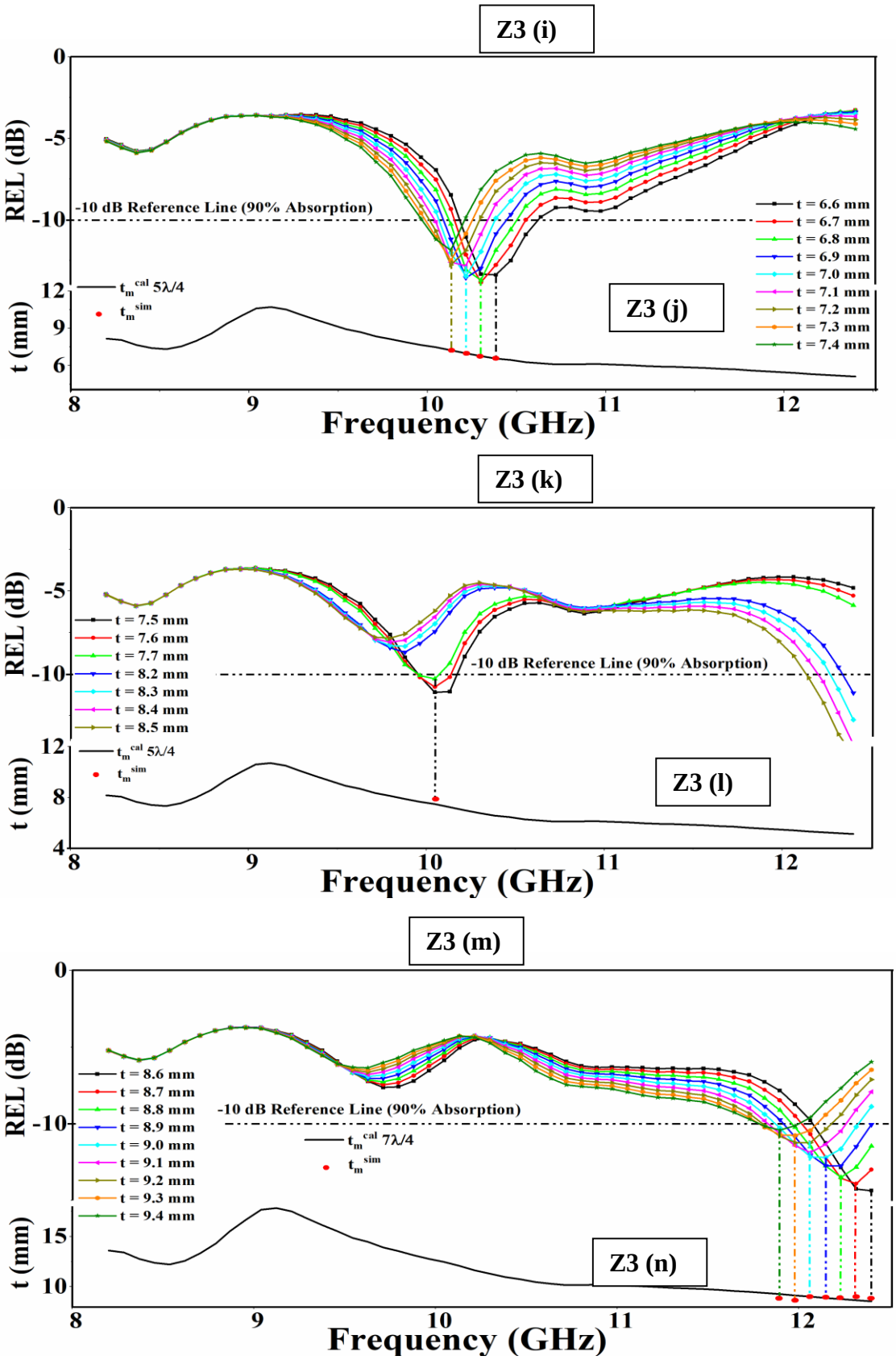

Figure 4.84 REL versus frequency for different thickness (Z3) and calculate thickness versus frequency for $BaCo_xCr_xFe_{12-2x}O_{19}$

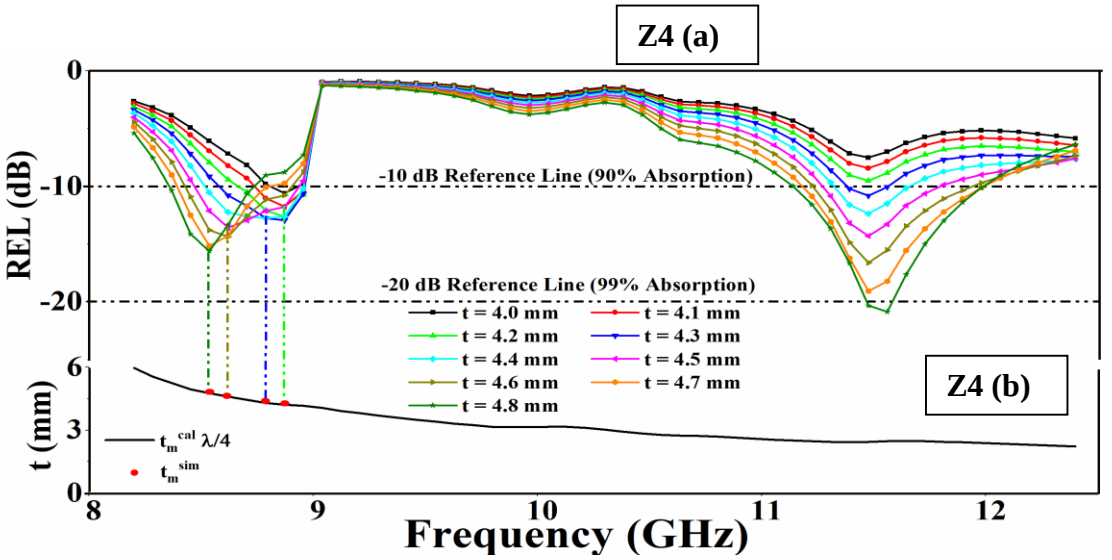
Z4 (a)
REL (dB)
-10 dB Reference Line (90% Absorption)
-20 dB Reference Line (99% Absorption)
t = 4.0 mm
t = 4.1 mm
t = 4.2 mm
t = 4.3 mm
t = 4.4 mm
t = 4.5 mm
t = 4.6 mm
t = 4.7 mm
t = 4.8 mm
Z4 (b)
t (mm)
t_m^{cal} λ/4
t_m^{sim}
Frequency (GHz)

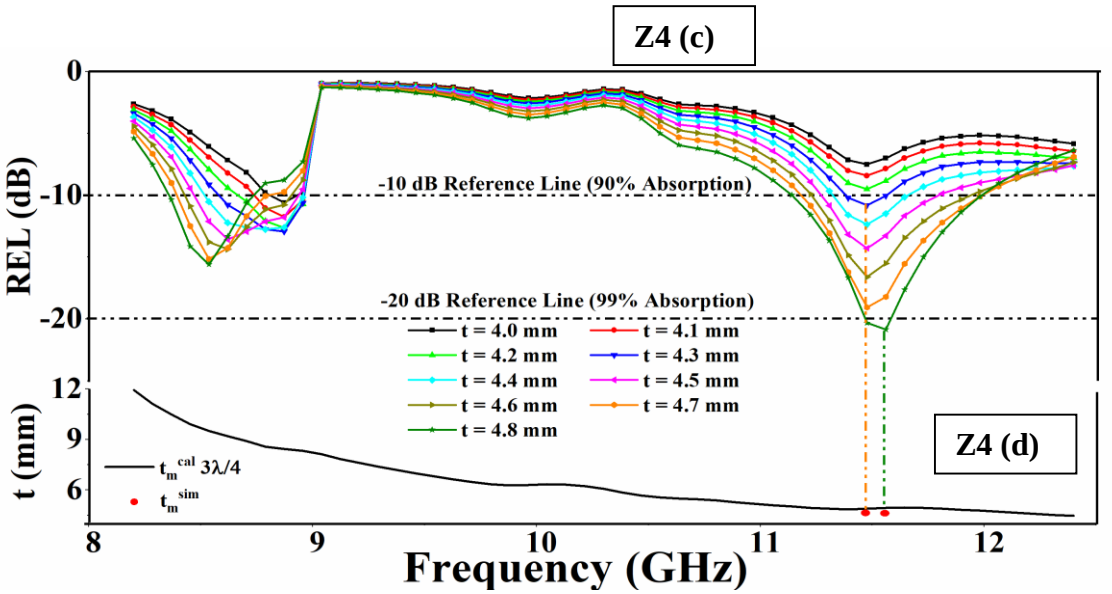
Z4 (c)
REL (dB)
-10 dB Reference Line (90% Absorption)
-20 dB Reference Line (99% Absorption)
t = 4.0 mm
t = 4.1 mm
t = 4.2 mm
t = 4.3 mm
t = 4.4 mm
t = 4.5 mm
t = 4.6 mm
t = 4.7 mm
t = 4.8 mm
Z4 (d)
t (mm)
t_m^{cal} 3λ/4
t_m^{sim}
Frequency (GHz)

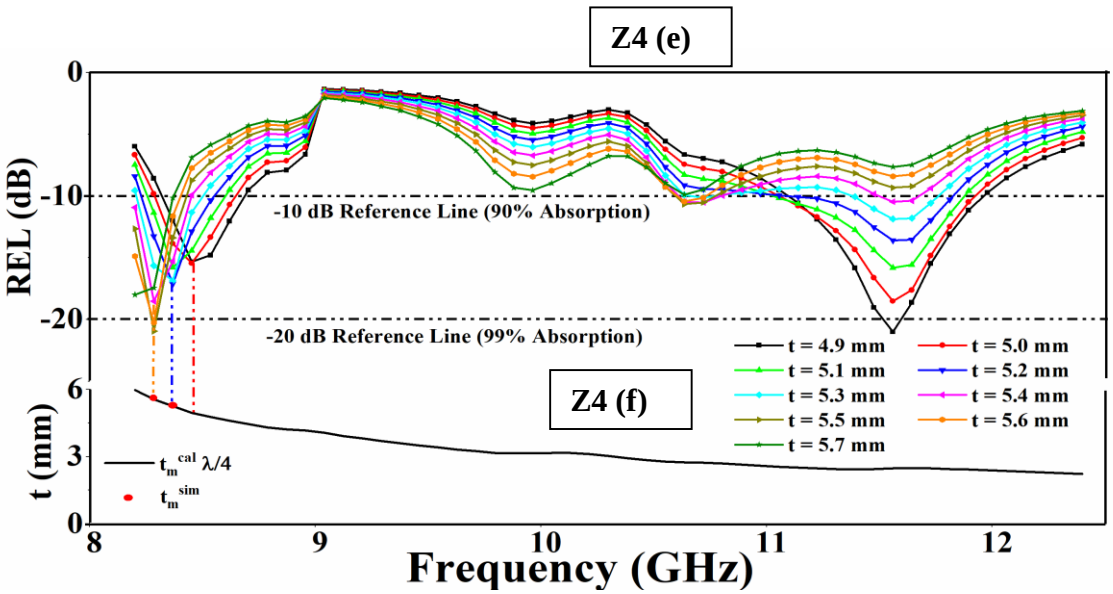
Z4 (e)
REL (dB)
-10 dB Reference Line (90% Absorption)
-20 dB Reference Line (99% Absorption)
t = 4.9 mm
t = 5.0 mm
t = 5.1 mm
t = 5.2 mm
t = 5.3 mm
t = 5.4 mm
t = 5.5 mm
t = 5.6 mm
t = 5.7 mm
Z4 (f)
t (mm)
t_m^{cal} λ/4
t_m^{sim}
Frequency (GHz)

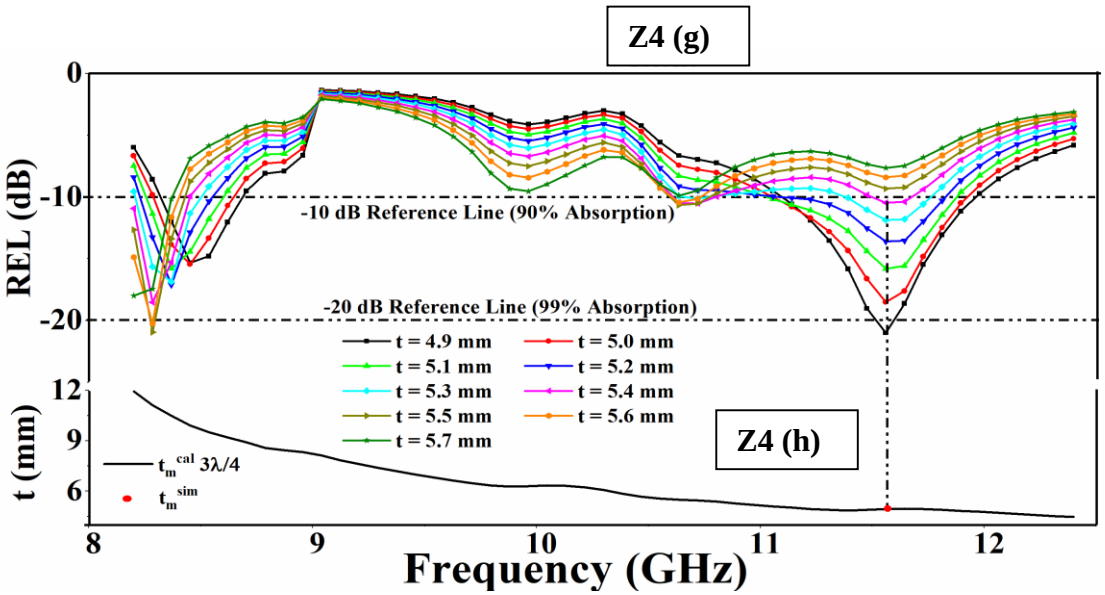
Z4 (g)
REL (dB)
-10 dB Reference Line (90% Absorption)
-20 dB Reference Line (99% Absorption)
t = 4.9 mm
t = 5.0 mm
t = 5.1 mm
t = 5.2 mm
t = 5.3 mm
t = 5.4 mm
t = 5.5 mm
t = 5.6 mm
t = 5.7 mm
Z4 (h)
t (mm)
t_m^{cal} 3λ/4
t_m^{sim}
Frequency (GHz)

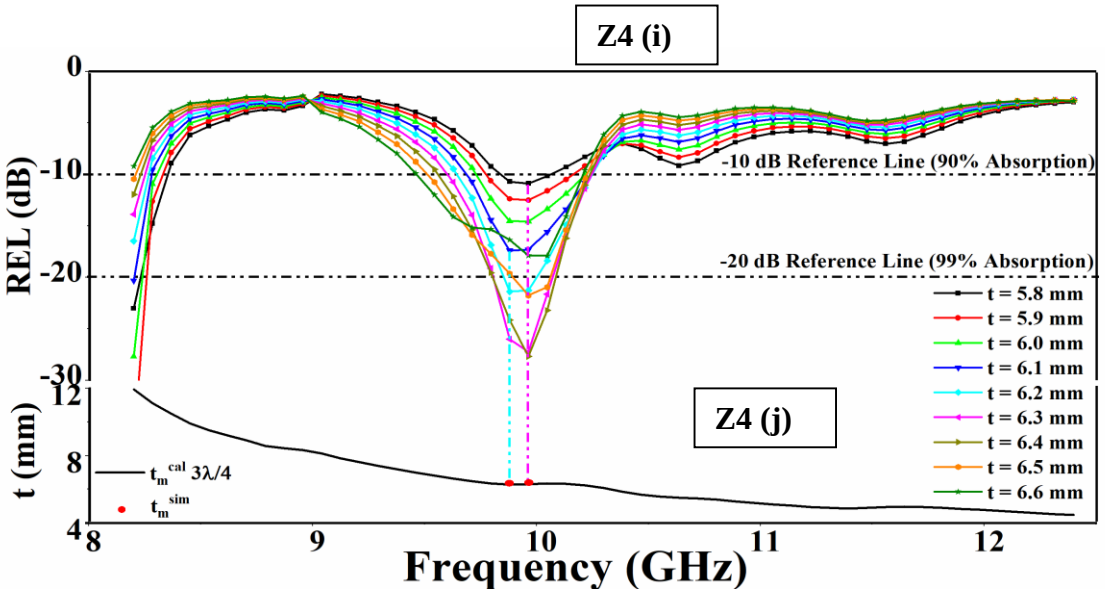
Z4 (i)
REL (dB)
-10 dB Reference Line (90% Absorption)
-20 dB Reference Line (99% Absorption)
t = 5.8 mm
t = 5.9 mm
t = 6.0 mm
t = 6.1 mm
t = 6.2 mm
t = 6.3 mm
t = 6.4 mm
t = 6.5 mm
t = 6.6 mm
Z4 (j)
t (mm)
t_m^{cal} 3λ/4
t_m^{sim}
Frequency (GHz)

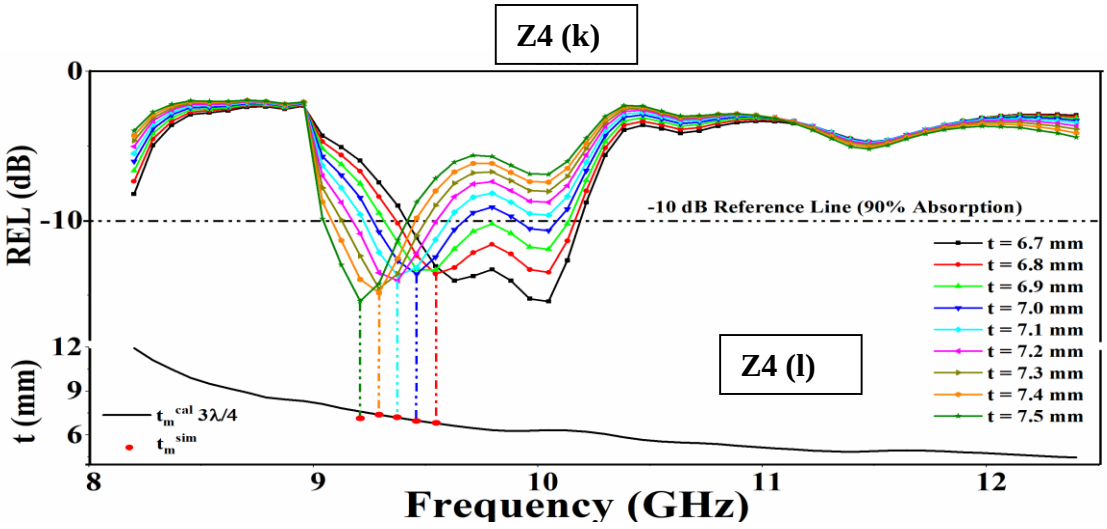
Z4 (k)
REL (dB)
-10 dB Reference Line (90% Absorption)
t = 6.7 mm
t = 6.8 mm
t = 6.9 mm
t = 7.0 mm
t = 7.1 mm
t = 7.2 mm
t = 7.3 mm
t = 7.4 mm
t = 7.5 mm
Z4 (l)
t (mm)
t_m^{cal} 3λ/4
t_m^{sim}
Frequency (GHz)

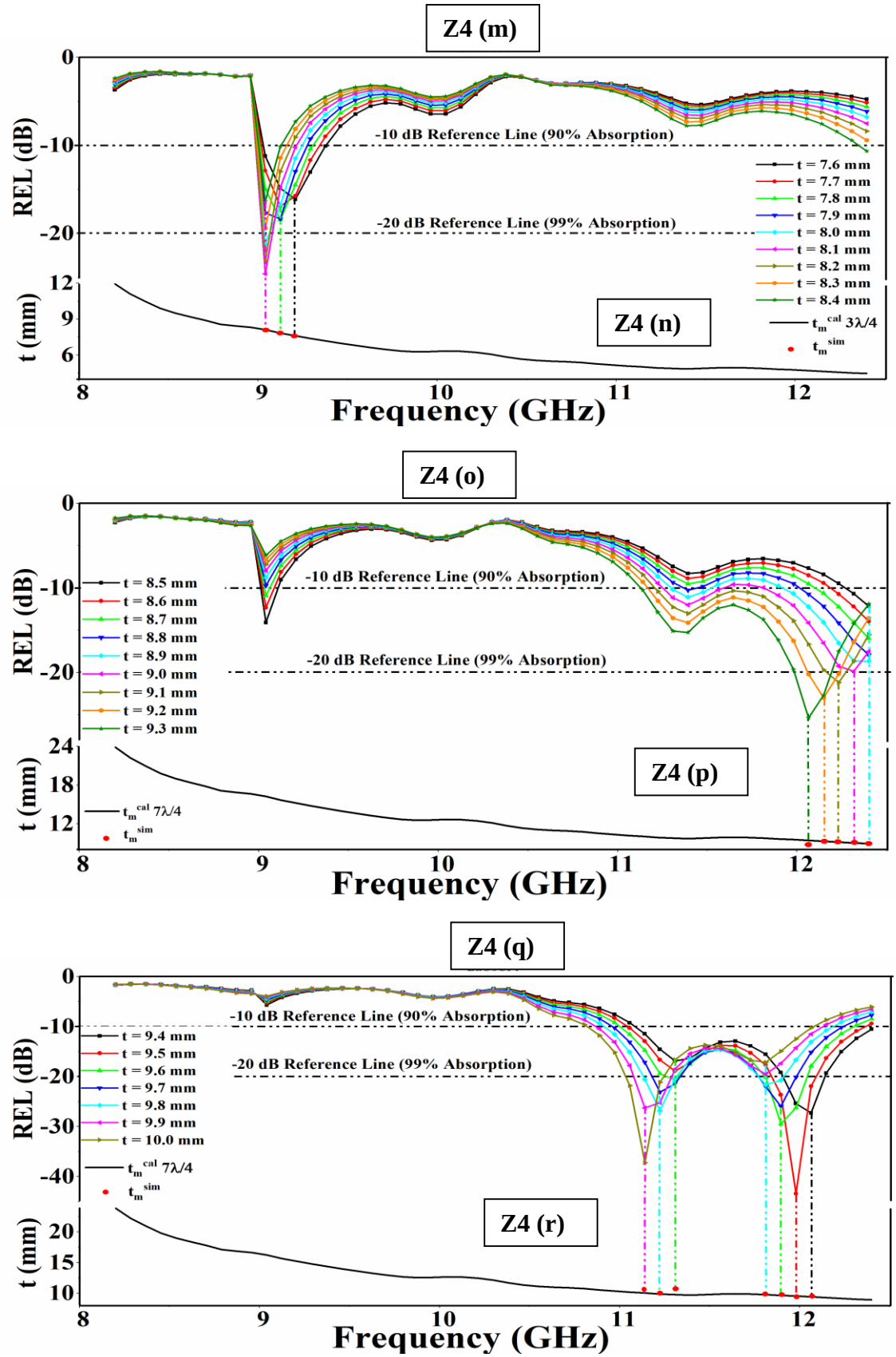

Figure 4.85 REL versus frequency for different thickness (Z4) and calculate thickness versus frequency for $BaCo_xCr_xFe_{12-2x}O_{19}$

Matching thicknesses of 4.3 mm and 6.7 mm provide peak REL values of -21.93 dB at 8.79 GHz and -12.4 dB at 9.88 GHz, respectively. The -10 dB bandwidth spans from 0.12 GHz to 0.21 GHz, indicating moderate absorption efficiency. For the -20 dB bandwidth, a very narrow range of 0.02 GHz is observed at a thickness of 4.3 mm.

Z2 shows impressive absorption with a maximum REL of -40.8 dB at 10.05 GHz with a matching thickness of 6.1 mm. Additional significant REL values are observed for thicknesses of 8.4 mm, 8.6 mm, and 9.6 mm, with REL values of -22.71 dB, -22.47 dB, and -24.91 dB, respectively. This sample exhibits broad bandwidths ranging from 0.15 GHz to 0.45 GHz for REL > -10 dB, demonstrating effective absorption over a wide frequency range.

Z3 shows strong absorption with multiple thicknesses ranging from 2.5 mm to 8.9 mm, providing REL values as low as -31.08 dB at 12.15 GHz. Broad bandwidths are also observed, with a -10 dB bandwidth reaching up to 1.34 GHz, indicating this composition is highly effective across a wide frequency range. Additionally, the composition shows a peak of -12.68 dB at 12.16 GHz for a thickness of 8.9 mm, ensuring significant microwave absorption in higher-frequency bands.

With a maximum REL of -43.4 dB at 11.98 GHz and a matching thickness of 9.5 mm, Z4 exhibits exceptional microwave absorption. The -10 dB bandwidth spans up to 1.34 GHz, which indicates highly efficient absorption across the frequency range. Other notable REL values for thicknesses of 4.8 mm, 6.4 mm, and 7.9 mm are -20.89 dB, -27.72 dB, and -18.35 dB, respectively, for frequencies in the 9.04 GHz to 12.06 GHz range.

The observed microwave absorption characteristics are closely tied to the quarter-wavelength mechanism. By comparing the calculated thicknesses (t_{cal}) with the simulated thicknesses (t_{sim}), we observe a clear correspondence between peak REL values and the $\lambda/4$, $3\lambda/4$, and $5\lambda/4$ thicknesses for the compositions Z1 to Z4. The matching frequency and thickness values confirm that the quarter-wavelength criterion is valid for these hexaferrites, as shown in Figure 4.82 to Figure 4.85.

Based on Table 4.27, the quarter wavelength criterion for composition Z1 is evident at thicknesses ranging from 4.3 mm to 6.7 mm, with a -10 dB bandwidth spanning from 0.12 GHz to 0.21 GHz. A reflection loss (REL) of -21.93 dB is reported within a -20 dB bandwidth of 0.02 GHz.

Table 4.27 REL with matching thickness/frequency, BW, and PBW for $BaCo_xCr_xFe_{12-2x}O_{19}$ (Z1 to Z4).

Sample Name	Matching Thickness (mm)	Maximum REL (dB)	Matching frequency (GHz)	Frequency Band for REL > -10 dB (GHz)	Bandwidth for RL > -10 dB (GHz)	Frequency Band REL > -20 dB (GHz)	Bandwidth for REL > -20 dB (GHz)	BTR	PBW (%)
Z1	4.3	-21.93	8.79	8.73-8.85	0.12	8.78-8.8	0.02	1.08 E-04	1.37
	6.7	-12.4	9.88	9.82-10.03	0.21	-	-	9.55 E-05	2.13
Z2	6.1	-40.8	10.05	9.98-10.19	0.21	10-10.11	0.11	1.02 E-04	2.09
	6.6	-14.3	10.04	10.01-10.16	0.15	-	-	6.70 E-05	1.49
	8.4	-22.71	9.88	9.72-10	0.28	9.84-9.91	0.07	1.03 E-04	2.83
	8.6	-22.47	9.8	9.66-10.01	0.35	9.77-9.89	0.12	1.26 E-04	3.57
	9.3	-14.79	9.46	9.27-9.72	0.45	-	-	1.61 E-04	4.76
	9.6	-24.91	9.38	9.21-9.61	0.4	9.32-9.47	0.15	1.41 E-04	4.26
Z3	2.5	-16.66	9.88	9.48-10.19	0.71	-	-	8.82 E-04	7.19
	2.7	-30.12	9.71	9.35-10.07	0.72	9.62-9.84	0.22	8.50 E-04	7.42
	3	-18.32	9.55	9.27-9.84	0.57	-	-	6.25 E-04	5.97
	5.3	-31.08	12.15	-	-	12.04-12.3	0.26	9.94 E-05	2.14
	5.6	-18.47	11.9	11.02-12.25	1.23	-	-	4.88 E-04	10.34
	5.7	-15.97	11.81	10.8-12.14	1.34	-	-	5.38 E-04	11.35
	6.8	-13.63	10.3	10.15-10.55	0.4	-	-	1.65 E-04	3.88
	7.5	-11.01	10.05	9.96-10.17	0.21	-	-	8.29 E-05	2.09
	8.9	-12.68	12.16	11.91-12.41	0.5	-	-	1.14 E-04	4.11
Z4	4.8	-20.89	11.56	11.14-11.99	0.85	11.47-11.59	0.12	3.98 E-04	7.35
	4.9	-20.99	11.57	11.09-11.95	0.86	11.51-11.61	0.1	3.97 E-04	7.43
	6.4	-27.72	9.96	9.57-	0.68	9.8-	0.29	3.25	6.83

				10.25		10.09		E-04	
	7.5	-15.27	9.21	9.05-9.42	0.37	-	-	1.74 E-04	4.02
	7.9	-18.35	9.13	9-9.27	0.27	-	-	1.23 E-04	2.96
	8.1	-24.54	9.04	8.99-9.21	0.22	9.02-9.08	0.06	9.84 E-05	2.43
	9.3	-25.34	12.06	11.13-12.47	1.34	11.99-12.19	0.2	3.11 E-04	11.11
	9.5	-43.4	11.98	11.03-12.37	1.34	11.84-12.09	0.25	3.10 E-04	11.19

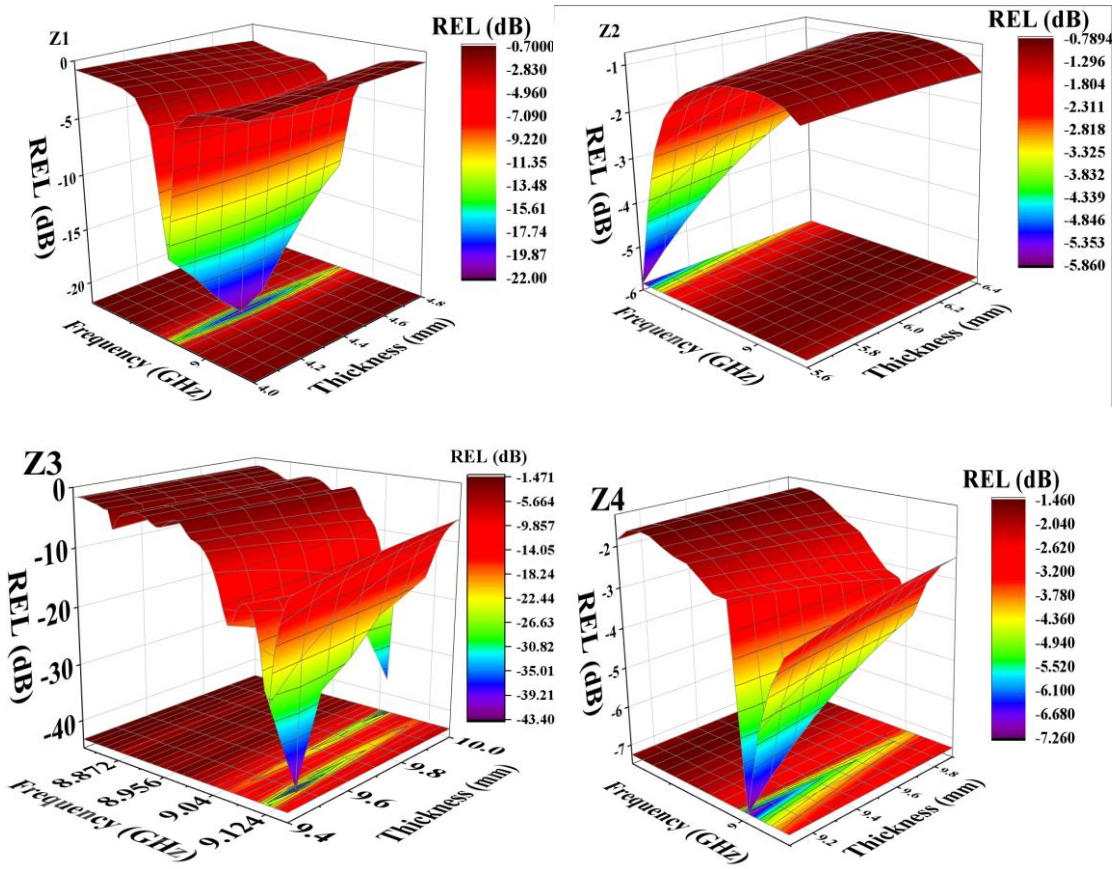

Figure 4.86 Three-dimensional (3D) plots of reflection loss at various frequencies and thicknesses for all samples of BaCoCr-series.

As illustrated in Figure 4.82 Z1(a), the reflection loss peaks for composition Z1 occur at 8.79 GHz for thicknesses between 3.8 mm and 4.6 mm. Similarly, peaks at 9.880 GHz are observed for thicknesses between 6.4 mm and 7.0 mm. Figures 4.82 Z1 (a) and 4.82 Z1(c) further confirm peak REL values at thicknesses of 4.3 mm and 6.7 mm, corresponding to RELs of -21.93 dB and -12.42 dB, respectively.

For composition Z2, the -10 dB peaks are observed across thicknesses ranging from 6.1 mm to 9.6 mm, with a -10 dB bandwidth ranging from 0.15 GHz to 0.45 GHz. Significant REL values of -40.8 dB, -22.71 dB, -22.47 dB, and -24.91 dB are reported for the -20 dB bandwidth, with bandwidths of 0.11 GHz, 0.07 GHz, 0.12 GHz, and 0.15 GHz, respectively. As seen in Figure 4.83 Z2 (a), Z2(c), and Z2 (e), the reflection loss peaks for composition Z2 occur at the same frequency of 10.05 GHz for thicknesses between 5.4 mm and 7.0 mm, at 9.88 GHz for thicknesses between 7.9 mm and 8.5 mm, and at 9.37 GHz for thicknesses between 9.4 mm and 10.00 mm. Furthermore, Figures 4.83 Z2 (i) and Z2 (k) show that as thickness increases from 8.8 mm to 9.4 mm and from 9.4 mm to 10.00 mm, the REL peaks shift toward the lower frequency region, following the quarter-wavelength process. The calculated thickness (t_{cal}) and simulated thickness (t_{sim}) demonstrate an inverse relationship between frequency and material thickness, as illustrated by the vertical comparison lines across the graphs.

For composition Z3, REL values span thicknesses from 2.5 mm to 8.9 mm, with a bandwidth of 0.4 GHz to 1.34 GHz at corresponding frequencies of 9.55 GHz to 12.15 GHz. Peak REL values of -31.08 dB are observed for a -20 dB bandwidth of 0.22 GHz and 0.26 GHz. In Figures 4.84 Z3(a) and Z3(c), it is noted that as thickness increases from 1.8 mm to 2.5 mm, the peak height also increases. However, as thickness increases from 2.7 mm to 3.5 mm and from 6.6 mm to 9.4 mm, the peak height decreases. As shown in Figures 4.84 Z3(a), Z3(c), Z3(i), Z3(k), and Z3(m), the REL peaks shift to the left in the lower frequency region as thickness increases. Additionally, Figure 4.84 Z3(g) shows a W-shaped curve between 10.00 GHz and 12.00 GHz, a feature that is favourable for applications such as electromagnetic interference (EMI) shielding, where broad absorption is desirable.

Composition Z4 exhibits bandwidths of 0.85 GHz at a thickness of 4.8 mm for the 11.14 GHz – 11.9 GHz frequency band, and bandwidths of 0.37 GHz and 0.27 GHz for thicknesses of 7.5 mm and 7.9 mm, respectively, corresponding to -10 dB. REL values of -20.89 dB, -20.99 dB, -27.72 dB, -24.54 dB, -25.4 dB, and a maximum of -43.4 dB are observed within the -20 dB bandwidth range of 0.1 GHz to 0.29 GHz. As indicated in Figures 4.85 Z4(c) and Z4(g), reflection loss peaks for composition Z4 are observed at the same frequency for thicknesses between 4.0 mm and 4.8 mm, and

4.9 mm to 5.7 mm. Figures 4.85 Z4(a), Z4(e), Z4(k), Z4(m), and Z4(o) demonstrate that the REL peaks shift to lower frequencies as thickness increases from 4.0 mm to 4.8 mm, 4.9 mm to 5.7 mm, 6.7 mm to 7.5 mm, and beyond. Peak heights increase with thickness from 4.0 mm to 6.6 mm and from 7.6 mm to 9.3 mm; however, for thicknesses between 4.9 mm and 5.7 mm, peak heights decrease as thickness increases.

For instance, composition Z1, with thicknesses ranging from 4.3 mm to 6.7 mm, shows a -10 dB bandwidth of 0.12 GHz to 0.21 GHz, while Z2, with thicknesses from 6.1 mm to 9.6 mm, exhibits a much broader -10 dB bandwidth range of 0.15 GHz to 0.45 GHz. The effective absorption for all compositions is governed by the inverse relationship between frequency and material thickness, confirming the applicability of the $\lambda/4$ mechanism.

5.3.3.4 Impedance matching mechanism

The variation in impedance observed in the samples is attributed to differences in their permittivity and permeability compared to free space. These discrepancies directly affect the microwave absorption capabilities of the material. When the impedance of the material closely matches that of free space (Z_o = 377 Ω), a larger portion of the incident microwave signal is absorbed, while a significant mismatch leads to most of the signal being reflected off the surface. Therefore, impedance matching is crucial in developing effective microwave absorbers.

The reflection loss (REL) and $|Z_{in}|$ values across various frequencies for the processed samples are presented in Figure 4.87. The corresponding $|Z_{in}|$ values at the maximum reflection loss for each composition (Z1 to Z4) are summarized in Table 4.28. For each composition, the most prominent REL peaks align with the principles of impedance matching.

For Z1 at a thickness of 4.3 mm, the peak REL of -21.93 dB at 8.79 GHz corresponds to an impedance of Z_{in} = 440.99 Ω. However, no REL peak is observed at 11.56 GHz where Z_{in} = 366.43 Ω, despite this being closer to Z_o than the impedance at the lower frequency. In Z2, an REL peak of -40.8 dB at 10.05 GHz corresponds to Z_{in} = 370.27 Ω. For Z3, a peak REL of -31.08 dB at 12.15 GHz is associated with Z_{in} = 357.55 Ω. In Z4, a significant REL peak of -43.4 dB at 11.98 GHz corresponds to Z_{in} = 372.33 Ω.

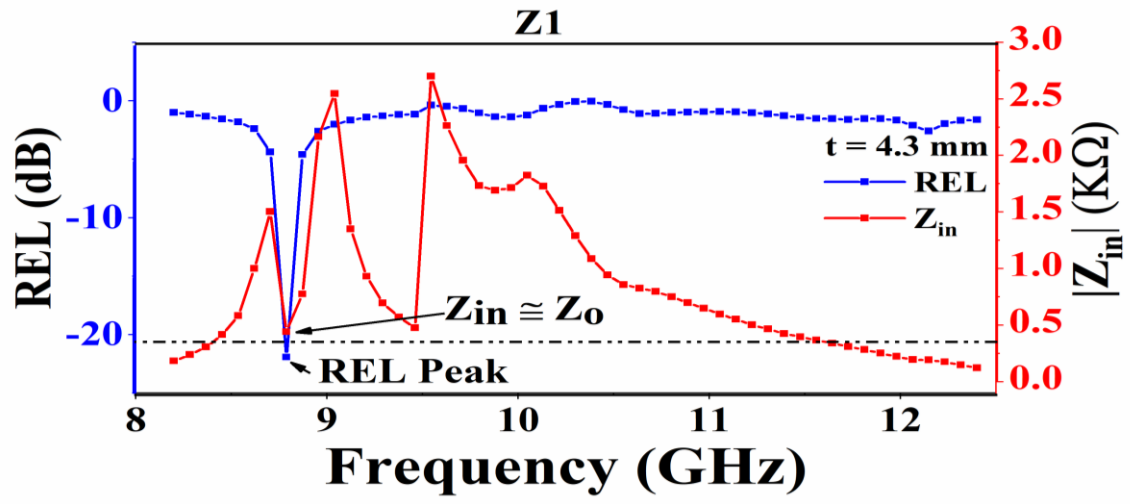
Z1
REL (dB)
|Z_in| (KΩ)
t = 4.3 mm
REL
Z_in
Zin ≅ Zo
REL Peak
Frequency (GHz)

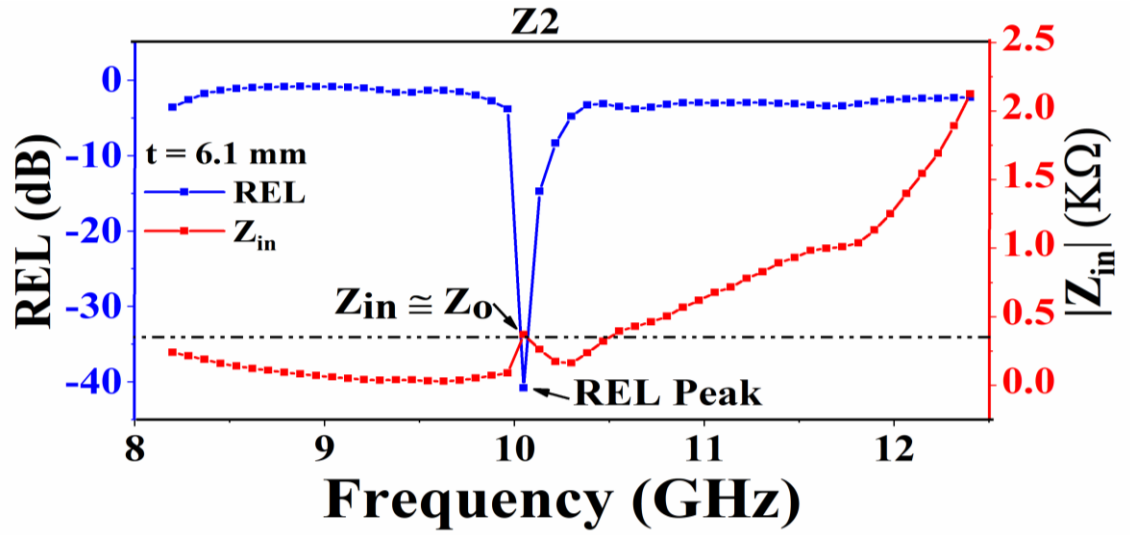
Z2
REL (dB)
|Z_in| (KΩ)
t = 6.1 mm
REL
Z_in
Zin ≅ Zo
REL Peak
Frequency (GHz)

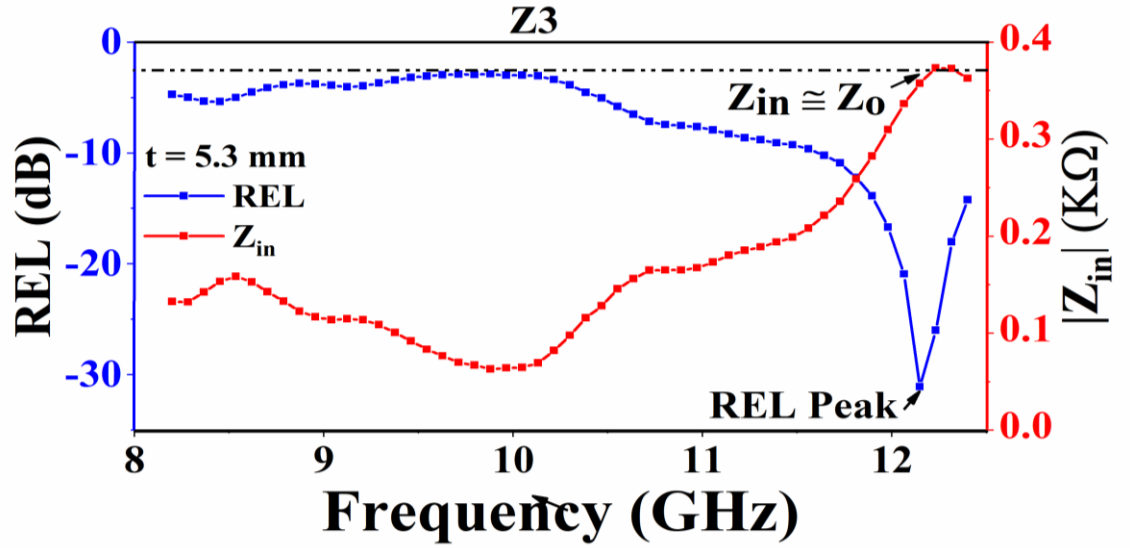
Z3
REL (dB)
|Z_in| (KΩ)
t = 5.3 mm
REL
Z_in
Zin ≅ Zo
REL Peak
Frequency (GHz)

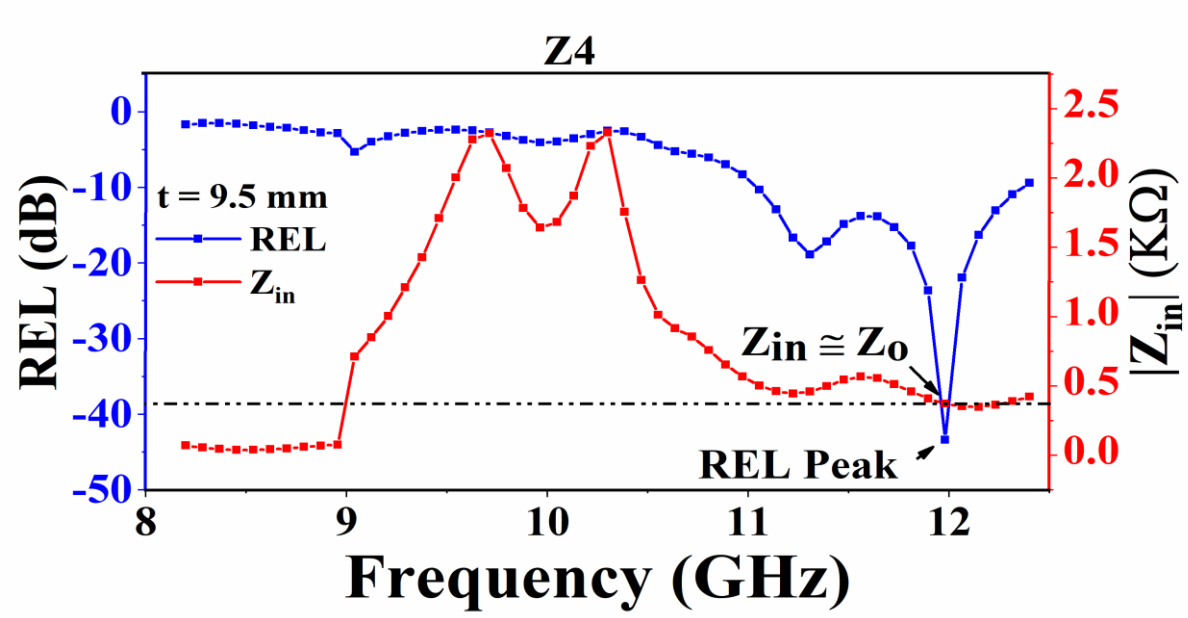

Figure 4.87 Z_{in} and REL curve against frequency for $BaCo_xCr_xFe_{12-2x}O_{19}$.

The complexity of Z_{in} arises from its real and imaginary components (Z_{real} and Z_{img}), both of which influence the impedance behaviour. The values of Z_{real} and Z_{img} for each composition are provided in Table 4.28, and their corresponding graphs are illustrated in Figure 4.88. Effective impedance matching requires that Z_{real} approach 377 Ω and Z_{img} approach zero.

For Z1, with a thickness of 4.3 mm, the maximum REL is -21.93 dB at a frequency of 8.79 GHz, and the real and imaginary impedance components are Z_{real} = 440.73 Ω and Z_{img} = 15.11 Ω, respectively. The higher Z_{real} indicates some impedance mismatch with free space, resulting in moderate absorption.

In Z2, at a thickness of 6.1 mm, the maximum REL reaches -40.8 dB at 10.05 GHz, with Z_{real} = 370.27 Ω and Z_{img} = 1.04 Ω. This close impedance matching to free space significantly enhances the absorption, leading to a stronger reflection loss.

Z3 shows a peak REL of -31.08 dB at 12.15 GHz and a thickness of 5.3 mm. The impedance values are Z_{real} = 357.55 Ω and Z_{img} = 6.48 Ω. While Z_{real} is slightly lower than Z_o, the absorption remains high due to the overall good impedance match.

For Z4, the maximum REL of -43.4 dB at 11.98 GHz corresponds to a thickness of 9.5 mm, with Z_{real} = 372.33 Ω and Z_{img} = -1.98 Ω. These values are very close to the ideal impedance, indicating excellent microwave absorption properties in this composition.

In conclusion, the absorption performance in these ferrite materials is closely linked to the degree of impedance matching, where closer alignment of Z_{real} to 377 Ω and Z_{img} to zero leads to higher reflection losses and better absorption. Z2 and Z4 demonstrate the best impedance matching and highest reflection losses, making them more effective in microwave absorption applications.

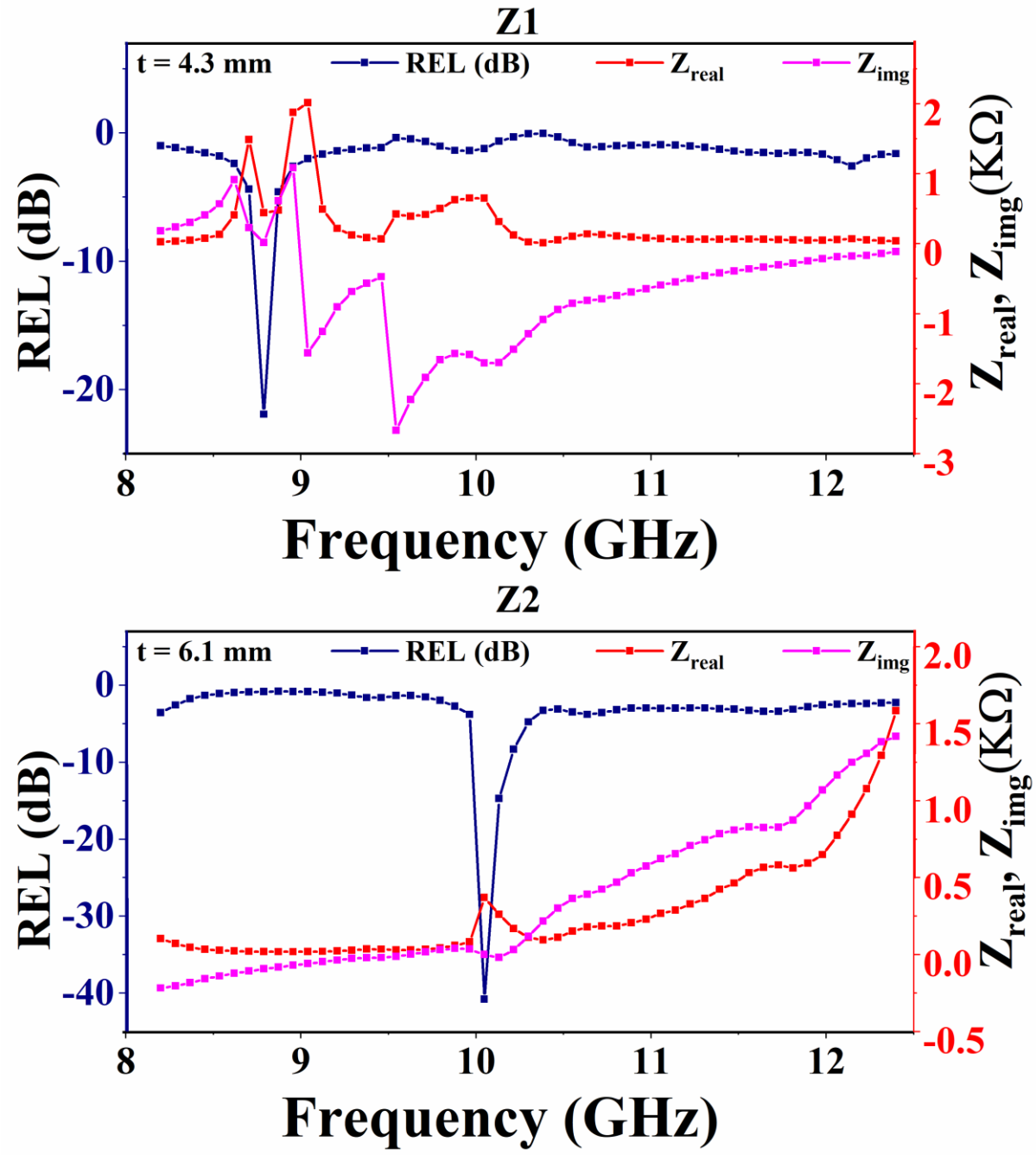

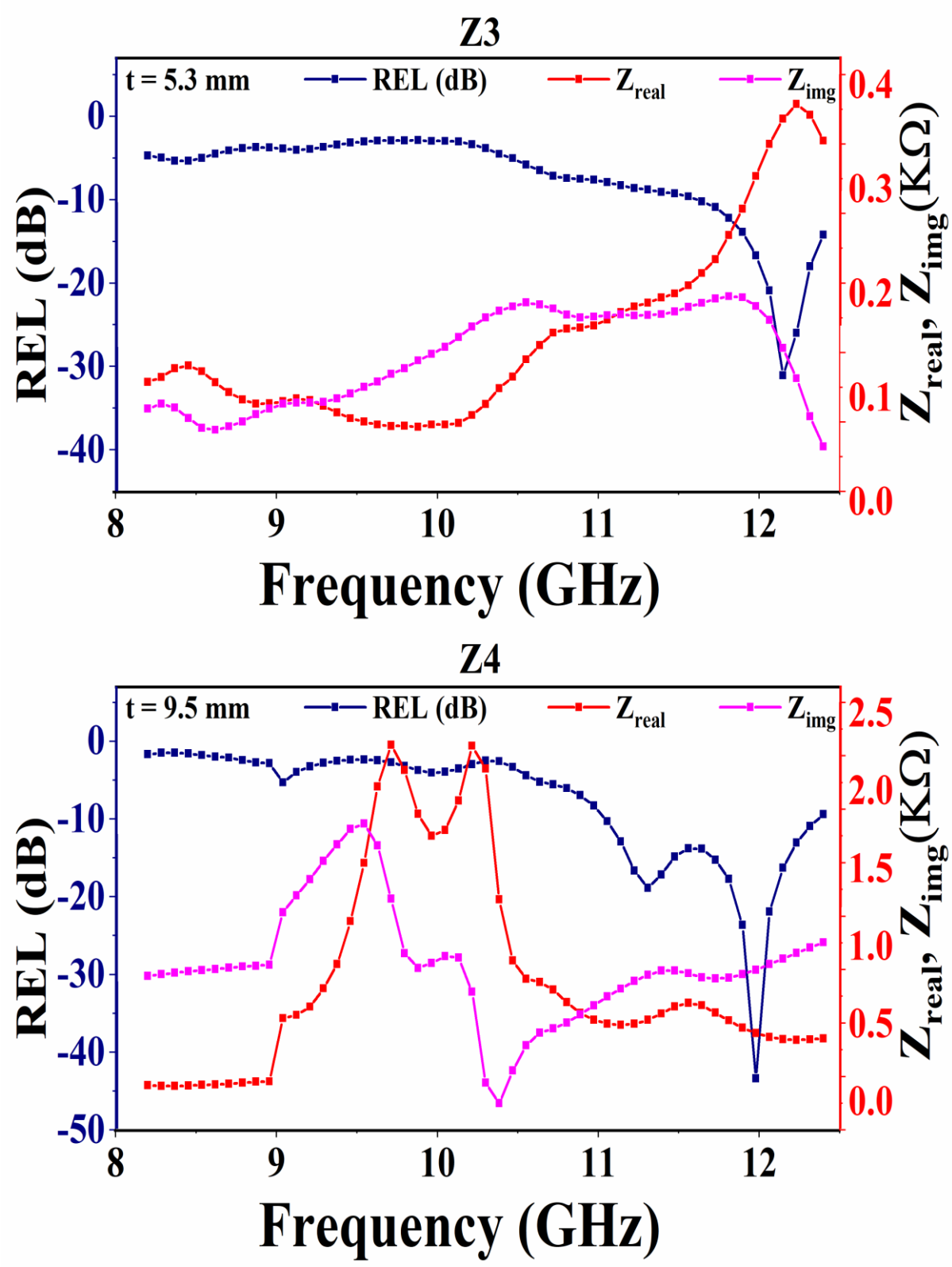

Figure 4.88 Z_{real}, Z_{imag}, and REL v/s frequency for $BaCo_xCr_xFe_{12-2x}O_{19}$.

Table 4.28 Z_{in}, Z_{real}, and Z_{imag} values corresponding to REL_{max} for $BaCo_xCr_xFe_{12-2x}O_{19}$.

Sample Name	Matching Thickness (mm)	Maximum REL (dB)	Matching frequency (GHz)	Zreal (Ω)	Zimg (Ω)	|Zin| (Ω)
Z1	4.3	-21.93	8.79	440.73	15.11	440.99
Z2	6.1	-40.8	10.05	370.27	1.04	370.27
Z3	5.3	-31.08	12.15	357.55	6.48	357.61
Z4	9.5	-43.4	11.98	372.33	-1.98	372.34

5.3.3.5 Eddy Current Loss

Z1, Z2, and Z4 curves seem to stay constant at or near zero, while Z3 shows a significant spike around 8.704 GHz with values like 2.19×10^6 ms. After this peak, Z3 gradually decreases to smaller values as the frequency increases beyond 9 GHz. Z1 shows relatively small values throughout the frequency range, with a slight peak around 8.79 GHz (0.81) and then a smooth decay. Z2 Follows a similar but slightly different pattern to Z1, with smaller values overall. It decays more smoothly after 8.70 GHz. Z4 Shows a steady decay pattern, with much smaller values compared to Z3, and slightly less fluctuation than Z1 and Z2.It is crucial to take into account that when the frequency rises and the C_0 stays constant, especially in the low frequency range of Z3, there will be an effect on the loss of eddy current. The graphs of all the compositions exhibit constancy beyond a frequency of 9.88 GHz, suggesting that the absorption of ferrite compositions is influenced by eddy current loss.

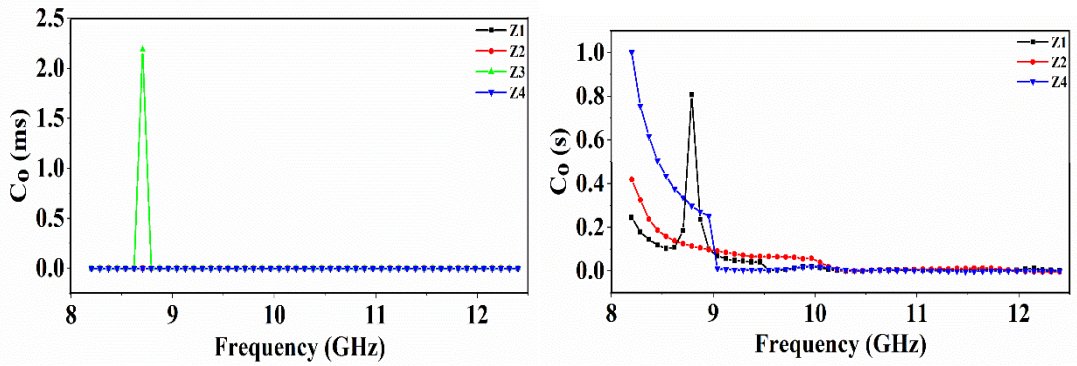

Figure 4.89 C_0 versus frequency curve for $BaCo_xCr_xFe_{12-2x}O_{19}$.

4.4.5.6 Bandwidth to Thickness Ratio

Highest BTR and PBW: Z3 exhibits the highest BTR values (up to 8.82×10^{-4}) and PBW values (up to 11.35%) at various thicknesses. At a thickness of 2.5 mm, Z3 shows a notable BTR of 8.82×10^{-4} with a PBW of 7.19%, which occurs at a

matching frequency of 9.88 GHz. Z4 exhibits substantially higher REL values (up to -43.4 dB at 11.98 GHz) but with lower BTR values compared to Z3. Z4 has a broad frequency range for REL > -10 dB, especially at greater thicknesses. The PBW values range up to 11.19% for thicker samples (9.5 mm at 11.98 GHz). Z1 has relatively low BTR values, ranging from 1.08×10^{-4} to 9.55×10^{-5}, with lower PBW percentages (1.37% to 2.13%). The frequency range is between 8.79 and 9.88 GHz for Z1. Z1 shows a smaller bandwidth for REL > -20 dB (up to 0.02 GHz). Z2 exhibits a moderate BTR range from 6.7×10^{-5} to 8.82×10^{-4}, with PBW percentages ranging from 1.49% to 4.76%. The matching frequency for Z2 spans from 9.38 GHz to 10.05 GHz for different thicknesses. The REL values are relatively lower than Z3 but still significant.

4.4.5.7 S – Parameter

When the input signal is applied at input port 1 of the test waveguide from VNA, the two-port S_{11} parameter accounts for the reflected signal from the same input port 1 from the sample fitted in the test waveguide of the VNA. S_{21} accompanies the attenuation in the signal traveling from input port 1 to output port 2.

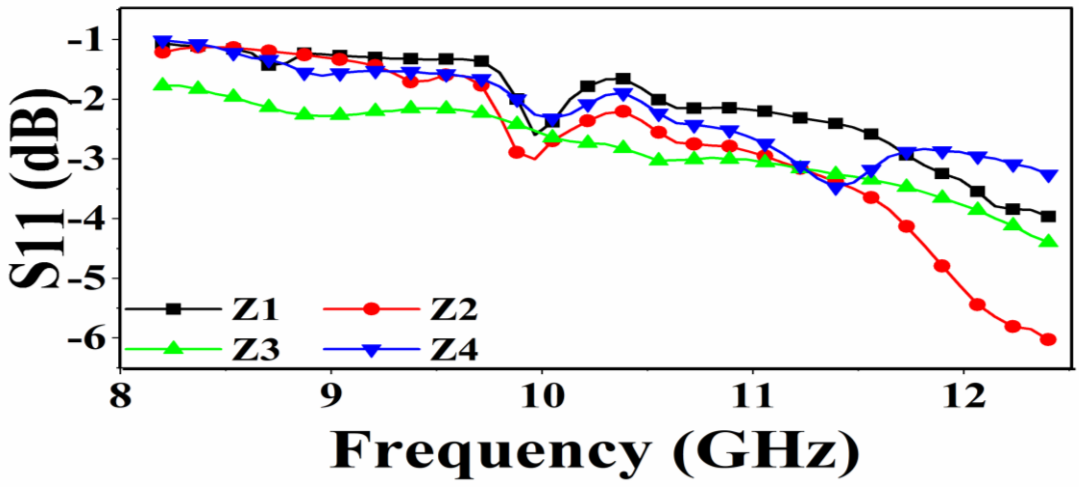

Figure 4.90 S_{11} versus frequency curve for $BaCo_xCr_xFe_{12-2x}O_{19}$.

The S_{11} for Z1 shows a gradual decline as frequency increases. It starts at around -1.06 dB at 8.2 GHz and drops steadily to about -3.96 dB at 12.4 GHz. Z2 shows a steep decline in S_{11} after 9.88 GHz, with values falling from -2.88 dB at 9.88 GHz to around -6.03 dB at 12.4 GHz. Z3 shows a more gradual decline in S_{11}, starting around -1.77 dB at 8.2 GHz and gradually reaching around -4.39 dB at 12.4 GHz. Z4 has

stable performance across the frequency range, with a smooth decline starting at around -1.01 dB at 8.2 GHz and reaching -3.26 dB at 12.4 GHz.

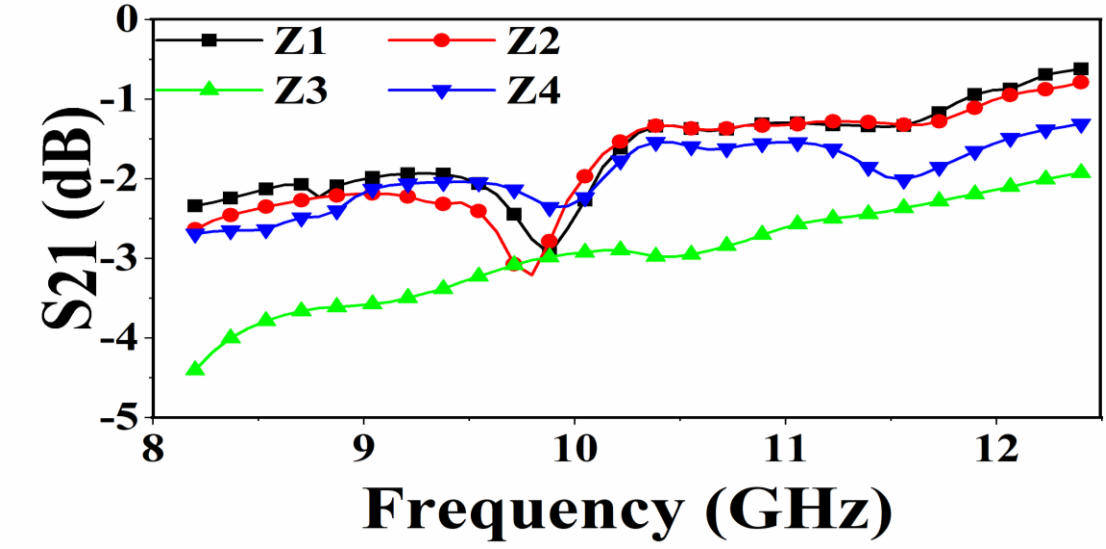

Figure 4.91 S_{21} versus frequency curve for $BaCo_xCr_xFe_{12-2x}O_{19}$.

Z1 shows a consistent S_{21} behaviour with values ranging between -2.5 dB to -1 dB across most of the frequency range. Z2 experiences a significant dip in S_{21} around 10 GHz, where the transmission drops to about -3 dB, but after that point, it recovers and improves steadily. Z3 consistently shows the lowest S_{21} values, meaning it experiences more attenuation compared to the other samples. It starts around -4.4 dB at 8.2 GHz and only gradually improves to -2 dB by 12 GHz. Z4 starts with similar behaviour to Z1, but after 9.5 GHz, it reaching approximately -1.5 dB at 12 GHz.

4.5 Co^{2+}- Al^{3+} substituted $BaCo_xAl_xFe_{12-2x}O_{19}$ / PANI Composite.

In this section, we will be utilizing the sol-gel combustion method to synthesize a hexaferrite with Co and Al substitutions. The composition of this hexaferrite will be $BaCo_xAl_xFe_{12-2x}O_{19}$. Displayed in Table 4.29 are the sample names/codes for various levels of substitution in $BaCo_xAl_xFe_{12-2x}O_{19}$.

Table 4.29. Presents the assignment of sample names corresponding to various substitution levels in $BaCo_xAl_xFe_{12-2x}O_{19}$ hexaferrite.

Sample Composition **$BaCo_xAl_xFe_{12-2x}O_{19}$**	Sample Code Name	Sample Code (WP-series)
x= 0.0	**$BaFe_{12}O_{19}$**	WP1
x = 0.8	**$BaCo_{0.8}Al_{0.8}Fe_{10.4}O_{19}$**	WP2
x = 1.0	**$BaCoAlFe_{10}O_{19}$**	WP3

4.5.1 Field Emission Scanning Electron Microscopy

The structure in Figure 4.92(a) i.e WP1 appears to consist of relatively large, irregular, and elongated grains. The surface seems rough with a high level of agglomeration, suggesting a potential strong interaction between the particles. These grain clusters indicate a well-packed morphology, which can contribute to improved electrical and magnetic properties due to a reduction in grain boundaries that may act as scattering sites for charge carriers.

The grains in Figure 4.92(b) i.e WP2 are smaller and appear to be more dispersed compared to the WP1. There are visible voids or porosities between the grain clusters, which may impact the overall density and could contribute to lower conductivity due to reduced inter-particle contact. This porosity could also enhance dielectric relaxation as the grain boundaries act as sites for charge accumulation.

In Figure 4.92(c) i.e WP3 shows a more compact and uniform arrangement of smaller grains with few visible pores. This compactness suggests higher packing density, which may lead to better inter-grain connectivity and potentially higher conductivity. The smaller grain size could lead to a greater contribution from grain boundaries in electrical and dielectric behaviour, as these interfaces become more pronounced in materials with smaller grains.

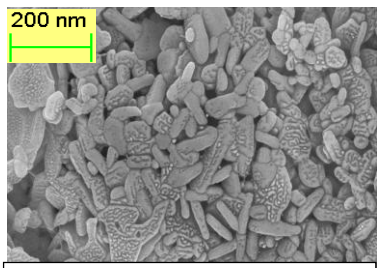

Figure 4.92(a) SEM for WP1

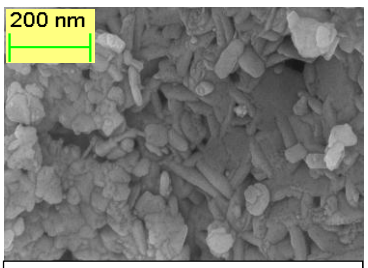

Figure 4.92(b) SEM for WP2

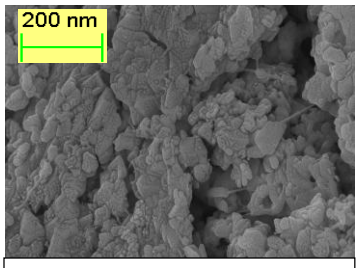

Figure 4.92(c) SEM for WP3

Figure 4.92 SEM Micrographs of $BaCo_xAl_xFe_{12-2x}O_{19}$ Ferrites (WP1 (x = 0.0), WP2 (x = 0.8), WP3 (x = 1.0)).

4.5.2 Electrical Characterization

4.5.2.1 Dielectric constant

From the figure 4.93, it is observed that the dielectric constant and loss have increased significantly compared to pure ferrites. This enhancement can be attributed to the presence of PANI, a dielectric material with a high dielectric constant, which contributes to the overall increase in the dielectric constant and loss in the composites.

The synthesized WP1, WP2, and WP3 hexaferrite composites show distinct frequency-dependent behaviours. WP1 consistently exhibits the highest values of ε' i.e 12791.13, while WP2 and WP3 display lower values across the frequency range i.e 203.05 and 52.31 respectively. With the substitution of Co^{2+} and Al^{3+} in WP2 and WP3, a notable reduction in ε' is observed. Figure 4.93(b) demonstrates the behaviour of the imaginary part of the dielectric constant (ε'') as a function of frequency. Similar to ε', the dielectric loss ε'' shows significant frequency dependence at lower frequencies, with WP1 again exhibiting the highest values i.e 172173.3. At higher frequencies, ε'' becomes nearly frequency-independent for WP2 and WP3, while WP1 shows a gradual decline, indicating reduced energy dissipation and as the frequency increases, ε' becomes almost independent of frequency, especially beyond 10^5 Hz.

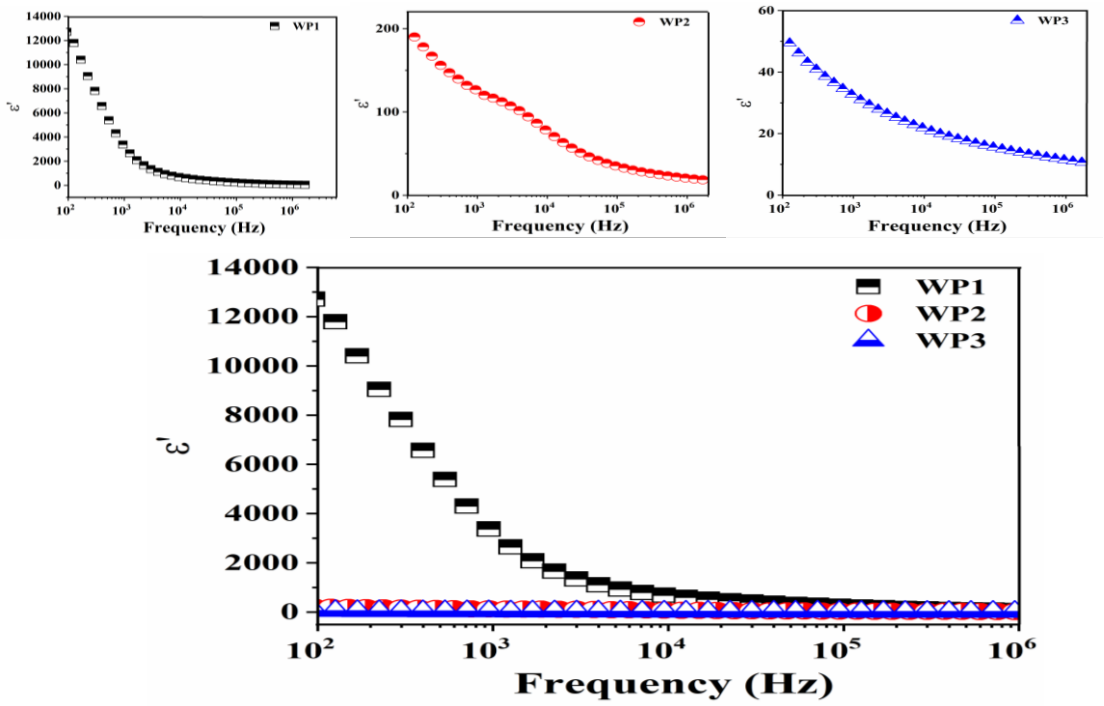

Figure 4.93(a) Dielectric Constant Dependence on Frequency in $BaCo_xAl_xFe_{12-2x}O_{19}$ (WP1 (x = 0.0), WP2 (x = 0.8), WP3 (x = 1.0)) Hexaferrites

The Figure 4.93(c) shows the variation of the loss tangent (tan δ) as a function of frequency for the WP1, WP2, and WP3 samples. The loss tangent, which represents the ratio of the dielectric loss (ε'') to the dielectric constant (ε'), is an indicator of energy dissipation within the material. The WP2 sample exhibits the highest values of tan δ i.e 28.7, especially at lower frequencies.

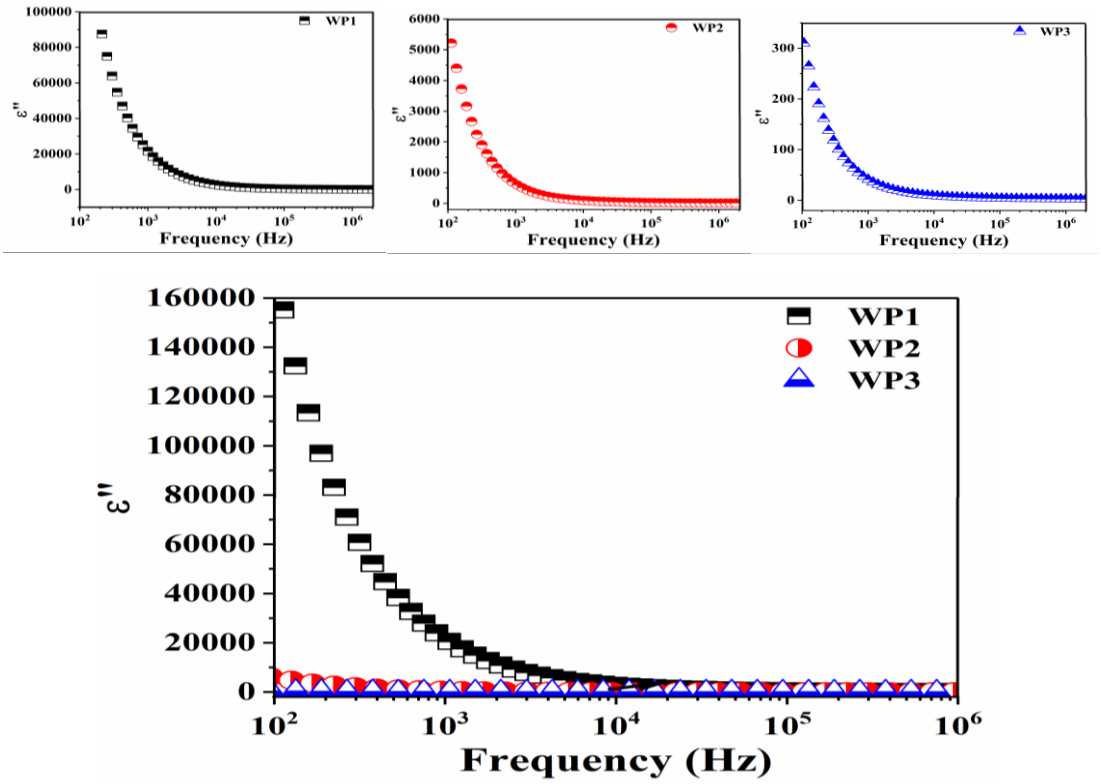

Figure 4.93(b) Dielectric Loss Dependence on Frequency in $BaCo_xAl_xFe_{12-2x}O_{19}$ (WP1 (x = 0.0), WP2 (x = 0.8), WP3 (x = 1.0)) Hexaferrites

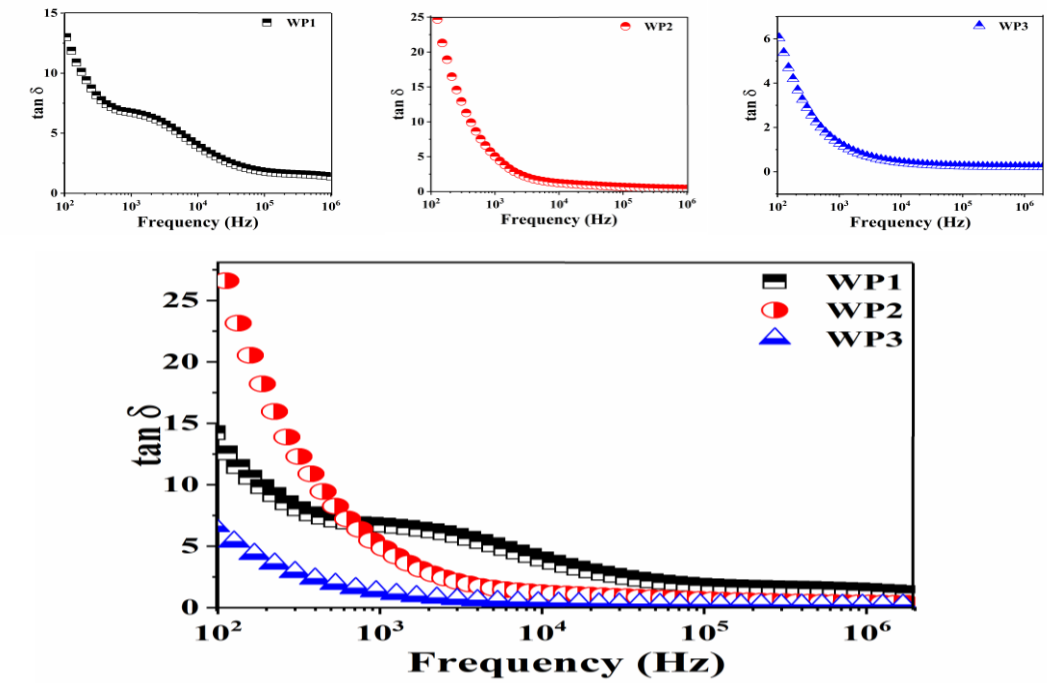

Figure 4.93(c) Dielectric Loss Tangent Dependence on Frequency in $BaCo_xAl_xFe_{12-2x}O_{19}$ (WP1 (x = 0.0), WP2 (x = 0.8), WP3 (x = 1.0)) Hexaferrites

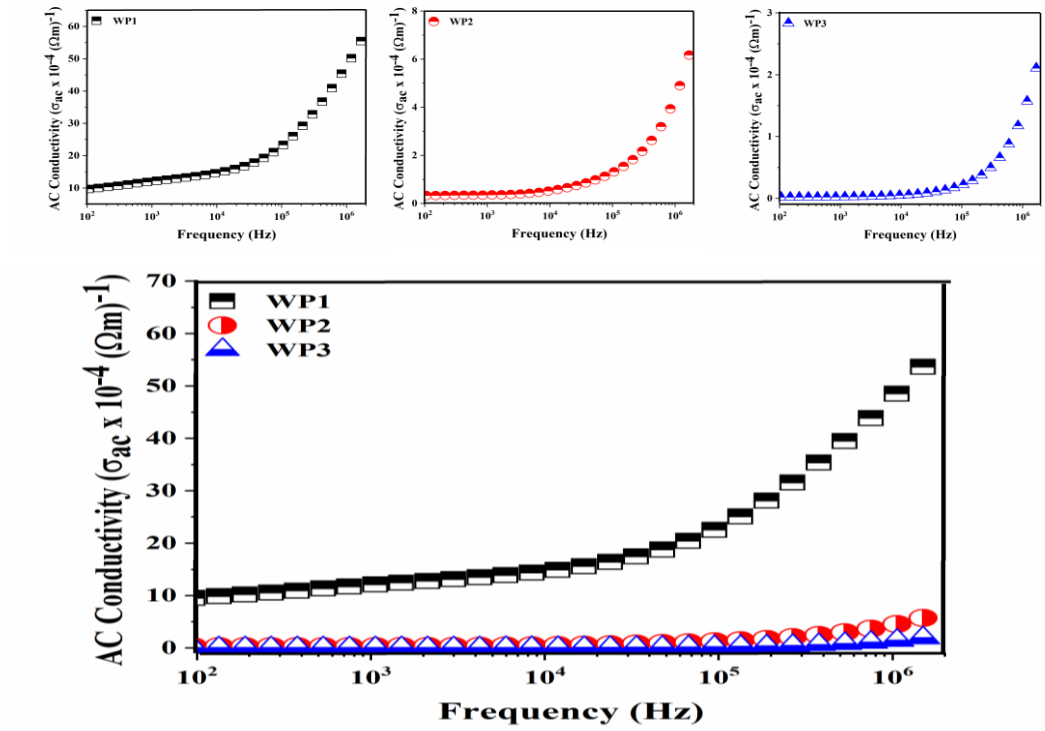

Figure 4.93(d) AC Conductivity Dependence on Frequency in $BaCo_xAl_xFe_{12-2x}O_{19}$ (WP1 (x = 0.0), WP2 (x = 0.8), WP3 (x = 1.0)) Hexaferrites

This high value suggests considerable energy dissipation in WP2, likely due to a higher degree of dielectric loss. WP1 shows moderate tan δ values, peaking around 10 at low frequencies. The loss tangent decreases steadily as the frequency increases, indicating a reduction in energy dissipation at higher frequencies. This sample shows an intermediate behaviour compared to WP2 and WP3, likely due to the influence of less disruptive doping or the balance between conductivity and polarization mechanisms. WP3 consistently displays the lowest values of tan δ across the frequency range, suggesting minimal energy dissipation.

The Figure 4.93(d) shows the variation of AC conductivity (σ_{ac}) as a function of frequency for the samples, WP1, WP2, and WP3. WP1 exhibits the highest AC conductivity across all frequencies. The AC conductivity increases gradually at lower frequencies and then rises sharply beyond around 10^5Hz. At higher frequencies, the conductivity reaches a peak value of approximately 58×10^{-3} $(\Omega \cdot m)^{-1}$**.** This sharp increase at higher frequencies suggests that WP1 has a more pronounced frequency-dependent conduction mechanism, likely due to enhanced hopping or charge carrier mobility. WP2 shows moderate AC conductivity compared to WP1. Although its

conductivity is relatively low at lower frequencies, it begins to increase more noticeably beyond 10^5Hz. However, the increase is much more gradual compared to WP1, and the maximum value reached is significantly lower, around 6.94×10^{-4} $(\Omega \cdot m)^{-1}$**.** This indicates that WP2 has fewer charge carriers compared to WP1. WP3 has the lowest AC conductivity among the three samples**.** The conductivity remains nearly flat across the entire frequency range, indicating that the material is much more resistive and less responsive to the alternating electric field. The maximum AC conductivity for WP3 is around 2.44×10^{-4} $(\Omega \cdot m)^{-1}$**,** highlighting its highly insulating behaviour compared to WP1 and WP2.

4.5.2.2 Electric modulus analysis

Figure 4.94(a) shows the variation of M' (real part of the electric modulus) as a function of frequency for Co- and Al-doped hexaferrite composites. The M' values for all samples tend to approach zero at lower frequencies, indicating a strong dipolar polarization and minimal contribution from electrode polarization and conductivity. This behaviour reflects the dominance of long-range mobility and dipolar relaxation at low frequencies. As the frequency increases, M' rises steadily before levelling off, indicating the transition to localized charge relaxation and short-range mobility. This trend aligns with the AC conductivity described earlier, where conductivity is minimal at low frequencies and maximal at high frequencies. WP3, among all samples, shows the highest M' values i.e 9.22 x 10^{-2}, suggesting greater resistance to charge carrier movement and higher conductive relaxation strength, while WP1 exhibits the lowest M' i.e 9.42 x 10^{-3}, indicating higher charge mobility and lower resistance.

In Figure 4.94(b), the imaginary part of the electric modulus (M'') is plotted against frequency. WP3 consistently shows the highest M'' values, reflecting significant energy dissipation and stronger conductivity relaxation effects. WP2 displays intermediate behaviour, while WP1 has the lowest M'' values, indicating lower losses and faster charge conductivity relaxation. Notably, the value in M'' increase at higher frequencies with increasing doping. WP1, with the smallest peak height, demonstrates weaker inter-grain connectivity and less effective polarization.

Figure 4.94(c) reveals the Cole-Cole plot (imaginary vs. real modulus), which reflects the conductivity relaxation processes and charge transport mechanisms in the doped

composites. The WP3 sample exhibits the largest diameter of the semicircular arc, indicating a higher conductivity relaxation strength and stronger interaction between charge carriers and the electric field. WP3 exhibits the highest peak in M", indicating that the relaxation processes and grain boundary effects are most pronounced in this sample. In contrast, WP1 shows a much smaller arc diameter, confirming its lower resistance and more effective charge mobility. WP1 has the lowest peak height, which reflects the least significant relaxation processes and suggests weaker grain contributions and strong grain boundary contribution. The behaviour of WP2 falls between these extremes, reflecting moderate conductivity relaxation behaviour. WP2 shows a lower peak height compared to WP3 but higher than WP1, suggesting intermediate conductivity relaxation. The peaks for WP2 and WP3 are shifted towards higher M' values compared to WP1, indicating that the relaxation processes occur at higher frequencies. This shift suggests that doping influences the charge mobility and grain dynamics, with WP3 showing the most significant shift, implying higher frequency relaxation. WP1 shows the peak at lower M' values, indicating slower relaxation and more influence from grain boundary processes.

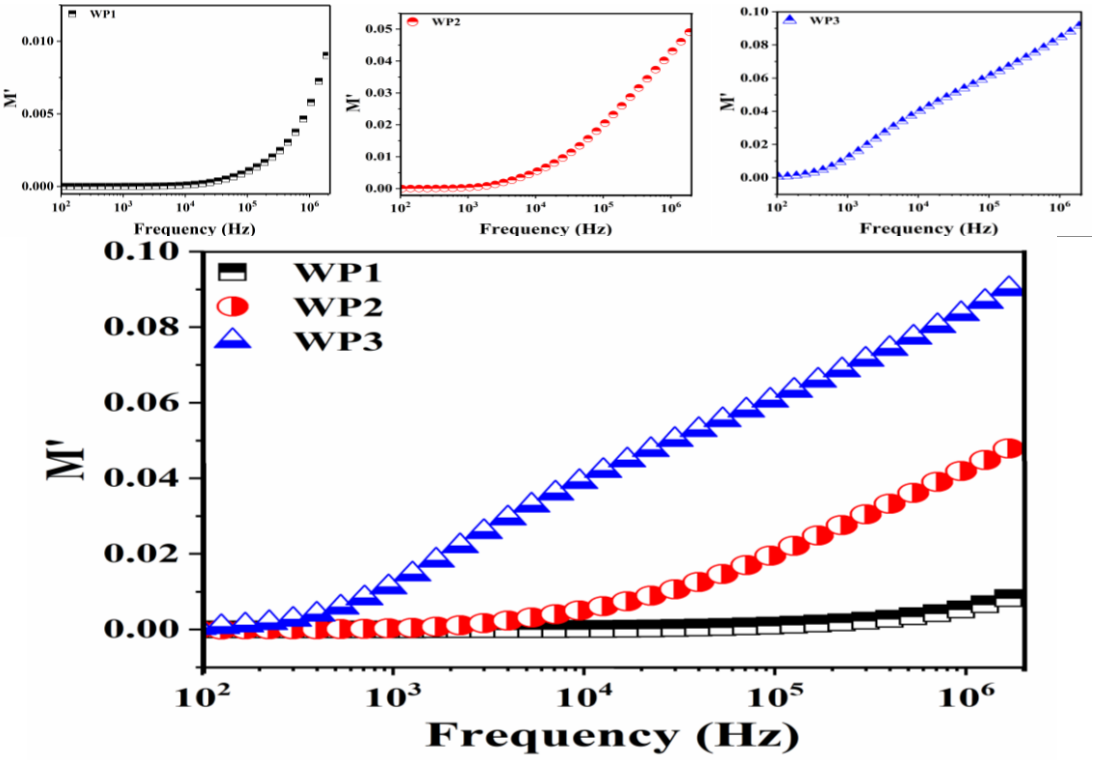

Figure 4.94(a) Real Modulus (M′) Dependence on Frequency in $BaCo_xAl_xFe_{12-2x}O_{19}$ (WP1 (x = 0.0), WP2 (x = 0.8), WP3 (x = 1.0)) Hexaferrites

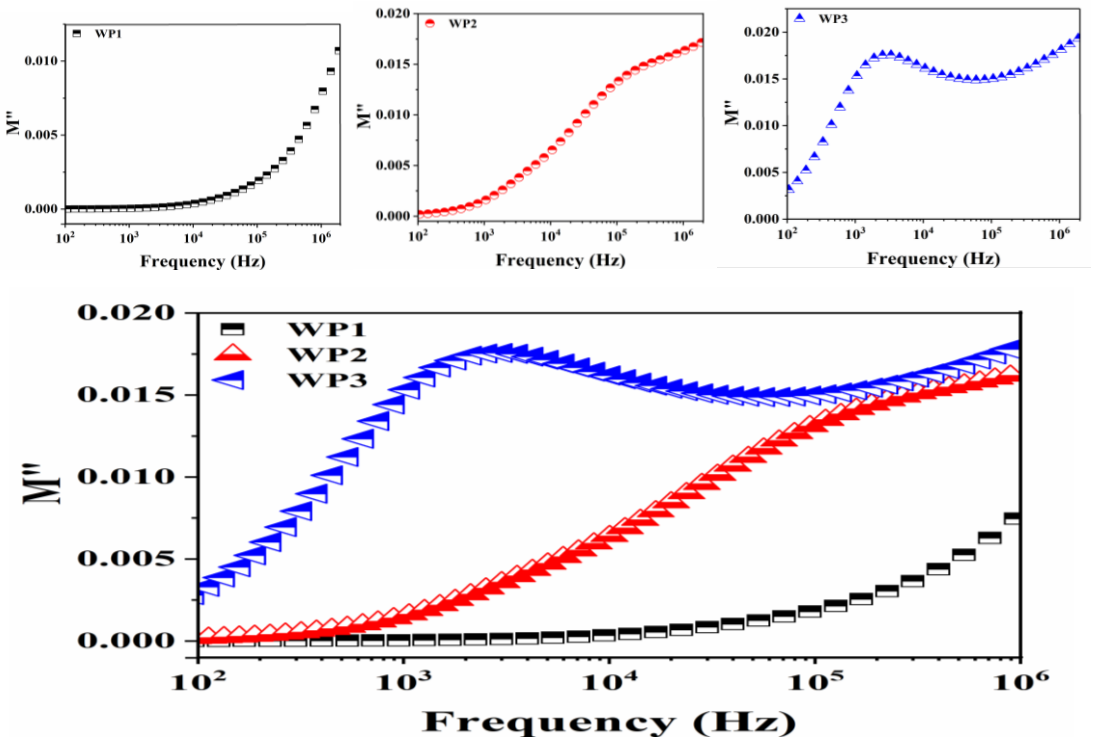

Figure 4.94(b) Imaginary Modulus (M'') Dependence on Frequency in $BaCo_xAl_xFe_{12-2x}O_{19}$ (WP1 (x = 0.0), WP2 (x = 0.8), WP3 (x = 1.0)) Hexaferrites

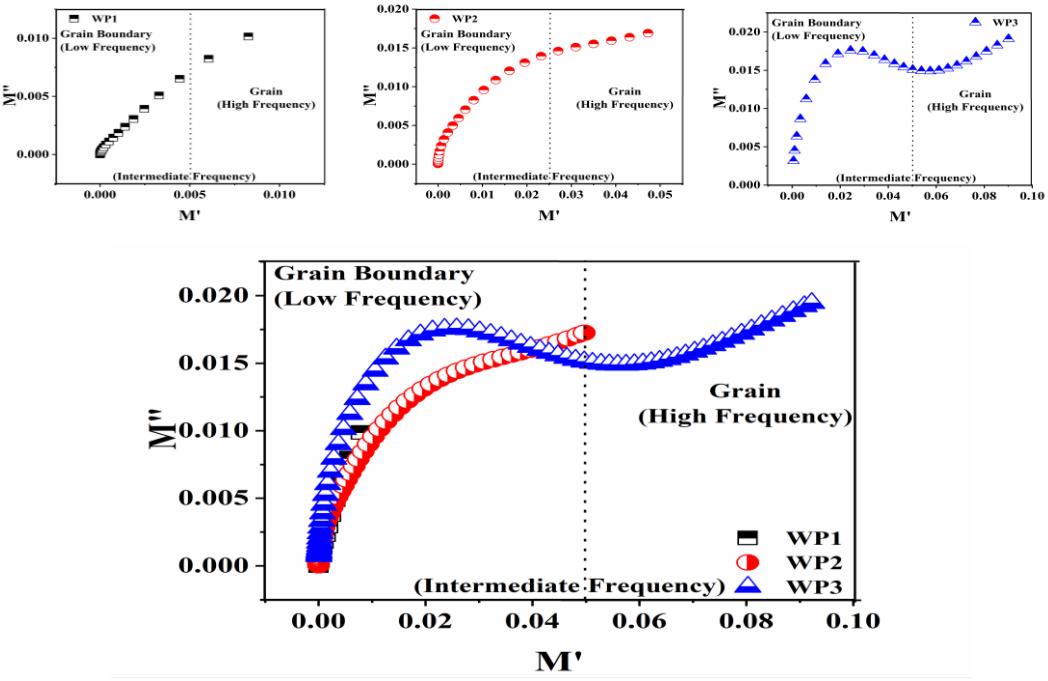

Figure 4.94(c) Cole-Cole Impedance Plots of $BaCo_xAl_xFe_{12-2x}O_{19}$ (WP1 (x = 0.0), WP2 (x = 0.8), WP3 (x = 1.0)) Hexaferrites at 900°C, 5h.

4.5.2.3 Impedance spectroscopy

The frequency-dependent behaviour of Z' and Z''' for Co-Al doped hexaferrite composites is depicted in Figure 4.95(a) and Figure 4.95(b). As the frequency increases, both Z' (real impedance) and Z'' (imaginary impedance) decrease, indicating enhanced conductivity due to an increase in electron hopping between localized ions. WP3 exhibits the highest impedance at low frequencies, reaching up to $6.10\times10^{7}\,\Omega$, followed by WP2 with a moderate impedance and WP1 showing the lowest impedance values. Beyond 10^{4} Hz, the Z'' values for all three composites level off, indicating that the impedance reaches a saturation point. This could imply that at high frequencies, the impedance becomes dominated by bulk material properties rather than grain boundary effects. The drop in Z'' values with higher Co-Al doping levels can be attributed to a reduction in polarization effects. WP2 shows a pronounced peak in Z'' at approximately 10^{4} Hz. This peak suggests a relaxation process, likely due to the contribution of grain boundaries and other interfacial effects that dominate the impedance response at this frequency. WP2 exhibits a wide range of frequency response, with Z'' values rising sharply from lower frequencies and reaching a peak before declining gradually. This behaviour suggests a significant contribution from grain boundaries and dipolar relaxation in WP2, which dominates the impedance behaviour in this frequency range.

Figure 4.95(c) illustrates the Cole-Cole (Nyquist) plots (Z'' vs Z') of the Co-Al doped hexaferrite composites. The low-frequency region reflects the resistive contributions from the grains of the material, while the high-frequency region reflects the grain boundary contributions. WP3 shows a significant contribution from grains in the low-frequency region, as indicated by the large arc in the graph. This suggests higher resistance or impedance due to the bulk material (grains) at low frequencies. As frequency increases, the grain boundary contribution becomes more prominent, leading to a reduction in the impedance as shown by the drop on the right-hand side of the plot (high-frequency region). WP2 displays a smaller arc compared to WP3, indicating grain contribution at low frequencies. The non-ideal (non-Debye) semicircular arcs suggest that the materials exhibit distributed relaxation times. WP3's larger arc implies more grain-related impedance, while WP1's smaller arc indicates less resistive grain effects and faster charges carrier relaxation.

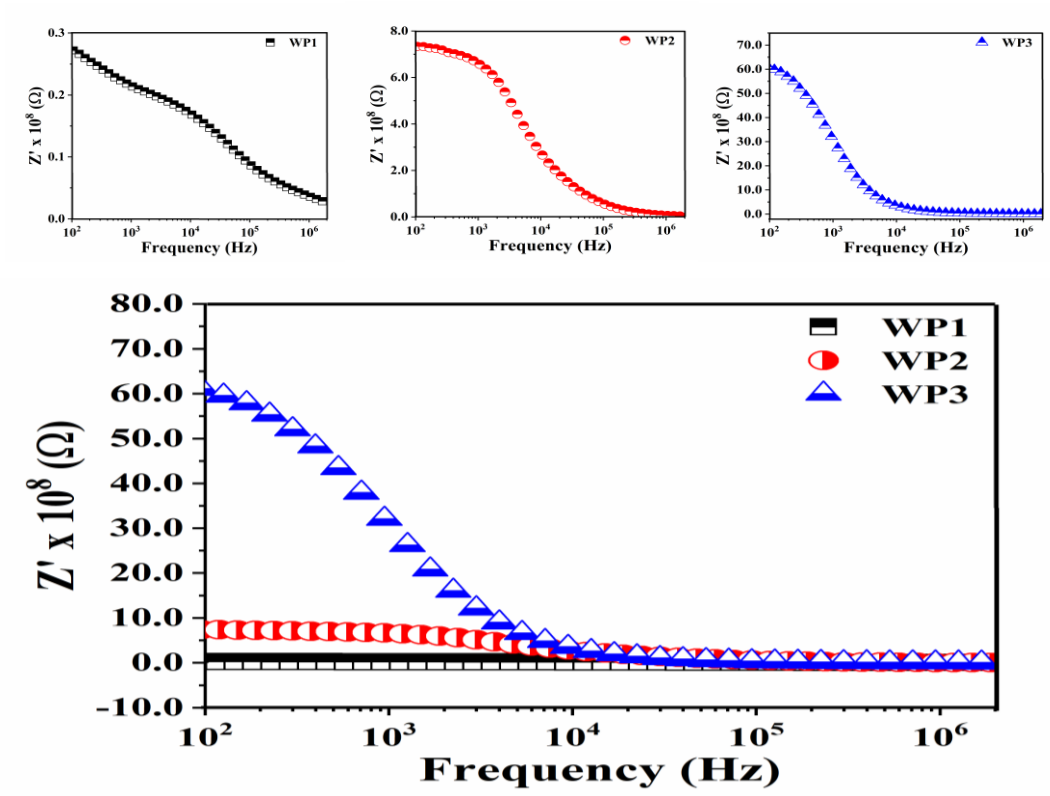

Figure 4.95(a) Real Impedance (Z′) Dependence on Frequency in $BaCo_xAl_xFe_{12-2x}O_{19}$ (WP1 (x = 0.0), WP2 (x = 0.8), WP3 (x = 1.0)) Hexaferrites

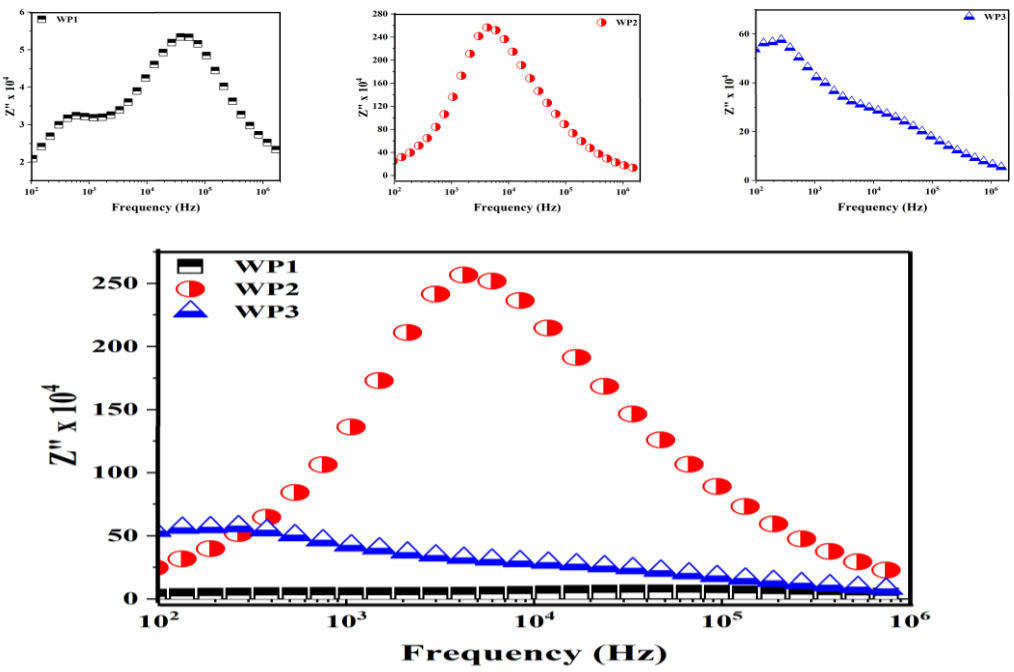

Figure 4.95(b) Imaginary Impedance (Z′) Dependence on Frequency in $BaCo_xAl_xFe_{12-2x}O_{19}$ (WP1 (x = 0.0), WP2 (x = 0.8), WP3 (x = 1.0)) Hexaferrites

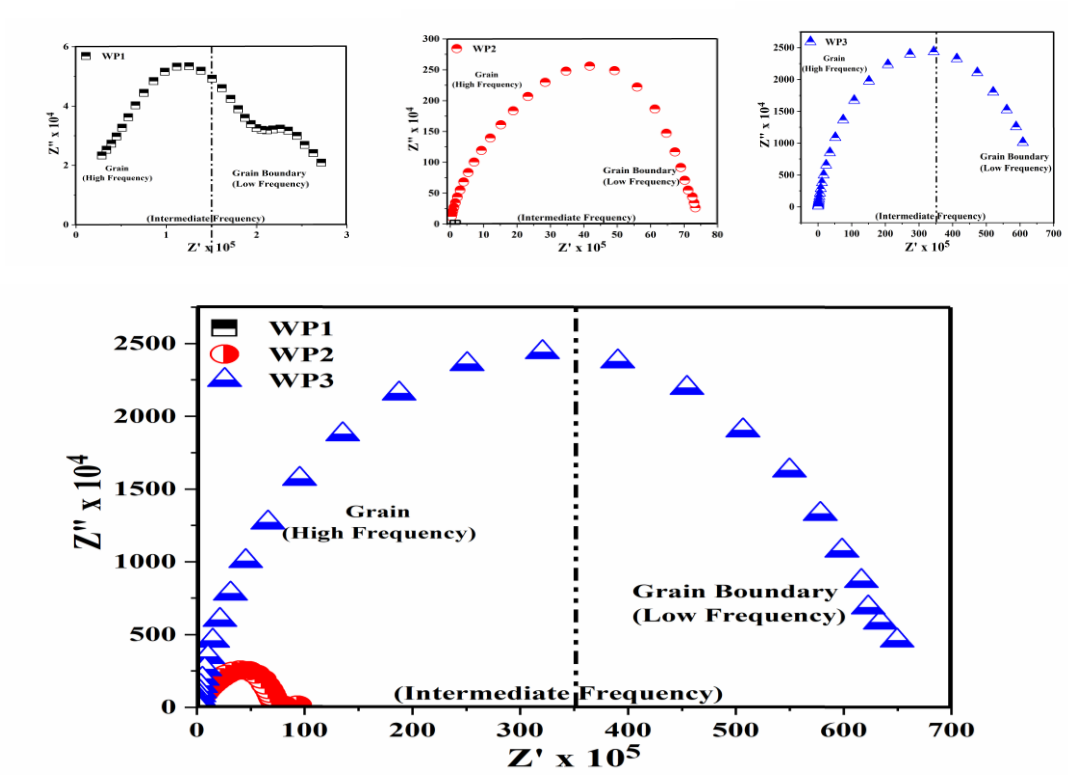

Figure 4.95(c) Cole-Cole Impedance Plots of $BaCo_xAl_xFe_{12-2x}O_{19}$ (WP1 (x = 0.0), WP2 (x = 0.8), WP3 (x = 1.0)) Hexaferrites after Heat Treatment at 900°C for 5 Hours.

4.5.2.4 Computational Impedance Simulation and Validation

Figure 4.96 illustrates the results of an analogous circuit analysis conducted on complex impedance data acquired via Electrochemical Impedance Spectroscopy (EIS) software [49]. The analogous circuit consists of a series arrangement of two parallel sub-circuits:

Initial sub-circuit: Represents the resistance and capacitance of individual grains (R_g & C_g).

Second sub-circuit: Depicts the resistance and capacitance of discrete grain boundaries (R_{gb} & C_{gb}).

This model precisely reflects the behaviour seen in the mixtures, as demonstrated by the strong correlation between measured and simulated/fitted curves in the images. Table 4.30 displays the resistance, and capacitance values derived from the EIS data for both grains and grain borders. These parameters measure the electrical response of the microstructural characteristics within the mixtures.

Table 4.30 Extracted Grain and Grain Boundary Parameters from EIS Modelling

Composite	R_g (MΩ)	R_{gb} (MΩ)	C_g (µF)	C_{gb} (µF)
WP1	0.21	0.02	440059.67	3.94
WP2	6.53	1.20	152.93	87.41
WP3	6.71	56.37	67.35	26.19

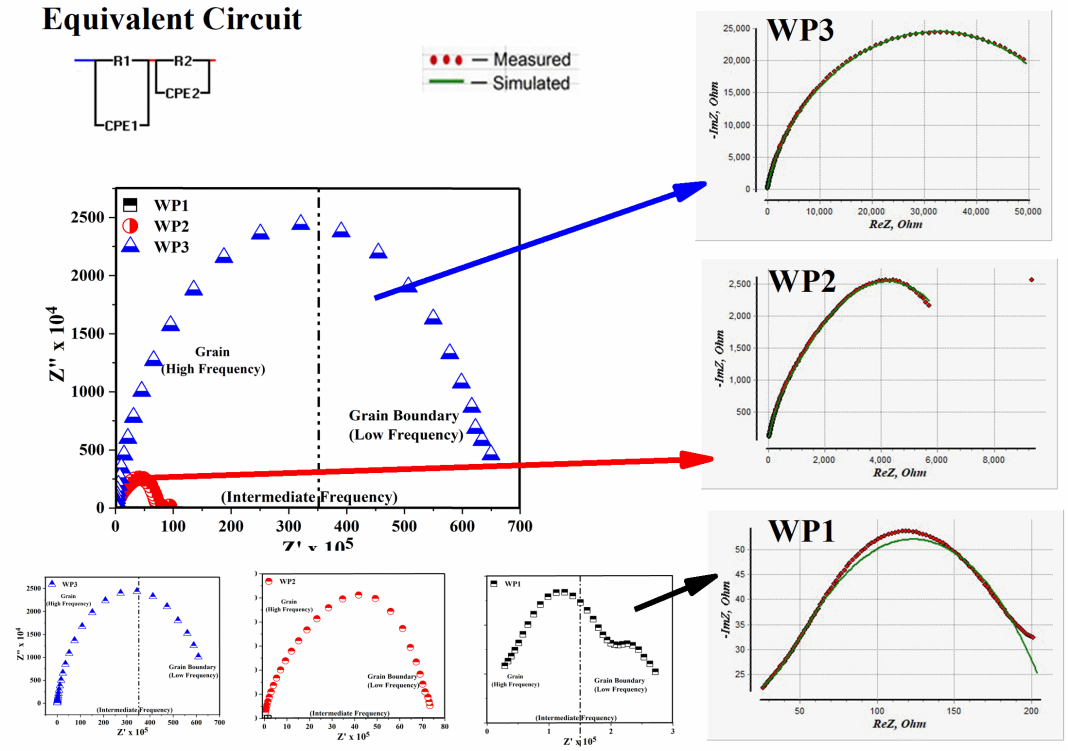

Figure 4.96 Measured and Fitted Impedance Data with Equivalent Circuit (WP1 to WP3)

4.5.2.5 Investigating the Relationship between EIS Data and Microstructure

The larger, well-defined grains seen in the Figure 4.92 (a) i.e WP1 suggest a dominant contribution from the grains themselves (R_g, C_g). Larger grains typically promote easier charge transfer across the material, meaning that R_g (grain resistance) is lower among all the sample i.e 0.21 MΩ and C_g is highest between WP1, WP2 and WP3 i.e 440059.67 µF. Grain boundaries are less prominent due to the large grain size, which could result in lower R_{gb} (grain boundary resistance) i.e 0.018 MΩ. The large and compact grains reduce the area available for grain boundaries, thus making the grain boundary capacitance C_{gb} small i.e 3.94 µF. The grains in Figure 4.92 (b) i.e WP2 are

smaller and more dispersed, which likely increases R_g from 0.211 MΩ to 6.53 MΩ as smaller grains introduce more scattering sites and barriers for electron flow. The visible porosity and the less compact structure suggest a significant contribution from grain boundaries, both in terms of resistance (R_{gb}) and capacitance (C_{gb}). The increased number of grain boundaries introduces more interfaces that contribute to highest C_{gb} i.e 87.41 µF and increase grain boundary resistance from 0.018 MΩ to 1.20 MΩ, as grain boundaries typically have higher resistivity and can store more charge. The grains in Figure 4.92 (c) are small but tightly packed, leading to improved inter-grain connectivity. Despite the dense packing, the smaller grains increase the surface area of the grain boundaries, leading to highest R_{gb} i.e 56.37 MΩ and higher C_{gb} i.e 26.20 MΩ . The grain boundaries likely dominate the electrical behaviour at higher frequencies due to their higher resistance.

4.5.2.6 Investigating the Relationship between EIS Data and Electric Parameters

Higher R_g corresponds to lower conductivity within the grains. In Co-Al-doped composites, this implies that electron hopping and charge carrier mobility within the grain interiors are hindered. R_g is low in WP1, it indicates that the grain interiors dominate the overall conduction, leading to better electrical conductivity, as seen in WP1, where R_g is significantly lower than in WP2 and WP3. This behaviour can be linked to efficient electron hopping between localized ions inside the grains. A high R_{gb} results in lower overall conductivity, where grain boundaries play a more prominent role. For instance, WP3 exhibits very high R_{gb}, indicating that grain boundaries dominate the overall impedance and conductivity of the material. This behaviour suggests that the Co-Al doping has altered the structure and behaviour of the grain boundaries, leading to increased impedance at these interfaces.

A high grain R_g and grain boundary resistance R_{gb} (as in WP2 and WP3) will reduce the real permittivity ε' because fewer charge carriers contribute to polarization, especially at high frequencies as shown in Figure 4.93(a). Highest C_g in WP1 increases ε' at low frequencies due to greater charge storage in grains as shown in Figure 4.93.

Higher R_g and R_{gb} shift the relaxation peaks in M' to higher frequencies as indicate in Cole Cole plot, indicating that the system takes longer to respond to the external field. In WP2 and WP3, the higher grain boundary resistance leads to a delayed response,

resulting in a shift of M′ peaks to higher frequencies. High grain and grain boundary resistances increase M″ at higher frequencies, indicating stronger relaxation effects. In WP2 and WP3, the higher R_{gb} results in larger M″ values at high frequencies. Higher C_g will reduce M″ at low frequencies, indicating better charge storage and lower losses within the grains. High C_{gb} increases M″ at high frequencies, reflecting higher energy dissipation at the grain boundaries.

Higher R_g and R_{gb} result in larger Z′ values, particularly at low frequencies where the grain effects are more significant. WP2 and WP3, with their higher grain boundary resistance, show elevated Z′, indicating reduced conductivity. Higher C_g reduces Z′ at low frequencies, improving conductivity within the grains. Higher C_{gb} increases Z′ at low frequencies, reflecting higher impedance due to grain boundary contributions. Higher C_{gb} increases Z″ at lower frequencies, indicating more significant energy dissipation due to grain boundaries.

4.5.3 Magnetic Analysis

The impact of Co^{2+} and Al^{3+} substitution in $BaCo_xAl_xFe_{12-2x}O_{19}$ / PANI Hexaferrite is significant in tuning the magnetic properties of the material due to differences in electronegativity, magnetic moments, and site preferences of the substituted ions. The replacement of Fe^{3+}ions (with higher magnetic moments) by Co^{2+} and Al^{3+} ions (with lower or non-magnetic moments) at specific crystallographic sites results in changes in saturation magnetization (M_s), coercivity (H_c), remanence magnetization (M_r), anisotropy field (H_a), and remanence ratio (M_r/M_s). Substituting Co^{2+} and Al^{3+} ions for Fe^{3+} significantly affects the overall magnetic characteristics of hexaferrite samples. The Al^{3+} ions, with a lower electronegativity (1.61) than Co2+ (1.88), prefer occupying tetrahedral sites, whereas Co^{2+} predominantly occupies octahedral sites. This selective site occupancy disrupts the Fe^{3+} superexchange interactions, impacting the magnetic properties as follows:

The saturation magnetization (M_s) shows a decreasing trend from WP1 to WP3:

WP1: M_s = 45.92 emu/g, **WP2**: M_s = 38.05 emu/g, **WP3**: M_s = 32.36 emu/g

The initial decrease in M_s is attributed to the replacement of Fe^{3+} (5 μB) ions by weaker magnetic Co^{2+} (3 μB) and non-magnetic Al^{3+} ions. This reduces the total magnetization as the number of Fe^{3+} ions at key magnetic sites is diminished. The reduction in M_s continues with increasing substitution, indicating that the addition of

Co^{2+} and Al^{3+} weakens the overall magnetic structure, likely due to a disruption in the superexchange interactions between Fe^{3+} ions.

Coercivity (H_c) values decrease with increasing substitution, indicating that less energy is required to reverse the magnetic domains in the material:

WP1: H_c = 5382.78 Oe, **WP2**: H_c = 3181.82 Oe, **WP3**: H_c = 2928.91 Oe

The reduction in H_c is linked to the decreasing anisotropy field (H_a) caused by the substitution of Fe^{3+} ions with Co^{2+} and Al^{3+}. At lower levels of substitution, the magnetic domains are harder to reverse due to stronger superexchange interactions. However, with further substitution, the disruption in the crystal structure leads to a softer magnetic behaviour, lowering the coercivity.

Remanent magnetization (M_r) represents the amount of magnetization retained by the material after the external magnetic field is removed. The values show a decreasing trend with increasing substitution:

WP1: M_r = 23.45 emu/g, **WP2**: M_r = 19.17 emu/g, **WP3**: M_r = 16.78 emu/g

The reduction in M_r is attributed to the weakening of magnetic interactions due to the substitution of Fe^{3+} with Co^{2+} and Al^{3+}. This substitution disrupts the alignment of magnetic moments in the material, resulting in lower remanent magnetization. The remanence ratio (M_r/M_s) is a critical factor in determining the magnetic behaviour of the material. A value of M_r/M_s<0.5 suggests a multi-domain nature, indicating that the material consists of multiple magnetic domains. In the case of the Co-Al doped samples, all M_r/M_s values are close to or below 0.5, which confirms the multi-domain behaviour:

WP1: M_r/M_s = 0.5107, **WP2**:M_r/M_s = 0.5038, **WP3**: M_r/M_s = 0.5187

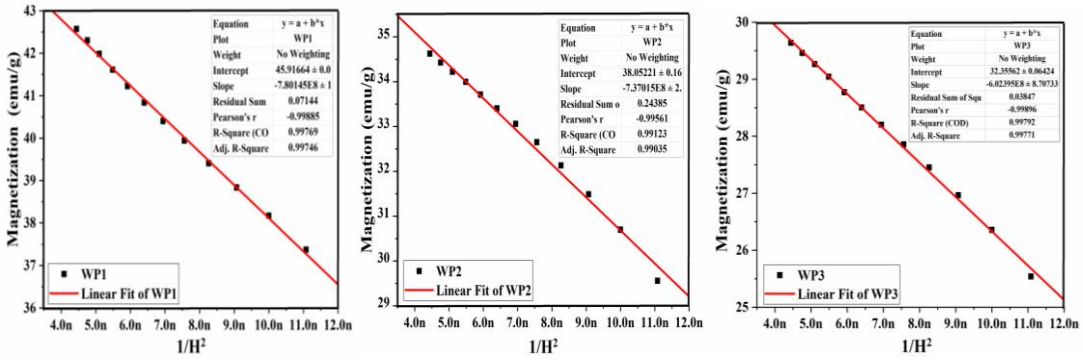

Figure 4.97 M_s versus 1/ H^2 plots for all hexaferrite samples.

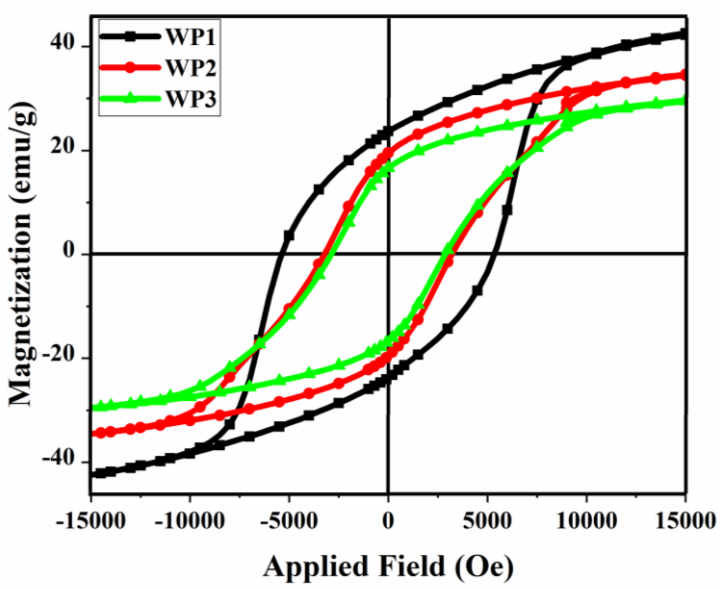

Figure 4.98 Hysteresis loops of WP1, WP2 and WP3 hexaferrite.

Table 4. 31 Magnetic parameters M_s, H_c, H_a, M_r and M_r/M_s value of all hexaferrite samples.

sample	M_s	H_c	H_a = sqrt(-15B)	H_a (kOe)	M_r	M_r/M_s
WP1	45.92	5382.78	15964.24	15.9642	23.45	0.511
WP2	38.05	3181.82	17044.88	17.0449	19.17	0.504
WP3	32.36	2928.91	16711.35	16.7113	16.78	0.518

4.5.4 Electromagnetic Characteristics

4.5.4.1 Complex permeability and complex permittivity

The Figure 4.99 displays plots of (ε'),(ε"), (μ'), and (μ") against frequency. The dielectric constant (ε') decreases with increasing frequency across all samples. WP1 consistently has the highest dielectric constant, followed by WP2 and WP3. The values of ε' at 12 GHz are 4.55, 4.0, and 3.15 for WP1, WP2, and WP3, respectively. The reduction in ε' with frequency is indicative of the limited ability of the material to store electrical energy at higher frequencies. The dielectric loss (ε"), which represents energy dissipation, WP1 shows the highest dielectric loss, with values peaking near 10 GHz. WP2 and WP3 have lower values, with WP3 exhibiting the lowest energy losses. These peaks suggest the presence of relaxation processes, which are related to charge hopping between Fe^{2+} and Fe^{3+} ions. The electron hopping within the Fe^{2+}/Fe^{3+} pairs and the grain boundary effects contribute to the observed loss behavior. The magnetic permeability (μ') increases with frequency for all samples, with WP3 showing the highest values. WP1 and WP2 have lower values, though WP2 exhibits a

significant fluctuation at lower frequencies. WP3's higher permeability suggests better magnetic alignment and fewer magnetic voids, while WP2's instability at lower frequencies. The magnetic loss (μ"), representing magnetic energy dissipation, peaks sharply around 9 GHz for WP2, with a lower peak observed for WP1. WP3 shows the lowest magnetic losses, reflecting its stable magnetic structure. The peaks in μ" can be attributed to ferromagnetic resonance and exchange coupling between Fe^{3+} and Fe^{2+} ions, processes influenced by the doping.

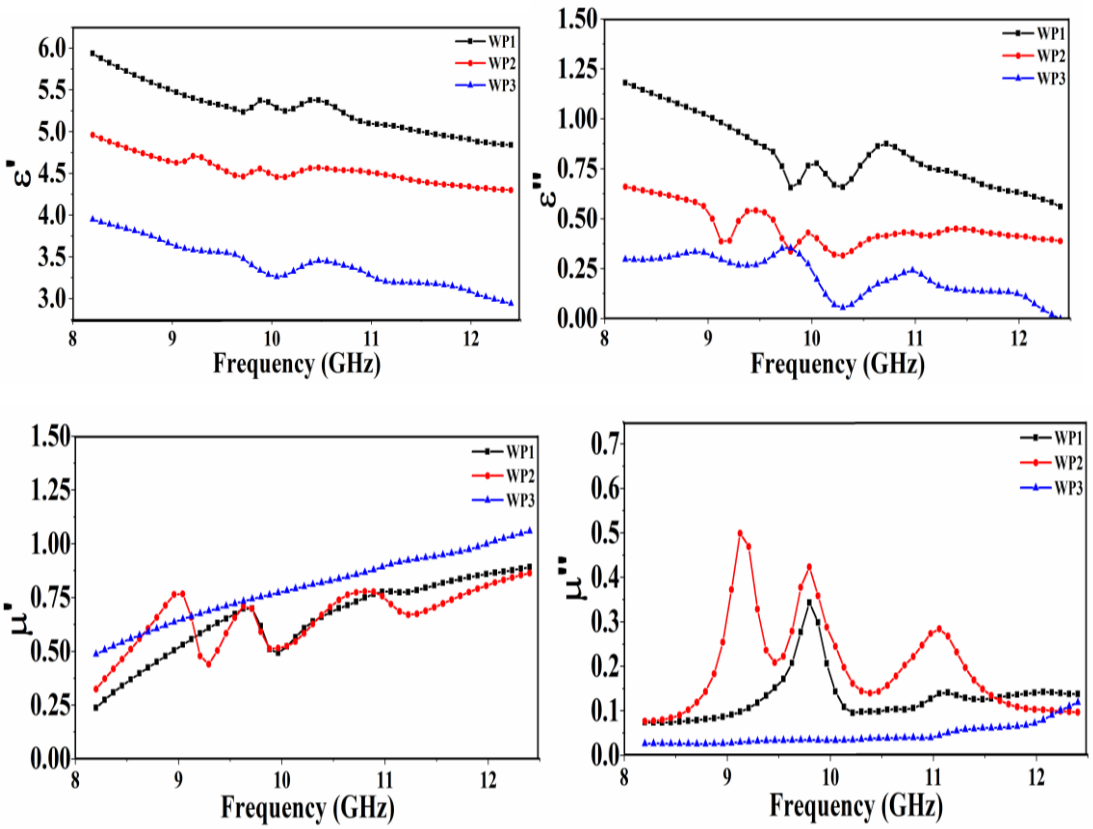

Figure 4.99 Complex permittivity and permeability versus frequency plots for $BaCo_xAl_xFe_{12-2x}O_{19}$ / PANI.

4.5.4.2 Microwave absorption in $BaCo_xAl_xFe_{12-2x}O_{19}$ / PANI

4.5.4.3 Quarter Wavelength Mechanism

We analyzed graphs that illustrate the reflection loss of various materials at different thicknesses and frequencies, showcasing the amount of microwave energy reflected by each material. These graphs provided crucial insights into the microwave absorption properties of the ferrites we synthesized. Figures 4.100 and subsequent figures present the detailed results for these ferrites. By carefully examining these graphs, we were able to quantify several key characteristics of the materials, such as

their reflection loss performance, frequency ranges, and thicknesses for optimal microwave absorption. A summary of these properties is provided in Table 4.32.

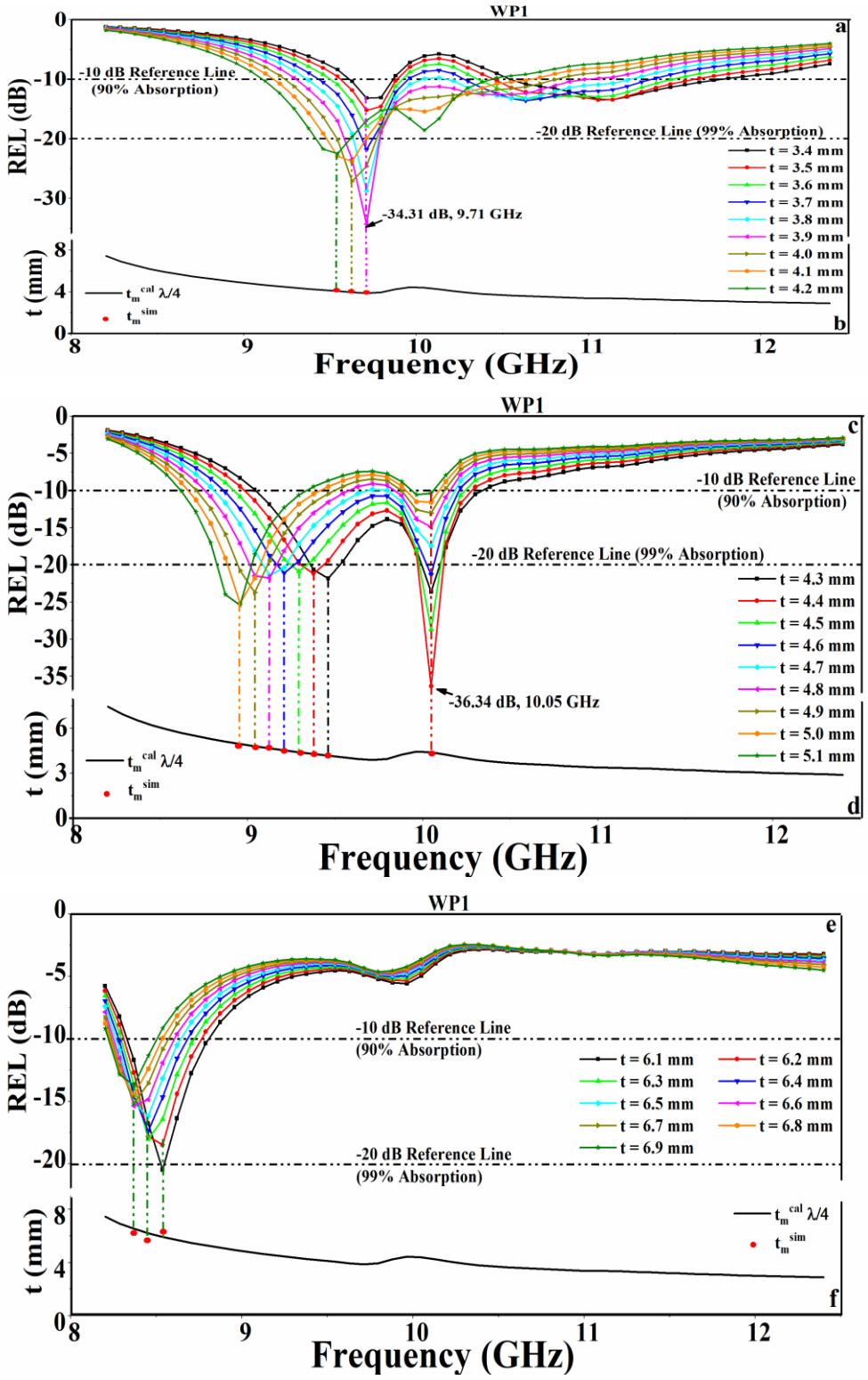

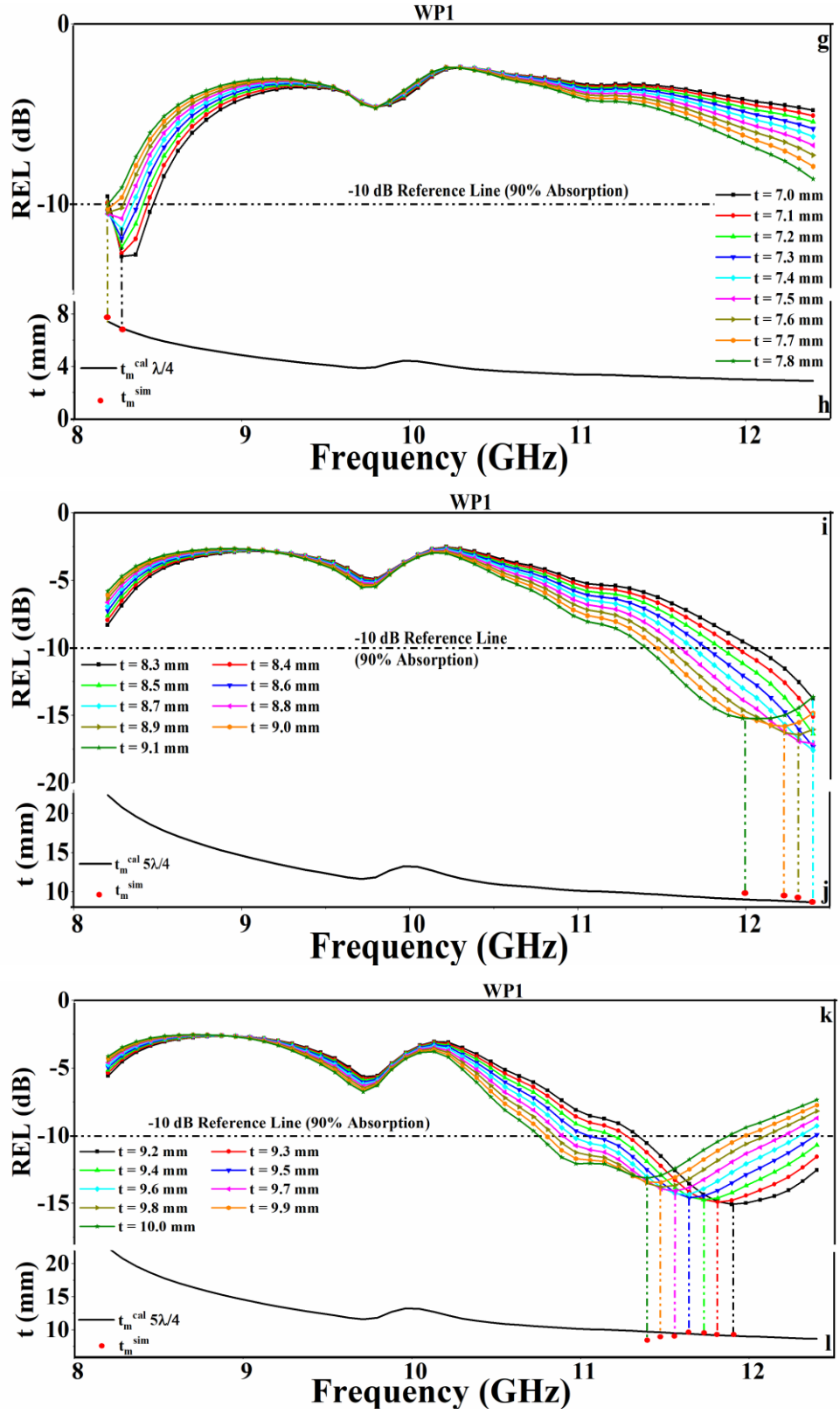

Figure 4.100 REL versus frequency for different thickness (WP1) and calculate thickness versus frequency for $BaCo_xAl_xFe_{12-2x}O_{19}$/PANI

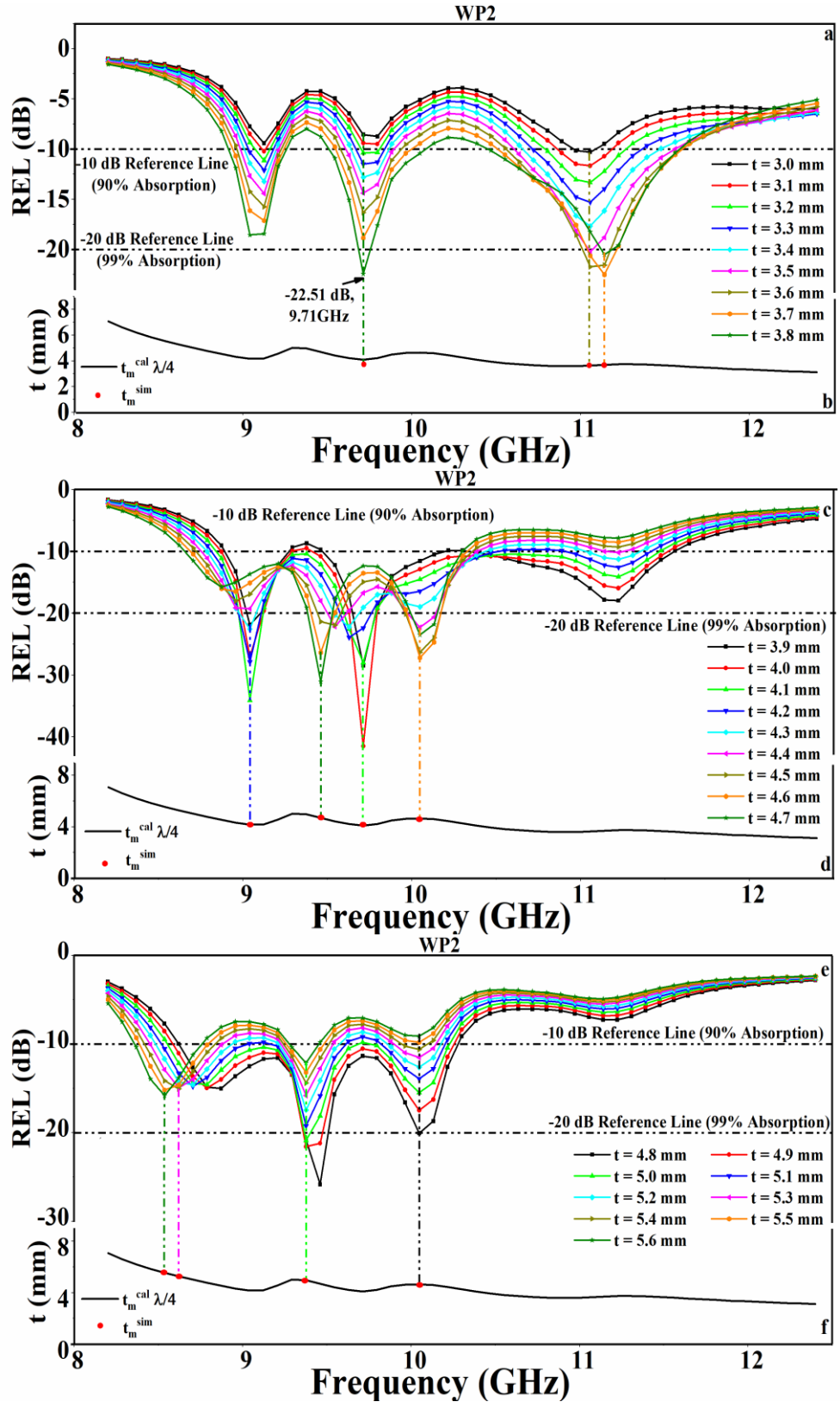
WP2
a
REL (dB)
-10 dB Reference Line
(90% Absorption)
-20 dB Reference Line
(99% Absorption)
-22.51 dB,
9.71GHz
t = 3.0 mm
t = 3.1 mm
t = 3.2 mm
t = 3.3 mm
t = 3.4 mm
t = 3.5 mm
t = 3.6 mm
t = 3.7 mm
t = 3.8 mm
t (mm)
t_m^{cal} λ/4
t_m^{sim}
b
Frequency (GHz)
WP2
c
-10 dB Reference Line (90% Absorption)
-20 dB Reference Line (99% Absorption)
t = 3.9 mm
t = 4.0 mm
t = 4.1 mm
t = 4.2 mm
t = 4.3 mm
t = 4.4 mm
t = 4.5 mm
t = 4.6 mm
t = 4.7 mm
d
WP2
e
-10 dB Reference Line (90% Absorption)
-20 dB Reference Line (99% Absorption)
t = 4.8 mm
t = 4.9 mm
t = 5.0 mm
t = 5.1 mm
t = 5.2 mm
t = 5.3 mm
t = 5.4 mm
t = 5.5 mm
t = 5.6 mm
f

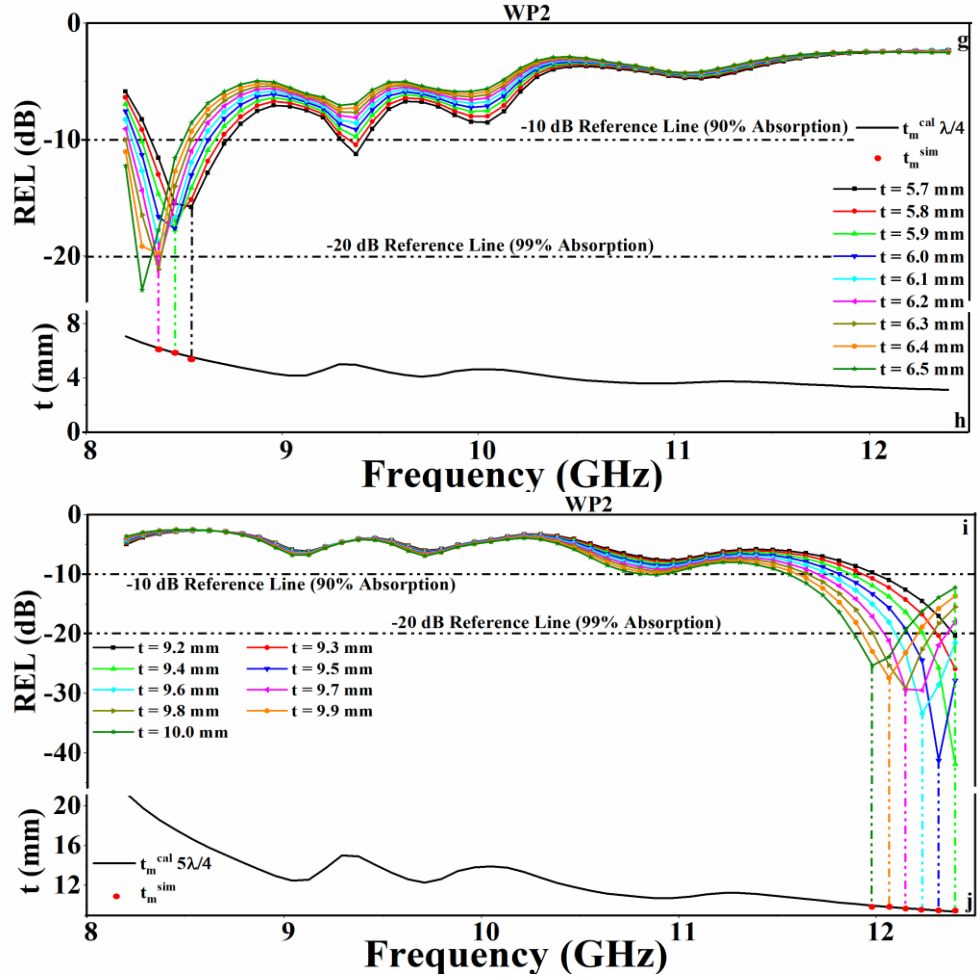

Figure 4.101 REL versus frequency for different thickness (WP2) and calculate thickness versus frequency for $BaCo_xAl_xFe_{12-2x}O_{19}$/PANI

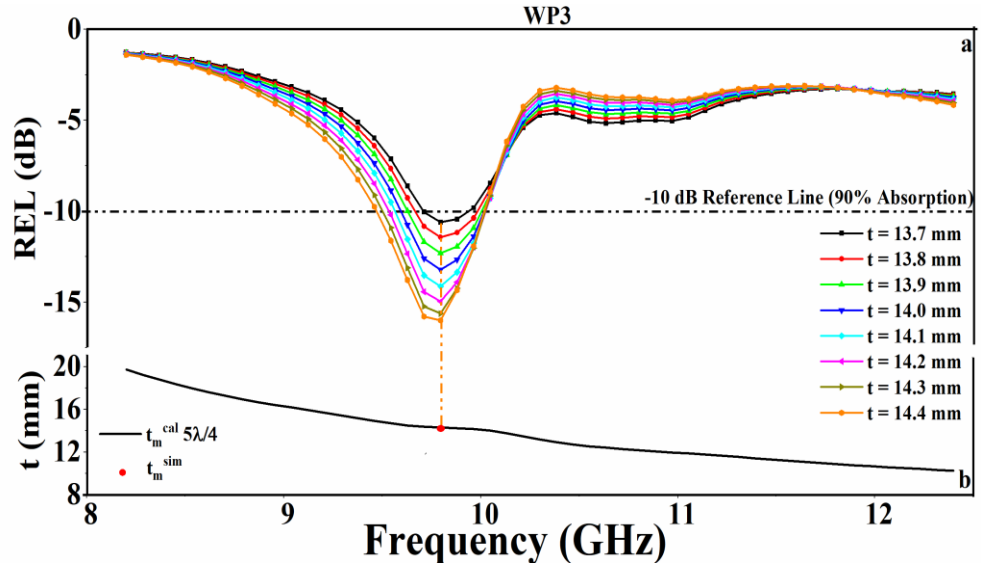

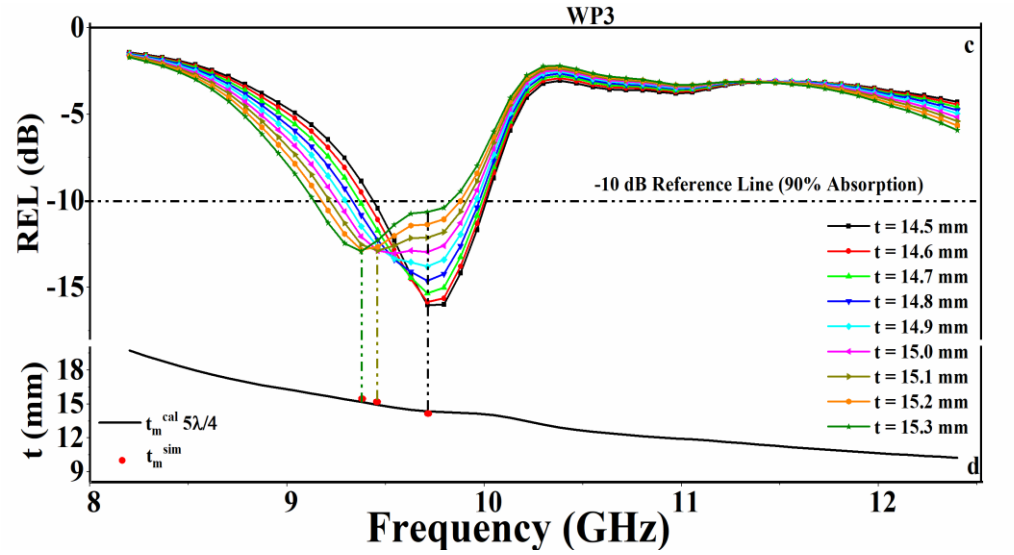

Figure 4.102 REL versus frequency for different thickness (WP3) and calculate thickness versus frequency for $BaCo_xAl_xFe_{12-2x}O_{19}$/PANI

Composition WP1 demonstrates a broad range of reflection loss (REL) values across various thicknesses. At a thickness of 3.5 mm, WP1 achieves a maximum REL of -15.15 dB at a frequency of 9.71 GHz, with a bandwidth of 0.32 GHz for REL > -10 dB. As the thickness increases to 3.9 mm, the REL significantly improves to -34.31 dB at the same frequency, with a broader bandwidth of 1.69 GHz for REL > -10 dB and 0.21 GHz for REL > -20 dB, indicating a marked improvement in absorption. Further increases in thickness continue to demonstrate high REL values. For instance, at 4.0 mm, WP1 shows an REL of -26.93 dB at 9.63 GHz with a bandwidth of 1.57 GHz for REL > -10 dB and 0.24 GHz for REL > -20 dB. At 4.4 mm, WP1 exhibits a very high REL of -36.34 dB at 10.05 GHz with a narrow bandwidth of 0.15 GHz for REL > -20 dB, indicating strong absorption at higher frequencies. At higher thicknesses, such as 5.1 mm and beyond, the REL decreases, with WP1 exhibiting an REL of -25.36 dB at 8.95 GHz and a bandwidth of 0.72 GHz for REL > -10 dB. The material shows effective microwave absorption even at higher thicknesses, confirming its suitability for a wide range of applications.

For composition WP2, the maximum REL performance is achieved at a thickness of 4.0 mm, where the REL reaches an impressive -41.38 dB at 9.71 GHz, with a bandwidth of 2.12 GHz for REL > -10 dB and 0.15 GHz for REL > -20 dB, demonstrating excellent broadband absorption. At lower thicknesses, such as 3.5 mm, WP2 shows an REL of -20.2 dB at 11.05 GHz with a bandwidth of 0.96 GHz for REL > -10 dB. As the

thickness increases, WP2 continues to show high absorption, with an REL of -30.9 dB at 9.46 GHz at 4.7 mm, along with a bandwidth of 1.64 GHz for REL > -10 dB and 0.15 GHz for REL > -20 dB, indicating strong performance across a range of frequencies. At thicker samples, WP2 remains effective. For instance, at 5.9 mm, WP2 exhibits an REL of -17.55 dB at 8.45 GHz with a bandwidth of 0.37 GHz for REL > -10 dB, confirming its ability to provide moderate broadband absorption even at higher thicknesses.

Composition WP3 displays strong absorption characteristics across a range of thicknesses, with the best REL occurring at 14.5 mm, where it reaches -16.01 dB at 9.71 GHz with a bandwidth of 0.56 GHz for REL > -10 dB. At a slightly thinner thickness of 14.4 mm, WP3 shows a similar REL of -16.0 dB at 9.79 GHz, confirming the stability of its performance. At 15.1 mm, WP3 exhibits an REL of -12.85 dB at 9.46 GHz with a wider bandwidth of 0.7 GHz for REL > -10 dB, indicating good broadband absorption capabilities. The material continues to show effective microwave absorption as thickness increases, with an REL of -12.89 dB at 15.3 mm and a bandwidth of 0.69 GHz for REL > -10 dB.

Table 4.32 REL with matching thickness/frequency, BW, and PBW for $BaCo_xAl_xFe_{12-2x}O_{19}$ (WP1 to WP3).

Sample Name	Matching Thickness (mm)	Maximum REL (dB)	Matching frequency (GHz)	Frequency Band for REL > -10 dB (GHz)	Bandwidth for RL > -10 dB (GHz)	Frequency Band REL > -20 dB (GHz)	Bandwidth for REL > -20 dB (GHz)	BTR	PBW (%)
WP1	3.5	-15.15	9.71	9.56-9.88	0.32	---	-	2.90E-04	3.30
	3.9	-34.31	9.71	9.3-10.99	1.69	9.58-9.79	0.21	1.27E-03	17.40
	4	-26.93	9.63	9.24-10.81	1.57	9.53-9.77	0.24	1.18E-03	16.30
	4.2	-22.52	9.54	9.108-10.45	1.34	9.41-9.62	0.21	1.01E-03	14.07
	4.3	-21.87	9.46	9.05-10.35	1.3	9.35-9.52	0.17	9.68E-04	13.74
	4.4	-21.21	9.38	8.98-10.28	1.3	9.3-9.43	0.13	9.60E-04	13.86
	4.4	-36.34	10.05	---	-	9.97-10.12	0.15	1.01E-04	1.49
	4.5	-20.82	9.29	8.92-10.24	1.32	9.24-9.34	0.1	9.63E-04	14.21
	4.6	-21.14	9.21	8.86-10.21	1.35	9.17-9.27	0.1	9.73E-04	14.66
	4.7	-21.43	9.12	8.81-9.67	0.86	9.08-9.22	0.14	6.44E-04	9.43

	4.9	-23.71	9.04	8.71-9.49	0.78	8.94-9.12	0.18	5.78E-04	8.63
	5.1	-25.36	8.95	8.62-9.34	0.72	8.82-9.02	0.2	5.26E-04	8.04
	6.1	-20.54	8.54	8.33-8.81	0.48	8.52-8.55	0.03	3.22E-04	5.62
	6.3	-18.04	8.45	8.29-8.72	0.43	---	-	2.83E-04	5.09
	6.6	-15.29	8.37	8.24-8.61	0.37	---	-	2.37E-04	4.42
	7	-12.89	8.28	8.21-8.47	0.26	---	-	1.60E-04	3.14
	8.7	-17.56	12.4	---	-	---	-	-	-
	9.2	-15.12	11.9	---	-	---	-	-	-
	9.6	-14.58	11.64	11.05-12.39	1.34	---	-	3.06E-04	11.51
	9.8	-13.79	11.47	10.84-12.19	1.35	---	-	3.13E-04	11.77
	10	-13.15	11.39	10.75-11.87	1.12	---	-	2.63E-04	9.83
WP2	3.5	-20.2	11.05	10.6-11.56	0.96	---	-	6.72E-04	8.69
	3.6	-21.69	11.05	10.56-11.59	1.03	11-11.17	0.17	7.01E-04	9.32
	3.7	-22.56	11.14	10.51-11.59	1.08	11.04-11.21	0.17	7.19E-04	9.69
	3.8	-22.51	9.71	9.51-10.09	0.58	9.68-9.76	0.08	4.77E-04	5.97
	4	-41.38	9.71	9.39-11.51	2.12	9.64-9.79	0.15	1.47E-03	21.83
	4.1	-33.99	9.03	8.84-11.47	2.63	8.97-9.12	0.15	1.90E-03	29.13
	4.6	-27.31	10.05	8.69-10.34	1.65	9.97-10.17	0.2	1.20E-03	16.42
	4.7	-30.9	9.46	8.66-10.3	1.64	9.38-9.53	0.15	1.17E-03	17.34
	4.8	-25.92	9.46	8.63-10.28	1.65	9.36-9.51	0.15	1.16E-03	17.44
	4.9	-21.54	9.38	8.58-10.25	1.67	9.36-9.47	0.11	1.16E-03	17.80
	5.3	-14.86	8.62	8.45-8.87	0.42	---	-	3.17E-04	4.87
	5.6	-15.89	8.53	8.36-8.75	0.39	---	-	2.86E-04	4.57
	5.7	-15.8	8.54	8.33-8.72	0.39	---	-	2.83E-04	4.57
	5.9	-17.55	8.45	8.28-8.65	0.37	---	-	2.63E-04	4.38
	6.3	-21.13	8.36	8.2-8.56	0.36	8.35-8.38	0.03	2.44E-04	4.31
	9.5	-41.53	12.31	---	-	---	-	-	-
	9.7	-29.26	12.14	---	-	12.04-12.36	0.32	6.65E-05	2.64
	9.9	-27.46	12.06	---	-	11.92-12.23	0.31	6.44E-05	2.57
	10	-25.46	11.98	---	-	11.88-12.13	0.25	5.20E-05	2.09
WP3	14.4	-16	9.79	9.46-10.02	0.56	---	-	1.23E-04	5.72
	14.5	-16.01	9.71	9.44-10	0.56	---	-	1.23E-04	5.77
	15.1	-12.85	9.46	9.21-9.91	0.7	---	-	1.52E-04	7.40
	15.3	-12.89	9.37	9.13-9.82	0.69	---	-	1.51E-04	7.36

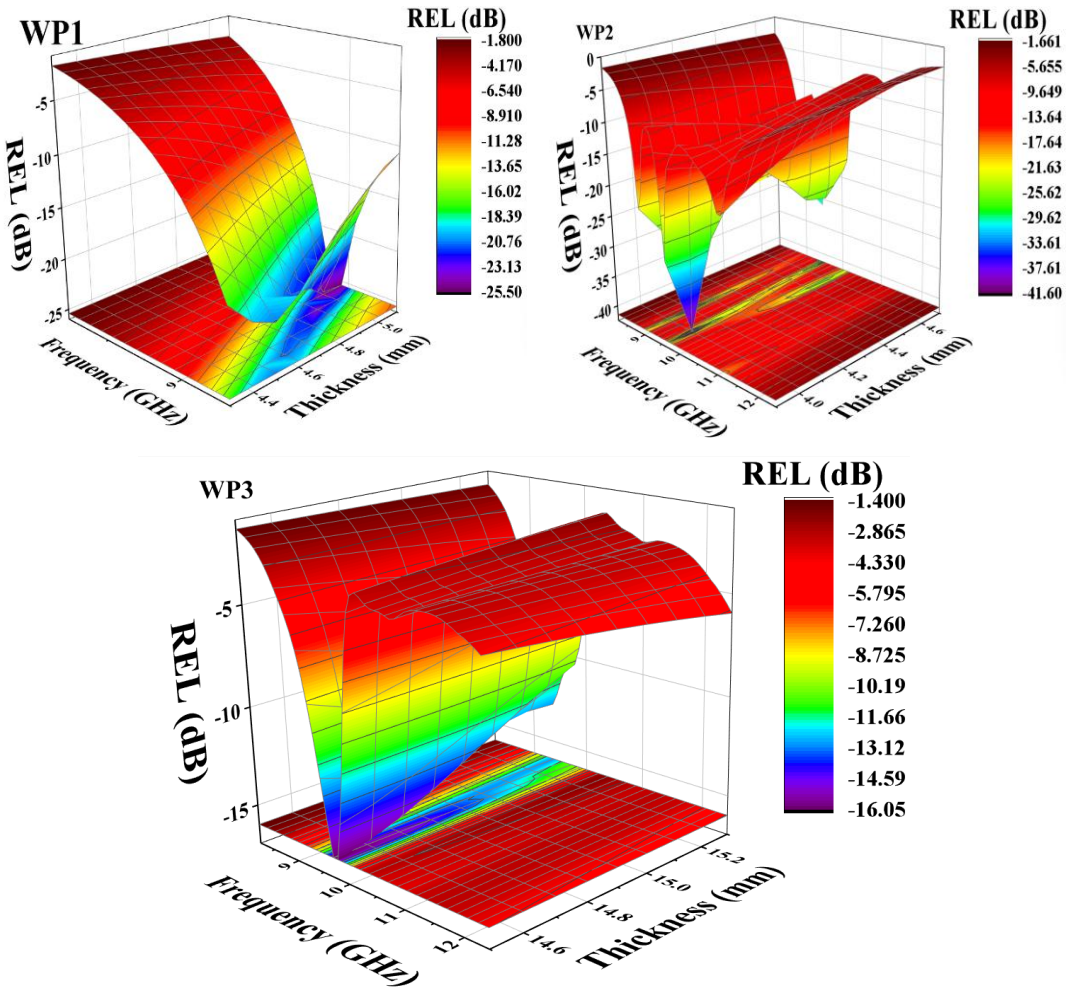

Figure 4.103 Three-dimensional (3D) plots of reflection loss at various frequencies and thicknesses for all samples of BaCoAl / PANI-series.

According to the Table 4.32, the quarter-wavelength criterion for composition WP1 is observed at thicknesses ranging from 3.5 mm to 10.0 mm, with a -10 dB bandwidth varying from 0.26 GHz to 1.69 GHz. Maximum REL values between -12.89 dB and -36.34 dB are recorded, with the -20 dB bandwidth ranging from 0.03 GHz to 0.24 GHz. As illustrated in Figure 4.100 WP1(a), the reflection loss peaks for WP1 occur at 9.71 GHz for thicknesses of 3.5 mm, 3.9 mm, and 4.0 mm. Similar peaks are observed at higher frequencies, such as 10.05 GHz at 4.4 mm, with a notable decrease in peak height as thickness increases, as shown in Figure 4.100 WP1(c). As shown in Figures 4.100 WP1(a), WP1(e), WP1(g), WP1(i) and WP(k) in the higher thickness range (3.9 mm to 4.2 mm, 6.1 mm to 6.9 mm, 7.0 mm to 7.8 mm, 8.3 mm to 9.1 mm and 9.2mm to 10.00 mm respectively), the REL peaks shift toward lower frequencies, with peak heights gradually decreasing. This behaviour is consistent with the quarter-

wavelength mechanism, where increasing thickness results in a corresponding shift in peak absorption to lower frequencies. The relationship between the quarter-wavelength mechanism and REL is confirmed by comparing the calculated thickness (tcal) and simulated thickness (tsim) using equations 1.7, with strong agreement between both values.

For WP2, the -10 dB bandwidth ranges from 0.36 GHz to 2.63 GHz across thicknesses from 3.5 mm to 10.0 mm. Maximum REL values between -14.86 dB and -41.53 dB are recorded, with -20 dB bandwidths varying between 0.03 GHz and 0.32 GHz. As illustrated in Figure 4.101 WP2 (a), the reflection loss peaks for WP2 occur at 9.71 GHz for thicknesses of 3.8 mm to 3.0 mm. Similar peaks are observed at higher frequencies, such as 9.71 GHz at 4.0 mm, 9.46 GHz at 4.8 mm, 8.62 GHz at 5.0 mm with a notable decrease in peak height as thickness increases, as shown in Figure 4.101 WP2(c), WP2 (e) and WP2 (e) respectively. As shown in Figure 4.101 WP2 (c), WP2 (e) and WP2 (i) the reflection loss peaks shift to lower frequencies as the thickness increases, particularly in the 9.05 GHz range for thicknesses between 4.1 mm and 4.7 mm, 9.71 GHz range for thicknesses between 3.8 mm and 4.1 mm., 10.05 GHz range for thicknesses between 4.8 mm and 5.6 mm and 12.00 GHz range for thicknesses between 9.5 mm and 10.0 mm respectively. A W-shaped curve is also evident in the range of 9.00 GHz to 10 GHz for thickness range from 3.9 mm to 4.7 mm and 4.8mm to 5.6 mm as shown in Figure 4.101 WP2 (c) and WP2 (e) respectively, indicating broad absorption that is beneficial for electromagnetic interference (EMI) shielding applications.

In the case of WP3, the REL values range between -12.85 dB and -16.01 dB for thicknesses between 14.4 mm and 15.3 mm. The bandwidth for REL > -10 dB varies between 0.56 GHz and 0.7 GHz. Figures 4.102 WP3(a) and WP3(c) show that as the thickness increases from 14.4 mm to 15.3 mm, the peak height at 9.46 GHz decreases, confirming that higher thicknesses result in lower reflection loss peaks.

The results for all compositions indicate that both -10 dB and -20 dB REL bands are influenced by the quarter-wavelength mechanism, with calculated and simulated thicknesses demonstrating good agreement with reflection loss peaks.

4.5.4.4 Impedance matching mechanism

The impedance of a material varies due to differences in its permittivity and permeability compared to free space. This variation affects the material's absorption properties. When these properties are mismatched, most of the incident signal is reflected, while only a small portion penetrates the material. However, if the permittivity and permeability are closely matched, more of the signal enters the material and is absorbed. Therefore, impedance matching is crucial for designing an efficient absorber. Figures 4.104 show the reflection loss (REL) and $|Z_{in}|$ versus frequency for the prepared samples, while Table 4.33 lists the corresponding Z_{in} values at the maximum REL for each composition. Across all compositions (WP1 to WP3), the highest REL peaks align with the impedance matching principle.

For composition WP1, with a thickness of 4.4 mm, the peak REL of -36.34 dB occurs at 10.05 GHz, where the input impedance $|Z_{in}|$ is 382.30 Ω. This value is very close to the characteristic impedance of free space (Z_0 = 377 Ω), which explains the strong absorption observed at this frequency. The real part of the impedance (Z_{real} = 382.16 Ω) is near the ideal value of 377 Ω, while the imaginary part (Z_{img} = 10.36 Ω) is relatively small, further indicating effective impedance matching. The proximity of Z_{in} to the free-space impedance supports the efficient microwave absorption in WP1 at this thickness and frequency.

In the case of WP2, at a thickness of 4.0 mm, the maximum REL reaches -41.38 dB at 9.71 GHz. The corresponding $|Z_{in}|$ is 370.80 Ω, which is slightly below the free-space impedance. The real part (Z_{real} = 370.80 Ω) is quite close to 377 Ω, while the imaginary part (Z_{img} = -1.04 Ω) is very small, almost zero. This near-zero imaginary component reflects near-perfect impedance matching, which is consistent with the strong microwave absorption observed. The slight deviation of the real component from 377 Ω is likely responsible for the minimal reflection observed, but the impedance matching is still effective enough to result in significant absorption at this frequency. However, in WP2, no REL peaks are observed at 11.14 GHz because Z_{real} = 379.16 Ω and Z_{img} = -127.96 Ω deviate significantly from the target values of 377 Ω and zero. This indicates that the differences in absorption properties are caused by the mismatch between Z_{real}, Z_{img}, and the ideal values.

The reflection loss behaviour of WP1, WP2, and WP3 demonstrates that impedance matching plays a critical role in determining the absorption efficiency of each composition. For WP1 and WP2, the close proximity of $|Z_{in}|$ to the characteristic impedance of free space, with minimal imaginary components, results in strong absorption peaks at their respective frequencies. In contrast, WP3 exhibits higher real and imaginary impedance values, leading to lower absorption efficiency. These findings confirm that optimizing the real and imaginary components of impedance is essential for improving the microwave absorption properties of materials, particularly in the case of compositions doped with Co-Al, which show non-monotonic impedance behaviour. The results highlight the importance of achieving the right balance between permittivity and permeability to enhance impedance matching and maximize absorption efficiency.

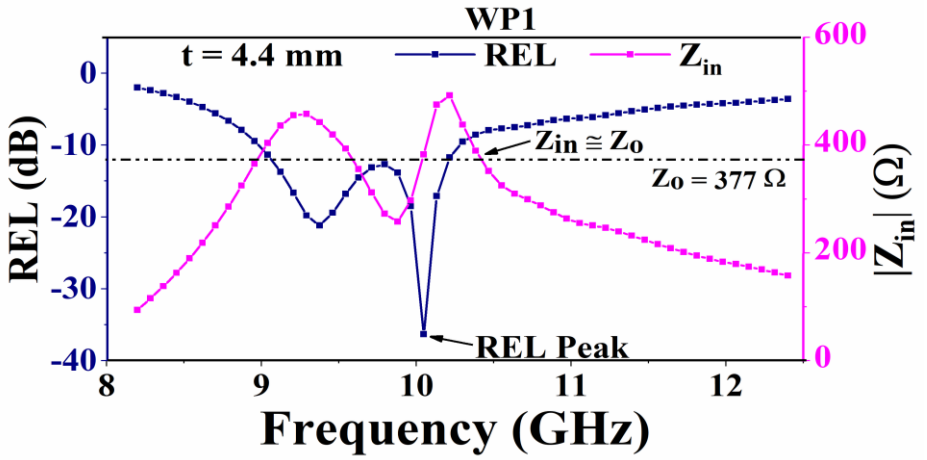

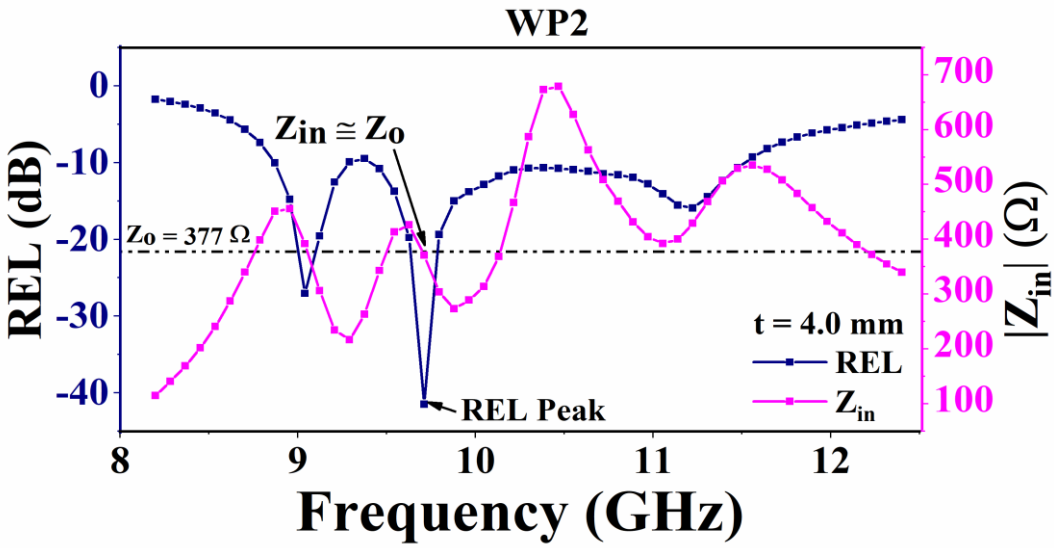

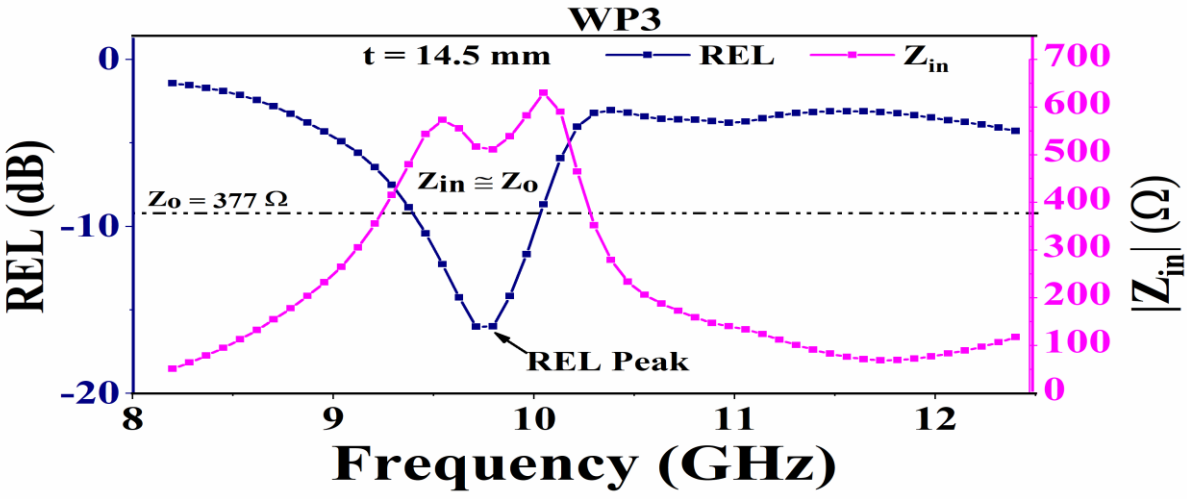

Figure 4.104 Zin and REL curve against frequency for $BaCo_xAl_xFe_{12-2x}O_{19}$ /PANI.

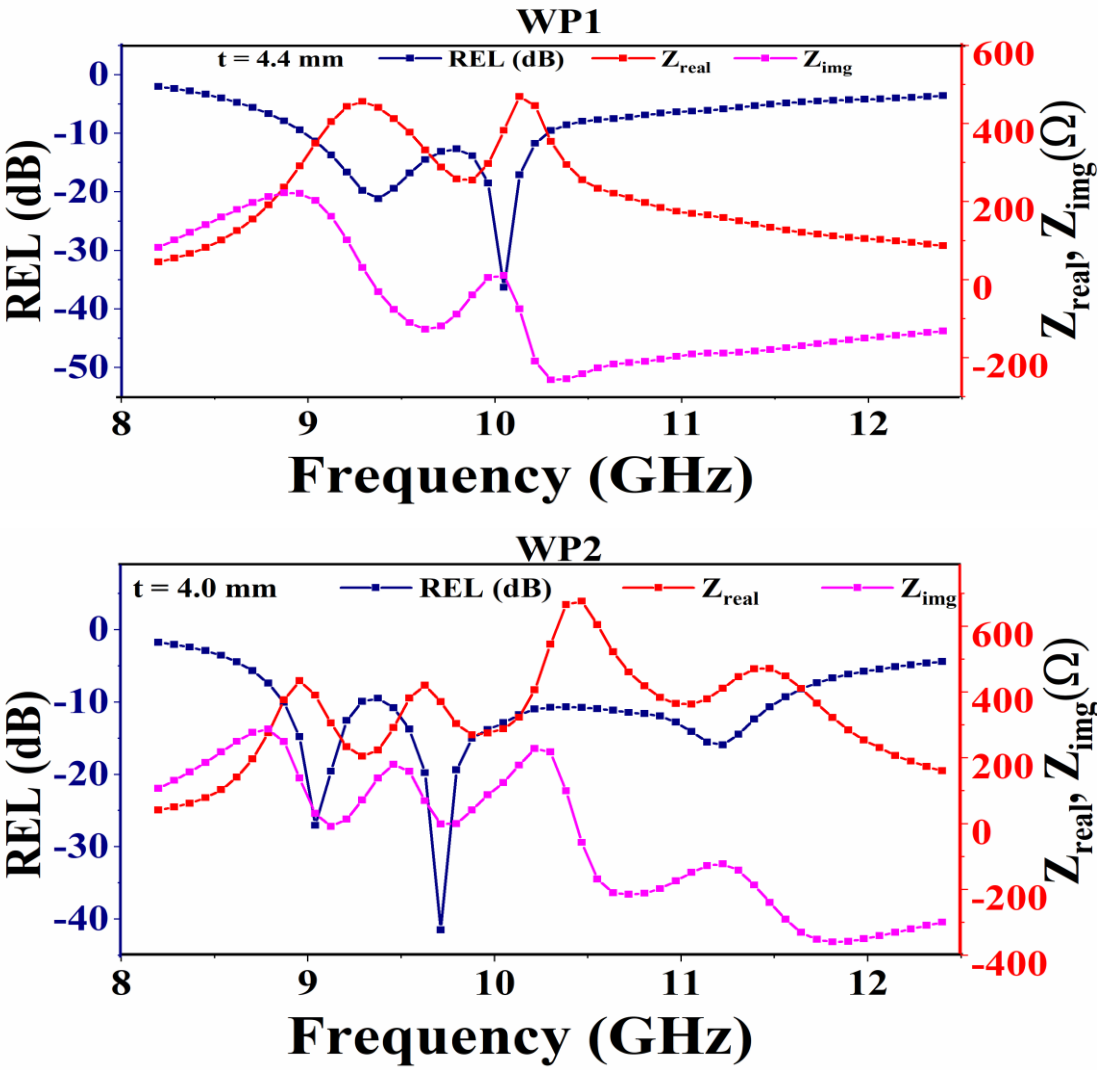

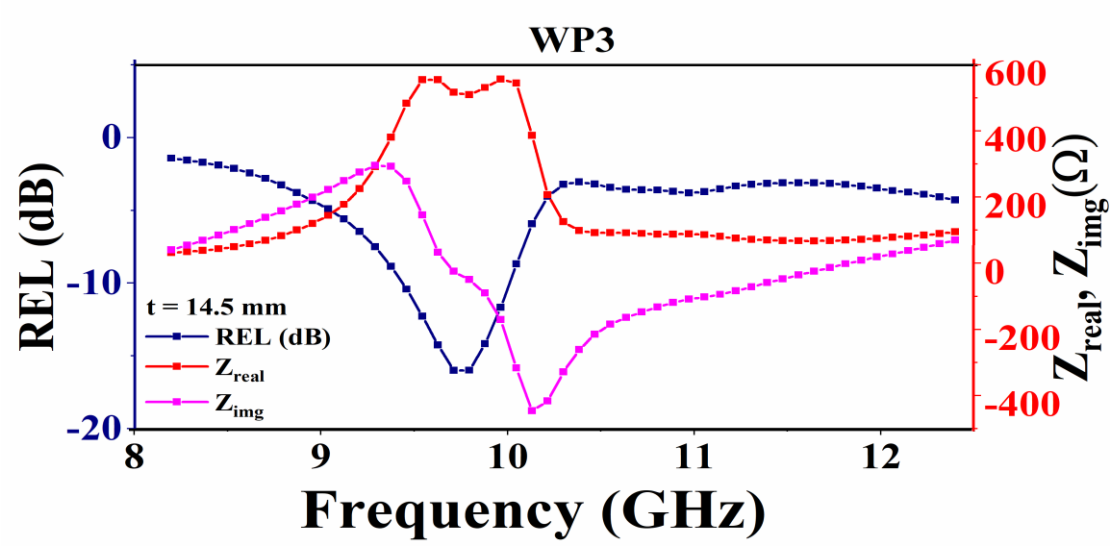

Figure 4.105 Z_{real}, Z_{imag}, and REL v/s frequency for $BaCo_xAl_xFe_{12-2x}O_{19}$ /PANI.

Table 4.33 Z_{in}, Z_{real}, and Z_{imag} values corresponding to REL_{max} for $BaCo_xAl_xFe_{12-2x}O_{19}$/PANI.

Sample Name	Matching Thickness (mm)	Maximum REL (dB)	Matching frequency (GHz)	Z_{real} (Ω)	Z_{img} (Ω)	$\|Z_{in}\|$ (Ω)
WP1	4.4	-36.34	10.05	382.16	10.36	382.30
WP2	4	-41.38	9.71	370.80	-1.04	370.80
WP3	14.5	-16.01	9.71	516.22	-25.03	516.83

4.5.4.5 Eddy Current Loss

For WP1, the values show a stable trend across the frequency range, with two notable peaks. The first peaks occur around 11.1 GHz, while the second, slightly larger peak, appears near 9.71 GHz, where C0 reaches approximately 1.6 ns. This indicates moderate energy interaction at these frequencies, with WP1 maintaining relatively stable C0 values across the higher frequency range.

WP2 exhibits a more dramatic response at lower frequencies, with a prominent peak at around 9.54 GHz, where C0 reaches its maximum value of approximately 2.22 ns. Following this peak, the values drop off sharply. WP2 shows strong energy interaction at lower frequencies, which could contribute to eddy current losses. After this peak, C0 stabilizes at higher frequencies, but still presents another peaks near 10 GHz and 11.1 GHz.

For WP3, the C0 values remain consistently low and stable throughout the frequency range, with a very small peak at approximately 9.46 GHz, where C0 reaches around

0.13 ns. WP3's stable behaviour across the frequency spectrum suggests minimal energy dissipation and makes it suitable for applications requiring low losses.

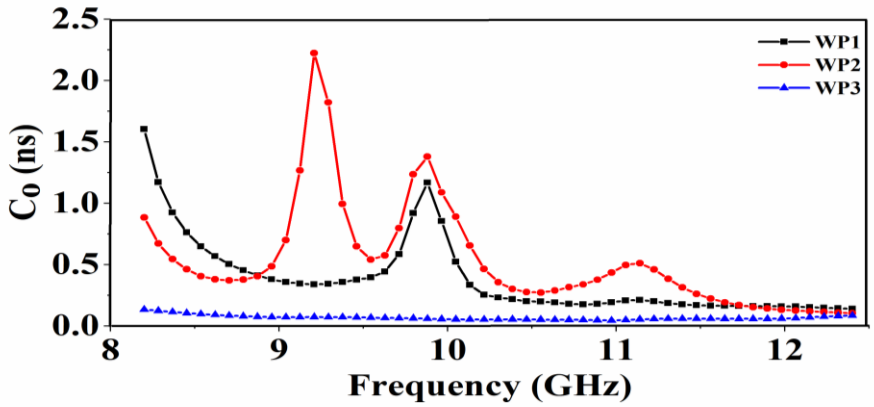

Figure 4.106 C_0 versus frequency curve for $BaCo_xAl_xFe_{12-2x}O_{19}$ / PANI.

4.5.4.6 Bandwidth to Thickness Ratio

The BTR (Bandwidth to Thickness Ratio) and PBW (Percentage Bandwidth) values for the prepared compositions are summarized in the table. For composition WP1, the BTR ranges from 1.01E-04 to 1.27E-03, with a PBW spanning between 1.49% and 17.40%. WP1 demonstrates its strongest performance at a thickness of 3.9 mm, with a reflection loss (REL) of -34.31 dB at 9.71 GHz, achieving a BTR of 1.27E-03 and PBW of 17.40%. The bandwidth for REL > -20 dB is 0.21 GHz at this thickness. WP1 shows relatively good absorption performance over a range of thicknesses between 3.5 mm and 10 mm, with stable reflection loss values across the frequency range from 8.28 GHz to 12.4 GHz.

WP2 exhibits a BTR range between 5.20E-05 and 1.90E-03, with a PBW spanning from 2.09% to 29.13%. WP2 shows its highest absorption performance at 4.0 mm thickness, achieving a maximum REL of -41.38 dB at 9.71 GHz. At this point, it demonstrates a BTR of 1.47E-03 and PBW of 21.83%, with a bandwidth of 0.15 GHz for REL > -20 dB. WP2 covers a frequency range between 8.36 GHz and 12.31 GHz, making it highly effective for broader microwave absorption applications.

For WP3, the BTR ranges from 1.23E-04 to 1.52E-04, with a PBW between 5.72% and 7.40%. WP3 shows its peak performance at 14.5 mm thickness, where it reaches a maximum REL of -16.01 dB at 9.71 GHz, with a BTR of 1.23E-04 and PBW of 5.77%. WP3's absorption capabilities are more limited in terms of frequency range,

focusing primarily on frequencies around 9.37 GHz to 9.79 GHz, but it maintains stable performance over thicker sample sizes.

In conclusion, WP2 demonstrates the highest BTR and PBW values, indicating broader and more efficient microwave absorption, especially at lower thicknesses. WP1 also shows effective absorption characteristics over a wider range of frequencies, while WP3 remains stable but performs best with thicker samples.

4.5.4.6 S – Parameter

When the input signal is applied at input port 1 of the test waveguide from VNA, the two-port S_{11} parameter accounts for the reflected signal from the same input port 1 from the sample fitted in the test waveguide of the VNA. S_{21} accompanies the attenuation in the signal traveling from input port 1 to output port 2.

The S_{11} values for WP1 start at around -2 dB at 8 GHz and gradually decrease as frequency increases, reaching about -3 dB at 12 GHz. The Figure 4.107 shows consistent behaviour across the frequency range, with minimal dips, suggesting WP1 has moderate reflection loss. WP2 shows more significant reflection loss as frequency increases. Starting at -2 dB, the values dip to approximately -7.0 dB around 12 GHz. The curve has a steady downward slope, indicating WP2 has much better absorption properties than WP1, especially in the higher frequency range (10-12 GHz). WP3 starts at -2 dB at 8 GHz and steadily decreases, reaching -8 dB near 12 GHz. The S_{21} values for WP1 range between -2 dB to -4 dB across the frequency range. WP2 shows relatively stable S_{21} values starting around -2.5 dB at 8 GHz, improving to -1.5 dB near 12 GHz. WP3, S_{21} values starting at -2 dB at 8 GHz and steadily improving to -0.5 dB near 12 GHz. This shows that WP3 has the least signal attenuation and the least energy loss over the frequency range.

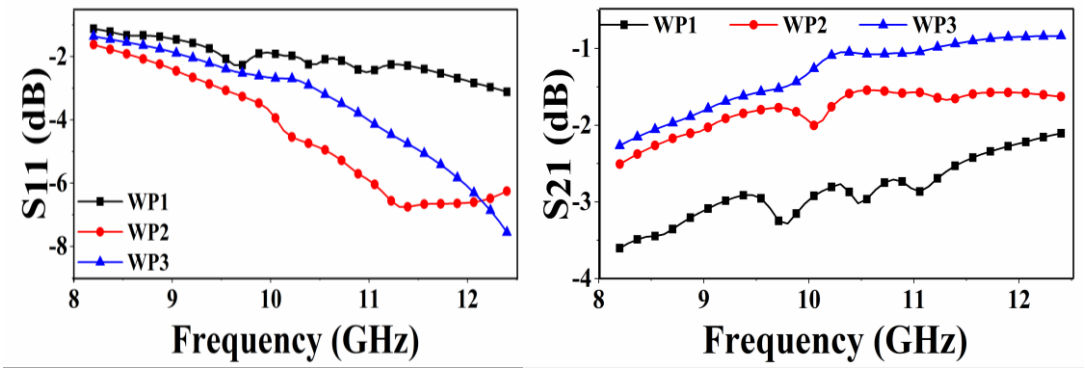

Figure 4.107 S_{11} and S_{21} versus frequency curve for $BaCo_xAl_xFe_{12-2x}O_{19}$ / PANI.

4.6 Co^{2+}- Ce^{3+} substituted $BaCo_xCe_xFe_{12-2x}O_{19}$ / PANI Composite.

In this section, we will be utilizing the sol-gel combustion method to synthesize a hexaferrite with Co and Ce substitutions. The composition of this hexaferrite will be $BaCo_xCe_xFe_{12-2x}O_{19}$. Displayed in Table 4.1 are the sample names/codes for various levels of substitution in $BaCo_xCe_xFe_{12-2x}O_{19}$.

Table 4.34. Presents the assignment of sample names corresponding to various substitution levels in $BaCo_xCe_xFe_{12-2x}O_{19}$ hexaferrite.

Sample Composition **$BaCo_xCe_xFe_{12-2x}O_{19}$**	Sample Code Name	Sample Code (X-series)
x= 0.0	**$BaFe_{12}O_{19}$**	XP1
x = 0.6	**$BaCo_{0.6}Ce_{0.6}Fe_{10.8}O_{19}$**	XP2
x = 1.0	**$BaCoCeFe_{10}O_{19}$**	XP3

4.6.1 Field Emission Scanning Electron Microscopy

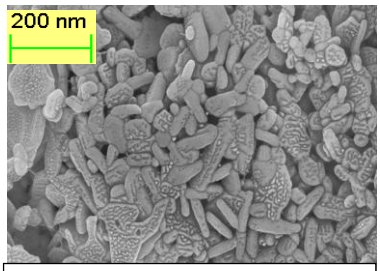

Figure 4.108(a) SEM for XP1

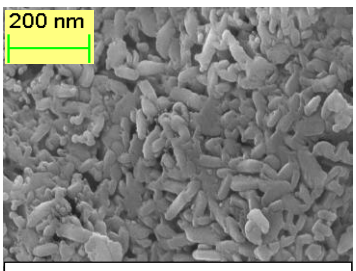

Figure 4.108(b) SEM for XP2

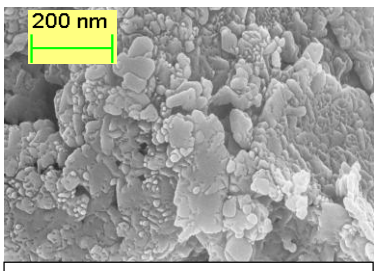

Figure 4.108(c) SEM for XP3

Figure 4.108 SEM Micrographs of $BaCo_xCe_xFe_{12-2x}O_{19}$ Ferrites.

This SEM has shown in Figure 4.108(a) reveals an aggregation of grains with distinct polygonal and elongated shapes. The grains appear well-defined, with clear boundaries between them. The presence of sharp-edged particles suggests that the material has been processed with minimal sintering or has a relatively low level of grain boundary fusion. The distribution of grains seems relatively homogeneous, which could contribute to consistent electrical properties across the sample. The SEM Figure 4.108(b) shows a similar grain structure to the first, but with a denser packing of the grains. The particles are more irregular in shape, and there is evidence of increased grain boundary contact. This suggests that the material may have undergone some level of sintering, leading to stronger grain interactions. In Figure 4.108(c) reveals a significant increase in grain fusion and coalescence compared to the XP1 and XP2. The grains have formed larger, more continuous structures, which suggest that the material has undergone higher levels of sintering or consolidation.

4.6.2 Electrical Characterization

4.6.2.1 Dielectric constant

Figure 109(a) illustrates the variation of the real part of the dielectric constant (ε') as a function of frequency and sample composition over the frequency range from 20 Hz to 2 MHz for the Co^{2+} and Ce^{3+} doped hexaferrites. From the figure 4.109, it is evident

that the dielectric constant (ε') shows significant variation across the frequency range for all samples (XP1, XP2, and XP3). XP1 exhibits the highest dielectric constant values, peaking at approximately 12,791.13 at lower frequencies. In contrast, XP2 and XP3 display much lower dielectric constant values, with XP2 at around 7295.51 and XP3 at approximately 4700.94 at the lowest frequency.

Figure 4.109(b) illustrates XP1 again demonstrates the highest dielectric loss values, reaching up to 172173.3 at the lowest frequencies. XP2 and XP3, however, show significantly lower dielectric losses, with XP2 at approximately 30054.24 and XP3 at around 18148.79. As frequency increases, ε" decreases and levels off, especially for XP2 and XP3, indicating a stabilization of the dielectric loss at higher frequencies.

Figure 4.109(c) presents the variation of the loss tangent (tan δ) with frequency for the Co^{2+} and Ce^{3+} doped hexaferrite samples. XP1 exhibits the highest tan δ values, peaking at approximately 13.46 at lower frequencies, indicating significant energy dissipation. XP2 shows a moderate loss tangent, peaking at 4.57, while XP3 displays the lowest tan δ values, starting at 3.86. The lower tan δ values for XP3 suggest minimal energy dissipation, which could be due to the reduced dielectric losses caused by the doping. As frequency increases, tan δ decreases for all samples, indicating reduced energy dissipation at higher frequencies. For XP1, the relaxation peak appears around the lower frequency range (below 10^3 Hz), which suggests strong dielectric relaxation at lower frequencies. XP2 shows a broader and less intense relaxation peak than XP1, indicating a more distributed relaxation behaviour. XP3 displays the weakest relaxation peak, implying that the material is highly resistive and experiences minimal dielectric relaxation. The XP1 sample shows a broad peak, indicating that dielectric losses occur over a wider frequency range. This suggests that a variety of relaxation mechanisms are active across this range. The XP2 sample exhibits a slightly narrower peak compared to XP1, but broader than XP3. This implies that XP2 experiences dielectric loss over a moderate frequency range. The XP3 sample has the narrowest peak, indicating that dielectric losses are confined to a smaller frequency range. This implies that fewer relaxation mechanisms are active in XP3.

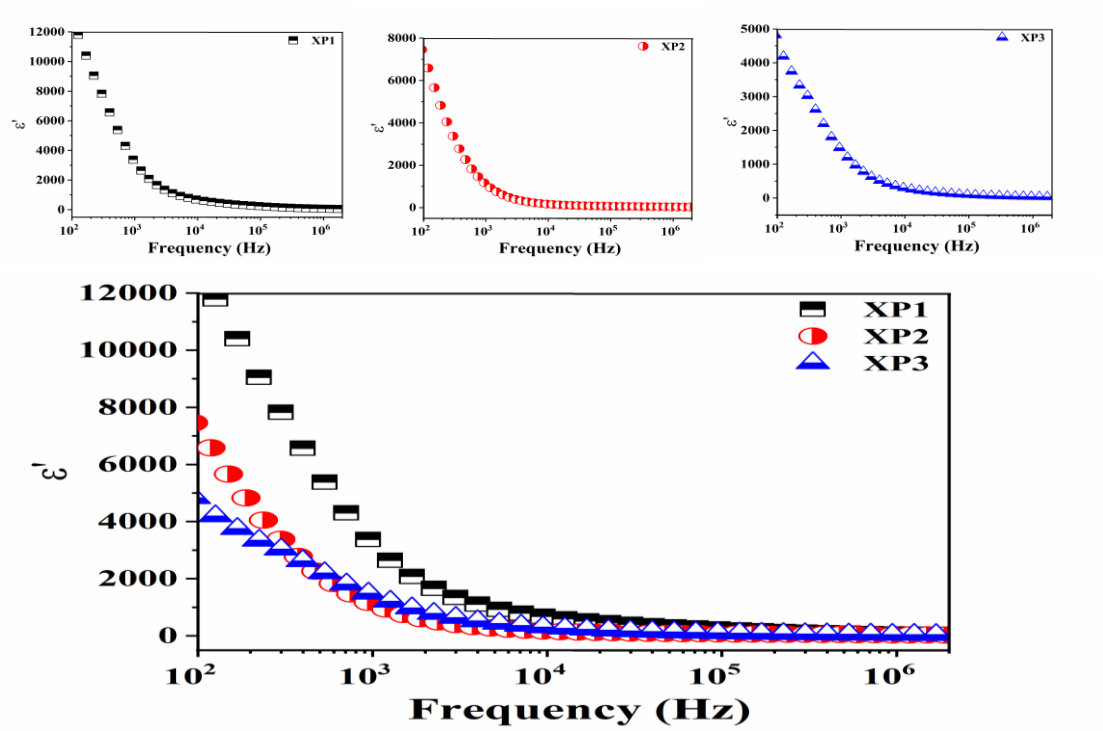

Figure 4.109(a) Dielectric Constant Dependence on Frequency in $BaCo_xCe_xFe_{12-2x}O_{19}$ (XP1 (x = 0.0), XP2 (x = 0.6), XP3 (x = 1.0)) Hexaferrites

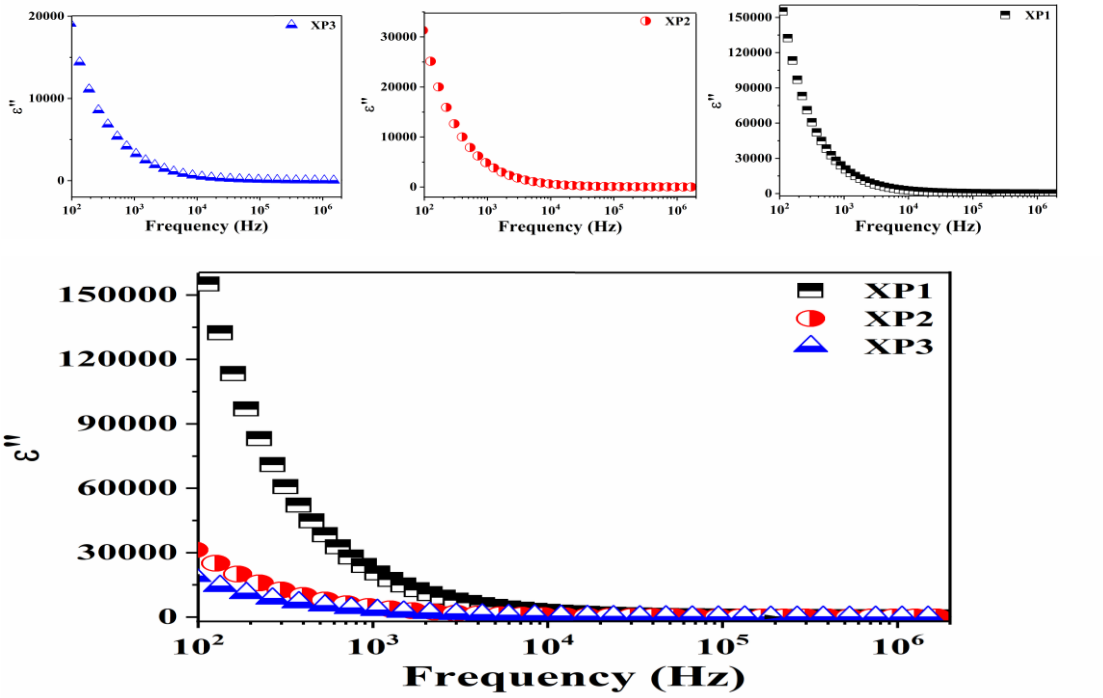

Figure 4.109(b) Dielectric Loss Dependence on Frequency in $BaCo_xCe_xFe_{12-2x}O_{19}$ (XP1 (x = 0.0), XP2 (x = 0.6), XP3 (x = 1.0)) Hexaferrites

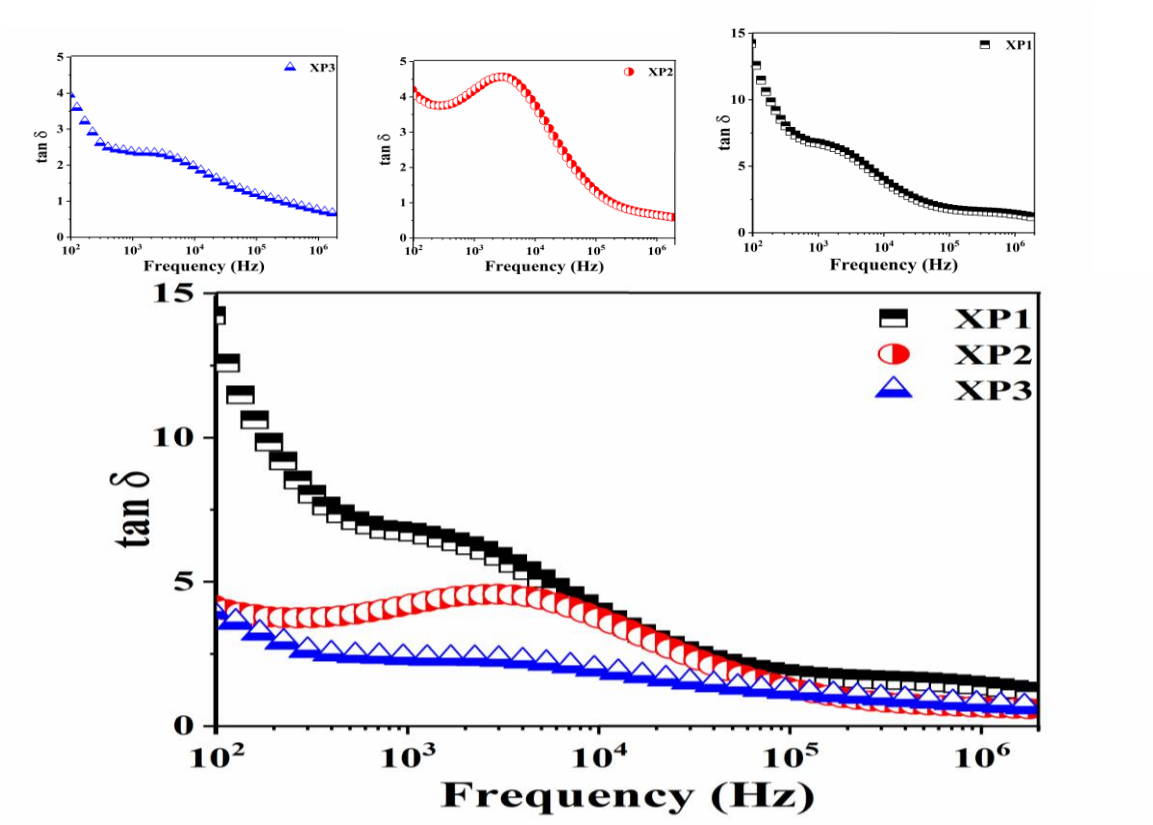

Figure 4.109(c) Dielectric Loss Tangent Dependence on Frequency in $BaCo_xCe_xFe_{12-2x}O_{19}$ (XP1 (x = 0.0), XP2 (x = 0.6), XP3 (x = 1.0)) Hexaferrites

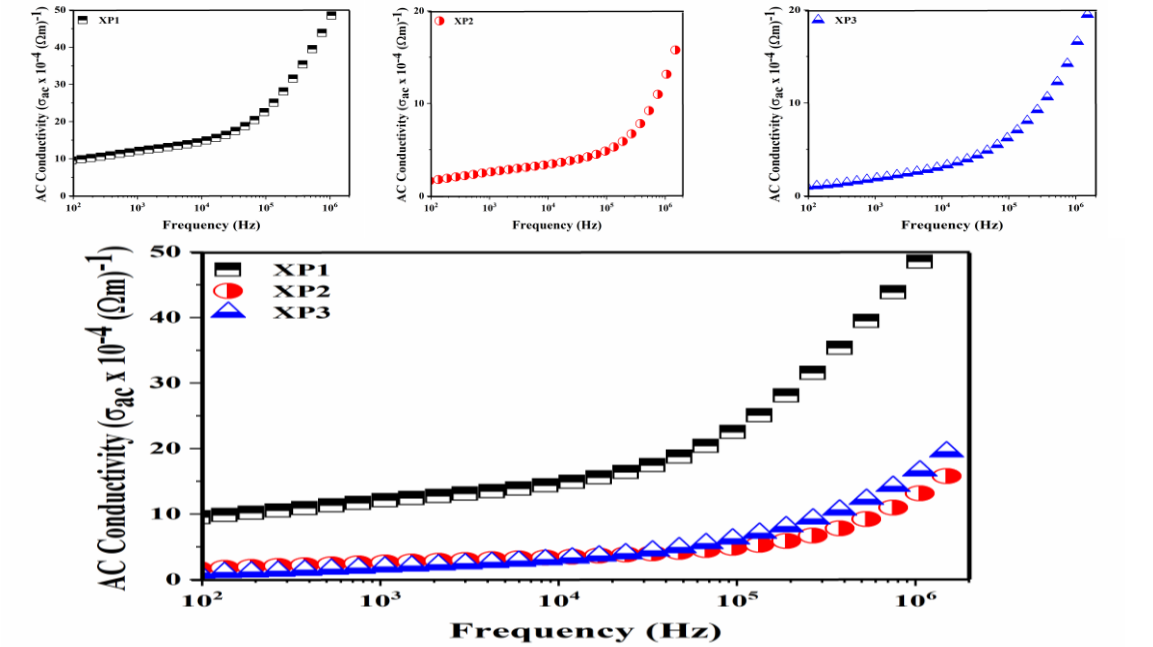

Figure 4.109(d) AC Conductivity Dependence on Frequency in $BaCo_xCe_xFe_{12-2x}O_{19}$ (XP1 (x = 0.0), XP2 (x = 0.6), XP3 (x = 1.0)) Hexaferrites

Figure 4.109(d) shows the variation in AC conductivity (σ_{ac}) as a function of frequency for the XP1, XP2, and XP3 samples. XP1 exhibits the highest AC conductivity, which increases significantly as the frequency increases, peaking at around 5.84×10^{-3} $(\Omega \cdot m)^{-1}$ at the highest frequency. This suggests enhanced charge carrier mobility and hopping mechanisms at higher frequencies. XP2 and XP3 show much lower AC conductivities, with XP2 reaching a maximum value of approximately 1.84×10^{-4} $(\Omega \cdot m)^{-1}$ and XP3 at 2.24×10^{-4} $(\Omega \cdot m)^{-1}$**.** The lower conductivity values for XP2 and XP3 suggest that the Co^{2+} and Ce^{3+} dopants have a more insulating effect on the ferrite structure, reducing charge mobility and conduction, especially at lower frequencies.

4.6.2.2 Electric modulus analysis

The figure 4.110(a) illustrates the variation of M' (real part of the electric modulus) as a function of frequency for Co and Ce-doped hexaferrite composites (XP1, XP2, XP3). At lower frequencies, the M' values for all samples tend to approach zero, indicating dominant interfacial (Maxwell-Wagner) polarization and minimal contributions from conductivity and electrode polarization. This behavior highlights the influence of long-range charge mobility and the interfacial polarization process, where the accumulation of charges at grain boundaries plays a significant role at lower frequencies. As the frequency increases, the M' values rise gradually before leveling off, reflecting the transition from long-range to short-range localized charge relaxation. This behavior aligns with the trends in AC conductivity, where conductivity is minimal at low frequencies but increases at higher frequencies due to enhanced charge carrier hopping and mobility. Among the samples, XP2 shows the highest M' values, reaching up to approximately 0.02633 at the highest frequencies. This suggests that XP2 has greater resistance to charge carrier movement, indicating higher relaxation strength and more localized charge mobility. In contrast, XP1 exhibits the lowest M' values, approximately 0.00942 at the same frequency, indicating higher charge mobility and lower resistance to carrier movement. XP3 shows intermediate behavior, with its M' values between those of XP1 and XP2, reflecting moderate charge mobility and relaxation strength.

The imaginary part of the electric modulus, M", which represents the energy dissipation and conductivity relaxation, is plotted as a function of frequency in the figure 4.110(b). XP2 consistently exhibits the highest M" values i.e 0.01529 across the entire frequency range, reflecting significant energy dissipation and strong conductivity relaxation processes. This suggests that XP2 has more pronounced charge relaxation dynamics and greater interaction between charge carriers and the electric field, leading to higher energy losses. XP3 displays moderate M" values, indicating intermediate energy dissipation and conductivity relaxation compared to

XP2 and XP1. XP1, with the lowest M" values i.e 0.01099, reflects the least energy dissipation, indicating faster charge carrier relaxation and lower overall losses.

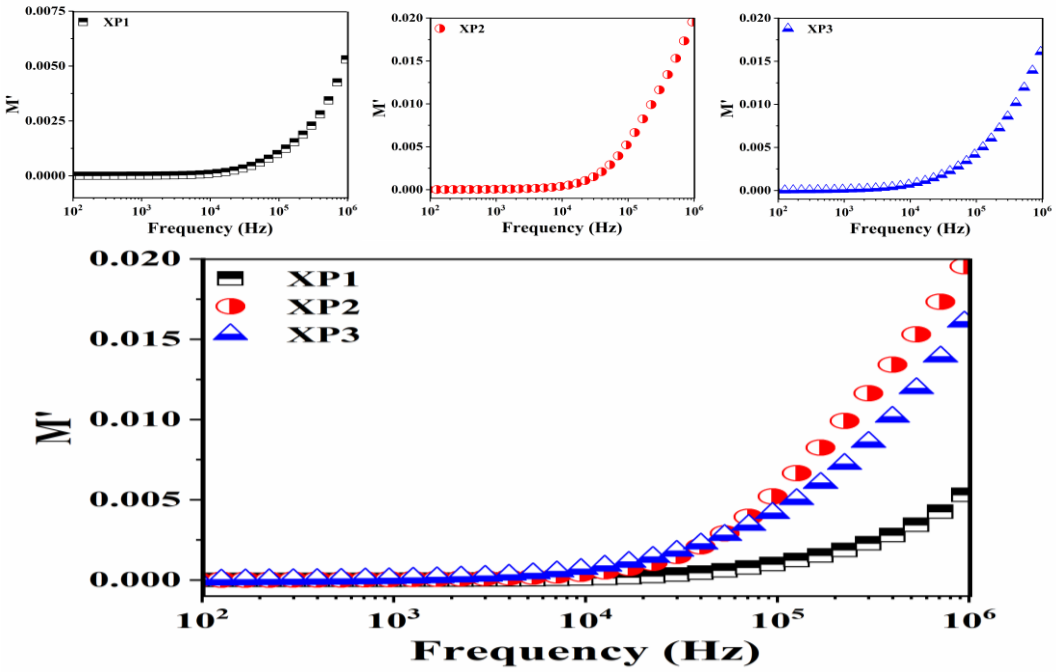

Figure 4.110(a) Real Modulus (M′) Dependence on Frequency in $BaCo_xCe_xFe_{12-2x}O_{19}$ (XP1 (x = 0.0), XP2 (x = 0.6), XP3 (x = 1.0)) Hexaferrites.

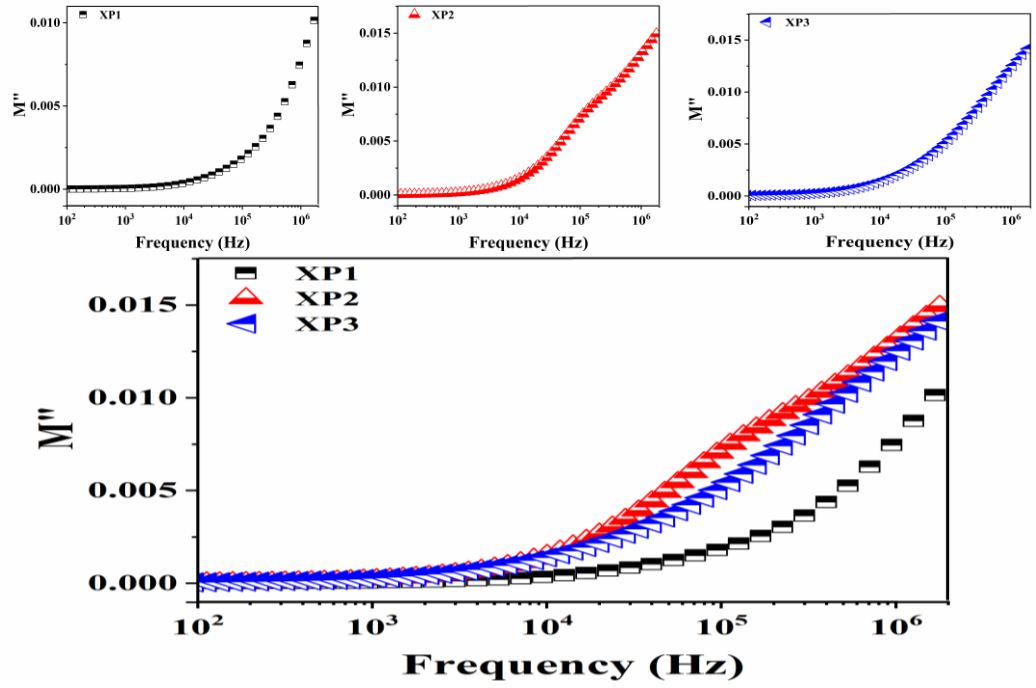

Figure 4.110(b) Imaginary Modulus (M") Dependence on Frequency in $BaCo_xCe_xFe_{12-2x}O_{19}$ (XP1 (x = 0.0), XP2 (x = 0.6), XP3 (x = 1.0)) Hexaferrites

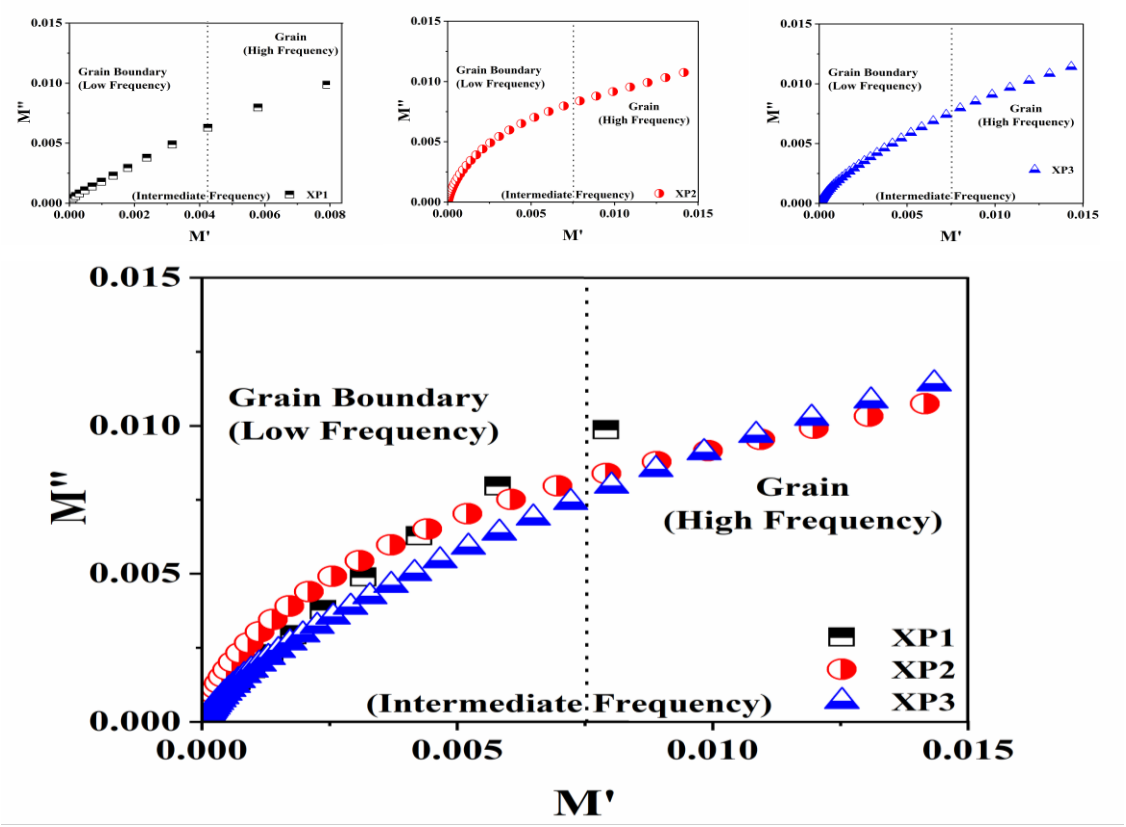

Figure 4.110(c) Cole-Cole Impedance Plots of $BaCo_xCe_xFe_{12-2x}O_{19}$ (XP1 (x = 0.0), XP2 (x = 0.6), XP3 (x = 1.0)) Hexaferrites at 900°C, 5h.

At higher frequencies, M" increases steadily for all samples, with a more noticeable increase in XP2. This suggests that the conductivity relaxation becomes more dominant as the frequency increases, with the strongest effects observed in XP2. The peak height for XP1 is the smallest, indicating weaker inter-grain connectivity and less effective polarization, which correlates with its lower energy dissipation and faster relaxation behaviour.

The Cole-Cole plot, which depicts the imaginary modulus (M") versus the real modulus (M'), reveals the conductivity relaxation processes and charge transport mechanisms in the Co and Ce-doped composites. The semicircular arcs in the plot reflect the conductivity relaxation strength and charge dynamics in each sample. XP3 exhibits the largest semicircular arc, indicating stronger conductivity relaxation and greater interaction between charge carriers and the electric field. This corresponds to the highest M" peak for XP3, which implies significant grain boundary effects and pronounced relaxation processes within the material. In contrast, XP1 displays a much

smaller arc diameter, suggesting lower resistance, more effective charge mobility, and weaker grain boundary effects. XP1's lower peak height further reflects less significant relaxation processes, with a more prominent contribution from grain boundary effects rather than grains. XP2 falls between XP1 and XP3 in terms of its behaviour. The arc diameter and peak height for XP2 are smaller than XP3 but larger than XP1, indicating intermediate conductivity relaxation behaviour. The shift of the peaks for XP2 and XP3 towards higher M' values compared to XP1 suggests that the relaxation processes in XP2 and XP3 occur at higher frequencies. This shift indicates that doping with Co and Ce enhances the charge mobility and increases the frequency at which the relaxation processes occur. In contrast, XP1 shows slower relaxation processes with more influence from grain boundaries.

4.6.2.3 Impedance spectroscopy

The frequency-dependent behaviour of Z′ (real impedance) and Z″ (imaginary impedance) for Co and Ce-doped hexaferrite composites is clearly shown in Figure 4.111.. Among the samples, XP3 shows the highest impedance at low frequencies, reaching values up to approximately $5.8\times10^5\,\Omega$, followed by XP2 with moderate impedance, while XP1 exhibits the lowest impedance values. This behaviour is consistent with increased grain boundary effects at low frequencies. At frequencies beyond 10^6 Hz, the Z″ values for all three composites begin to plateau, suggesting that the impedance reaches a saturation point. The decrease in Z″ values at higher frequencies indicates a reduction in polarization effects. XP2, in particular, displays a prominent peak in Z″ around 10^2 Hz and 10^5 Hz, which is likely indicative of a relaxation process driven by grain and grain boundaries respectively and interfacial effects that influence the impedance response within this frequency range.

The Cole-Cole (Nyquist) plots, showing Z″ versus Z′ for the Co and Ce-doped hexaferrite composites, further elucidate the contributions of grain and grain boundary effects. At lower frequencies, the plots reflect the resistive contributions from the grains (bulk material), while at higher frequencies, the grain boundary contributions become more dominant. XP3, with a large arc in the low-frequency region, highlights a significant grain contribution, implying higher resistance or impedance due to bulk material at lower frequencies. As the frequency increases, the influence of grain boundaries becomes more prominent, leading to a reduction in impedance, as indicated by the rightward drop on the high-frequency side of the plot. XP2, with a smaller arc compared to XP3, shows a moderate grain contribution at low frequencies, while XP1, which has the smallest arc, suggests lower resistive grain effects and faster charge carrier relaxation. XP3 exhibits a single prominent relaxation peak, which is characterized by a significant rise and fall in the impedance values. This peak suggests that XP3 undergoes a dominant relaxation process, likely associated with grain boundary effects, at a specific frequency. XP2 shows double relaxation peaks, implying that there is two relaxation processes

occurring within the sample. This suggests complex charge dynamics, where different mechanisms are contributing at different frequencies. XP1 displays a relatively weak and less distinct peak.

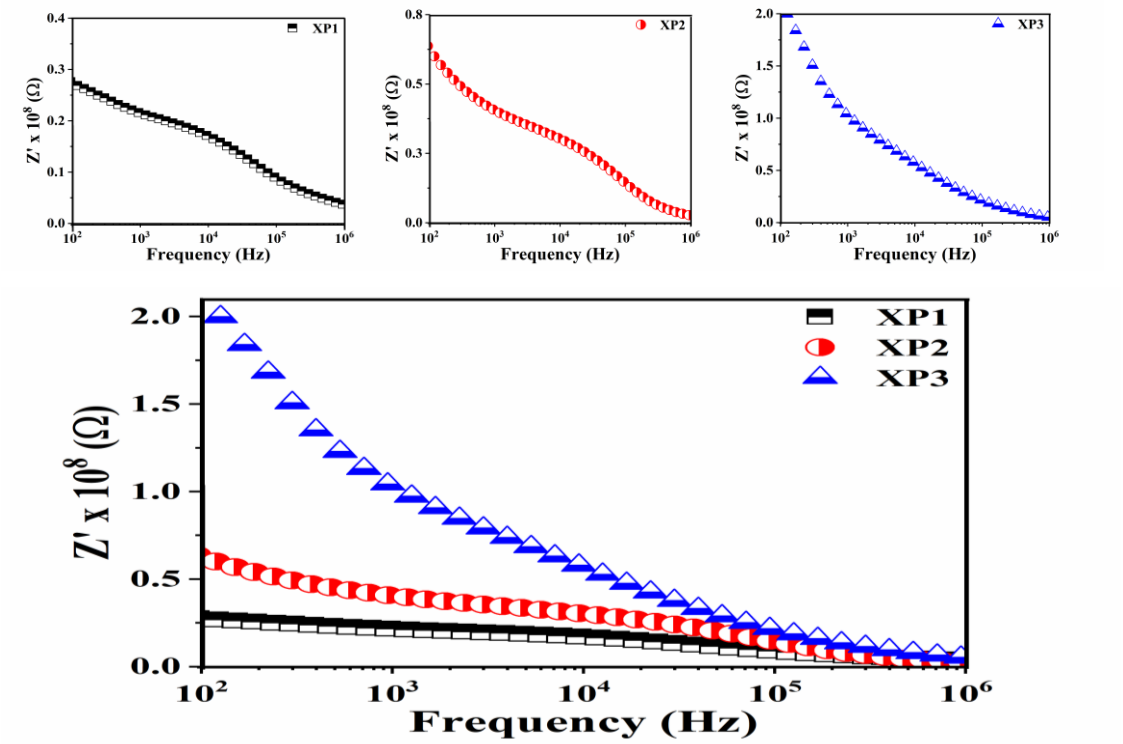

Figure 4.111(a) Real Impedance (Z′) Dependence on Frequency in $BaCo_xCe_xFe_{12-2x}O_{19}$ (XP1 (x = 0.0), XP2 (x = 0.6), XP3 (x = 1.0)) Hexaferrites

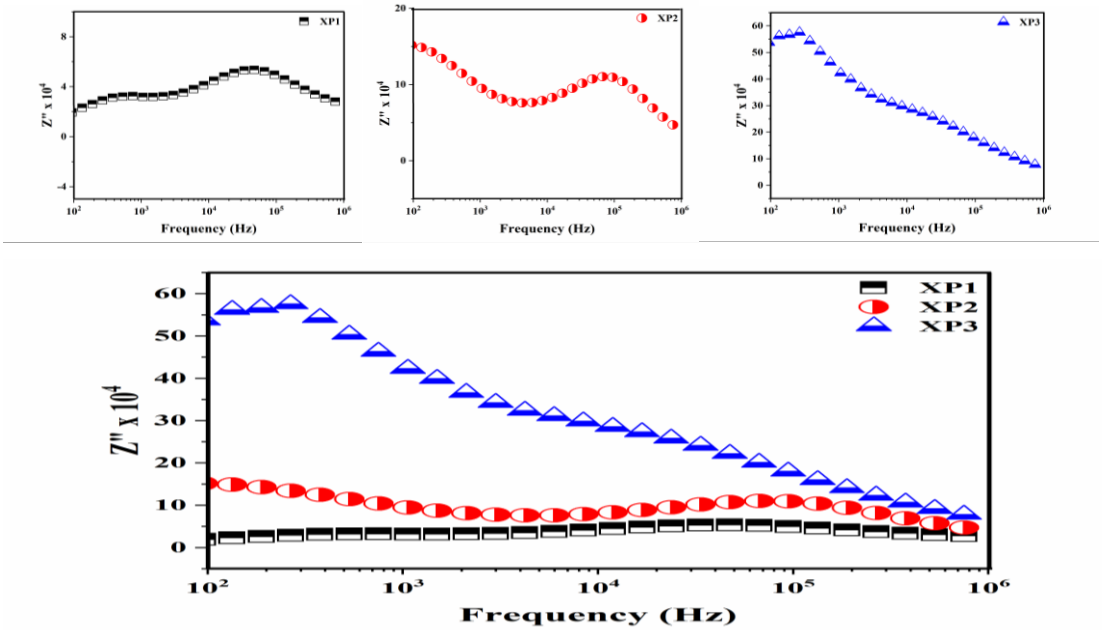

Figure 4.111(b) Imaginary Impedance (Z′) Dependence on Frequency in $BaCo_xCe_xFe_{12-2x}O_{19}$ (XP1 (x = 0.0), XP2 (x = 0.6), XP3 (x = 1.0)) Hexaferrites.

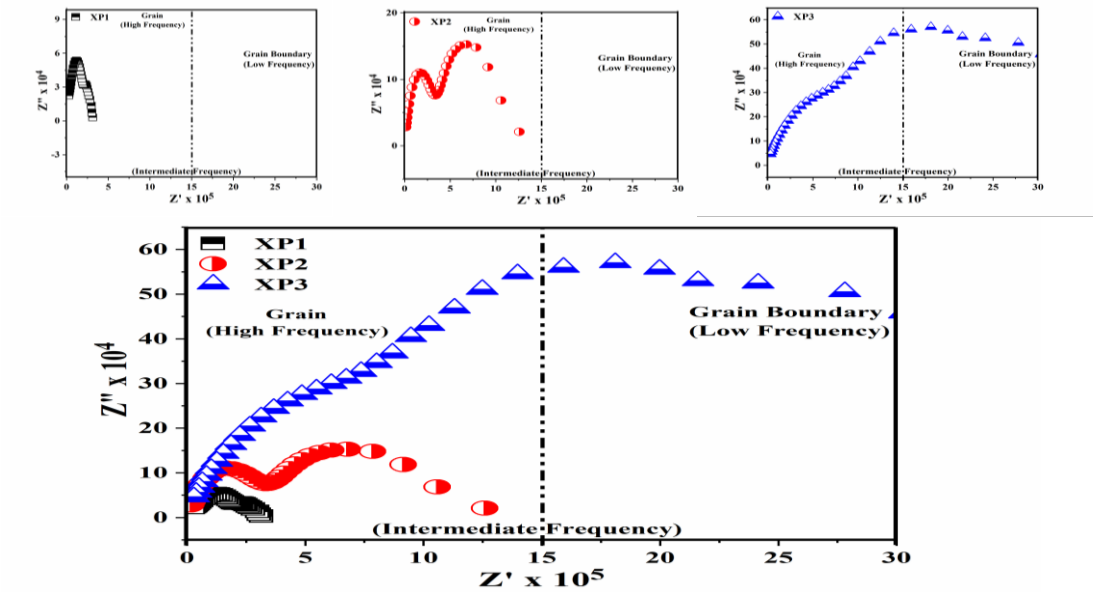

Figure 4.111(c) Cole-Cole Impedance Plots of $BaCo_xCe_xFe_{12-2x}O_{19}$ (XP1 (x = 0.0), XP2 (x = 0.6), XP3 (x = 1.0)) Hexaferrites after Heat Treatment at 900°C for 5 Hours.

4.6.2.4 Computational Impedance Simulation and Validation

The Figure 4.112 presents the results of an equivalent circuit analysis based on complex impedance data obtained using Electrochemical Impedance Spectroscopy (EIS) software [49].

In this model, the CPE parameter "P" and the resistance "R" are used along with the phase shift "n," which ranges between 0 and 1 for a capacitor. This approach accurately represents the behavior of the composite materials, as evidenced by the strong agreement between the experimental and fitted impedance curves shown in the Figure 4.112. Table 4.35 provides the resistance and capacitance values for both grains and grain boundaries, derived from the EIS data. These parameters offer insights into the electrical response and microstructural properties of the composites under investigation.

Table 4.35 Extracted Grain and Grain Boundary Parameters from EIS Modelling

Composite	R_g (MΩ)	R_{gb} (MΩ)	C_g (μF)	C_{gb} (μF)
XP1	0.21	0.02	0.44 x 10^6	3.94

XP2	0.28	1.06	0.61 x 10^3	32.33 x 10^{10}
XP3	0.61	2.13	0.031 x 10^6	6.85 x 10^6

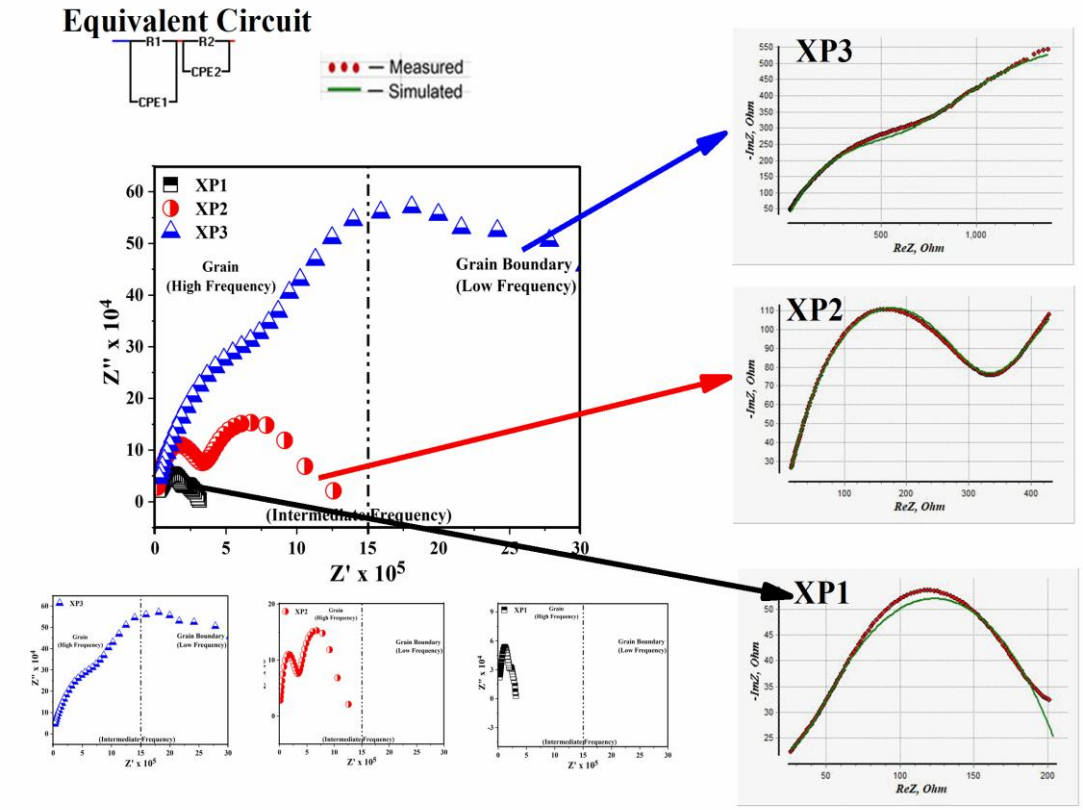

Figure 4.112 Measured and Fitted Impedance Data with Equivalent Circuit (XP1 to XP3)

4.6.2.5 Investigating the Relationship between EIS Data and Microstructure

The low grain resistance (R_g = 0.21 MΩ) and very low grain boundary resistance (R_{gb} = 0.02 MΩ) suggest that the charge carriers move more freely between grains in XP1, consistent with the distinct grains seen in the Figure 4.108(a). The small, well-separated grains reduce the impedance, explaining the moderate grain boundary capacitance (C_{gb} = 3.94 μF) and high grain capacitance (C_g = 0.44 × 10^6 μF). The high capacitance could be due to the large surface area of the smaller grains, which allows for better polarization within the material. The denser grain packing in XP2, as observed in the Figure 4.108(b), correlates with the moderate grain resistance (R_g = 0.28 MΩ) and higher grain boundary resistance (R_{gb} = 1.06 MΩ). The grain boundary resistance is higher due to the grain contact points, which act as barriers to charge carrier movement. The significantly lower grain capacitance (C_g = 0.61×10^3 μF) and

extraordinarily high grain boundary capacitance (C_{gb} = 32.33×10^{10} μF) suggest that the grain boundaries dominate the electrical response in XP2. This behavior is consistent with the more interconnected grain structure seen in the Figure 4.108(b), where grain boundaries play a significant role in the impedance. The larger, fused grains in XP3 correlate with the highest grain resistance (R_g = 0.61 MΩ) and grain boundary resistance (R_{gb} = 2.13 MΩ) due to the reduced grain boundary area and the larger grains acting as obstacles to charge mobility. The lower grain capacitance (C_g = 0.031×10^6 μF) aligns with the larger grain size, as larger grains typically exhibit reduced surface area for polarization. The moderate grain boundary capacitance (C_{gb} = 6.85×10^6 μF) reflects the reduced role of grain boundaries in the electrical response, as the fused grains reduce the overall number of grain boundaries in the material.

4.6.2.6 Investigating the Relationship between EIS Data and Electric Parameters

R_g represents the resistance within individual grains of the material. Lower grain resistance typically suggests better electron mobility within the grains, indicating higher conductivity. In XP1, the grain resistance is the lowest (R_g = 0.21 MΩ), indicating higher electrical conductivity within the grains. This can be correlated with its relatively high saturation magnetization (M_s) and coercivity (H_c), as lower resistance supports stronger superexchange interactions. For XP2 and XP3, R_g increases, with XP3 having the highest grain resistance (R_g = 0.61 MΩ). This indicates that XP3 has reduced conductivity within the grains, which may lead to weaker magnetic interactions and higher resistivity in the material.

R_{gb} reflects the resistance at the boundaries between grains. Higher grain boundary resistance generally correlates with poorer charge transport across grain boundaries, leading to increased resistivity. XP1 has the lowest grain boundary resistance (R_{gb} = 0.02 MΩ), indicating efficient charge transport across grain boundaries, which enhances the overall electrical conductivity of the material. In XP2 and XP3, the grain boundary resistance increases significantly, with XP3 having the highest R_{gb} value (2.13 MΩ). This suggests that XP3 suffers from greater interfacial polarization and higher resistivity at grain boundaries, limiting the mobility of charge carriers and weakening magnetic interactions.

C_g is a measure of the material's ability to store charge within the grains. Higher grain capacitance reflects greater polarization within the grains, which can impact dielectric

properties. XP1 has a relatively high grain capacitance (C_g = 0.44 x 10^6 µF), which suggests strong charge storage capabilities within the grains.

C_{gb} represents the material's ability to store charge at grain boundaries. High grain boundary capacitance can indicate enhanced interfacial polarization, leading to greater dielectric loss but also stronger relaxation effects. XP1 shows the lowest grain boundary capacitance (C_{gb} = 3.94 µF), indicating minimal interfacial polarization and efficient charge transport across grain boundaries. XP2 and XP3 show significantly higher C_{gb} values, with XP2 reaching an extremely high value (C_{gb} = 32.33 x 10^{10} µF). This suggests that XP2 experiences significant interfacial polarization, which may dominate its impedance behaviour and lead to lower overall conductivity.

4.6.3 Magnetic Analysis

The magnetic properties of Co-Ce doped hexaferrite PANI composites (XP1, XP2, and XP3) can be analyzed using hysteresis Figure 4.113 and table 4.36, which display key parameters such as saturation magnetization (M_s), coercivity (H_c), anisotropy field (H_a), remanent magnetization (M_r), and the remanence ratio (M_r/M_s). The substitution of Co^{2+} and Ce^{3+} ions into the hexaferrite structure influences these magnetic parameters by altering superexchange interactions between Fe^{3+} ions.

The saturation magnetization (M_s) indicates the maximum magnetization achieved by the material when all magnetic moments are aligned. In the Co-Ce doped samples: XP1 shows the highest M_s value of 45.92 emu/g, suggesting a higher net magnetic moment, likely due to stronger Fe^{3+}-Fe^{3+} superexchange interactions. XP3 has an intermediate M_s of 33.42 emu/g, reflecting a decrease in magnetic strength as Co^{2+} and Ce^{3+} substitution weakens the magnetic interactions. XP2 exhibits the lowest M_s of 14.93 emu/g, indicating the most significant reduction in net magnetic moment among the samples. This reduction in M_s with increasing substitution is attributed to the fact that Co^{2+} and Ce^{3+} ions have lower magnetic moments than Fe^{3+}, disrupting the strong Fe^{3+}-Fe^{3+} superexchange interactions that contribute to higher M_s.

XP1 has the lowest grain resistance (R_g = 0.21 MΩ) and the lowest grain boundary resistance (R_{gb} = 0.02 MΩ), indicating a higher conductivity within both grains and grain boundaries. The high conductivity corresponds to the highest saturation magnetization (M_s = 45.92 emu/g) observed in XP1. The lower resistance allows for better electron hopping, enhancing the magnetic interactions, leading to higher M_s.

XP2 shows a moderate increase in both R_g (0.28 MΩ) and R_{gb} (1.06 MΩ). This increase in resistance is associated with a significant drop in saturation magnetization (M_s = 14.93 emu/g). The higher resistance indicates reduced conductivity, which weakens the superexchange interactions, resulting in a lower overall magnetization. This effect is likely due to the disruption of Fe^{3+} superexchange interactions by the Ce and Co doping, leading to lower magnetization. XP3 displays the highest grain and grain boundary resistance values (R_g = 0.61 MΩ, R_{gb} = 2.13 MΩ). Despite the high resistance, the saturation magnetization (M_s = 33.42 emu/g) increases compared to XP2. The increased R_g and R_{gb} values indicate more resistive grain and grain boundary contributions, which may reduce electron hopping and weaken superexchange interactions. However, the higher M_s compared to XP2 suggests that Ce doping influences the distribution of magnetic ions in a way that compensates for the increased resistance, allowing some recovery of magnetic interactions.

Coercivity (H_c) represents the resistance of the magnetic domains to switching when exposed to an external magnetic field. The trend observed is: XP1 has the highest coercivity at 5382.78 Oe, suggesting strong magnetic anisotropy and domain stability. XP2 and XP3 show decrease coercivity values of 3803.83 Oe and 2723.86 Oe, respectively, indicating that with increasing substitution, the magnetic domains become easier to reverse, likely due to a softening of the magnetic structure. The decrease in coercivity reflects the reduced strength of Fe^{3+}-Fe^{3+} exchange interactions as Co^{2+} and Ce^{3+} ions replace Fe^{3+} at specific crystallographic sites, making the domains more susceptible to reversal. XP1 has the highest anisotropy field of 15.96 kOe, indicating strong magnetocrystalline anisotropy. XP2 and XP3 show lower Ha values of 14.10 kOe and 13.70 kOe, respectively, signifying a gradual reduction in anisotropy with increased doping of Co^{2+} and Ce^{3+}.

XP1 has the highest coercivity (H_c = 5382.78 Oe) and the highest anisotropy field (H_a = 15.96 kOe), which correlates with the lower resistance values for both grains and grain boundaries (R_g = 0.21 MΩ, R_{gb} = 0.02 MΩ). The higher conductivity within the grains and across the grain boundaries supports stronger magnetic interactions, leading to higher coercivity and anisotropy. XP2 shows a notable drop in both H_c (3803.83 Oe) and H_a (14.10 kOe), which is associated with the increased grain boundary resistance (R_{gb} = 1.06 MΩ) and the high grain boundary capacitance (C_{gb} =

32.33 x 10^{10} µF). The reduced conductivity and the increased polarization at the grain boundaries weaken the magnetic interactions, resulting in lower coercivity and anisotropy. XP3 has the lowest coercivity (H_c = 2723.86 Oe) and the lowest anisotropy field (H_a = 13.70 kOe). The increased resistances (R_g = 0.61 MΩ, R_{gb} = 2.13 MΩ) and the higher grain boundary capacitance (C_{gb} = 6.85 x 10^6 µF) lead to weaker magnetic domain interactions, making it easier to reverse the magnetic domains and contributing to the lower coercivity.

The remanence ratio (M_r/M_s) provides insight into the magnetic domain structure. A ratio below 0.5 generally indicates multi-domain behaviour, while values greater than 0.5 suggest single-domain or pseudo-single-domain behaviour. XP1 and XP3 both exhibit a ratio of 0.511, while XP2 has a slightly higher ratio of 0.519. All values are close to 0.5, suggesting that the materials exhibit multi-domain.

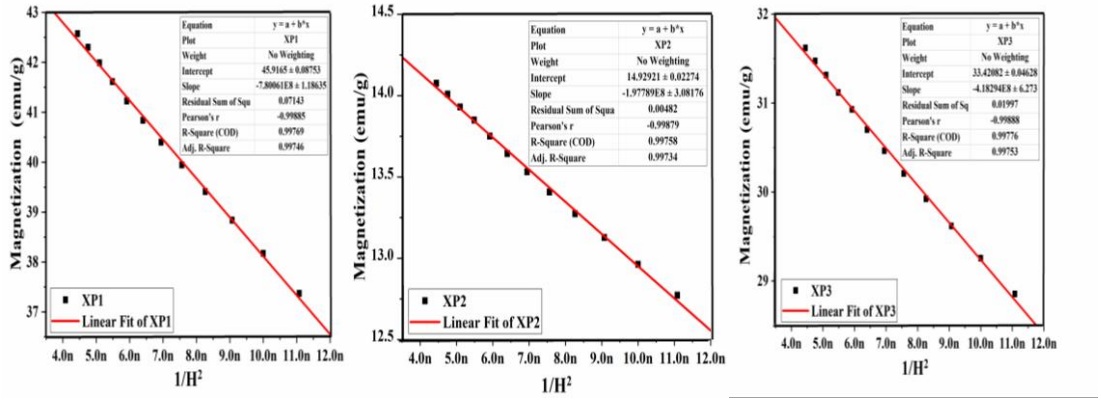

Figure 4.113 M_s versus 1/ H^2 plots for all hexaferrite samples.

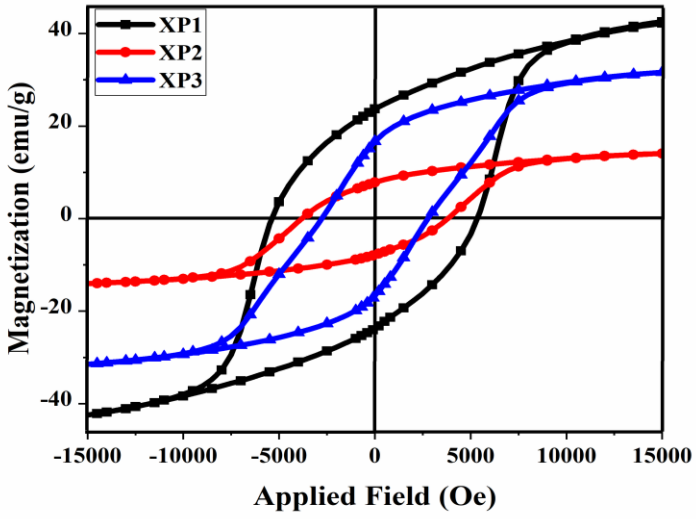

Figure 4.114 Hysteresis loops of XP1, XP2 and XP3 hexaferrite.

Table 4.36 Magnetic parameters M_s , H_c , H_a, M_r, and M_r / M_s value of all hexaferrite samples.

sample	M_s	H_c	H_a=sqrt(-15B)	H_a (kOe)	M_r	M_r/M_s
XP1	45.92	5382.78	15963.40	15.96	23.45	0.511
XP2	14.93	3803.83	14097.05	14.10	7.747	0.519
XP3	33.42	2723.86	13701.81	13.70	17.09	0.511

4.6.4 Electromagnetic Characteristics

4.6.4.1 Complex permeability and complex permittivity

The Figure 4.115 displays plots of (ε'),(ε"), (μ'), and (μ") against frequency. The real permittivity (ε') for XP1 starts high at around 5.9 at 8 GHz and gradually decreases as the frequency increases, dropping to about 4.9 by 12 GHz. There are no significant peaks or dips, indicating a consistent and smooth decrease in permittivity with increasing frequency. XP2 shows a much lower permittivity compared to XP1, starting around 4.3 at 8 GHz and gradually decreasing to 3.2 by 12 GHz. The trend for XP2 shows a steady decline in permittivity with no sharp fluctuations or changes, indicating a smooth response across the frequency range. XP3 starts at a value of 5.25 but exhibits some fluctuation between 9 GHz and 11 GHz, where it dips and peaks. After 11 GHz, XP3 shows a slight recovery and then stabilizes around 4.5 as the frequency approaches 12 GHz. The graph for ε" shows a clear decreasing trend across the frequency range of 8 GHz to 12 GHz for all samples (XP1, XP2, XP3). XP1 starts at approximately 1.18 at 8 GHz and gradually decreases, ending near 0.5 at 12 GHz. XP2 follows a steady decline, starting from around 0.51 at 8 GHz and gradually decreases, ending near -1.32 at 12 GHz. XP3 begins at 0.55 and fluctuates, first rising and then stabilizing around 0.5 at 12 GHz. This indicates that XP1 has the largest dielectric loss, while XP2 and XP3 exhibit more moderate values, with XP2 crossing into negative regions as frequency increases. Starting at a value of around 0.24 at 8 GHz, μ' for XP1 gradually increases up to approximately 0.77 at 9.6 GHz. After this point, there is a sharp dip, dropping down to a lower value of around 0.47 at 10 GHz. From there, μ' begins to rise steadily again, reaching around 0.87 by 12 GHz. XP2 exhibits a relatively higher μ' across the frequency range compared to XP1. It starts at around 0.57 at 8 GHz and shows a smooth increase up to around 1.03 by 12 GHz, indicating a steady increase in the real part of the permeability over this frequency

range. For XP3, μ' starts at around 0.7 at 8 GHz and gradually increases to about 1.05 at around 10.0 GHz. However, μ' then declines slightly after this point, reaching approximately 0.89 by 12 GHz, showing a peak followed by a gradual decline.

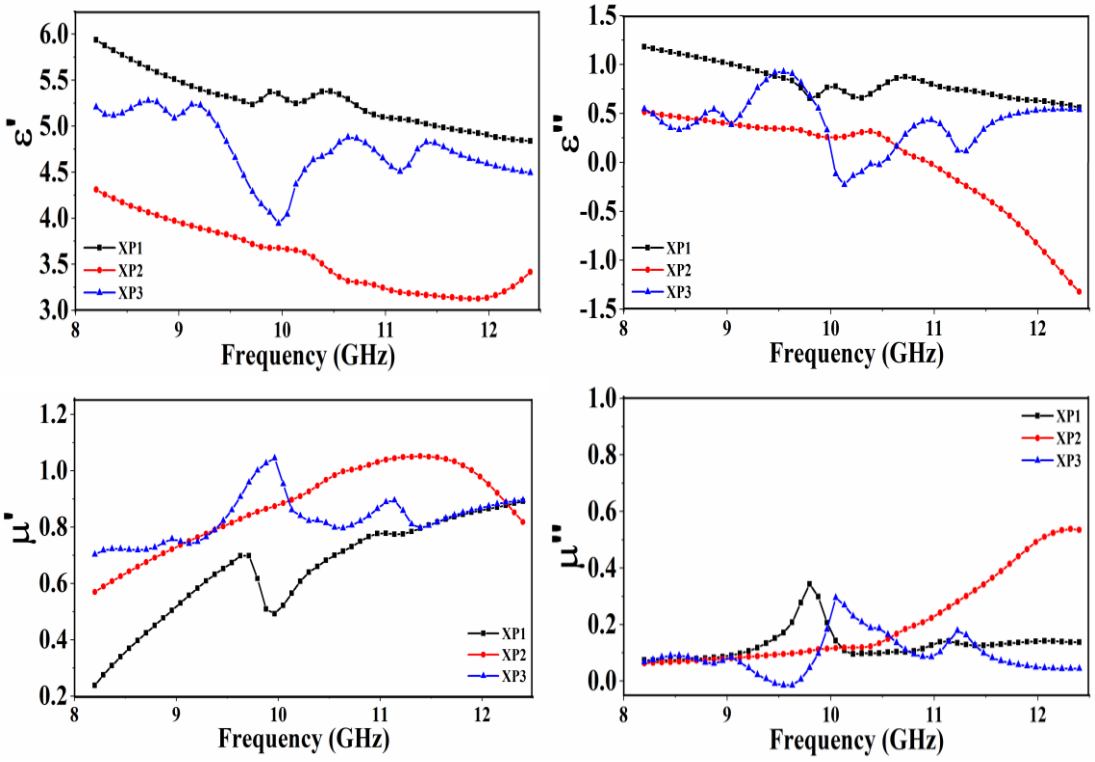

Figure 4.115 Complex permittivity and permeability versus frequency plots for $BaCo_xCe_xFe_{12-2x}O_{19}$ / PANI

The Figure 4.115 for XP1 shows a small peak around 10 GHz, starting at around 0.1 at 8 GHz, peaking near 0.4 at 10 GHz, and then dropping back to around 0.2 at 12 GHz. This indicates a localized resonance effect around 10 GHz, contributing to increased magnetic losses at this frequency. XP2 starts low around 0.1 at 8 GHz and steadily increases, showing a gradual upward trend from around 0.2 at 9 GHz to approximately 0.6 by the time it reaches 12 GHz. This suggests that XP2 experiences increasing magnetic losses as the frequency rises. XP3 starts at a higher value of approximately 0.1 at 8 GHz, shows a peak near 10 GHz (around 0.4), and then gradually decreases, ending around 0.15 at 12 GHz.

4.6.4.2 Microwave absorption in $BaCo_xCe_xFe_{12-2x}O_{19}$ / PANI

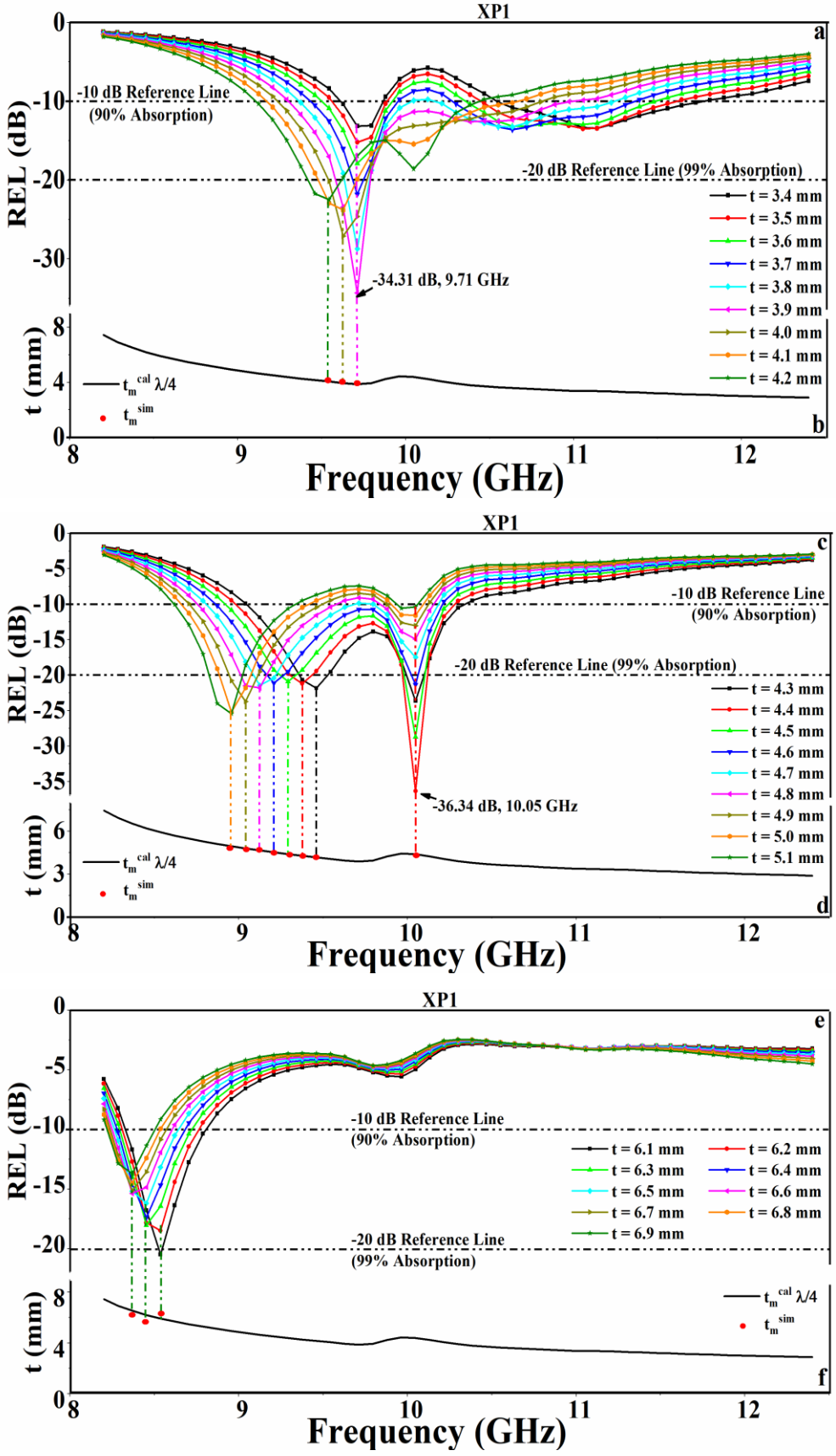

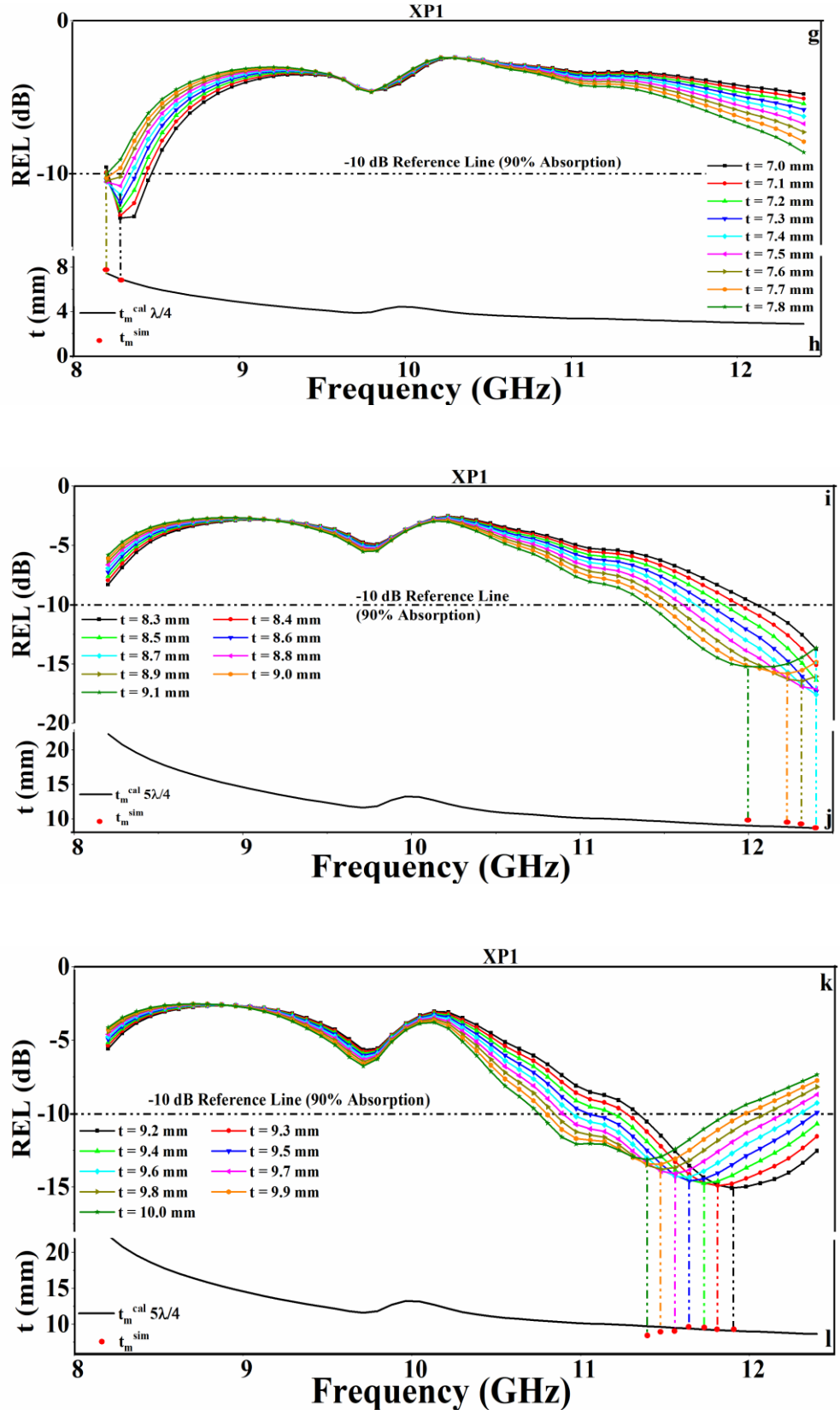

Figure 4.116 REL versus frequency for different thickness (XP1) and calculate thickness versus frequency for $BaCo_xCe_xFe_{12-2x}O_{19}$

4.6.4.3 Quarter Wavelength Mechanism

We examined graphs that displayed the reflection loss of various materials at different thicknesses and frequencies, illustrating the amount of microwave energy they reflected. These graphs provided valuable insights into the absorption of microwaves by the materials. Figures 4.116 and so on display the results for the ferrites we produced. Through a careful examination of these graphs, we were able to determine and quantify several characteristics of the materials. There is a table that provides a summary of these properties, which can be found in Table 4.37.

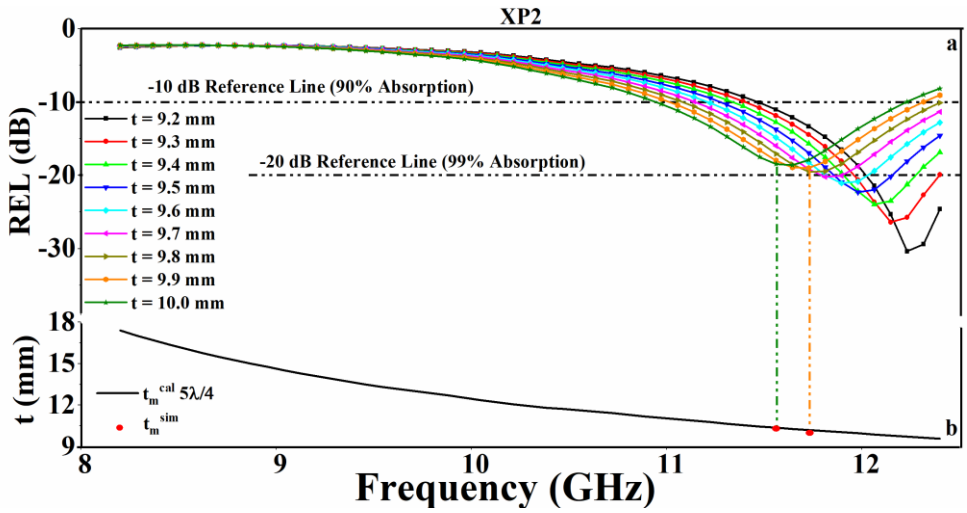

Figure 4.117 REL versus frequency for different thickness (XP2) and calculate thickness versus frequency for $BaCo_xCe_xFe_{12-2x}O_{19}$

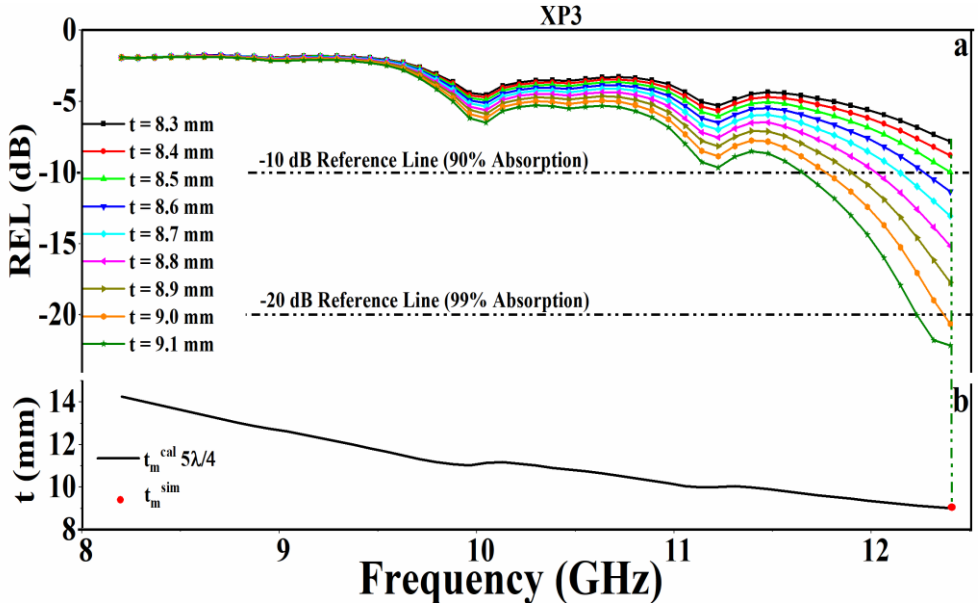

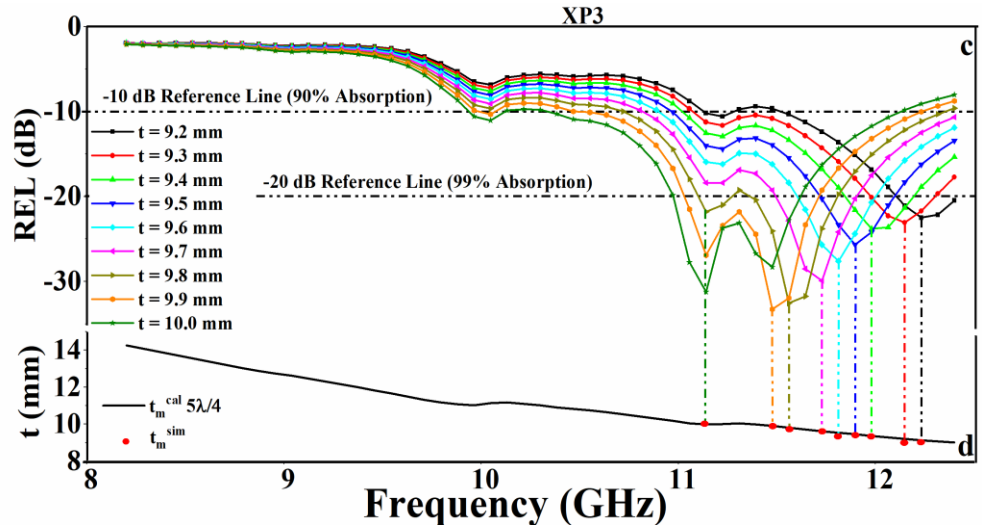

Figure 4.118 REL versus frequency for different thickness (XP3) and calculate thickness versus frequency for $BaCo_xCe_xFe_{12-2x}O_{19}$

Composition XP1 demonstrates a broad range of reflection loss (REL) values across various thicknesses. At a thickness of 3.5 mm, WP1 achieves a maximum REL of -15.15 dB at a frequency of 9.71 GHz, with a bandwidth of 0.32 GHz for REL > -10 dB. As the thickness increases to 3.9 mm, the REL significantly improves to -34.31 dB at the same frequency, with a broader bandwidth of 1.69 GHz for REL > -10 dB and 0.21 GHz for REL > -20 dB, indicating a marked improvement in absorption. Further increases in thickness continue to demonstrate high REL values. For instance, at 4.0 mm, WP1 shows an REL of -26.93 dB at 9.63 GHz with a bandwidth of 1.57 GHz for REL > -10 dB and 0.24 GHz for REL > -20 dB. At 4.4 mm, XP1 exhibits a very high REL of -36.34 dB at 10.05 GHz with a narrow bandwidth of 0.15 GHz for REL > -20 dB, indicating strong absorption at higher frequencies. At higher thicknesses, such as 5.1 mm and beyond, the REL decreases, with XP1 exhibiting an REL of -25.36 dB at 8.95 GHz and a bandwidth of 0.72 GHz for REL > -10 dB. The material shows effective microwave absorption even at higher thicknesses, confirming its suitability for a wide range of applications.

For XP2, the matching thicknesses range from 9.3 mm to 10 mm, with a maximum REL of -26.43 dB at 12.14 GHz for a thickness of 9.3 mm. The bandwidth for REL > -20 dB spans from 0.22 GHz to 0.43 GHz, with maximum performance at 12.14 GHz, where the reflection loss is relatively high. For higher thicknesses, the bandwidth increases, but reflection loss slightly decreases compared to XP1. For XP3, the

matching thicknesses range from 9.1 mm to 10 mm, with a maximum REL of -33.29 dB at 11.48 GHz for a thickness of 9.9 mm. The bandwidth for REL > -10 dB reaches 1.75 GHz, while the bandwidth for REL > -20 dB extends to 0.67 GHz.

XP3 shows the highest reflection loss among all compositions, especially at higher frequencies (11.48 GHz to 12.41 GHz), and demonstrates better absorption across the frequency range with the greatest bandwidth performance at higher thicknesses. XP1 performs well in the lower frequency ranges with moderate reflection loss, while XP2 shows improved reflection loss at higher frequencies but lower bandwidth. XP3 stands out with superior absorption and reflection loss in the higher frequency ranges, particularly at greater thicknesses, making it the most effective in terms of energy absorption.

According to the data, the quarter-wavelength criterion for composition XP1 is observed at thicknesses ranging from 3.5 mm to 10.0 mm, with a -10 dB bandwidth varying from 0.26 GHz to 1.69 GHz. Maximum REL values between -12.89 dB and -36.34 dB are recorded, with the -20 dB bandwidth ranging from 0.03 GHz to 0.24 GHz. As illustrated in Figure 4.116 XP1(a), the reflection loss peaks for XP1 occur at 9.71 GHz for thicknesses of 3.5 mm, 3.9 mm, and 4.0 mm. Similar peaks are observed at higher frequencies, such as 10.05 GHz at 4.4 mm, with a notable decrease in peak height as thickness increases, as shown in Figure 4.116 XP1(c). As shown in Figures 4.116 XP1(a), XP1(e), XP1(g), XP1(i) and XP(k) in the higher thickness range (3.9 mm to 4.2 mm, 6.1 mm to 6.9 mm, 7.0 mm to 7.8 mm, 8.3 mm to 9.1 mm and 9.2mm to 10.00 mm respectively), the REL peaks shift toward lower frequencies, with peak heights gradually decreasing. This behaviour is consistent with the quarter-wavelength mechanism, where increasing thickness results in a corresponding shift in peak absorption to lower frequencies.

For XP2, the -10 dB bandwidth ranges from 1.29 GHz to 1.34 GHz across thicknesses from 9.3 mm to 10.0 mm. Maximum REL values between -18.43 dB and -26.43 dB are recorded, with -20 dB bandwidths varying between 0.22 GHz and 0.43 GHz. As shown in figure 4.117 XP2 (a), the reflection loss peaks shift to lower frequencies as the thickness increases and height of peak also decrease with thickness, particularly in the range of 11.5 GHz to 12.5 GHz for thicknesses between 9.2 mm and 10.00 mm.

In the case of XP3, the REL values range between -22.22 dB and -33.29 dB for thicknesses between 9.1 mm and 10.0 mm. The bandwidth for REL > -10 dB varies between 1.57 GHz and 1.7 GHz and bandwidth for REL > -20 dB varies between 0.3 GHz and 0.67 GHz. As shown in figure 4.118 XP3 (c), the reflection loss peaks shift to lower frequencies as the thickness increases and height of peak also increase with thickness, particularly in the range of 11.00 GHz to 12.5 GHz for thicknesses between 9.2 mm and 10.00 mm. A W-shaped curve is also evident in the range of 11.00 GHz to 12.2 GHz for thicknesses ranging from 9.7 mm to 10.00 mm, indicating broad absorption that is advantageous for electromagnetic interference (EMI) shielding applications.

Table 4.37 REL with matching thickness/frequency, BW, and PBW for $BaCo_xCe_xFe_{12-2x}O_{19}$ (XP1 to XP3).

Sample Name	Matching Thickness (mm)	Maximum REL (dB)	Matching frequency (GHz)	Frequency Band for REL > -10 dB (GHz)	Band width for RL > -10 dB (GHz)	Frequency Band REL > -20 dB (GHz)	Band width for REL > -20 dB (GHz)	BTR	PBW (%)
XP1	3.5	-15.15	9.71	9.56-9.88	0.32	---	-	2.90E-04	3.30
	3.9	-34.31	9.71	9.3-10.99	1.69	9.58-9.79	0.21	1.27E-03	17.40
	4	-26.93	9.63	9.24-10.81	1.57	9.53-9.77	0.24	1.18E-03	16.30
	4.2	-22.516	9.54	9.108-10.45	1.342	9.41-9.62	0.21	1.01E-03	14.07
	4.3	-21.87	9.46	9.05-10.35	1.3	9.35-9.52	0.17	9.68E-04	13.74
	4.4	-21.21	9.38	8.98-10.28	1.3	9.3-9.43	0.13	9.60E-04	13.86
	4.4	-36.34	10.05	---	-	9.97-10.12	0.15	1.01E-04	1.49
	4.5	-20.82	9.29	8.92-10.24	1.32	9.24-9.34	0.1	9.63E-04	14.21
	4.6	-21.14	9.21	8.86-10.21	1.35	9.17-9.27	0.1	9.73E-04	14.66
	4.7	-21.43	9.12	8.81-9.67	0.86	9.08-9.22	0.14	6.44E-04	9.43
	4.9	-23.71	9.04	8.71-9.49	0.78	8.94-9.12	0.18	5.78E-04	8.63
	5.1	-25.36	8.95	8.62-9.34	0.72	8.82-9.02	0.2	5.26E-04	8.04
	6.1	-20.54	8.54	8.33-8.81	0.48	8.52-8.55	0.03	3.22E-04	5.62
	6.3	-18.04	8.45	8.29-8.72	0.43	---	-	2.83E-04	5.09
	6.6	-15.29	8.37	8.24-8.61	0.37	---	-	2.37E-04	4.42
	7	-12.89	8.28	8.21-8.47	0.26	---	-	1.60E-04	3.14
	8.7	-17.56	12.4	---	-	---	-	-	-

	9.2	-15.12	11.9	---	-	---	-	-	-
	9.6	-14.58	11.64	11.05-12.39	1.34	---	-	3.06E-04	11.51
	9.8	-13.79	11.47	10.84-12.19	1.35	---	-	3.13E-04	11.77
	10	-13.15	11.39	10.75-11.87	1.12	---	-	2.63E-04	9.83
XP 2	9.3	-26.43	12.14	---	-	11.96-12.39	0.43	9.36E-05	3.54
	9.4	-23.77	12.06	---	-	11.91-12.27	0.36	7.86E-05	2.99
	9.5	-22.26	11.98	---	-	11.86-12.15	0.29	6.36E-05	2.42
	9.6	-21.19	11.73	---	-	11.81-12.03	0.22	4.84E-05	1.88
	9.8	-19.63	11.73	11.06-12.4	1.34	---	-	2.99E-04	11.42
	9.9	-18.97	11.64	11-12.31	1.31	-	-	2.93E-04	11.25
	10	-18.43	11.57	10.94-12.23	1.29	---	-	2.89E-04	11.15
XP 3	9.1	-22.22	12.41	---	-	---	-	-	-
	9.2	-22.47	12.24	---	-	12.1-12.4	0.3	6.52E-05	2.45
	9.3	-23.17	12.15	---	-	11.98-12.31	0.33	7.22E-05	2.72
	9.4	-23.78	11.98	---	-	11.84-12.2	0.36	7.95E-05	3.01
	9.5	-25.78	11.89			11.71-12.09	0.38	8.48E-05	3.20
	9.6	-27.69	11.81			11.6-11.99	0.39	8.76E-05	3.30
	9.7	-29.99	11.73	10.83-12.4	1.57	11.49-11.91	0.42	3.62E-04	13.38
	9.8	-32.53	11.57	10.74-12.36	1.62	11.35-11.82	0.47	3.74E-04	14.00
	9.9	-33.29	11.48	10.47-12.22	1.75	11.04-11.71	0.67	4.14E-04	15.24
	10	-31.29	11.14	10.33-12.12	1.79	10.97-11.62	0.65	4.29E-04	16.07

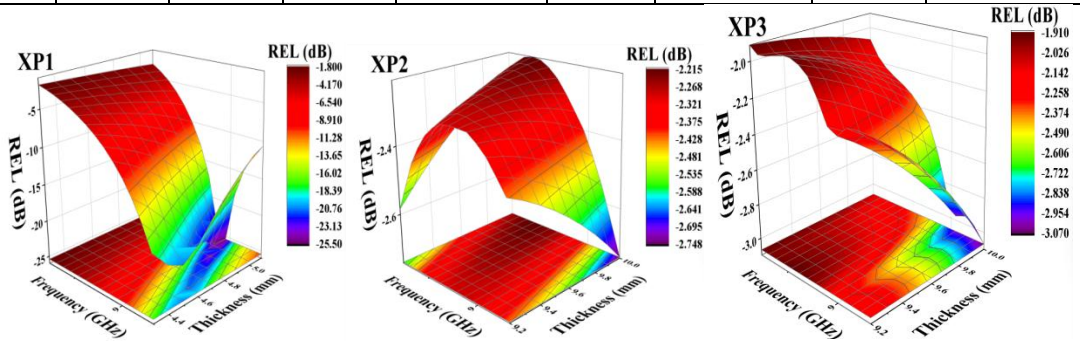

Figure 4.119 Three-dimensional (3D) plots of reflection loss at various frequencies and thicknesses for all samples of BaCoCe-series.

4.6.4.4 Impedance matching mechanism

The material's impedance varies because its permittivity/permeability is different from that of free space. The distinction between these two influences the material's absorption properties. A smaller portion of the incident signal penetrates the material and the majority is discarded from the surface as a result of these two being out of alignment. But if they are mostly the same, some of it enters the material and is absorbed by it. For this reason, researching impedance matching is necessary in order to create an efficient absorber.

Plots of reflection loss and $|Z_{in}|$ v/s frequency for the prepared samples are shown in Figure 4.120. The Z_{in} values that correspond to the maximum reflection loss of the various compositions are listed in Table 4.38. In every composition (XP1 to XP3), the highest REL peaks adhere to the impedance matching technique.

For XP1, at a matching thickness of 4.4 mm, the maximum REL value is -36.34 dB at a frequency of 10.05 GHz, with corresponding Z_{real} = 382.16 Ω and Z_{img} = 10.36 Ω, resulting in an input impedance of $|Z_{in}|$ = 382.30 Ω. This indicates that XP1 has relatively good absorption properties at this frequency, as its input impedance is close to the impedance of free space (377 Ω). For XP2, at a matching thickness of 9.3 mm, the maximum REL value is -26.43 dB at a frequency of 12.14 GHz, with Z_{real} = 411.75 Ω and Z_{img} = 14.97 Ω, giving $|Z_{in}|$ = 412.02 Ω.

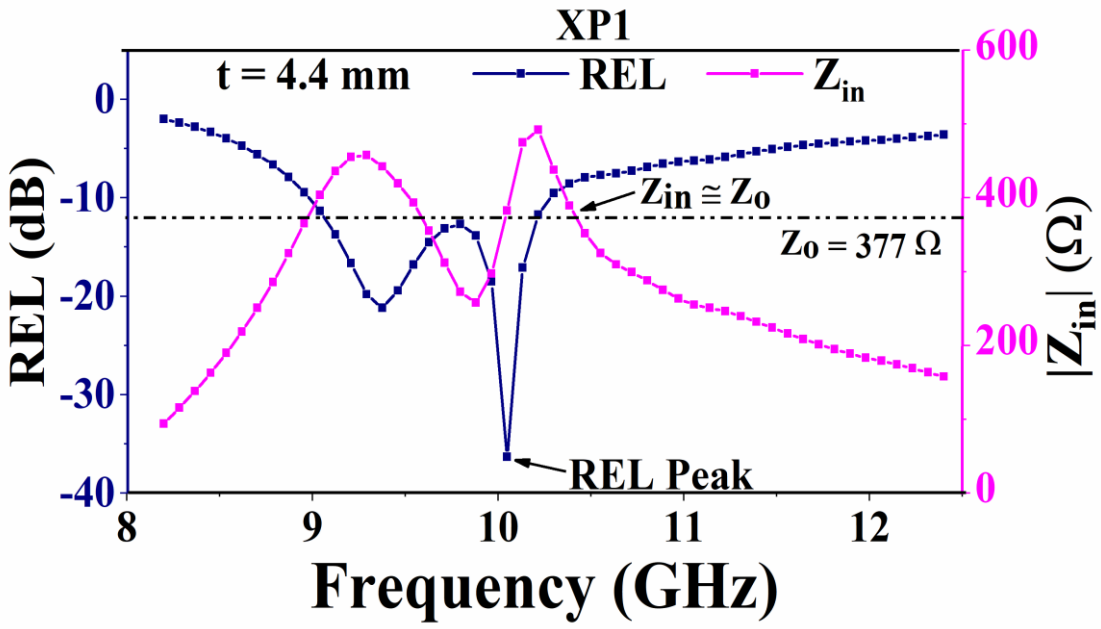

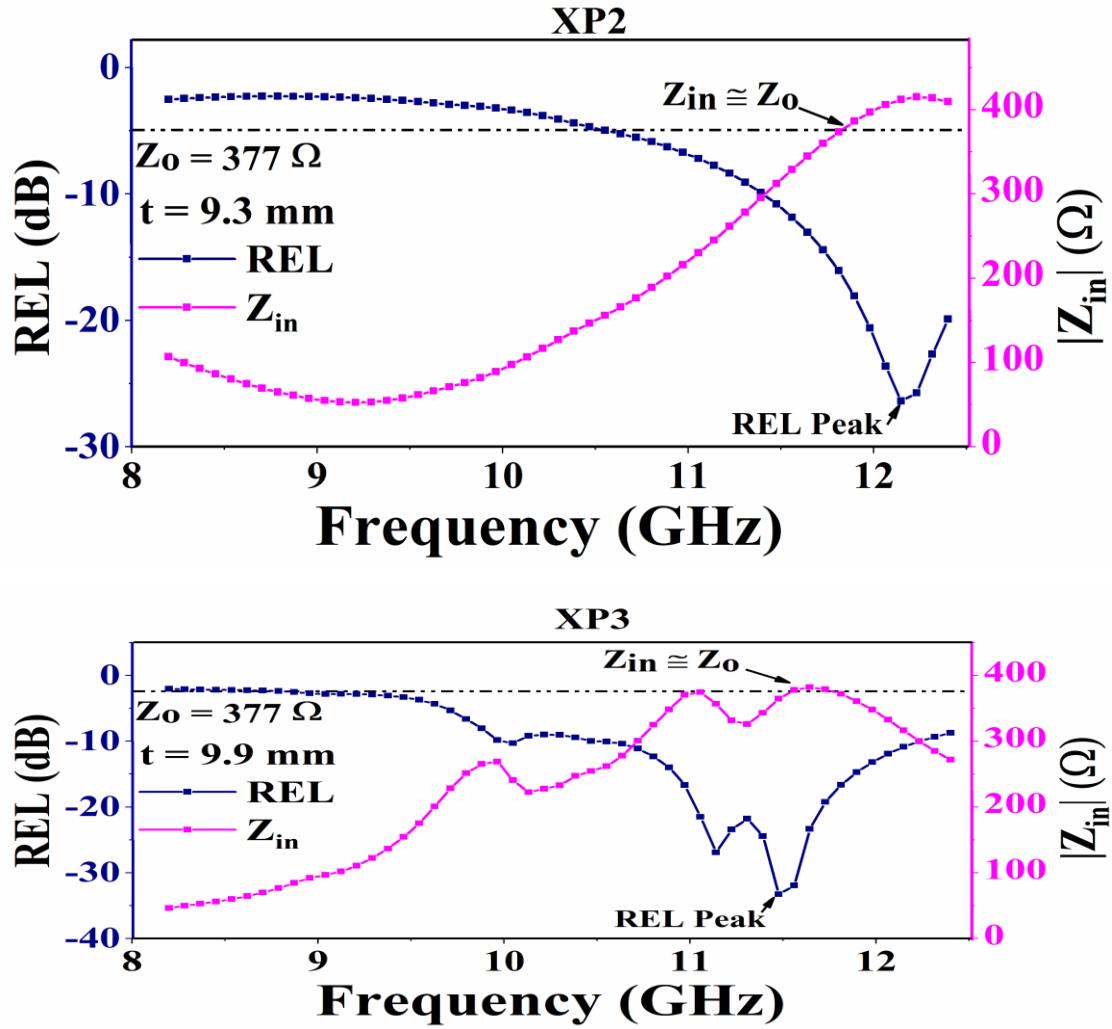

Figure 4.120 Z_{in} and REL curve against frequency for $BaCo_xCe_xFe_{12-2x}O_{19}$ / PANI

Although the REL is lower compared to XP1, the input impedance deviates more from 377 Ω, suggesting somewhat less efficient impedance matching at this frequency. For XP3, at a matching thickness of 9.9 mm, the maximum REL value is -33.29 dB at a frequency of 11.48 GHz, with Z_{real} = 364.24 Ω and Z_{img} = 9.78 Ω, resulting in $|Z_{in}|$ = 364.37 Ω. XP3 shows a strong reflection loss and a relatively well-matched impedance close to 377 Ω, indicating efficient absorption at this frequency. In conclusion, XP1 and XP3 show stronger REL peaks and better impedance matching compared to XP2, which has slightly higher input impedance values, leading to less optimal absorption.

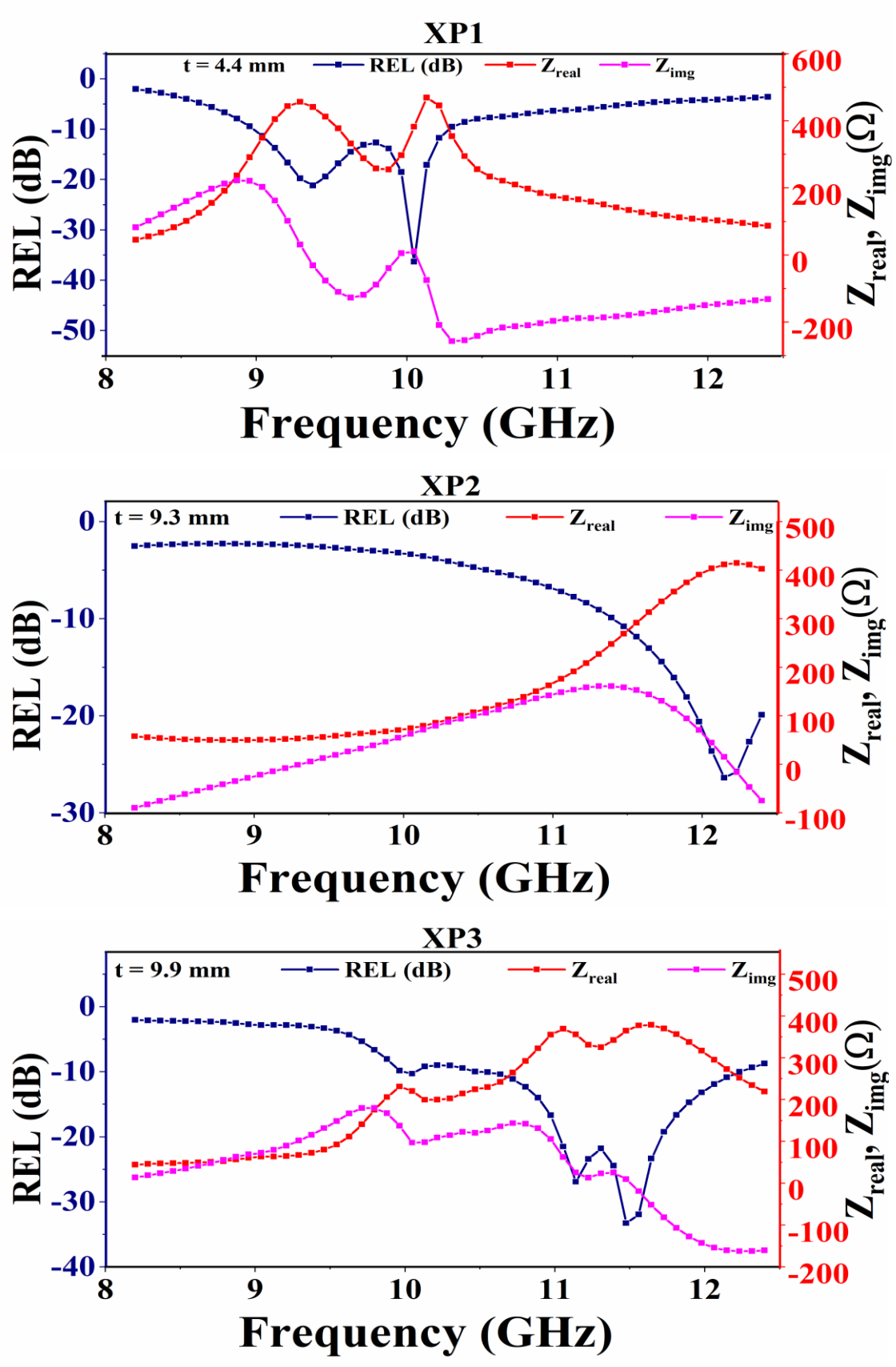

Figure 4.121 Z_{real}, Z_{imag}, and REL v/s frequency for $BaCo_xCe_xFe_{12-2x}O_{19}$ / PANI

Table 4.38 Z_{in}, Z_{real}, and Z_{imag} values corresponding to REL_{max} for $BaCo_xCe_xFe_{12-2x}O_{19}$ / PANI

Sample Name	Matching Thickness (mm)	Maximum REL (dB)	Matching frequency (GHz)	Z_{real} (Ω)	Z_{img} (Ω)	$\|Z_{in}\|$ (Ω)
XP1	4.4	-36.34	10.05	382.16	10.36	382.30
XP2	9.3	-26.43	12.14	411.75	14.97	412.02
XP3	9.9	-33.29	11.48	364.24	9.78	364.37

4.6.4.5 Eddy Current Loss

XP1 exhibits a sharp peak at around 8 GHz with a maximum C_0 value of approximately 1.7 ns, followed by a dip near 10 GHz. After 10.0 GHz, the C_0 value gradually declines and stabilizes near 0 ns for frequencies beyond 11 GHz. XP2 shows a gradual and consistent increase in C_0 as the frequency increases, starting from a value slightly below 0 at 8 GHz and reaching about 0.5 ns at 12 GHz. The curve is smooth and shows no significant fluctuations, indicating a more stable behaviour compared to XP1. XP3 starts with C_0 values around 0.2 ns at 8 GHz and experiences a slight dip near 9 GHz. It then fluctuates around 0 ns, with minor variations across the frequency range, before rising steadily after 11 GHz to reach around 0.3 ns at 12 GHz.

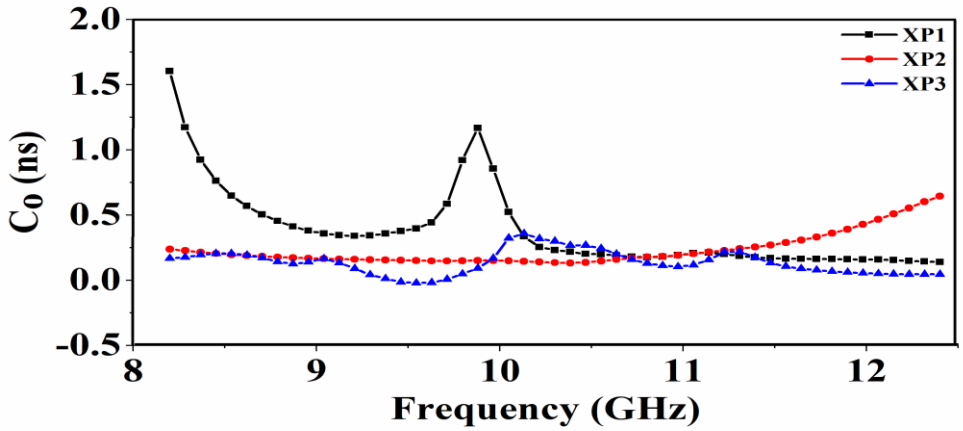

Figure 4.122 C_0 versus frequency curve for $BaCo_xAl_xFe_{12-2x}O_{19}$ / PANI

4.6.4.6 Bandwidth to Thickness Ratio

Wide bandwidths with reduced thickness play a crucial role in the characterization and design of an absorber. Instead of focusing just on raising REL values, one should strive for a low thickness after reaching the REL≥-10 dB. This makes figuring out the bandwidth to thickness ratio (BTR) and percentage bandwidth (PBW) crucial.

The BTR (Bandwidth to Thickness Ratio) and PBW (Percentage Bandwidth) values for the prepared compositions are summarized in the table. For composition XP1, the BTR ranges from 1.01E-04 to 1.27E-03, with a PBW spanning between 1.49% and 17.40%. XP1 demonstrates its strongest performance at a thickness of 3.9 mm, with a reflection loss (REL) of -34.31 dB at 9.71 GHz, achieving a BTR of 1.27E-03 and PBW of 17.40%. The bandwidth for REL > -20 dB is 0.21 GHz at this thickness. XP1 shows relatively good absorption performance over a range of thicknesses between 3.5 mm and 10 mm, with stable reflection loss values across the frequency range from 8.28 GHz to 12.4 GHz.

XP2 exhibits a BTR range between 4.84E-05 and 2.99E-03, with a PBW spanning from 1.88% to 11.4%. XP2 shows its highest absorption performance at 9.3 mm thickness, achieving a maximum REL of -26.43 dB at 12.14 GHz. At this point, it demonstrates a BTR of 9.36E-05 and PBW of 3.54%, with a bandwidth of 0.43 GHz for REL > -20 dB.

For XP3, the BTR ranges from 6.52E-05 to 4.29E-04, with a PBW between 2.45% and 16.1%. XP3 shows its peak performance at 9.9 mm thickness, where it reaches a maximum REL of -33.29 dB at 11.48 GHz, with a BTR of 4.14E-04 and PBW of 15.24%.

4.6.4.6 S – Parameter

When the input signal is applied at input port 1 of the test waveguide from VNA, the two-port S_{11} parameter accounts for the reflected signal from the same input port 1 from the sample fitted in the test waveguide of the VNA. S_{21} accompanies the attenuation in the signal traveling from input port 1 to output port 2. The S_{11} values for XP1 start at around -2 dB at 8 GHz and show minimal fluctuation across the frequency range, ending near -2.5 dB at 12 GHz. XP2 starting at -2 dB and dropping as low as -7 dB by 12 GHz. For XP3, the S_{11} values begin at -4 dB at 8 GHz, initially decrease to a low of -6 dB near 9.5 GHz, and then increase steadily to around -2 dB by 12 GHz. In terms of S_{21}, XP1 values range between -2 dB to -3.5 dB across the frequency range. XP2 shows relatively stable S_{21} values, starting at -2.5 dB at 8 GHz, with a slight dip around 10.00 GHz, but improving to -1.5 dB near 12 GHz. XP3 shows steady improvement in S_{21}, starting at -2 dB and reached upto -3.0 dB at 12 GHz.

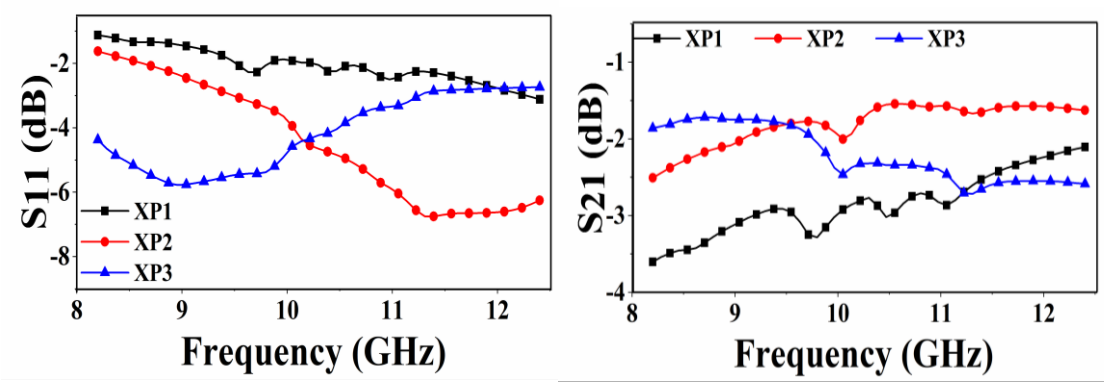

Figure 4.123 S_{11} and S_{21} versus frequency curve for $BaCo_xCe_xFe_{12-2x}O_{19}$ / PANI.

4.7 Co^{2+}- Cd^{2+} substituted $BaCo_xCd_xFe_{12-2x}O_{19}$ hexaferrite / PANI

This section will use the sol-gel combustion technique to produce a hexaferrite compound with replacements of Co and Cd. By composition, the hexaferrite will consist of $BaCo_xCd_xFe_{12-2x}O_{19}$. Table 4.39 presents the numerical values assigned to different degrees of substitution in $BaCo_xCd_xFe_{12-2x}O_{19}$.

Table 4.39. Presents the assignment of sample names corresponding to various substitution levels in $BaCo_xCd_xFe_{12-2x}O_{19}$ hexaferrite.

Sample Composition **$BaCo_xCd_xFe_{12-2x}O_{19}$**	Sample Code Name	Sample Code (Y-series)
x= 0.0	**$BaFe_{12}O_{19}$**	YP1
x = 0.6	**$BaCo_{0.6}Cd_{0.6}Fe_{10.8}O_{19}$**	YP2

4.7.1 Field Emission Scanning Electron Microscopy

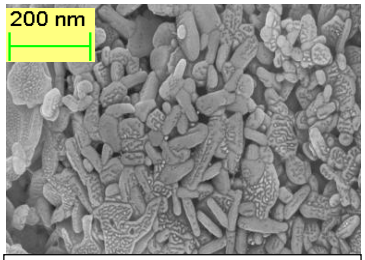

Figure 4.124(a) SEM for YP1

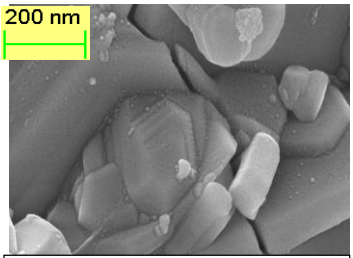

Figure 4.124(b) SEM for YP2

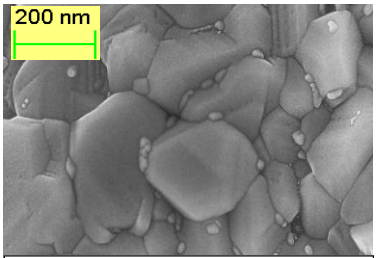

Figure 4.124(c) SEM for YP3

Figure 4.124 SEM Micrographs of $BaCo_xCd_xFe_{12-2x}O_{19}$ Ferrites (YP1 (x = 0.0), YP2 (x = 0.6), YP3 (x = 1.0)).

The Figure 4.124(a) shows the fine grain structure with high porosity in YP1 results in a material with a high density of grain boundaries, which significantly influences its dielectric and conductive properties.

The Figure 4.124(b) i.e YP2, the coarse grains and dense grain boundary network in YP2 provide a robust and interconnected microstructure, favouring high grain boundary polarization and charge storage capacity.

The Figure 4.124(c) i.e YP3, the moderate grain size and isolated grain boundaries in YP3 create a less interconnected structure. This morphology limits the grain boundary effects, leading to less charge storage and polarization compared to YP2.

4.7.2 Electrical Characterization

4.7.2.1 Dielectric constant

The Figure 4.125 illustrates the variation of the real part of the dielectric constant (ε') as a function of frequency and sample composition for $BaCo_xCd_xFe_{12-2x}O_{19}$ hexaferrites (YP1 with x = 0.0, YP2 with x = 0.6, and YP3 with x = 1.0) over the frequency range from 100 Hz to 2 MHz. In Figure 4.125(a), the YP1, dielectric constant (ε') starts at a moderate value (12,791.13) at low frequencies and decreases steadily with increasing frequency, down to 44.94 at 2 MHz. YP2 exhibits a very high dielectric constant (461,887.40) at low frequencies, which rapidly decreases as frequency increases, reaching 156.73 at 2 MHz. YP3 shows a much lower dielectric constant (66.45 at low frequencies) compared to YP1 and YP2. This stable and minimal dielectric constant is indicative of a highly ordered structure with fewer defects and grain boundaries. As the Co and Cd substitution increases (x = 1.0), the material appears to become more crystalline and less susceptible to polarization, resulting in a stable dielectric response over the entire frequency range. Beyond 10^5 Hz, all samples exhibit frequency-independent behaviour. This indicates that at higher frequencies, the charge carriers in the materials cannot respond quickly enough to the alternating electric field, leading to a stabilization of the dielectric constant. The dielectric loss (ε'') starts high (172,173.30 at low frequencies) and decreases significantly to 52.44 at 2 MHz. YP2 shows much larger losses (134630 at low frequencies), which gradually decrease to 417.53 at 2 MHz. Even at higher frequencies, YP2 still exhibits relatively high losses compared to YP1 and YP3, indicating persistent conduction or relaxation losses within the material. YP3 demonstrates minimal dielectric losses, starting with very low values (which could be attributed to inductive behaviour) at very low frequencies and stabilizing at a low value (7.97 at 2 MHz). The low ε'' across the frequency range suggests that the

substitution of Co and Cd enhances the crystallinity and reduces the number of active polarization mechanisms, leading to lower energy dissipation.

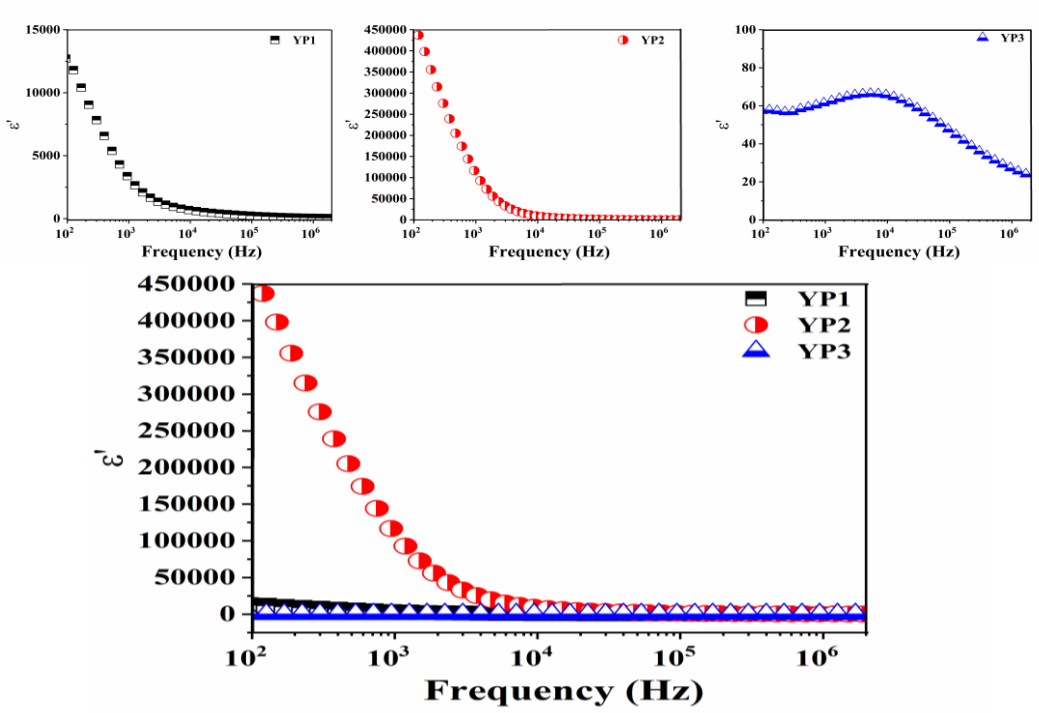

Figure 4.125(a) Dielectric Constant Dependence on Frequency in $BaCo_xCd_xFe_{12-2x}O_{19}$ (YP1 (x = 0.0), YP2 (x = 0.6), YP3 (x = 1.0)) Hexaferrites.

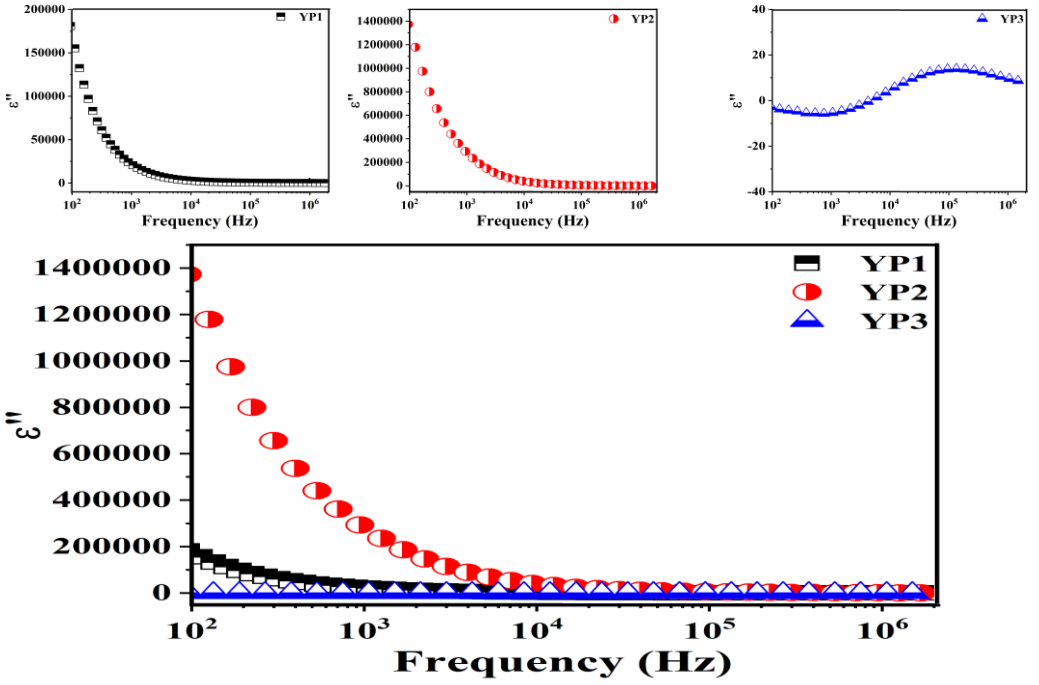

Figure 4.125(b) Dielectric Loss Dependence on Frequency in $BaCo_xCd_xFe_{12-2x}O_{19}$ (YP1 (x = 0.0), YP2 (x = 0.6), YP3 (x = 1.0)) Hexaferrites.

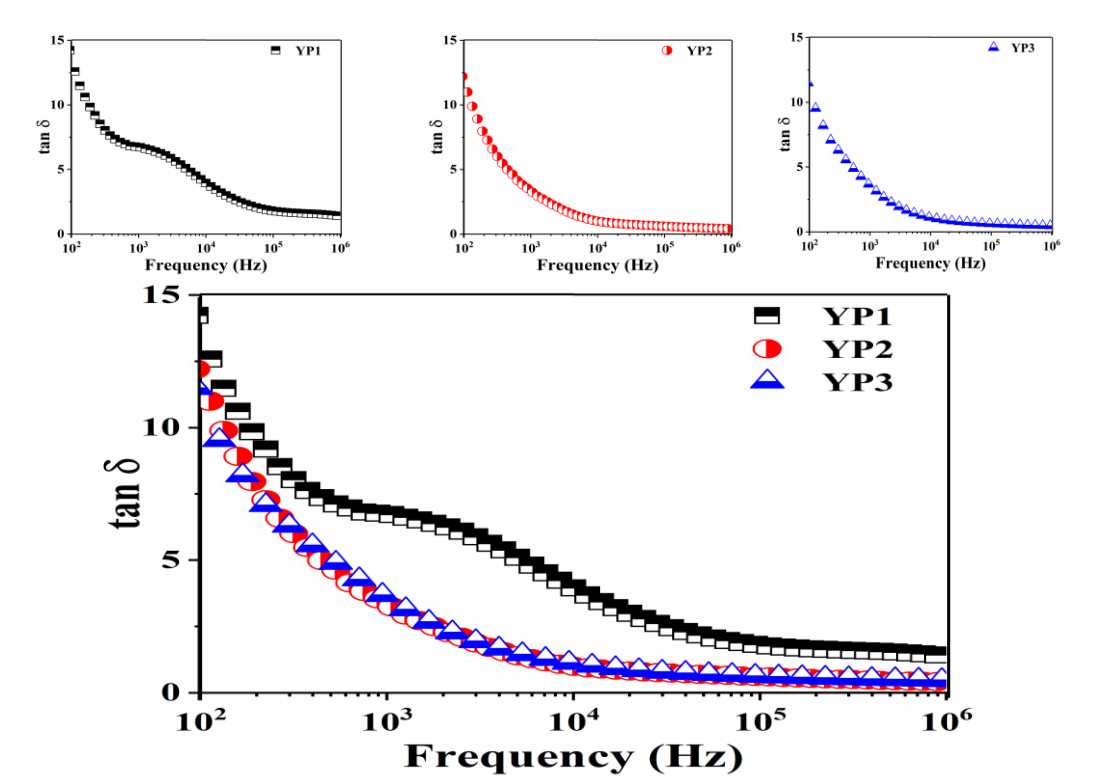

Figure 4.125(c) Dielectric Loss Tangent Dependence on Frequency in $BaCo_xCd_xFe_{12-2x}O_{19}$ (YP1 (x = 0.0), YP2 (x = 0.6), YP3 (x = 1.0)) Hexaferrites.

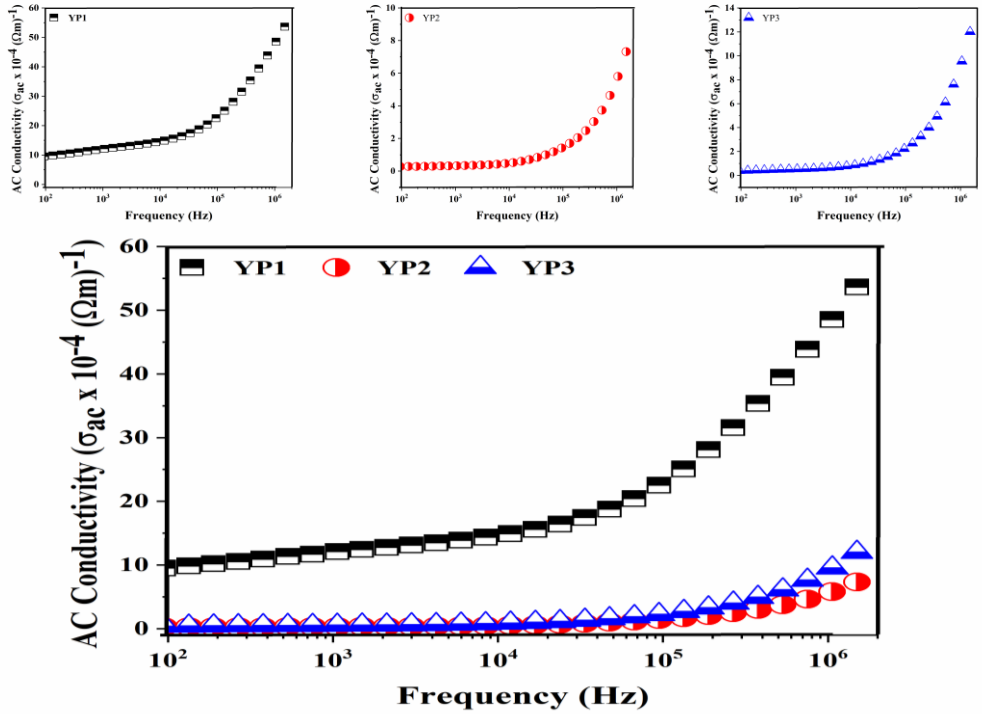

Figure 4.125(d) AC Conductivity Dependence on Frequency in $BaCo_xCd_xFe_{12-2x}O_{19}$ (YP1 (x = 0.0), YP2 (x = 0.6), YP3 (x = 1.0)) Hexaferrites.

The loss tangent (tan δ), which indicates the ratio of dielectric loss to the dielectric constant, follows a similar trend as ε". YP1 shows the highest peak for tan δ at lower frequencies, reaching a value of approximately 13 at 100 Hz. This indicates that YP1 exhibits the highest energy dissipation, likely due to the significant polarization effects occurring in the undoped structure. YP2 has a lower peak height compared to YP1, with a maximum tan δ of approximately 10. YP3 displays the lowest tan δ peak, with a maximum value of approximately 9. YP1 shows the most gradual decrease in tan δ across the frequency range, suggesting a broader distribution of relaxation times. This implies that a wide range of polarization mechanisms are contributing to the dielectric loss. YP2 shows a faster decline in tan δ with increasing frequency compared to YP1, suggesting a more limited range of relaxation processes. YP3 exhibits the sharpest drop in tan δ with frequency, indicating a narrower distribution of relaxation times. This suggests that the material has fewer active polarization mechanisms and is more resistant to energy dissipation at higher frequencies.

YP1 shows the highest conductivity (9.60×10^{-4} $\Omega \cdot m^{-1}$) at 100 Hz, increasing steadily with frequency. This high conductivity is attributed to the relatively low grain boundary resistance, allowing for effective charge transport across the material. The high grain capacitance also indicates good polarization and charge mobility within the grains. YP2 shows the lowest initial conductivity (2.72×10^{-5} $\Omega \cdot m^{-1}$), but its conductivity increases significantly at higher frequencies, reflecting the onset of a frequency-dependent conduction mechanism. The combination of lowest grain resistance and lowest grain boundary resistance suggests that charge carriers move easily within and across the grains at higher frequencies, leading to a sharp rise in conductivity. YP3 exhibits moderate conductivity (3.90×10^{-5} $\Omega \cdot m^{-1}$), which increases with frequency but remains lower than YP1. The high grain boundary resistance in YP3 limits the movement of charge carriers across the material, resulting in lower overall conductivity compared to YP1, despite having a relatively low grain resistance.

4.7.2.2 Electric modulus analysis

The real part of the electric modulus (M') reflects the material's resistive behaviour and conductivity response across different frequencies. M′ increases with increasing frequency for all samples (YP1, YP2, and YP3). This is typical in dielectric materials

where the ability of the charge carriers to follow the external electric field decreases at higher frequencies.

YP1: At 2 MHz, M′ reaches approximately 0.00942, YP2: At 2 MHz, M′ is 0.000788.

YP3: At 2 MHz, M′ reaches 0.03849, the highest among the entire sample

The higher M′ in YP3 suggests that YP3 has greater higher grain boundary resistance (R_{gb}), which could be attributed to structural in homogeneities due to Cd doping. The grain boundaries act as barriers to the flow of charge carriers, which reduces long-range mobility and increases the resistive nature of the material, which is reflected in the increasing M′ values. In YP1 and YP2, the lower grain boundary resistance allows better charge carrier mobility, resulting in lower M′ values.

M″, which represents the energy dissipation in the material, also increases with frequency in all samples. It reflects the relaxation process where the charges trapped at grain boundaries or interfaces are unable to follow the alternating electric field at higher frequencies.

YP1: M″ reaches 0.01099 at 2 MHz, YP2: M″ reaches 0.0021 at 2 MHz, YP3: M″ reaches 0.01319 at 2 MHz.

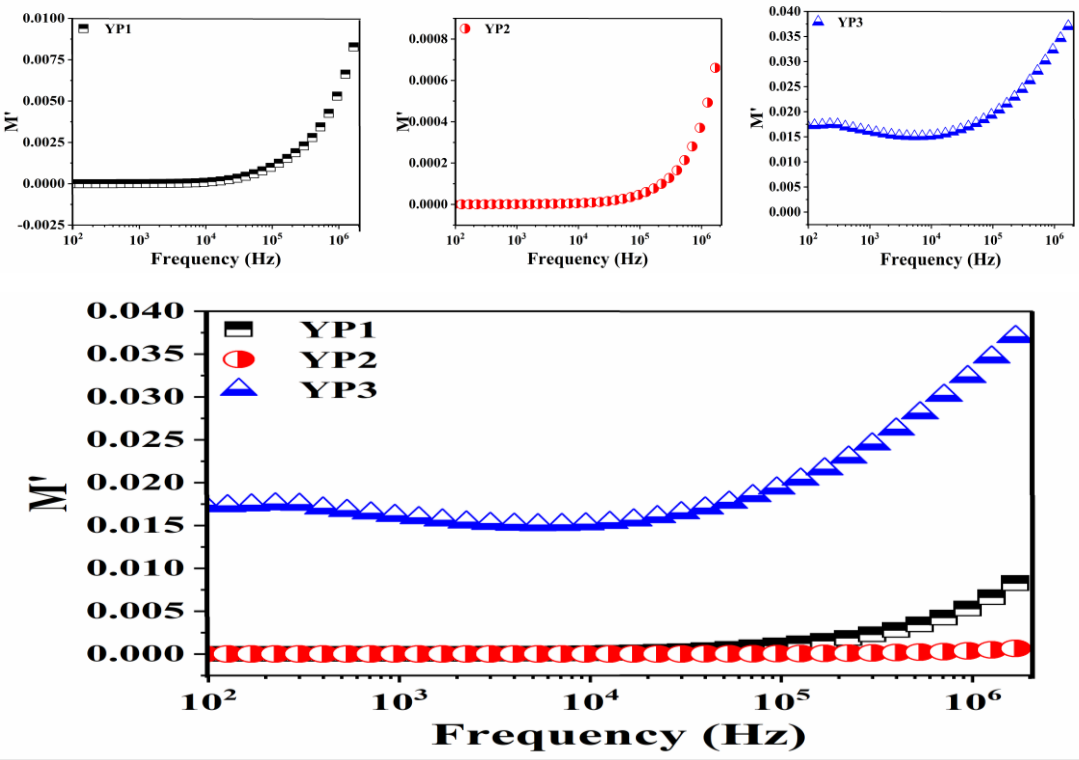

Figure 4.126 (a) Real Modulus (M′) Dependence on Frequency in $BaCo_xCd_xFe_{12-2x}O_{19}$ (YP1 (x = 0.0), YP2 (x = 0.6), YP3 (x = 1.0)) Hexaferrites

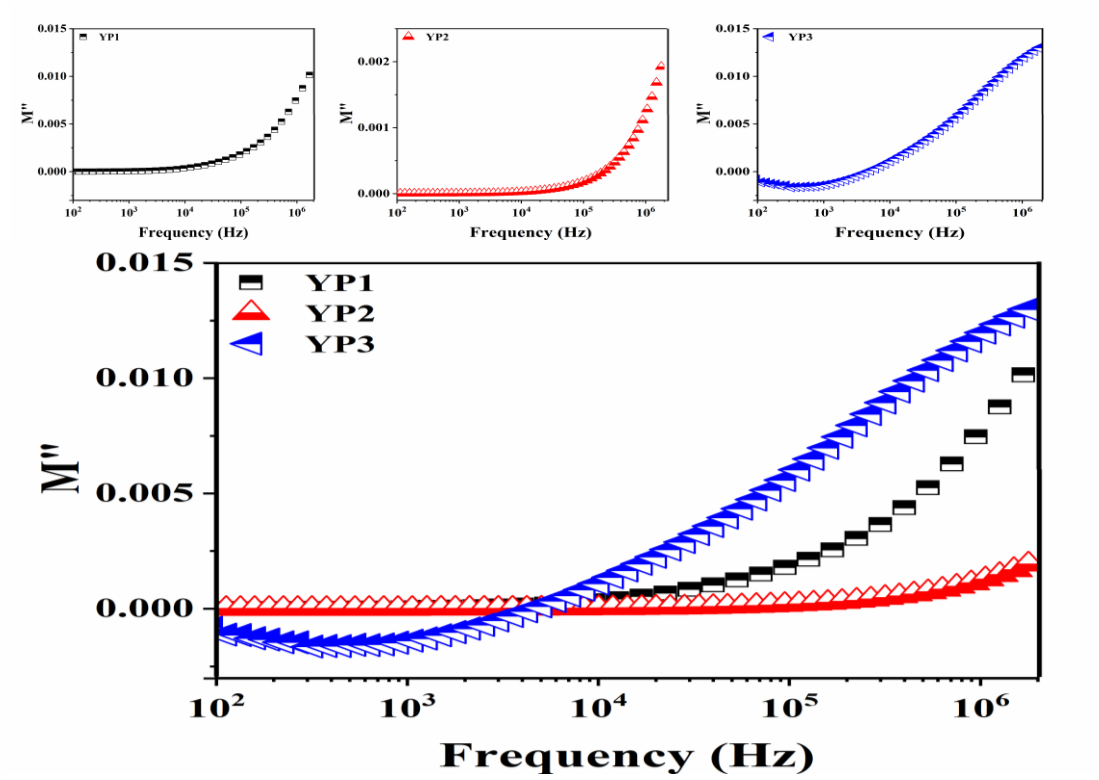

Figure 4.126(b) Imaginary Modulus (M") Dependence on Frequency in $BaCo_xCd_xFe_{12-2x}O_{19}$ (YP1 (x = 0.0), YP2 (x = 0.6), YP3 (x = 1.0)) Hexaferrites

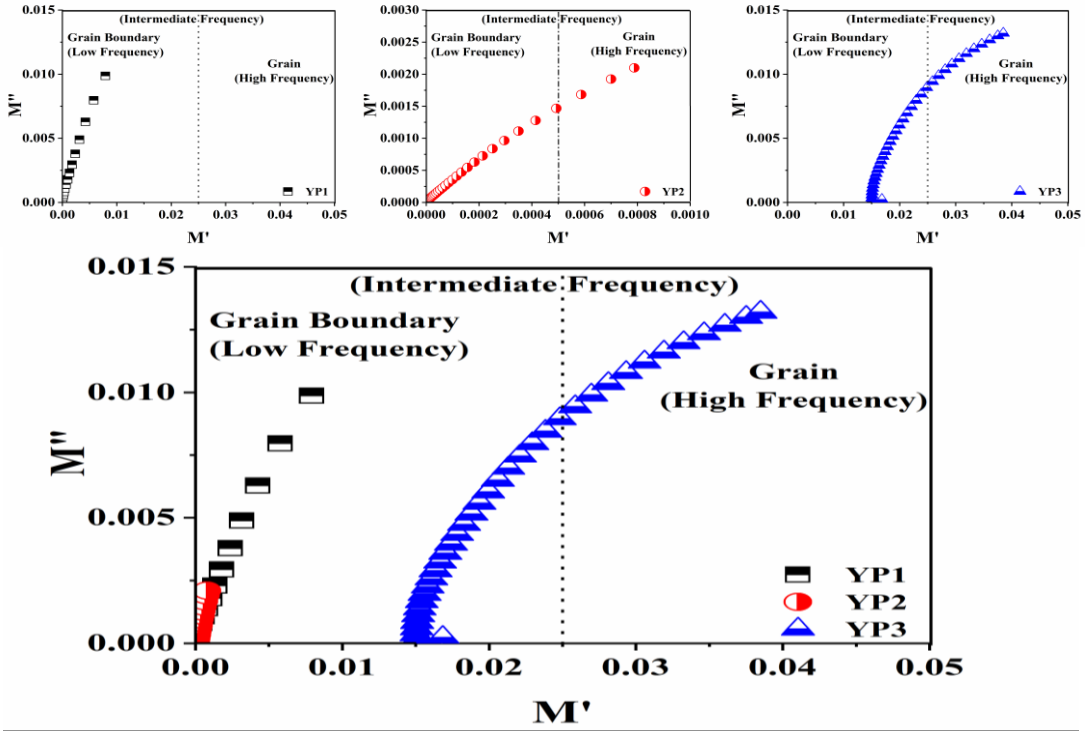

Figure 4.126(c) Cole-Cole Impedance Plots of $BaCo_xCd_xFe_{12-2x}O_{19}$ (YP1 (x = 0.0), YP2 (x = 0.6), YP3 (x = 1.0)) Hexaferrites at 900°C, 5h.

The Cole-Cole plot for YP1 shows a smaller arc compared to YP3, indicating that YP1 is more influenced by grain boundary effects, as its arc is concentrated in the low-frequency region. This suggests that the charge transport in YP1 is hindered by grain boundaries, leading to higher grain boundary resistance. YP2 exhibits a slightly smaller arc compared to YP1, indicating that grain boundary effects are still significant but slightly less pronounced than in YP1. The smaller arc suggests that while YP2 is also dominated by grain boundary effects (as it ends in the low-frequency region), it has slightly lower grain boundary resistance compared to YP1, which contributes to marginally better charge transport. The Cole-Cole plot for YP3 shows a larger arc, indicating a broader distribution of relaxation times and more contribution from the grain (bulk) region at higher frequencies. This is consistent with lower grain boundary resistance in YP3, where the bulk properties (grain effects) dominate the relaxation process as the frequency increases.

4.7.2.3 Impedance spectroscopy

The Z' values for all samples decrease with increasing frequency. This decrease is typical for dielectric materials, as the impedance tends to reduce when the material becomes more conductive at higher frequencies. The reduction in Z' suggests that at high frequencies, the grain conductivity improves due to the higher mobility of charge carriers. YP1, at low frequency (100 Hz), Z' is approximately 273,580 **Ω,** indicating significant resistive behaviour at low frequencies due to the dominance of grain boundary effects. YP2, shows lower resistive behaviour with Z' around 29,645 Ω at 100 Hz, indicating higher conductivity through grains. The Z'' values for all samples generally decrease with increasing frequency, but the trend varies depending on the frequency range and the specific sample. At low frequencies, the impedance (Z'') is higher due to grain boundary effects. At higher frequencies, Z'' decreases, indicating that the grains' conductivity starts dominating over the grain boundary contributions. YP1, at 100 Hz, Z'' is 6.64×10^3 Ω, showing significant resistive and capacitive contributions. YP2, displays even lower Z'' values (e.g., 2.96×10^3 Ω at 100 Hz), indicating efficient charge carrier mobility through grains. YP3, exhibits significantly higher Z'' values and shows a mix of inductive and resistive behaviour, indicating that grain boundaries significantly hinder charge mobility.

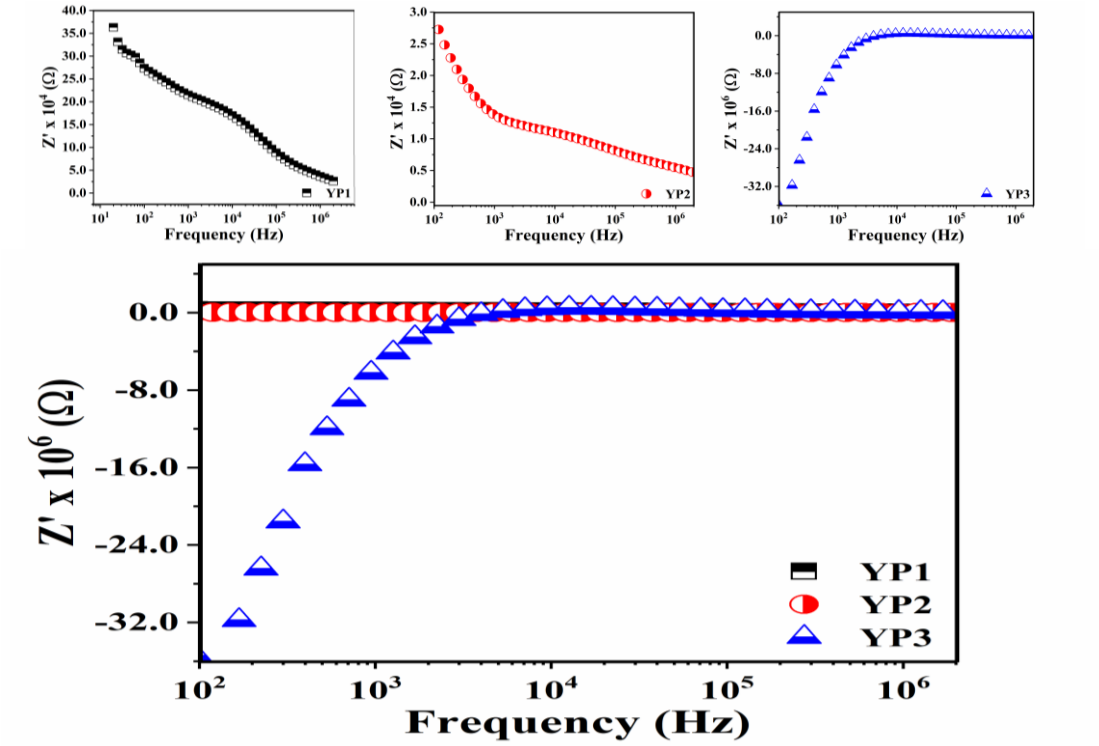

Figure 4.127(a) Real Impedance (Z′) Dependence on Frequency in $BaCo_xCd_xFe_{12-2x}O_{19}$ (YP1 (x = 0.0), YP2 (x = 0.6), YP3 (x = 1.0)) Hexaferrites.

The Cole-Cole plot (Nyquist plot) is generated by plotting Z″ (imaginary) versus Z′ (real) components of impedance. It provides insight into the relaxation behaviour, grain, and grain boundary contributions, and overall conduction mechanisms in the material. The Cole-Cole plot for YP1 shows a semicircular arc, typical of materials with Debye-like relaxation behaviour. The arc's size is moderate, indicating a balanced interaction between grains and grain boundaries. The arc's shape suggests efficient energy dissipation and a clear relaxation process. YP2's Cole-Cole plot shows a smaller semicircular arc compared to YP1, indicating lower impedance and energy dissipation. The efficient charge transport through grains results in minimal contribution from grain boundaries, leading to a sharper, smaller arc in the plot. The Cole-Cole plot for YP3 displays a large and broad arc, consistent with the high Z″ values and substantial grain boundary contributions. The plot suggests that grain boundaries dominate the relaxation behaviour, resulting in significant energy loss and a prolonged relaxation time. The large arc reflects the high resistive nature of the grain boundaries.

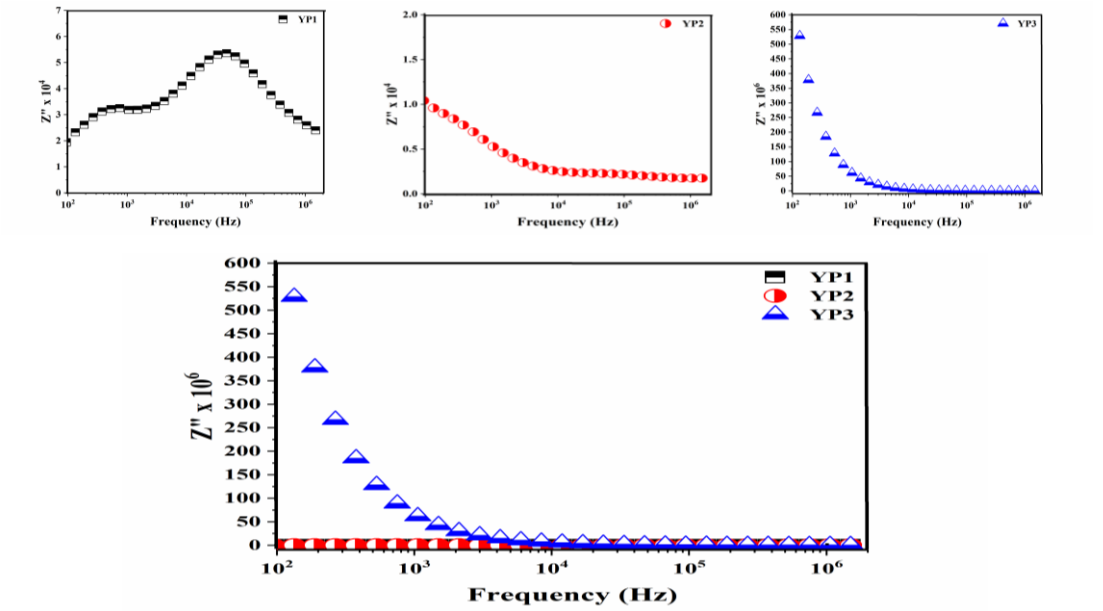

Figure 4.127(b) Imaginary Impedance (Z′) Dependence on Frequency in $BaCo_xCd_xFe_{12-2x}O_{19}$ (YP1 (x = 0.0), YP2 (x = 0.6), YP3 (x = 1.0)) Hexaferrites.

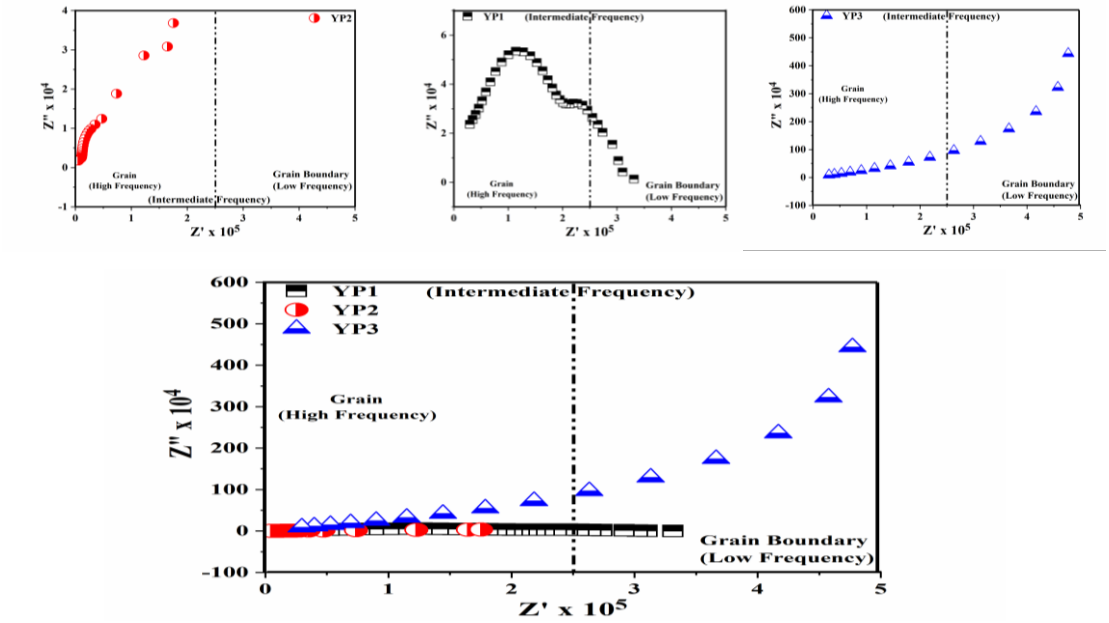

Figure 4.127(c) Cole-Cole Impedance Plots of $BaCo_xCd_xFe_{12-2x}O_{19}$ (YP1 (x = 0.0), YP2 (x = 0.6), YP3 (x = 1.0)) Hexaferrites after Heat Treatment at 900°C for 5 Hours.

4.7.2.4 Computational Impedance Simulation and Validation

Figure 4.128 illustrates the results of an analogous circuit analysis conducted on complex impedance data acquired via Electrochemical Impedance Spectroscopy (EIS) software [49].

This model precisely reflects the behaviour seen in the mixtures, as demonstrated by the strong correlation between measured and simulated/fitted curves in the images. Table 4.40 displays the resistance, and capacitance values derived from the EIS data for both grains and grain borders. These parameters measure the electrical response of the microstructural characteristics within the mixtures.

Table 4.40 Extracted Grain and Grain Boundary Parameters from EIS Modelling

Composite	R_g (MΩ)	R_{gb} (MΩ)	C_g (μF)	C_{gb} (μF)
YP1	0.211	0.018	4.400×10^5	3.935
YP2	0.005	0.013	4284.707	2.390×10^{10}
YP3	0.207	81.200	540.09	9.117

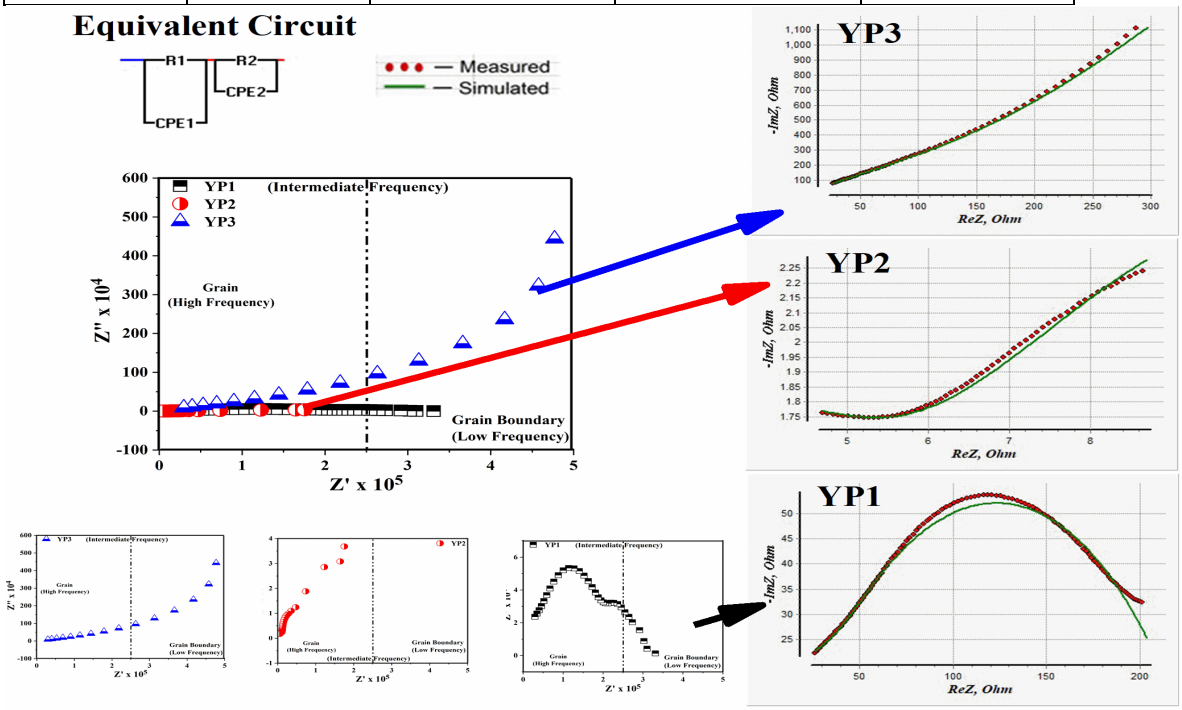

Figure 4.128 Measured and Fitted Impedance Data with Equivalent Circuit (YP1 to YP3)

4.7.2.5 Investigating the Relationship between EIS Data and Microstructure

For YP1:

R_g = 0.211 MΩ, The moderate resistance of grains suggests that the grains are relatively small but still provide sufficient connectivity. However, due to higher

porosity, there might be interruptions in the conduction paths, leading to this moderate resistance.

R_{gb} = 0.018 MΩ, The low grain boundary resistance indicates that the grain boundaries are conductive, likely due to the presence of smaller grains and higher grain boundary area. The high porosity might contribute to this, as the grain boundaries become pathways for conduction despite the interruptions within the grains themselves.

C_g = 4.4×10^5 μF, The large grain capacitance reflects that the grains, despite being small, have a high surface area and can store a significant amount of charge. This is consistent with the presence of fine grains, which provide a larger effective area for charge storage.

C_{gb} = 3.935 μF, The moderate grain boundary capacitance suggests that while grain boundaries are conductive, they are not the primary sites for polarization. This is because the grain boundaries in YP1 may not have as much stored charge as the grains themselves.

For YP2:

R_g = 0.005 MΩ, The extremely low grain resistance suggests that the grains are well-connected and larger, providing efficient conduction paths. The morphology supports this with large, continuous grains minimizing interruptions in conduction.

R_{gb} = 0.013 MΩ, The grain boundary resistance is low, indicating that the grain boundaries in YP2 are well-connected and conductive. The dense packing and fewer grain boundaries help maintain lower resistance.

C_g = 4284.707 μF, The grain capacitance is relatively small compared to YP1, consistent with larger grains having less surface area relative to volume for charge storage.

C_{gb} = 2.39×10^{10} μF, The extremely high grain boundary capacitance is a critical feature of YP2. This suggests that the grain boundaries in YP2 have a significant capacity to store charges. This is likely due to the dense, compact nature of the grain boundary regions, which facilitate polarization.

For YP3:

R_g = 0.207 MΩ, The resistance of grains is similar to YP1, suggesting that the grain connectivity is not as high as in YP2 but is still sufficient for conduction.

R_{gb} = 81.2 MΩ, The very high grain boundary resistance indicates that grain boundaries are less connected and isolated in YP3. This could be due to the presence of defects or non-continuous grain boundary networks, limiting charge transport across these boundaries.

C_g = 540.09 μF, The moderate grain capacitance correlates with the moderate grain size. The grains do not offer as much surface area for charge storage as in YP1 but are more effective than YP2.

C_{gb} = 9.117 μF, The low grain boundary capacitance indicates that the grain boundaries in YP3 are not major sites for charge storage. This further aligns with the morphology where grain boundaries are isolated, limiting their ability to store charge.

4.7.2.6 Investigating the Relationship between EIS Data and Electric Parameters

The high C_g in YP1 contributes significantly to ε′ at higher frequencies as the grains dominate the response. The relatively low R_{gb} means that grain boundaries allow charge carriers to pass through more easily, maintaining a lower dielectric constant at low frequencies compared to other samples. In YP2, the extremely high C_{gb} value causes a substantial increase in ε′ at low frequencies due to grain boundary polarization. The low R_g and R_{gb} values ensure efficient charge transport, which sustains ε′ even as frequency increases. YP3 has a moderate R_g and very high R_{gb}, meaning the grain boundaries are less conductive, leading to lower ε′ at low frequencies compared to YP2. However, the moderate C_g value indicates that grains contribute modestly to the dielectric constant at higher frequencies.

With R_g relatively high and R_{gb} low, ε″ in YP1 is influenced mainly by the grain boundaries at low frequencies. The low R_{gb} facilitates charge movement, resulting in lower dielectric losses at low frequencies. The large C_g value can contribute to moderate ε″ at higher frequencies when grains dominate. The extremely high C_{gb} value and low resistances (R_{gb}) in YP2 lead to very high ε″ at low frequencies due to the grain boundary polarization effects. The low resistances allow charge carriers to move freely, increasing losses. As frequency rises, the grain contributions (with a smaller C_g) take over, decreasing ε″. The high R_{gb} in YP3 causes charge carriers to be trapped at grain boundaries, leading to increased ε″ at low frequencies compared to YP1 but still lower than YP2. At higher frequencies, the moderate C_g value keeps ε″ from rising sharply as the grain boundaries become less influential.

YP1, has the highest grain resistance (0.211 MΩ), which indicates higher resistance to charge carrier motion within the grains. This corresponds to moderate M′ and M″ values. YP2, has the lowest grain resistance (0.005 MΩ), suggesting more efficient charge transport through the grains. This correlates with the lower M′ and M″ values. YP3, has the highest grain boundary resistance (81.2 MΩ), indicating that grain boundaries in YP3 act as significant barriers to charge movement. This is reflected in the highest M′ and M″ values, as well as the largest arc in the Cole-Cole plot. YP1, shows moderate grain boundary resistance (0.018 MΩ), suggesting that grain boundaries do not act as major barriers in YP1, reflected in the moderate relaxation and energy loss behaviour. YP2, has the lowest grain boundary resistance (0.013 MΩ), indicating that grain boundaries do not significantly hinder charge transport, which is why M′ and M″ are lower in YP2 compared to YP1 and YP3. YP1, has the highest grain capacitance (4.4×10^{5} μF), indicating that YP1 can store more charge within its grains. This contributes to its moderate M′ values at low frequencies. YP2, has the highest grain boundary capacitance (2.39×10^{10} μF), which correlates with better charge storage at grain boundaries, reducing energy dissipation and explaining the lower M″ values. YP1, has the lowest grain boundary capacitance (3.935 μF), indicating less charge storage at grain boundaries, contributing to moderate energy dissipation.

YP1 has moderate grain resistance (R_g) and high capacitance (C_g), resulting in balanced behaviour between resistive and capacitive elements. This explains the high initial Z′ values and the subsequent decline as frequency increases. YP2's lower grain resistance (R_g = 0.005 MΩ) allows for better conduction, keeping Z′ and Z″ lower across frequencies. The values suggest that grains dominate the conduction behaviour more effectively than grain boundaries. YP3's high R_{gb} value causes significant resistive and reactive impedances at low frequencies, making grain boundaries the dominant factor. This explains the large negative Z′ values initially and the gradual reduction as frequency increases. YP1 and YP2 show a mix where the grain boundaries play a lesser role due to lower R_{gb}, leading to a reduction in impedance and reactance as the frequency increases, showcasing efficient energy dissipation and charge movement primarily through the grains.

4.7.3 Magnetic Analysis

The impact of Co^{2+} and Cd^{3+} substitution in $BaCo_xCd_xFe_{12-2x}O_{19}$ PANI Hexaferrite significantly influence the magnetic properties of the material. This substitution changes the overall magnetic characteristics, including saturation magnetization (M_s), coercivity (H_c), and remanent magnetization (M_r), as well as the anisotropy field (H_a).

Magnetic Saturation (M_s): YP1 has the highest magnetic saturation (M_s) value of 45.92, indicating a strong magnetic response. The high density of fine grains increases the grain boundary density, enhancing domain wall movement and allowing more magnetic domains to align in response to an external magnetic field, which explains the higher M_s. YP2 has the lowest M_s value of 28.92. The coarse grain structure results in fewer grain boundaries compared to YP1, reducing the number of domain walls and magnetic domains available for alignment, thus lowering the overall M_s. YP3 has an intermediate M_s value of 42.92. The moderate grain size and isolated grain boundaries offer a balance between the high domain wall density of YP1 and the low density of YP2, leading to a moderate magnetic response.

Coercivity (H_c): YP1 has the highest coercivity (H_c) value of 5382.77. The fine grains and high grain boundary density contribute to greater resistance against domain wall movement, requiring a stronger field to demagnetize the material. The H_c value of YP2 is significantly lower than YP1 (598.09). The larger grain size and compact structure result in fewer pinning centers, allowing domain walls to move more freely, thus requiring less external field for demagnetization. YP3 has the lowest coercivity value (208.48). The isolated grain boundaries result in minimal resistance to domain wall movement, making it easier to demagnetize the material with a weaker external field.

Anisotropy Field (H_a): The anisotropy field (H_a) of YP1 is also the highest (15.96 kOe). The fine grains and dense grain boundaries lead to greater structural anisotropy, increasing the energy required for domain alignment along specific axes. YP2 has a moderate anisotropy field of 10.89 kOe. The lower grain boundary density reduces the structural anisotropy compared to YP1, requiring less energy for domain alignment. YP3 has the lowest Ha value (9.32 kOe). The moderate grain size and lack of connectivity among grain boundaries result in a lower structural anisotropy, reducing the energy required for domain alignment.

Remanence (M_r): YP1 has a relatively high remanence value (23.45). The numerous grain boundaries serve as pinning centres for magnetic domains, allowing a significant portion of domains to remain aligned even after the external field is removed. YP2 shows a moderate M_r value (10.61). The fewer grain boundaries mean fewer pinning centres, leading to lower retention of aligned domains after the external field is removed. YP3 shows a moderate M_r value of 13.29, which is higher than YP2 but lower than YP1. The isolated grain boundaries provide limited pinning, allowing some domains to remain aligned post-external field removal, but not as effectively as in YP1.

M_r/M_s Ratio: The ratio of M_r/M_s (0.511) is the highest among the samples, indicating a higher retention of magnetization due to the fine grain structure and high density of grain boundaries acting as effective pinning sites. M_r/M_s ratio is 0.367, which is lower than YP1 in YP2. The lower ratio reflects the reduced ability of the coarse grains and fewer grain boundaries to retain magnetization. The M_r/M_s ratio of YP3 is the lowest (0.307). The moderate grain size and isolated grain boundaries make it less effective at retaining magnetization, reflecting the limited pinning effect.

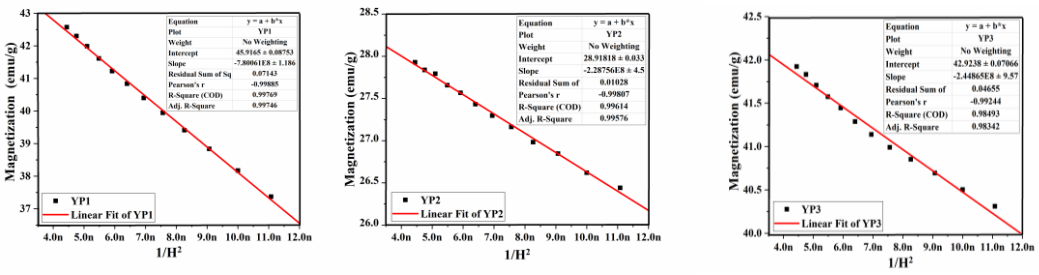

Figure 4.129 M_s versus 1/ H^2 plots for all hexaferrite samples.

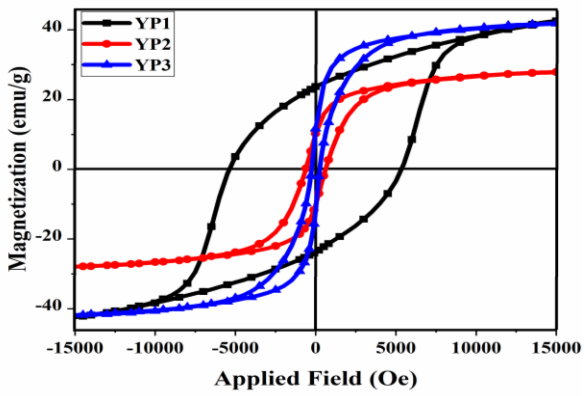

Figure 4.130 Hysteresis loops of Y1, Y2 and Y3 hexaferrite.

Table 4.41 Magnetic parameters M_s, H_c, H_a, M_r and M_r/M_s value of all hexaferrite samples.

Composite	M_s	H_c	H_a=sqrt(-15B)	H_a (kOe)	M_r	M_r/M_s
YP1	45.92	5382.77	15963.40	15.96	23.45	0.511
YP2	28.92	598.09	10892.97	10.89	10.61	0.367
YP3	42.92	208.48	9321.61	9.32	13.29	0.307

4.7.4 Electromagnetic Characteristics

4.7.4.1 Complex permeability and complex permittivity

The figures 4.131 illustrate the frequency dependence of complex permittivity (ε′, ε″) and complex permeability (μ′, μ″) for the compositions YP1 to YP3. These variations are a direct result of Co-Cd doping in $BaCo_xCd_xFe_{12-2x}O_{19}$ / PANI. The ε′ values for YP1 are the lowest among the three, starting at around 5.9 at lower frequencies and gradually decreasing to around 5.1 at higher frequencies (around 12 GHz). There is a slight dip at around 10 GHz. The ε′ values for YP2 are the highest, starting at approximately 6.9 and peaking at around 7.7 near 10 GHz, followed by a moderate decrease at higher frequencies. The ε′ values for YP3 lie between YP1 and YP2, starting around 6.4, and exhibit a dip around 10 GHz, similar to YP1, but with a smaller range of variation. YP1 displays a relatively stable trend. The values of ε″ gradually decrease from around 1.18 to 0.56 over the frequency range from 8 to 12 GHz. There is no sharp peak or significant resonance, indicating stable energy dissipation across the range. YP2 shows significant variations. It starts at 0.49, increases and exhibits a pronounced small peak near 9.5 GHz then again decrease and reached upto 0.0. Again start sharply rises to around 1.35 near 10.5 GHz, and then continues to rise more gradually toward higher frequencies, reaching up to 1.7 at 12 GHz. The sharp rise at 10.5 GHz is indicative of strong dielectric loss or energy dissipation, potentially due to a relaxation or resonance effect around this frequency. YP3 also demonstrates interesting behaviour but with much less energy dissipation compared to YP2. The trend starts near 0.99, decreases steadily, even dipping into negative values near 11 GHz (indicating possible anomalous loss mechanisms), and continues decreasing toward the end of the frequency range. The μ′ values for YP1 show a steady increase from approximately 0.24 at 8 GHz to around 0.89 at 12 GHz, with a slight dip around 10 GHz. This suggests that YP1 undergoes a gradual

enhancement in magnetic response as frequency increases, with some magnetic disturbance near 10 GHz. YP2 exhibits a relatively stable trend across the frequency range, starting at around 0.56 and gradually rising to about 0.77 at 12 GHz. There is a very slight dip between 9 and 10 GHz, but the trend is overall smooth with no significant peaks or anomalies. YP3 starts around 0.47 at 8 GHz and increases steadily, reaching around 0.75 at 12 GHz. The trend follows a relatively smooth path but with a small dip near 10 GHz, similar to YP1. YP1 shows a small, but distinct, peak in magnetic loss around 10 GHz. Starting from a low value around 0.07 at 8 GHz, it rises to about 0.34 at 10 GHz, after which it gradually decreases and flattens out toward higher frequencies. YP2 also has a notable peak near 10 GHz, though smaller than YP1's. It rises from around 0.28 at 8 GHz, peaks at around 0.29 at 10 GHz, and then slowly decreases, flattening out toward higher frequencies similar to YP1. YP3 shows a different behavior, with relatively higher μ″\mu"μ″ values compared to YP1 and YP2 across the frequency range. It starts at around 0.34 at 8 GHz and remains more stable, with a gradual increase to around 0.45 at 12 GHz. There is no sharp peak in magnetic losses like in YP1 or YP2, indicating more stable dissipation across the entire frequency range.

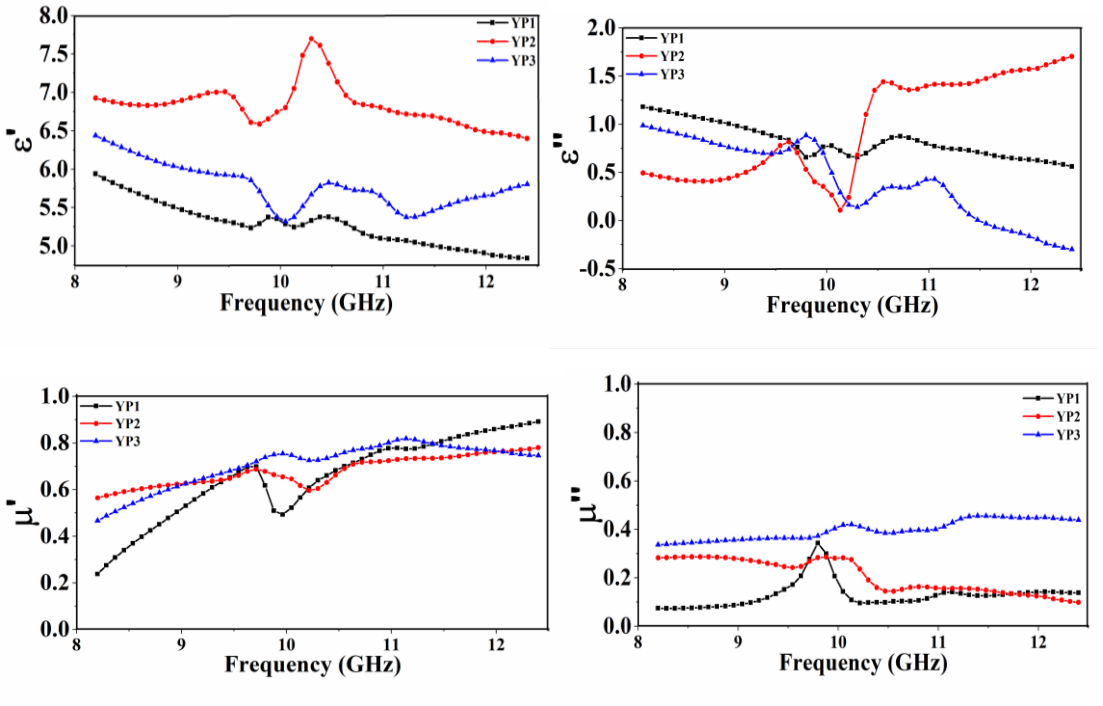

Figure 4.131 Complex permittivity and permeability versus frequency plots for $BaCo_xCd_xFe_{12-2x}O_{19}$ / PANI.

4.7.4.2 Microwave absorption and Quarter Wavelength Mechanism in $BaCo_xCd_xFe_{12-2x}O_{19}$ / PANI

The YP1 composite demonstrates significant reflection loss (REL) performance at various thicknesses, and the optimal absorption occurs at a thickness of 4.4 mm, where a maximum REL of -36.34 dB is achieved at a matching frequency of 10.05 GHz. This is the highest REL observed for YP1, reflecting its strong absorption capacity at this thickness. Interestingly, the frequency band for REL > -20 dB is quite narrow, spanning from 9.97 to 10.12 GHz (a bandwidth of 0.15 GHz), indicating focused absorption around this frequency range. As the thickness decreases to 3.9 mm, YP1 still maintains strong absorption, with an REL of -34.31 dB at 9.71 GHz. At this thickness, YP1 shows a broader frequency band for REL > -10 dB, ranging from 9.3 to 10.99 GHz with a bandwidth of 1.69 GHz. The frequency band for REL > -20 dB is 0.21 GHz (from 9.58 to 9.79 GHz). As the thickness increases from 4.4 mm to 5.1 mm, the maximum REL decreases to -25.36 dB at 8.95 GHz, with a frequency band for REL > -10 dB ranging from 8.62 to 9.34 GHz. At 6.1 mm, the REL further decreases to -20.54 dB, showing that while YP1 can still absorb efficiently at higher thicknesses, the absorption capacity decreases as the material gets thicker. This trend aligns with the quarter-wavelength mechanism, where the optimal absorption often shifts as the material thickness changes.

YP2 shows excellent absorption performance, with the maximum REL occurring at a thickness of 3.2 mm, where an REL of -55.54 dB is achieved at 10.56 GHz. This is the highest observed REL among the YP composites. The frequency band for REL > -10 dB spans from 8.96 to 12.41 GHz, offering a wide bandwidth of 3.45 GHz. Additionally, the frequency band for REL > -20 dB is from 10.0 to 11.06 GHz (a bandwidth of 1.06 GHz), showcasing efficient absorption over a wide frequency range. The BTR at this thickness is 2.91E-03, and the PBW is 32.67%, indicating outstanding performance for EMI shielding applications. At a slightly lower thickness of 3.0 mm, YP2 still demonstrates strong absorption, with an REL of -35.66 dB at 11.31 GHz, and a bandwidth for REL > -10 dB that is narrower compared to 3.2 mm. This behaviour demonstrates how the material's absorption efficiency is highly dependent on the thickness, with thinner layers providing slightly different performance across the frequency range.

The YP3 composite also performs very well, with a maximum REL of -48.79 dB at 10.89 GHz when the thickness is 3.0 mm. The frequency band for REL > -10 dB spans from 10.65 to 11.69 GHz, showing an absorption bandwidth of 1.04 GHz. At this thickness, the frequency band for REL > -20 dB is from 10.39 to 11.42 GHz, with a bandwidth of 1.03 GHz, indicating focused, high-efficiency absorption over this range. At thinner thicknesses, such as 2.8 mm, YP3 still performs well, with an REL of -32.19 dB at 11.47 GHz. The bandwidth for REL > -10 dB at this thickness is 1.08 GHz, slightly narrower than at 3.0 mm. As thickness increases beyond 3.0 mm, the REL decreases, and the absorption efficiency becomes slightly less pronounced, although YP3 still maintains strong absorption across a wide frequency range.

YP1 demonstrates optimal absorption at 4.4 mm with a maximum REL of -36.34 dB, but it still performs well across a wide range of thicknesses, maintaining strong absorption at different frequencies, which makes it versatile for electromagnetic shielding. YP2 shows the highest absorption capacity, reaching -55.54 dB at 3.2 mm, making it ideal for lightweight applications that require thin materials with high absorption. YP3 offers a balance between thickness and absorption performance, with its maximum REL of -48.79 dB occurring at 3.0 mm, providing strong broadband absorption.

According to the data, the quarter-wavelength criterion for composition YP1 is observed at thicknesses ranging from 3.5 mm to 10.0 mm, with a -10 dB bandwidth varying from 0.26 GHz to 1.69 GHz. Maximum REL values between -12.89 dB and -36.34 dB are recorded, with the -20 dB bandwidth ranging from 0.03 GHz to 0.24 GHz. As illustrated in Figure YP1(a), the reflection loss peaks for YP1 occur at 9.71 GHz for thicknesses of 3.5 mm, 3.9 mm, and 4.0 mm. Similar peaks are observed at higher frequencies, such as 10.05 GHz at 4.4 mm, with a notable decrease in peak height as thickness increases, as shown in Figure YP1(c). As shown in Figures YP1(a), YP1(e), YP1(g), YP1(i) and YP(k) in the higher thickness range (3.9 mm to 4.2 mm, 6.1 mm to 6.9 mm, 7.0 mm to 7.8 mm, 8.3 mm to 9.1 mm and 9.2mm to 10.00 mm respectively), the REL peaks shift toward lower frequencies, with peak heights gradually decreasing. This behaviour is consistent with the quarter-wavelength mechanism, where increasing thickness results in a corresponding shift in peak absorption to lower frequencies. In Figure (a and b) of YP2, as thickness

increases from 2.6 mm to 3.4 mm, peaks shift to lower frequencies. For the 2.8 mm thickness, the peak absorption occurs at a higher frequency, close to 12.3 GHz. As thickness increases to 3.4 mm, the peak shifts towards a lower frequency, around 10 GHz. In Figure (c and d) of YP2, as the thickness increases from 3.5 mm to 4.3 mm, the absorption peaks shift even further towards lower frequencies and also height of peak reduces as thickness increase. In Figure (a and b) for YP3, as the thickness increases from 2.1 mm to 2.9 mm, the absorption peaks shift to lower frequencies from 12.5 GHz to 11 GHz. In Figure (c and d) for YP3, peak shifting towards lower frequencies continues as thickness increases from 3.0 mm to 3.8 mm and height of peak also reduces as thickness increase. The 3.0 mm material reaches close to -20 dB (99% absorption), while the 3.8 mm material has a shallower peak around 10 dB (90% absorption). The absorption peaks shift even further towards lower frequencies as thickness increases from 3.9 mm to 4.7 mm as shown in Figure (e and f) for YP3. The peak height continues to decrease as thickness increases.

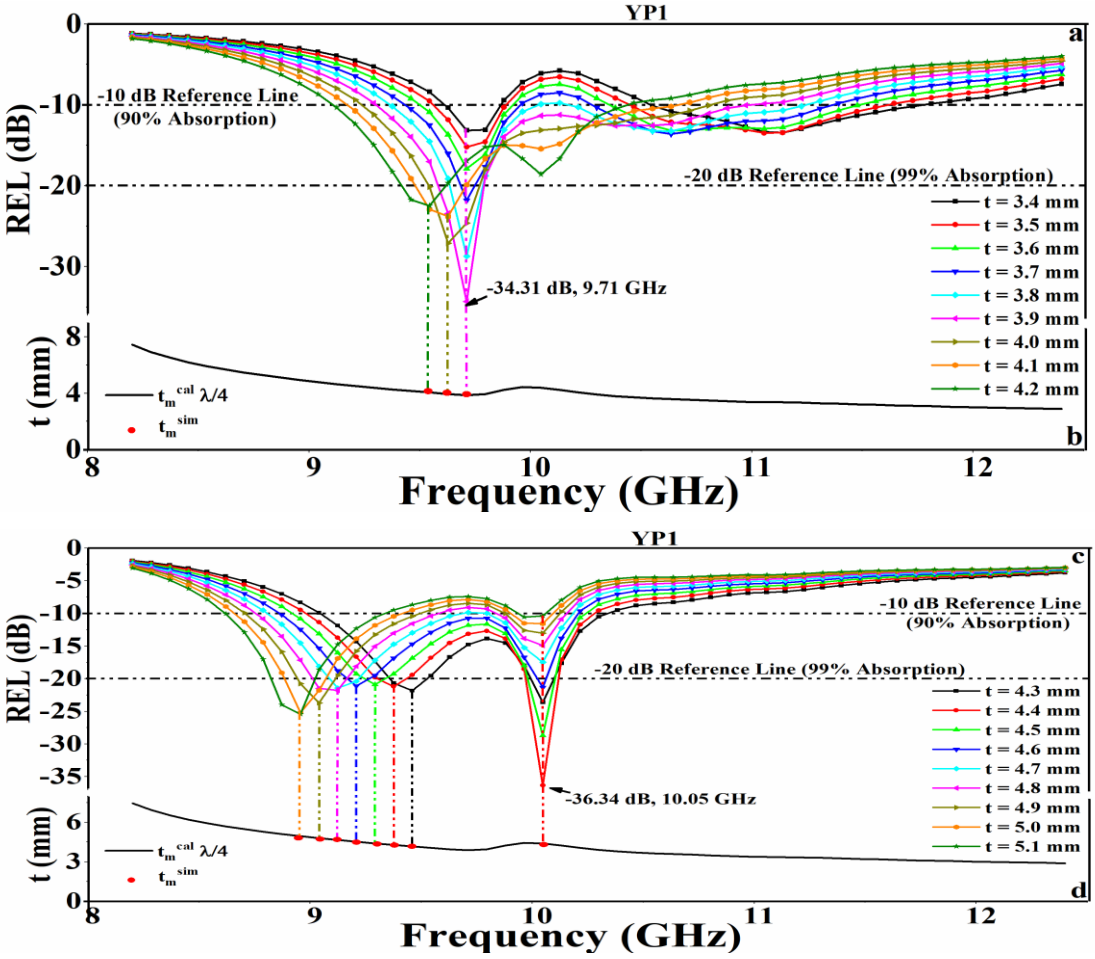

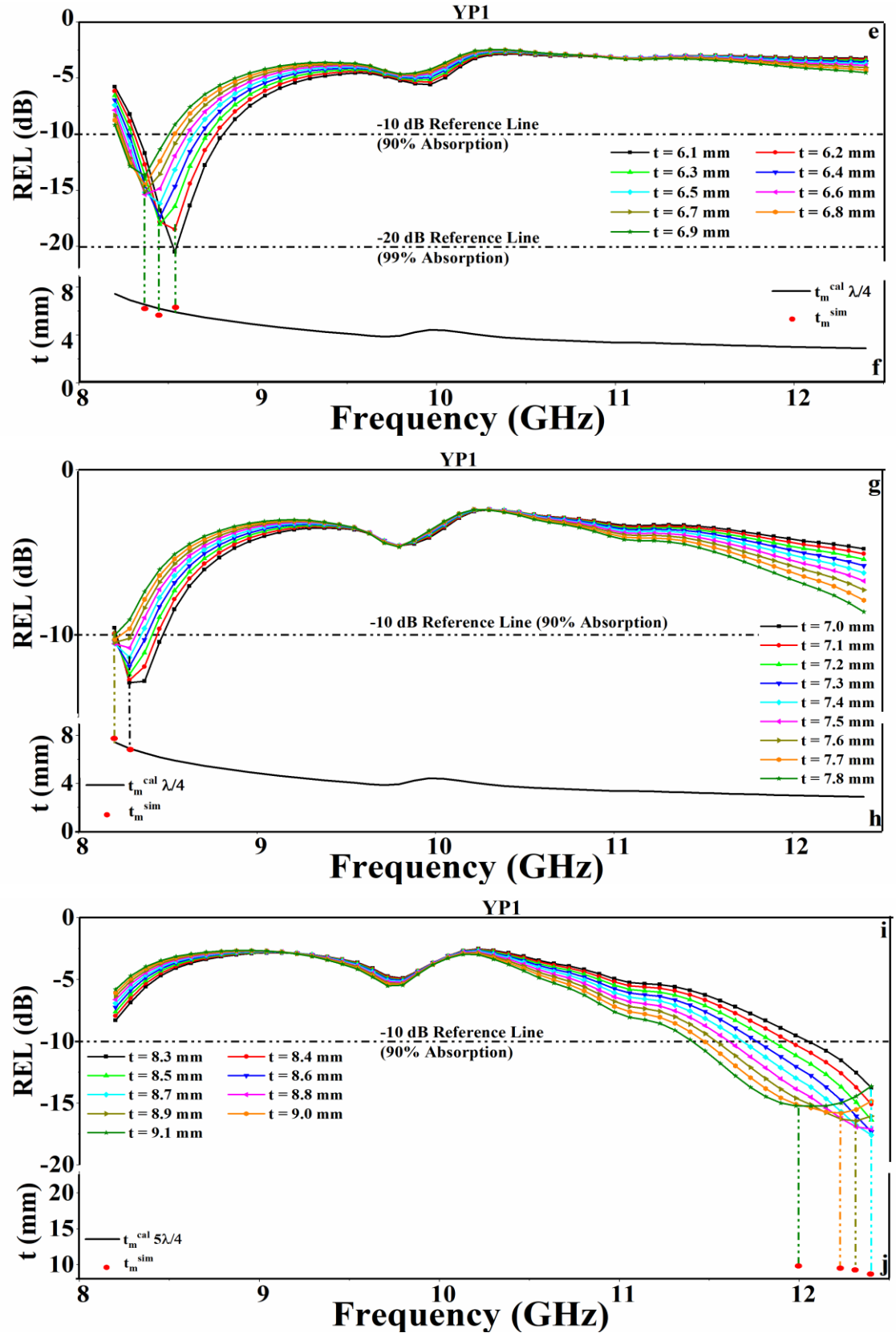
YP1
e
REL (dB)
-10 dB Reference Line
(90% Absorption)
-20 dB Reference Line
(99% Absorption)
t = 6.1 mm
t = 6.2 mm
t = 6.3 mm
t = 6.4 mm
t = 6.5 mm
t = 6.6 mm
t = 6.7 mm
t = 6.8 mm
t = 6.9 mm
t (mm)
t_m^{cal} λ/4
t_m^{sim}
f
Frequency (GHz)
YP1
g
REL (dB)
-10 dB Reference Line (90% Absorption)
t = 7.0 mm
t = 7.1 mm
t = 7.2 mm
t = 7.3 mm
t = 7.4 mm
t = 7.5 mm
t = 7.6 mm
t = 7.7 mm
t = 7.8 mm
t (mm)
t_m^{cal} λ/4
t_m^{sim}
h
Frequency (GHz)
YP1
i
REL (dB)
-10 dB Reference Line
(90% Absorption)
t = 8.3 mm
t = 8.4 mm
t = 8.5 mm
t = 8.6 mm
t = 8.7 mm
t = 8.8 mm
t = 8.9 mm
t = 9.0 mm
t = 9.1 mm
t (mm)
t_m^{cal} 5λ/4
t_m^{sim}
j
Frequency (GHz)

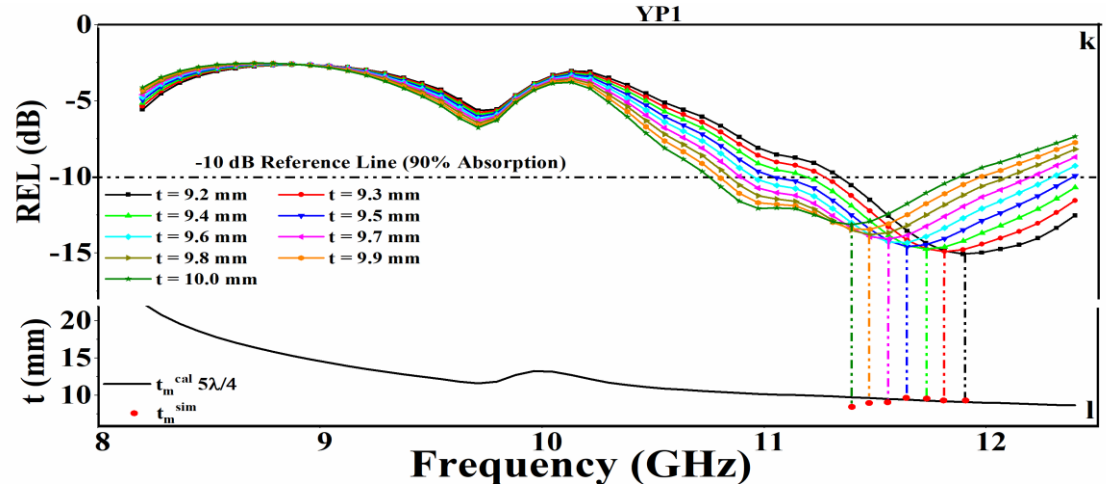

Figure 4.132 REL versus frequency for different thickness (YP1) and calculate thickness versus frequency for $BaCo_xCd_xFe_{12-2x}O_{19}$ / PANI

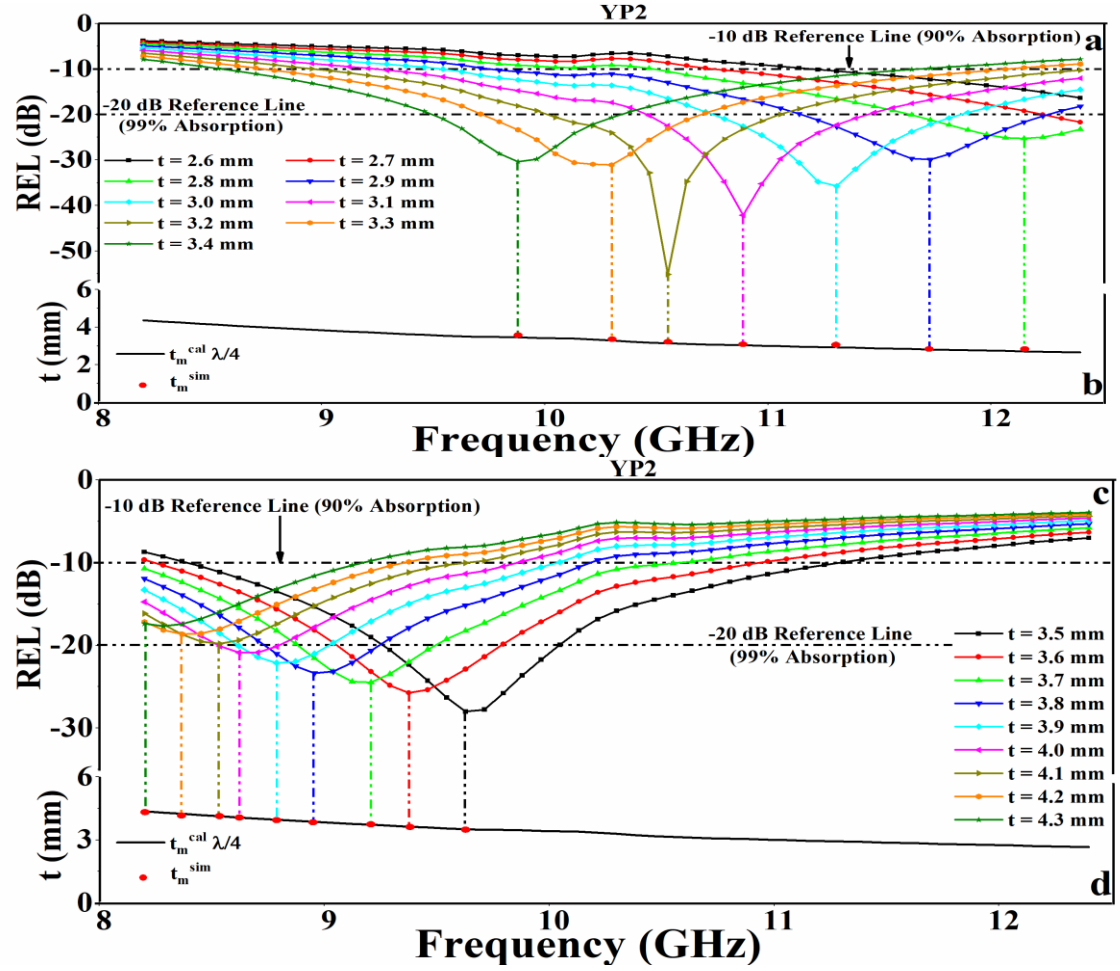

Figure 4.133 REL versus frequency for different thickness (YP2) and calculate thickness versus frequency for $BaCo_xCd_xFe_{12-2x}O_{19}$ / PANI

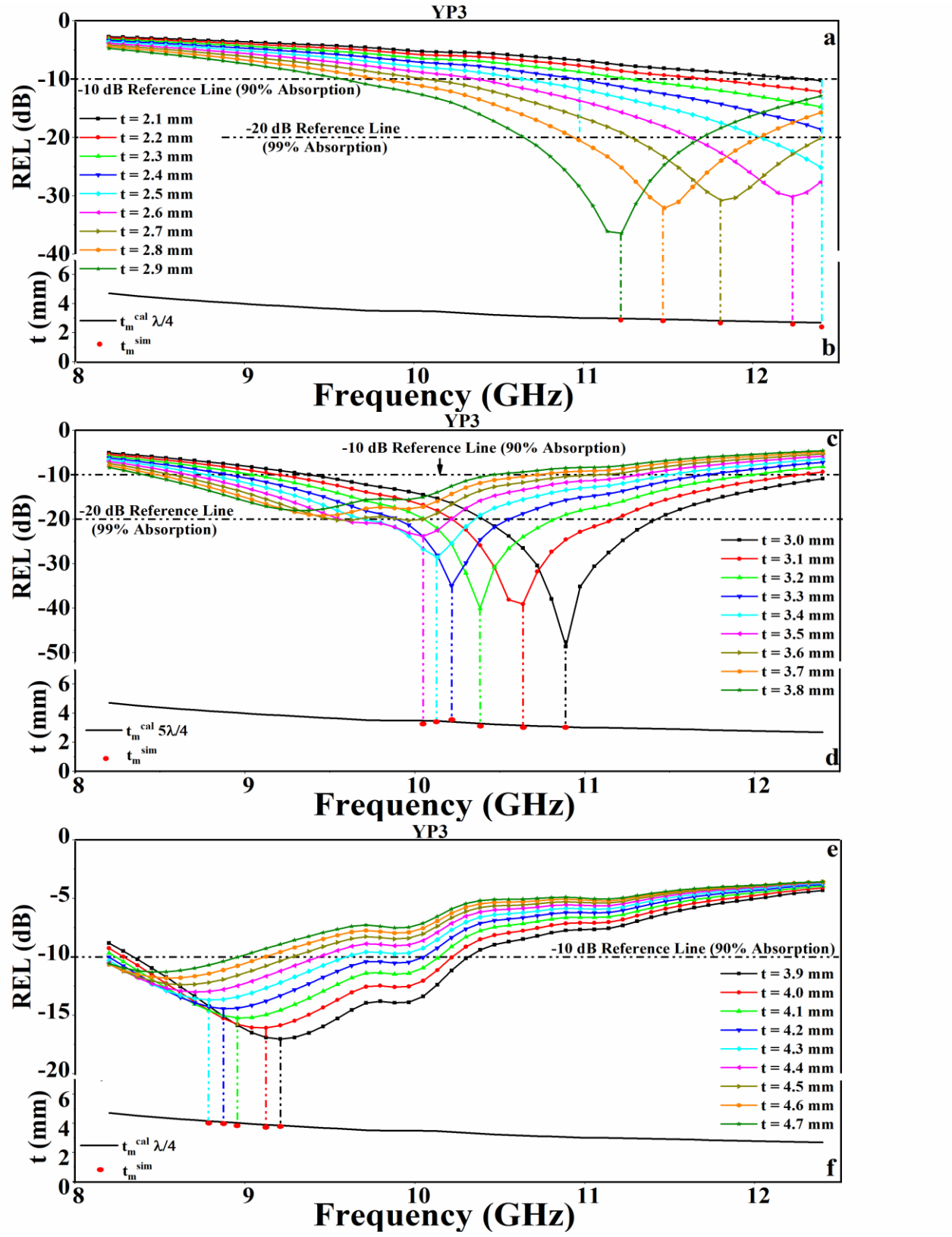

Figure 4.134 REL versus frequency for different thickness (YP3) and calculate thickness versus frequency for $BaCo_xCd_xFe_{12-2x}O_{19}$ / PANI

Table 4.42 REL with matching thickness/frequency, BW, and PBW for $BaCo_xCd_xFe_{12-2x}O_{19}$ (YP1 to YP3).

Sample Name	Matching Thickness (mm)	Maximum REL (dB)	Matching frequency (GHz)	Frequency Band for REL > -10 dB (GHz)	Band width for RL > -10 dB (GHz)	Frequency Band REL > -20 dB (GHz)	Bandwidth for REL > -20 dB (GHz)	BTR	PBW (%)
YP1	3.5	-15.15	9.71	9.56-9.88	0.32	---	-	2.90E-04	3.30
	3.9	-34.31	9.71	9.3-10.99	1.69	9.58-9.79	0.21	1.27E-03	17.40
	4	-26.93	9.63	9.24-10.81	1.57	9.53-9.77	0.24	1.18E-03	16.30
	4.2	-22.516	9.54	9.108-10.45	1.342	9.41-9.62	0.21	1.01E-03	14.07
	4.3	-21.87	9.46	9.05-10.35	1.3	9.35-9.52	0.17	9.68E-04	13.74
	4.4	-21.21	9.38	8.98-10.28	1.3	9.3-9.43	0.13	9.60E-04	13.86
	4.4	-36.34	10.05	---	-	9.97-10.12	0.15	1.01E-04	1.49
	4.5	-20.82	9.29	8.92-10.24	1.32	9.24-9.34	0.1	9.63E-04	14.21
	4.6	-21.14	9.21	8.86-10.21	1.35	9.17-9.27	0.1	9.73E-04	14.66
	4.7	-21.43	9.12	8.81-9.67	0.86	9.08-9.22	0.14	6.44E-04	9.43
	4.9	-23.71	9.04	8.71-9.49	0.78	8.94-9.12	0.18	5.78E-04	8.63
	5.1	-25.36	8.95	8.62-9.34	0.72	8.82-9.02	0.2	5.26E-04	8.04
	6.1	-20.54	8.54	8.33-8.81	0.48	8.52-8.55	0.03	3.22E-04	5.62
	6.3	-18.04	8.45	8.29-8.72	0.43	---	-	2.83E-04	5.09
	6.6	-15.29	8.37	8.24-8.61	0.37	---	-	2.37E-04	4.42
	7	-12.89	8.28	8.21-8.47	0.26	---	-	1.60E-04	3.14
	8.7	-17.56	12.4	---	-	---	-	-	-
	9.2	-15.12	11.9	---	-	---	-	-	-
	9.6	-14.58	11.64	11.05-12.39	1.34	---	-	3.06E-04	11.51
	9.8	-13.79	11.47	10.84-12.19	1.35	---	-	3.13E-04	11.77
	10	-13.15	11.39	10.75-11.87	1.12	---	-	2.63E-04	9.83
YP2	2.8	-25.46	12.15	---	-	---	-	-	-
	2.9	-30.02	11.72	---	-	11.13-12.24	1.11	8.43E-04	9.47
	3	-35.66	11.31	---	-	10.76-11.85	1.09	8.55E-04	9.64
	3.1	-42.51	10.89	---	-	10.46-11.43	0.97	7.85E-04	8.91
	3.2	-55.54	10.56	8.96-12.41	3.45	10-11.06	1.06	2.91E-03	32.67

	3.3	-30.82	10.29	8.73-12.08	3.35	9.72-10.69	0.97	2.89E-03	32.56
	3.4	-30.28	9.88	8.55-11.66	3.11	9.49-10.34	0.85	2.75E-03	31.48
	3.5	-28	9.63	8.39-11.31	2.92	9.26-10.04	0.78	2.64E-03	30.32
	3.6	-25.69	9.38	8.25-10.93	2.68	9.06-9.78	0.72	2.48E-03	28.57
	3.7	-24.29	9.2	---	-	8.88-9.49	0.61	5.87E-04	6.63
	3.8	-23.46	8.95	---	-	8.73-9.24	0.51	4.99E-04	5.70
	3.9	-22.05	8.79	---	-	8.62-9.03	0.41	4.05E-04	4.66
	4	-20.9	8.63	---	-	8.53-8.79	0.26	2.60E-04	3.01
YP3	2.6	-30.11	12.24	---	-	---	-	-	-
	2.7	-30.77	11.81	11.28-12.4	1.12	---	-	8.90E-04	9.48
	2.8	-32.19	11.47	10.96-12.04	1.08	---	-	8.77E-04	9.42
	2.9	-36.53	11.23	10.65-11.69	1.04	---	-	8.64E-04	9.26
	3	-48.79	10.89	---	-	10.39-11.42	1.03	8.68E-04	9.46
	3.1	-38.89	10.64	9.21-12.25	3.04	10.21-11.18	0.97	2.61E-03	28.57
	3.2	-40.15	10.38	9.05-11.96	2.91	10.05-10.81	0.76	2.52E-03	28.03
	3.3	-35.09	10.22	8.91-11.71	2.8	9.88-10.55	0.67	2.44E-03	27.40
	3.4	-28.65	10.13	8.79-11.49	2.7	9.66-10.36	0.7	2.36E-03	26.65
	3.5	-23.82	10.05	8.68-11.31	2.63	9.57-10.22	0.65	2.30E-03	26.17
	3.6	-20.31	9.59	8.57-11.08	2.51	9.52-10.04	0.52	2.20E-03	26.17
	3.7	-19.19	9.46	8.49-10.72	2.23	---	-	1.99E-03	23.57
	3.8	-18.05	9.29	8.41-10.45	2.04	---	-	1.83E-03	21.96
	3.9	-17.05	9.21	8.35-10.31	1.96	---	-	1.75E-03	21.28
	4	-16.13	9.12	8.28-10.12	1.84	---	-	1.65E-03	20.18
	4.1	-15.29	8.95	8.24-10.14	1.9	---	-	1.66E-03	21.23
	4.2	-14.51	8.88	8.2-10.03	1.83	---	-	1.59E-03	20.61
	4.3	-13.81	8.79	8.2-9.58	1.38	---	-	1.23E-03	15.70

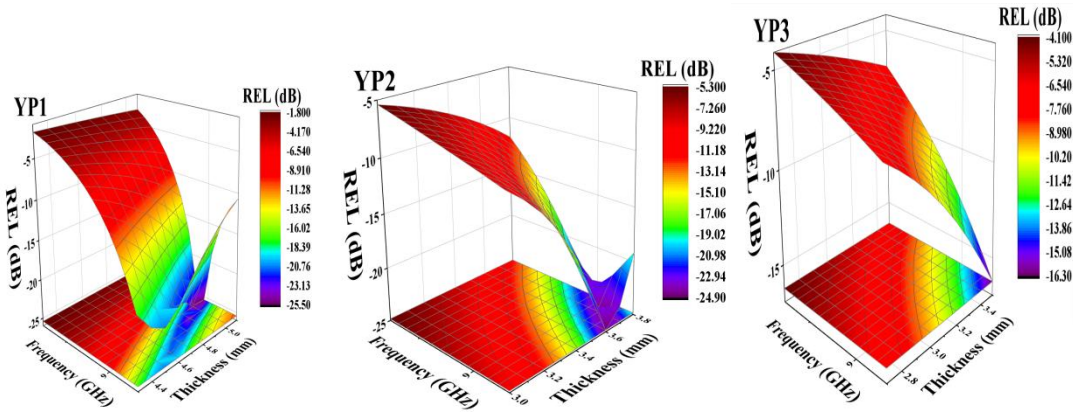

Figure 4.135 Three-dimensional (3D) plots of reflection loss at various frequencies and thicknesses for all samples of BaCoCd-series.

4.7.4.3 Impedance matching mechanism

The variation in the impedance of a material is primarily determined by its permittivity and permeability, which differ from that of free space. This distinction significantly influences the absorption characteristics of the material. When there is a mismatch between the permittivity and permeability, a large portion of the incident electromagnetic wave is reflected, with only a small fraction penetrating the material. However, when the material's impedance closely matches that of free space (377 Ω), a portion of the wave is absorbed by the material. This highlights the importance of impedance matching in developing efficient absorbers. The reflection loss (REL) and impedance (Z_{in}) versus frequency plots for the prepared samples (YP1 to YP3) illustrate the relationship between these two factors. The highest REL peaks in each composition align with the impedance matching principle, wherein Z_{in} closely approaches the free-space impedance (Z_0 = 377 Ω).

For the YP1 sample, with a thickness of 4.4 mm, the maximum REL peak of -36.34 dB is observed at 10.05 GHz, where the impedance Zin = 382.30 Ω, which is close to Z0. Interestingly, the combination of Zreal = 382.16 Ω and Zimg = 10.36 Ω suggests near-ideal matching conditions, allowing for significant absorption at this frequency. However, no notable REL peaks occur at frequencies slightly below or above this value, indicating that efficient absorption is closely tied to both the impedance match and the specific frequency. In YP2, with a thickness of 3.2 mm, a maximum REL of -55.54 dB is observed at 10.56 GHz, where the impedance Zin = 376.33 Ω, almost perfectly matching Z0. The near-zero imaginary component Zimg = 1.13 Ω further

confirms the excellent impedance matching, which results in highly efficient absorption. The exceptionally deep absorption observed in YP2 is due to this precise matching, highlighting how a small imaginary impedance component enhances absorption. The YP3 sample, with a thickness of 3.0 mm, exhibits a significant reflection loss of -48.79 dB at 10.89 GHz, with Zin = 376.48 Ω, showing a minimal deviation from Z0. Despite this, strong absorption is observed due to the small imaginary component of Zimg = -2.74 Ω, which is close to the ideal zero value.

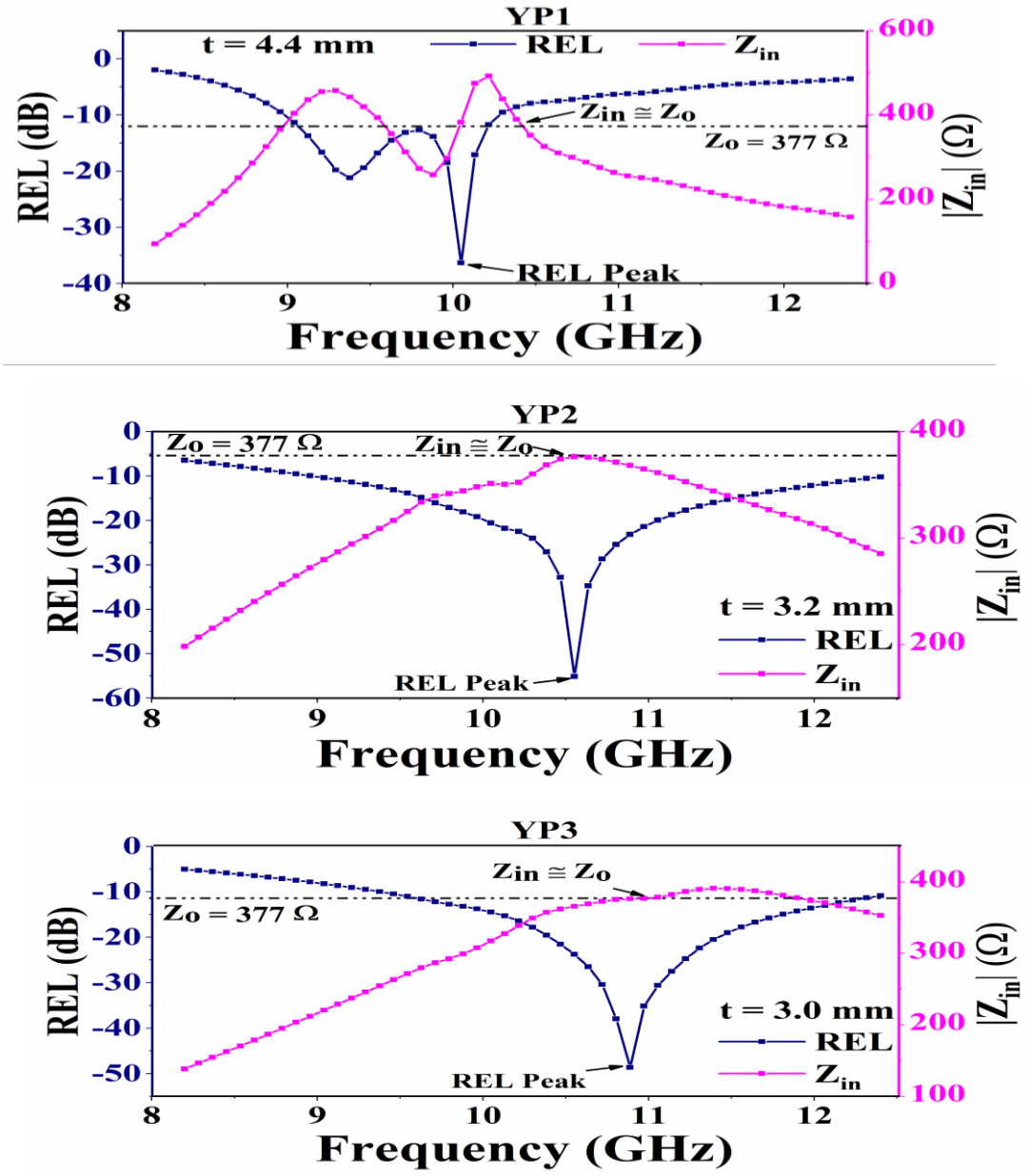

Figure 4.136 Z_{in} and REL curve against frequency for $BaCo_xCd_xFe_{12-2x}O_{19}$ / PANI

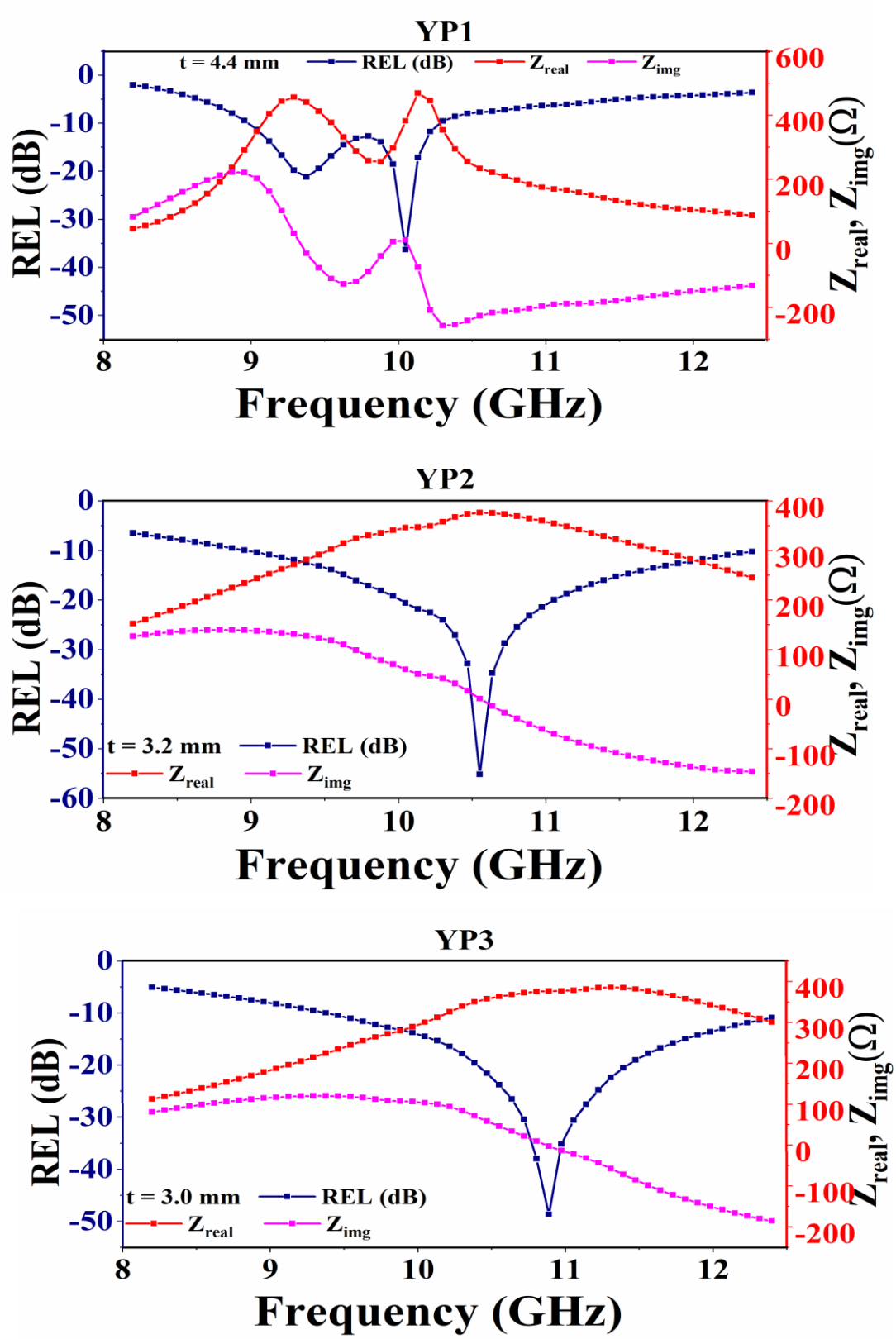

Figure 4.137 Z_{real}, Z_{imag}, and REL v/s frequency for $BaCo_xCd_xFe_{12-2x}O_{19}$ / PANI

Table 4.43 Z_{in}, Z_{real}, and Z_{imag} values corresponding to REL_{max} for $BaCo_xCd_xFe_{12-2x}O_{19}$.

Sample Name	Matching Thickness (mm)	Maximum REL (dB)	Matching frequency (GHz)	Zreal (Ω)	Zimg (Ω)	|Zin| (Ω)
YP1	4.4	-36.34	10.05	382.16	10.36	382.30
YP2	3.2	-55.54	10.56	376.33	1.13	376.33
YP3	3	-48.79	10.89	376.47	-2.74	376.48

4.7.4.4 Eddy Current Loss

All three samples (YP1, YP2, and YP3) exhibit a decreasing trend in C0 as frequency increases from 8 GHz to 12.5 GHz. This indicates a reduction in the time constant C0 with increasing frequency, which is typical as energy absorption becomes more efficient at higher frequencies. YP1 shows a prominent peak around 10 GHz, indicating a significant increase in C0 at this frequency, followed by a steep decrease beyond 10 GHz. This suggests a strong resonance effect at 10 GHz. After the peak at 10 GHz, the curve drops and levels off at a relatively low value compared to YP2 and YP3, indicating more efficient absorption at higher frequencies. YP2 exhibits a smoother transition across the frequency range, with a minor peak around 10 GHz, but the overall curve stays relatively stable. The curve for YP2 remains consistently higher than YP1 across the frequency range, indicating relatively slower energy absorption, but without any sharp resonance effects as in YP1. YP3 displays the highest values of C0 across the entire frequency range, indicating less efficient absorption compared to YP1 and YP2. The curve for YP3 has no sharp peak, instead showing a gradual decrease in C0 as frequency increases, suggesting a more distributed and less resonant absorption mechanism.

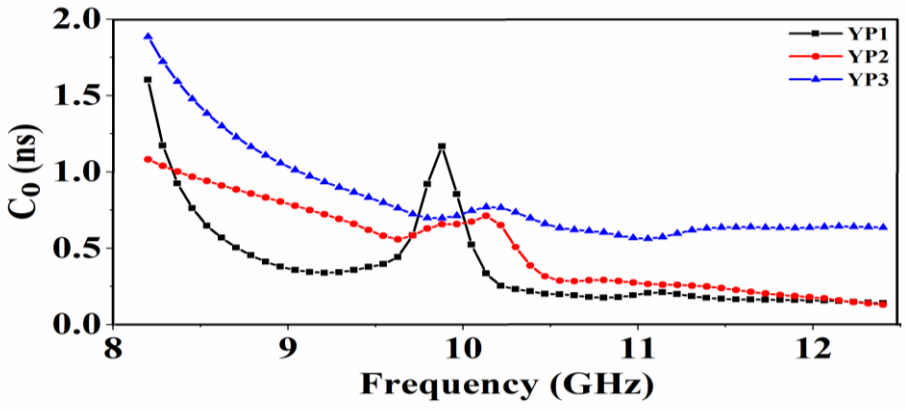

Figure 4.138 C_0 versus frequency curve for $BaCo_xCd_xFe_{12-2x}O_{19}$ / PANI

4.7.4.5 Bandwidth to Thickness Ratio

Wide bandwidths with reduced thickness play a crucial role in the characterization and design of an absorber. Instead of focusing just on raising REL values, one should strive for a low thickness after reaching the REL≥-10 dB. This makes figuring out the bandwidth to thickness ratio (BTR) and percentage bandwidth (PBW) crucial.

The BTR (Bandwidth to Thickness Ratio) and PBW (Percentage Bandwidth) values for the prepared compositions are summarized in the table. For composition YP1, the BTR ranges from 1.01E-04 to 1.27E-03, with a PBW spanning between 1.49% and 17.40%. YP1 demonstrates its strongest performance at a thickness of 3.9 mm, with a reflection loss (REL) of -34.31 dB at 9.71 GHz, achieving a BTR of 1.27E-03 and PBW of 17.40%. The bandwidth for REL > -20 dB is 0.21 GHz at this thickness. YP1 shows relatively good absorption performance over a range of thicknesses between 3.5 mm and 10 mm, with stable reflection loss values across the frequency range from 8.28 GHz to 12.4 GHz.

YP2 exhibits a BTR range between 2.60E-04 and 2.91E-03, with a PBW spanning from 3.01% to 32.67%. YP2 shows its highest absorption performance at 3.2 mm thickness, achieving a maximum REL of -55.54 dB at 10.56 GHz. At this point, it demonstrates a BTR of 2.91E-03 and PBW of 32.67%, with a bandwidth of 1.06 GHz for REL > -20 dB.

For YP3, the BTR ranges from 8.64E-04 to 2.61E-03, with a PBW between 9.26% and 28.57%. YP3 shows its peak performance at 3.0 mm thickness, where it reaches a maximum REL of -48.79 dB at 10.89 GHz, with a BTR of 8.68E-04 and PBW of 9.46%.

4.7.4.6 S – Parameter

For YP1, the S11 value is relatively high, starting around -1 dB, which is highest among all samples. As the frequency increases, the S11 value fluctuates between -2 dB and -1 dB, showing moderate reflection throughout this frequency range. For YP2, the S11 value decreases steadily from -2.5 dB to around -3.5 dB, indicating improving impedance matching as the frequency increases. However, beyond 10 GHz, the S11 value increases again, reaching -2 dB. YP3 shows the moderate S11 values, starting at -2 dB at 8 GHz and decreasing to -4 dB at 12 GHz. This indicates stronger impedance matching across the entire frequency range. For YP1, at lower frequencies (around 8

GHz), the S21 value is around -3.5 dB. As frequency increases, the S21 curve fluctuates, but rises overall to about -2 dB. YP2 starts with an S21 value of around -4.5 dB at 8 GHz, and rises up to 10 GHz. However, after 10 GHz, the value decreases again ending at around -5 dB. For YP3, the S21 remains relatively stable throughout the frequency range, starting at -4.8 dB at 8 GHz and staying below -4 dB up to 12 GHz.

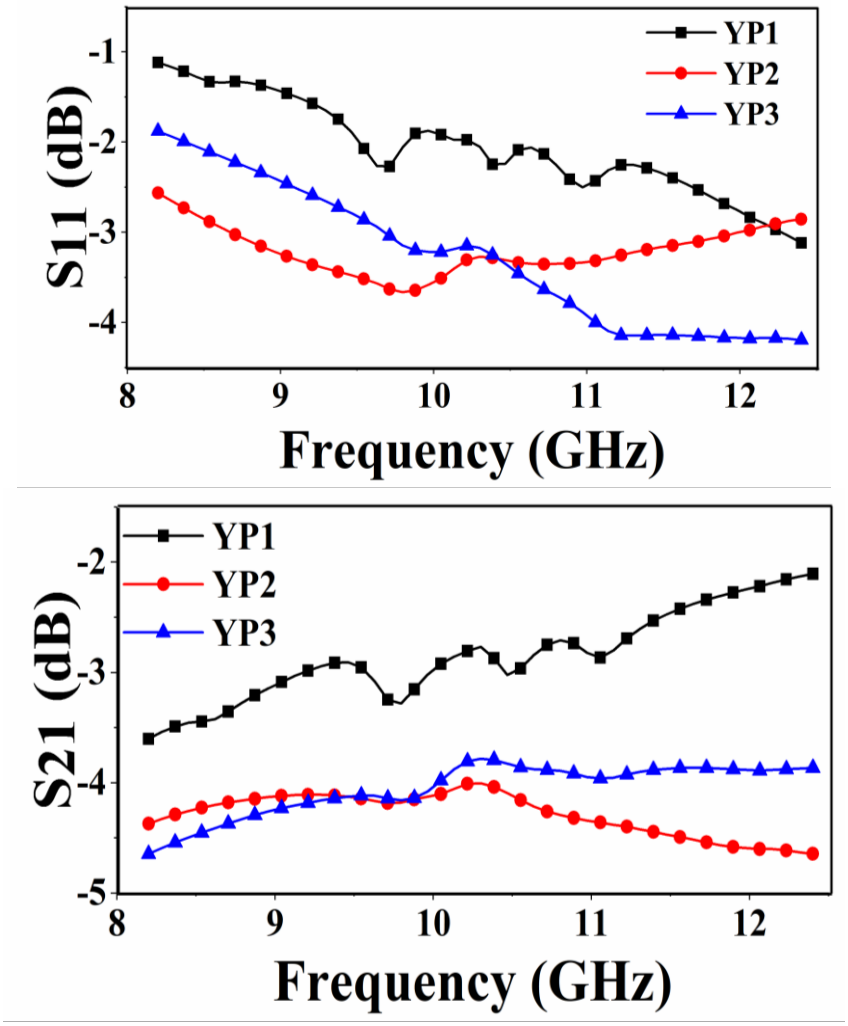

Figure 4.139 S_{11} and S_{21} versus frequency curve for $BaCo_xCd_xFe_{12-2x}O_{19}$ / PANI

4.8 Co^{2+}- Cr^{3+} substituted $BaCo_xCr_xFe_{12-2x}O_{19}$ hexaferrite / PANI

In this section, we will utilize the sol-gel combustion method to fabricate a hexaferrite compound with Co and Cr substitutions. The composition of the hexaferrite will be $BaCo_xCr_xFe_{12-2x}O_{19}$. Table 4.44 displays the sample names/codes for various levels of substitution in $BaCo_xCr_xFe_{12-2x}O_{19}$.

Table 4.44. Presents the assignment of sample names corresponding to various substitution levels in $BaCo_xCr_xFe_{12-2x}O_{19}$ hexaferrite.

Sample Composition $BaCo_xCr_xFe_{12-2x}O_{19}$	Sample Code Name	Sample Code (Z-series)
x= 0.0	$BaFe_{12}O_{19}$	ZP1
x = 0.6	$BaCo_{0.6}Cr_{0.6}Fe_{10.8}O_{19}$	ZP2
x = 0.8	$BaCo_{0.8}Cr_{0.8}Fe_{10.4}O_{19}$	ZP3

4.8.1 Field Emission Scanning Electron Microscopy

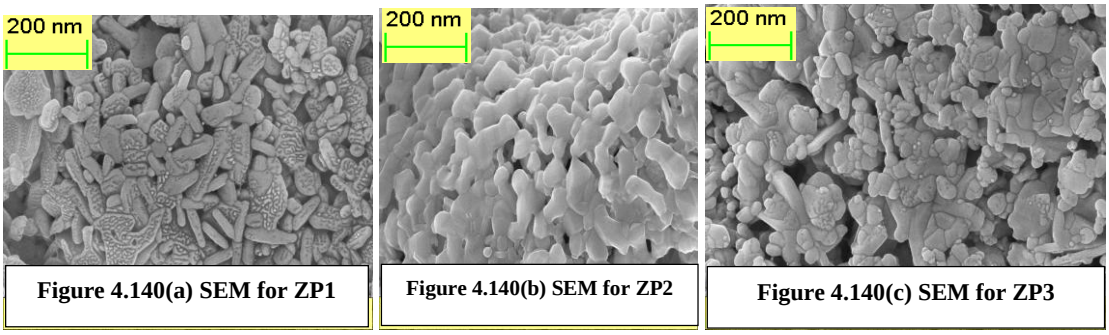

Figure 4.140(a) SEM for ZP1

Figure 4.140(b) SEM for ZP2

Figure 4.140(c) SEM for ZP3

Figure 4.140 SEM Micrographs of $BaCo_xCr_xFe_{12-2x}O_{19}$ Ferrites (ZP1 (x = 0.0), ZP2 (x = 0.6), ZP3 (x = 0.8)).

The Figure 4.140(a) i.e ZP1 shows grains that are fairly well defined with sharp edges. These grains are uniformly distributed, which suggests efficient crystallization. The relatively clear grain boundaries indicate limited interference between grains, contributing to better magnetic alignment and higher magnetization.

The Figure 4.140(b) i.e ZP2 depicts more rounded grains with reduced crystallinity compared to ZP1. There is increased porosity, which could introduce grain boundary effects and increase resistance. This could also increase grain boundary resistance. This structure reduces magnetization due to grain boundary interference.

The Figure 4.140(c) i.e ZP3 displays irregularly shaped grains, showing significant porosity and aggregation. These characteristics suggest a stronger grain boundary influence and the poor grain connectivity results in lower saturation magnetization.

4.8.2 Electrical Characterization

4.8.2.1 Dielectric constant

From the Figure 4.141(a) showing the real part of the dielectric constant (ε') for the ZP1, ZP2, and ZP3 samples, ZP1 has the highest dielectric constant, while ZP3 and ZP2 have significantly lower values. The dielectric constant decreases as frequency increases, which is a common behaviour in materials where the ability of charge

carriers to follow the alternating electric field diminishes at higher frequencies. At lower frequencies (around 100 Hz), ZP1 exhibits a maximum value of approximately 12791.13, while ZP2 and ZP3 show values of around 418.00 and 640.13 respectively. The lower values for ZP2 and ZP3 may result from structural modifications due to doping, which can disrupt charge transport mechanisms and reduce the dielectric constant. Beyond 10^5 Hz, all samples exhibit frequency-independent behaviour. The imaginary part of the dielectric constant (ε") indicates energy losses in the material. The ZP1 sample again shows the highest values for ε", peaking around 172,173.3 at low frequencies (100 Hz) and then steadily declining as frequency increases. ZP2 and ZP3 display much lower ε" values, around 4,881.14 and 6,997.38, respectively, at low frequencies, and drop off more quickly compared to ZP1. As frequency increases, the imaginary part of the dielectric constant for all samples becomes relatively constant, suggesting the dominance of conduction losses at high frequencies. The loss tangent (tan δ), which represents the ratio of dielectric loss to dielectric constant, follows a similar trend as ε". ZP1 has the highest tan δ values at low frequencies (13.46 at 100 Hz), reflecting higher energy dissipation, while ZP2 and ZP3 show lower values around 11.68 and 10.93, respectively. The tan δ values decrease with increasing frequency for all samples, indicating reduced energy dissipation at higher frequencies. The peak width, which gives an indication of the relaxation time spread, is broader for ZP1 compared to ZP2 and ZP3. This suggests that ZP1 has a broader distribution of relaxation times, meaning a wider range of processes contribute to energy dissipation over a range of frequencies. ZP1 shows a more prominent relaxation peak, which indicates stronger dielectric relaxation processes compared to ZP2 and ZP3. The shift in peak heights and widths suggests that the doping affects the dielectric relaxation mechanisms, with ZP1 being the least disrupted in its charge transport mechanisms, while ZP2 and ZP3 are more resistive, resulting in lower tan δ values. AC conductivity increases with frequency for all samples, with ZP1 showing the highest conductivity across the frequency range. At 100 Hz, ZP1's conductivity is approximately 9.6×10^{-4} $(\Omega \cdot m)^{-1}$, while ZP2 and ZP3 exhibit much lower values around 2.7×10^{-5} and 3.9×10^{-5} $(\Omega \cdot m)^{-1}$ and reached up-to the height value of 0.00584 $(\Omega \cdot m)^{-1}$, 0.000892 $(\Omega \cdot m)^{-1}$ and 0.00146 $(\Omega \cdot m)^{-1}$ respectively. Conductivity

for all samples shows a steep rise after 10^5 Hz, indicating the onset of a frequency-dependent conduction mechanism.

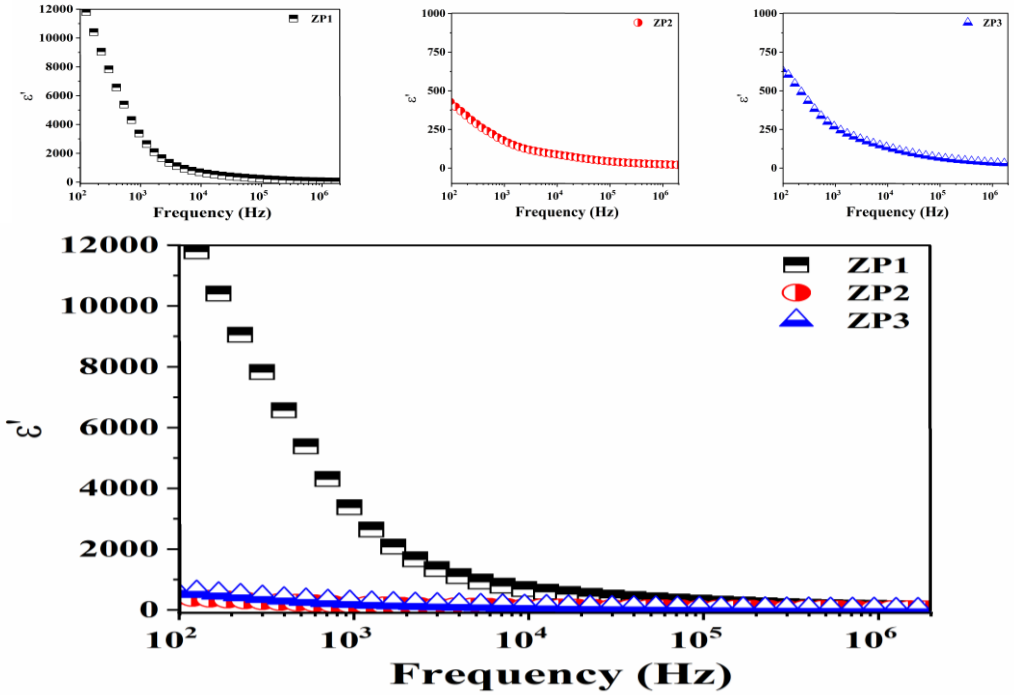

Figure 4.141(a) Dielectric Constant Dependence on Frequency in $BaCo_xCr_xFe_{12-2x}O_{19}$ (ZP1 (x = 0.0), ZP2 (x = 0.6), ZP3 (x = 0.8)) Hexaferrites.

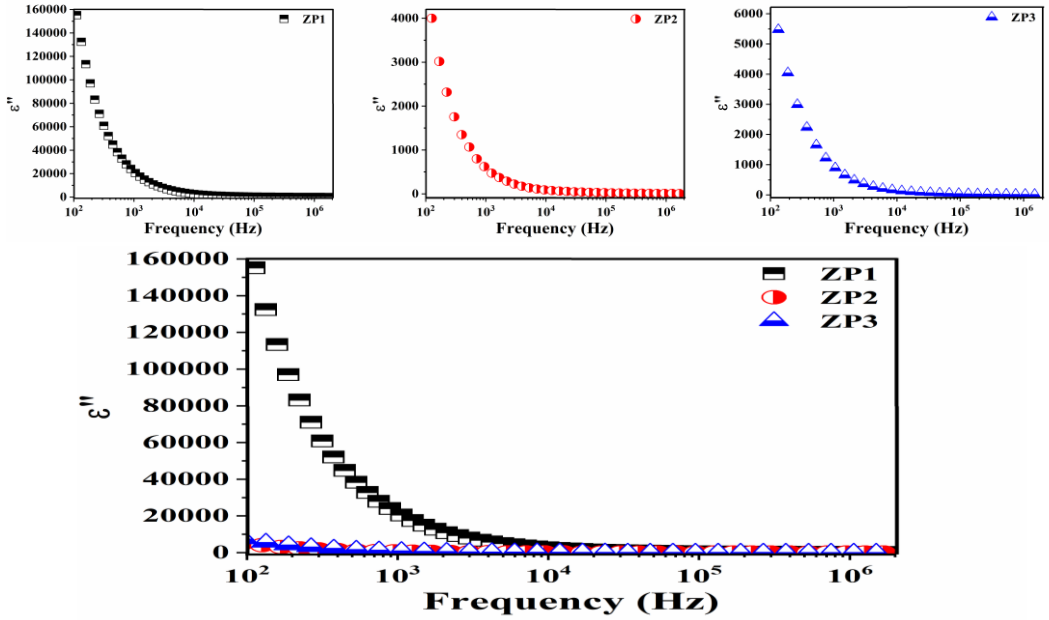

Figure 4.141(b) Dielectric Loss Dependence on Frequency in $BaCo_xCr_xFe_{12-2x}O_{19}$ (ZP1 (x = 0.0), ZP2 (x = 0.6), ZP3 (x = 0.8)) Hexaferrites.

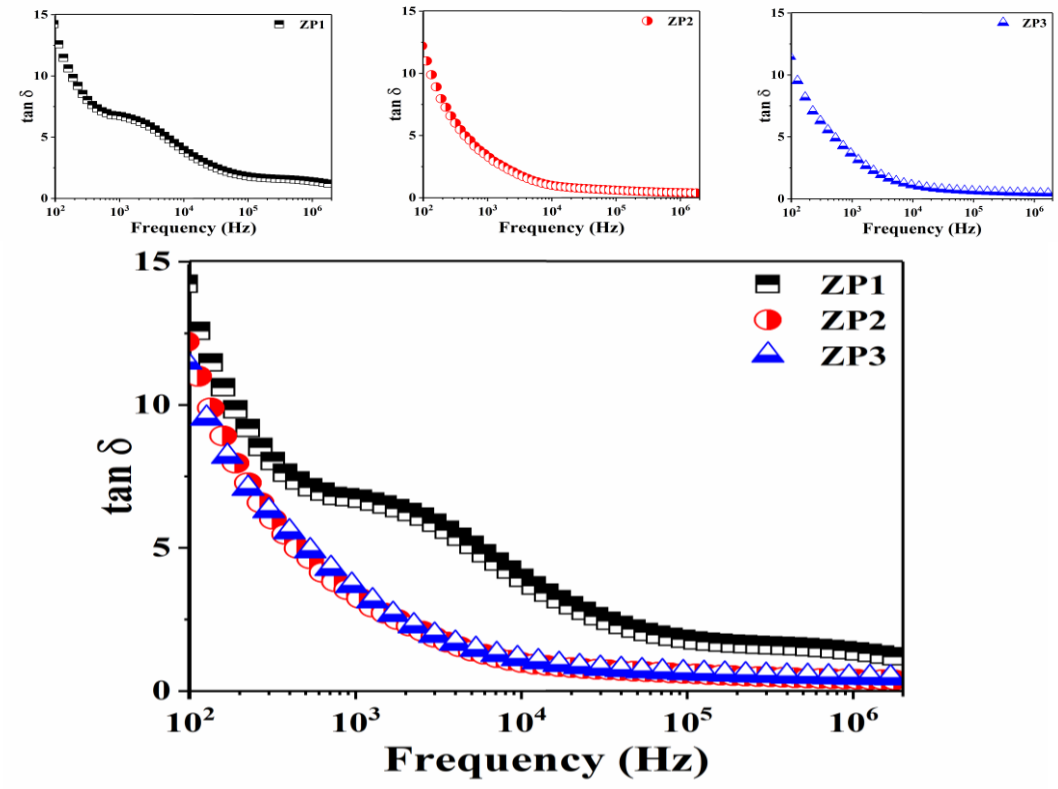

Figure 4.141(c) Dielectric Loss Tangent Dependence on Frequency in $BaCo_xCr_xFe_{12-2x}O_{19}$ (ZP1 (x = 0.0), ZP2 (x = 0.6), ZP3 (x = 0.8)) Hexaferrites.

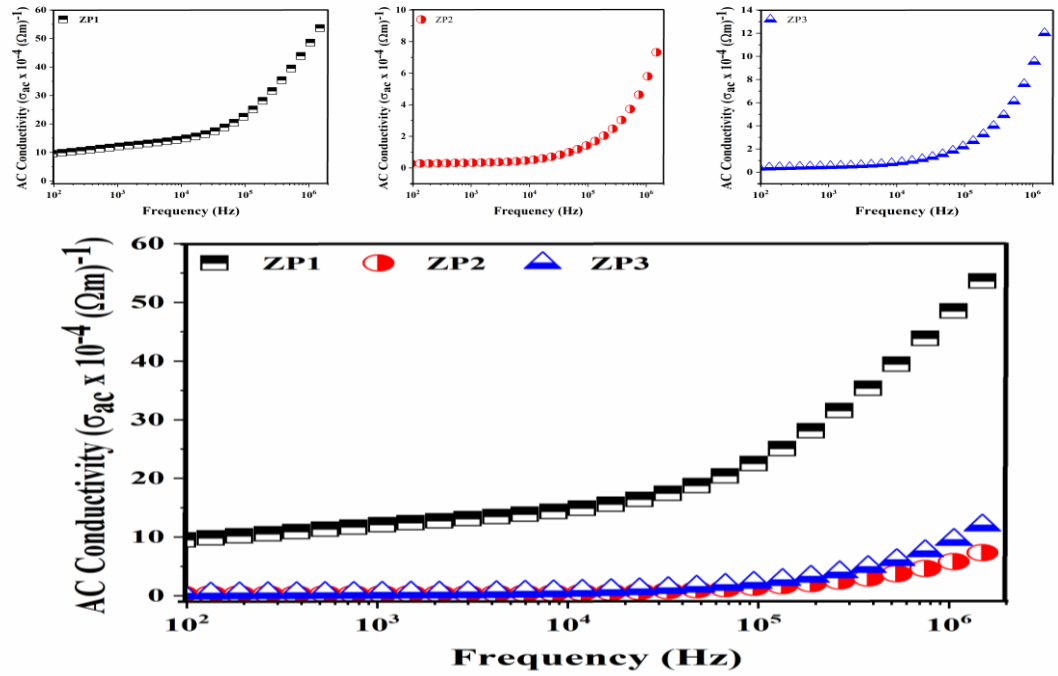

Figure 4.141(d) AC Conductivity Dependence on Frequency in $BaCo_xCr_xFe_{12-2x}O_{19}$ (ZP1 (x = 0.0), ZP2 (x = 0.6), ZP3 (x = 0.8)) Hexaferrites.

4.8.2.2 Electric modulus analysis

In the low-frequency region, M' values for all ZP1, ZP2, and ZP3 samples tend to approach zero, signifying minimal resistive effects. This indicates that at lower frequencies, charge carriers exhibit long-range mobility, with minimal resistivity. Essentially, the low-frequency range corresponds to high conductivity, as charge carriers can move more freely. As the frequency increases, M' begins to rise, particularly beyond the intermediate frequency range (~10^3 to 10^4 Hz), indicating an increasing resistance to charge carrier movement. This shift reflects the transition from long-range mobility to more localized charge relaxation mechanisms. ZP1 consistently exhibits the lowest values of M′ across the frequency range. For example, at 100 Hz, M′ is 4.29×10^{-7}, while at 2 MHz, it increases to 9.42×10^{-3}. ZP2 and ZP3 show higher values of M′, with ZP2 having the highest values. For instance, ZP2 starts at 1.74×10^{-5} at 100 Hz and reaches 0.04178 at 2 MHz, while ZP3 starts at 1.30×10^{-5} and reaches 0.02842. ZP1 exhibits the lowest M' values across the frequency range, indicating lower resistivity and higher conductivity, allowing for more efficient charge transport.

The imaginary part of the electric modulus (M") provides insight into the energy dissipation due to conductivity relaxation. As seen in the Figure 4.142(b), M" increases steadily with frequency, indicating stronger conductivity relaxation effects at higher frequencies. ZP2 consistently shows the highest M" values, at 100 Hz is 2.03×10^{-4}, and it reaches 0.04178 at 2 MHz reflecting greater energy dissipation and more pronounced conductivity relaxation effects. This suggests that ZP2 has stronger interactions between the charge carriers and the applied electric field, leading to slower relaxation processes. ZP1, on the other hand, exhibits the lowest M" values, at 100 Hz, ZP1 has $M'' = 5.78\times10^{-6}$, and this increases to 1.09×10^{-2} at 2 MHz indicating that it experiences the least energy dissipation and faster conductivity relaxation. The M" peak for ZP1 is smaller and shifted towards lower frequencies, which correlates with faster charge transport mechanisms and lower resistivity. ZP3 shows intermediate behaviour, with M" values falling between ZP1 and ZP2. This gradual increase in M" with increased doping (Cr and Co) highlights the impact of doping on the conductivity relaxation process, making it more pronounced in ZP2 compared to the other samples.

The Cole-Cole plot (M'' vs. M') provides a clear visualization of the conductivity relaxation processes and charge transport mechanisms in the doped composites. ZP3 exhibits the largest semicircular arc, indicating a higher degree of conductivity relaxation and greater resistivity. The large arc diameter for ZP3 suggests stronger interactions between the charge carriers and the electric field, leading to more prominent relaxation processes and a slower response to the alternating field. This behaviour is consistent with its high M' and M'' values, especially at high frequencies. In contrast, ZP1 shows a smaller arc, indicating less significant relaxation processes and lower resistivity. The small arc reflects the efficient charge mobility and quicker relaxation processes in ZP1, which corresponds to its lower M' and M'' values. ZP2 exhibits an intermediate arc size, reflecting its moderate conductivity relaxation behaviour, falling between ZP1 and ZP3. The peaks for ZP2 and ZP3 are shifted towards higher M' values compared to ZP1, suggesting that relaxation processes occur at higher frequencies due to the influence of doping. This shift implies that Co and Cr doping increases the relaxation frequency, with ZP3 showing the most significant shift.

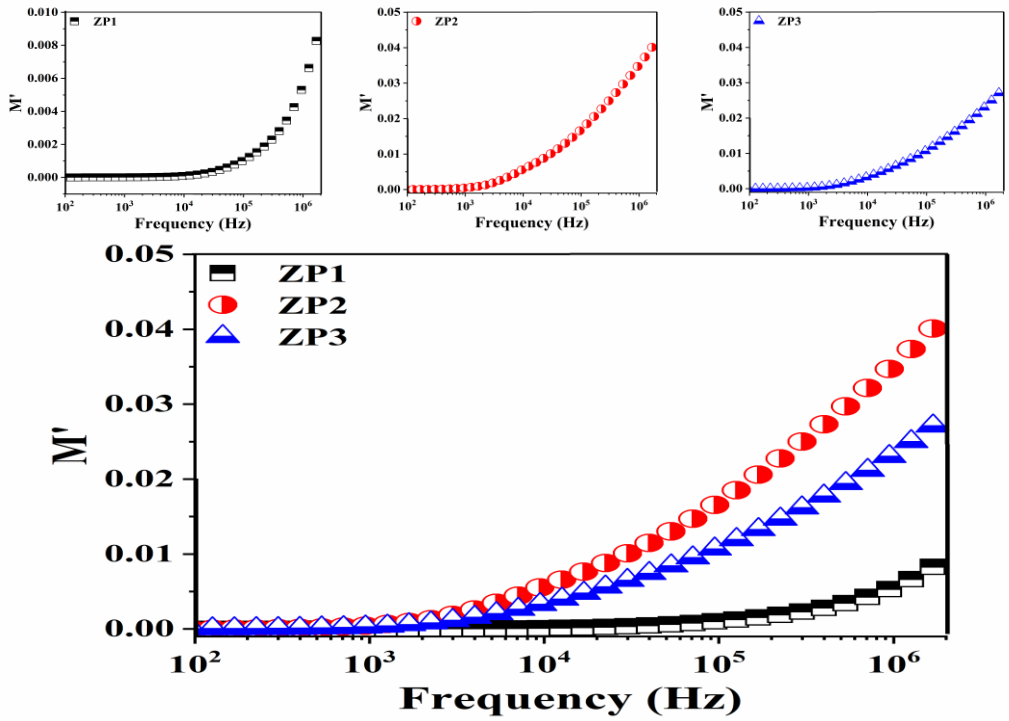

Figure 4.142(a) Real Modulus (M′) Dependence on Frequency in $BaCo_xCr_xFe_{12-2x}O_{19}$ (ZP1 (x = 0.0), ZP2 (x = 0.6), ZP3 (x = 0.8)) Hexaferrites

The plot is divided into two regions: low-frequency (grain boundary effects) and high-frequency (grain effects). At lower frequencies, the Cole-Cole plot shows that the grain boundary dominates the behaviour, with ZP1 showing more pronounced effects compared to ZP2 and ZP3. The grain boundary effects decrease with increasing frequency, and grain effects take over in the high-frequency region. This is typical for materials where grain boundary conduction dominates at lower frequencies, while at higher frequencies, conduction occurs within the grains themselves. ZP1 shows a small arc with the lowest M′ and M″ values, indicating that it has the least significant grain boundary resistance and higher conductivity. This reflects that ZP1 has higher charge mobility due to reduced grain boundary contribution. The arc for ZP2 and ZP3 is larger than ZP1, suggesting that ZP2 and ZP3 has a moderate grain boundary contribution and intermediate charge mobility. The diameter of the semicircular arcs in the Cole-Cole plot indicates the strength of the relaxation processes. ZP3 and ZP2 exhibit the larger arc diameter, suggesting stronger conductivity relaxation and more significant interaction between charge carriers and the electric field. On the other hand, ZP1 shows the smallest arc, indicating that it has weaker relaxation processes and higher conductivity with less resistance from the grain boundaries.

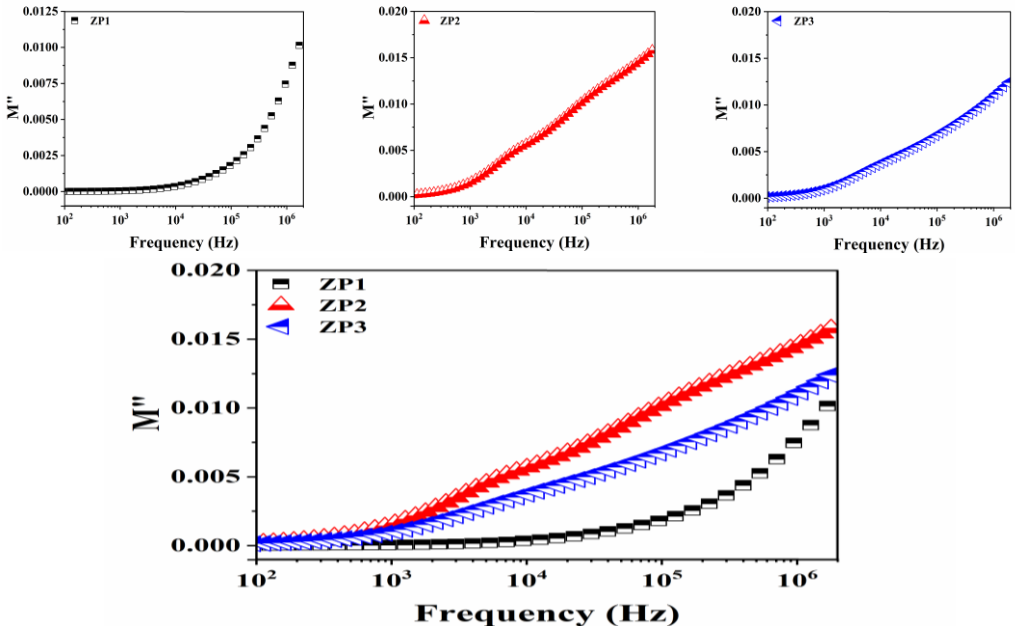

Figure 4.142(b) Imaginary Modulus (M") Dependence on Frequency in $BaCo_xCr_xFe_{12-2x}O_{19}$ (ZP1 (x = 0.0), ZP2 (x = 0.6), ZP3 (x = 0.8)) Hexaferrites

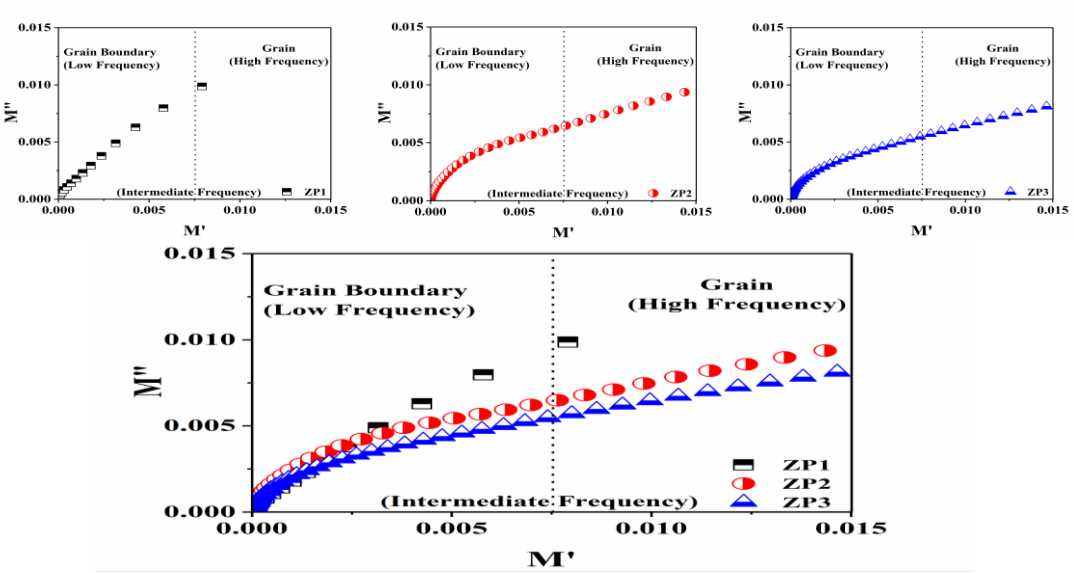

Figure 4.142(c) Cole-Cole Impedance Plots of $BaCo_xCr_xFe_{12-2x}O_{19}$ (ZP1 (x = 0.0), ZP2 (x = 0.6), ZP3 (x = 0.8)) Hexaferrites at 900°C, 5h.

4.8.2.3 Impedance spectroscopy

The real impedance (Z′) for ZP1 decreases with increasing frequency, from around 273,580 Ω at 100 Hz to 26,097 Ω at 2 MHz. This decrease suggests that ZP1 becomes more conductive at higher frequencies. ZP2 exhibits the highest values of Z' at low frequencies, starting from approximately 9.67 MΩ at 100 Hz and reducing to around 38.26 kΩ at 2 MHz indicating substantial resistive contributions due to grain boundary effects. ZP3 displays intermediate Z' values, Its starts at around 4.82 MΩ at 100 Hz and reduces to around 21.66 kΩ at 2 MHz suggesting less pronounced grain boundary resistivity compared to ZP2, but higher than ZP1. This suggests that ZP3 has moderate grain boundary resistivity and grain conduction. ZP2 shows the highest peak in Z″ (312.9×10^4 Ω), indicating significant energy dissipation and a strong relaxation process. This is the most pronounced among the three samples, reflecting a higher degree of impedance from grain boundaries. ZP3 exhibits a smaller peak (131.35×10^4 Ω) than ZP2, but still larger than ZP1, indicating moderate energy dissipation and relaxation effects. ZP2's peak occurs around the frequency of 10^4 Hz, reflecting the frequency at which the grain boundary resistive effects are strongest. This indicates that ZP2 experiences maximum impedance due to charge transport resistance at this frequency. ZP3's peak also appears near 10^4 Hz, but the height is lower than ZP2, suggesting less pronounced resistive relaxation. The grain boundary effects are still

significant but less so than in ZP2. ZP2 shows the broadest peak in Z″, indicating that the resistive relaxation process occurs over a wider frequency range, which suggests significant grain boundary contributions that persist over a broad spectrum of frequencies. The broadness of this peak implies substantial grain boundary impedance. ZP1 has the best performance with minimal Z″ values, indicating high conductivity with negligible grain boundary impedance, thus the most effective charge transport.

The Cole-Cole plot, ZP2 displays the largest semicircular arc, corresponding to a higher contribution from grain boundary effects and a slower relaxation process. The larger arc suggests that ZP2 has a significant amount of resistive grain boundary regions, contributing to slower charge transport and higher energy dissipation. ZP3 has a smaller arc compared to ZP2, indicating that its grain boundary contribution is less dominant, and it has more efficient charge transport across the grains. ZP1 shows a much smaller semicircular arc, which suggests very minimal grain boundary effects. This is consistent with ZP1 having the lowest resistivity and energy dissipation. The grain effects dominate in this sample, providing faster charge transport and better overall conductivity.

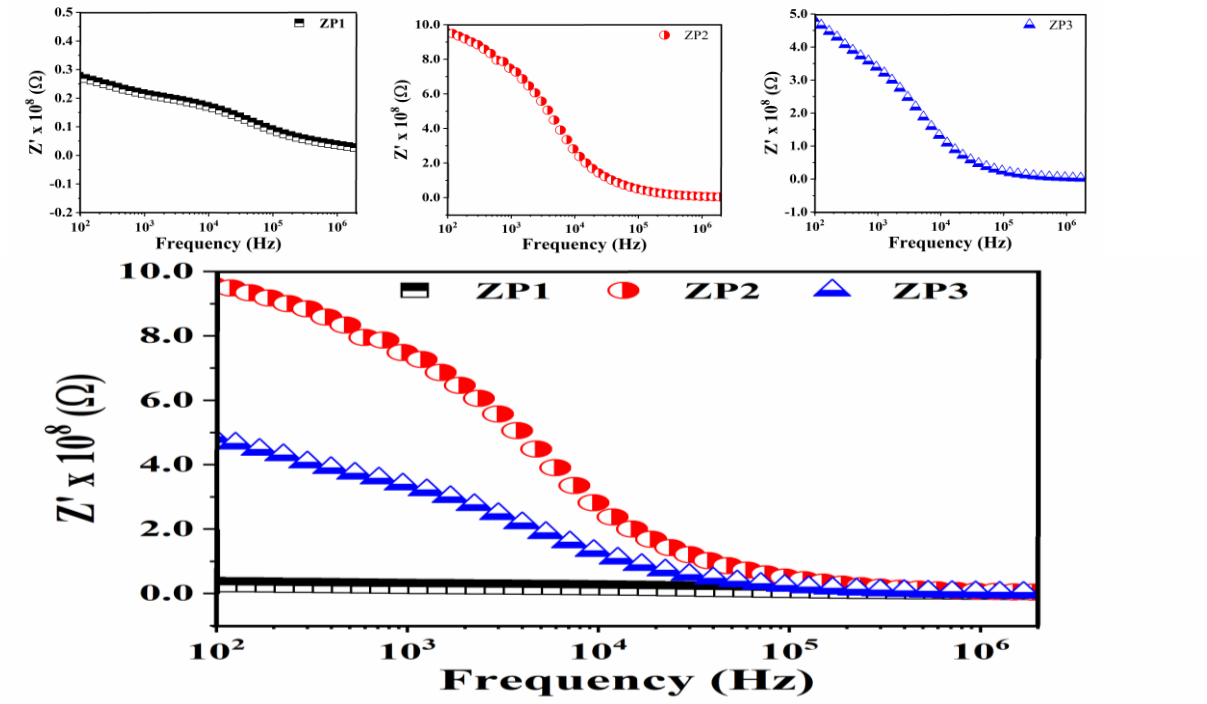

Figure 4.143(a) Real Impedance (Z′) Dependence on Frequency in $BaCo_xCr_xFe_{12-2x}O_{19}$ (ZP1 (x = 0.0), ZP2 (x = 0.6), ZP3 (x = 0.8)) Hexaferrites.

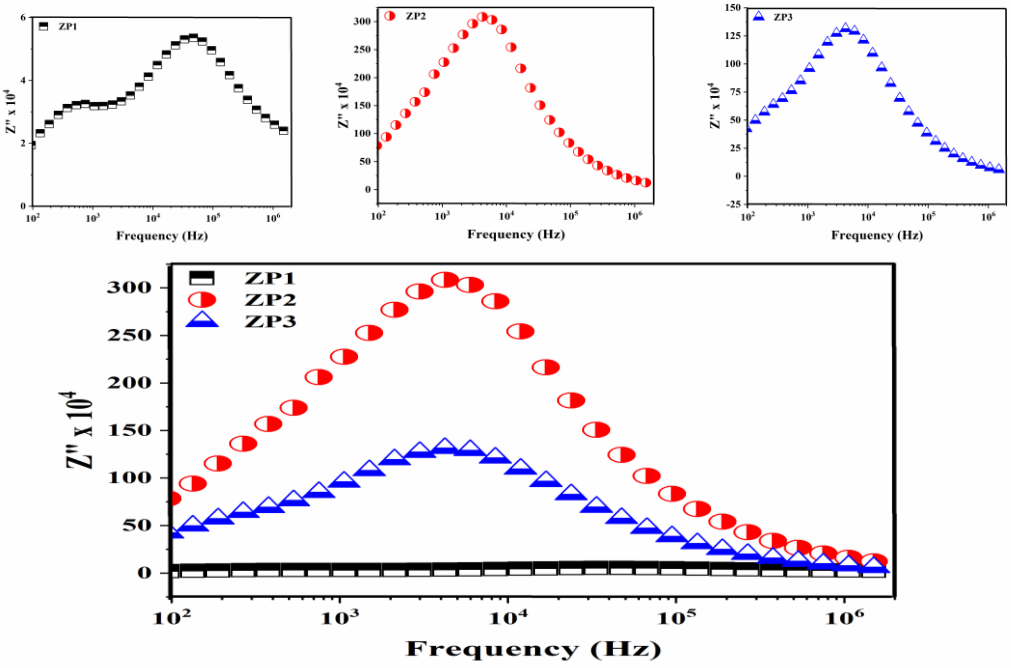

Figure 4.143(b) Imaginary Impedance (Z′) Dependence on Frequency in $BaCo_xCr_xFe_{12-2x}O_{19}$ (ZP1 (x = 0.0), ZP2 (x = 0.6), ZP3 (x = 0.8)) Hexaferrites.

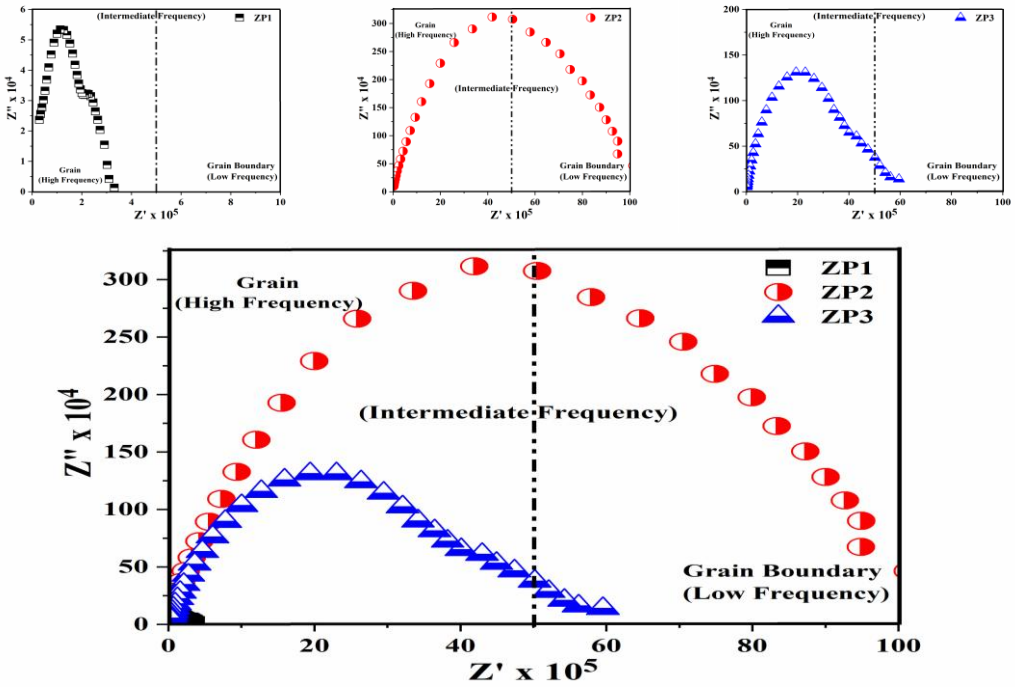

Figure 4.143(c) Cole-Cole Impedance Plots of $BaCo_xAl_xFe_{12-2x}O_{19}$ (ZP1 (x = 0.0), ZP2 (x = 0.6), ZP3 (x = 0.8)) Hexaferrites after Heat Treatment at 900°C for 5 Hours.

Computational Impedance Simulation and Validation

Figure 4.144 illustrates the results of an analogous circuit analysis conducted on complex impedance data acquired via Electrochemical Impedance Spectroscopy (EIS) software [49].

This model precisely reflects the behaviour seen in the mixtures, as demonstrated by the strong correlation between measured and simulated/fitted curves in the images. Table 4.45 displays the resistance, and capacitance values derived from the EIS data for both grains and grain borders. These parameters measure the electrical response of the microstructural characteristics within the mixtures.

Table 4.45 Extracted Grain and Grain Boundary Parameters from EIS Modelling

Composite	R_g (MΩ)	R_{gb} (MΩ)	C_g (μF)	C_{gb} (μF)
ZP1	0.211	0.02	440059.67	3.94
ZP2	0.30	8.88	85.24	288.10
ZP3	4.03	0.09	1491.85	579.18

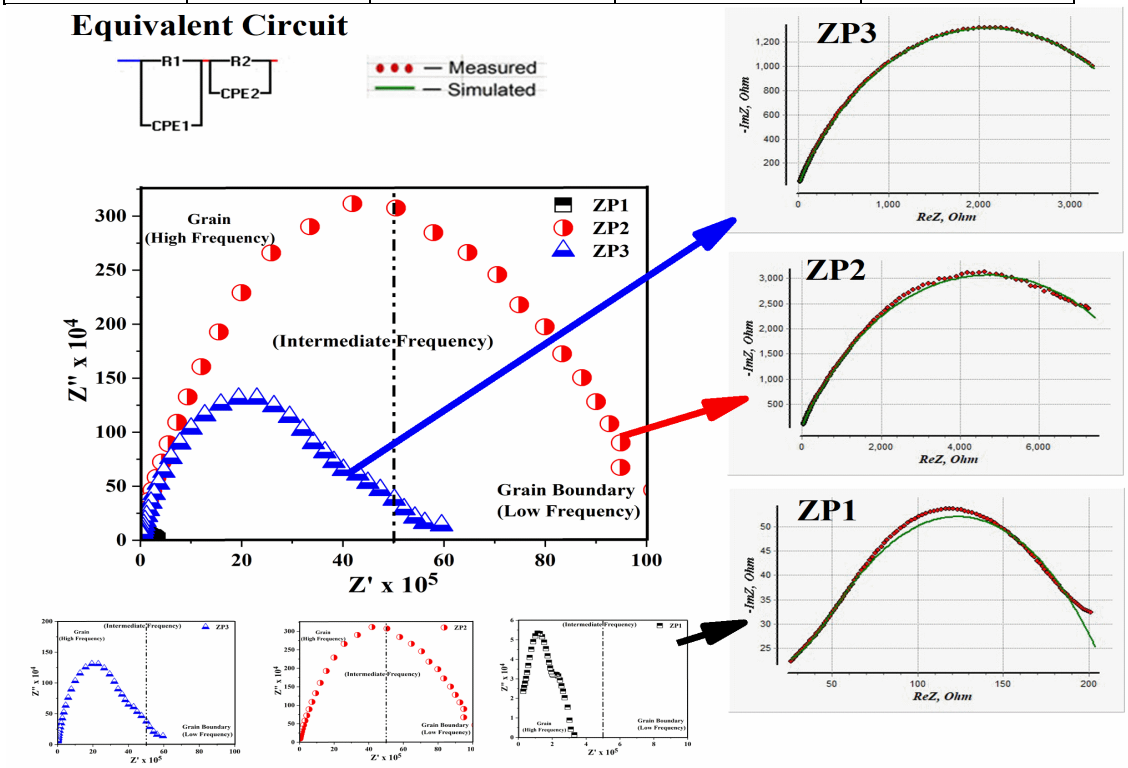

Figure 4.144 Measured and Fitted Impedance Data with Equivalent Circuit (ZP1 to ZP3)

4.8.2.4 Investigating the Relationship between EIS Data and Microstructure

The ZP1 shows large, well-defined grains with compact surfaces which result in lower resistance to grain conduction. The minimal grain boundary area further contributes to lower grain boundary resistance R_{gb} = 0.02 MΩ. This compact structure reduces grain boundary capacitance C_{gb} = 3.94 µF, while the large grains store a high amount of charge, reflected in the exceptionally high grain capacitance C_g = 440059.67 µF. ZP2 shows a porous structure with many grain boundaries and irregular grain shapes, indicating more space between grains and less compactness. The porous structure leads to highest grain boundary resistance R_{gb} = 8.88 MΩ because of increased grain boundary areas, which act as barriers to charge movement. The lower compactness contributes to higher grain boundary capacitance C_{gb} = 288.10 µF. However, the grain capacitance C_g = 85.24 µF is significantly reduced compared to ZP1, indicating less efficient charge storage in the grains. ZP3 presents a more uniform, compact structure with smaller and tightly packed grains. The smaller and closely packed grains lead to higher grain resistance R_g = 4.03 MΩ due to limited charge mobility within the grains. The compact structure also explains the relatively low grain boundary resistance R_{gb} = 0.09 MΩ and the higher capacitance values (both C_g = 1491.85 µF and C_{gb} = 579.18 µF) since the grain boundary regions are well defined, and the grains are capable of storing moderate amounts of charge.

Investigating the Relationship between EIS Data and Electric Parameters

The large C_g = 440059.67 µF and Lower grain resistance (R_g = 0.211 MΩ) in ZP1 implies a very high charge storage capability and more efficient conduction within the grains, leading to an extremely high ε′ = 12791.13, meaning a strong dielectric response. The minimal grain boundary resistance R_{gb} i.e 0.02 MΩ helps in easy charge movement across grains, but because so much energy is stored in the grains (due to high capacitance), this leads to substantial dielectric losses as energy is lost in the grain regions. The low grain and grain boundary resistances enhance the overall conductivity. With R_g = 0.211 MΩ and R_{gb} = 0.02 MΩ, ZP1 shows the highest conductivity among the samples due to the minimal resistance to both grain and grain boundary conduction. The higher grain boundary resistance R_{gb} (8.88 MΩ) significantly hinders charge movement across grain boundaries, leading to a reduction in ε′ from 12791.13 to 418.00 due to inefficient charge storage. The higher grain

boundary resistance R_{gb} (8.88 MΩ) also reduces the overall conductivity of ZP2, making it less conductive compared to ZP1 and ZP3. The conductivity σ = 0.000892 is lowest due to the significant barriers at the grain boundaries. C_g for ZP2 is 85.24 µF, which is much lower than the other samples (ZP1 and ZP3). This lower capacitance indicates a smaller ability to store charge in the grains compared to ZP1 and ZP3. ε″ is related to energy dissipation, and since ZP2 has lower capacitance C_g, it experiences less dielectric loss compared to ZP1. The data also shows that ε″ is the lowest in ZP2, indicating the least energy dissipation or dielectric loss. R_g (grain resistance) in ZP2 is 0.30 MΩ, higher than ZP1 but lower than ZP3, which suggests that ZP2 has moderate resistance to charge flow through the grains. The conductivity of ZP3 is improved compared to ZP2 due to the lower R_{gb} but is lower than ZP1 because of the moderate R_g.

M′ and M″ are inversely related to ε′, the high capacitance C_g and low grain boundary resistance in ZP1 result in lower values for M′ and M″, signifying that ZP1 has minimal resistance to carrier relaxation in the grains. In ZP2, the higher R_{gb} results in higher values for M′ and M″, as charge carriers face greater resistance when trying to relax across grain boundaries. This increases the relaxation times, causing the peaks in M′ and M″ to shift to lower frequencies. Relaxation processes in ZP3 are relatively efficient due to the balance between grain and grain boundary capacitances. The moderate C_g and C_{gb} values result in intermediate M′ and M″, as charge carriers experience moderate resistance in both grain and boundary regions.

ZP1 exhibits very low R_{gb}, which significantly reduces both Z′ (real impedance) and Z″ (imaginary impedance). The large grain capacitance further enhances this effect, as grains can support better conduction with lower impedance values. Z′ and Z″ would remain relatively low across the frequency range, indicating excellent conductivity behaviour. The significantly higher R_{gb} increases Z′ (real part of impedance) and Z′’(imaginary part). The grains themselves can still store charge due to C_g = 85.24 µF, but the large R_{gb} creates a barrier that contributes to higher impedance. Both Z′ and Z″ will show higher peaks at lower frequencies compared to ZP1.

4.8.3 Magnetic Analysis

The impact of Co^{2+} and Cr^{3+} substitution in $BaCo_xCr_xFe_{12-2x}O_{19}$ PANI Hexaferrite significantly influence the magnetic properties of the material. This substitution

changes the overall magnetic characteristics, including saturation magnetization (M_s), coercivity (H_c), and remanent magnetization (M_r), as well as the anisotropy field (H_a). The changes are linked to the substitution of Fe^{3+} (which has higher magnetic moments – 5.92 μB) by Co^{2+} (3.87 μB) and Cr^{3+} ions (3.87 μB), modifying the crystal structure and magnetic exchange interactions.

The saturation magnetization (M_s) shows a decreasing trend from ZP1 to ZP3:

ZP1: M_s = 45.92 emu/g, **ZP2**: M_s = 30.25 emu/g, **ZP3**: M_s = 22.55 emu/g

M_s decreases with increasing Co^{2+} and Cr^{3+} substitution. This is due to the replacement of Fe^{3+} (with a magnetic moment of 5 μB) by Co^{2+} and Cr^{3+}. The reduction in M_s indicates that the magnetic exchange interactions are weakened as Fe^{3+} ions, which contribute more to the magnetization, are progressively replaced. ZP1, with the highest M_s, indicates stronger magnetic interactions due to a higher concentration of Fe^{3+} ions. ZP3, with the lowest M_s, reflects the largest substitution of Fe^{3+} ions by Co^{2+} and Cr^{3+}, leading to a further reduction in the material's net. The substitution of Co^{2+} and Cr^{3+} for Fe^{3+} in $BaCo_xCr_xFe_{12-2x}O_{19}$/PANI hexaferrite modifies the relative contributions of these sublattices, altering M_a and M_b values and therefore influencing the overall saturation magnetization (M_s). Fe^{3+} (5 μB) in the spin-up and spin-down sublattices plays a dominant role in magnetic order due to its higher magnetic moment. Co^{2+} (3 μB) has a smaller magnetic moment and tends to occupy octahedral sites (12k↑) in the crystal structure, which are typically associated with the spin-up sublattice (M_a). The substitution of Co^{2+} at these sites decreases the contribution of M_a. Cr^{3+} (0 μB or 3.87 μB depending on crystal site), as a non-magnetic or weakly magnetic ion, replaces Fe^{3+} at the tetrahedral or octahedral sites, further reducing M_a or M_b depending on where Cr^{3+} substitutes. The result is a net reduction in M_a, with a potentially slight effect on M_b (due to the specific sites occupied by Cr^{3+}), leading to an overall decrease in M_s. As Fe^{3+} ions (with high magnetic moments) are replaced by ions with lower or zero magnetic moments, the net magnetization decreases. ZP1 has the highest M_s (45.92 emu/g) because it retains more Fe^{3+} in key sites (both M_a and M_b), resulting in a higher net magnetization. The substitution of Co^{2+} and Cr^{3+} in ZP1 is relatively minimal, preserving the magnetic strength. The low R_g (0.211 MΩ) and R_{gb} (0.02 MΩ) allow efficient charge movement within the grains and across the grain boundaries. This efficient charge movement

preserves the alignment of the magnetic domains, contributing to the stronger superexchange interactions between Fe^{3+} ions and resulting in a higher saturation magnetization (M_s = 45.92 emu/g) and higher coercivity (H_c = 5382.78 Oe). ZP2 shows a drop in M_s (30.25 emu/g) and H_c (2470.95 Oe) because more Fe^{3+} is substituted by Co^{2+} and Cr^{3+}, reducing the contributions from the spin-up sublattice M_a. The higher grain boundary resistance (R_{gb} = 8.88 MΩ) also disrupts the superexchange interactions between Fe^{3+} ions, further reducing the overall magnetization. ZP3 exhibits the highest grain resistance (R_g = 4.03 MΩ) and a moderate grain boundary resistance (R_{gb} = 0.09 MΩ). The high R_g indicates poor charge movement within the grains, which can disrupt the alignment of magnetic domains, leading to a lower saturation magnetization (M_s = 22.55 emu/g) and coercivity (H_c = 1889.95 Oe). The combined effect of reduced M_a and relatively constant M_b results in a significant reduction in net magnetization. When a material contains weak magnetic ions the overall contribution to the saturation magnetization decreases.

Coercivity (H_c) values decrease with increasing substitution, indicating that less energy is required to reverse the magnetic domains in the material:

ZP1: H_c = 5382.78 Oe, **ZP2**: H_c = 2470.95 Oe, **ZP3**: H_c = 1889.95 Oe

Coercivity decreases as Co^{2+} and Cr^{3+} substitution increases. The reduction in H_c is linked to the softening of magnetic behaviour due to weaker superexchange interactions. In ZP1, the higher coercivity is supported by stronger magnetic pinning, which is linked to lower grain boundary resistance (R_{gb} = 0.02 MΩ). In ZP2 and ZP3, the higher R_{gb} values (8.88 MΩ for ZP2 and 0.09 MΩ for ZP3) reduce the ability to pin domain walls effectively, leading to a softer magnetic response and lower coercivity. The anisotropy field H_a not only decreases with decreasing H_c, but it is also strongly influenced by the material's coercivity. Thus, the lower the coercivity of the sample, the lower the anisotropy field.

Remanent magnetization (M_r) represents the amount of magnetization retained by the material after the external magnetic field is removed. The values show a decreasing trend with increasing substitution:

ZP1: M_r = 23.84 emu/g, **ZP2**: M_r = 15.44 emu/g, **ZP3**: M_r = 11.53 emu/g

The remanent magnetization (M_r) shows a decreasing trend, consistent with the substitution of Fe^{3+} ions by Co^{2+} and Cr^{3+}. The weakening of magnetic interactions reduces the material's ability to retain magnetization after the removal of the external field. ZP1 retains the highest M_r, while ZP3 has the lowest, due to the progressive disruption of magnetic domains caused by increasing Co^{2+} and Cr^{3+} content.

The remanence ratio (M_r/M_s) is a critical factor in determining the magnetic behaviour of the material. A value of $M_r/M_s<0.5$ suggests a multi-domain nature, indicating that the material consists of multiple magnetic domains. In the case of the Co-Cr doped samples, all M_r/M_s values are close to or below 0.5, which confirms the multi-domain behaviour:

ZP1: $M_r/M_s = 0.519$, **ZP2**:$M_r/M_s = 0.510$, **ZP3**: $M_r/M_s = 0.511$

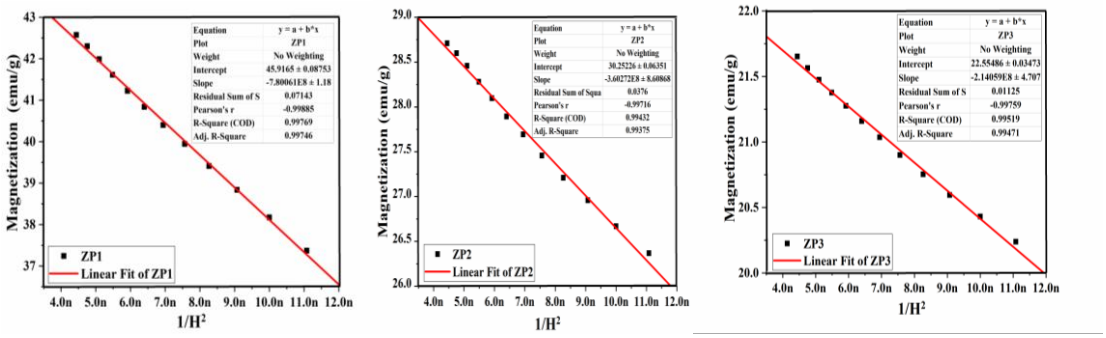

Figure 4.145 M_s versus 1/ H^2 plots for all hexaferrite samples.

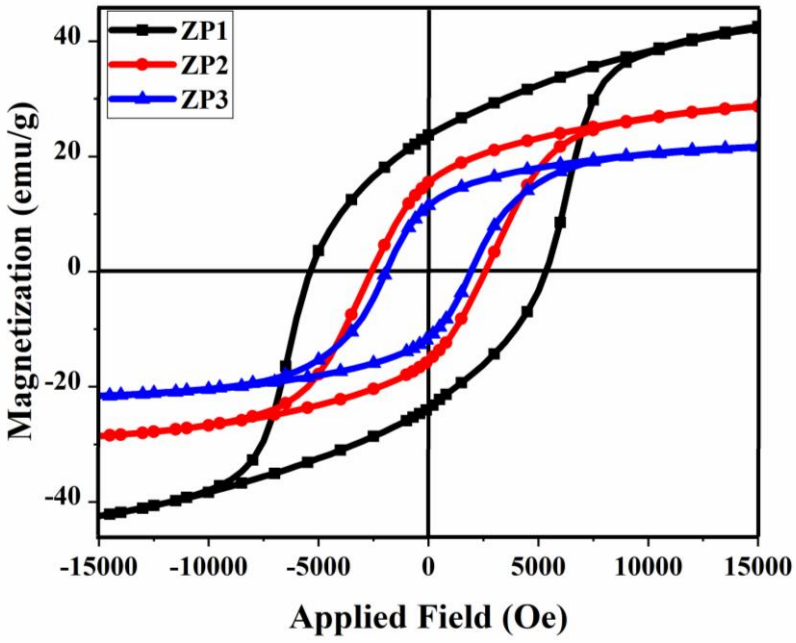

Figure 4.146 Hysteresis loops of ZP1, ZP2 and ZP3 hexaferrite.

Table 4.46 Magnetic parameters M_s, H_c, H_a, M_r and M_r/M_s value of all hexaferrite samples.

sample	M_s	H_c	H_a=sqrt(-15B)	H_a (kOe)	M_r	M_r/M_s
ZP1	45.92	5382.78	15963.40	23.45	23.84	0.519
ZP2	30.25	2470.95	13365.40	15.69	15.44	0.510
ZP3	22.55	1889.95	11931.42	11.24	11.53	0.511

4.8.4 Electromagnetic Characteristics

4.8.4.1 Complex permeability and complex permittivity

The figure 4.147 displays plots of (ε'),(ε"), (μ'), and (μ") against frequency. ZP1 displays the highest dielectric constant (ε') across the frequency range, starting from 5.94 at 8 GHz and decreasing to 4.84 at 12 GHz. ZP1 exhibits a relatively stable trend with minor fluctuations, indicating strong dielectric polarization and stable electron hopping within the material. This higher dielectric constant suggests that ZP1 has a greater ability to store electrical energy. ZP2 has the lowest dielectric constant among the three samples. It starts at 4.86 at 8 GHz and decreases steadily to around 4.00 at 12 GHz. The steady decline in ε' indicates a reduced capacity for energy storage at higher frequencies. ZP3 shows intermediate values of ε', starting at 5.30 at 8 GHz and decreasing to 4.04 at 12 GHz. ZP3 has a more dynamic variation, with a slight dip at around 9.5-10 GHz, indicating dielectric relaxation behaviour. ZP1 shows the highest dielectric loss values among the three samples. At 8 GHz, the value of ε" starts at 1.1803, and as frequency increases, the dielectric loss gradually decreases. Around 10 GHz, the dielectric loss reaches a dip at approximately 0.6378 before stabilizing slightly above 0.64 at 12 GHz. The overall trend for ZP1 shows a gradual decrease with some fluctuations, likely due to relaxation processes or resonance mechanisms in the material. ZP2 exhibits lower dielectric loss values compared to ZP1. At 8 GHz, the ε" value starts at 0.6588, maintaining a relatively steady range through the 8-9 GHz range. However, around 10 GHz, a notable increase occurs, with ε" peaking at 0.8325 around 9.5 GHz. After this peak, the dielectric loss gradually drops back to around 0.4652 at 12 GHz. ZP3, interestingly, displays a lower dielectric loss in comparison to ZP1 and ZP2, starting at 0.6631 at 8 GHz and maintaining a fairly

steady trend up to around 10 GHz. Afterward, the ε" values for ZP3 decrease sharply, even reaching negative values (approximately -0.8 at 12 GHz).

For the real part of permeability (μ'), ZP1 starts at 0.2376 at 8 GHz and increases steadily to 0.8702 at 12 GHz, showing a strong enhancement in its magnetic response. ZP2 begins at 0.3653 and increases to 0.8597 by 12 GHz, while ZP3 starts at 0.5011 and climbs to 1.0352 at 12 GHz, indicating the strongest magnetic response among the three. This trend of increasing μ' across all samples suggests improved magnetic storage capabilities at higher frequencies, particularly in ZP3, which exhibits the highest values. ZP1 reaches a sharp peak of approximately 0.4 at 9.5 GHz, indicating strong ferromagnetic resonance, after which it rapidly declines. On the other hand, ZP3 does not exhibit a distinct peak at 9.5 GHz but rather shows a continuous rise in magnetic loss after 10 GHz, reaching approximately 0.4 at 12 GHz and continuing to increase. The higher magnetic losses in ZP1 and ZP3 beyond 9 GHz suggest substantial energy dissipation due to magnetic resonance, with ZP3 showing the highest loss at higher frequencies.

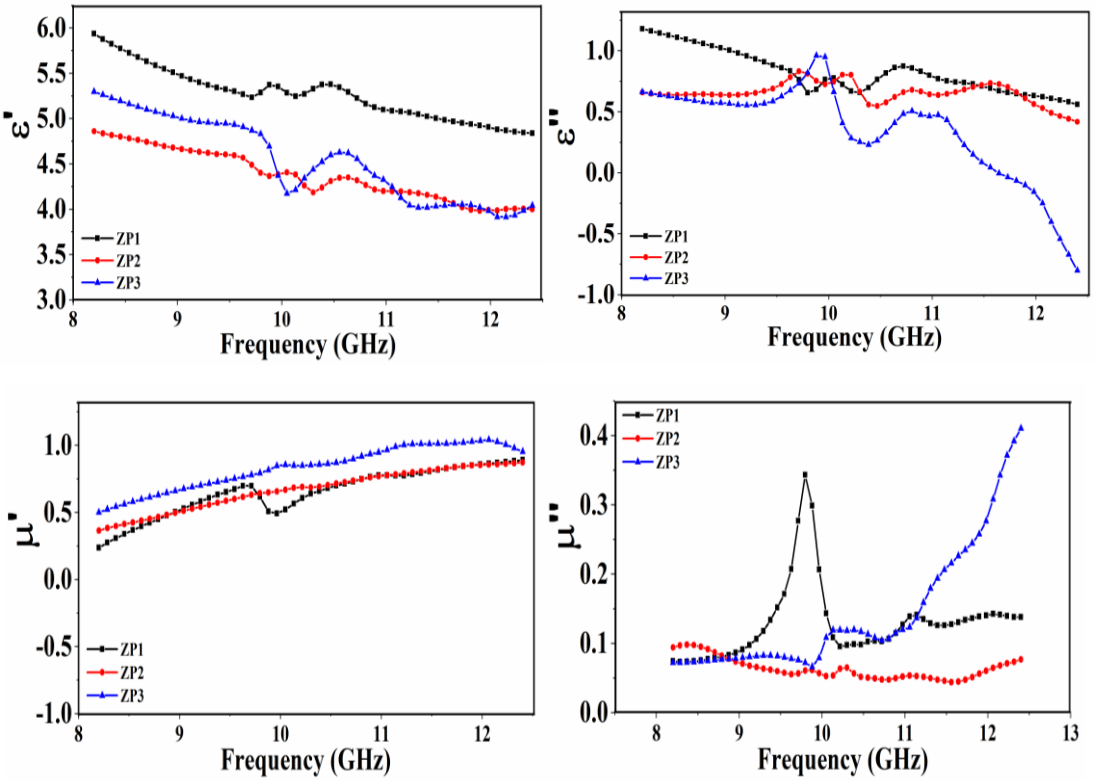

Figure 4.147 Complex permittivity and permeability versus frequency plots for $BaCo_xCr_xFe_{12-2x}O_{19}$ (ZP1 to ZP3).

4.8.4.2 Microwave absorption in $BaCo_xCr_xFe_{12-2x}O_{19}$ / PANI

4.8.4.3 Quarter Wavelength Mechanism

We analyzed graphs depicting the reflection loss of several materials at varying thicknesses and frequencies, therefore illuminating the magnitude of microwave energy they reflected. The presented figures provide significant insights into the microwave absorption characteristics of the materials. The findings for the ferrites we manufactured are reported in Figures 4.148 and subsequent figures. By conducting a meticulous analysis of these graphs, we successfully identified and measured several properties of the materials. For a concise overview of these characteristics, please refer to Table 4.47.

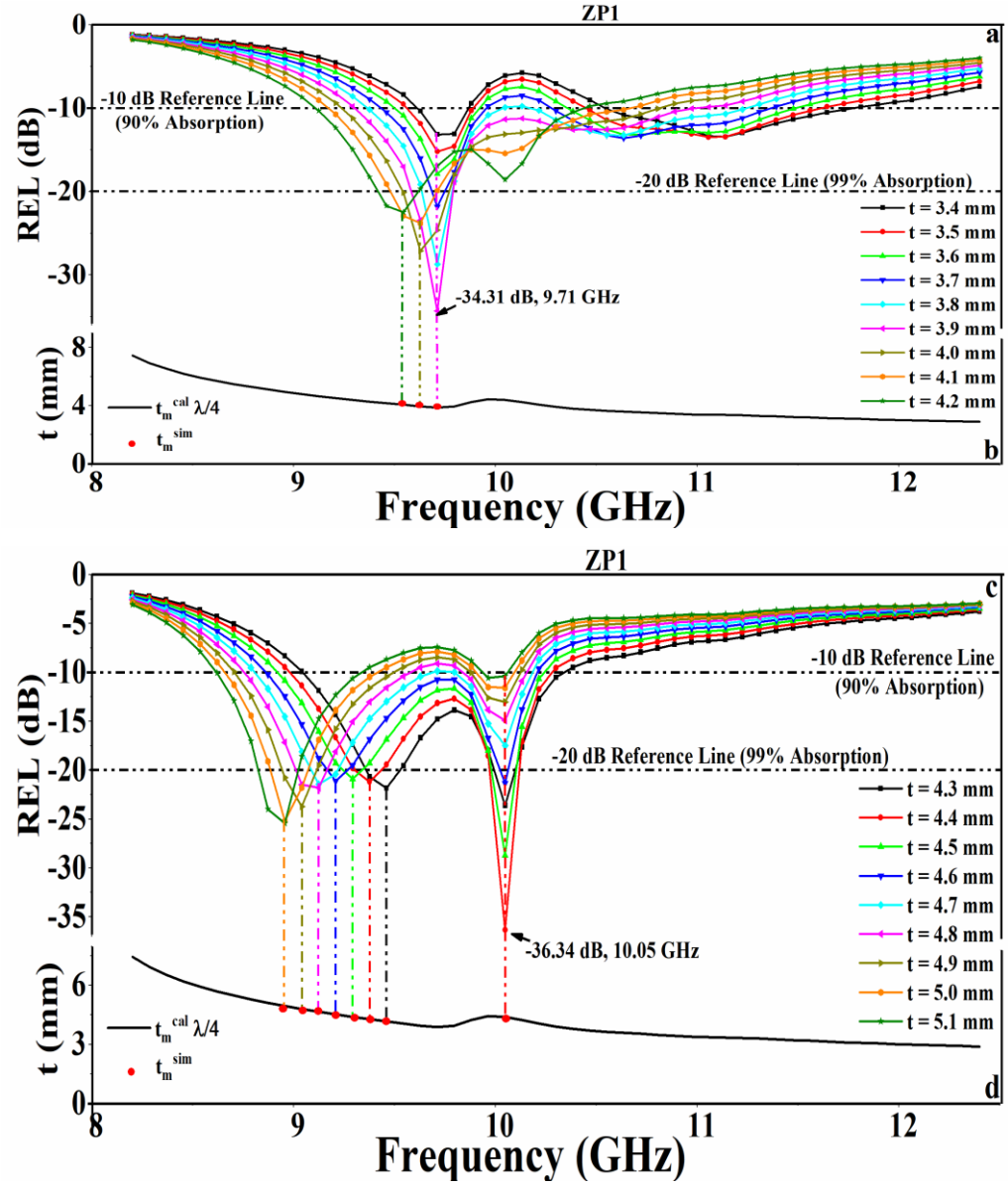

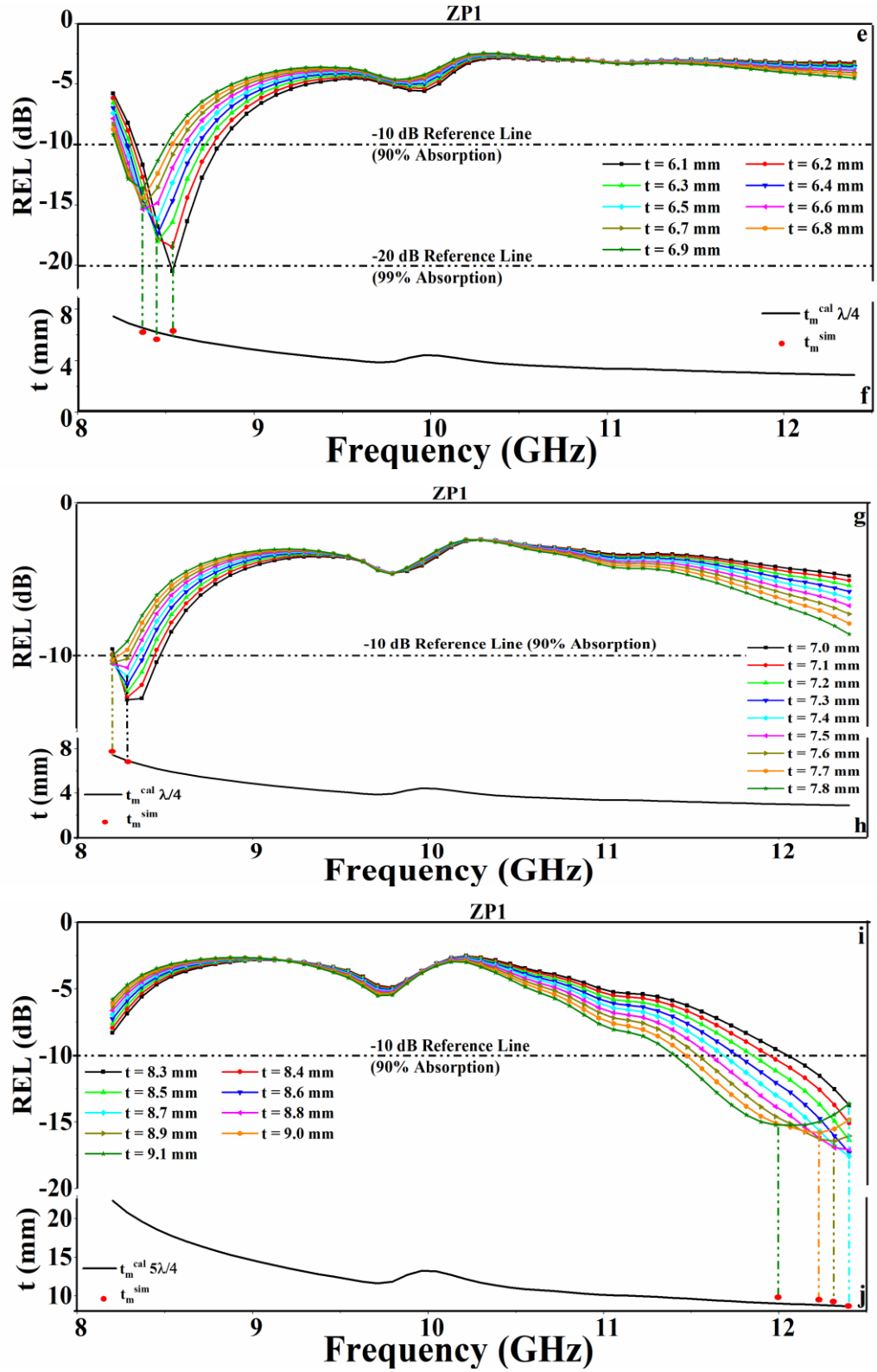
ZP1
e
REL (dB)
-10 dB Reference Line
(90% Absorption)
-20 dB Reference Line
(99% Absorption)
t = 6.1 mm
t = 6.2 mm
t = 6.3 mm
t = 6.4 mm
t = 6.5 mm
t = 6.6 mm
t = 6.7 mm
t = 6.8 mm
t = 6.9 mm
t (mm)
t_m^{cal} λ/4
t_m^{sim}
f
Frequency (GHz)
ZP1
g
REL (dB)
-10 dB Reference Line (90% Absorption)
t = 7.0 mm
t = 7.1 mm
t = 7.2 mm
t = 7.3 mm
t = 7.4 mm
t = 7.5 mm
t = 7.6 mm
t = 7.7 mm
t = 7.8 mm
t (mm)
t_m^{cal} λ/4
t_m^{sim}
h
Frequency (GHz)
ZP1
i
REL (dB)
-10 dB Reference Line
(90% Absorption)
t = 8.3 mm
t = 8.4 mm
t = 8.5 mm
t = 8.6 mm
t = 8.7 mm
t = 8.8 mm
t = 8.9 mm
t = 9.0 mm
t = 9.1 mm
t (mm)
t_m^{cal} 5λ/4
t_m^{sim}
j
Frequency (GHz)

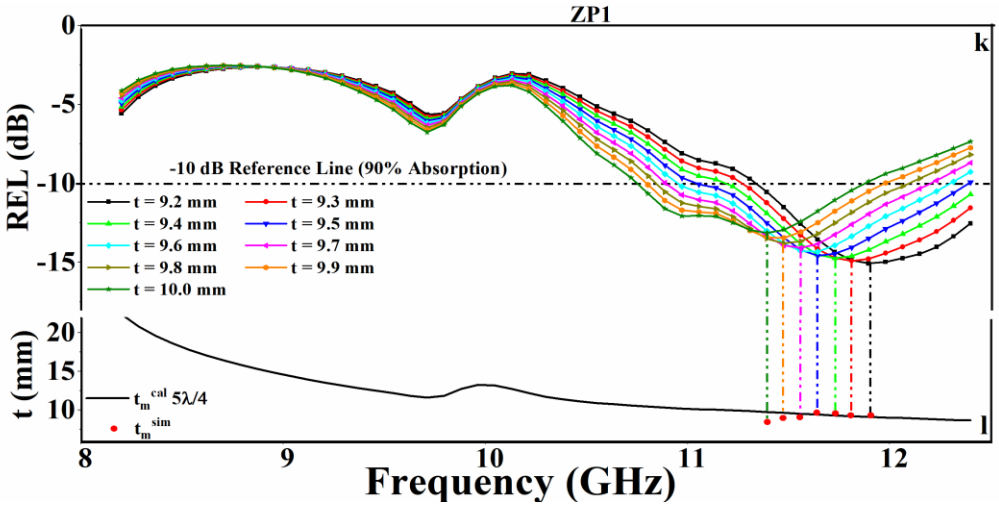

Figure 4.148 REL versus frequency for different thickness (ZP1) and calculate thickness versus frequency for $BaCo_xCr_xFe_{12-2x}O_{19}$ / PANI

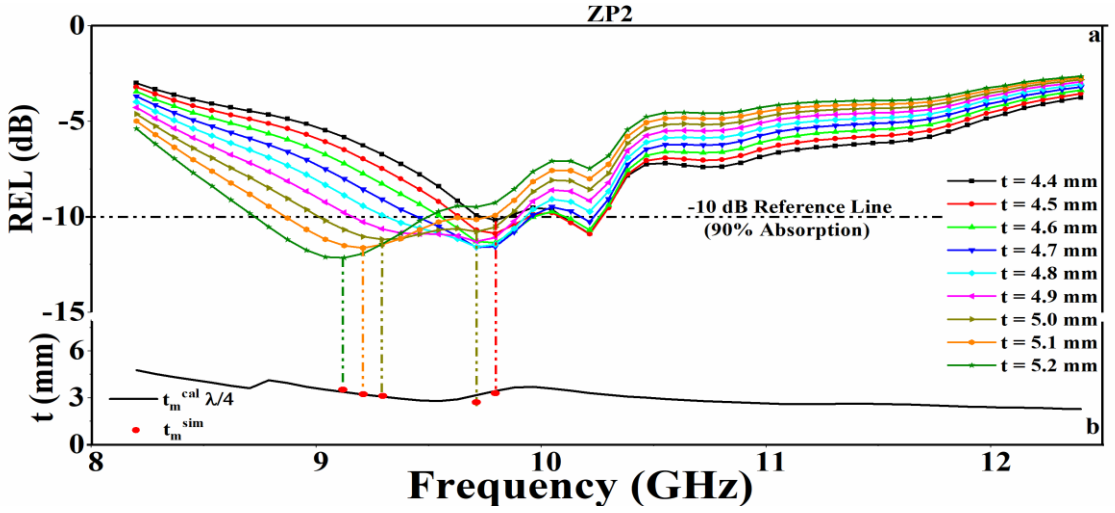

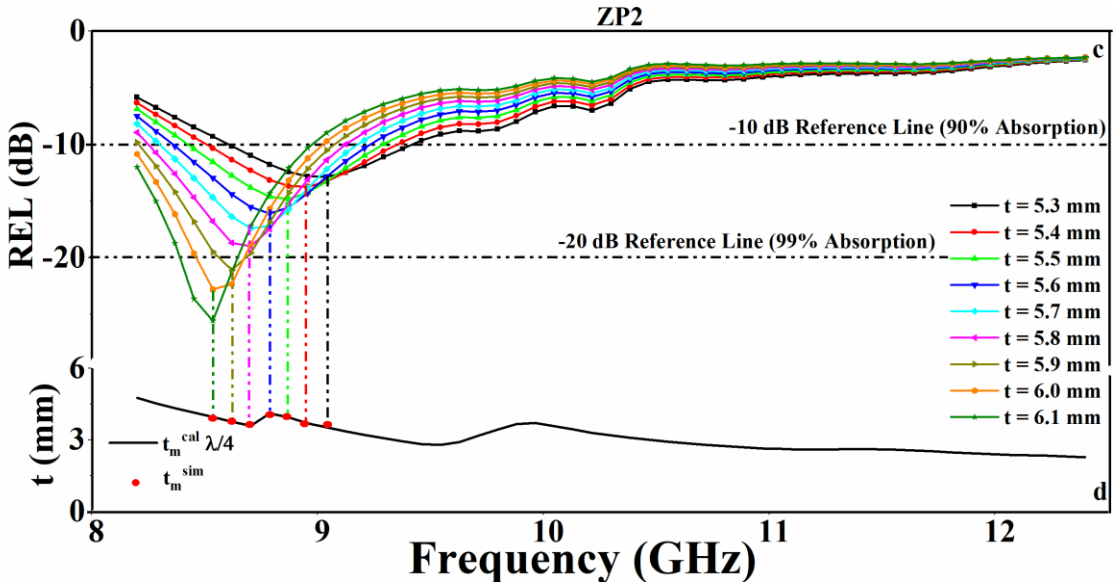

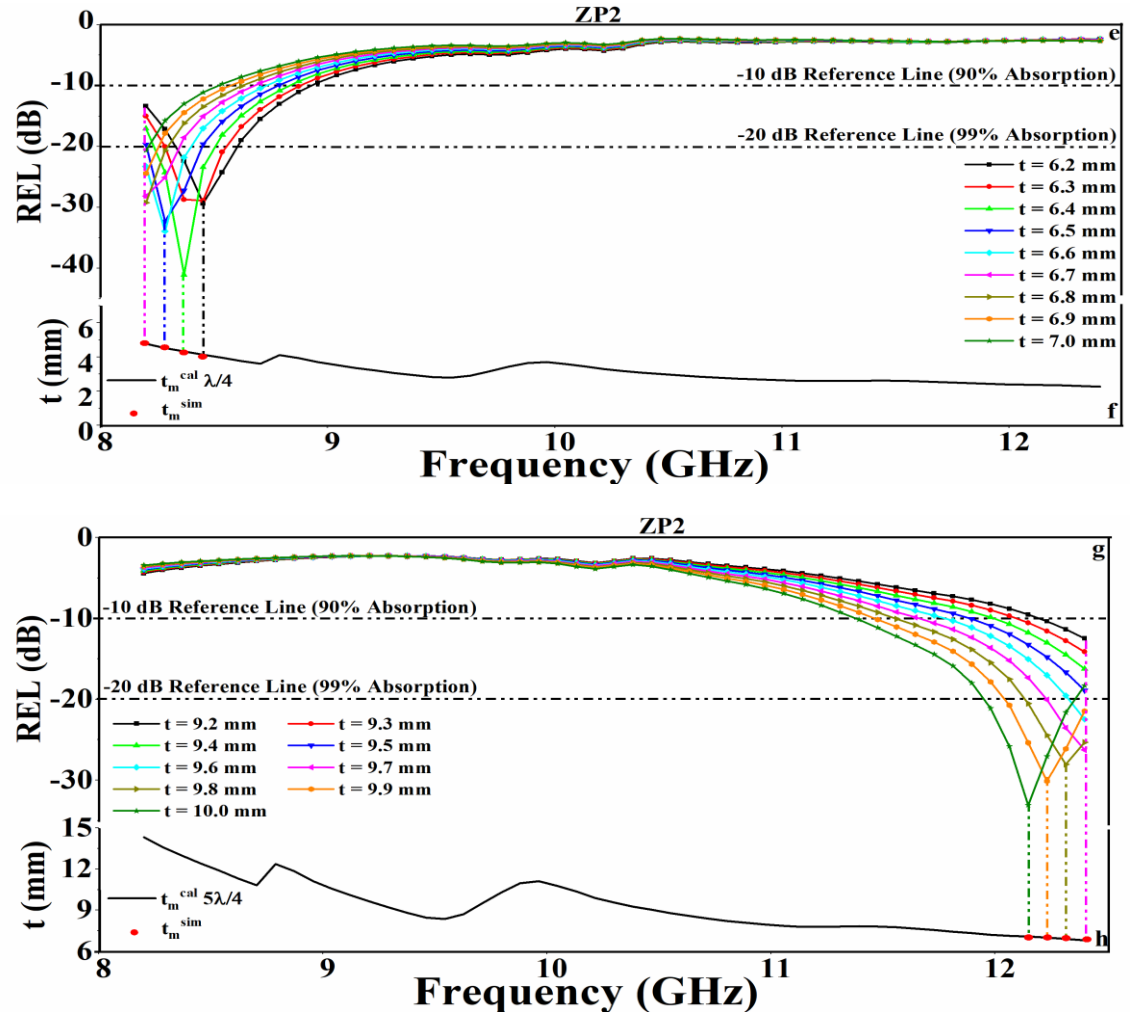

Figure 4.149. REL versus frequency for different thickness (ZP2) and calculate thickness versus frequency for $BaCo_xCr_xFe_{12-2x}O_{19}$ / PANI

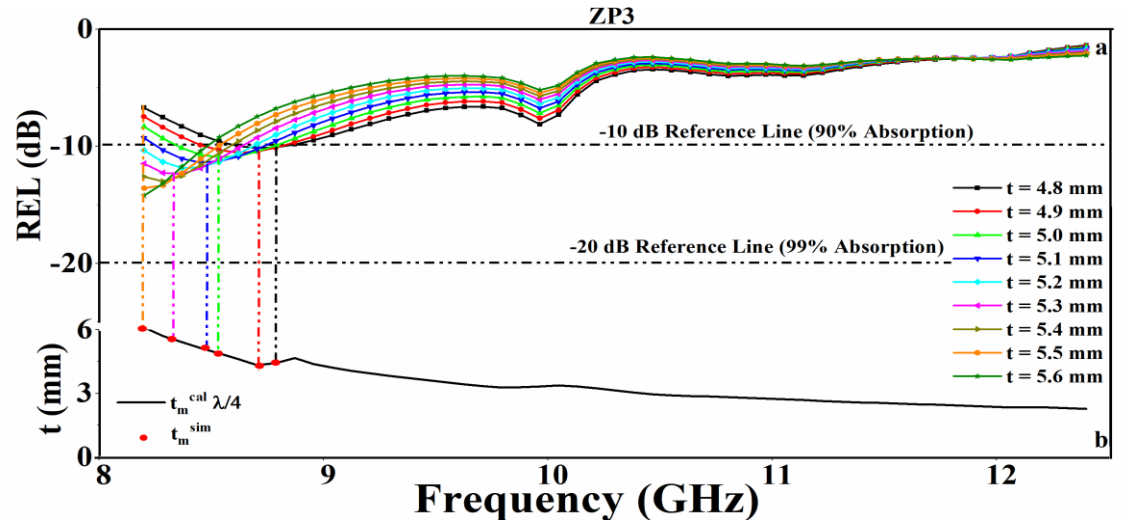

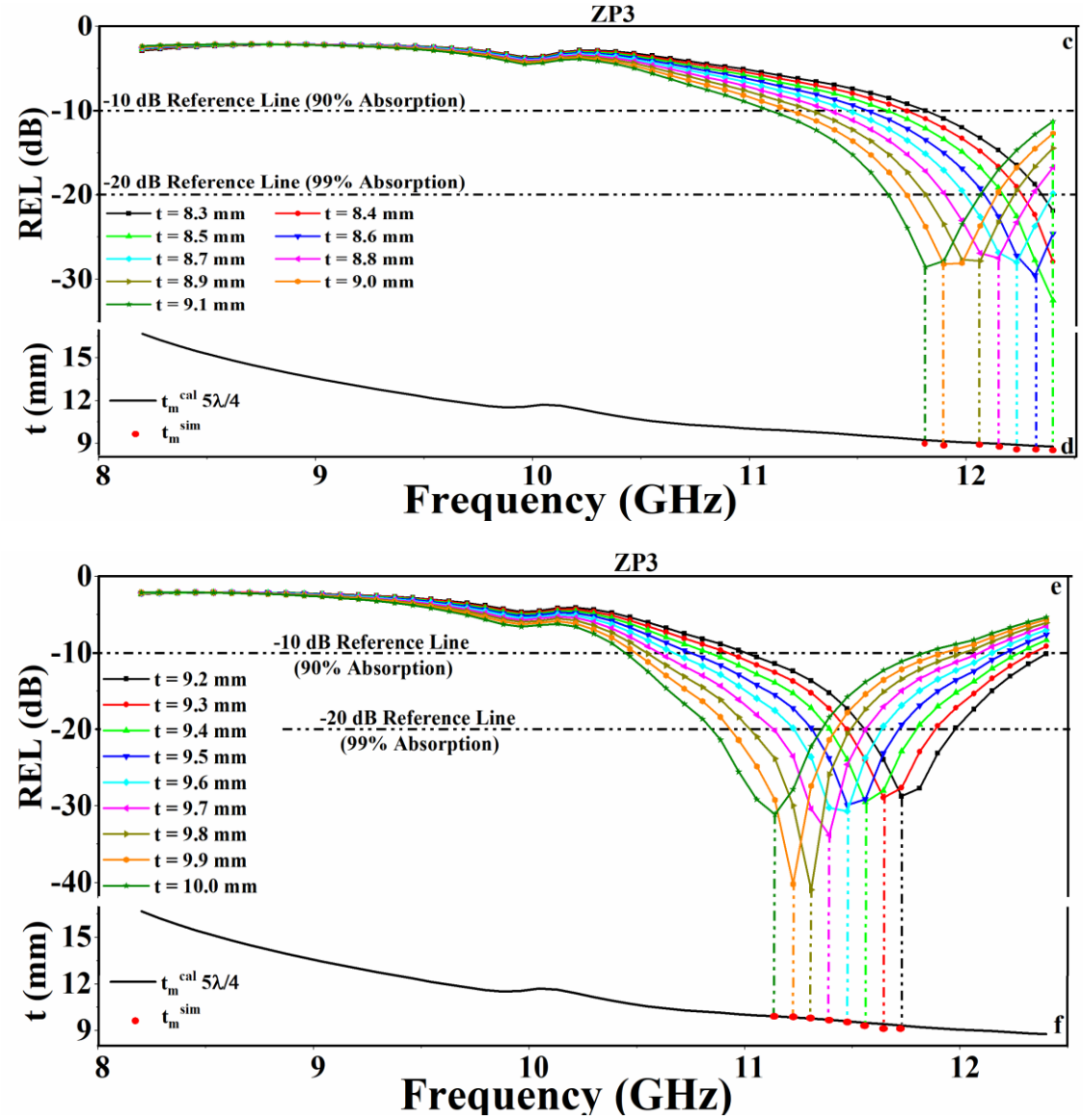

Figure 4.150 REL versus frequency for different thickness (ZP3) and calculate thickness versus frequency for $BaCo_xCr_xFe_{12-2x}O_{19}$ / PANI

For ZP1, the maximum reflection loss (REL) is observed at 4.4 mm, reaching -36.34 dB at 10.05 GHz, which is the best-performing thickness for this composition. The lowest REL occurs at a thickness of 7 mm, where the REL is -12.89 dB at 8.28 GHz, indicating relatively lower absorption. At 3.5 mm, the REL is -15.15 dB at 9.71 GHz, with a -10 dB bandwidth from 9.56 to 9.88 GHz (0.32 GHz). At 3.9 mm, the REL improves significantly to -34.31 dB at 9.71 GHz, with a -10 dB band from 9.3 to 10.99 GHz (1.69 GHz) and a -20 dB band from 9.58 to 9.79 GHz (0.21 GHz). At 4.2 mm, the REL is -22.52 dB at 9.54 GHz, with a -10 dB band from 9.108 to 10.45 GHz (1.342 GHz) and a -

20 dB band from 9.41 to 9.62 GHz (0.21 GHz). 4.6 mm, the REL reaches -21.14 dB at 9.21 GHz, with the -10 dB band spanning from 8.86 to 10.21 GHz and a -20 dB band from 9.17 to 9.27 GHz. At 6.1 mm, the REL is -20.54 dB at 8.54 GHz, with a -10 dB band from 8.33 to 8.81 GHz (0.48 GHz) and a -20 dB band from 8.52 to 8.55 GHz (0.03 GHz) At larger thicknesses, such as 9.6 mm, the maximum REL is -14.58 dB at 11.64 GHz, with a -10 dB band from 11.05 to 12.39 GHz and a bandwidth of 1.34 GHz, highlighting its strong performance across a wide frequency range.

For ZP2, the maximum REL occurs at 6.4 mm, with -41.09 dB at 8.37 GHz, making it the best-performing thickness for this sample. The lowest REL occurs at 4.5 mm, where the REL is -10.88 dB at 9.79 GHz. At 4.5 mm, the REL is -10.88 dB at 9.79 GHz, with a -10 dB band from 9.63 to 9.94 GHz (0.31 GHz). Increasing the thickness to 5.1 mm improves the REL to -11.62 dB at 9.21 GHz, with a -10 dB band from 8.86 to 9.76 GHz, demonstrating broader absorption across this range. At 5.3 mm, the REL improves to -12.89 dB at 9.04 GHz, with a -10 dB band from 8.6 to 9.41 GHz (0.81 GHz). At 5.9 mm, the REL reaches -21.18 dB at 8.62 GHz, with a -10 dB band from 8.2 to 9.07 GHz (0.87 GHz) and a -20 dB band from 8.55 to 8.68 GHz (0.13 GHz). At 6.1 mm, the REL improves further to -25.53 dB at 8.54 GHz, with a -20 dB band from 8.39 to 8.64 GHz (0.25 GHz). For even thicker samples, such as 9.9 mm, the REL remains significant at -30.13 dB at 12.23 GHz.

For ZP3, the maximum REL is observed at 9.8 mm, reaching -41.01 dB at 11.31 GHz, while the lowest REL occurs at 4.8 mm, where the REL is -10.15 dB at 8.7 GHz. At 4.8 mm, the REL is -10.15 dB at 8.7 GHz, with a -10 dB band from 8.59 to 8.85 GHz (0.26 GHz). At 5 mm, the REL improves to -10.95 dB at 8.53 GHz, with a -10 dB band from 8.34 to 8.79 GHz (0.45 GHz). At 8.7 mm, the REL reaches -28.01 dB at 12.23 GHz, with a -10 dB band from 11.98 to 12.4 GHz (0.42 GHz). At 9.9 mm, ZP3 maintains strong performance with an REL of -40.4 dB at 11.22 GHz, with the -10 dB band from 10.5 to 11.92 GHz and the -20 dB band from 10.93 to 11.42 GHz, further illustrating its wide absorption capabilities.

The study investigates the correlation between REL peaks and the λ/4 mechanism by comparing the computed thickness (t_m^{cal}) with the simulated thickness (t_m^{sim}). The inclusion of REL peaks in the thickness-frequency graphs enables a clear comparison between the computed and simulated thickness lines. The observed reflection loss peaks,

particularly for compositions ZP1, ZP2, and ZP3, align well with the λ/4 and 5λ/4 mechanisms for n=1 and 5, confirming that the λ/4 resonance plays a crucial role in the absorption behaviour of the doped compositions.

Table 4.47 REL with matching thickness/frequency, BW, and PBW for $BaCo_xCr_xFe_{12-2x}O_{19}$ (Z1 to Z5).

Sample Name	Matching Thickness (mm)	Maximum REL (dB)	Matching frequency (GHz)	Frequency Band for REL > -10 dB (GHz)	Bandwidth for RL > -10 dB (GHz)	Frequency Band REL > -20 dB (GHz)	Bandwidth for REL > -20 dB (GHz)	BTR	PBW (%)
ZP1	3.5	-15.15	9.71	9.56-9.88	0.32	---	-	2.90E-04	3.30
	3.9	-34.31	9.71	9.3-10.99	1.69	9.58-9.79	0.21	1.27E-03	17.40
	4	-26.93	9.63	9.24-10.81	1.57	9.53-9.77	0.24	1.18E-03	16.30
	4.2	-22.516	9.54	9.108-10.45	1.342	9.41-9.62	0.21	1.01E-03	14.07
	4.3	-21.87	9.46	9.05-10.35	1.3	9.35-9.52	0.17	9.68E-04	13.74
	4.4	-21.21	9.38	8.98-10.28	1.3	9.3-9.43	0.13	9.60E-04	13.86
	4.4	-36.34	10.05	---	-	9.97-10.12	0.15	1.01E-04	1.49
	4.5	-20.82	9.29	8.92-10.24	1.32	9.24-9.34	0.1	9.63E-04	14.21
	4.6	-21.14	9.21	8.86-10.21	1.35	9.17-9.27	0.1	9.73E-04	14.66
	4.7	-21.43	9.12	8.81-9.67	0.86	9.08-9.22	0.14	6.44E-04	9.43
	4.9	-23.71	9.04	8.71-9.49	0.78	8.94-9.12	0.18	5.78E-04	8.63
	5.1	-25.36	8.95	8.62-9.34	0.72	8.82-9.02	0.2	5.26E-04	8.04
	6.1	-20.54	8.54	8.33-8.81	0.48	8.52-8.55	0.03	3.22E-04	5.62
	6.3	-18.04	8.45	8.29-8.72	0.43	---	-	2.83E-04	5.09
	6.6	-15.29	8.37	8.24-8.61	0.37	---	-	2.37E-04	4.42
	7	-12.89	8.28	8.21-8.47	0.26	---	-	1.60E-04	3.14
	8.7	-17.56	12.4	---	-	---	-	-	-
	9.2	-15.12	11.9	---	-	---	-	-	-
	9.6	-14.58	11.64	11.05-12.39	1.34	---	-	3.06E-04	11.51
	9.8	-13.79	11.47	10.84-12.19	1.35	---	-	3.13E-04	11.77
	10	-13.15	11.39	10.75-11.87	1.12	---	-	2.63E-04	9.83
ZP2	4.5	-10.88	9.79	9.63-9.94	0.31	---	-	2.16E-04	3.17
	4.7	-11.59	9.71	9.45-9.95	0.5	---	-	3.39E-04	5.15
	5	-11.17	9.29	9.01-9.85	0.84	---	-	5.68E-04	9.04
	5.1	-11.62	9.21	8.86-9.76	0.9	---	-	6.12E-04	9.77

	5.2	-12.17	9.12	8.72-9.49	0.77	---	-	5.37E-04	8.44
	5.3	-12.89	9.04	8.6-9.41	0.81	---	-	5.67E-04	8.96
	5.4	-13.7	8.95	8.51-9.35	0.84	---	-	5.86E-04	9.39
	5.5	-14.72	8.87	8.42-9.29	0.87	---	-	6.07E-04	9.81
	5.6	-16.04	8.79	8.36-9.22	0.86	---	-	5.98E-04	9.78
	5.8	-18.92	8.7	8.25-9.12	0.87	---	-	5.98E-04	10.00
	5.9	-21.18	8.62	8.2-9.07	0.87	8.55-8.68	0.13	5.95E-04	10.09
	6.1	-25.53	8.54	---	-	8.39-8.64	0.25	1.70E-04	2.93
	6.2	-29.17	8.45	8.2-8.45	0.25	---	-	1.75E-04	2.96
	6.4	-41.09	8.37	8.24-8.5	0.26	---	-	1.74E-04	3.11
	6.5	-32.17	8.28	8.33-8.6	0.27	---	-	1.74E-04	3.26
	6.7	-28.01	8.2	---	-	---	-	-	-
	9.9	-30.13	12.23	---	-	---	-	-	-
	10	-33.07	12.15	11.94-12.35	0.41	---	-	8.34E-05	3.37
ZP3	4.8	-10.15	8.7	8.59-8.85	0.26	---	-	2.14E-04	2.99
	4.9	-10.54	8.62	8.45-8.83	0.38	---	-	3.12E-04	4.41
	5	-10.95	8.53	8.34-8.79	0.45	---	-	3.68E-04	5.28
	5.1	-11.41	8.45	8.25-8.74	0.49	---	-	4.00E-04	5.80
	8.7	-28.01	12.23	11.98-12.4	0.42	---	-	9.75E-05	3.43
	8.8	-27.61	12.15	11.9-12.31	0.41	---	-	9.54E-05	3.37
	8.9	-27.94	12.06	11.81-12.22	0.41	---	-	9.58E-05	3.40
	9	-28.27	11.89	11.72-12.14	0.42	---	-	9.84E-05	3.53
	9.1	-28.6	11.81	11.64-12.07	0.43	---	-	1.01E-04	3.64
	9.2	-28.61	11.73	10.99-12.41	1.42	11.47-11.89	0.42	3.40E-04	12.11
	9.3	-28.83	11.64	10.92-12.34	1.42	11.47-11.89	0.42	3.40E-04	12.20
	9.4	-29.23	11.56	10.82-12.27	1.45	11.39-11.79	0.4	3.49E-04	12.54
	9.6	-30.67	11.48	10.68-12.14	1.46	10.68-12.14	1.46	3.52E-04	12.72
	9.7	-33.74	11.39	10.61-12.09	1.48	11.13-11.56	0.43	3.57E-04	12.99
	9.8	-41.01	11.31	10.55-12.02	1.47	11.02-11.49	0.47	3.55E-04	13.00
	9.9	-40.4	11.22	10.5-11.92	1.42	10.93-11.42	0.49	3.44E-04	12.66
	10	-30.97	11.14	10.44-11.84	1.4	10.84-11.35	0.51	3.40E-04	12.57

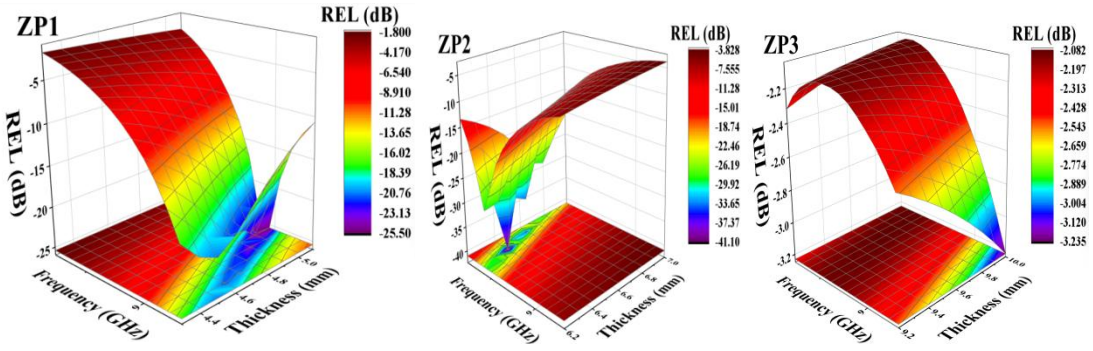

Figure 4.151 Three-dimensional (3D) plots of reflection loss at various frequencies and thicknesses for all samples of BaCoCr-series.

According to the Table 4.47, the quarter-wavelength criterion for composition ZP1 is observed at thicknesses ranging from 3.5 mm to 10.0 mm, with a -10 dB bandwidth varying from 0.26 GHz to 1.69 GHz. Maximum REL values between -12.89 dB and -36.34 dB are recorded, with the -20 dB bandwidth ranging from 0.03 GHz to 0.24 GHz. As illustrated in Figure 4.148 ZP1(a), the reflection loss peaks for ZP1 occur at 9.71 GHz for thicknesses of 3.5 mm, 3.9 mm, and 4.0 mm. Similar peaks are observed at higher frequencies, such as 10.05 GHz at 4.4 mm, with a notable decrease in peak height as thickness increases, as shown in Figure 4.148 ZP1(c). As shown in Figures 4.148 ZP1(a), ZP1(e), ZP1(g), ZP1(i) and ZP(k) in the higher thickness range (3.9 mm to 4.2 mm, 6.1 mm to 6.9 mm, 7.0 mm to 7.8 mm, 8.3 mm to 9.1 mm and 9.2mm to 10.00 mm respectively), the REL peaks shift toward lower frequencies, with peak heights gradually decreasing. This behaviour is consistent with the quarter-wavelength mechanism, where increasing thickness results in a corresponding shift in peak absorption to lower frequencies.

For ZP2, the -10 dB bandwidth spans from 0.25 GHz to 0.90 GHz across thicknesses ranging from 4.5 mm to 10.0 mm. The maximum REL values, ranging from -10.89 dB to -41.09 dB, indicate a broad absorption range, and the -20 dB bandwidth varies between 0.13 GHz and 0.25 GHz. As shown in Figure 4.149 ZP2(a) and ZP2 (c), the reflection loss peaks shift to lower frequencies with increasing thickness and height of peaks also increase, especially in the range of 8.00 GHz to 10.00 GHz for thicknesses between 4.4 mm and 5.2 mm and 5.3 mm and 6.1 mm respectively.

In the case of ZP3, REL values range between -10.15 dB and -41.01 dB for thicknesses between 4.8 mm and 10.0 mm, with the maximum REL recorded at 9.8

mm with -41.01 dB at 11.31 GHz. The bandwidth for REL > -10 dB varies between 0.26 GHz and 1.48 GHz. In Figure 4.150 ZP3 (a), it is illustrated that as the thickness increases from 4.8 mm to 5.6 mm, the peak height increases and shifts toward a lower frequency, specifically within the range of 8.0 GHz to 9.00 GHz. This trend demonstrates the typical behaviour of the quarter-wavelength mechanism, where increasing thickness leads to a corresponding shift in absorption peaks to lower frequencies. Similarly, in Figures 4.150 ZP3(c) and ZP3(e), the reflection loss (REL) peaks shift toward the left (i.e., lower frequency regions) as the thickness increases from 8.3 mm to 10.0 mm. This leftward shift suggests that, as the material's thickness increases, the absorption frequency decreases, aligning with the inverse relationship between frequency and material thickness. This characteristic is crucial for applications requiring broader bandwidth and effective electromagnetic absorption over a wider frequency range.

4.8.4.4 Impedance matching mechanism

The variation in impedance of the material arises from its distinction in permittivity/permeability from that of free space. The differentiation between these two factors affects the absorption characteristics of the substrate. Due to the misalignment of these two elements, only a tiny fraction of the incident signal manages to pass through the material, while the bulk is reflected off the surface. However, if they are substantially same, a portion of it penetrates the substance and is thus absorbed by it. Therefore, it is essential to do research on impedance matching to development an effective absorber.

Figure 4.152 displays the plots of reflection loss and $|Z_{in}|$ v/s frequency for the processed samples. The Z_{in} values associated with the maximum reflection loss for the different compositions are shown in Table 4.48. Within each composition (ZP1 to ZP3), the most prominent REL peaks conform to the impedance matching approach.

For a thickness of 4.4 mm in composition ZP1, the REL peak of -36.34 dB at 10.05 GHz corresponds to an impedance value of Z_{real} = 382.16 Ω and Z_{img} = 10.36 Ω, resulting in a total impedance of Z_{in} = 382.30 Ω. This impedance is slightly higher than the ideal Z_0 = 377 Ω, indicating a less than perfect impedance matching. For composition ZP2, at a thickness of 6.4 mm, the REL peak of -41.09 dB at 8.37 GHz corresponds to Z_{real} = 382.67 Ω and Z_{img} = −3.62 Ω, giving a total impedance of Z_{in} =

382.69 Ω. This value is also slightly above Z_0 = 377 Ω, suggesting good, but not perfect, impedance matching. In the case of ZP3, for a thickness of 9.8 mm, the REL peak of -41.01 dB at 11.31 GHz corresponds to an impedance of Z_{real} = 381.48 Ω and Z_{img} = −5.11 Ω giving a total impedance of Z_{in} = 381.51 Ω. This impedance value is closer to Z_0 = 377 Ω, indicating better impedance matching and effective absorption. The variation in the input impedance Z_{in} is primarily driven by its real (Z_{real}) and imaginary (Z_{img}) components. In all three compositions (ZP1, ZP2, and ZP3), the real and imaginary components of impedance demonstrate the role of impedance matching in achieving high reflection loss. Particularly for ZP2 and ZP3, the impedance values are close to the ideal Z_0, leading to the strongest absorption performance with REL values as low as -41.09 dB and -41.01 dB, respectively.

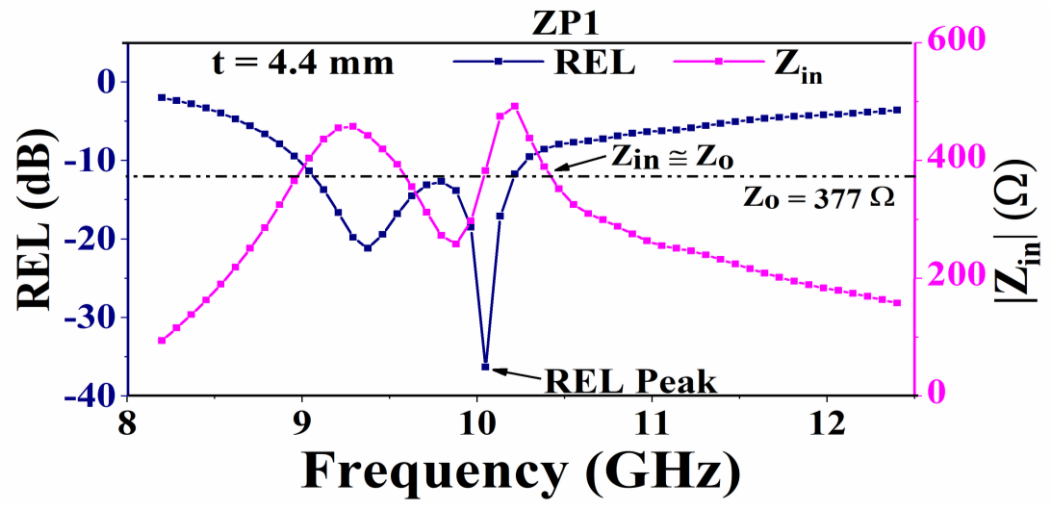

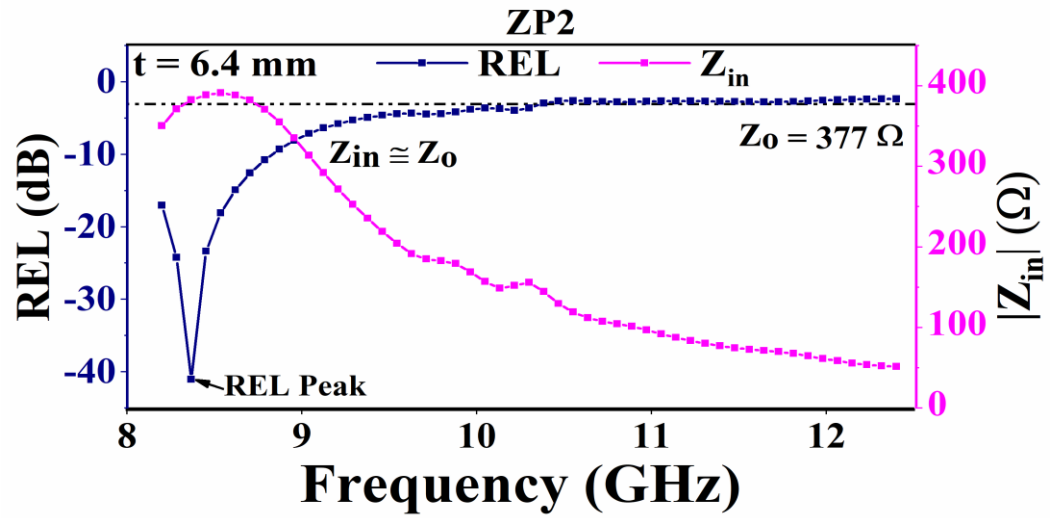

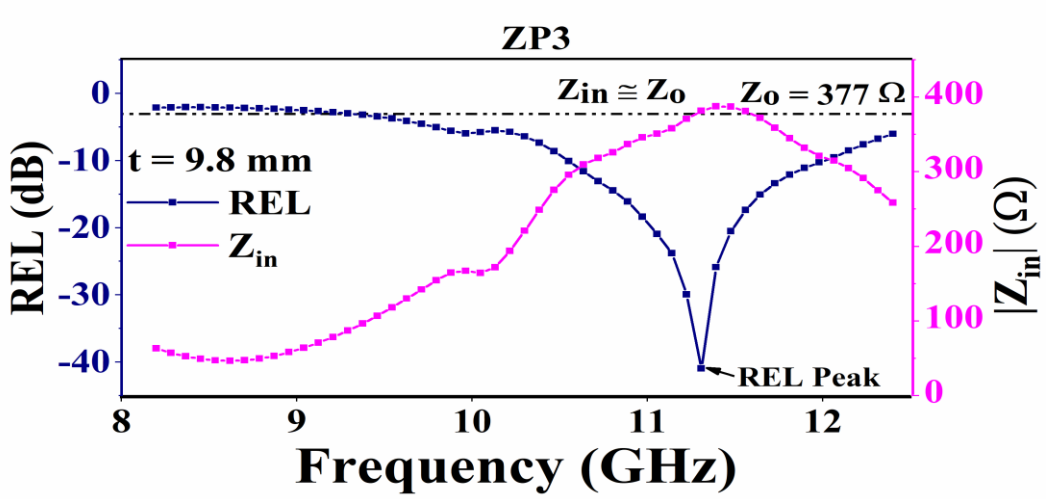

Figure 4.152 Z_{in} and REL curve against frequency for $BaCo_xCr_xFe_{12-2x}O_{19}$ / PANI.

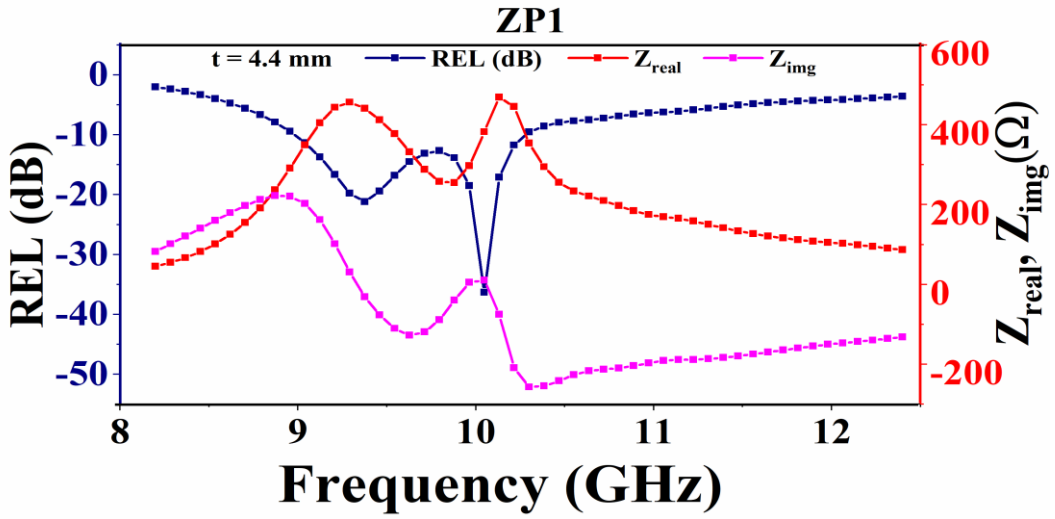

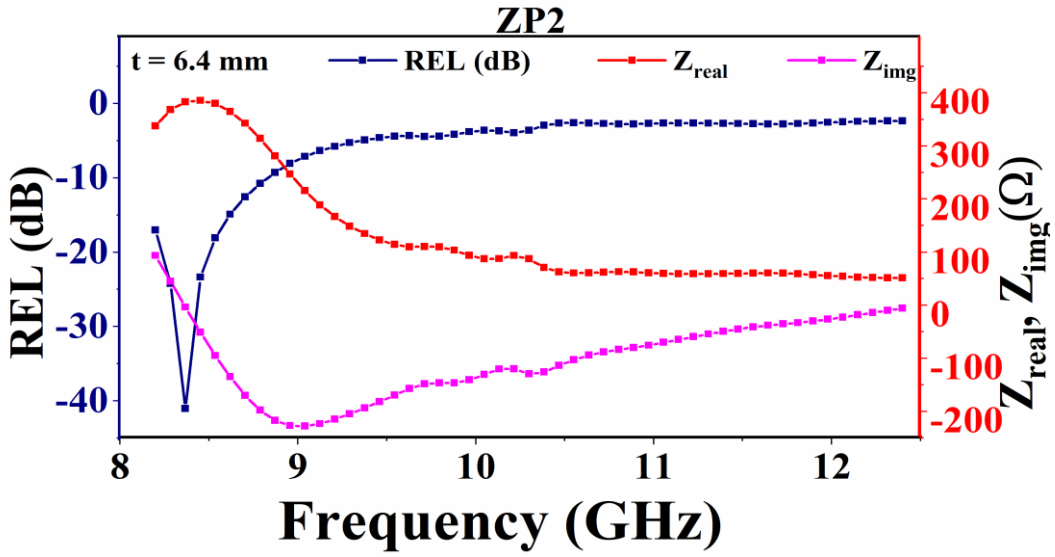

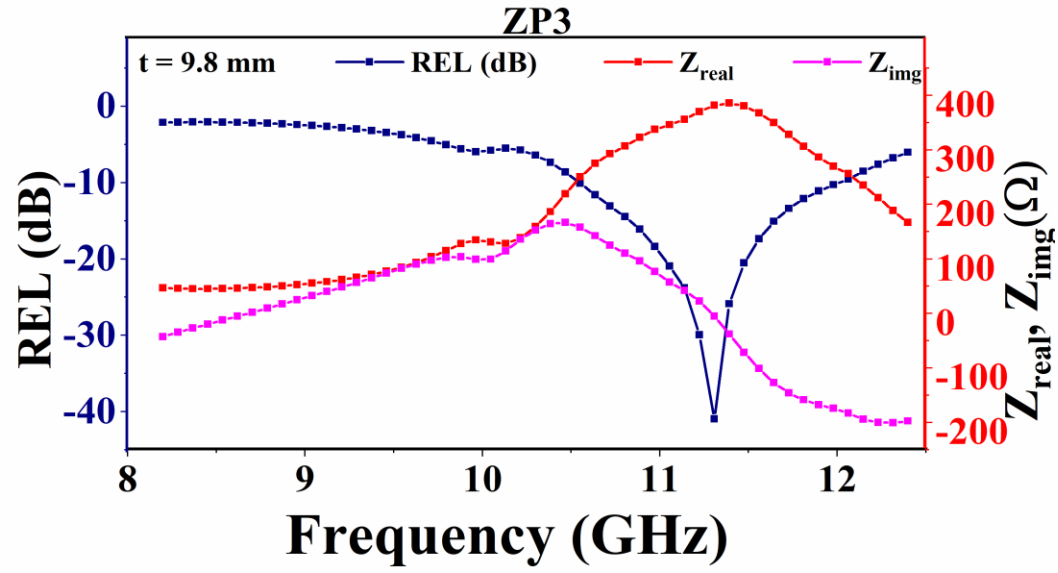

Figure 4.153 Z_{real}, Z_{imag}, and REL v/s frequency for $BaCo_xCr_xFe_{12-2x}O_{19}$ / PANI

Table 4.48 Z_{in}, Z_{real}, and Z_{imag} values corresponding to REL_{max} for $BaCo_xCr_xFe_{12-2x}O_{19}$ / PANI.

Sample Name	Matching Thickness (mm)	Maximum REL (dB)	Matching frequency (GHz)	Zreal (Ω)	Zimg (Ω)	|Zin| (Ω)
ZP1	4.4	-36.34	10.05	382.16	10.36	382.30
ZP2	6.4	-41.09	8.37	382.67	-3.62	382.69
ZP3	9.8	-41.01	11.31	381.48	-5.11	381.51

4.8.4.5 Eddy Current Loss

The Figure 4.154 shows the variation of C0 over a frequency range from 8 to 12.5 GHz for three samples: ZP1, ZP2, and ZP3. The curve for ZP1 shows a prominent peak around 9.7 GHz, where C0 reaches close to 1.6 ns. This indicates a sharp increase in the parameter C0 at this frequency, possibly due to a resonance or enhanced relaxation phenomenon in the sample. After the peak, C0 quickly decreases, stabilizing around 0.5 ns for frequencies above 10 GHz. ZP2 shows a generally flat and steady trend compared to ZP1, with C0 values consistently around 0.4 ns across the frequency range. This indicating a more stable or less frequency-sensitive response in this range. ZP3 has the lowest values of C0 across the frequency spectrum, generally staying close to zero. This implies minimal or no significant relaxation phenomena in this frequency range. The slight upward trend near 12 GHz indicates a marginal increase in C0 at higher frequencies, but the values remain lower than both ZP1 and ZP2.

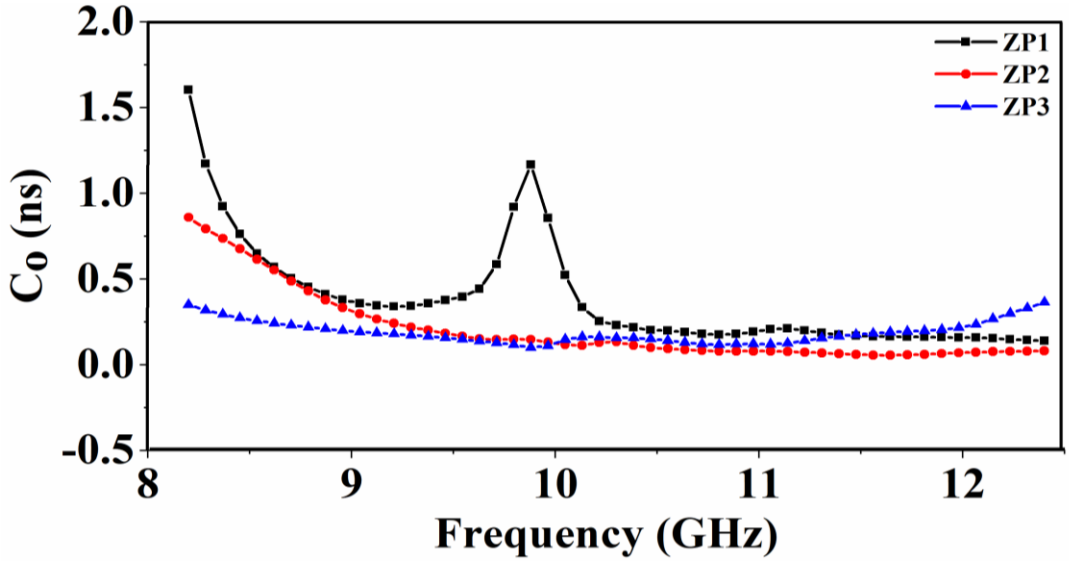

Figure 4.154 C_0 versus frequency curve for $BaCo_xCr_xFe_{12-2x}O_{19}$ / PANI.

4.8.4.6 Bandwidth to Thickness Ratio

The characterization and design of an absorber are significantly influenced by the large bandwidths achieved with lower thickness. Rather than only concentrating on increasing REL values, it is advisable to aim for a reduced thickness after the REL reaches -10 dB. Therefore, it is essential to determine the bandwidth to thickness ratio (BTR) and percentage bandwidth (PBW).

The BTR and PBW values for the prepared compositions ZP1, ZP2, and ZP3 are listed in the table 4.47. Among the three, ZP1 exhibits the highest BTR, with a value of 1.27E-03 and a PBW of 17.40% at a frequency of 9.71 GHz with an REL = -34.31 dB for a thickness of 3.9 mm.

Remarkably, ZP2 shows a maximum REL of -41.09 dB at a frequency of 8.37 GHz with a thickness of 6.4 mm, and although it has a lower BTR than ZP1, it demonstrates consistent performance with a BTR ranging from 8.34E-05 to 6.12E-04 and a PBW between 2.93% and 10.1% for frequencies spanning 8.2 GHz to 12.23 GHz. In addition, ZP3 exhibits a BTR ranging from 9.54E-05 to 4.00E-04 and a PBW ranging from 2.90% to 13.0% for frequencies between 8.45 GHz and 12.23 GHz, for thicknesses ranging between 4.8 mm and 10 mm. Overall, the results indicate that the reflection loss, bandwidth, and power bandwidth (PBW) of ZP1, ZP2, and ZP3 vary significantly with changes in thickness and frequency, with ZP1 achieving the best performance in terms of overall absorption at higher frequencies and thicknesses.

4.3.5 S – Parameter

When the input signal is applied at input port 1 of the test waveguide from VNA, the two-port S_{11} parameter accounts for the reflected signal from the same input port 1 from the sample fitted in the test waveguide of the VNA. S_{21} accompanies the attenuation in the signal traveling from input port 1 to output port 2. ZP1 shows a relatively stable reflection loss between -2 dB and -4 dB over the entire frequency range from 8 GHz to 12 GHz. ZP2 exhibits a dip around 9.5 GHz, where S_{11} reaches approximately -3 dB. After this, the value stabilizes around -2 dB for frequencies up to 12 GHz. ZP3 shows a deeper dip in S_{11} around 9.5 GHz, reaching a value close to -4 dB, which is the lowest among the three samples. This suggests that ZP3 has better impedance matching around this frequency. Beyond 9.5 GHz values decrease and reach upto -8 dB. ZP1 exhibits the lowest transmission among the three samples, with values ranging between -2 dB and -3 dB over the 8 GHz to 12 GHz range. There is a relatively flat trend in S_{21}, with minor variations. For the S_{21} parameters, ZP1 shows values ranging from -2.5 dB to -3.5 dB across the frequency range. ZP2 has a similar trend, starting at around -3 dB at 8 GHz and improving to -2 dB at 12 GHz, indicating relatively better compared to ZP1. ZP3 demonstrates similar pattern as ZP2, with S_{21} values improving from -3 dB at 8 GHz to about -2 dB at 12 GHz.

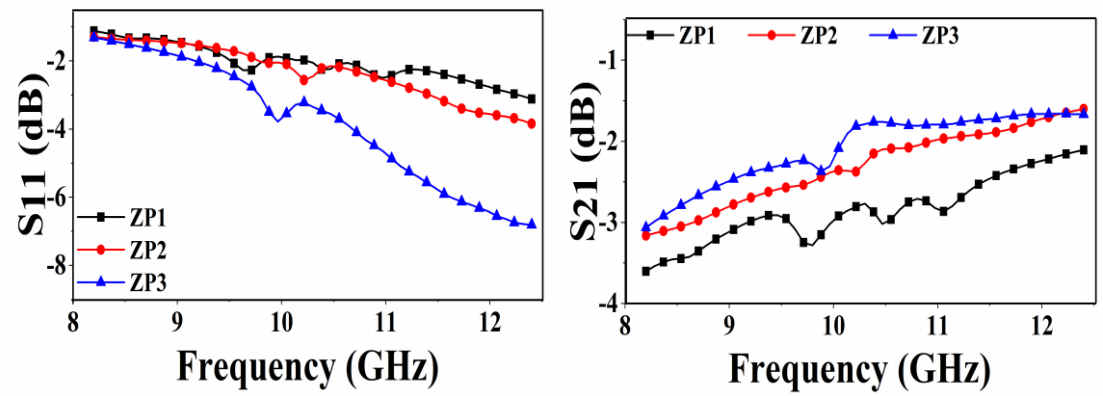

Figure 4.155 S_{11} and S_{21} versus frequency curve for $BaCo_xCr_xFe_{12-2x}O_{19}$ / PANI.

Conclusion

The results validate the effectiveness of Co-M substitutions in tailoring the structural, dielectric, magnetic, and microwave absorption properties of BaFe12O19 hexaferrites. Key conclusions include:

- Enhanced Performance through Substitution: Dopants significantly improved dielectric stability, grain boundary polarization, and magnetic alignment, contributing to superior electromagnetic absorption.
- Optimal Microwave Absorption: Samples like YP2 (-55.54 dB at 10.56 GHz) and X3 (-49.46 dB at 12.15 GHz) demonstrated exceptional performance, making them suitable for EMI shielding and broadband applications.
- PANI Composites: Integration of PANI into hexaferrites further enhanced charge mobility, conductivity relaxation, and impedance matching, confirming their viability for advanced electromagnetic applications.

This chapter establishes the synthesized hexaferrites and their composites as promising candidates for practical applications in EMI shielding, broadband microwave absorption, and related fields.

CHAPTER 5

SUMMARY AND CONCLUSION

This research thoroughly explores how Co-M (M = Al, Ce, Cd, Cr) co-substitution affects the structure, electrical properties, magnetic behavior, and microwave absorption capabilities of $BaFe_{12}O_{19}$ M-type hexaferrites and their polyaniline (PANI) composites. We systematically examined how different dopants and the addition of PANI change the core features of these materials, highlighting their significant promise for cutting-edge electromagnetic applications like EMI shielding.

Co-Al Doped $BaCo_xAl_xFe_{12-2x}O_{19}$ Hexaferrites (W Series)

We made these hexaferrites using the sol-gel combustion method, confirming their M-type hexagonal structure across all doping levels. We saw a consistent drop in unit cell volume (from 698.68×106 pm^3 in W0 to 690.89×106 pm^3 in W5) and smaller lattice parameters ('a' from 5.8937 A˚ to 5.8725 A˚, 'c' from 23.2261 A˚ to 23.1333 A˚). Crystallite sizes, derived from the Scherrer equation, ranged from 37.31 nm to 43.40 nm, with smaller sizes in doped samples suggesting internal stress.

FESEM imaging showed a change in grain shape: W0 had large, fused grains, while doped samples (W3, W4, W5) had smaller, needle-like grains. This change likely increases interfacial resistance, which helps absorb electromagnetic waves. Co-Al doping also created more voids and grain boundaries, affecting how the material responds to electric fields and its impedance. Dielectric permittivity (ε' and ε'') decreased with frequency, with doped samples having lower values (e.g., W1's ε' fell from 107.31 to 5.60 at 2 MHz). Prominent peaks in ε'' for W1 pointed to increased interfacial polarization.

Analysis of the electric modulus (M′) showed it increased with frequency. W4 and W5 had higher M′ at low frequencies, indicating strong grain boundary polarization. The peaks in the imaginary modulus (M″) shifted to higher frequencies, suggesting faster conductivity relaxation. Impedance components (Z′ and Z″) were higher at low frequencies due to considerable space charge polarization, dropping with frequency, which aligns with Koop's double-layer model. W4 and W5 showed significant influence from grain boundaries. AC conductivity (σ_{ac}) increased with frequency, indicating better electron hopping between Fe^{2+} and Fe^{3+} ions.

Magnetic properties displayed a non-linear trend for saturation magnetization (M_s): it first dropped from 87.97 emu/g (W0) to 50.28 emu/g (W1), then rose to 72.06 emu/g (W4), before settling at 58.32 emu/g (W5). Coercivity (H_c) decreased with more doping (from 4671 Oe in W0 to 2826.38 Oe in W5), implying that dopants made domain wall movement easier. The anisotropy field (H_a) peaked at 17.51 kOe in W4, likely due to stronger grain boundary effects.

Regarding microwave absorption, W5 performed best, showing a maximum reflection loss (REL) of −46.55 dB at 10.05 GHz with a 3.1 mm thickness. Impedance matching (Zin) for W5 was nearly perfect (379.49Ω), greatly reducing reflection and improving absorption.

Co-Ce Doped $BaCo_xCe_xFe_{12-2x}O_{19}$ Hexaferrites (X Series)

These Co-Ce substituted hexaferrites also had an M-type hexagonal structure, with minor changes in lattice parameters. The 'a' parameter went from 5.8937 A˚ (X0) to 5.8898 A˚ (X5), and the 'c' parameter from 23.2261 A˚ to 23.1998 A˚, leading to a unit cell volume decrease from 698.68 A˚3 (X0) to 696.97 A˚3 (X5). Crystallite size decreased from 43.39 nm for X0 to 33.73 nm for X5, showing controlled grain growth.

FESEM observations indicated that Co-Ce doping caused grain clumping and uneven grain distribution, especially with voids in heavily doped samples. This structure, particularly the many grain boundaries, affected dielectric and magnetic traits by boosting impedance and polarization. Both dielectric constant (ε′) and dielectric loss (ε″) dropped with frequency, signaling dielectric relaxation. X0's ε′ went from 83.48 at 100 Hz to 12.38 at 2 MHz, while X5 decreased from 130.03 to 4.13 in the same range, suggesting it's good for EMI shielding due to less polarization.

Electric modulus (M′) showed increased grain boundary polarization at low frequencies, especially for X4 and X5. The imaginary modulus (M″) peaks moved to higher frequencies with more Co-Ce doping, indicating quicker conductivity relaxation. Impedance spectroscopy showed high values at low frequencies, with Z′ and Z″ dropping as frequency increased. Cole-Cole plots for X1, X2, and X3 showed semicircles, pointing to strong grain boundary resistance.

AC conductivity (σ_{ac}) grew with frequency because of electron hopping, with σ_{ac} values significantly rising at higher doping levels, particularly in X2, which helps

dissipate energy in EMI uses. Magnetic analysis showed that Co-Ce substitution affected properties; saturation magnetization (M_s) dropped from 105.29 emu/g (X0) to 65.36 emu/g (X4), while coercivity (H_c) went from 5382 Oe (X0) to 2511 Oe (X5). Remanent magnetization (M_r) also fell, hinting at weaker magnetic coupling. Co-Ce doping impacted magnetic anisotropy (H_a), crucial for EMI shielding.

Microwave absorption analysis showed X3 had the best absorption, with a reflection loss (REL) of −49.46 dB at 12.15 GHz (7.4 mm thick), and ideal impedance matching with Zin values of 375.26Ω.

Co-Cd Doped $BaCo_xCd_xFe_{12-2x}O_{19}$ Hexaferrites (Y Series)

The Co-Cd substituted hexaferrites had an M-type hexagonal structure with slight lattice contraction. The unit cell volume shrank from 698.68 pm^3 (Y0) to 695.51 pm^3 (Y5), reflecting how different ion sizes can boost magnetic and dielectric properties.

FESEM analysis showed varied grain sizes. Doping led to larger grains in heavier-doped samples (especially Y3). This merging led to Y3 having the highest grain capacitance and fewer grain boundaries, affecting how it behaves electrically and magnetically. Dielectric properties showed ε′ and ε″ decreasing with frequency, indicating dielectric relaxation. Y0 had the highest ε′ at 83.48 (100 Hz), while Y5 dropped to 3.59 at 2 MHz, showing space charge polarization consistent with the Maxwell-Wagner model. Y2's ε″ peaked at 56.71 at 100 Hz, indicating strong energy storage.

In Electric Modulus (M′ and M″) analyses, Y5 had the highest M′ values at 2 MHz (0.24), suggesting energy storage from grain boundary resistance. Y5 also had the highest M″ (0.06), showing strong conductivity relaxation dynamics. Non-Debye relaxation in Cole-Cole plots for Y2, Y3, and Y5 confirmed better charge movement. Impedance spectroscopy showed notable grain and grain boundary resistance. Y0 had maximum Z′ at low frequencies (239.48 MΩ), and Y5 had the highest Z″ (1100 MΩ). This high impedance in Y5 was linked to lower AC conductivity, improving its dielectric properties and absorption.

AC conductivity (σ_{ac}) increased with frequency across all samples, driven by electron hopping. Y1 had the highest σ_{ac} ($0.00022\Omega m^{-1}$), linked to lower grain boundary resistance, while Y5 had the lowest, indicating restricted charge movement, which is good for insulation. Magnetic properties showed a non-linear trend. Y1 had the

highest saturation magnetization (M_s) at 101.60 emu/g, and Y5 the lowest. Coercivity (H_c) dropped from 4596.72 Oe (Y0) to 228.98 Oe (Y5), with a corresponding decrease in anisotropy, meaning less resistance to magnetic reversal.

For microwave absorption, Y4 achieved an optimal REL of −40.49 dB at 10.39 GHz with a thickness of 1.7 mm. Impedance matching for Y4 was nearly perfect, with Z_{real} and Z_{img} values at 382.24Ω and 5.55Ω, respectively. The quarter-wavelength mechanism worked well, showing strong EMI shielding potential.

Co-Cr Doped $BaCo_xCr_xFe_{12-2x}O_{19}$ Hexaferrites (Z Series)

The Co-Cr substituted hexaferrites maintained a hexagonal M-type structure, with a gradual reduction in lattice parameters and unit cell volume (from 699.00 $A^{\circ 3}$ in Z0 to 696.37 $A^{\circ 3}$ in Z5). This shrinking is because smaller Co^{2+} (0.72 A˚) and Cr^{3+} (0.63 A˚) ions replaced Fe^{3+}, creating internal stress that affected magnetic and dielectric behavior.

FESEM observations revealed notable morphological changes. Z0 had large, distinct grains, but more Co-Cr substitution (Z1 to Z5) resulted in more needle-like and unevenly shaped grains. This change increased grain boundary density, impacting dielectric characteristics and charge movement, especially in Z3 and Z4. Dielectric properties showed the expected Maxwell-Wagner polarization effect, with ε′ (from 83.48 in Z0 at 100 Hz to 25.50 in Z5) and ε″ (from 121.68 in Z0 to 19.48 in Z5) decreasing with frequency, showing less polarization and more resistance in doped samples. Z2, for instance, maintained effective charge polarization with ε′ at 55.38 and ε″ at 20.08 at 100 Hz.

Electric Modulus (M′ and M″) analyses indicated that higher frequencies increased M′ values. Z1 through Z5 showed clear M″ peaks, meaning efficient charge mobility and relaxation, with Z5 being particularly efficient. In impedance analysis, Z′ and Z″ dropped with frequency, showing less polarization and better conductivity in Z4 and Z5. Z0 had high initial impedance (Z′ = 190.09 MΩ, Z″ = 480.66 MΩ), while Z4 and Z5 showed lower resistance, suggesting better dielectric relaxation and absorption.

The AC conductivity of these samples increased with frequency due to electron hopping between Fe^{2+} and Fe^{3+} ions. Z2 had high σ_{ac} values, showing enhanced electronic and ionic conduction. Regarding magnetic properties, saturation magnetization (M_s) decreased non-monotonically from 79.99 emu/g (Z0) to 24.17

emu/g (Z5), due to weaker superexchange interactions. Interestingly, Z3's M_s increased to 64.46 emu/g, linked to less porosity and better magnetic ordering. Coercivity (H_c) and anisotropy field (H_a) also dropped with doping, making magnetic domain wall movement easier.

Microwave absorption performance was best in Z2 and Z4. Z2 achieved a REL of −40.8 dB at 10.05 GHz (6.1 mm thick) and Z4 reached −43.4 dB at 11.98 GHz (9.5 mm thick). These strong REL values, along with wide −10 dB bandwidths and near-ideal impedance matching (Z2: 370.27Ω, Z4: 372.33Ω), confirm the effectiveness of Co-Cr substituted hexaferrites for EMI shielding.

PANI Composites (WP, XP, YP, ZP Series)

The Co-Al substituted $BaCo_xAl_xFe_{12-2x}O_{19}$/PANI composites displayed significant shifts in structural, dielectric, magnetic, and microwave absorption properties, tailored to improve functionality in electromagnetic applications. In dielectric properties, WP1 exhibited the highest dielectric constant (ε') of 12,791.13 at lower frequencies due to strong polarization, while ε' dropped to 203.05 (WP2) and further to 52.31 (WP3), a reduction linked to the disrupted Fe^{3+} polarization by Co-Al substitution. The dielectric loss (ε'') followed a similar frequency-dependent pattern, with WP1 reaching a peak value of 172,173.3, indicative of high energy dissipation, while WP2 and WP3 presented lower ε'' values, enhancing energy retention, particularly at high frequencies.

The electric modulus analysis showed an increase in M' with frequency, with WP3 having the highest real modulus (M') of 9.22×10^{-2}, indicating significant resistive behaviour and strong relaxation dynamics. In contrast, WP1 exhibited a lower M' of 9.42×10^{-3}, reflecting high charge mobility. Imaginary modulus (M'') values corroborated this trend, with WP3 displaying higher energy dissipation due to stronger relaxation effects, while WP1 showed minimal energy loss, highlighting faster charge relaxation.

Impedance spectroscopy demonstrated a decline in both real and imaginary impedance values as frequency increased, indicating enhanced electron hopping and a reduction in overall impedance. WP3 presented the highest impedance values, with $Z' = 6.10 \times 10^7$ Ω at lower frequencies, dominated by grain boundary impedance. WP1, in contrast, demonstrated the lowest impedance, reflecting more effective charge

transport and lower interfacial resistance. Cole-Cole plot analysis for WP3 displayed larger semicircular arcs, indicating higher grain boundary resistance, whereas WP1's smaller arc suggested more efficient charge mobility.

In magnetic properties, WP1 showed the highest saturation magnetization (M_s) at 45.92 emu/g, coercivity (H_c) at 5382.78 Oe, and remanent magnetization (M_r) at 23.45 emu/g due to strong Fe^{3+} superexchange interactions. These values decreased with increased Co-Al substitution, with WP3 displaying M_s, H_c, and M_r values of 32.36 emu/g, 2928.91 Oe, and 16.78 emu/g respectively, reflecting the weakened magnetic alignment caused by non-magnetic Al^{3+} ions.

Microwave absorption properties were also significantly influenced by Co-Al substitution, with WP1 achieving a maximum reflection loss (REL) of -36.34 dB at 10.05 GHz at a thickness of 4.4 mm. WP2 reached an even higher REL of -41.38 dB at 9.71 GHz with a broader -10 dB bandwidth, optimizing it for EMI shielding applications. WP3, however, required a thicker profile of 14.5 mm to achieve maximum absorption at -16.01 dB, indicating lower efficiency. Impedance matching further revealed that WP1 and WP2 closely approximated the characteristic impedance of free space, with $|Z_{in}|$ values at 382.30 Ω (WP1) and 370.80 Ω (WP2), confirming near-perfect impedance alignment for optimal absorption.

The Co-Ce substituted $BaCo_xCe_xFe_{12-2x}O_{19}$/PANI composites (XP1, XP2, and XP3) demonstrated significant adjustments in structural, dielectric, magnetic, and microwave absorption properties, aligning them for advanced electromagnetic applications. The dielectric constant (ε') was highest in XP1 at 12,791 at low frequencies, indicating strong charge polarization. However, with Co and Ce substitutions, ε' values dropped significantly to 7295.51 (XP2) and 4700.94 (XP3), attributed to the disrupted Fe^{3+}-Fe^{2+} electron hopping due to dopant ions, which hindered polarization effects. The dielectric loss (ε") showed a similar trend, with XP1 displaying the highest dissipation at 172,173.3, while XP2 and XP3 presented lower values of 30,054.24 and 18,148.79 respectively, favouring energy retention over dissipation.

Electric modulus (M') analysis revealed that XP2 had the highest M' value of 0.02633, reflecting increased resistance to charge movement, while XP1 showed a lower M' of 0.00942, indicating enhanced charge mobility. In terms of imaginary modulus (M"),

XP2 displayed higher values at 0.01529, associated with stronger conductivity relaxation, while XP1 showed minimal energy dissipation, ideal for applications where charge mobility is paramount.

Impedance spectroscopy showed an increase in impedance values with substitution. XP3 had the highest Z' reaching 5.8 x 10^5 Ω at low frequencies, correlating with higher grain boundary resistance, whereas XP1 demonstrated the lowest impedance, enhancing conductivity. The Cole-Cole plot for XP3 displayed a large semicircular arc, indicating significant impedance contributions from grain boundaries, whereas XP1's smaller arc signified efficient charge mobility.

Magnetic properties varied across the series, with saturation magnetization (M_s) declining from 45.92 emu/g (XP1) to 14.93 emu/g (XP2), then stabilizing at an intermediate level of 33.42 emu/g (XP3). This decrease reflects weaker magnetic interactions as Fe^{3+} was replaced by Co^{2+} and Ce^{3+}. Coercivity (H_c) followed a similar trend, with XP1 exhibiting the highest value of 5382.78 Oe, indicative of strong domain stability, while H_c decreased to 2723.86 Oe in XP3, favouring easier magnetic reversal due to weakened magnetic domain boundaries.

Microwave absorption properties showed maximum absorption potential in XP1, with a reflection loss (REL) of -36.34 dB at 10.05 GHz at a thickness of 4.4 mm. XP3 achieved a strong REL of -33.29 dB at 11.48 GHz with a thicker profile, reflecting its peak absorption at higher frequencies, while XP2 recorded a moderate maximum REL of -26.43 dB at 12.14 GHz. Impedance matching parameters, with near-optimal values of Z_{in} for XP1 (382.30 Ω), aligned closely with the characteristic impedance of free space, confirming effective microwave absorption.

The Co-Cd substituted $BaCo_xCd_xFe_{12-2x}O_{19}$/PANI composites (YP1, YP2, and YP3) displayed notable modifications in structural, dielectric, magnetic, and microwave absorption properties, enhancing their potential for electromagnetic applications. In terms of dielectric properties, YP1 had a moderate initial dielectric constant (ε') of 12,791 at low frequencies, decreasing with frequency. YP2 showed an exceptionally high ε' of 461,887 at low frequencies, but this value rapidly declined with frequency due to robust polarization effects. YP3 maintained a low, stable dielectric constant of 66.45, ideal for applications demanding high-frequency stability and minimal polarization sites. Dielectric loss (ε'') was highest in YP2 at 134,630, suggesting

substantial energy dissipation, while YP3 presented minimal ε'' at 7.97 across frequencies.

The electric modulus analysis showed YP3 with the highest M' (0.03849), indicating significant grain boundary resistance, while YP2 had the lowest M' at 0.000788, reflecting enhanced charge mobility. Imaginary modulus (M'') values were highest for YP3 at 0.01319, linked to energy dissipation from grain boundary barriers, while YP2 showed minimal M'' due to greater charge mobility. Cole-Cole plots confirmed Debye-type relaxation, with YP3's larger arc suggesting higher grain boundary impedance.

Impedance spectroscopy results showed YP1 with the highest impedance values of 273,580 Ω (Z') and 6.64 x 10^3 Ω (Z''), reflecting substantial resistance due to grain boundaries. YP2 exhibited lower impedance values, indicative of higher grain conductivity. Magnetic properties followed a similar trend, with YP1 showing the highest saturation magnetization (M_s) of 45.92 emu/g and coercivity (H_c) of 5382.77 Oe, while YP2 showed the lowest Ms and H_c, linked to larger grains and easier domain wall movement.

Microwave absorption performance was optimal in YP2, achieving the highest reflection loss (REL) of -55.54 dB at 10.56 GHz with a thickness of 3.2 mm, marking it as ideal for EMI shielding. YP1 and YP3 followed with REL values of -36.34 dB and -48.79 dB, suitable for lower and higher frequency applications, respectively. The impedance matching for YP2 was near-perfect with Z_{in} of 376.33 Ω, ensuring minimal reflection loss.

The Co-Cr substituted $BaCo_xCr_xFe_{12-2x}O_{19}$/PANI composites (ZP1, ZP2, and ZP3) presented diverse dielectric, magnetic, and microwave absorption properties, enhancing their suitability for electronic and electromagnetic applications. The dielectric constant (ε') followed a decreasing trend with substitution. ZP1 exhibited the highest ε' of 12,791, reflecting robust charge polarization. However, ε' values declined to 418 (ZP2) and 640 (ZP3), suggesting that Co and Cr doping reduced the material's polarization capacity. The dielectric loss (ε'') was highest for ZP1 at 172,173, indicating substantial energy dissipation, while ZP2 and ZP3 presented significantly lower values, which are favourable for applications requiring low dielectric loss.

The electric modulus showed ZP2 with the highest M' values, suggesting strong grain boundary resistance, while ZP1 exhibited the lowest M', indicating enhanced conductivity. Imaginary modulus (M") analysis showed ZP2 with the highest M" values, reflecting slower charge relaxation, while ZP1's low M" confirmed its efficiency in charge mobility.

Impedance spectroscopy confirmed ZP1 as the least resistive with Z' and Z" values starting at 273.5 kΩ and decreasing to 26.1 kΩ at high frequencies. ZP2 and ZP3 demonstrated higher impedance, correlating with increased grain boundary resistance. Magnetic properties saw M_s decreasing from 45.92 emu/g (ZP1) to 22.55 emu/g (ZP3), with a similar reduction in coercivity, indicating that Co-Cr substitution reduced magnetic hardness.

Microwave absorption properties were optimized with ZP2 and ZP3, where ZP2 achieved a peak REL of -41.09 dB at 8.37 GHz (6.4 mm thickness), aligning with quarter-wavelength theory for optimal impedance matching. ZP3 followed closely with an REL of -41.01 dB at 11.31 GHz (9.8 mm thickness). Impedance matching for both ZP2 and ZP3 showed near-ideal Z_{in} values, minimizing reflection losses.

Co-Al Substituted $BaCo_xAl_xFe_{12-2x}O_{19}$ Hexaferrites and PANI Composites (W and WP Series)

Hexaferrites (W Series): Structural analysis indicated a progressive decrease in lattice parameters with Co-Al substitution, with unit cell volume decreasing from 698.68 × 10^6 pm^3 in W0 to 690.89 × 10^6 pm^3 in W5. Saturation magnetization (M_s) decreased non-linearly, with W4 reaching 72.06 emu/g, while reflection loss (REL) peaked at -46.55 dB at 10.05 GHz (3.1 mm thickness) in W5, showing optimal microwave absorption.

PANI Composites (WP Series): The WP series demonstrated strong dielectric and impedance properties. The WP2 composite achieved a maximum REL of -41.38 dB at 9.71 GHz, with near-perfect impedance matching at $Z_{in} \approx 370.80$ Ω (4.0 mm thickness), highlighting its EMI shielding potential.

Co-Ce Substituted $BaCo_xCe_xFe_{12-2x}O_{19}$ Hexaferrites and PANI Composites (X and XP Series)

Hexaferrites (X Series): The Co-Ce substitutions resulted in enhanced grain boundary polarization and controlled grain morphology. Saturation magnetization

(Ms) declined from 105.29 emu/g in X0 to 65.36 emu/g in X4, while the X3 composite exhibited a peak REL of -49.46 dB at 12.15 GHz at a thickness of 7.4 mm, demonstrating high EMI shielding effectiveness.

PANI Composites (XP Series): PANI addition enhanced charge mobility and conductivity relaxation. XP1 showed a maximum REL of -36.34 dB at 10.05 GHz (4.4 mm thickness), supported by near-ideal impedance matching (Z_{in} = 382.30 Ω), reinforcing its suitability for high-frequency microwave absorption.

Co-Cd Substituted $BaCo_xCd_xFe_{12-2x}O_{19}$ Hexaferrites and PANI Composites (Y and YP Series)

Hexaferrites (Y Series): Structural analyses indicated that Co-Cd substitution led to significant morphological changes and increased dielectric response. Y4 exhibited optimal reflection loss with REL = -40.49 dB at 10.39 GHz (1.7 mm thickness), while M_s reached a high of 101.60 emu/g in Y1, suitable for EMI shielding applications.

PANI Composites (YP Series): With the PANI integration, dielectric properties and impedance matching improved markedly. YP2 achieved the highest REL value of -55.54 dB at 10.56 GHz (3.2 mm thickness) with optimal impedance matching ($Z_{in} \approx$ 376.33 Ω), showing superior broadband absorption capabilities.

Co-Cr Substituted $BaCo_xCr_xFe_{12-2x}O_{19}$ Hexaferrites and PANI Composites (Z and ZP Series)

Hexaferrites (Z Series): Co-Cr substitutions modified the grain morphology and reduced magnetic hardness, with M_s decreasing from 79.99 emu/g in Z0 to 24.17 emu/g in Z5. The Z4 composition achieved significant microwave absorption with an REL of -43.4 dB at 11.98 GHz (9.5 mm thickness), underscoring its high-performance EMI shielding potential.

PANI Composites (ZP Series): PANI addition supported enhanced dielectric properties and reduced impedance, optimizing charge mobility and impedance matching. ZP2 reached an REL of -41.09 dB at 8.37 GHz with optimal impedance matching (Z_{in} = 382.69 Ω, 6.4 mm thickness), making it ideal for EMI shielding and high-frequency applications.

All $BaCo_xM_xFe_{12-2x}O_{19}$ hexaferrites and their corresponding PANI composites displayed significant tunability across structural, dielectric, magnetic, and microwave absorption parameters.

Optimal Microwave Absorption: YP2 (-55.54 dB at 10.56 GHz) and X3 (-49.46 dB at 12.15 GHz) demonstrated exceptional absorption, highlighting their potential in EMI shielding applications.

Ideal Impedance Matching: Both PANI and non-PANI composites, especially those with Co-Al (W5, WP2) and Co-Cd (YP2), achieved near-free-space impedance matching, enhancing absorption and reducing reflection losses.

These comprehensive findings confirm that Co-M substitutions in $BaFe_{12}O_{19}$ based hexaferrites, with or without PANI composites, create materials highly suitable for advanced electromagnetic applications, including EMI shielding and broadband microwave absorption.

Series Type - Hexaferrites	**Optimal Sample**	**Max REL (dB)**	**Frequency (GHz)**	**Thickness (mm)**	**M_s (emu/g)**	**H_c (Oe)**	**Optimal Impedance Matching (Zin ≈ 377 Ω)**	**Key Strengths**
Co-Al (W)	W5	-46.55	10.05	3.1	58.32 (W5)	2826.38 (W5)	Yes (W5: 379.49 Ω)	Tunable M_s, significant REL
Co-Ce (X)	X3	-49.46	12.15	7.4	65.36 (X4)	2511 (X5)	Yes (X3: 375.26 Ω)	High REL, grain boundary polarization
Co-Cd (Y)	Y4	-40.49	10.39	1.7	101.60 (Y1)	228.98 (Y5)	Yes (Y4: 382.24 Ω)	Excellent impedance match, controlled grain size
Co-Cr (Z)	Z4	-43.4	11.98	9.5	64.46 (Z3)	1514.02 (Z5)	Yes (Z4: 372.33 Ω)	Broad bandwidth, reduced magnetic hardness
PANI Composites								
Co-Al/PANI (WP)	WP2	-41.38	9.71	4	32.36 (WP3)	2928.91 (WP3)	Yes (WP2: 370.80 Ω)	Enhanced dielectric loss, EMI shielding

Co-Ce/PANI (XP)	XP1	-36.34	10.05	4.4	45.92 (XP1)	5382.78 (XP1)	Yes (XP1: 382.30 Ω)	Strong polarization, high-frequency absorption
Co-Cd/PANI (YP)	YP2	-55.54	10.56	3.2	Low (YP2)	Low (YP2)	Yes (YP2: 376.33 Ω)	Exceptional REL, broadband potential
Co-Cr/PANI (ZP)	ZP2	-41.09	8.37	6.4	22.55 (ZP3)	Low (ZP3)	Yes (ZP2: 382.69 Ω)	Optimal impedance matching, low dielectric loss

Outcomes with Applications

1. **Radar Absorption (Stealth Technology):**

   Reason: High REL values (up to -41 dB) and effective impedance matching ($Z \approx 377\ \Omega$) in Cr and Cd-doped samples.

   Application: Aircraft, ship, and vehicle stealth technologies to reduce radar signatures.

2. **Electromagnetic Shielding:**

   Reason: Broadband absorption and strong dielectric properties in Al and Ce-doped samples.

   Application: Shielding devices to protect sensitive electronic equipment from electromagnetic interference.

3. **High-Frequency Magnetic Devices:**

   Reason: Soft magnetic behaviour and reduced coercivity in Cr-doped samples.

   Application: Inductors and transformers in high-frequency electronic circuits.

4. **Environmental Applications:**

   Reason: Adjusted porosity and controlled dielectric loss could support pollutant trapping in electromagnetic absorptive filters.

   Application: Environmental pollutant remediation using electromagnetic wave-assisted techniques.

5.1 Future Scope

- Innovations in manufacturing techniques, particularly improved processing technologies, may influence the cost-effectiveness and scalability of M-type hexaferrite for practical applications.
- The appropriate design of a multi-functional electromagnetic absorber utilizing M-type hexaferrite, incorporating other advantageous characteristics such as mechanical strength, lightweight composition, and thermal stability.
- Studies may concentrate on optimizing the dielectric and magnetic properties of M-type hexaferrite composites via substitution, diverse synthesis techniques, or manipulation of grain size and morphology to attain superior microwave absorption efficacy in high-frequency bands Ku (12-18 GHz), K (18-26 GHz), or Ka (26-40 GHz).

REFERENCES

[1]. Gurbuz, A., Onar, N., Ozdemir, I., Karaoglanli, A., & Celik, E. (2012, January 1) Structural, Thermal and Magnetic Properties of Barium-ferrite Powders Substituted with Mn, Cu or Co and X (X = Sr and Ni) Prepared by the Sol-gel Method | GCRIS Database | Pamukkale University. https://hdl.handle.net/11499/8616.

[2]. Williams, J., Adetunji, J., & Gregori, M. (2000, October). Mossbauer spectroscopic determination of magnetic moments of Fe^{3+} and Co^{2+} in substituted barium hexaferrite, $Ba(Co,Ti)_xFe_{(12-2x)}O_{19}$. Journal of Magnetism and Magnetic Materials, 220(2–3), 124–128. https://doi.org/10.1016/s0304-8853(00)00458-3

[3]. Nakanishi T. ,Okube M., Toyoda T., Nakao A. and Sasaki B.,(2008), Site occupancy in $BaTiMnFe_{10}O_{19}$ hexa-ferrite , Photon Factory Activity Report2007 # 25 part B http://pfwww.kek.jp/acr2007pdf/part_b/pf07b187.pdf

[4]. Bsoul, I. (2009, January 1), Preparation of Nanocrystalline $BaFe_{12-2x}Co_xTi_xO_{19}$ by Ball Milling Method and Their Magnetic Properties. http://repository.yu.edu.jo/handle/123456789/955

[5]. Ashima, Sanghi, S., Agarwal, A., & Reetu. (2012, February). Rietveld refinement, electrical properties and magnetic characteristics of Ca–Sr substituted barium hexaferrites. Journal of Alloys and Compounds, 513, 436–444. https://doi.org/10.1016/j.jallcom.2011.10.071

[6]. Chaudhari, H. N., Dhruv, P. N., Singh, C., Meena, S. S., Kavita, S., & Jotania, R. B. (2020, September 15). Effect of heating temperature on structural, magnetic, and dielectric properties of Magnesium ferrites prepared in the presence of Solanum Lycopersicum fruit extract. Journal of Materials Science: Materials in Electronics, 31(21), 18445–18463. https://doi.org/10.1007/s10854-020-04389-1

[7]. Kaur, R., Dhillon, N., Singh, C., Narang, S. B., & Chandra, M. (2015, January). Microwave and electrical characterization of M-type $Ba_{0.5}Sr_{0.5}Co_xRu_xFe_{(12-2x)}O_{19}$ hexaferrite for practical applications. Solid State Communications, 201, 72–75. https://doi.org/10.1016/j.ssc.2014.10.012

[8]. Singh, C., Bindra-Narang, S., Hudiara, I. S., Sudheendran, K., & Raju, K. C. J. (2011, October 4). Microwave and electrical behavior of Co^{2+} and Ru^{4+} ions substituted Ba-Sr sintered ferrite. Journal of Electroceramics, 27(3–4), 120–125. https://doi.org/10.1007/s10832-011-9656-5

[9]. Gupta, T., Chauhan, C. C., Kagdi, A. R., Meena, S. S., Jotania, R. B., Singh, C., & Basak, C. (2020, April). Investigation on structural, hysteresis, Mossbauer properties and electrical parameters of lightly Erbium substituted X-type $Ba_2Co_2ErFe_{28}O_{46}$ hexaferrites. Ceramics International, 46(6), 8209–8226. https://doi.org/10.1016/j.ceramint.2019.12.049

[10]. Dhruv, P. N., Pullar, R. C., Singh, C., Carvalho, F. E., Jotania, R. B., Meena, S. S., & Singh, J. (2021, January). Design and development of Ga-substituted Z-type hexaferrites for microwave absorber applications: Mössbauer, static and dynamic properties. Ceramics International, 47(1), 1145–1162. https://doi.org/10.1016/j.ceramint.2020.08.23.

[11]. Chawla, S. K., Kaur, P., Mudsainiyan, R. K., Meena, S. S., & Yusuf, S. M. (2014, December 5). Effect of Fuel on the Synthesis, Structural, and Magnetic Properties of M-Type Hexagonal $SrFe_{12}O_{19}$ Nanoparticles. Journal of Superconductivity and Novel Magnetism, 28(5), 1589–1599. https://doi.org/10.1007/s10948-014-2893-5

[12]. Gupta, M., Anu, Mudsainiyan, R., & Randhawa, B. (2018, January). Li doping induced physico-chemical modulations in Cd ferrite ($CdLi_x Fe_{(2-x)}O_{4-x}$) synthesized using aqueous ammonia assisted co-precipitation route. Materials Science and Engineering: B, 227, 1–8. https://doi.org/10.1016/j.mseb.2017.10.001

[13]. Shikha, P., Komal, Kang, T. S., & Randhawa, B. (2017, April). Mn doping induced physico-chemical changes in La Ce ferrite nanofabricated by ionic liquid assisted hydrothermal route. Journal of Alloys and Compounds, 701, 788–796. https://doi.org/10.1016/j.jallcom.2017.01.138

[14]. Mudsainiyan, R. K., Gupta, M., & Chawla, S. (2016). Physico-chemical and Magnetic Properties of Co-Zr Doped Ba-hexaferrites Using Self Combustion

and Urea Assisted Method – A Comparative Study. Materials Today: Proceedings, 3(2), 507–512. https://doi.org/10.1016/j.matpr.2016.01.128

[15]. Mudsainiyan, R., Chawla, S., Meena, S., Sharma, N., Singh, R., & Das, A. (2014, December). Cations distribution and magnetic properties of Co–Zr doped $BaCo_xZr_xFe_{(12-2x)}O_{19}$ prepared via citrate precursor sol–gel route. Ceramics International, 40(10), 16617–16626. https://doi.org/10.1016/j.ceramint.2014.08.022

[16]. Pullar, R. C. (2012). Hexagonal ferrites: A review of the synthesis, properties and applications of hexaferrite ceramics. Progress in Materials Science, 57(7), 1191–1334. https://doi.org/10.1016/j.pmatsci.2012.04.001

[17]. Da Rocha Caffarena, V., Capitaneo, J. L., Ogasawara, T., & Pinho, M. S. (2008). Microwave absorption properties of Co, Cu, Zn: substituted hexaferrite polychloroprene nanocomposites. Materials Research, 11(3), 335–339. https://doi.org/10.1590/s1516-14392008000300017

[18]. Liu, Y., Lin, Y., & Yang, H. (2019). Facile fabrication for core-shell $BaFe_{12}O_{19}$@C composites with excellent microwave absorption properties. Journal of Alloys and Compounds, 805, 130–137. https://doi.org/10.1016/j.jallcom.2019.07.006

[19]. Pratap, V., Soni, A., Dayal, S., Abbas, S., Siddiqui, A., & Prasad, N. (2018). Electromagnetic and absorption properties of U-type barium hexaferrite-epoxy composites. Journal of Magnetism and Magnetic Materials, 465, 540–545. https://doi.org/10.1016/j.jmmm.2018.06.027

[20]. Afghahi, S. S. S., Shokuhfar, A., Saberi, B., & Javidan, A. (2014). Iron–cobalt–graphite core–shell nanoparticles as efficient electromagnetic wave absorbers at X-band frequency range. Micro & Nano Letters, 9(6), 412–416. https://doi.org/10.1049/mnl.2013.0723

[21]. Thakur, M., Singh, C., & Srivastava, A. K. (2024). Tunable structural, morphological, and hysteresis characteristics of $SrFe_{12}O_{19}/Fe_3O_4$ composites. Journal of Materials Science Materials in Electronics, 35(9). https://doi.org/10.1007/s10854-024-12395-w

[22]. Naqvi, S. T. A., Singh, C., Godara, S. K., Jotania, R. B., Kaur, V., & Sood, A. K. (2024a). Functionalization of morphology in optimization of dielectric,

electrical/impedance modulus, and relaxation mechanisms of Co-Ni doped M-type Sr nanoferrites. Physica Scripta, 99(5), 055558. https://doi.org/10.1088/1402-4896/ad3aaf

[23]. Wang, J., Wang, B., Feng, A., Jia, Z., & Wu, G. (2020). Design of morphology-controlled and excellent electromagnetic wave absorption performance of sheet-shaped ZnCo2O4 with a special arrangement. Journal of Alloys and Compounds, 834, 155092. https://doi.org/10.1016/j.jallcom.2020.155092

[24]. Ali-Sharbati, N., & Khani, J. V. (2013). Influence of Ho substitution on structural, magnetic and microwave absorption properties of PbM-type hexaferrites nanoparticles. Journal of Materials Science Materials in Electronics, 25(1), 244–248. https://doi.org/10.1007/s10854-013-1578-3

[25]. Dumitru, I., & Caltun, O. F. (2023). Ferrites use in magnetic recording. In Elsevier eBooks (pp. 733–745). https://doi.org/10.1016/b978-0-12-823717-5.00017-6.

[26]. Wei F., Lu M., and Yang Z., "The temperature dependence of magnetic properties of Zn-Ti substituted Ba-ferrite particles for magnetic recording," 1999.

[27]. Nakagawa, S., Matsushita, N., & Naoe, M. (2001). Perpendicular magnetic recording media using hexagonal ferrite thin films deposited on Pt underlayers and interlayers. Journal of Magnetism and Magnetic Materials, 235(1–3), 337–341. https://doi.org/10.1016/s0304-8853(01)00371-7

[28]. Ong, C., Fang, H., Yang, Z., & Li, Y. (2000). Magnetic relaxation in Zn–Sn-doped barium ferrite nanoparticles for recording. Journal of Magnetism and Magnetic Materials, 213(3), 413–417. https://doi.org/10.1016/s0304-8853(00)00013-5.

[29]. Rethinasabapathy, M., Vilian, A. E., Hwang, S. K., Kang, S., Cho, Y., Han, Y., Rhee, J., & Huh, Y. S. (2020). Cobalt ferrite microspheres as a biocompatible anode for higher power generation in microbial fuel cells. Journal of Power Sources, 483, 229170. https://doi.org/10.1016/j.jpowsour.2020.229170

[30]. Singh, N., Kansal, M. K., Kumar, P., Dabas, S., & Verma, V. (2023). Effect of Sn doping on structural, magnetic and power loss properties of lithium ferrites for high frequency applications. Physics Open, 16, 100155. https://doi.org/10.1016/j.physo.2023.100155

[31]. Ghanem, A. A., & Abdellatif, S. O. (2023). Experimentally verified numerical model for asymmetric ferrite core wireless power transfer with on-chip interfacing circuits. e-Prime - Advances in Electrical Engineering Electronics and Energy, 5, 100262. https://doi.org/10.1016/j.prime.2023.100262

[32]. Sharma, K., Aggarwal, N., Kumar, N., & Sharma, A. (2023). A review paper: Synthesis techniques and advance application of Mn-Zn nano-ferrites. Materials Today Proceedings. https://doi.org/10.1016/j.matpr.2022.12.088

[33]. Huang, S., Li, L., Zhang, X., Wu, X., Tang, J., Lan, M., Ren, W., & Chang, X. (2023). Effects of ytterbium substitution on the structural, electrical and magnetic properties of Ni–Zn–Co ferrites for microwave equipment. Ceramics International, 49(17), 28758–28763. https://doi.org/10.1016/j.ceramint.2023.06.135

[34]. Naz, K., Khan, J. K., Khalid, M., Akhtar, M. S., Gilani, Z. A., Asghar, H. N. U. H. K., Mersal, G. A., Ibrahim, M. M., Muhammad, A., & Ashiq, M. (2022). Structural, dielectric, impedance and electric modulus analysis of Ni substituted copper spinel ferrites nanoparticles for microwave device applications. Materials Chemistry and Physics, 285, 126091. https://doi.org/10.1016/j.matchemphys.2022.126091

[35]. Bobyl, A., Suris, R., Karmanenko, S., Semenov, A., Melkov, A., Konuhov, S., & Olshevski, A. (2002). The ferrite/superconductor layered structure for tunable microwave devices. Physica C Superconductivity, 372–376, 508–510. https://doi.org/10.1016/s0921-4534(02)00734-7

[36]. Amiri, M., Salavati-Niasari, M., & Akbari, A. (2019). Magnetic nanocarriers: Evolution of spinel ferrites for medical applications. Advances in Colloid and Interface Science, 265, 29–44. https://doi.org/10.1016/j.cis.2019.01.003

[37]. Amiri, S., & Shokrollahi, H. (2012). The role of cobalt ferrite magnetic nanoparticles in medical science. Materials Science and Engineering C, 33(1), 1–8. https://doi.org/10.1016/j.msec.2012.09.003

[38]. Manjunatha, K., Chethan, B., Wu, S. Y., Ubaidullah, M., Shaikh, S. F., Al-Enizi, A. M., Alanazi, N. B., Pandit, B., Bajorek, A., & Angadi, J., V. (2023). Effect of Eu^{3+} and Sc^{3+} on the structure, microstructure and humidity sensing properties of copper ferrites for sensor applications. Ceramics International, 49(24), 40236–40243. https://doi.org/10.1016/j.ceramint.2023.09.359

[39]. Jain, A., Singh, C., Godara, S. K., Jotania, R. B., Kaur, V., & Sood, A. K. (2024b). Modulating Electrical Response and Impedance in Co-Cr Substituted M-Phase Barium Hexaferrites: Examining Microstructure, Grain Boundaries, Charge Transport, and Computational Modeling. Ceramics International. https://doi.org/10.1016/j.ceramint.2024.08.044

[40]. Gomes, H. C., Teixeira, S. S., & Graça, M. (2022). Synthesis of calcium ferrite for energy storage applications. Journal of Alloys and Compounds, 921, 166026. https://doi.org/10.1016/j.jallcom.2022.166026.

[41]. Ghanem, A. A., & Abdellatif, S. O. (2023b). Experimentally verified numerical model for asymmetric ferrite core wireless power transfer with on-chip interfacing circuits. e-Prime - Advances in Electrical Engineering Electronics and Energy, 5, 100262. https://doi.org/10.1016/j.prime.2023.100262.

[42]. Li, J., Gao, F., Wang, G., Yang, Y., Sun, Y., Su, H., Han, X., Zhang, H., & Li, Q. (2021). Enhancement of microstructure and magnetic properties of MgCd ferrite via Sm-Ga ions substitution for microwave devices. Materials Research Bulletin, 142, 111414. https://doi.org/10.1016/j.materresbull.2021.111414

[43]. Guo, H., Zhang, L., Yan, Y., Zhang, J., Wang, J., Wang, S., Li, L., & Wu, X. (2022b). Effect of lanthanum substitution on structural, magnetic, and electric properties of Ni–Zn–Co ferrites for radio frequency and microwave devices. Ceramics International, 48(15), 22516–22522. https://doi.org/10.1016/j.ceramint.2022.04.275.

[44]. Naz, K., Khan, J. K., Khalid, M., Akhtar, M. S., Gilani, Z. A., Asghar, H. N. U. H. K., Mersal, G. A., Ibrahim, M. M., Muhammad, A., & Ashiq, M. (2022c). Structural, dielectric, impedance and electric modulus analysis of Ni substituted copper spinel ferrites nanoparticles for microwave device

applications. Materials Chemistry and Physics, 285, 126091. https://doi.org/10.1016/j.matchemphys.2022.126091.

[45]. Behera, P., & Ravi, S. (2018). Impedance spectroscopy and magnetic properties of Mg doped Y-type barium hexaferrite. Journal of Materials Science Materials in Electronics, 29(23), 20206–20215. https://doi.org/10.1007/s10854-018-0153-3

[46]. Sahu, B. B., Patri, S. K., Behera, B., & Maharana, B. (2018). Electrical properties of Y-type hexaferrite. Journal of Advanced Dielectrics, 08(03), 1850022. https://doi.org/10.1142/s2010135x18500224.

[47]. Guo, F. Y., Ji, G. J., Xu, J. J., Zou, H. F., Gan, S. C., & Xu, X. C. (2014). Influence of Tb substitution on electromagnetic and microwave absorption properties of barium hexaferrites. Materials Research Innovations, 18(2), 112–119. https://doi.org/10.1179/1433075x12y.0000000064.

[48]. Drofenik, M., Kristl, M., Žnidaršić, A., & Lisjak, D. (2007). Barium Hexaferrite Prepared by Hydrothermal Synthesis. Materials Science Forum, 555, 183–187. https://doi.org/10.4028/www.scientific.net/msf.555.183.

[49]. Mohebbi, E., Hasani, S., Nouri-Khezrabad, M., & Ziarati, A. (2022). The effect of agarose agent on the structural, magnetic and optical properties of barium hexaferrite nano-particles synthesized by sol-gel auto-combustion method. Ceramics International, 49(6), 9757–9770. https://doi.org/10.1016/j.ceramint.2022.11.149.

[50]. Lei, Y., Wang, W., Tan, G., Shang, X., Huang, X., & Man, Q. (2022). Effects of dysprosium substitution on the structure, magnetic properties and microwave absorption properties of Z-type hexaferrite $Ba_3Co_2Fe_{24}O_{41}$ synthesized by the sol–gel method. Journal of Materials Research and Technology, 20, 1603–1615. https://doi.org/10.1016/j.jmrt.2022.07.112.

[51]. Braham, Z. C., Kermad, A., Korso, S. E., Ramdani, M. R., Boudjemaa, A., Bachari, K., & Braham, A. C. (2023). Enhancing structural properties of simple perovskite materials based on zirconate and titanate prepared by sol-gel method. Materials Chemistry and Physics, 310, 128460. https://doi.org/10.1016/j.matchemphys.2023.128460.

[52]. Marjeghal, M. A., Sedghi, A., & Baghshahi, S. (2023). The effect of the citric acid to metal nitrates molar ratio on the structural and magnetic properties of strontium hexaferrite nanoparticles synthesized by the sol-gel combustion method. Journal of Alloys and Compounds, 968, 171765. https://doi.org/10.1016/j.jallcom.2023.171765.

[53]. Kausar, R., Khan, M. A., Gulbadan, S., Junaid, M., Hussain, A., Manzoor, A., Somaily, H., Attia, M. S., & Amin, M. A. (2022). Investigation into the structural and magnetic features of nickel doped U-type hexaferrites prepared through sol–gel method. Journal of Magnetism and Magnetic Materials, 549, 169054. https://doi.org/10.1016/j.jmmm.2022.169054.

[54]. Akharame, M. O., Fatoki, O. S., Opeolu, B. O., Olorunfemi, D. I., & Oputu, O. U. (2018). Polymeric Nanocomposites (PNCs) for Wastewater Remediation: An Overview. Polymer-Plastics Technology and Engineering, 57(17), 1801–1827. https://doi.org/10.1080/03602559.2018.1434666.

[55]. Beygisangchin, M., Rashid, S. A., Shafie, S., Sadrolhosseini, A. R., & Lim, H. N. (2021). Preparations, Properties, and Applications of Polyaniline and Polyaniline Thin Films—A Review. Polymers, 13(12), 2003. https://doi.org/10.3390/polym13122003.

[56]. Shakir, M. F., Khan, A. N., Khan, R., Javed, S., Tariq, A., Azeem, M., Riaz, A., Shafqat, A., Cheema, H. M., Akram, M. A., Ahmad, I., & Jan, R. (2019). EMI shielding properties of polymer blends with inclusion of graphene nano platelets. Results in Physics, 14, 102365. https://doi.org/10.1016/j.rinp.2019.102365.

[57]. Borhan, A. I., Ghercă, D., Iordan, A. R., & Palamaru, M. N. (2023). Classification and types of ferrites. In Elsevier eBooks (pp. 17–34). https://doi.org/10.1016/b978-0-12-823717-5.00026-7

[58]. Khan, M., Waqas, M., Naeem, M., Hasan, Iqbal, M., Mahmood, A., Ramay, S. M., Al-Masry, W., Abubshait, S. A., Abubshait, H. A., & Mahmood, Q. (2020). Magnetic behavior of Ga doped yttrium iron garnet ferrite thin films deposited by sol-gel technique. Ceramics International, 46(17), 27318–27325. https://doi.org/10.1016/j.ceramint.2020.07.217

[59]. Yousaf, M., Noor, A., Xu, S., Akhtar, M. N., & Wang, B. (2020). Magnetic characteristics and optical band alignments of rare earth (Sm^{+3}, Nd^{+3}) doped garnet ferrite nanoparticles (NPs). Ceramics International, 46(10), 16524–16532. https://doi.org/10.1016/j.ceramint.2020.03.219.

[60]. Yang, Y., Xu, D., Kong, L., Qiao, J., Li, B., Ding, X., Liu, J., Liu, W., & Wang, F. (2021). Construction of Ni-Zn bimetal sulfides Heterostructured-hybrids for High-performance electromagnetic wave absorption. Journal of Colloid and Interface Science, 606, 1410–1420. https://doi.org/10.1016/j.jcis.2021.08.095.

[61]. Zong, B., & Niu, X. (2020). Analysis of structure and magnetic behavior in M-type hexaferrite compounds $Sr_{1-x}Y_xFe_{10}CoTiO_{19}$. Journal of Materials Science Materials in Electronics, 31(7), 5290–5297. https://doi.org/10.1007/s10854-020-03089-00.

[62]. Tian, F., Gao, Y., Wang, A., Xiang, L., Man, Q., Xu, H., & Shen, B. (2023b). Effect of Mn substitution on structural, magnetic and microwave absorption properties of Co_2Y hexagonal ferrite. Journal of Magnetism and Magnetic Materials, 587, 171229. https://doi.org/10.1016/j.jmmm.2023.171229.

[63]. Ramzan, A., Naz, S., Zubair, A., Sadiq, I., Abbas, Q., Sadiq, F., Shahbaz, M., Saeed, S., Idrees, M., Hussain, S., Riaz, S., & Naseem, S. (2023). Raveling out the effect of Pr3+ ions substitution on different properties of nano-sized hexagonal ferrites. Materials Science and Engineering B, 297, 116717. https://doi.org/10.1016/j.mseb.2023.116717

[64]. Gui, D., & Ren, X. (2023b). Investigation on electromagnetic properties of La–Al co-doped Co_2W hexagonal ferrites for microwave absorption. Ceramics International, 49(9), 14079–14089. https://doi.org/10.1016/j.ceramint.2022.12.289.

[65]. Junaid, M., Jan, H. A., Batoo, K. M., Jabeen, R., & Hussain, S. (2023). Band–gap reduction of aluminum substituted M−type hexagonal ferrite to study its characteristics. Results in Chemistry, 6, 101133. https://doi.org/10.1016/j.rechem.2023.101133.

[66]. Jing, X., Chen, Z., Zhao, Q., Li, Z., Xiong, X., Yang, X., Wang, Q., Huang, H., Jiang, H., Zhao, T., & Gong, H. (2024). Praseodymium dysprosium co-

doped M-type strontium ferrite: Intentionally manufacturing heterophase growth to improve microwave absorption performance. Materials Today Chemistry, 39, 102151. https://doi.org/10.1016/j.mtchem.2024.102151

[67]. Wang, H., & Han, J. (2024b). Structural Elucidation and Evaluation of Magnetic and Dielectric Properties of Lu–La Co-substituted M-Type Hexagonal Ferrites Synthesized by Chemical Co-precipitation Method. Physica Status Solidi (A). https://doi.org/10.1002/pssa.202300969

[68]. Jin, Y., Xiao, W., Ma, L., Liang, X., Ma, S., Sun, W., Zhang, P., Cui, J., & Wang, D. (2024). Effect of Ce doping on electromagnetic characteristics and absorbing properties of M-type barium ferrite. Materials Today Communications, 108596. https://doi.org/10.1016/j.mtcomm.2024.108596.

[69]. Wei, H., Huang, Z., Cui, J., Zhang, P., Ma, S., Sun, W., Liang, X., Zhang, Y., & Wu, Y. (2024). Tailoring electromagnetic wave absorption properties of M-type barium ferrite through Nd^{3+}–(Nb^{5+}/Ta^{5+}) cosubstitution. Materials Today Communications, 39, 109378. https://doi.org/10.1016/j.mtcomm.2024.109378

[70]. Panwar, M., Khan, H. M., Bano, N., Zahid, M., Mazhar, M. E., Bilal, M., Saleem, M. I., Solre, G. F., Gomez, P., & Li, Z. (2024). Influence of bismuth and cobalt doping on structural, dielectric, and magnetic properties of M-type calcium hexagonal ferrites. Journal of Alloys and Compounds, 994, 174623. https://doi.org/10.1016/j.jallcom.2024.174623

[71]. Yang, X., Chen, Z., Zhou, D., Xiong, X., Jing, X., Zhao, T., Gong, H., & Shen, B. (2024). Effect of the interaction of Fe- and Ce-contents on the structure and magnetic properties of M-type strontium ferrites. Ceramics International, 50(18), 32465–32476. https://doi.org/10.1016/j.ceramint.2024.06.055

[72]. Chen, Z., Xu, N. B., Li, Z., Zhou, N., Gong, H., & Jing, X. (2023). The influence of Ho doping on the morphology and magnetic properties of M-type strontium ferrite with different Fe/Sr. Materials Chemistry and Physics, 312, 128635. https://doi.org/10.1016/j.matchemphys.2023.128635

[73]. Kayalvizhi, K., Kennedy, L. J., & Ratna, D. (2024). Negative permittivity and permeability behaviour of $SrFe_{12}O_{19}$/rGO metacomposite for microwave absorption in 2–18 GHz range. Ceramics International.

https://doi.org/10.1016/j.ceramint.2024.02.104

[74]. Yang, H., Jian, Z., Li, K., Chang, H., Yang, W., & Liu, S. (2024). Band gap, ferromagnetic resonance and strong microwave absorption of $BaFe_{12-2}ZnSnO_{19}$ compounds and enhanced dielectric loss in $BaFe_{12-2}ZnSnO_{19}$/carbon nano tube composites. Journal of Magnetism and Magnetic Materials, 596, 171997. https://doi.org/10.1016/j.jmmm.2024.171997

[75]. Wei, S., Wang, X., Wang, B., Wang, Y., Liang, Y., Liu, Z., Zhang, H., Xu, Q., & Mou, H. (2024). Constructing and optimizing epoxy resin-based carbon Nanotube/Barium ferrite microwave absorbing coating system. Materials Research Bulletin, 179, 112928. https://doi.org/10.1016/j.materresbull.2024.112928

[76]. Shu, R., Nie, L., Zhao, Z., & Yang, X. (2023). Synthesis of nitrogen-doped reduced graphene oxide/magnesium ferrite/polyaniline composite aerogel as a lightweight, broadband and efficient microwave absorber. Journal of Material Science and Technology, 175, 115–124. https://doi.org/10.1016/j.jmst.2023.08.015.

[77]. Mudasar, M., Zh, X., Sy, L., Li, X., & Cheng, X. (2024). Tailoring permittivity and permeability of M-type hexagonal ferrite and 2D Ti3C2Tx MXene composites for broadband microwave stealth performance. Materials Chemistry and Physics, 315, 129031. https://doi.org/10.1016/j.matchemphys.2024.129031

[78]. Bala, M., Shivling, V., & Tyagi, S. (2024). Enhancing X-band microwave absorption properties with nickel ferrite and carbon-based composites. Ceramics International, 50(18), 34123–34132. https://doi.org/10.1016/j.ceramint.2024.06.231

[79]. Yunasfi, N., Dewi, S. H., Mashadi, N., Winatapura, D. S., Setiawan, J., Mulyawan, A., Gunanto, Y. E., & Adi, W. A. (2024). Exploring the structural and magnetic properties of La-doped nickel ferrite for microwave absorbing application. Journal of Magnetism and Magnetic Materials, 603, 172267. https://doi.org/10.1016/j.jmmm.2024.172267

[80]. Kaur, M., & Bahel, S. (2023). Characterization of sol-gel synthesized $Zn_{0.25}Co_{0.75}(NiZr)_xFe_{2-2x}O_4$ ($0.05 \leq x \leq 0.25$) spinel ferrites based microwave

absorbers in Ka frequency band. Journal of Physics and Chemistry of Solids, 184, 111671. https://doi.org/10.1016/j.jpcs.2023.111671

[81]. Siddique, M. A., Irfan, M., Rasool, R. T., Arshad, M., Ashraf, G. A., Akhtar, M. N., Manzoor, S., Raza, M. R., & Khan, M. A. (2024). Role of Zn cations substitution on structural, vibrational, elastic, dielectric, bandwidth, and microwave absorbance of Co–Cd ferrites at high frequencies. Materials Chemistry and Physics, 315, 128972. https://doi.org/10.1016/j.matchemphys.2024.128972

[82]. Akhtar, M. N., Alomayrah, N., Baqir, M., Irfan, M., Khan, M. A., Almohammedi, A., Alelyani, M., Yousaf, M., Alrowaili, Z., & Al-Buriahi. (2024). Design and Tuneable Magnetodielectric ferrite-based Meta-Absorbers for high-frequency microwave absorption applications. Materials Research Bulletin, 174, 112716. https://doi.org/10.1016/j.materresbull.2024.112716

[83]. Ijaz, M., Albalawi, K., Ghori, U., Saleh, E. a. M., Moharam, M., El-Zahhar, A. A., Asif, S. U., & Ullah, H. (2023). Influence of ferromagnetic cobalt on microstructural and magnetic trends of sol–gel routed rare earth and aluminium based BaSr-Hexaferrites ($Ba_{0.6}Sr_{0.3}Er_{0.1}Fe_{11.5-x}Al_{0.5}Co_xO_{19}$). Materials Science and Engineering B, 299, 116933. https://doi.org/10.1016/j.mseb.2023.116933

[84]. Khan, M. Z., Gul, I. H., & Tahir, F. A. (2023). Encapsulation of Ba–Sr hexaferrite nanoparticlesand MWCNTs in conductive polymer matrix for improved dielectric spectroscopy, electromagnetic shielding and microwave absorption applications. Ceramics International, 49(17), 27796–27814. https://doi.org/10.1016/j.ceramint.2023.05.266

[85]. Thanh, T. D., Tran, N., Chinh, N. T. V., Anh, N. T. N., Manh, D. H., & Tuan, N. Q. (2023). Excellent microwave absorption performances of cobalt-doped $SrFe_{12}O_{19}$ hexaferrite with varying incident angles. Journal of Alloys and Compounds, 952, 170060. https://doi.org/10.1016/j.jallcom.2023.170060

[86]. Tian, F., Gao, Y., Wang, A., Xiang, L., Man, Q., Xu, H., & Shen, B. (2023). Effect of Mn substitution on structural, magnetic and microwave absorption properties of Co_2Y hexagonal ferrite. *Journal of Magnetism and Magnetic Materials*, *587*, 171229. https://doi.org/10.1016/j.jmmm.2023.171229

[87]. Liu, X., Ji, R., Yang, M., Chen, W., Chen, H., Song, X., Liu, J., Zhang, M., & Zhang, L. (2022). Facilitating enhanced microwave absorption properties of barium hexaferrite/polyaniline composites based on tunable interfacial polarization by rare earth doping. Journal of Alloys and Compounds, 937, 168391. https://doi.org/10.1016/j.jallcom.2022.168391

[88]. Verma, S., Singh, A., Sharma, S., Kaur, P., Godara, S. K., Malhi, P. S., Ahmed, J., Babu, P., & Singh, M. (2022). Magnetic and structural analysis of BaZnxZrxFe12–2xO19 (x = 0.1–0.7) hexaferrite samples for magnetic applications. Journal of Alloys and Compounds, 930, 167410. https://doi.org/10.1016/j.jallcom.2022.167410

[89]. Khan, K., Abbas, H., & Nadeem, K. (2022). Magnetic exchange coupling and effect of grain and grain boundaries on conduction mechanism of $(MgFe_2O_4)_{100-x}$ /$(BaFe_{12}O_{19})_x$ nanocomposites. Ceramics International, 49(9), 13982–13993. https://doi.org/10.1016/j.ceramint.2022.12.280

[90]. Gupta, A., & Roy, P. (2023). Effect of Zn2+ ion substitution in Al3+-substituted rare-earth free Sr-hexaferrite for different permanent magnet applications. Inorganic Chemistry Communications, 155, 111114. https://doi.org/10.1016/j.inoche.2023.111114

[91]. Sahu, S., Mohapatra, P. P., Singh, H. K., & Dobbidi, P. (2023). Enhanced microwave absorbing performance of Sr^{2+} substituted Nickel-Cobalt nano ferrite for radar and stealth applications. *Materials Science and Engineering B*, *294*, 116514. https://doi.org/10.1016/j.mseb.2023.116514

[92]. Caliskan, S., Almessiere, M., Baykal, A., Gungunes, H., Slimani, Y., Hassan, M., Klygach, D., Kostishin, V., Trukhanov, S., Trukhanov, A., & Gondal, M. (2023). Impact of vanadium substitution on structural, magnetic, microwave absorption features and hyperfine interactions of SrCo hexaferrites. Journal of Alloys and Compounds, 960, 170578. https://doi.org/10.1016/j.jallcom.2023.170578

[93]. Rana, K., Thakur, S., Tomar, M., Gupta, V., & Thakur, A. (2023). Effect of low sintering temperature on the structural and magnetic properties of M-type strontium hexaferrite. Journal of Magnetism and Magnetic Materials, 587, 171289. https://doi.org/10.1016/j.jmmm.2023.171289.

[94]. Gulbadan, S., Khan, M. A., Ashraf, G. A., Mahmood, K., Shahid, M., Irfan, M., & Ahmad, A. (2022). Insight of structural, dielectric and spectroscopic characteristics of $Ba_{0.6}Sr_{0.4-x}Yb_xFe_{12-y}Co_yO_{19}$ M-type hexaferrite. *Ceramics International*, *49*(4), 6487–6499. https://doi.org/10.1016/j.ceramint.2022.10.162

[95]. Ramírez-Ayala, M., Guerrero, A. L., Herrera-González, A., Pérez-Juache, T., López-Juárez, R., Elizalde-Galindo, J., Salazar-Muñoz, V., Palomares-Sánchez, S., & Reyes-López, S. (2023). Study of neodymium addition on the magnetic and structural properties of strontium hexaferrite synthesized by the Pechini method. Journal of Magnetism and Magnetic Materials, 582, 170985. https://doi.org/10.1016/j.jmmm.2023.170985

[96]. Mironovich, A., Kostishin, V., Al-Khafaji, H., Timofeev, A., Ril, A., & Shakirzyanov, R. (2023). Study of structure, cation distribution and magnetic properties of Ni substituted M-type barium hexaferrite. Materialia, 32, 101898. https://doi.org/10.1016/j.mtla.2023.101898.

[97]. Gui, D., & Ren, X. (2023). Investigation on electromagnetic properties of La–Al co-doped Co_2W hexagonal ferrites for microwave absorption. *Ceramics International*, *49*(9), 14079–14089. https://doi.org/10.1016/j.ceramint.2022.12.289

[98]. Nishkala, K., Rao, R. R., Mutalik, S., Murari, & Daivajna, M. D. (2023). Investigations on structural, Mossbauer, dielectric, and ferroelectric properties of La doped barium hexaferrite. Physica B Condensed Matter, 664, 414954. https://doi.org/10.1016/j.physb.2023.414954.

[99]. Fasate, S. K., Salunke, P. S., Rode, S., Alone, S., & Jadhav, K. (2023). Electrical, dielectric and magnetic properties of Mn2+ substitution in barium hexaferrites nanoparticles. Materials Today Proceedings, 92, 980–985. https://doi.org/10.1016/j.matpr.2023.04.590.

[100]. Chagas, P., Catique, L., Lira, V. C. C., Vega-Garcia, A., Marinho-Castellanos, P., Anglada-Riveira, J., Leyet, Y., Peña-Garcia, R., & Guerrero, F. (2023). Effect of Sn-substitution on the electrical conductivity of $SrFe_{12-x}Sn_xO_{19}$ ($0.0 \leq x \leq 1.0$) hexaferrite. Physica B Condensed Matter, 661, 414961. https://doi.org/10.1016/j.physb.2023.414961.

[101]. Bilovol, V., Sikora, M., & Berent, K. (2023). Exchange coupling in $SrFe_{12}O_{19}/CoFe_2O_4$ composites: Effect of component proportions. Journal of Magnetism and Magnetic Materials, 568, 170384. https://doi.org/10.1016/j.jmmm.2023.170384

[102]. Zhang, W., Li, J., Li, J., Guo, J., Wang, Y., Zu, P., & Li, P. (2021). Structural, optical, dielectric, and magnetic properties of $Sr_{0.7}La_{0.3}Zn_{0.3}Fe_{11.7}AlO_{19}$ hexaferrite synthesized by the solid-state reaction method. *Journal of Solid State Chemistry*, *306*, 122766. https://doi.org/10.1016/j.jssc.2021.122766

[103]. Akhtar, M. N., Yousaf, M., Lu, Y., Mahmoud, M. Z., Iqbal, J., Khan, M. A., Khallidoon, M. U., Ullah, S., & Hussien, M. (2021). Magnetic, structural, optical band alignment and conductive analysis of graphene-based REs (Yb, Gd, and Sm) doped NiFe2O4 nanocomposites for emerging technological applications. *Synthetic Metals*, *284*, 116994. https://doi.org/10.1016/j.synthmet.2021.116994

[104]. Khan, M. Z., Abbas, H., Nadeem, K., Iqbal, A., & Papst, I. (2022). Concentration dependent exchange coupling in $BaFe_{12}O_{19}/NiFe_2O_4$ nanocomposites. Journal of Alloys and Compounds, 922, 166105. https://doi.org/10.1016/j.jallcom.2022.166105

[105]. Singh, H. K., Mohapatra, P. P., Sahu, S., & Dobbidi, P. (2022). Dielectric and temperature dependent magnetic studies of Al^{3+} substituted $Ba_{0.4}La_{0.1}Sr_{0.5}Al_xFe_{12-x}O_{19}$ hexaferrite for microwave application. Materials Science and Engineering B, 284, 115876. https://doi.org/10.1016/j.mseb.2022.115876.

[106]. Hassan, Z., Sadiq, I., Hussain, R., Sadiq, F., Idrees, M., Hussain, S., Riaz, S., & Naseem, S. (2022). Determination of dual magnetic phases and the study of structural, dielectric, electrical, surface morphological, optical properties of Ce3+ substituted hexagonal ferrites. *Journal of Alloys and Compounds*, *906*, 164324. https://doi.org/10.1016/j.jallcom.2022.164324

[107]. Shakir, H. F., Shahzad, M., Aziz, H. R., Rizwan, M. S., Shahid, S., Ali, S. H., & Zhao, T. (2022). In-situ polymerization and EMI shielding property of barium hexaferrite/pyrrole nanocomposite. Journal of Alloys and Compounds, 902, 163847. https://doi.org/10.1016/j.jallcom.2022.163847

[108]. Chauhan, C. C., Gupta, T., Meena, S. S., Desimone, M. F., Das, A., Sandhu, C. S., Jotania, K. R., & Jotania, R. B. (2021). Tailoring magnetic and dielectric properties of $SrFe_{12}O_{19}/NiFe_2O_4$ ferrite nanocomposites synthesized in presence of Calotropis gigantea (crown) flower extract. Journal of Alloys and Compounds, 900, 163415. https://doi.org/10.1016/j.jallcom.2021.163415

[109]. Singh, J., Singh, C., Bai, Y., Kaur, D., Narang, S. B., Raju, K. J., Dhruv, P. N., Jotania, R., Joseph, A., & Joshi, R. (2022). Role of phase, grain morphology and impedance properties in tailoring of Barium Strontium hexaferrites for microwave absorber/attenuator applications. *Materials Science and Engineering B, 281*, 115679. https://doi.org/10.1016/j.mseb.2022.115679

[110]. Dilshad, M., Khan, H. M., Zahid, M., Honey, S., Assiri, M. A., & Imran, M. (2022). Structural, optical and dielectric properties of aluminum-substituted $SrAl_{2x}Fe_{12-2x}O_{19}$ x = (0.0,0.2,0.4,0.6,0.8,1.0) M-type hexagonal ferrites. *Journal of Materials Science Materials in Electronics*, *33*(27), 21519–21530. https://doi.org/10.1007/s10854-022-08943-x

[111]. Godara, S. K., Kaur, V., Jasrotia, R., Suman, N., Thakur, S., Singh, V. P., Ahmed, J., Alshehri, S. M., Pandit, B., Singh, M., Kaur, P., Mohammed, J., Kaur, M. P., & Sood, A. K. (2022). Effect of Ca^{2+} exchange at Ba^{2+} site on the structural, dielectric, morphological and magnetic traits of BaM nanohexaferrites. Journal of Magnetism and Magnetic Materials, 564, 170049. https://doi.org/10.1016/j.jmmm.2022.170049

[112]. Basha, D. B., Kumar, N. S., Naidu, K. C. B., & Kumar, G. R. (2022). Structural, electrical, and magnetic properties of nano $Sr_{1-x}La_xFe_{12}O_{19}$ (x = 0.2–0.8). *Scientific Reports*, *12*(1). https://doi.org/10.1038/s41598-022-15250-2

[113]. Yousaf, M., Lu, Y., Hu, E., Wang, B., Akhtar, M. N., Noor, A., Akbar, M., Shah, M. Y., Wang, F., & Zhu, B. (2021). Tunable magneto-optical and interfacial defects of Nd and Cr-doped bismuth ferrite nanoparticles for microwave absorber applications. *Journal of Colloid and Interface Science*, *608*, 1868–1881. https://doi.org/10.1016/j.jcis.2021.09.182

[114]. Zahid, M., Khan, H. M., Sadiq, I., Rehman, A. U., Waheed, A., Mazhar, E., Assiri, M. A., Imran, M., Usmani, N., & Khan, I. (2021). Structural Elucidation with Improved Dielectric and Magnetic Properties of Sol–Gel Synthesized Cr^{3+} Substituted M-Type Sr2+ Hexaferrites. *Journal of Materials Engineering and Performance*, *31*(2), 1530–1539. https://doi.org/10.1007/s11665-021-06263-5

[115]. Purnama, B., Arilasita, R., Rikamukti, N., Utari, N., Budiawanti, S., Suharno, N., Wijayanta, A. T., Suharyana, N., Djuhana, D., Suharyadi, E., Tanaka, T., & Matsuyama, K. (2022). Annealing temperature dependence of crystalline structure and magnetic properties in nano-powder strontium-substituted cobalt ferrite. Nano-Structures & Nano-Objects, 30, 100862. https://doi.org/10.1016/j.nanoso.2022.100862

[116]. Singh, C., Nikolic, M. V., Narang, S. B., Sombra, A. S. B., Zhou, D., Trukhanov, S., Panina, L., Singh, J., & Trukhanov, A. (2021). Controllable morphology, dielectric, magnetic and reflection loss characteristics of ferrite/wax composites for low-loss applications. Journal of Alloys and Compounds, 888, 161611. https://doi.org/10.1016/j.jallcom.2021.161611

[117]. Kumar, S., Verma, V., & Walia, R. (2021). Magnetization and thickness dependent microwave attenuation behaviour of Ferrite-PANI composites and embedded composite-fabrics prepared by in situ polymerization. *AIP Advances*, *11*(1). https://doi.org/10.1063/9.0000022

[118]. Bozorgmehr, M., Gordani, G. R., Ghasemi, A., & Tavoosi, M. (2021). An assessment of electromagnetic properties of substituted hexaferrite/SWCNTs nanocomposite. Journal of Magnetism and Magnetic Materials, 527, 167709. https://doi.org/10.1016/j.jmmm.2020.167709

[119]. Fang, G., Liu, C., Yang, Y., Peng, K., Xu, G., & Zhang, Y. (2020). Broad microwave absorption bandwidth achieved by exchange coupling interaction between hard and soft magnetic materials. Ceramics International, 47(2), 2879–2883. https://doi.org/10.1016/j.ceramint.2020.09.011

[120]. Tran, N., Lee, M., Jeong, W., Phan, T., Tuan, N., & Lee, B. (2021). Thickness independent microwave absorption performance of La-doped $BaFe_{12}O_{19}$ and

polyaniline composites. Journal of Magnetism and Magnetic Materials, 538, 168299. https://doi.org/10.1016/j.jmmm.2021.168299

[121]. Rostami, M., Jafarpour, M., & Ara, M. H. M. (2021). An investigation on the microwave absorption properties of Co–Al–Ti substituted barium hexaferrite-MWCNT nanocomposites. Journal of Alloys and Compounds, 872, 159656. https://doi.org/10.1016/j.jallcom.2021.159656

[122]. Aggarwal, N., & Narang, S. B. (2021). Microwave absorption analysis of Mg–Zr-substituted Ni–Zn spinel ferrites in the X-band. Journal of Physics and Chemistry of Solids, 159, 110289. https://doi.org/10.1016/j.jpcs.2021.110289

[123]. Widanarto, W., Ekaputra, A. I., Effendi, M., Cahyanto, W. T., Ghoshal, S. K., Kurniawan, C., Handoko, E., & Alaydrus, M. (2020). Neodymium ions activated barium ferrite composites for microwave X-band absorber applications: Synthesis and characterizations. Composites Communications, 19, 51–55. https://doi.org/10.1016/j.coco.2020.02.008

[124]. Feng, G., Zhou, W., Li, Y., Qing, Y., Luo, F., Zhu, D., Huang, Z., & Zhou, Y. (2019). Lanthanum-substituted $Ba_{0.4}Ca_{0.6}Fe_{11.4}Co_{0.6}O_{19}$ ceramics with enhanced microwave absorption. Journal of Materials Science Materials in Electronics, 31(1), 621–627. https://doi.org/10.1007/s10854-019-02567-4

[125]. Phan, T., Tran, N., Nguyen, H., Yang, D., Dang, N., & Lee, B. (2019). Crystalline and electronic structures and magnetic properties of $BaCo_{1-x}Mn_xFe_{11}O_{19}$ hexaferrites. Journal of Alloys and Compounds, 816, 152528. https://doi.org/10.1016/j.jallcom.2019.152528

[126]. Guan, G., Zhang, K., Gong, L., Chen, X., Li, X., Wang, Q., Wang, Y., & Xiang, J. (2019). Electromagnetic wave absorption enhancement of double-layer structural absorbers based on carbon nanofibers and hollow Co_2Y hexaferrite microfibers. Journal of Alloys and Compounds, 814, 152302. https://doi.org/10.1016/j.jallcom.2019.152302

[127]. Anand, S., Pauline, S., & Prabagar, C. J. (2020). Zr doped Barium hexaferrite nanoplatelets and RGO fillers embedded Polyvinylidenefluoride composite films for electromagnetic interference shielding applications. Polymer Testing, 86, 106504. https://doi.org/10.1016/j.polymertesting.2020.106504

[128]. Jing, Z., Qinghong, R., & Atassi, Y. (2020). Design of ternary-component X-band microwave absorber based on FeCo/Sr hexaferrite/PANI nanocomposite in silicon resin matrix. Journal of Magnetism and Magnetic Materials, 512, 167037. https://doi.org/10.1016/j.jmmm.2020.167037.

[129]. Ma, T., Cui, Y., Sha, Y., Liu, L., Ge, J., Meng, F., & Wang, F. (2020). Facile synthesis of hierarchically porous rGO/MnZn ferrite composites for enhanced microwave absorption performance. *Synthetic Metals*, *265*, 116407. https://doi.org/10.1016/j.synthmet.2020.116407

[130]. Zhang, Y., Liu, C., Zhao, X., Yao, M., Miao, X., & Xu, F. (2019). Enhanced microwave absorption properties of barium ferrites by Zr^{4+}-Ni^{2+} doping and oxygen-deficient sintering. *Journal of Magnetism and Magnetic Materials*, *494*, 165828. https://doi.org/10.1016/j.jmmm.2019.165828

[131]. Jiao, Z., Yao, Z., Zhou, J., Qian, K., Lei, Y., Wei, B., & Chen, W. (2020). Enhanced microwave absorption properties of Nd-doped NiZn ferrite/polyaniline nanocomposites. *Ceramics International*, *46*(16), 25405–25414. https://doi.org/10.1016/j.ceramint.2020.07.010

[132]. Shu, R., Zhang, J., Guo, C., Wu, Y., Wan, Z., Shi, J., Liu, Y., & Zheng, M. (2019). Facile synthesis of nitrogen-doped reduced graphene oxide/nickel-zinc ferrite composites as high-performance microwave absorbers in the X-band. *Chemical Engineering Journal*, *384*, 123266. https://doi.org/10.1016/j.cej.2019.123266

[133]. Khadour, M., Atassi, Y., & Abdallah, M. (2020). Preparation and characterization of a flexible microwave absorber based on MnNiZn ferrite ($Mn_{0.1}Ni_{0.45}Zn_{0.45}Fe_2O_4$) in a thermoset polyurethane matrix. *SN Applied Sciences*, *2*(2). https://doi.org/10.1007/s42452-020-2004-0

[134]. Moradnia, M., Fathi, M., Mehdipour, M., & Shokrollahi, H. (2020). Analyzing the Microwave Absorption Properties of $BaFe_{12}O_{19}$, $Ba4MnZnFe_{36}O_{60}$ and $NiFe_2O_4$ Particles. *Journal of Electronic Materials*, *49*(10), 5957–5963. https://doi.org/10.1007/s11664-020-08317-1

[135]. He, Y., Pan, S., & Yu, J. (2020). Research on magnetic and microwave absorbing properties of Co2Y ferrite fabricated by sol–gel process. *Journal of*

Sol-Gel Science and Technology, *96*(3), 521–528. https://doi.org/10.1007/s10971-020-05235-w

[136]. Handoko, E., Sugihartono, I., Marpaung, M. A., Cahyana, U., Aritonang, S., Zulkarnain, J., Rusmono, R., Taufiq, A., Sunaryono, S., & Alaydrus, M. (2019). Enhanced Microwave Absorbing Capabilities of Multilayer Absorbers Based on $BaFe_{12}O_{19}$ and Fe_3O_4 Materials Science Forum, 966, 338–343. https://doi.org/10.4028/www.scientific.net/msf.966.338

[137]. Veisi, S. S., Yousefi, M., Amini, M., Shakeri, A., & Bagherzadeh, M. (2018). Magnetic and microwave absorption properties of Cu/Zr doped M-type Ba/Sr hexaferrites prepared via sol-gel auto-combustion method. Journal of Alloys and Compounds, 773, 1187–1194. https://doi.org/10.1016/j.jallcom.2018.09.189

[138]. Arora, A., Narang, S. B., & Pubby, K. (2019b). Enhanced Microwave Absorption Properties of Doped M-Type Barium Hexagonal Ferrites in Ka-band Frequencies. Journal of Superconductivity and Novel Magnetism, 32(8), 2705–2709. https://doi.org/10.1007/s10948-019-5044-1

[139]. Mansour, S., Hemeda, O., Abdo, M., & Nada, W. (2017b). Improvement on the magnetic and dielectric behavior of hard/soft ferrite nanocomposites. Journal of Molecular Structure, 1152, 207–214. https://doi.org/10.1016/j.molstruc.2017.09.089

[140]. Tyagi, S., Pandey, V., Baskey, H. B., Tyagi, N., Garg, A., Goel, S., & Shami, T. C. (2017). RADAR absorption study of $BaFe_{12}O_{19}/ZnFe_2O_4$/CNTs nanocomposite. Journal of Alloys and Compounds, 731, 584–590. https://doi.org/10.1016/j.jallcom.2017.10.071

[141]. Patel, C. K., Solanki, N. P., Singh, C., Jotania, R. B., Chauhan, C. C., Kulkarni, S. D., & Shirsath, S. E. (2017). Structural phases, magnetic properties and Maxwell–Wagner type relaxation of $CoFe_2O_4/Sr_2Co_2Fe_{12}O_{22}$ ferrite composites. Materials Research Express, 4(7), 076105. https://doi.org/10.1088/2053-1591/aa7699

[142]. Malana, M. A., Qureshi, R. B., Ashiq, M. N., & Ehsan, M. F. (2015). Synthesis, structural, magnetic and dielectric characterizations of molybdenum

doped calcium strontium M-type hexaferrites. *Ceramics International*, *42*(2), 2686–2692. https://doi.org/10.1016/j.ceramint.2015.10.144

[143]. Mosleh, Z., Kameli, P., Poorbaferani, A., Ranjbar, M., & Salamati, H. (2015). Structural, magnetic and microwave absorption properties of Ce-doped barium hexaferrite. *Journal of Magnetism and Magnetic Materials*, *397*, 101–107. https://doi.org/10.1016/j.jmmm.2015.08.078

[144]. He, Z., Qi, S., Zhong, X., Ma, H., Wang, P., & Qiu, H. (2014). Preparation and microwave-absorbing properties of silver-coated strontium ferrite with polyaniline via in situ polymerization. *Journal of Alloys and Compounds*, *621*, 194–200. https://doi.org/10.1016/j.jallcom.2014.09.187

[145]. Durmus, Z., Kavas, H., Durmus, A., & Aktaş, B. (2015). Synthesis and micro-structural characterization of graphene/strontium hexaferrite ($SrFe_{12}O_{19}$) nanocomposites. *Materials Chemistry and Physics*, *163*, 439–445. https://doi.org/10.1016/j.matchemphys.2015.07.063

[146]. Fatima, N., Khan, H. M., Laref, A., Alhashim, H. H., Zahid, M., Nadeem, M., Akhtar, T., & Anjum, R. (2021). Synthesis And Characterization Of Cobalt Substituted W Type Hexagonal Ferrites. Digest Journal of Nanomaterials and Biostructures, 16(1), 93–100. https://doi.org/10.15251/djnb.2021.161.93

[147]. Cheng, J. (2012). Synthesis Of $La_xSr_{1-x}TiO_3$ Anode Materials By Sol-Gel Auto-Combustion Method. Journal of the Chilean Chemical Society, 57(1), 969–971. https://doi.org/10.4067/s0717-97072012000100003

[148]. Dunn, B., & Zink, J. I. (2007). Sol–Gel Chemistry and Materials. Accounts of Chemical Research, 40(9), 729. https://doi.org/10.1021/ar700178b

[149]. Whittig L. D. and Allardice W. R., “2 X-Ray Diffraction Techniques,” 1986.

[150]. Bunaciu, A. A., Udriştioiu, E. G., & Aboul-Enein, H. Y. (2015). X-Ray Diffraction: Instrumentation and Applications. Critical Reviews in Analytical Chemistry, 45(4), 289–299. https://doi.org/10.1080/10408347.2014.949616

[151]. Borisov, S. V., & Podberezskaya, N. V. (2012). X-ray diffraction analysis: A brief history and achievements of the first century. Journal of Structural Chemistry, 53(S1), 1–3. https://doi.org/10.1134/s0022476612070013

[152]. T, T. T. C., Sharma, J., Mohammed, J., Kumar, S., & Srivastava, A. K. (2017). Effect of temperature on the magnetic properties of nano-sized M-type barium hexagonal ferrites. AIP Conference Proceedings. https://doi.org/10.1063/1.4990307

[153]. Augustin, M., & Balu, T. (2017). Estimation of Lattice Stress and Strain in Zinc and Manganese Ferrite Nanoparticles by Williamson–Hall and Size-Strain Plot Methods. International Journal of Nanoscience, 16(03), 1650035. https://doi.org/10.1142/s0219581x16500356

[154]. Kaur, T., Kaur, B., Bhat, B. H., Kumar, S., & Srivastava, A. (2014). Effect of calcination temperature on microstructure, dielectric, magnetic and optical properties of $Ba_{0.7}La_{0.3}Fe_{11.7}Co_{0.3}O_{19}$ hexaferrites. Physica B Condensed Matter, 456, 206–212. https://doi.org/10.1016/j.physb.2014.09.003

[155]. Yakowitz, H., & Heinrich, K. F. J. (1968). Quantitative electron probe microanalysis: Absorption correction uncertainty. Microchimica Acta, 56(1), 182–200. https://doi.org/10.1007/bf01216121

[156]. Buršík, J., Kužel, R., Knížek, K., & Drbohlav, I. (2013). Oriented Y-type hexagonal ferrite thin films prepared by chemical solution deposition. Journal of Solid State Chemistry, 203, 100–105. https://doi.org/10.1016/j.jssc.2013.04.026

[157]. Burgei, W., Pechan, M. J., & Jaeger, H. (2003). A simple vibrating sample magnetometer for use in a materials physics course. American Journal of Physics, 71(8), 825–828. https://doi.org/10.1119/1.1572149

[158]. Grossinger, R. (1982). Correlation between the inhomogeneity and the magnetic anisotropy in polycrystalline ferromagnetic materials. Journal of Magnetism and Magnetic Materials, 28(1–2), 137–142. https://doi.org/10.1016/0304-8853(82)90037-3.

[159]. Mahmood, S. H., Ghanem, A. A., Bsoul, I., Awadallah, A., & Maswadeh, Y. (2017). Structural and magnetic properties of $BaFe_{12-2x}Cu_xMn_xO_{19}$hexaferrites. Materials Research Express, 4(3), 036105. https://doi.org/10.1088/2053-1591/aa646c

[160]. Ghahfarokhi, S. M., Ranjbar, F., & Shoushtari, M. Z. (2013). A study of the properties of $SrFe_{12-x}Co_xO_{19}$ nanoparticles. Journal of Magnetism and Magnetic Materials, 349, 80–87. https://doi.org/10.1016/j.jmmm.2013.08.036.

[161]. Descamps S. X., Parra J. M., Ramon S., and Calvet G., "Early Proceedings of the AGACSE 2015 Conference."

[162]. Long, J., Nand, A., & Ray, S. (2021). Application of Spectroscopy in Additive Manufacturing. Materials, 14(1), 203. https://doi.org/10.3390/ma14010203

[163]. Nasri, M., Henchiri, C., Dhahri, R., Khelifi, J., Rahmouni, H., Dhahri, E., Omari, L., Tozri, A., & Berber, M. R. (2021). Structural, dielectric, electrical and modulus spectroscopic characteristics of $CoFeCuO_4$ spinel ferrite nanoparticles. Materials Science and Engineering B, 272, 115331. https://doi.org/10.1016/j.mseb.2021.115331.

[164]. Pradhan, A. K., Nath, T. K., & Saha, S. (2017). Impedance spectroscopy and electric modulus behavior of Molybdenum doped Cobalt–Zinc ferrite. Materials Research Express, 4(7), 076107. https://doi.org/10.1088/2053-1591/aa7c8c

[165]. Sayed, M., & Martens, J. (2013). Vector network analyzers. In Cambridge University Press eBooks (pp. 98–129). https://doi.org/10.1017/cbo9781139567626.006

[166]. Thakur, M., Singh, C., Martinson, K. D., Buryanenko, I. V., Semenov, V. G., Mishra, S. R., Azim, M. F., Srivastava, A. K., & Popkov, V. I. (2023). Significantly improved magnetic parameters of Co–La co-doped strontium hexagonal ferrites for recording applications: structural, hysteresis, and mossbauer performance metrics. Journal of Materials Science Materials in Electronics, 34(29). https://doi.org/10.1007/s10854-023-11328-3.

[167]. Sozeri, H., Genç, F., Unal, B., Baykal, A., & Aktaş, B. (2015). Magnetic, electrical and microwave properties of Mn–Co substituted $Ni_xZn_{0.8-x}Fe_2O_4$ nanoparticles. Journal of Alloys and Compounds, 660, 324–335. https://doi.org/10.1016/j.jallcom.2015.11.123.

[168]. Zhang, Y., Xu, F., Tan, G., Zhang, J., Wang, T., & Li, F. (2014). Improvement of microwave-absorbing properties of Co_2Z barium ferrite composite by

coating Ag nanoparticles. Journal of Alloys and Compounds, 615, 749–753. https://doi.org/10.1016/j.jallcom.2014.06.165.

[169]. Shen, G., Xu, Z., & Li, Y. (2005). Absorbing properties and structural design of microwave absorbers based on W-type La-doped ferrite and carbon fiber composites. Journal of Magnetism and Magnetic Materials, 301(2), 325–330. https://doi.org/10.1016/j.jmmm.2005.07.007.

[170]. Kuruva, P., Reddy Matli, P., Mohammad, B., Reddigari, S., & Katlakunta, S. (2015, May). Effect of Ni–Zr codoping on dielectric and magnetic properties of $SrFe_{12}O_{19}$ via sol–gel route. Journal of Magnetism and Magnetic Materials, 382, 172–178. https://doi.org/10.1016/j.jmmm.2015.01.050

[171]. Kingery W. D., Bowen H. K. and Uhlmann D. R., "Introduction to Ceramics," 2nd Edition, John Wiley and Sons, New York, 1976, 457p.

[172]. Jain, A., Singh, C., Godara, S. K., Jotania, R. B., Kaur, V., & Sood, A. K. (2024d). Investigating grain and grain boundary effects on charge transport and dielectrics in $BaCo_xAl_xFe_{12-2x}O_{19}$ nanoferrites. Physica B Condensed Matter, 690, 416211. https://doi.org/10.1016/j.physb.2024.416211

[173]. Louati, B., Gargouri, M., Guidara, K., & Mhiri, T. (2005, May). AC electrical properties of the mixed crystal $(NH_4)_3H(SO_4)_{1.42}(SeO_4)_{0.58}$. Journal of Physics and Chemistry of Solids, 66(5), 762–765. https://doi.org/10.1016/j.jpcs.2004.09.011

[174]. Jonscher, A. K. (1999, January 1). Dielectric relaxation in solids. Journal of Physics D: Applied Physics, 32(14), R57–R70. https://doi.org/10.1088/0022-3727/32/14/201

[175]. Funke, K. (1993, January). Jump relaxation in solid electrolytes. Progress in Solid State Chemistry, 22(2), 111–195. https://doi.org/10.1016/0079-6786(93)90002-9

[176]. Lodhi, M. Y., Khan, M. A., Akhtar, M. N., Warsi, M. F., Mahmood, A., & Ramay, S. M. (2018, February). Role of Nd-Ni on structural, spectral and dielectric properties of strontium-barium based nano-sized X-type ferrites. Ceramics International, 44(3), 2968–2975. https://doi.org/10.1016/j.ceramint.2017.11.049

[177]. Macdonald, J. R. & Department of Physics and Astronomy, University of North Carolina. (1992). Impedance Spectroscopy. In Annals of Biomedical Engineering (Vol. 20, pp. 289–305). https://jrossmacdonald.com/jrm/wp-content/uploads/187ImpSpectroscopy.pdf Kaiser, M. (2012, February). Electrical conductivity and complex electric modulus of titanium doped nickel–zinc ferrites. Physica B: Condensed Matter, 407(4), 606–613. https://doi.org/10.1016/j.physb.2011.11.043

[178]. Padmasree K., Kanchan D., & Kulkarni A. (2006, February). Impedance and Modulus studies of the solid electrolyte system $20CdI_2$–$80[xAg_2O$–$y(0.7V_2O_5$–$0.3B_2O_3)]$, where $1\leq x/y\leq 3$. Solid State Ionics, 177(5–6), 475–482. https://doi.org/10.1016/j.ssi.2005.12.019

[179]. Jain, A., Singh, C., Godara, S. K., Jotania, R. B., Parmar, D., Kaur, V., & Sood, A. K. (2024c). Structural elucidation, morphological properties, dielectric properties and their physical interpretation of Cerium-substituted Cobalt and Barium-based M-type hexagonal nano ferrites. Physica Scripta, 99(8), 085952. https://doi.org/10.1088/1402-4896/ad5ed4.

[180]. Bagum, A., Hossen, M. B., & Chowdhury, F. (2016). Complex impedance and electric modulus studies of Al substituted $Co_{0.4}Cu_{0.2}Zn_{0.4}Al_xFe_{2-x}O_4$ ferrites prepared by auto combustion technique. Ferroelectrics, 494(1), 19–32. https://doi.org/10.1080/00150193.2016.1137467

[181]. Costa, M., Pires Júnior, G., & Sombra, A. (2010, September). Dielectric and impedance properties' studies of the of lead doped (PbO)-Co2Y type hexaferrite ($Ba_2Co_2Fe_{12}O_{22}$ (Co_2Y)). Materials Chemistry and Physics, 123(1), 35–39. https://doi.org/10.1016/j.matchemphys.2010.03.026

[182]. Pervaiz, E., & Gul, I. H. (2013, June 10). Influence of Rare Earth (Gd^{3+}) on Structural, Gigahertz Dielectric and Magnetic Studies of Cobalt ferrite. Journal of Physics: Conference Series, 439, 012015. https://doi.org/10.1088/1742-6596/439/1/012015

[183]. Bai, Y., Zhou, J., Gui, Z., & Li, L. (2004, July). Electrical properties of non-stoichiometric Y-type hexagonal ferrite. Journal of Magnetism and Magnetic Materials, 278(1–2), 208–213. https://doi.org/10.1016/j.jmmm.2003.12.1389

[184]. Jonscher, A. K. (1999, January 1). Dielectric relaxation in solids. Journal of Physics D: Applied Physics, 32(14), R57–R70. https://doi.org/10.1088/0022-3727/32/14/201

[185]. Zhou, Y., Liu, W., Zhao, X., & Zhang, Z. (2004, July). Phase transformation, structure and magnetic properties of (Nd,Pr)–Fe–V–B alloys and their nitrides prepared by mechanical alloying. Journal of Magnetism and Magnetic Materials, 278(1–2), 1–8. https://doi.org/10.1016/j.jmmm.2003.11.020

[186]. Chourashiya, M., Patil, J., Pawar, S., & Jadhav, L. (2008, May). Studies on structural, morphological and electrical properties of $Ce_{1-x}Gd_xO_{2-(x/2)}$. Materials Chemistry and Physics, 109(1), 39–44. https://doi.org/10.1016/j.matchemphys.2007.10.028

[187]. Raymond, O., Font, R., Portelles, J., Suárez-Almodovar, N., & Siqueiros, J. M. (2006, June 15). Frequency-temperature response of ferroelectromagnetic $Pb(Fe_{1/2}Nb_{1/2})O_3$ ceramics obtained by different precursors. III. Dielectric relaxation near the transition temperature. Journal of Applied Physics, 99(12), 124101. https://doi.org/10.1063/1.2201853

[188]. Nikolic, M., Sekulic, D., Nikolic, N., Slankamenac, M., Aleksic, O., Danninger, H., Halwax, E., Pavlovic, V., & Nikolic, P. (2013). Structural and electrical properties of Ti doped α-Fe_2O_3. Science of Sintering, 45(3), 281–292. https://doi.org/10.2298/sos1303281n

[189]. Ahmad, S. I., Rauf, A., Mohammed, T., Bahafi, A., Kumar, D. R., & Suresh, M. B. (2019). Dielectric, impedance, AC conductivity and low-temperature magnetic studies of Ce and Sm co-substituted nanocrystalline cobalt ferrite. Journal of Magnetism and Magnetic Materials, 492, 165666. https://doi.org/10.1016/j.jmmm.2019.165666M.

[190]. Iqbal, M. J., Nadeem, M., & Hassan, M. M. (2013). Low temperature ac electrical study of $Pr_{0.5-x}La_xCa_{0.5}MnO_3$ (x = 0.0–0.4) ceramics by employing impedance spectroscopy. Journal of Applied Physics, 114(11). https://doi.org/10.1063/1.4821957

[191]. Nongjai, R., Khan, S., Asokan, K., Ahmed, H., & Khan, I. (2012). Magnetic and electrical properties of In doped cobalt ferrite nanoparticles. Journal of Applied Physics, 112(8). https://doi.org/10.1063/1.4759436

[192]. Liu, C., Liu, X., Feng, S., Rehman, K. M. U., Li, M., Zhang, C., Li, H., & Meng, X. (2017). Microstructure and magnetic properties of M-type strontium hexagonal ferrites with Y-Co substitution. Journal of Magnetism and Magnetic Materials, 436, 126–129. https://doi.org/10.1016/j.jmmm.2017.04.040

[193]. Mund, H., & Ahuja, B. (2016). Structural and magnetic properties of Mg doped cobalt ferrite nano particles prepared by sol-gel method. Materials Research Bulletin, 85, 228–233. https://doi.org/10.1016/j.materresbull.2016.09.027.

[194]. Chauhan, C. C., Gupta, T., Gor, A. A., Jotania, K. R., & Jotania, R. B. (2021). Effect of calcination temperature on structural and magnetic properties of lightly lanthanum substituted M-type strontium cobalt hexaferrites. Materials Today Proceedings, 47, 715–718. https://doi.org/10.1016/j.matpr.2020.12.1184.

[195]. Nongjai, R., Khan, S., Asokan, K., Ahmed, H., & Khan, I. (2012b). Magnetic and electrical properties of In doped cobalt ferrite nanoparticles. Journal of Applied Physics, 112(8). https://doi.org/10.1063/1.4759436

[196]. Rane, M. V., Bahadur, D., Nigam, A., & Srivastava, C. (1999). Mössbauer and FT-IR studies on non-stoichiometric barium hexaferrites. Journal of Magnetism and Magnetic Materials, 192(2), 288–296. https://doi.org/10.1016/s0304-8853(98)00533-2

[197]. Singh, C., Narang, S. B., Hudiara, I., Bai, Y., & Marina, K. (2009). Hysteresis analysis of Co–Ti substituted M-type Ba–Sr hexagonal ferrite. Materials Letters, 63(22), 1921–1924. https://doi.org/10.1016/j.matlet.2009.06.002.

[198]. Lee, J., Lee, E. J., Hwang, T., Kim, J., & Choa, Y. (2020). Anisotropic characteristics and improved magnetic performance of Ca–La–Co-substituted strontium hexaferrite nanomagnets. Scientific Reports, 10(1). https://doi.org/10.1038/s41598-020-72608-0

[199]. Kumar, S., Manglam, M. K., Supriya, S., Satyapal, H. K., Singh, R. K., & Kar, M. (2018). Lattice strain mediated dielectric and magnetic properties in La doped barium hexaferrite. Journal of Magnetism and Magnetic Materials, 473, 312–319. https://doi.org/10.1016/j.jmmm.2018.10.085

[200]. Ghzaiel, T. B., Dhaoui, W., Pasko, A., & Mazaleyrat, F. (2016). Effect of non-magnetic and magnetic trivalent ion substitutions on BaM-ferrite properties synthesized by hydrothermal method. Journal of Alloys and Compounds, 671, 245–253. https://doi.org/10.1016/j.jallcom.2016.02.071

[201]. Ghasemi, A., & Morisako, A. (2007). Static and high frequency magnetic properties of Mn–Co–Zr substituted Ba-ferrite. Journal of Alloys and Compounds, 456(1–2), 485–491. https://doi.org/10.1016/j.jallcom.2007.02.101

[202]. Guler, P., Ertug, B., Isikci, N. I., & Kara, A. (2020). Effect of Rare-Earth Co-Doping on the Microstructural and Magnetic Properties of $BaFe_{12}O_{19}$. Advances in Materials Science, 20(3), 23–35. https://doi.org/10.2478/adms-2020-0014

[203]. Ashiq, M. N., Iqbal, M. J., & Gul, I. H. (2009). Structural, magnetic and dielectric properties of Zr–Cd substituted strontium hexaferrite ($SrFe_{12}O_{19}$) nanoparticles. Journal of Alloys and Compounds, 487(1–2), 341–345. https://doi.org/10.1016/j.jallcom.2009.07.140

[204]. Jasrotia, R., Singh, V. P., Kumar, R., Singha, K., Chandel, M., & Singh, M. (2019). Analysis of Cd^{2+} and In^{3+} ions doping on microstructure, optical, magnetic and mo¨ssbauer spectral properties of sol-gel synthesized BaM hexagonal ferrite based nanomaterials. Results in Physics, 12, 1933–1941. https://doi.org/10.1016/j.rinp.2019.01.088

[205]. Jadhav, G. L., Khirade, P. P., Chavan, A. R., Kale, C. M., & Jadhav, K. M. (2021). Structural, Optical and Magnetic Properties of Diamagnetic Cd^{2+} Incorporated Cobalt Ferrite Thin Films Deposited by Spray Pyrolysis. Journal of Electronic Materials, 50(11), 6525–6534. https://doi.org/10.1007/s11664-021-09199-7

[206]. Murthy, V. R. K., & Sobhanadri, J. (1976, August 16). Dielectric properties of some nickel-zinc ferrites at radio frequency. Physica Status Solidi (A), 36(2), K133–K135. https://doi.org/10.1002/pssa.2210360247

[207]. Irfan, M. (2016, March 30). Hysteresis and electric modulus analysis of y^{3+} doped mnni-y-type hexagonal ferrite. Ceramics - Silikaty, 34–40. https://doi.org/10.13168/cs.2016.0005

[208]. Singh, C., Jain, A., Godara, S., Jotania, R., Kaur, V., & Sood, A. (2023c). Physical Interpretation of the morphology in the relaxation mechanism of Ba Hexagonal Nano-Ferrites (BaCoxCdxFe12-2xO19): Impedance Modelling, AC conductivity, dielectric modulus, and electrical modulus parameters. *Research Square (Research Square)*. https://doi.org/10.21203/rs.3.rs-3159066/v1